Distribution Category:
Magnetic Fusion Energy
(UC-20)

ANL/FPP/TM-154

ARGONNE NATIONAL LABORATORY
9700 South Cass Avenue
Argonne, Illinois 60439

A DEMONSTRATION TOKAMAK POWER PLANT STUDY

Interim Report

March 1982

STARFIRE/DEMO TEAM

Team Leaders

M. Abdou	ANL
C. Baker	ANL
J. Brooks	ANL
D. DeFreece	MDAC
D. Ehst	ANL
R. Mattas	ANL
G. Morgan	MDAC
D. Smith	ANL
C. Trachsel	MDAC

Major Contributors

V. Bailey	PI	P. Finn	ANL
S. Ball	PI	Y. Gohar	ANL
K. Barry	RMP	J. Jung	ANL
D. Bhadra	GA	R. Lari	ANL
M. Billone	ANL*	S. Majumdar	ANL
K. Black	MDAC	B. Merrill	EG&G
C. Boley	ANL	D. Mikkelsen	PPPL
Y. Cha	ANL	B. Misra	ANL
C. Chu	GA	V. Peuron	GA
R. Clemmer	ANL	J. Rest	ANL
C. Dillow	MDAC	V. Stubblefield	MDAC
K. Evans	ANL	L. Turner	ANL

---

*Consultant from Northwestern University

ANL - Argonne National Laboratory
EG&G - EG&G Idaho, Inc.
GA - General Atomic Company
MDAC - McDonnell Douglas Astronautics Co./East
PI - Physics International Company
PPPL - Princeton Plasma Physics Laboratory
RMP - The Ralph M. Parsons Company

FOREWORD

This document is an interim report on the STARFIRE/DEMO Study, which was begun in FY 1981 with the basic goal of providing a technical perspective and conceptual design of a tokamak reactor to follow a tokamak Fusion Engineering Device (FED). The study will be completed in September, 1981, and a final report will be issued soon thereafter.

The first phase of the study was concluded with a two-day workshop held at ANL on January 20-21, 1982. The purpose of the workshop was to review the work of the first year of the DEMO Study and provide recommendations for the work to be carried out during the remainder of FY 1982. The basic format of the workshop was as follows: The participants were divided into five working groups, which examined in detail specific key issues of the DEMO Study. Each group listened to a presentation by a member of the DEMO team and then discussed and formulated recommendations which were summarized by the group chairman, who was not a member of the DEMO team. The workshop agenda, working group chairmen, list of participants, and recommendations are presented in the Appendices.

This document was provided in draft form to the workshop participants prior to the workshop. Some minor changes have been made to the draft report since the workshop, but no major changes were made as a result of the workshop recommendations. Rather, these recommendations will be used in directing the work for the remainder of FY 1982. It should be noted, therefore, that the DEMO parameters listed herein should not be identified as the reference DEMO design. The reference design will be developed for inclusion in the final report at the conclusion of the study.

ACKNOWLEDGMENTS

We would like to express our appreciation to C. Karney (PPPL) for the use of a ray tracing code. We would also like to thank D. Riser (MDAC) for the preparation of certain illustrations. In addition, a special thank you is extended to C. Hytry, L. Legerski, M. Pagnusat (ANL) and R. Seger (MDAC) for the typing and assembly of this report.

Table of Contents

Table of Contents (continued)

CHAPTER 1

INTRODUCTION

Chapter 1

Table of Contents

Chapter 1

List of Figures

List of Tables

1.0 Introduction

This document represents an interim report on the STARFIRE/DEMO Study, which was undertaken at the completion of the STARFIRE Commercial Tokamak Fusion Power Plant Study in October, 1980 [1]. Major contributors to the DEMO Study include Argonne National Laboratory and McDonnell Douglas Astronautics Company, with support from General Atomic Company, The Ralph M. Parsons Company, and Physics International Company. It should be noted that a substantial portion of this effort was redirected during the past year to permit the team to support the International Tokamak Reactor (INTOR) Study. This section outlines the STARFIRE/DEMO Study objectives and approach, role of the DEMO in the national magnetic fusion energy program, rationale for selection of key design features and parameters, and an overview of the key issues considered thus far in the study.

1.1 Study Objectives and Approach

The past several years has seen substantial progress in the U.S. and world fusion energy programs. In particular, successes in the tokamak research program have resulted in a high degree of confidence that the Tokamak Fusion Test Reactor (TFTR) will produce a $Q = 1$ experiment and, thus, culminate the demonstration of the scientific feasibility of fusion. This has stimulated a substantial effort on defining the next step in the tokamak development program as well as defining a program to demonstrate the engineering feasibility of fusion energy. This activity has centered around the concept of a Fusion Engineering Device (FED) [2] and has been supported by the INTOR project. [3] At the same time, the STARFIRE Study and other tokamak reactor designs have examined the potential commercial applications of the tokamak approach. We have, then, a situation where one has a firm picture of the current research program (ongoing experiments and TFTR), a pre-conceptual design of FED and INTOR, and a perspective on the long-range goal of a commercial reactor (e.g., STARFIRE).

A major issue for the U.S. magnetic fusion energy program is the determination of the step or steps between FED and a commercial tokamak reactor. While we are concerned here with the development path for tokamaks, it is recognized that there are other viable commercial reactor concepts. By attempting to better understand the development steps for tokamaks, it is further anticipated that much useful information will be generated of

relevance to the other magnetic fusion concepts. Also, a better definition of the post-FED step will provide very useful feedback to the FED project in terms of its mission and desirable design features. In fact, features viewed as desirable for commercial reactors (e.g., RF heating with current drive and pumped limiters) are being considered for the FED.

The basic goal of this study is to provide a technical perspective and conceptual design of the tokamak device that might follow the FED. The role of such a device in the overall program is discussed further in the next section. The effort has focused on designing the key features of such a device with the objective of providing design information for guiding the research and development efforts. During the FY 1981 period, emphasis was placed on the following five key areas: (1) DEMO objectives and parameters, (2) steady-state operation with various current drive options, (3) impurity control options, (4) first wall/blanket design options, and (5) overall device configuration. The approach has been to examine several options in sufficient detail to provide an adequate basis for a more in-depth study of a selected set of options during the remainder of FY 1982. While a reference conceptual design for the DEMO will be developed, less emphasis will be placed on a single design point (as was done in the STARFIRE study) and more emphasis will be placed on exploring major design features. Certain areas (e.g., plant design) will receive relatively little effort. However, a sufficiently detailed design will be developed to provide a reasonable preliminary cost estimate for the DEMO.

1.2 Role of the DEMO

The objectives and requirements of the DEMO can only be viewed as a part of a comprehensive fusion research and development plan. Because the required research and development programs are substantial and because the time scale involved is long, the fusion development plan has to remain flexible. Consequently, the missions (and even the number) of the various devices to be constructed between now and fusion commercialization cannot be firmly determined at this time. The focusing and sharpening of the objectives and features of the specific devices will occur as a part of an evolutionary process over a number of years. One purpose of this study is to define a set of objectives for the DEMO that can serve as input to this evolutionary process.

Given that the number of steps between TFTR and a commercial tokamak reactor cannot be completely defined, and given the ongoing FED activity, it was decided that this study should focus on the step after FED. This approach would then provide a basis for determining the next reasonable step after FED and, by examining the requirements for a commercial reactor, provide a perspective on the number of steps between FED and a commercial-grade device.

The perspective adopted for the DEMO study is that, before several commercial planta are built with solely private financing, there will likely be a device, which we termed a First Commercial Demonstration Reactor (FCDR), that will be built and operated with government funds or perhaps with some combination of government and private funds. This device would be a commercial reactor in all known aspects, except for the fact that as a still somewhat first-of-a-kind machine it would be developmental in nature and would surely result in definition of many design improvements. The primary function of FCDR would be to convince utilities that fusion is ready for commercialization and can be taken over by utilities at acceptable risk. DEMO's role in this scenario would be to demonstrate commercial reactor features and subsystems and show that the risk in developing an FCDR is acceptable to the fusion development program. DEMO's objectives are than determined on a "roll-forward" basis from FED; it does not necessarily have to achieve the degree of reliability and performance expected of a fully commercial demonstration reactor.

With the foregoing in mind, let us examine the role of the DEMO. We have adopted the point of view that the principal goal of FCDR is to demonstrate economic competitiveness. This leads to some important conclusions. The DEMO does not need to produce economically competitive electric power. It needs only to demonstrate that it extrapolates to an economically competitive system. This will be done during the design and development effort for DEMO and during early operation. A primary requirement for FCDR to be economically competitive is that it achieve a plant availability factor of ~ 65-75%. Minimizing the risk in achieving such an availability factor in FCDR requires that: (a) extrapolation of technologies from the DEMO to FCDR should be straightforward--practically all technologies to be used in FCDR must be demonstrated in the DEMO; (b) extrapolation of performance parameters between the DEMO and FCDR should be minimized; and (c) achievement by DEMO of a sufficiently high availability during initial operation so that the additional improvement in availability required for FCDR can be shown to be a reasonable

extrapolation, after modifications that were identified during the operation and construction of DEMO and the data obtained from tests in other development programs are incorporated.

The above considerations provide incentives for constructing as advanced a DEMO as necessary to minimize the risk for FCDR. On the other hand, there are incentives for constructing a "less-advanced" DEMO in order to minimize the risk associated with the construction and operation of the DEMO itself. The extrapolation from FED to the DEMO must be kept reasonable. An examination of the results of FED and commercial reactor studies carried out over the past several years indicate that the advances required in technology, component reliability, and availability between FED and FCDR are very substantial. To minimize the risk associated with FCDR, the burden of demonstrating the required advances in physics and technology beyond FED will have to be borne by the DEMO and complementary development programs. All FCDR technology and physics requirements which are not demonstrated in FED will represent risks deferred from FED that must be taken in the DEMO. Therefore, results derived from the STARFIRE/DEMO study should provide feedback into defining the requirements on FED.

In reviewing past demonstration devices, a range of two to ten is typical for the step size (scale factor) in reactors from demo (pilot) to commercial. When only power plants are considered, the step size range reduces to approximately three to five. This range of step sizes was exhibited by the LWR (60 to 180 to 500 MWe). The Phoenix (French breeder) demo has an output of 230 MWe, and the Creys Malville commercial plant will have an output of about 1200 MWe. The Clinch River Breeder Reactor is designed for 350 MWe, and design studies for the Prototype Large Breeder Reactor show outputs of approximately 1000 MWe. A further example of step size is obtained by comparing the Fort St. Vrain HTGR, with an output of 330 MWe, to the next units which were designed for 800 to 1200 MWe. Based on these prior examples, a fusion demo sized for 200 to 300 MWe would be appropriate.

For the purposes of this study, we have made some broad assumptions concerning FED and the fusion development program:

(1) FED construction and operation will demonstrate integrated technologies for confining, heating, fueling, and burn

control of the plasma. These include superconducting magnets, RF or other plasma heating technology, pellet injection or an alternative, vacuum, and tritium processing (except tritium recovery from the blanket).

(2) A credible impurity control system will be developed through testing in FED and complementary physics and engineering facilities.

(3) Although FED may not be operated in steady state, sufficient testing will be performed in FED and other complementary facilities to demonstrate the feasibility of steady-state operation before the construction of the DEMO.

(4) Tritium-breeding blanket technology will be aggressively pursued by testing in fission reactors and other complementary facilities in order to select no more than three blanket concepts. Testing in FED will provide sufficient information to confirm the selection of the blanket design for the DEMO.

(5) There will be insufficient time prior to construction of the DEMO to develop and qualify a structural material other than stainless steel. A combination of testing in FED, fission reactors, and other complementary facilities will provide the required information for stainless steel. Other materials will have to be qualified for special applications such as limiters or divertor collector plates.

(6) An availability factor of about 20% or more will be achieved in FED. Learning experience from complementary technology development efforts and early FED operation will confirm the design extrapolation to the DEMO.

(7) FED, together with parallel development, will provide a sufficient data base to permit safe operation of the DEMO.

Based on the above assumptions, we can state the following broad objectives for the DEMO:

(1) Demonstration of a level of performance for all components in an integrated power plant system which is satisfactorily

extrapolatable to a first commercial demonstration reactor.

(2) Demonstrate system availability at a level which will be satisfactorily extrapolatable to a first commercial demonstration reactor.

(3) Demonstrate that the tritium-breeding, power-producing blanket can operate at conditions required for commercial reactors; i.e., a net tritium breeding ratio greater than unity, an acceptably low tritium inventory in the blanket, a sufficiently high temperature operation to permit acceptable thermal conversion efficiency, and other requirements similar to other components (e.g., reliability, safety, lifetime, etc.).

(4) Demonstrate safe and environmentally acceptable operation.

(5) Demonstrate compatibility with utility grid operations including off-normal conditions.

1.3 Selection of Key Design Features and Parameters

Satisfying the DEMO objectives defined in the previous section requires that the DEMO design features and performance be as close as practicable to those of a commercial reactor. Two practical constraints must be clearly recognized: (1) the DEMO capital cost should be minimized; (2) the DEMO performance requirements should be consistent with a fusion research and development plan which realistically accounts for financial and time schedule considerations. The capital cost constraint primarily affects the selection of the DEMO size (physical size and thermal power). The constraint of a realistic fusion R&D plan has its major influence on the selection of the availability goal for the DEMO. The plant availability depends on the reliability and lifetime of all reactor components. Therefore, achieving high availability is judged to be the most costly and time-consuming phase of fusion development.

For given technological (e.g., maximum magnetic field) and physics (e.g., maximum beta) constraints, the minimum size that can be considered for the DEMO is defined primarily by ignition requirements. The FED (10 T case) and INTOR designs shown in Table 1-1 provide the range for such a minimum. For a

Table 1-1. Range of Parameters for DEMO

	TFTR	FED	INTOR	DEMO	STARFIRE
MWth	20 Fusion	180/450	620	800-1000	4000
MWe (Net)	--	--	> 10	200-300	1240
R (m)	2.5	5.0	5.2	5.0-5.3	7.0
r_p (m)	0.9	1.3	1.2	1.2-1.3	1.9
Plasma Elongation	1.0	1.6	1.6	1.6	1.6
B_{max} (T)	--	8/10	12	10	11
Wall Loading (MW/m^2)	0.2	0.4/1.0	1.3	1.5-2.0	3.6
Availability	--	0.1-0.2	0.35	0.50	0.75
β	0.012	0.052	0.056	0.06-0.08	0.067
Q (Plasma)	> 1	5/50	60	> 10	35
Plasma Heating	Neutral Beam	RF	Neutral Beam (RF Backup)	RF or REB	RF
Impurity Control	--	Pumped Limiter	Single-null Divertor	Limiter or Divertor	Pumped Limiter
Operating Mode	Pulsed 1.5-s burn	Pulsed 100/50-s burn	Pulsed 100-s burn	Steady-state Driver?	Steady-state RF Driver
Lifetime	4×10^3 Pulses	5×10^4 Pulses	10^6 Pulses	20 y	40 y
Tritium Breeding Ratio	--	Experiment	0.6	> 1.0	> 1.0
First Wall/Blanket Material	SS (304 LN)	SS (316)	SS (316)	SS	SS (PCA)
Coolant	H_2O	H_2O	H_2O	H_2O	H_2O

maximum magnetic field, $B_m \simeq 10$ T, and plasma elongation $\kappa = 1.6$, the major and minor radii are in the range of $R \simeq 5.0\text{-}5.2$ and $a \simeq 1.2\text{-}1.3$. For the DEMO, we selected $B_m = 10$ T in order to reduce the design risks and cost associated with higher fields. Furthermore, results from STARFIRE, INTOR, FED, and other studies [5] indicate that $\kappa = 1.6$ is a reasonable compromise between the benefits (higher beta) of increased elongation and the equilibrium field (EF) coils requirements, particularly when all these coils are placed outside the TF coils. The optimum blanket/shield thickness for a wide range of DEMO conditions was found previously to be $\Delta^i_{BS} = 1.2$ m.[6] FED and INTOR operate at an average toroidal β of $\sim 0.052\text{-}0.056$. With these values defined, the minimum size device produces a neutron wall load, $W_n \sim 1.0\text{-}1.3$ MW/m^2.

The size of FED and INTOR, slightly increased to assure a comfortable ignition margin, is adequate for the DEMO except for the somewhat low value of the neutron wall load. Based on the results of STARFIRE and other studies (see, for example, Ref. 5), commercial tokamaks will likely operate with $W_n \sim 3.0\text{-}4.0$ MW/m^2. The importance of the neutron wall load is that it directly impacts the power density and, hence, the performance characteristics and failure rate of the first wall and blanket. Therefore, it is very desirable to demonstrate high wall load operation in the DEMO. A higher wall load can be achieved only by: (a) increasing the power density in the plasma (i.e., increasing B_m or β) and/or (b) increasing the physical size of the device ($W_n \sim \beta^2 B^4 a$). Both will increase the capital cost of the DEMO. In general, better economics is obtainable for fusion reactors by increasing the plasma power density rather than increasing the reactor physical size. In particular, tokamaks are most attractive at higher beta operation. We assume in this study that substantial improvement in beta beyond that predicted for FED and INTOR will be achievable in the DEMO. Therefore, $\beta = 0.08$ has been selected as the goal for the DEMO.

With $R = 5.2$ m, $a = 1.3$ m, $\kappa = 1.6$, $\Delta^i_{BS} = 1.2$ m, $B_m = 10$ T, and $\beta = 0.08$, the neutron wall load is in the range $W_n \sim 1.5\text{-}2.0$ MW/m^2, depending on the operating conditions selected for the plasma. Table 1-2 shows the variation of the fusion power and neutron wall load with the average plasma electron temperature, $\bar{T}_e$. The fusion power and neutron wall load peak at $\bar{T}_e = 8$ KeV with values of 1320 MW and 2.6 MW/m^2, respectively. The fusion power and neutron wall load are lower at higher temperatures. However, the

Table 1-2. Plasma Power Balance for DEMO
(P_{aux} = 0 and Z_{eff} = 1.42)

$\bar{T}_e$, keV	4	6	8	10	12	14	16	18
P_f, MW	955	1270	1320	1230	1080	917	766	637
$\bar{n}_e$, 10^{20} m^{-3}	5.24	3.42	2.48	1.90	1.50	1.23	1.03	0.883
W_n, MW/m^2	1.91	2.54	2.64	2.46	2.16	1.83	1.53	1.27
$\bar{n}_D$, 10^{20} m^{-3}	2.23	1.46	1.06	0.806	0.639	0.520	0.435	0.371
α_{emp}	0.44	0.23	0.26	0.33	0.44	0.61	0.83	0.97

electron density, $\bar{n}_e$, also decreases in going to higher $\bar{T}_e$, and the power required for a non-inductive current drive also decreases (see Sec. 2). Further trade-off studies are required to select the plasma operating point. For the purpose of the present phase of the the study, we selected $\bar{T}_e \sim 14$ KeV which yields a fusion power of ~ 920 MW and a neutron wall load of ~ 1.8 MW/m^2. This wall load is about a factor of two higher than that in FED (see the 10 T case in Table 1-1) and is half of that in STARFIRE. Higher wall loads are desirable in most respects and can be achieved by further increases in the size of the device but with a substantial increase in the capital cost. Preliminary analysis indicates that, for the conditions defined above, the capital cost of the DEMO is directly proportional to the neutron wall load. The inability to test for higher power density in the DEMO blanket without substantial increase in the capital cost is one of the major difficulties in fusion development.

Table 1-3 shows the major design parameters tentatively selected for the DEMO. The major emphasis in the DEMO study so far has been on examining key design issues. Therefore, the reference set of design parameters given in this section serves only as a framework for investigating the design options and parameters for key reactor components. Development of a detailed and consistent reference design will be undertaken in FY 1982 after the subsystems investigations are completed.

A major conclusion of the economic analysis for STARFIRE is that the greatest uncertainties in the economics of future tokamak power plants concern the plant availability factor. For fusion reactors to be economically competitive, a plant availability of 65-75% must be achieved. Yet, there is practically no quantitative data base for making a reliable prediction of the achievable availability factor in power-producing tokamaks. The availability factor is crucially dependent on component lifetime and reliability (low frequency of component failure) and maintainability (short downtime to replace failed components). The data base for the lifetime and reliability of components must be obtained primarily from the technology development program. Definitive information on reactor maintainability will come primarily from experience with operation and maintenance of future fusion devices such as FED. In the DEMO study, the great importance of the availability factor has been recognized in two ways. First, a plant

Table 1-3. Major Design Parameters for DEMO

Fusion power, MW	920
Thermal power, MW	1050
Net electric power, MW	250-300
Average neutron wall load, MW/m^2	1.8
Overall plant availability, %	50
Major radius, m	5.2
Plasma half-width, m	1.3
Plasma elongation (b/a)	1.6
Plasma half-height, m	2.08
Plasma volume, m^3	272
First wall surface area, m^2	400
Plasma average toroidal beta	0.08
Plasma current, MA	9.01
Inboard wall-to-magnet thickness, Δ^i_{BS}, m	1.2
Outer blanket/shield thickness, m	2.0
Scrape-off thickness, m	0.2 (inboard), 0.165 (outboard)
Maximum toroidal magnetic field, T	10
Number of TF coils	8
Major radius of TF mid-outboard leg (R_2), m	11.6

availability goal of 50% was adopted for the DEMO. Given that FED is planned for ~ 20% availability, this DEMO goal provides an ambitious target for technology development. Since FCDR will be required to achieve 65-75% availability, the selected DEMO goal of 50% is a necessary minimum in order not to burden FCDR with "high risk" extrapolations. Second, every effort is being taken in the DEMO study to incorporate design features and select design and technology options that enhance the probability of achieving high availability. The single most important design feature selected to maximize component lifetime and reliability in the DEMO is steady-state plasma operation. By eliminating cyclic loads, steady-state operation significantly enhances the reliability of key components such as the first wall, blanket, limiters, divertors, and magnets. In addition, the frequency of plasma

disruption is greatly reduced for two reasons: (a) most plasma disruptions occur during startup and shutdown; and (b) a non-inductive current driver will permit current density profile control, thus providing effective measures for controlling plasma disruptions. Accommodating the thermal energy dump and the electromagnetic forces associated with plasma disruptions currently represents a key engineering design problem, particularly for the first wall, limiter, and divertor.

Component lifetime and reliability are also enhanced in the DEMO by locating, whenever feasible, key components away from the harsh radiation environment. All the EF coils (all superconducting) are located outside the TF coils, except for some small CF coils which are located inside the TF coils but outside the radiation shield. All vacuum pumps are located in the reactor building basement where the radiation field is low.

The STARFIRE strategy of simplifying the reactor design in order to enhance component reliability and maintainability continues to be adopted in the DEMO. This has been a key approach in developing the non-inductive current drive, blanket, and impurity control concepts as discussed in the next section. Other features adopted to enhance maintainability include modularity, locating the vacuum boundary at the shield with all mechanical seals at the exterior, and placing all service connections outside the vacuum boundary.

As discussed in Sec. 5, there is a tradeoff between maintainability and capital cost in selecting the reactor configuration. The configuration developed for the DEMO favors better maintainability. This is reflected particularly in the choice of the low number (8) of TF coils and the use of one blanket/shield sector per TF coil which result in the use of larger TF coils.

Design selections for the current drive, first wall, blanket, impurity control, and configuration have been the subject of extensive tradeoff studies. The key issues in these studies are discussed in the next section.

1.4 Key Design Issues for Major Components

The DEMO effort in FY 1981 focused primarily on in-depth investigations of the key issues for the DEMO elements that require extensive development in

parallel to and beyond FED. These elements are: (1) non-inductive current driver, (2) impurity control and exhaust, (3) first wall and breeder blanket, and (4) reactor configuration and maintainability. These elements will have the largest impact on the capital cost and availability of the DEMO. Some of these components (e.g., breeder blanket and current driver) may not be used in FED, while for others (e.g., impurity control and configuration) the FED solution must be checked for suitability to commercial systems.

Significant design and research and development efforts have been devoted over the past decade to the systems of impurity control and exhaust, breeder blanket, and, to a lesser extent, non-inductive current drive. However, it must be recognized that the state of the art for these systems is not advanced enough to select a single design option, nor is it possible at this time to assure that any of the presently proposed concepts will eventually prove viable. There is a lack of important data in many critical areas and limited experimental verification of theoretical predictions in other areas. In addition, there are some design problems for which more attractive solutions must be developed.

Given the state of the art for the components discussed above and recognizing the role of the DEMO in fusion development, it was judged undesirable for the DEMO study effort to focus on developing the details of a single design point. Rather, it is more beneficial for the national fusion program to utilize the DEMO design study as a framework for identifying key research and development paths for critical subsystems. The approach for each component is to: (1) investigate design options; (2) identify key problems and develop design solutions whenever possible; (3) select the most promising two or three design concepts; (4) characterize the critical problems and identify key experimental and analytical data required for resolving these problems; and (5) describe the overall R&D paths including the major milestones. The DEMO effort to date has focused on items (1) through (3). Items (4) and (5) will be addressed in the later part of the study.

The following subsections provide a brief overview of the DEMO study effort in the areas of current drive, impurity control, first wall and breeder blanket, and reactor configuration and maintainability. The details of the work are presented in Sec. 2 through Sec. 5. This overview is concerned only with key issues in selection of design options.

1.4.1 Steady State/Current Driver Options

Theory and experiments indicate the possibility that toroidal plasma currents may be maintained in tokamaks with non-inductive external momentum sources to the electrons. This suggests that steady state may be an achievable mode of operation for tokamaks. Steady-state operation offers many technological and engineering benefits in commercial reactors. Among these are: (1) component and system reliability is increased; (2) material fatigue is eliminated as a serious concern; (3) likelihood of plasma disruptions is reduced; (4) higher neutron wall load is acceptable; (5) thermal energy storage is not required; (6) the need for an intermediate coolant loop is reduced or eliminated; (7) electrical energy storage is significantly reduced or eliminated; and (8) a full-size ohmic heating solenoid is not needed, and external placement of the EF coils is simplified.

The penalty for steady-state operation comes primarily from potential problems associated with a non-inductive current driver; in particular: (1) the electrical power requirements; (2) the capital cost; and (3) reliability and engineering complexity of the current driver. The magnitude of these penalties varies from one current driver to another.

A large number of external drivers have been proposed which theoretically can sustain the toroidal current in a tokamak in a steady-state condition. Both plasma waves and particle beams have been suggested, and a survey of the most attractive candidates has been performed. We classify waves into three types for this discussion. High-phase-speed (HS) waves are those with toroidal phase velocities exceeding the electron thermal speed and which directly impart momentum to the circulating electrons. Examples of these waves, which have received some experimental tests for driving current, are the lower-hybrid wave (JFT-2, PLT), the magnetosonic wave (Synchromak), and the ion-cyclotron wave (Model C). Low-phase-speed (LS) waves are those with subthermal phase speeds which can supply electron momentum. The most studied example is the fast wave, which is the compressional Alfven wave (CAW) at low frequencies and which we term a low-speed (short parallel wavelength) magnetosonic wave above the ion cyclotron frequency. The third wave-current-drive classification refers to ICRH and ECRH techniques which heat plasma to create anisotropic resistivity, thereby indirectly driving currents. Beam-driven currents may be created by injection of neutral beams (Culham Levitron) or relativistic electron (REB) beams (SPAC-IV).

The driver power requirements have been compared on several levels, as the normalized current to power density ratio, $\hat{j}/\hat{p}$, as total current to power dissipated, I/P_{aux}, and as the net electric power, P_n, vs. plasma temperature. Here we summarize our findings and outline the logic which should be followed in order to identify the most attractive driver for the DEMO.

Figure 1-1 combines the $\hat{j}/\hat{p}$ plots for this study using a common independent variable, v_d/v_e, where v_d is the parallel velocity associated with the driver. This quantity, v_d/v_e, is important, as it must be carefully chosen to maximize $\hat{j}/\hat{p}$. Our discussion here focuses on only a subset of all the drivers examined in Sec. 2. The other drivers are the victims of poorly developed theory, problems with experimental verification, or simply dismal prospects for achieving a reasonable DEMO driver. Starting with the neutral beam (D°), we note from the figure that $\hat{j}/\hat{p}$ has a well defined maximum; fortunately, neutral beams have well controlled energies so v_d can likely be selected to maximize $\hat{j}/\hat{p}$. A concern with this driver is that $\hat{j}/\hat{p}$ may deteriorate by a factor of two if the neoclassical theory is inappropriate for some reason. Due to its similar physical current-drive process, ICRH results in $\hat{j}/\hat{p}$ values similar to those from neutral beams. However, if minority ^3He is used, neoclassical theory predicts $\hat{j}/\hat{p}$ would be much less for $\varepsilon = 0.1$ than for $\varepsilon = 0$ (where ε is the reciprocal of the local flux surface aspect ratio), and regions of reversed current density would also result. Furthermore, wave propagation and absorption determines the spatial variation of v_d/v_e, so it may be hard to arrange v_d/v_e in order to maximize $\hat{j}/\hat{p}$.

The relativistic electron beam (REB) is the most efficient driver if resistivity is greatly enhanced due to non-linear wave processes during pulsed injection. The dissipated power approaches the ohmic limit if v_d is properly chosen. Even if resistivity is not enhanced, the REB produces $\hat{j}/\hat{p}$ values comparable with other drivers. Good control of v_d/v_e is easily achieved, and neoclassical effects are irrelevant for this driver. In the limit $v_d \to c$, ECRH has $\hat{j}/\hat{p}$ identical to that of the REB (with $\alpha \equiv 1$), according to linear theory. In the strong heating limit ($D \equiv D^{QL}/D^c \gg 1$) the value of $\hat{j}/\hat{p}$ about doubles for ECRH. However, in the limit $v_d < v_e$ there are indications that electron trapping may seriously degrade the efficienty of ECRH current drive. Moreover, it may prove difficult to accurately launch

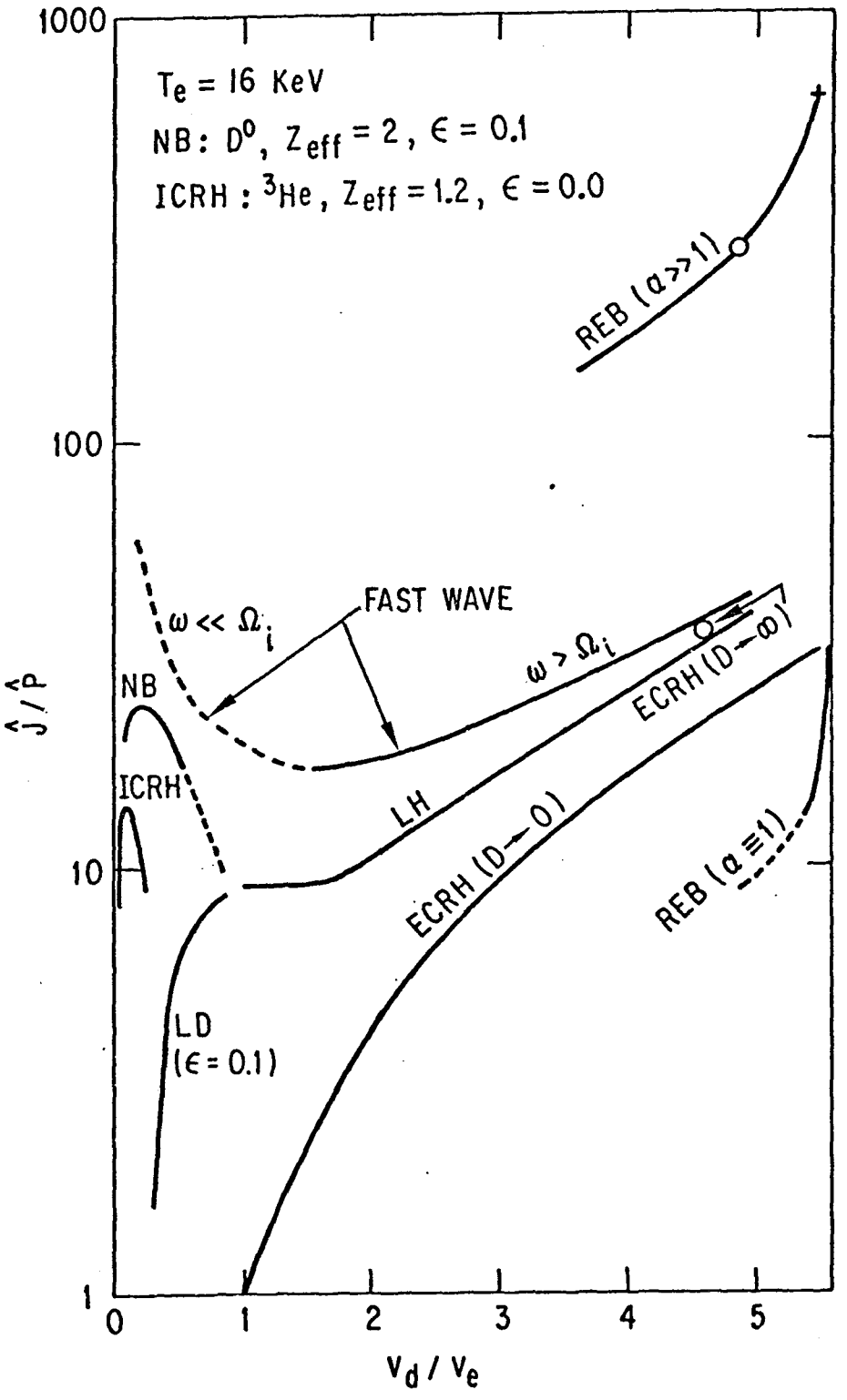

Fig. 1-1. Normalized current density to power density ratio for various drivers.

rays which have one-sided damping with $v_d \gg v_e$ in order to maximize $\hat{j}/\hat{p}$. Additionally, we point out the necessity of developing high power, high efficiency sources of ECRH if this method were to prove practical for a DEMO.

As Fig. 1-1 shows, the lower-hybrid (LH) driver has $\hat{j}/\hat{p}$ values some 33% larger than those due to ECRH at $v_d \geq 3v_e$ in the linear regime. This is due to the wave-particle momentum transfer which accompanies the ansitropic heating. Neoclassical trapping strongly reduces $\hat{j}/\hat{p}$ associated with the Landau damping of the LH driver when $v_d \leq v_e$; see the curve labeled LD. The principal defect with this driver, however, is the accessibility constraint inhibiting the generation of centrally peaked current profiles.

The low frequency ($\omega \ll \Omega_i$) limit of the fast wave is the CAW, which yields the largest $\hat{j}/\hat{p}$ values of all the waves when $\varepsilon = 0$ and $v_d \ll v_e$. It is important to operate in the linear regime ($D \ll 1$) as this makes fullest advantage of the transit time damping mechanism, which yields the greatest $\hat{j}/\hat{p}$ values. Neoclassical effects predominate when $v_d \ll v_e$ making predictions unreliable with this driver; hence, Fig. 1-1 shows this curve dotted. Above the ion cyclotron frequency we term the fast wave the high speed magnetosonic (HSMS) wave when $v_d \geq v_e$. In this regime $\hat{j}/\hat{p}$ values are seen to exceed those of the LH wave, which is due to the transit time damping mechanism. The HSMS has no accessibility constraint, and neoclassical trapping is of no concern.

The ratio of the plasma current to the driver power delivered to the plasma (I/P_{aux}) is more relevant than $\hat{j}/\hat{p}$ as it is obtained by integrating the current and power densities over the plasma cross section. This ratio depends on $\bar{T}_e$, $\bar{n}_e$, and the plasma profiles, and for comparison we give the values at $\bar{T}_e = 18$ keV and $\bar{n}_e = 0.84 \times 10^{20}\ m^{-3}$ for several DEMO drivers in Table 1-4.

A better figure of merit for the DEMO is the net power produced, P_n, which depends on the driver's power conversion efficiency, η_{aux}, and on the plasma temperature, since fusion power, P_f, and P_{aux} both vary with $\bar{T}_e$. As shown in Table 1-2, we desire 12 keV $\leq \bar{T}_e \leq$ 16 keV in order to keep the neutron wall load in the range $\sim$ 1.5 MW/m^2–2.1 MW/m^2. Figure 1-2 epitomizes our results for three likely drivers. The neutral beam (3 MeV D°) is seen to be quite sensitive to η_{aux}, an advanced electrostatic quadrupole-focused accelerator ($\eta_{NB} = 0.8$) yielding an acceptable $P_n \geq 100$ MW but an rf quadrupole-focused accelerator (with $\eta_{NB} = 0.35$) barely breaking even.

Table 1-4. I/P_{aux} for Selected Drivers of DEMO

(9MA, R_o = 5.2 m, $\bar{T}_e$ = 18 keV, $\bar{n}_e$ = .84 x 10^{20} m^{-3})

Driver	I/P_{aux} (A/W)	Comment
D° neutral beam	0.14	3 MeV; realization in DEMO requires negative ion source, electrostatic quadrupole focused accelerator, photo-detachment neutralizer
REB	4.9	γ_d = 4.0, 4 MJ per pulse, assumes $\alpha \gg 10^3$ and includes factor of two reduction for conservatism; two diodes penetrate blanket with 50 cm O.D.
^{3}He ICRH	0.08	
CAW	1.0	Ignores neoclassical trapping; requires antenna loops
HSMS	0.11	82 MHz, λ_{11} ~ 80 cm; no concern for neo-classical effects; good wave penetration; broad current density; 10 coax feeds through blanket with 23 cm O.D.; reentrant waveguides may be possible
LH	~ 0.1	(Based on STARFIRE design); centrally peaked current density difficult to achieve due to wave accessibility limitation

(Negative ions with a photodetachment neutralizer are a necessary development which we assumed.) The HSMS (fast wave) is likewise sensitive to η_{aux}, but the system may need less development to achieve η_{aux} = 0.7 than the negative ion source neutral beam. For both the D° beam and the HSMS the 12 keV-16 keV range of $\bar{T}_e$ tends to maximize P_n at the desired wall loading, suggesting that the design is an optimum. The REB needs so little driver power that P_n is insensitive to η_{aux}. This is an advantage since it is often difficult to accurately estimate η_{aux} for current drive systems. The circulating power is so small for the REB that P_n peaks near the 8 keV maximum of P_f. However, the reference DEMO has too large a thermal power (~1500 MW) at 8 keV, so an optimized design with the REB driver would call for a lower beta or magnetic

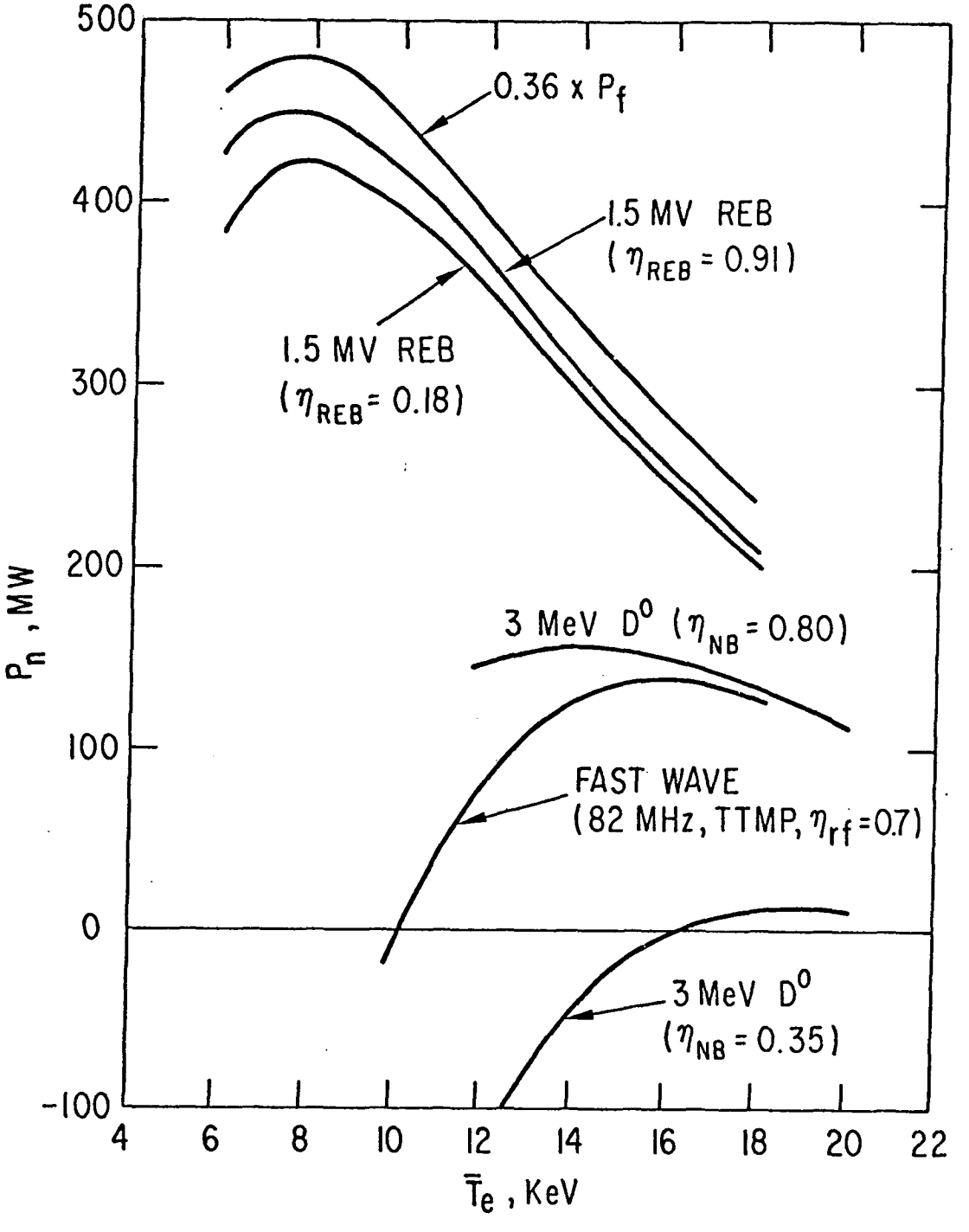

Fig. 1-2. Gross power (0.36 P_f) for DEMO reactor and net electric power for three driver candidates operating at different temperatures; R_o = 5.2 m and I = 9.01 MA. $P_n \equiv (0.36\ P_f) - 22 - P_d\ (\eta_{aux})^{-1}$, in MW.

field with operation at 8 keV.

We see that I/P_{aux} is not necessarily a good measure of driver performance. In particular, the REB has I/P_{aux} about 45 times larger than does the HSMS driver, yet P_n is only two or three times larger, as shown in Fig. 1-3, for $\eta_{aux} \sim 0.7$. Thus, the neutral beam and HSMS drivers may well satisfy the DEMO performance specifications ($P_n \geq 100$ MW).

The selection of the best driver may now narrow to consideration of engineering and equipment costs. Neutral beam lines introduce complexity into the reactor design, for tritium and neutrons are not well contained within the plasma chamber. In addition, neutral beams must be located within the reactor hall and will require fully remote maintenance. In contrast, the REB and HSMS systems have coaxial-transmission lines which can conveniently be routed outside the reactor hall and they incorporate vacuum windows. The vacuum windows in these structures assure good tritium containment, and the bends reduce radiation streaming. It is also desirable to select current drive systems which simultaneously can serve to provide auxiliary heating to ignition during reactor startup. As shown in App. 2-B, the REB system can be modified to operate at 20 Hz, yielding 80 MW of plasma heating during startup, and the system cost is estimated to be ~ $10 million (1981), exclusive of development costs. From Fig. 2-34, we see the HSMS system supplies over 80 MW of heating provided operation occurs at $\bar{T}_e < 18$ keV; if we assume normal operation occurs at $\bar{T}_e = 14$ keV, than about 150 MW of CW power is required. A cost analysis for this system has not been performed, but we note that a similar current drive system in Ref. 14 of Sec. 2 (at 154 MHz) was costed at $3.30 per watt delivered to the plasma, so a 150 MW system would cost ~ $495 million. Hence, the HSMS driver appears to be far more expensive than the REB. The couplers for the REB and the HSMS options have not been fully designed. As shown in Fig. 2-3, each has components inside the first wall, in the limiter shadow, and the engineering constraints may prove challenging.

Finally, we remark that theoretical work on pulsed power injections for wave and neutral beam drivers is presently underway. Preliminary results suggest the time averaged $I/\langle P_{aux} \rangle$ could increase modestly (by about factors of two to three), but a variety of difficulties appear which warrant further study.

1.4.2 Impurity Control System

The impurity control system must achieve adequate plasma composition control, must be reliable enough to achieve multiyear lifetimes, and should not adversely affect the other reactor systems. Besides having a major influence on the plasma, the impurity control system interacts with other reactor systems including the first wall, the vacuum system, the blanket, and possibly the magnet system. The system may also have a significant impact on tritium fueling, breeding, and reactor maintenance.

Based on the results of the FED, INTOR, and STARFIRE studies, two concepts have emerged as potentially viable for the impurity control and exhaust systems for tokamaks. These are a poloidal divertor and a pumped limiter. An improved poloidal divertor concept was developed in the INTOR Phase-1 study (for which the DEMO team has provided major technical support). The pumped limiter concept was developed in some detail in the STARFIRE study and more recently in the FED design. These two concepts for a poloidal divertor and pumped limiter served as the starting point for the DEMO effort.

The improved single-null poloidal divertor concept developed for INTOR [3] was reexamined in the context of the DEMO. The concept is applicable with minor modifications. The reference collector plate design uses tungsten tiles mechanically attached to a heat sink with low thermal conductance across the interface. Most conclusions regarding this concept remain valid. Details of the concept and identification of key issues are documented in Ref. 7. Most of the DEMO effort in FY 1981 was devoted to developing the pumped limiter concept. While efforts on the pumped limiter and divertor will continue in the remainder of FY 1982 with the objective of providing a comparison of the critical issues as well as the impact on the overall DEMO cost and availability for the two concepts, the initial DEMO reference concept is based on a pumped limiter.

The philosophy used in examining the limiter impurity control options was to vary the plasma edge conditions over a wide range and then to select the most appropriate engineering design for each set of conditions. The design geometry employed in this tradeoff study was that of the STARFIRE limiter [1]. Three plasma edge temperature conditions were selected for detailed study. They are designated as high (1500 eV), medium (100 eV), and

low (10 ev). Plasma analysis, using mostly 1-D transport calculations, show that the plasma edge temperature can be controlled, to some extent, by selecting the appropriate combination of plasma fueling method and pumping efficiency. The high edge temperature case can be produced by pellet fueling and relatively high efficiency pumping. The medium temperature case is obtained by gas puffing and moderate efficiency pumping. The physics of the very low edge temperature regime was not analyzed in detail, but it represents a very attractive case from the engineering standpoint because sputtering is insignificant. This low edge temperature may be achievable with enhancing radiation.

A separate limiter design was selected for each of the plasma edge conditions, and several major issues were identified and examined. A summary of the designs together with the major issues is presented in Table 1-5.

At high edge temperatures, the major issues involve either directly or indirectly the sputtering and redistribution of materials. First, significant sputtering and redeposition will necessitate that both the first wall and limiter surfaces are constructed from the same material. If different materials are used, the resultant redistribution of material will eventually produce a single composition on all exposed surfaces. The consequences of surface compositional changes are difficult to evaluate and could result in reduced component lifetimes. Second, sputtering considerations dictate that a low-Z material, such as Be, B, or C, be used as the surface coating material. Low-Z materials have the lowest sputtering rates under the high edge temperature conditions and, more importantly, are the only materials that exhibit a self-sputtering coefficient less than unity at the limiter surface. Beryllium has been selected as the surface material based upon its relatively good thermophysical properties, its low hydrogen permeability, and the expected lack of chemical sputtering. The relevant data base for low-Z materials is limited, however, and other low-Z materials are still under consideration. Detailed calculations indicate that the loss rate of material from the first wall will be ~ 0.5 mm/y, and the buildup of material on the limiter will be ~ 5 mm/y at 50% availability factor.

The major issues involving the buildup of material on the limiter include the structure and properties of redeposited material, and the influence of the redeposited material on the temperatures, stresses, and ultimately the

Table 1-5. Limiter Material Selections for Various Edge Temperatures

Edge Temperature	Limiter Materials	First-Wall Materials	Reasons for Selections	Critical Issues
High	Be-coating Cu-structure	Be-coating SS-structure	Low sputtering rate Self-sputtering <1 Low temperature and stresses Minimum impurity effect in plasma	Sputtering and redeposition rates Properties of redeposited material Temperature and stresses in limiter Irradiation effects in Cu Bonding between coating and structure
Medium	W-coating Cu-structure	W-coating SS-structure	Low sputtering rate Resistence to disruption effects Low temperature and stresses Thin limiter/first wall structure	W self sputtering Sputtering and redeposition rates High-Z concentration in plasma Irradiation effects in Cu Bonding between coating and structure
Low	Cu - structure	SS - structure	Simplified design and engineering Thin limiter/first wall structure	Physics uncertainties Irradiation effects in Cu

lifetime of the limiter. The interactions of the incoming particles with the limiter surface represent a complex set of phenomena. The incoming particles may be reflected from the surface, become trapped within the surface, produce lattice displacement damage, or sputter additional particles from the limiter. Recent experiments indicate that the limiter surface is likely to trap D, T, and/or He particles as the redeposited material builds up over time. The consequences of gas trapping are: (1) that the redeposited material will probably be less than 100% dense; (2) that the crystal structure is likely to be highly damaged; and (3) that the trapping of tritium could result in a high tritium inventory. At this time, it is not possible to predict the properties of redeposited material, and additional work in this area is needed. Initial temperature and stress calculations of the limiter leading edge with a 10 mm coating of beryllium indicate excessively high temperatures and stresses. There are several uncertainties in these calculations, however, including the properties of redeposited materials, the bond properties between the coating and structure, and the influence of cracks in the coating on the stresses. Additional work will be conducted to examine these uncertainties in more detail and to determine the allowable "buildup" thickness on the limiter.

None of the candidate low-Z materials can be considered to be a structural material; therefore, structural material must be identified for both the first wall and limiter. A modified austenitic stainless steel, Prime Candidate Alloy (PCA), has been selected as the first wall structural material as described in Sec. 4. PCA cannot be used for the limiter because it receives a high heat flux. The candidate limiter structural materials include copper alloys, aluminum alloys, and refractory metal alloys. The material that most closely matches the requirements for the limiter is a high strength copper alloy such as AMAX-MZC. The major issue involved in the use of copper alloys is the long-term effects of neutron irradiation. The irradiation data base is very limited, and the data indicate that irradiation effects could be severe. Additional experimental effort in this area is required to qualify copper alloys for use in fusion reactors. The selection of a copper alloy has been made with the assumptions that the coolant is low-temperature water. A copper alloy would be unacceptable with a liquid-metal coolant or with high temperature pressurized water conditions. If a liquid-metal coolant were used for DEMO, then a refractory metal alloy such as V-15Cr-5Ti or FS-85 (niobium)

would be required for compatibility.

At medium edge temperatures, the choice of the first wall and limiter coating is different. At energies of ~ 100 eV, the high-Z materials exhibit the lowest DT sputtering rates while satisfying the requirement of self-sputtering coefficients < 1 on the limiter surface. Preliminary analysis using the computer code described in Sec. 3.3 indicates that at medium edge temperatures, high-Z materials may exhibit low net erosion and low concentrations within the plasma. These conditions would occur when sputtered high-Z atoms are ionized near the surface (≤1 cm) and then returned to the limiter. Little or no sputtered material would be transported into the plasma. An edge temperature not much in excess of ~ 150 eV is required to avoid a self-sputtering coefficient >1. A major issue with the use of high-Z materials is the strict limitation on the allowable impurity concentration in the plasma. Preliminary calculations indicate that the high-Z concentration reaches an acceptable level of ~ 0.01%. However, because of the critical nature of this problem, it will be examined in more detail during the remainder of FY 1982.

Tungsten has been chosen as the high-Z material. The principal advantages of tungsten are its high melting point and its very low vaporization ratio. Calculations of plasma disruption effects on tungsten indicate that under most conditions tungsten will not reach its melting point. The predicted sputtering rate of tungsten on the first wall is ~ 0.2 mm/y, and the average buildup rate on the limiter is estimated to be ~ 1.5 mm/y at 100% duty factor. The low sputtering/redeposition rate means that the first wall and limiter structure can be designed to be thin, which will reduce the temperatures and stresses compared with the high edge temperature design. The properties and structure of redeposited material remains a major issue for tungsten.

Tungsten is not considered to be a structural material due to difficult fabrication and severe radiation embrittlement. The structural material selected for this design is AMAX-MZC, and the major concerns discussed previously for this material also apply here.

At low edge temperatures (~ 10 eV), all materials exhibit low sputtering rates so that they can be chosen independently of sputtering considerations. The limiter design for this edge temperature regime utilizes a single, thin

structural material, and it offers the longest material lifetime. AMAX-MZC is again selected as the structural material, with the major concern being long-term irradiation effects. The major concern for this regime is the uncertainty in achieving such low edge temperatures, and additional work will be conducted in this area.

Finally, the impact of the limiter position on the overall reactor design was examined. The critical issues include the effects on tritium breeding, reactor maintenance, interference with other components, and the influence of plasma disruptions. Because of the severe operating environment for the limiter, it is anticipated that it will have to be replaced more frequently than other components. Therefore, it is very desirable that the limiter be designed to be replaced without removing the rest of the first wall/blanket. The tritium breeding and reactor maintenance requirements are in conflict since reactor downtime for limiter replacement can be minimized by designing the limiter module to be non-breeding. Breeding materials with marginal breeding potential could be eliminated from consideration because of the loss of this breeding volume. The bottom limiter location, similar to the FED design, allows the most space for other reactor penetrations, but it is believed to be more susceptible to plasma disruptions than the outer midplane location. Since disruption effects are considered more serious than space conflict, the outer midplane location has been selected for DEMO.

1.4.3 First Wall/Breeder Blanket

A large number of blanket concepts that vary in material choices and design details were proposed (see, for examples, Ref. 1 and Ref. 8 through 17) over the past years. None of these concepts emerges as a clear choice. On the other hand, the fusion research and development program cannot pursue all these concepts. It is, therefore, necessary to make a critical assessment of breeder blanket options in order to select a limited number of concepts for further research and development. This is required now in order to assure timely development of breeder blankets because: (1) the need for a breeder blanket in near-term devices such as FED cannot completely be ruled out at present, and (2) perhaps more importantly, the testing of integrated blanket concepts for the DEMO will be performed in FED; and this will require extensive testing in non-fusion facilities over the next several years in

order to provide a detailed definition of breeder blanket modules to be tested in FED.

The assessment of blanket concepts in STARFIRE [1,8] and the present DEMO study, which also included an evaluation of the results of previous blanket studies, lead us to propose two development paths for the breeder blanket R&D program as shown in Table 1-6. Path 1 is for solid breeders and Path 2 is for liquid metals. The breeder materials for Path 1 are $LiAlO_2$ and Li_2O. For both solid breeders, the selected coolant and structural materials are pressurized water and austenitic stainless steel, respectively. For Path 2, the breeder materials are liquid lithium and the lead-rich Li-Pb eutectic (17 at % Li - 83 at % Pb). Liquid lithium serves as both the breeder and coolant. The choice of coolant for the Li-Pb breeder requires further evaluation. A number of issues must be resolved before a refractory alloy or stainless steel is selected for the liquid metal path.

Both the solid breeder and liquid metal paths need to be pursued for a number of years until a clear choice emerges. There are a number of critical issues for both paths that can only be resolved based on results from future experimental investigations. These critical issues are shown in Table 1-7. The issues in the table are limited to those concerning feasibility and do not include problems related to performance and economic attractiveness.

Three critical issues are identified for the two Path 1 solid breeders. The first two are common to all solid breeders. The first issue concerns the magnitude of the tritium inventory in the blanket. For idealized conditions and in the absence of radiation effects, the estimated tritium inventory is acceptably low (<100 g). However, radiation effects are expected to substantially increase the tritium inventory--possibly to unacceptable levels. The second issue relates to problems in the development of a mechanical design that is viable in the fusion reactor environment under practical normal and off-normal operating conditions. These problems arise mostly from the need to maintain the low-thermal-conductivity solid breeder in a narrow temperature range with controlled temperature gradients across the breeder/structure/coolant interfaces. Further narrowing of the theoretically predicted temperature range for solid breeders, which may be dictated as a result of future tritium recovery experiments under irradiation, could render the solid breeder designs impractical.

Table 1-6. Proposed R&D Paths for Breeder Blanket

	Breeder Material	Coolant	Structural Materials
Path 1 Solid Breeders	A) $LiAlO_2$ B) Li_2O	Water	Austenitic Stainless Steel
Path 2 Liquid Metals	A) Lithium B) 17Li-83Pb	Lithium ?	Refractory Alloy (Vanadium) or Stainless Steel (Ferritic or Austenitic)

Table 1-7. Critical Issues for the Breeder Blanket Development Paths

1. Solid Breeders

- Blanket Tritium Inventory
  Particularly, effects of radiation on tritium inventory
- Design Practicability
  A number of design problems related to maintaining the low-thermal-conductivity breeder material within the required narrow temperature range and controlling the temperature gradient at the breeder/structure/coolant interfaces
- For $LiAlO_2$: Tritium Breeding
  Achieving a net tritium breeding ratio greater than one
- For Li_2O: Reactivity with Water to Form LiOH
  - Difficulties in obtaining and maintaining high purity Li_2O
  - Consequences of corrosive effects of LiOH under off-normal events involving breeder/coolant interaction

2. Liquid Metals

A. Lithium

- Safety
  Consequences of lithium fire
- MHD Effects
- Compatibility with Structural Materials

B. 17Li-83Pb (Evaluation Not Complete)

- Compatibility with Structural Materials
- For Li-Pb Cooling
  - MHD effects
  - Tritium processing and containment
- For Water Cooling
  - Safety - large scale expulsion of Li-Pb from the blanket in off-normal Li-Pb/water contact
  - Tritium permeation to water as a result of tritium low solubility/high partial pressure
- For Sodium Cooling
  - Safety - chemical reactivity of sodium with water and air
  - MHD effects

The third critical issue for solid breeders is not the same for $LiAlO_2$ and Li_2O, and this is why selection of only one of them is not possible now. For the ternary ceramics, such as $LiAlO_2$, there are uncertainties concerning the feasibility of achieving a net tritium breeding ratio (TBR) greater than one. While theoretical calculations with the best available neutron multipliers (except beryllium) show that a TBR slightly greater than one is possible, the margin is so small that an experimental verification is necessary. Beryllium substantially enhances the breeding potential, but its acceptability depends on resolving uncertainties related to toxicity, resource limitations, and radiation damage effects. For Li_2O, the problems arising from the reactivity of Li_2O with water to form LiOH may hinder the viability of this breeder. This reactivity makes it difficult to obtain and maintain high purity Li_2O. In addition, the consequences of a water leak into the breeder region are of great concern. The formation of the corrosive LiOH could lead to rapid corrosion of adjacent structural material with a potential for a propagating-type failure.

The reasons for selecting pressurized water over helium cooling for the solid breeder path were discussed previously [1, 11]. Some of the key reasons reinforced in the present DEMO study are: (1) the required high operating temperature and large temperature rise for the helium coolant are not compatible with solid breeders, which must operate at moderate temperatures within a narrow range; (2) the large void space associated with the use of helium cooling, particularly in the inboard region of the reactor, results in a significant economic penalty compared to water cooling; and (3) no structural material which can be operated at high temperatures is resistant to radiation damage and is compatible with impurities in helium has been identified.

An advanced austenitic stainless steel (designated PCA in the alloy development program), similar to Type 316, is selected for the solid breeder development path. Structure temperatures in a water-cooled system can be maintained below the temperatures at which severe radiation damage occurs. However, steady-state operation is important for acceptable lifetime because of the relatively high thermal stress factor associated with austenitic stainless steel. The limitations on the lifetime of solid breeders resulting from Li burnup reduce the incentive for a very long lifetime structure. The

presently available extensive data and technology base for stainless steel combined with the ability to perform meaningful irradiation tests (with appropriate helium-to-DPA ratio) in fission reactors make its development for fusion the least expensive, the least time consuming, and perhaps the least risky compared to the development requirements of all other candidate structural materials.

The existence of critical issues associated with solid breeders makes it prudent to pursue in parallel research and development activities for liquid metals (Path 2). Liquid lithium offers unique advantages. It can simultaneously perform the functions of tritium production, heat deposition and, heat transport resulting in a simple system. Many of the early-generation design studies found the use of liquid lithium as both coolant and breeder to be logical since lithium in some form must be present in the blanket. As shown in Table 1-7, there are three critical issues that must be thoroughly investigated for liquid lithium. The first issue is safety. Lithium reacts vigorously with water (hydrogen is produced) and with air and concrete. Special design features (e.g., multiple barriers between liquid lithium and water and air, or completely eliminating moisture from the reactor building) to reduce the probability and consequences of lithium fires to acceptable levels need to be investigated. The second critical issue for liquid lithium (as a coolant) relates to the MHD effects. Flowing a liquid metal with high electrical conductivity in a magnetic field results in electromagnetic effects that can impact pumping power losses, system pressure, and loads on the structure. A number of design studies (e.g, Refs. 9 and 12) showed that liquid lithium blankets can be designed with low pressure drop. However, the validity of some key assumptions employed in the calculations and the practicability of the proposed design solutions need to be established experimentally. The third critical issue is the compatibility of liquid lithium with structural materials. Limited experimental data indicate that corrosion of stainless steel in a flowing liquid lithium environment may be unacceptably high. If this proves to be definitely the case, then a refractory alloy will have to be used. The development of a refractory alloy is a major issue itself because of the cost, time, and risk involved.

Because success in developing solid breeders and/or liquid lithium cannot be guaranteed, it is desirable to explore the possibility of another "backup"

path. Obviously, it has to be a lithium-containing liquid. The lead-rich 17Li-83Pb eutectic has the advantage of being much less reactive to water and air than liquid lithium. However, this 17Li-83Pb breeder poses a number of critical isues. The issue of compatibility with structural materials appears to be even more critical than that for liquid lithium discussed above. Our present analysis shows no clear choice for cooling the Li-Pb because each candidate coolant poses one or more potentially critical issues as shown in Table 1-7. For Li-Pb as the coolant, containment of relatively high pressure tritium and processing at the low tritium concentration in Li-Pb are key issues. The required mass flow rates are much higher for 17Li-83Pb than for liquid lithium. Although the electrical conductivity of Li-Pb is much lower than that of liquid lithium, the MHD effects are of concern. For pressurized-water cooling, there are two key issues. The first is the safety problems associated with the possibility of a large-scale expulsion of the Li-Pb breeder from the blanket as a result of Li-Pb/water contact. The second is the high tritium permeation rates through coolant containment structure into water. The tritium permeation rates result from the high tritium partial pressure caused by the very low solubility of tritium in 17Li-83Pb. Design solutions for limiting tritium permeation remain to be examined. The key issues with sodium cooling are the reactivity with water and air and MHD effects as discussed above for liquid lithium.

As mentioned earlier, the breeder-blanket effort in the DEMO study is focused on identifying and characterizing the breeder development paths and the critical issues that need to be resolved before a final blanket concept can be selected. Within the scope of the present effort it is not possible to analyze all four concepts shown in Table 1-6. However, the recent STARFIRE study provides an in-depth analysis of the $LiAlO_2$ design. The conclusions regarding the critical materials and design issues remain valid. This is also the case for liquid lithium, which was studied in detail in a number of previous studies. Therefore, the contribution of the DEMO effort was maximized in FY 1981 by focusing on Li_2O and 17Li-83Pb to bring the understanding of the material and design issues for these two materials to the same level as for $LiAlO_2$ and liquid lithium.

Section 4 documents the results of the evaluations for Li_2O and 17Li-83Pb. Summaries are given in Secs. 4.3.1 and 4.4.1 for Li_2O and 17Li-83Pb, respectively.

Two issues that are common to all the in-vessel components (first wall, limiter, divertor collector plate, etc.) are tritium permeation and plasma disruptions. These issues are treated in detail in Sec. 4.2. Below is a summary of the conclusions.

Tritium migration in the first wall, the primary tritium barrier for the coolant, is an issue of considerable importance, particularly for water coolant. Several models which have been developed to predict the migration rates yield values which can differ by four to five orders of magnitude. An evaluation of the boundary conditions for the pessimistic models indicated that the key issue was the assumed magnitude of the surface desorption rate constant. Based on limited experimental data for tritium implantation and migration, it appears that the desorption rate constants used in the pessimistic predictions are too small by orders of magnitude. Therefore, on the basis of the admittedly limited experimental data, the tritium migration rates for DEMO in all candidate structural materials with the water coolant are predicted to be <20 ci/d, an acceptable value. However, experimental studies are needed to confirm this prediction. More details are provided in Sec. 4.2.

There are presently considerable uncertainties concerning plasma disruptions. These uncertainties relate to frequency of occurrence, location of regions where the plasma energy dump occurs, energy density peaking factors, and decay time constants. There are also uncertainties in characterizing the response of materials to plasma disruption. Our DEMO design strategy for dealing with plasma disruptions consists of three elements: (1) reduce the likelihood of plasma disruptions; (2) design the in-vessel components to be as resistant to plasma disruptions as practicable without driving the DEMO design to features that would be unacceptable (e.g., breeding ratio less than one) in a commercial reactor system; and (3) in any case, the design must assure that no component will fail under the effect of a limited number of major disruptions. Our selection of steady-state mode of operation with a non-inductive current driver is believed to offer the possibility of eliminating, or at least reducing the likelihood of, major disruptions. Nevertheless, all DEMO components have been designed to withstand the electromagnetic loads from plasma disruptions. The response of the DEMO in-vessel components to the thermal energy dump from plasma

disruptions was analyzed. If the plasma energy were deposited uniformly over the first wall, the energy density would be ~ 75 J/cm^2, which is of no consequence to any of the in-vessel components. For a peaking factor of 5, the peak energy density on the first wall could be ~ 375 J/cm^2 if no energy was deposited on the limiter. The likely case appears to be [4] simultaneous plasma energy deposition on the first wall and limiter (or divertor collector plate), but the specifics of energy deposition profiles are highly uncertain. Tungsten, which is selected as the surface material for the divertor collector plate and for the limiter and first wall in the case of the 100 eV plasma-edge temperature, is the most resistant material to plasma disruptions. It does not experience any serious effects (melting, vaporization) for energy densities up to ~ 400 J/cm^2 and 700 J/cm^2 for thermal-decay time constants of 5 ms and 20 ms, respectively. On the other hand, beryllium, which is the recommended material for the case of the high plasma-edge temperature is much less resistant to disruption. Its response is approximately similar to that of stainless steel. For 20 ms decay time constant, the vaporization thickness is insignificant up to energy densities of ~ 400 J/cm^2, but a thin melt layer will develop at lower energy densities. The stability of this melt layer is of concern and needs to be investigated. We point out that the redeposition on the limiter of materials eroded by physical sputtering from the first wall improves the survivability of the limiter under disruption conditions.

1.4.4 Configuration and Maintenance

The most critical issues in the selection of the reactor configuration and maintenance approach for the DEMO are: (1) impact of DEMO's role in development of a commercial fusion reactor; (2) effect of the number of components on availability; (3) number of blanket sectors per TF coil; (4) number of TF coils; (5) TF coil shape; (6) location of the vacuum boundary; (7) full remote maintenance requirement; and (8) design concept for the anti-torque structure. Each issue and the rationale for selection of the DEMO design point is summarized below.

DEMO's role in the development of a commercial fusion reactor must be identified to permit definition of a DEMO design. A key assumption is that DEMO should use prototype commercial reactor systems to provide operational

experience with relevant systems, to provide design refinement and, hence, to permit the first commercial demonstration reactor to achieve the necessary 65-75% availability range.

DEMO has established a 50% availability goal and has emphasized maintainability even at the expense of modest increases in capital cost. For example, maintainability considerations lead to the choice of a minimum number of TF coils and one blanket sector per TF coil to improve reliability and minimize replacement time even though the coil stored energy and reactor building size was somewhat increased.

The availability of a reactor is believed to be closely related to the number of replaceable components that are used. Each replaceable component must be equipped with sensors, valves, piping, etc. which permit individual component operation and fault isolation. More pipes, valves, instrumentation, etc. will result in a less-reliable system, and this would reduce the overall reactor availability.

DEMO has chosen to minimize the number of TF coils (to eight) since the number of blanket sectors, limiters, coolant lines, etc. will be decreased proportionally. Additionally, only one large blanket sector per TF coil has been used to provide fewer components and simplify its replacement. A comparison of the relative replacement times and reliability for 8 and 16 blanket sectors is given in Table 1-8 to illustrate the above point. The replacement time for a complete first wall and blanket system in the case of 16 blanket sectors will take approximately two times longer than that for the 8-sector case because of the two-fold increase in operations, but the failure rates are expected to be approximately equal since key life-limiting effects (e.g., surface erosion) are independent of sector size. The number of fluid connections, isolation valves, etc. will also double and, as a result, both the replacement time and failure rate will increase by approximately two. Therefore, unless extremely high reliability connector, valves, etc. as well as long-life blanket sectors (life of plant) are developed, the reactor availability will be substantially increased by using a minimum number of sectors.

Table 1-8. A Minimum Number of Components Leads to Improved Availability

	8 Blanket Sectors	16 Blanket Sectors
First Wall/Blanket Replacement:		
Time	A	2A
Failure Rate	← ~ Equal →	
Connections:		
Number	~ 30/sector	~ 60/sector
Replacement Time	B	2B
Combined Failure Rate	C	2C

The major issue in selection of the number of blanket sectors per TF coil is a tradeoff between the capital cost associated with increased TF coil size for blanket access and the increase in availability that can result from use of fewer components and a simpler replacement method. A maximum increase of 4 m in overall reactor diameter results from installation of a single sector per TF coil which increases the reactor building cost by ~ $12 million and increases the TF coil cost by ~ 20% (~ $20 million). The increase in the stored energy of the poloidal field coils is modest for the case of the pumped limiter but remains to be evaluated for the divertor case. These costs must be offset by increases in availability. An increase of ~ 1% in the availability factor of a commercial reactor will offset this cost. It is believed this additional cost must be borne by DEMO so that enough confidence can be developed in the designs, maintenance equipment, and availability to justify extrapolation to a first commercial demonstration reactor that attracts industrial participation. Table 1-9 shows the value of R_2 (the horizontal major radius of the outer leg of the TF coil) as a function of the number of TF coils for three cases: (1) R_2 based on access requirements for one blanket sector per TF coil, (2) R_2 based on a field ripple at the plasma edge of 3% (peak to peak), and (3) R_2 based on a field ripple of 1.5%. A crossover in the requirements for the access and 3% ripple cases occurs at approximately eight coils. Access considerations for installation of one

Table 1-9. Outer Leg Radius (in m) as a Function of the Number of TF Coils

Number of TF Coils	R_2 Based on Access Requirements	R_2 Based on 3% Ripple Peak-to-Peak	R_2 Based on 1.5% Ripple Peak-to-Peak
7	11.4	11.8	13.0
8	11.6	11.1	12.1
9	11.8	10.6	11.4
10	12.0	10.2	10.9
12	12.3	9.6	10.1

sector per TF coil limits the outer leg radius to 11.6 m. Three percent ripple could be met with an 11.1 m radius. DEMO uses a 11.6 m outer radius TF coil and has a 2.1% peak-to-peak ripple at the outer plasma edge.

The TF coil shape can have a substantial impact on the total plant cost. The larger outer leg radius for blanket installation leads to a taller TF coil that increases stored TF and EF coil energy and increases the building volume unless the shape is modified from the conventional straight center post approach. DEMO has chosen to utilize a pure tension shape in areas away from the center post but has brought the center post out at the top and bottom of the reactor to provide additional support (see Fig. 1-4). The reduction in coil half-height is ~ 2 m and permits use of a shorter building and decreases the stored energy in the coil system. Additionally, the coil vacuum tank at the top of the reactor has been made to closely conform to the coil maximum height. Additionally, the inner leg of the coil has been formed as a segment of a toroidal annulus to permit location of the peak field closer to the plasma. This reduces the peak field requirements by ~ 1 T and minimizes stored energy.

Choice of the vacuum boundary location can influence the complexity of maintaining the reactor. Locations at the shield and TF coil vacuum tank have been considered. The advantages and disadvantages of each location are shown in Table 1-10. The major limitations of locating the vacuum boundary at the TF coil are increases in vacuum pumped volume, increased complexity of TF coil

Table 1-10. Vacuum Boundary Location Options

	At TF Coil	At Shield Interior
Pumped Volume	~ 1100 m^3	~ 300 m^3
Exposed Surface Area	~ 4400 m^2	~ 1500 m^2
Bakeout	<150°C Glow Discharge Only	~ 300 °C Heating by Coolant
Leakage in Door	Forced Outage	Forced Outage
Leaking in other Areas	Continued Operation	Forced Outage
Segment Joints	Intersector Contactor	Intersector Contactor
	Vacuum Gap	Dielectric Break or Resistance Control
Trim Coil Operation	Potential for Arcing	Operation in Air
TF Coil Replacement	Severely Complicates Removal	No Impact
Tritium Leakage	Unknown - May be Severe	Manageable

replacement and potential tritium permeation to the cryogens. A major advantage is the elimination of the need for a dielectric break joint.

Current trends toward reducing radiation exposure to workers may require full remote maintenance for commercial reactor operation. As a result, DEMO should demonstrate that its 50% availability can be achieved using remote maintenance. This places a major burden on both performance and reliability of the maintenance equipment. DEMO has chosen to utilize remote maintenance but, because of the developmental nature of DEMO, a hands-on capability will be provided for operations outside the bulk radiation shield.

A 4°K anti-torque structure provides the advantage of simplified blanket replacement and a simplified structure. However, it increases the difficulty of remotely replacing a TF coil and limits vertical access to the blanket because the vacuum tank blocks most access. This vacuum tank provides an enclosure for poloidal coils. DEMO is utilizing a 4°K anti-torque structure and a common vacuum tank that encloses the poloidal coils.

A cross-section of the DEMO reactor is shown in Fig. 1-4. Eight TF coils and eight blanket/shield sectors are used. All superconducting poloidal coils are located external to the TF coils. Four segmented copper control coils are located inside the TF coils and are supported at the top and bottom by the center post and follow a pure tension shape in all other areas. The eight vacuum pumps are located in the basement and can be maintained independently of the blanket. Six pumps operate while two are regenerated.

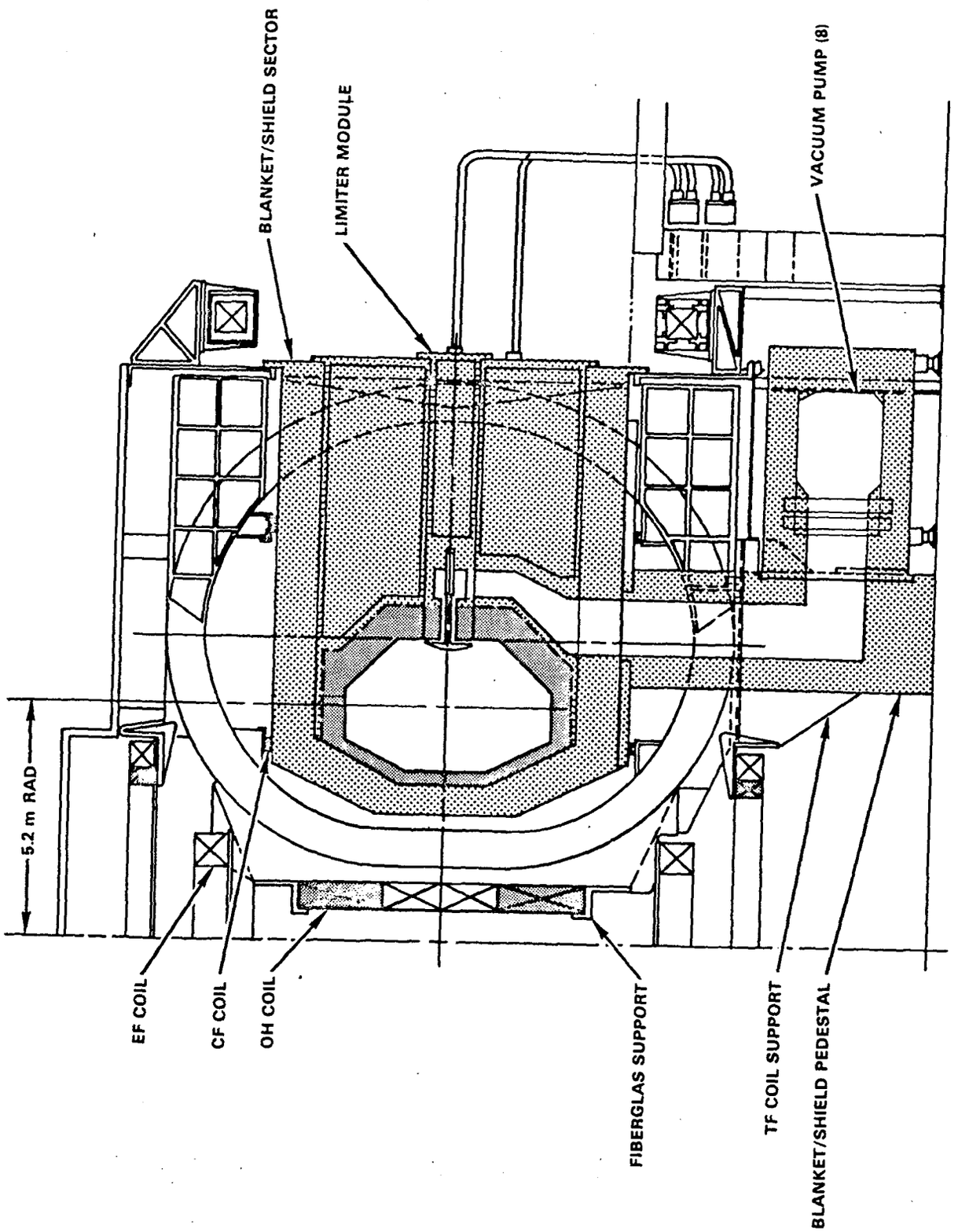

Fig. 1-3. DEMO reference design.

References for Chapter 1

1. C. C. Baker, et al., "STARFIRE - A Commercial Tokamak Fusion Power Plant Study," Argonne National Laboratory, ANL/FPP-80-1 (1980).

2. The Fusion Engineering Device, DOE/TIC-11600 (1981).

3. U.S. INTOR Conceptual Design, Phase I, USA-INTOR/81-1 (1981).

4. Reports from INTOR, Session III, Phase-2A, IAEA (December, 1981).

5. M. A. Abdou, et al., "Impact of Major Design Parameters on the Economics of Tokamak Power Plants," Proc. IAEA Workshop on Fusion Reactor Design Concepts, 1977, Madison, Wisconsin, IAEA-TC-145/44 (1978).

6. M. A. Abdou, "Radiation Considerations for Superconducting Fusion Magnets," J. Nucl. Mater., 72, 147 (1978).

7. M. A. Abdou, R. F. Mattas, et al., "Divertor Collector Plate and Channel," Chapter VIII, INTOR/NUC/81-8 (1981).

8. "STARFIRE - A Commercial Tokamak Reactor: Interim Report," Argonne National Laboratory, ANL/FPP-TM-125 (1979).

9. D. L. Smith, et al., "Fusion Reactor Blanket/Shield Design Study," Argonne National Laboratory, ANL/FPP-79-1 (1979).

10. J. S. Karbowski, et al., "Tokamak Blanket Design Study," Oak Ridge National Laboratory, ORNL/TM-7049 (1979).

11. M. A. Abdou and D. Graumann, "The Choice of Coolant in Commercial Tokamak Power Plants," Fourth Topical Meeting on the Technology of Controlled Nuclear Fusion, October, 1980, King of Prussia, Pennsylvania, CONF-801011, Vol. III (1981).

12. B. Badger, et al., "A Wisconsin Toroidal Fusion Reactor Design: UWMAK-I," University of Wisconsin, UWFDM-68 (1974).

13. B. Badger, et al., "UWMAK-II, A Conceptual Tokamak Power Reactor Design," University of Wisconsin, UWFDM-112 (1975).

14. B. Badger, et al., "UWMAK-III, A Noncircular Tokamak Power Reactor Design," University of Wisconsin, UWFDM-150 (1976).

15. B. Badger, et al., "NUWMAK, A Tokamak Reactor Design Study," University of Wisconsin, UWFDM-330 (1979).

16. D. R. Cohn, et al., "High Field Compact Tokamak Reactor (HFCTR)," Massachusetts Institute of Technology Plasma Fusion Center, RR-78-2 (1978).

17. B. Badger, et al., "WITAMIR-I, A Wisconsin Tandem Mirror Reactor Design," University of Wisconsin, UWFDM-400 (1980).

CHAPTER 2

STEADY-STATE CURRENT DRIVE

Chapter 2

Table of Contents

Chapter 2

List of Figures

List of Figures (continued)

List of Figures (continued)

Chapter 2

List of Tables

2.1 General Design Considerations

2.1.1 Introduction

High availability is crucial to the commercial success of any machine, and a major emphasis has been placed on this aspect of the DEMO design. It is expected that steady-state plasma operation will increase the availability of the reactor system compared to pulsed, ohmically driven discharges for the long plant lifetimes required. The present work documents a survey of a number of means proposed in the past few years to maintain steady-state tokamak operation. All the techniques considered here require some combination of external energy, momentum, or particle injection into the tokamak to maintain a toroidal plasma current in equilibrium against ohmic dissipation. The adaptation of different current drive techniques to the single DEMO reactor, as analyzed herein, enables a comparison of these several proposals in a common frame of reference. To an extent, our conclusions would also be valid if a current driver were sought for the FED[1] or a commercial reactor, since the DEMO is midway in size and toroidal current between these two cases.

Our survey concentrates on the calculation of electrical power required for each candidate current driver to sustain the toroidal current. Since the DEMO must produce net electric power, and since previous studies[2] suggested the circulating power may be substantial, this calculation of electric power requirements is the primary concern in our study. If any current drivers appear to have negligible power requirements ($\lesssim$1% of gross electric power) then the capital costs for these systems can be considered influential for discriminating among these drivers. Whenever possible the current drive system is sized to also provide auxiliary heating to ignition. Engineering problems have not been addressed in any detail, except for two drivers treated in the appendices. It is important to understand that the plasma physics theory of current drive has been developed to differing degrees of detail for the various drivers under consideration. In addition, the coupling of the driver to the plasma is not well understood for most of the drivers. Thus, our conclusions regarding the relative attractiveness of the driver options for the DEMO are obviously tentative.

Another shortcoming of this study is that most drivers are considered to operate in a purely steady-state mode; pulsed power injection may have benefits, and we expect our conclusions may be modified once pulsed power techniques are fully considered.

This report is organized with a discussion of the reactor design constraints and a description of the reference DEMO parameters in the next subsection. This is followed with discussions of current drivers requiring particle injection in Sec. 2.2. Wave driven currents are treated in Sec. 2.3. Table 2-1 displays all the options considered in this chapter.

2.1.2 Selection of DEMO Plasma Parameters

Plasma stability analysis for the lower-hydrid-wave-driven STARFIRE reactor suggested that the maximum stable volume averaged plasma beta, β, increases as the toroidal current is increased and attains a broad centrally peaked profile.[3] Consistent with the high performance goals of the DEMO, we require the driver system to generate a high current, high β plasma. We set $\beta = 0.08$, *ad hoc*, without quantitative justification of stability. We adopt an elongated plasma cross section with an elongation $\kappa = 1.6$ and a moderate D-shape characterized by a triangularity factor $d = 0.2$. (The exact geometry is defined in Ref. 4, where the equilibrium calculation is described in detail.) Larger values of d are desired for enhanced stability, but such highly shaped plasmas are extremely difficult to produce with equilibrium field (EFC) coils external to the toroidal field (TFC) coils. We examined equilibria with aspect ratios, A, equal to 3.6, 3.8, and 4.0; the cases considered have high current and small safety factors: $q_a \approx 1.0$ on axis and $q_b \sim 2.0$ at the limiter boundary, corresponding to a poloidal beta $\beta_p \approx 1.6$. According to elementary theory,[1] stability is expected for $\beta \lesssim \beta_p/A^2$. Our β is higher than the value for FED, reflecting our confidence that noninductive current drive will permit current density profile control to achieve the maximum beta with low-q, disruption-free operation.

The equilibria we consider have broad pressure profiles, $p = p_0\hat{\psi}^{1.4}$, where $\hat{\psi}$ is a normalized poloidal flux function[4] and p_0 is the central pressure. The pressure is the sum of the products of the constituent species' densities and temperatures; we assume fairly flat density profiles, $n = n_0\hat{\psi}^{0.3}$, and peaked temperature profiles, $T = T_0\hat{\psi}^{1.1}$. In the comparison of reactor performance at the three aspect ratios we have varied the plasma temperature and density, keeping β constant. The maximum toroidal field at the edge of the TFC is taken to be $B_M = 10$ T; the inboard blanket/shield thickness is $\Delta^i_{B/S} = 1.2$ m; and the scrape-off width on the inboard side is $\Delta^i_v = 0.2$ m. The results are shown in Fig. 2-1, where we have set the neutron wall load $W_n = 1.5$ MW/m^2 and calculated the required major radius, R. The results show

Table 2-1. DEMO Current Driver Options

	Parallel Momentum Input	Indirect Means (Heating, Canonical Angular Momentum, etc.)
Particle injection driven currents (Sec. 2.2)	Neutral beam (NB) Partially ionized heavy atom beam Pulsed relativistic electron beam (REB) Pulsed intense (charge neutral) ion beam	Bootstrap Preferential alpha loss
Wave-driven currents (Sec. 2.3)	Compressional Alfven wave (CAW), $\omega \ll \Omega_i$ Shear Alfven wave, $\omega \ll \Omega_i$ Low-speed magnetosonic ($\omega \gg \Omega_i$) wave ($\frac{\omega}{k_\parallel} < v_e$)	Minority ICRH Alpha Landau and transit time damping
	Lower hybrid wave, Ion cyclotron wave, $\omega \approx \Omega_i$ High-speed magnetosonic (HSMS) wave ($\frac{\omega}{k_\parallel} > v_e$)	ECRH Anisotropic reflection of synchrotron radiation

the DEMO needs a major radius in the 5-m range. The minor radius, a, must be about 1.3 m. All the cases in the figure are ignited, if electron energy containment follows empirical scaling, but the low temperature, high density regime yields a higher safety margin for ignition. On the other hand, current drive requirements favor high $\bar{T}_e$, low $\bar{n}_e$ operation (a super bar indicates a volume average), even though the current, I, increases slightly at higher $\bar{T}_e$. The largest aspect ratio (A = 4.0) in the figure results in the lowest current, smallest device for a given $\bar{T}_e$, and, since the DEMO cost must be minimized, we select A = 4.0 as the reference value for the device. The choice R = 5.2 m and a = 1.3 m results in the minimum size machine which guarantees ignition at the lower limit of wall load, W_n = 1.5 MW/m^2. Operation at higher wall loads (higher $\bar{n}_e$, lower $\bar{T}_e$) provides a greater ignition margin.

Table 2-2 summarizes the plasma geometry and MHD equilibrium selected for the DEMO. Figure 2-2 details the two-dimensional equilibrium solution for the magnetic fields and toroidal current density. These two-dimensional profiles of density and temperature are used in the power balance calculations presented below. Note the broad current density profile, j(R), in the equatorial plane (Fig. 2-2b) which results in the large plasma current, I = 9.01 MA. The peak of j(R) occurs at R = 6.14 m, 67 cm outboard of the magnetic axis. Two-dimensional current equilibria will not be calculated for the drivers considered in Secs. 2.2 and 2.3; the only toroidal effects considered will be current density modifications due to magnetically trapped electrons. Side and plan views of DEMO are shown in Figs. 2-3 and 2-4; the eight toroidal coils have smaller vertical dimensions than an equivalent set wound in constant tension.

In the survey of current driver performance it is necessary to examine a large number of plasma regimes: we consider $\bar{T}_e$ in the range 4 keV to 20 keV, and we examine plasma power balance with 0, 20, and 50 MW of auxiliary heating (P_{aux}) going either to electrons or ions, depending on the current driver considered. Consequently a time-independent power balance is computed for the volume-average plasma variables, and we employ global containment times. In the banana regime, assuming $\bar{T}_i \approx$ 12 keV, $\bar{n}_e = 1.5 \times 10^{20}$ m^{-3}, and Z_{eff} = 1.4, we estimate the ion energy containment time for a circular plasma to be one-third of the neoclassical value: $1/3\ \tau^{NC}_{U,DT} = 6$ s. For electron energy

Table 2-2. DEMO Parameters

Geometry:

R_0	= 5.2 m	
A	= 4.0	
a	= 1.3 m	
κ	= 1.6	
b	= κa = 2.08 m	
d	= 0.2	Triangularity
V_p	= 272 m^3	Plasma volume
A_w	= 400 m^2	First wall area
Δ_v	= 0.20 m 0.165 m	Scrapeoff (inboard) Scrapeoff (outboard, limiter region)
$\Delta^i_{B/S}$	= 1.2 m	Inboard blanket/shield
Δ^o_B	= 0.70 m	Outboard blanket
Δ^o_S	= 1.40 m	Outboard shield
R_1	= 2.1 m	Inboard leg TFC } 0.6% pp ripple at R + (a/2)
R_2	= 11.6 m	Outboard leg TFC } by approximate formula.
Δ_{TFC}	= 0.78 m	TFC thickness
Δ_{sup}	= 0.25 m	Support cylinder

8 TF coils assumed

MHD:

B_M	= 10.0 T	Maximum toroidal field, at magnet
B_0	= 4.81 T	Toroidal field at R_0
B_{mag}	= 4.57 T	Toroidal field at magnetic axis
I_0	= 9.01 MA	
β	= 0.08	Volume averaged beta
β_*	= 0.10	RMS beta
$q(\psi)$	= 1.02 1.92	Magnetic axis Limiter
α	= 1.4	Pressure profile: $p(\psi) = p_0\hat{\psi}^{1.4}$
γ	= 1.8	Diamagnetism $F(\psi) = RB_t$
δ	= 0.09487	$F^2(\psi) = F_0^2\left(1 - \delta\hat{\psi}^{\gamma}\right)$
α_J	= 0.6	$\alpha_J \equiv \delta\gamma F_0^2/\left(2\alpha p_0 \mu_0 R_0^2\right)$
β_p	= 1.58	
S	= 1.32	Shape factor
R_{mag}	= 5.47 m	Magnetic axis
L	= 10.6 μH	Self inductance

Profiles:

α_T	= 1.1	$T = T_0\hat{\psi}^{1.1}$, all temperatures
α_n	= 0.3	$n = n_0\psi^{0.3}$, all plasma densities
$n_{e,edge}$	= 1×10^{18} m^{-3}	
$T_{e,edge}$	= 1 keV	
$T_{i,edge}$	= 0.3 keV	
δ_p	= 4 cm	Density e-folding length in limiter shadow
δ_T	= 8 cm	Temperature e-folding length in limiter shadow
δ_E	= 2.67 cm	Heat flux e-folding length in limiter shadow

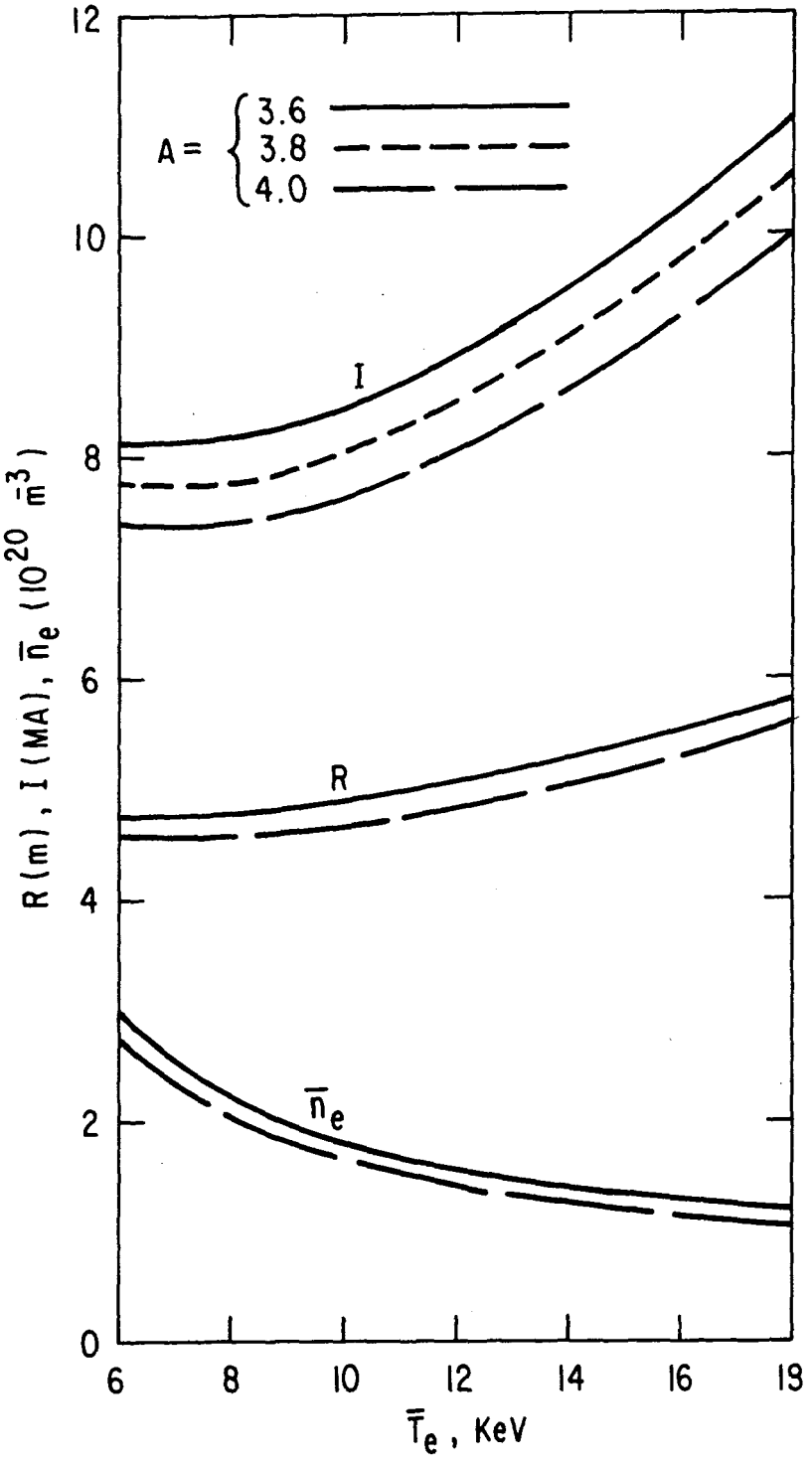

Fig. 2-1a. Major radius, toroidal current, and average density vs. plasma temperature for fixed β (= 0.08), B_{M_2} (= 10 T), and neutron wall load, W_n (= 1.5 MW/m^2) and for different aspect ratios.

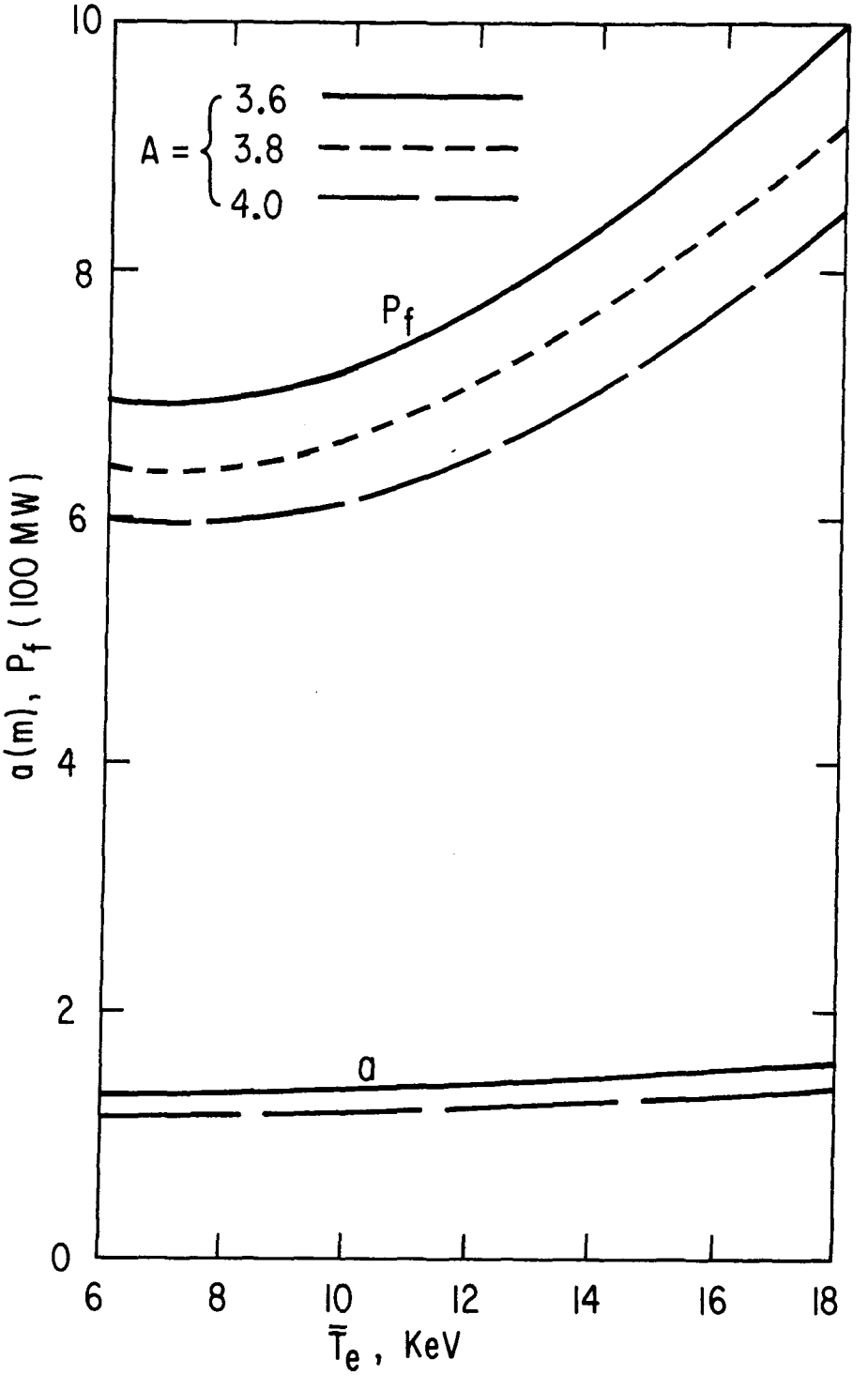

Fig. 2-1b. Fusion power and minor radius for the cases in Fig. 2-1a.

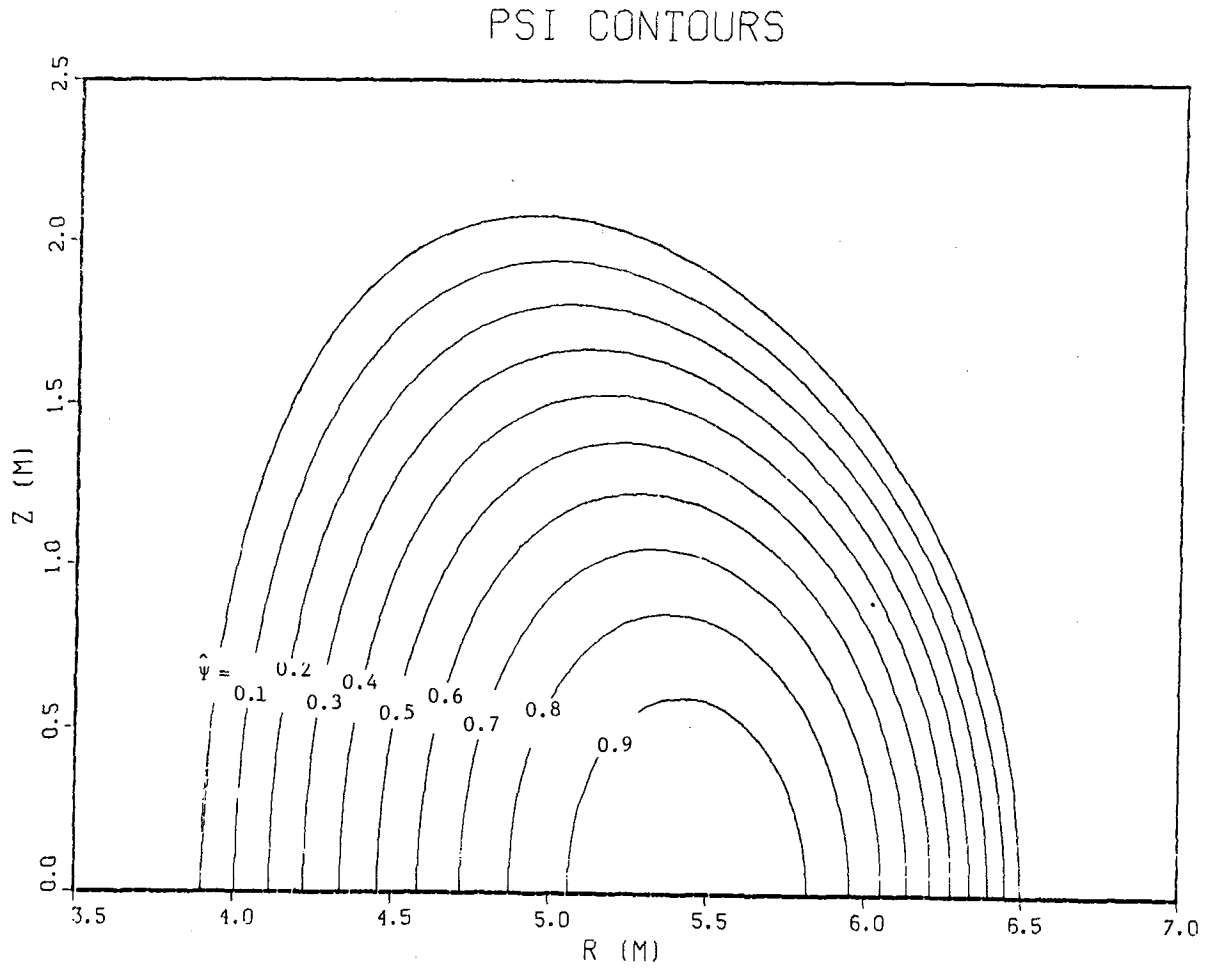

Fig. 2-2a. DEMO equilibrium poloidal flux.

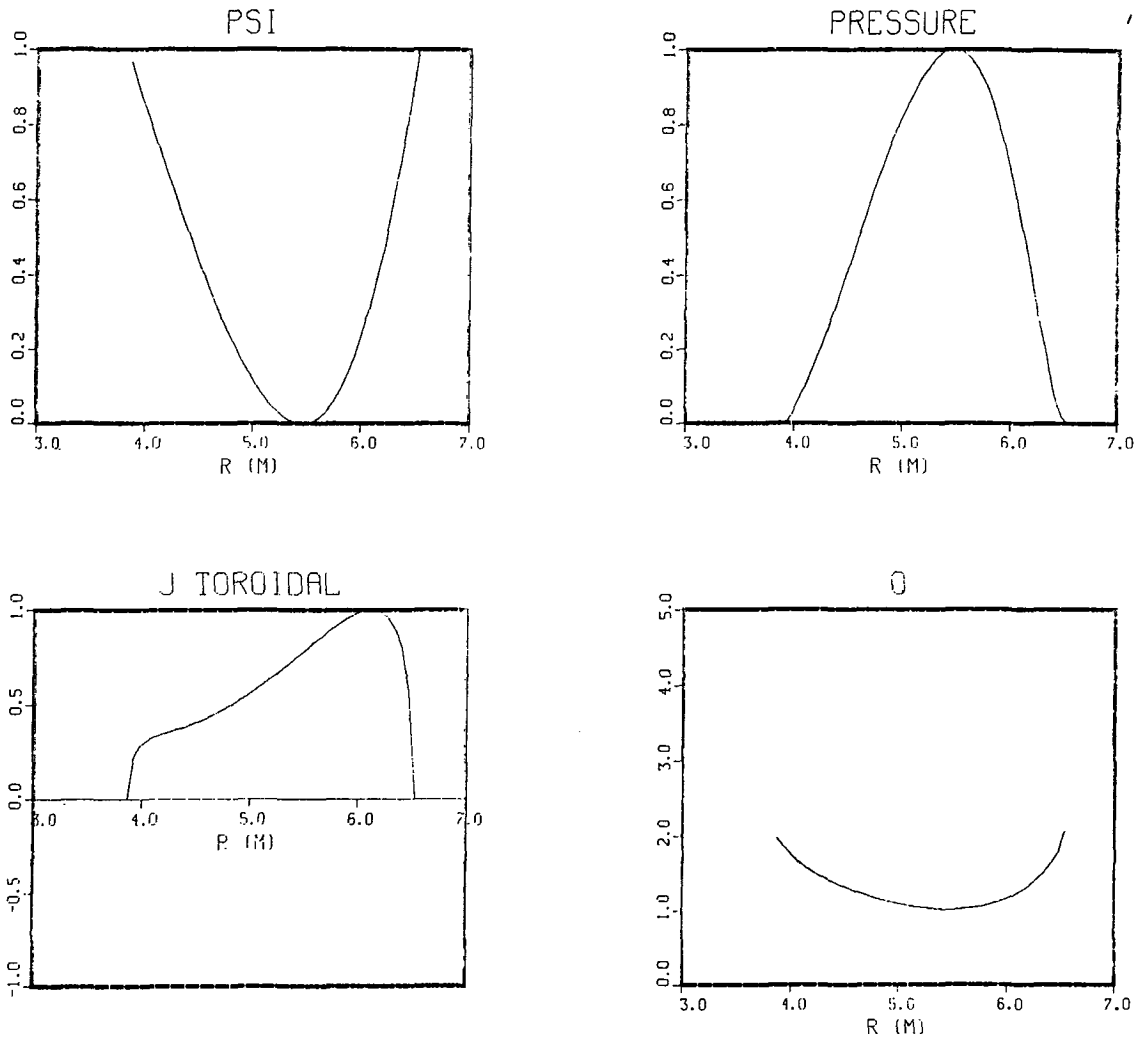

Fig. 2-2b. Equilibrium profiles in equatorial plane.

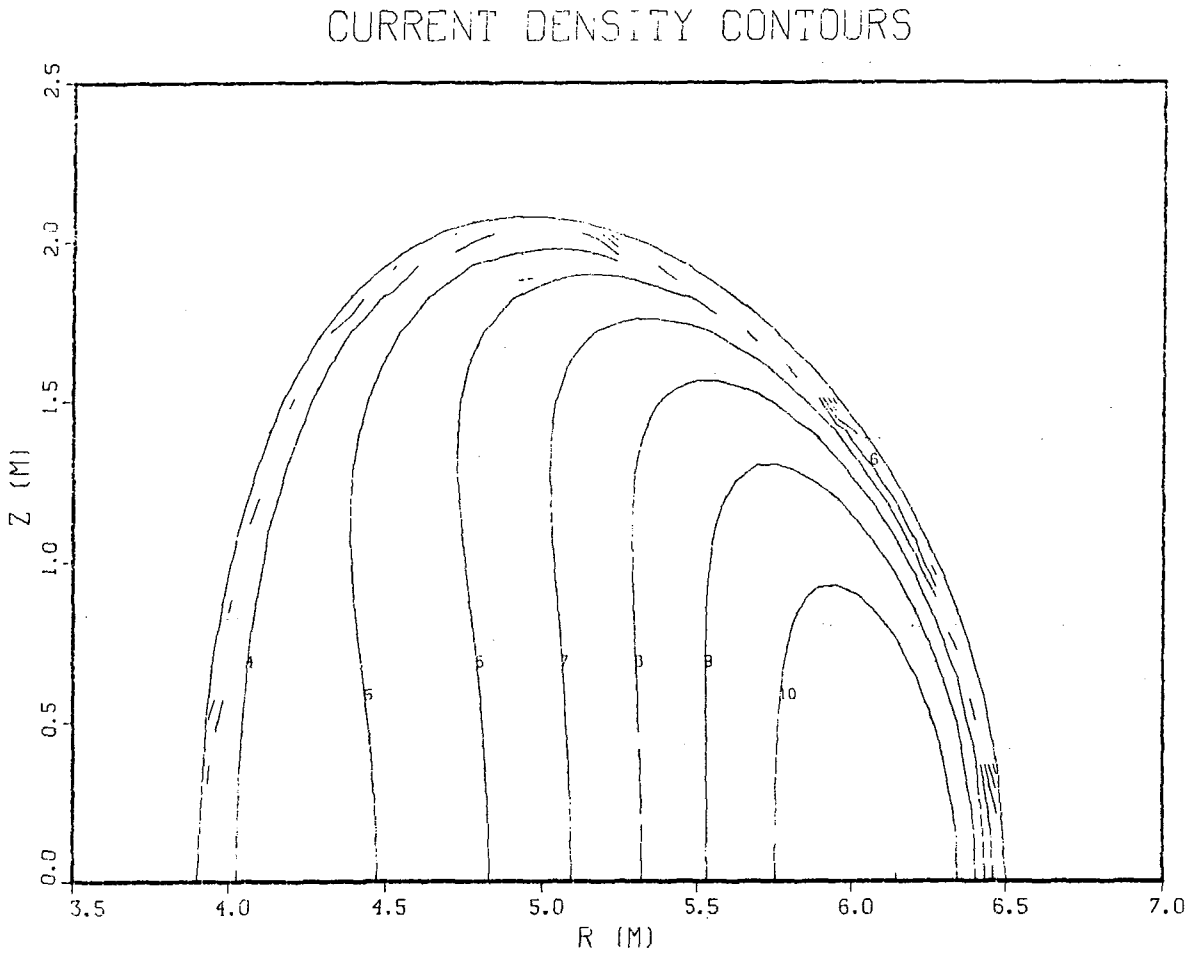

Fig. 2-2c. Two-dimensional current density contours.

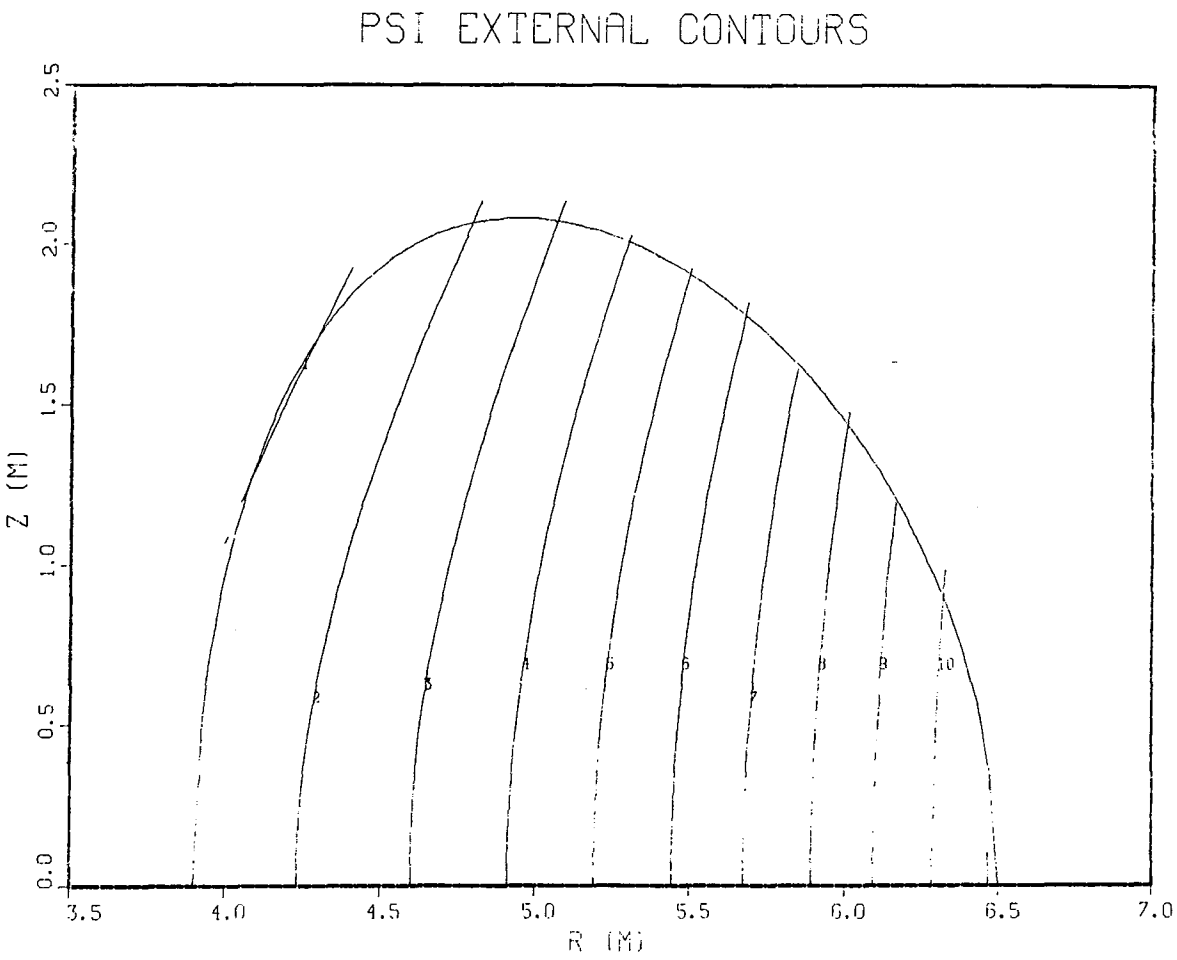

Fig. 2-2d. External magnetic field required for equilibrium.

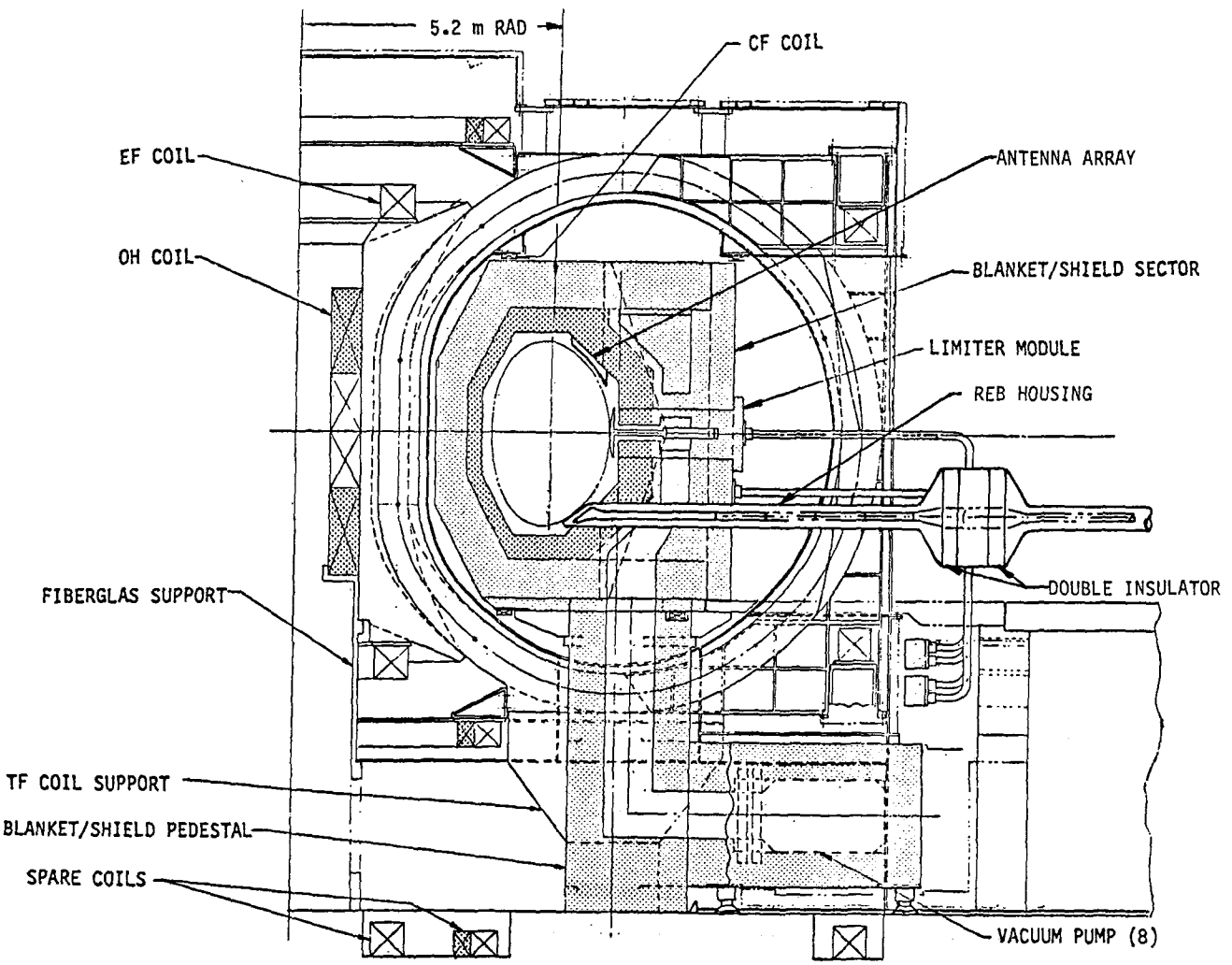

Fig. 2-3. View of DEMO showing typical locations and relative sizes of REB diode and antenna loop for fast wave (HSMS) launcher at 82 MHz.

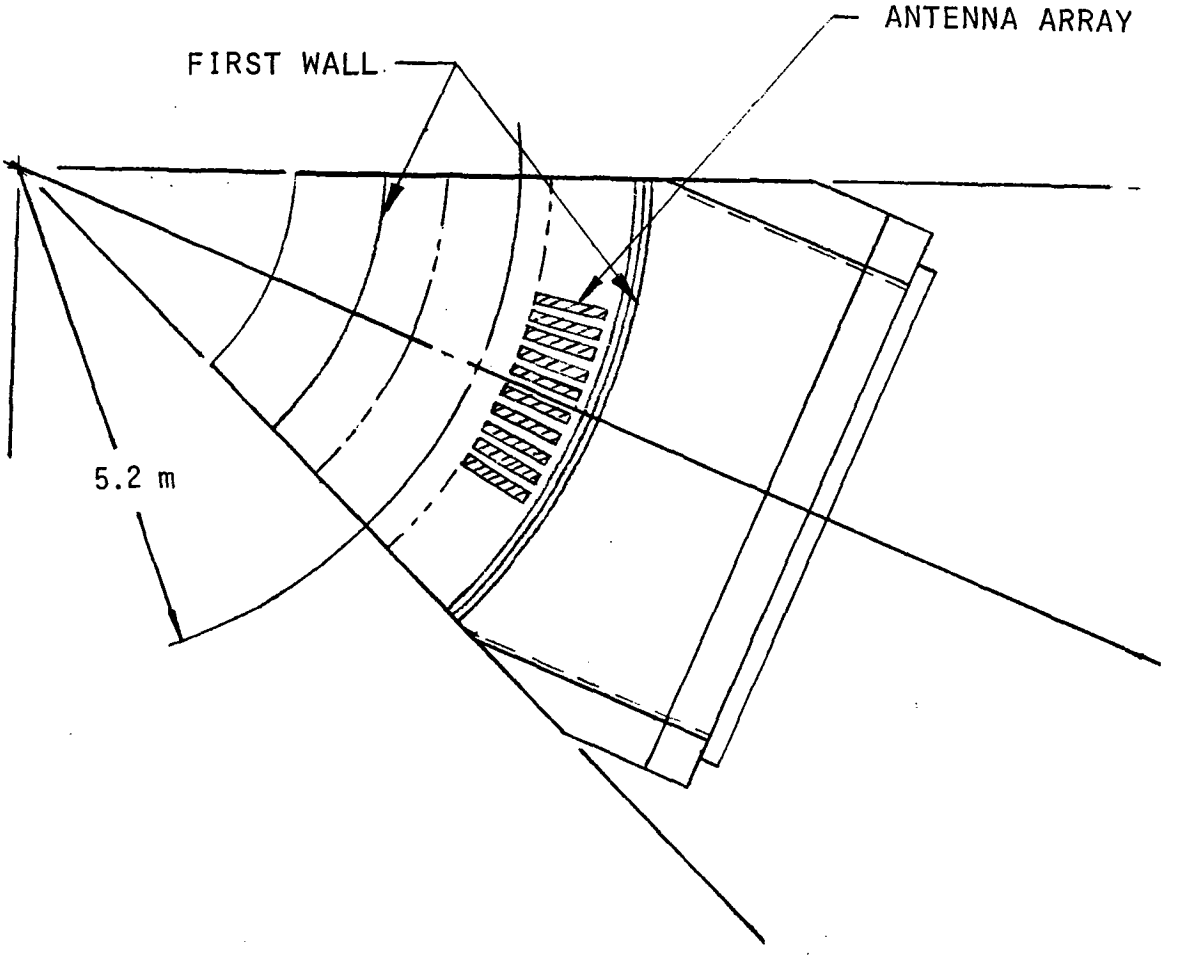

Fig. 2-4. Top view of DEMO showing spacing of elements in the traveling wave antenna (82 MHz, HSMS).

confinement we adopt the empirical scalings proposed in FED and INTOR studies:[1,5] $\tau_{U,e}^{EMP} = 0.5 \times 10^{-20}\ \bar{n}_e a^2 \times 2 \exp[-(2\ \beta_p/A)^2]$, or $\tau_{U,e}^{EMP} = 1.3$ s for $\bar{n}_e = 1.5 \times 10^{20}\ m^{-3}$, $a = 1.3$ m, and $\beta_p = 1.6$. The particle losses are due to diffusion and charge exchange, and, based on transport code simulations, we set $\tau_p \approx 0.4$ s. Noncircular boundaries[6] increases all these values by $2\kappa^2/(1 + \kappa^2)$, which is a factor 1.4 for $\kappa = 1.6$. (We note in Fig. 2-2a that the flux surfaces retain this elongation even near the magnetic axis, due to the broad current density profile.) Thus, $\tau_{U,DT}/\tau_{U,e} \approx 4$ and $\tau_p/\tau_{U,e} \approx 0.3$; we use these ratios in all our calculations and compute the value of $\tau_{U,e}$ required to achieve power balance. We specify a few percent of alpha particles and first-wall material in the plasma, resulting in a $Z_{eff} \approx 1.4$. For most cases examined, the required $\tau_{U,e}$ is less than that predicted by the empirical scaling, so, in fact, the plasma must be "spoiled" by the addition of an impurity (e.g., iodine) to increase the radiation and achieve power production balance.

Tables 2-3 and 2-4 illustrate the plasma parameters for two particular cases, no auxiliary heating and 50 MW of rf heating (45 MW to electrons and 5 MW to ions). Only parameters relevant to the current drive calculations are tabulated. Additional tables were compiled for other current drivers, e.g., neutral deuterium beam driven currents include 50 MW of auxiliary heating with the beam slowing down explicitly calculated and with suprathermal fusion included in the power balance. In special cases (D^0 driven currents), Z_{eff} is increased by the addition of argon to the plasma. For the case of ^3He minority heating the plasma is diluted by the addition of a 5% ^3He concentration.

Several points should be emphasized regarding the results. Notice fusion power peaks at $\bar{T}_e = 8$ keV and decreases rapidly going to higher $\bar{T}_e$ for the fixed tokamak geometry and β. However, the electron density, $\bar{n}_e$, also decreases in going to higher $\bar{T}_e$ so we expect the current driver power to decrease with increasing $\bar{T}_e$, since, as we shall see, the driver power is generally proportional to $\bar{n}_e$ for a fixed current and major radius. Also operation at 12 keV $\lesssim \bar{T}_e \lesssim$ 16 keV is necessary to achieve $1.5\ MW/m^2 \lesssim W_n \lesssim 2.0\ MW/m^2$. The quantity α_{emp} is the ratio of the required $\tau_{U,e}$ to that predicted by our empirical scaling, and we require $\alpha_{emp} \leq 1$ to achieve an ignited plasma. Thus, we see that operation at the lowest $\bar{T}_e$ values yields the greatest safety margin to guarantee ignition.

Table 2-3. Plasma Power Balance for DEMO; P_{aux} = 0 and Z_{eff} = 1.42

$\bar{T}_e$, keV	4	6	8	10	12	14	16	18
P_f, MW	955	1270	1320	1230	1080	917	766	637
$\bar{n}_e$, 10^{20} m^{-3}	5.24	3.42	2.48	1.90	1.50	1.23	1.03	0.883
W_n, MW/m^2	1.91	2.54	2.64	2.46	2.16	1.83	1.53	1.27
$\bar{n}_D$, 10^{20} m^{-3}	2.23	1.46	1.06	0.806	0.639	0.520	0.435	0.371
α_{emp}	0.44	0.23	0.26	0.33	0.44	0.61	0.83	0.97

Table 2-4. Plasma Power Balance for DEMO; P_{aux} = 50 MW (45 MW to Electrons and 5 MW to Ions), RF Heating, and Z_{eff} = 1.42

$\bar{T}_e$, keV	6	8	10	12	14	16	18
P_f, MW	1320	1370	1280	1130	973	827	703
$\bar{n}_e$, 10^{20} m^{-3}	3.42	2.48	1.90	1.51	1.24	1.04	0.900
W_n, MW/m^2	2.54	2.64	2.45	2.16	1.84	1.55	1.30
$\bar{n}_D$, $10^{20} m^{-3}$	1.46	1.06	0.811	0.644	0.528	0.443	0.381
α_{emp}	0.18	0.21	0.27	0.35	0.46	0.61	0.78

In the analysis of Secs. 2.2 and 2.3 the net electric production of the fusion power plant is estimated by the formula

$$P_n = 0.36 \times P_f - 22 - \left(P_{aux}/\eta_{aux}\right) , \qquad (2\text{-}1)$$

where all units are MW and η_{aux} is the efficiency of converting electric power to the requisite power, P_{aux}, absorbed by the plasma to sustain the 9-MA equilibrium. The gross electric output accounts for some energy multiplication in the blanket; 22 MW is assumed necessary to operate the plant (pumping, cryogenics, etc.). For reactor engineering considerations, a reference set of operating parameters (corresponding to the REB driver of Sec. 2.2) is included as Table 2-5.

2.2 Particle Beam Drivers

2.2.1 Neutral Atom Injection

The use of neutral beams to generate plasma currents was first proposed by Ohkawa,[7] and the theory has been refined to a great degree through the efforts of Cordey, et al.[8-9] Experiments on the Culham Levitron[10] and DITE[11] are in substantial agreement with the refined theory.

Upon injection of a neutral beam into the plasma the atoms are ionized and circulate toroidally, their radial deposition profile being determined by the plasma density and temperature profiles and by the neutral atom velocities. The circulating ions constitute a plasma current; however, momentum transfer to electrons pushes the electrons in the same direction, creating a reduction in the net current. In toroidal systems a fraction of the electrons are trapped; these do not contribute to the counter current if they receive momentum, and they also increase the friction on the circulating electrons. Thus toroidal effects can act to increase the net current relative to a straight field geometry. These effects are included in the approximate current density expression in terms of the fast ion (beam) current density, j_b,[8]

$$j = j_b\left\{1 - \frac{Z_b}{Z_{eff}}\left[1 - 1.46\sqrt{\epsilon}\left(1 + \frac{0.7}{Z_{eff}}\right)\right]\right\}, \qquad (2\text{-}2)$$

where the subscript b refers to the fast ion charge state. We define the local flux surface aspect ratio as ϵ^{-1} and note that this formula is valid only for $\epsilon \ll 1$, i.e. near the magnetic axis, where the current density is

Table 2-5. Plasma Performance: REB Current Drive

$\bar{T}_e$, kev	16	
$\bar{T}_i$, keV	19.4	
$\bar{n}_e$, m^{-3}	1.03×10^{20}	
$\bar{n}_{DT}$, m^{-3}	0.87×10^{20}	
$\bar{n}_\alpha/n_{DT}$	0.08	
n_{Be}/n_{DT}	0.04	
P_f, MW	766	Fusion power
$P_{neutron}$, MW	613	
P_{rad}, MW	~35	
P_{cx}, MW	~13	cx to first wall
P_{lim}, MW	~100	Charged particles to limiter
P_{aux}, MW	$\lesssim 5$	REB heating
P_{REB}, MW	2.2	REB current drive
R, Ω	5.80×10^{-9}	Plasma resistance
P_{net}, MW	$\lesssim 242$	Net electric
$\bar{W}_{neutron}$, MW/m^2	~1.5	Wall load
$\bar{J}_{neutron}$, $m^{-2}s^{-1}$	6.80×10^{17}	Neutron current density
$\bar{W}_{rad}$, MW/m^2	~0.1	
Z_{eff}	~1.4	
$\tau_{U,e}$, s	1.3	
ν_*	4×10^{-3}	
$\tau_{U,DT}$, s	6	One-third of neoclassical
τ_p, s	0.4	

highest. In addition, this result assumes fast ion velocities, v_b, much less than the electron thermal speed, $v_e = \sqrt{T_e/m_e}$, which is the regime of present interest. Thermal ion toroidal rotation, a component of the bootstrap current, is not included in Eq. 2-2.

The power density, p, consumed in the maintenance of j is a function of the neutral atom injection energy, Z_{eff}, and the slowing down time, τ_s, of the ions in the plasma. In order to facilitate the comparison of various current drivers we will frequently examine a normalized current drive efficiency $\hat{j}/\hat{p}$, where we define $\hat{j} = j/(n_e v_e e)$ and $\hat{p} = p/(n_e m_e v_e^2 \nu_0)$, with m_e and e the electron rest mass and charge and with $\nu_0 \equiv n_e \ell n \Lambda e^4/(2\pi\varepsilon_0^2 m_e v_e^3)$, $\ell n \Lambda$ being the Coulomb logarithm. Thus

$$j/p = \frac{2\pi\varepsilon_0^2 m_e v_e^2}{n_e e^3 \ell n \Lambda} (\hat{j}/\hat{p})$$

$$= 0.96 \times 10^{18} \frac{20}{\ell n \Lambda} \frac{T_e}{n_e} (\hat{j}/\hat{p}) \ . \qquad (2\text{-}3)$$

Unless otherwise specified, all units in this report are SI, except for plasma temperatures, which are in keV. The dimensionless quantity $\hat{j}/\hat{p}$ is a function of v_b/v_e, and we display a typical beam driver result in Fig. 2-5, which is adapted from Ref. 12. The figure demonstrates that there is an optimum beam energy, $v_b/v_e \approx 0.2$, which maximizes $\hat{j}/\hat{p}$. Furthermore, when $Z_b < Z_{eff}$, the neoclassical effects act to increase $\hat{j}/\hat{p}$. (When $Z_{eff} < Z_b$ the opposite is true, as evidenced by Eq. 2-2.) The functional form of Eq. 2-3 demonstrates that high temperatures and low densities raise the current drive efficiency, j/p, for a given $\hat{j}/\hat{p}$.

Equation 2-3 is local in minor radius, and we generalize the calculation with a spatial Monte Carlo simulation of the beam slowing down, integrating a more accurate form of Eq. 2-2 along test particle orbits:[9]

$$j = \frac{I_B}{N\pi\kappa a^2} \sum_{b=1}^{N} Z_b \int_0^{\tau_s} \frac{v_\parallel(t)}{2\pi R_0} \left\{ 1 - \frac{Z_b}{Z_{eff}} \left[1 - 1.55 \left(1 + \frac{0.55}{Z_{eff}} \right) \sqrt{\varepsilon} \right. \right.$$

$$\left. \left. - \left(0.20 + \frac{1.55}{Z_{eff}} \right) \varepsilon \right] \right\} \ ,$$

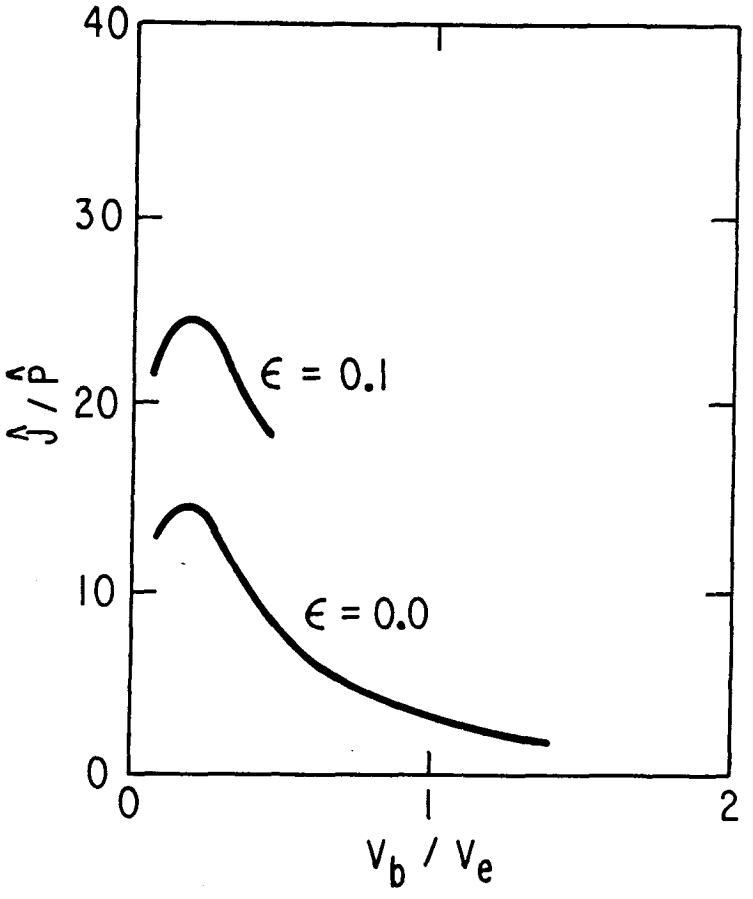

Fig. 2-5. D^0 injection into D-T plasma with $Z_{eff} = 2$.

where $v_{\parallel}$ is the fast ion toroidal velocity and I_B is the beam current injected. The code follows the neutral atoms, computes their position of ionization, includes finite Larmor radius effects, calculates the subsequent ionization and guiding center drifts, and slows the particles down. The actual flux surfaces of Fig. 2-2a are modeled for this calculation by concentric ellipses centered at R_0 with a = 1.3 m and b = 2.1 m. Plasma temperature and density is constant on flux surfaces and we model the profiles as

$$\begin{aligned} T(r) &= T_0\left[1 - (r/a)^2\right]^{1.1} \\ n(r) &= n_0\left[1 - (r/a)^2\right]^{0.3} \end{aligned} \tag{2-4}$$

across the equatorial plane. The beam is assumed cylindrically symmetric with a Gaussian current density of half-width 20 cm. The toroidal current density profile, j(r), is sensitive to the radius of tangency, ρ, to the plasma; the beam axis lies close to the equatorial plane. The code integrates j over the plasma cross section and computes the total current I for a given injection power P_b.

The most attractive regime appears to be for $Z_b < Z_{eff}$. From Eq. 2-2 it is obvious that j/j_b is maximized by minimizing Z_b/Z_{eff}. We selected a deuteron beam and increased the plasma impurity content until $Z_{eff} = 3.1$; higher Z_{eff} jeopardizes ignition and yields only small increases in I/P_b. The test equilibrium had $\bar{T}_e = 18$ keV and $\bar{n}_e = 0.84 \times 10^{20}$ m^{-3}, and the optimum injection energy, 3 MeV, resulted in $I/P_b = 0.14$ A/W with $\rho = 4.5$ m. (Suppression of neoclassical effects by setting $\varepsilon = 0$ resulted in a lower value, $I/P_b = 0.11$ A/W). Figure 2-6 displays the resulting current density profile. The extension of our results to other $\bar{T}_e$, $\bar{n}_e$ values would actually require additional numerical computation, but based on the functional dependence of Eq. 2-3 we can approximately extrapolate these results as

$$I/P_b = 0.14 \frac{\left(\bar{T}_e/18 \text{ keV}\right) \text{ A/W}}{\left(\bar{n}_e /0.84 \times 10^{20} \text{ m}^{-3}\right)} , \tag{2-5}$$

where we assume the deuteron beam energy is adjusted to keep $\hat{j}/\hat{p}$ constant.

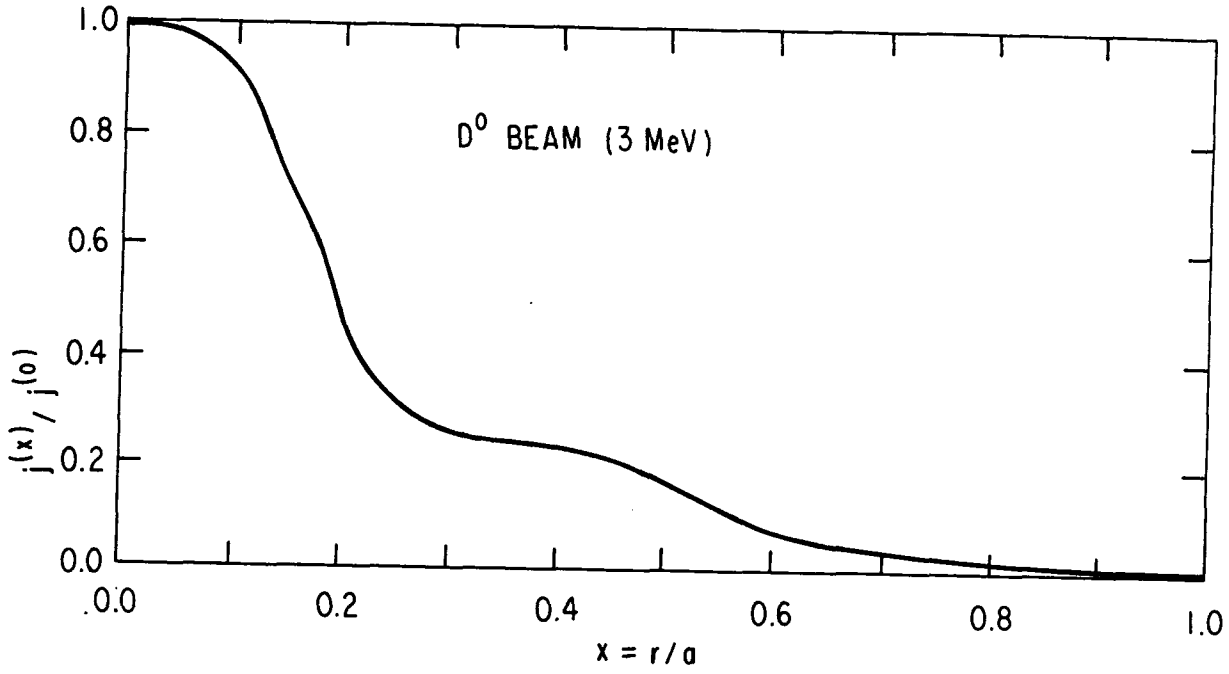

Fig. 2-6. Current density profile for 3 MeV D^0 injected into $\bar{n}_e = 0.84 \times 10^{20}\ m^{-3}$ with $Z_{eff} = 3.1$.

For comparison, we studied Si^0 injection into a plasma with $Z_{eff} = 1.6$ (due in part to a steady-state concentration of Si, $n_{Si}/n_{DT} \approx 0.1\%$). The beam is injected counter to the toroidal current at a shallow angle to the equatorial plane, with $\rho = 4.2$ m. For a 56-MeV beam injected into a $\bar{T}_e = 18$ keV, $\bar{n}_e = 0.88 \times 10^{20}$ m^{-3} plasma we find $I/P_b = 0.12$ A/W if neoclassical effects are suppressed. For the case in which neoclassical effects are present, $I/P_b = 0.047$ A/W, which is much poorer than the D^{-0} case cited previously.

Returning then to the D^0 beam, we have plotted P_b and the corresponding neutral beam current, I_b, based on Eq. 2-5, as well as the gross electric power production ($0.36 \times P_f$), over a range of operating regimes in Fig. 2-7. Plasma surface sources[13] are expected to deliver several hundred mA of D^- so we expect between ten and a hundred sources would be needed for the system. Electric quadrupole focused rf accelerators[13] seem well suited to handle the high energy, high current ion beams in a CW manner. These accelerators capture and transmit ~85-90% of the incident beam with power efficiencies ≈35%, and designs are being considered for beam lines which can carry 1-3 A. Several beam lines could be constructed in parallel to provide the full current. It appears that laser photodetachment will be mandatory in order to maximize the neutralization efficiency of the D^- beam, although the development of this system may be difficult in the relatively short time period leading to the DEMO design specification. We feel a realistic overall efficiency for delivering D_0 to the plasma with an rf accelerator would be $\eta_{aux} = 0.35$, and this value is used in Eq. 2-1 to estimate the net electric power production of the DEMO. From the figure we see that net electric power production is marginal at best and probably not possible at low temperatures. In contrast, there have been suggestions[14] that electrostatic quadrupole (ESQ) accelerators could be developed to deliver 2 MeV D^0 at η_{aux} at 0.80. If this is actually achievable it would dramatically alter our conclusions, permitting net power production at the 150-MW level in DEMO. Consequently, the success of neutral beam driven currents for steady-state operation of the DEMO hinges on the question of the accelerator/neutralizer efficiency. Negative ion sources, ESQ accelerators, and photodetachment laser neutralizers deserve more study by the neutral beam community prior to making a final judgment as to the suitability of neutral beams as the DEMO current drive system.

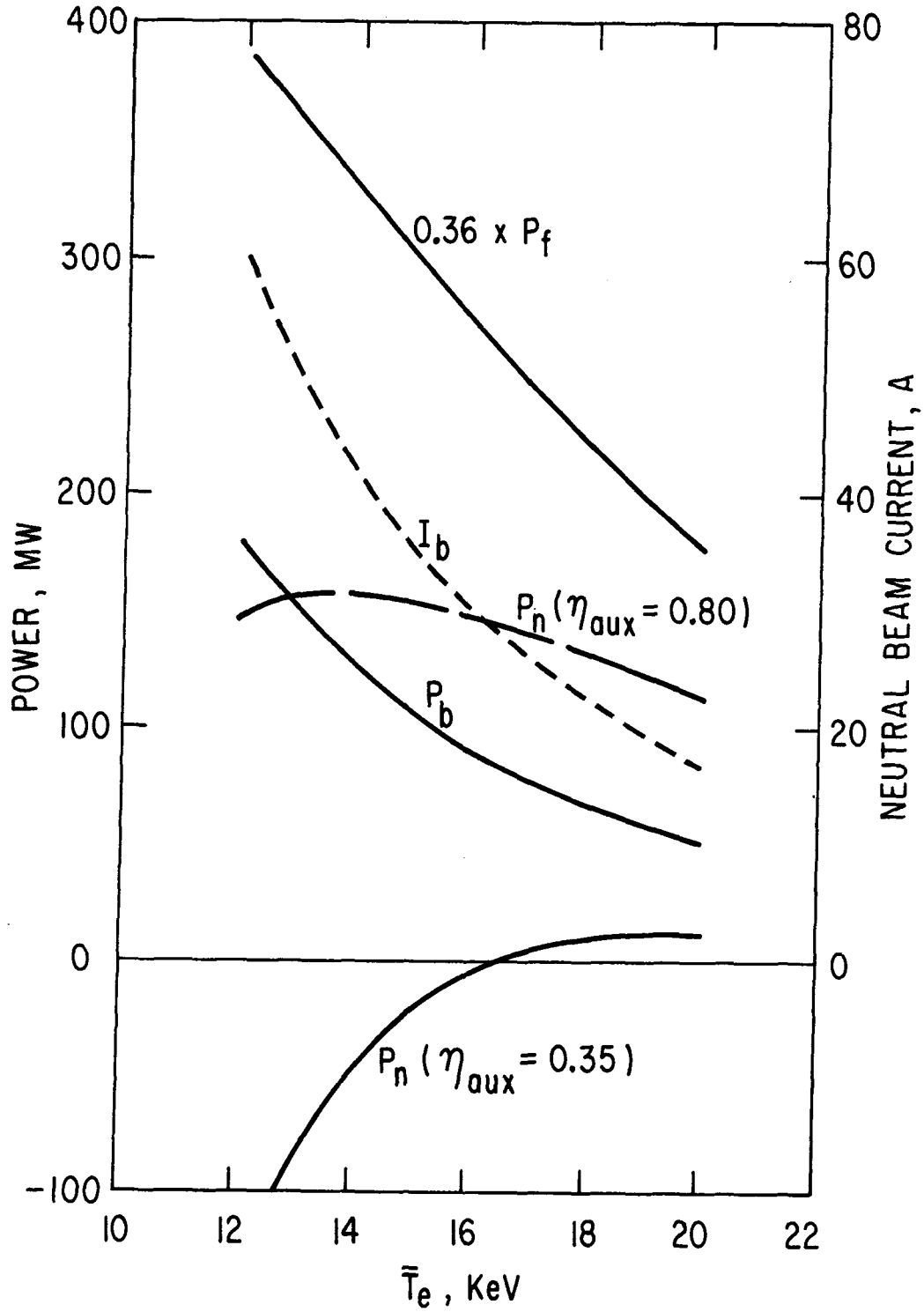

Fig. 2-7. D^0 at 2 MeV, Z_{eff} = 3.1, including neoclassical effects; gross electric power production is 0.36 x P_f, beam current and power are labeled I_b and P_b, and net electric power, P_n, is shown for two system efficiencies.

2.2.2 Pulsed Relativistic Electron Beam (REB) Injection

Toroidal equilibria with relativistic electron currents were first studied by Yoshikawa and Christofilos,[15] and Ikuta[16] explicitly proposed the application of the REB to steady-state tokamaks. REB dynamics in curved magnetic fields have been studied in theory and experiment by a number of authors,[17] and a variety of successful means have been used to inject and trap an REB in a full torus.[18] Subsequent experiments have produced long-lived toroidal equilibria by injection into plasmas both without[19] and with[20] preexisting toroidal current. The principal reactor-relevant study to date has emphasized only the auxiliary heating benefits of the REB to ignition-sized tokamaks.[21]

The theory presented here predicts a very high efficiency for generating current with the REB, and this appears to be due to two circumstances connected with the REB. First, the REB is naturally operated in a pulsed, repetitive mode (and consequently our interest will settle on the time-averaged power consumption as the figure of merit rather than the instantaneous power requirement). In the second place, we will see that the plasma resistivity must vary temporally in an appropriate fashion in order to greatly reduce the average power requirements relative to that needed for other drivers. Pulsed power injection with resistivity oscillations may be used to advantage with other current drivers, but the benefits for other drivers are not as dramatic and are harder to implement compared to CW power injection. Thus, the REB is the only major driver in this study which is assumed to be pulsed.

Generally speaking, REB injection into a plasma creates a double-humped electron distribution function. The thermal electron contribution is treated with a fluid equation; it is essentially a shifted Maxwellian with the drift speed determined by an electric field. At very high velocities ($v_{\parallel} \approx c$) there is a bump on the electron tail; these relativistic electrons are created by injection, and their slowing down is determined by collisions and any electric field.

The plasma thermal electron momentum balance is

$$m_e \dot{v}_d = eE - m_e v_d \nu_m \alpha \ , \qquad (2\text{-}6)$$

where v_d is the electron drift speed, E is the electric field, and ν_m is the momentum transfer rate from plasma electrons to ions, including neoclassical effects. (A dot indicates differentiation with respect to time.) The parameter α indicates a time variation of plasma resistivity, due to anomalies driven by wave phenomena. Generally, the nonthermal (beam) electron component also carries momentum; for cases of interest in this paper the collisional momentum transfer from nonthermal to thermal electrons is negligible. We multiply this equation by $n_e e/(m_e \nu_m \alpha)$ to get an equation for the plasma current density, $j_p = n_e e v_d$:

$$\frac{1}{\alpha\nu_m}\frac{dj_p}{dt} = \frac{E}{\alpha\eta} - j_p ,$$

where η is the neoclassical resistivity. We assume the current profile j_p never varies; i.e., the self-inductance is a constant: $\dot{L} = 0$. Then we integrate this last expression over the plasma cross section:

$$I_p + \frac{1}{\alpha\nu_m}\frac{dI_p}{dt} = \frac{V}{\alpha R} , \qquad (2\text{-}7)$$

where

$I_p = \int dS\, j_p$, the plasma (bulk) current;

$R = 2\pi R_0/[\int dS\, \eta^{-1}]$, the resistance; and

$V = 2\pi R_0 E$, the loop voltage.

The nonthermal (noninductive) component of current due to injection of the beam is denoted I_d, and the total current is the sum of the beam component plus the thermal portion:

$$I = I_p + I_d . \qquad (2\text{-}8)$$

Unlike purely steady-state current drive situations in which $d/dt \equiv 0$, the pulsed mode of operation introduces an electromotive force into the current drive calculations, and this electric field must be determined self-consistently by Lenz's law

$$V = -L\dot{I} . \qquad (2\text{-}9)$$

We desire an equation governing I after a short turn-on period required to establish the circulating beam; after turn-on we can combine Eqs. 2-7 - 2-9, and, provided $I_p >> \dot{I}_p/(\alpha\nu_m)$ (which can be shown a posteriori) we find

$$I = -\frac{L}{\alpha R}\frac{dI}{dt} + I_d \ . \tag{2-10}$$

We define an auxiliary time variable

$$\tau = \int_0^t \frac{\alpha(t')\,dt'}{L/R} \ , \tag{2-11}$$

so this becomes

$$I = -dI/d\tau + I_d \ , \tag{2-12}$$

which has the solution

$$I = e^{-\tau}\left[C + \int d\tau' e^{\tau'} I_d(\tau')\right] \ ; \tag{2-13}$$

C is a constant of integration, determined by initial conditions. The increase in total current during a fast turn-on (<<1 ms) is negligible so we set $I(\tau = 0) \equiv I_0$, the value before turning on the external power source. We define the driver current after turn-on as $I_d(\tau = 0) \equiv I_{do}$.

If $I_{do} > I_0$ the total current increases immediately after t = 0. This situation is depicted schematically in Fig. 2-8. Our interest focuses on the injection of an external amount of energy, $\mathscr{E}_d$, in a pulsed fashion. Thus, the driven current I_d initially exceeds I_0 but will decay to a value less than I_0; the time dependence of I_d will depend on the details of the injection scheme. As long as $I_d > I_0$, a period of duration Δt, the current increases. Once $t = \Delta t$ the increase in total current has reached its maximum, ΔI. Beyond this time, $\dot{I} < 0$ and a forward emf sustains the current. Provided the nonthermal current component has substantially vanished after $t = \Delta t$, the time period for I to decay back to its initial value is simply determined by the plasma inductance and resistance as

$$\delta t = (L/\alpha R)\,\ell n(1 + \Delta I/I_0) \ . \tag{2-14}$$

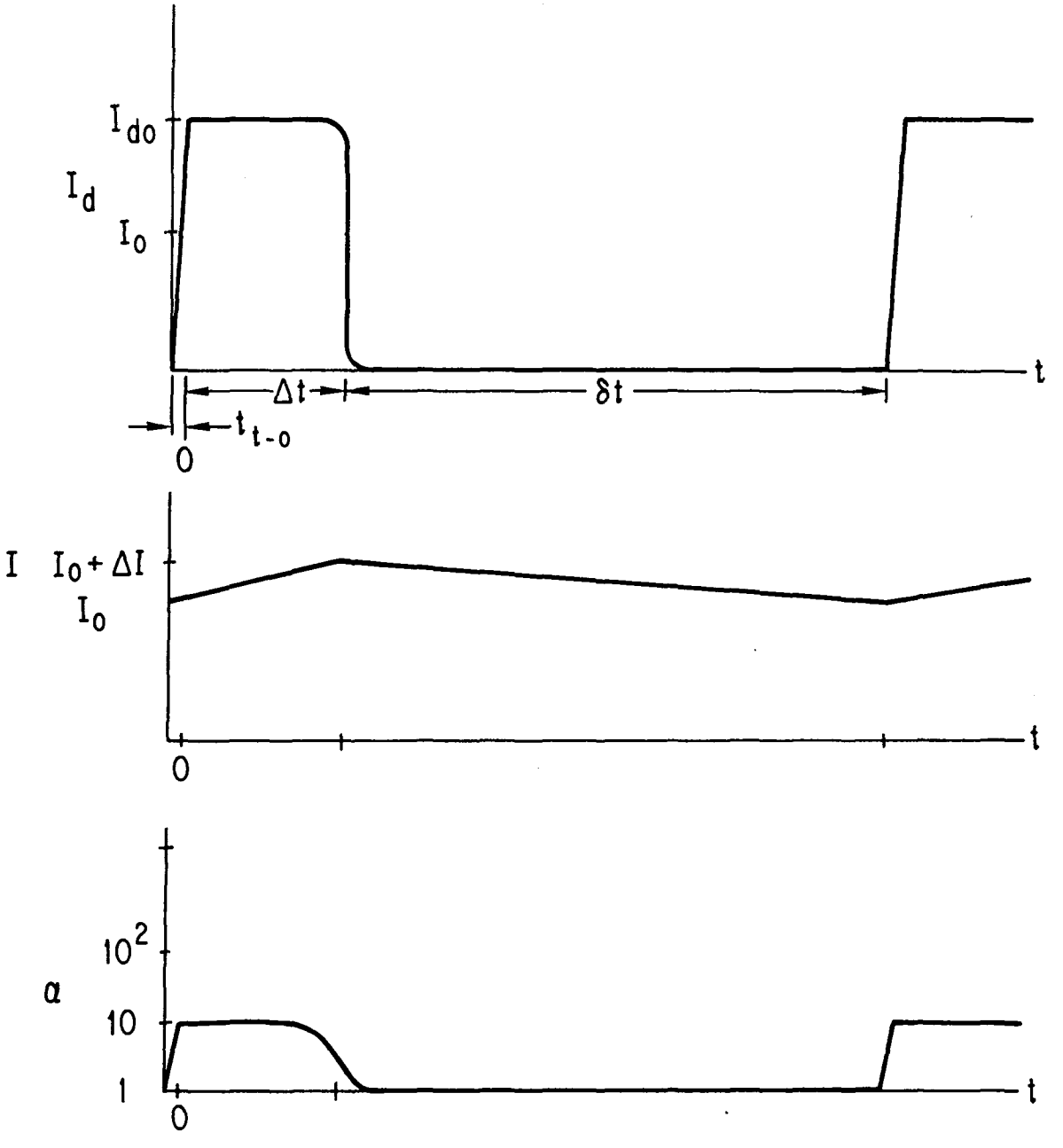

Fig. 2-8. Schematic time dependence of driver current, total current, and resistivity enhancement.

(For this discussion we assume α is unity after $t = \Delta t$.) Our goal is to identify the pulsed driver scenario which maximizes the interpulse period, $\Delta t + \delta t$, for a given $\mathcal{E}_d$, thus minimizing the time-averaged driver power,

$$\langle P_d \rangle = \mathcal{E}_d/(\Delta t + \delta t) \quad , \tag{2-15}$$

required to maintain a given value of I_0.

Before presenting the detailed solution to this problem it may be more transparent to take a heuristic form for $I_d(t)$ which illustrates the importance of the resistance variation, α, to the success of this pulsed current drive scheme. Thus, we model the driver current as

$$I_d = \begin{cases} I_{do} , & 0 < t < \Delta t \\ I_{do} e^{-\nu(t-\Delta t)}, & \Delta t < t \end{cases} , \tag{2-16}$$

with

$$\alpha = \begin{cases} \text{constant} > 1 , & 0 < t < \Delta t \\ 1 , & \Delta t < t \end{cases} . \tag{2-17}$$

The solution for $0 < t < \Delta t$ to Eq. 2-13 is

$$I = I_0 e^{-t/(L/\alpha R)} + I_{do}\left[1 - e^{-t/(L/\alpha R)}\right] . \tag{2-18}$$

If I_d only exists for a short period $\Delta t \ll L/(\alpha R)$ then the increase in total current is

$$\begin{aligned} \Delta I &= I(t = \Delta t) - I_0 \\ &= (I_{do} - I_0)\alpha\Delta t/(L/R) . \end{aligned} \tag{2-19}$$

The solution to Eq. 2-13 for the period $\Delta t < t$ is

$$I = (I_0 + \Delta I)e^{-(t-\Delta t)/(L/R)} + \frac{I_{do}\left[e^{-\nu(t-\Delta t)} - e^{-(t-\Delta t)/(L/R)}\right]}{1 - \nu L/R} .$$

We will assume the current driver decay period, ν^{-1}, is very short compared to the period δt before the next pulse, which may be easily achieved in practice. In addition, in a hot plasma we will assume $\delta t \ll L/R$. With these approximations we find the period $t - \Delta t = \delta t$ by equating the last expression with I_0:

$$\delta t = \left[\frac{\Delta I}{I_0 + \Delta I}\right] (L/R) .$$

Since $\delta t \ll (L/R)$, this can be rewritten as

$$\delta t = \frac{\Delta I}{I_0} (L/R) , \qquad (2\text{-}20)$$

which, of course, is the limiting case of Eq. 2-14 when $\alpha = 1$. Substituting Eq. 2-19 we find

$$\delta t = \left[(I_{do}/I_0) - 1\right]\alpha\Delta t . \qquad (2\text{-}21)$$

This last equation is important and demonstrates a variety of possibilities for extending the interpulse period δt, thereby reducing the average power, $\langle P_d \rangle$. One mechanism, treated in Ref. 22, assumes a constant resistance ($\alpha = 1$) for all times and relies on plasma density reduction during the Δt period to maximize the quantity I_{d0}/I_0 in Eq. 2-21. The penalty associated with this approach is that the fusion power density varies as n^2 and will consequently vary greatly due to the density cycling. We do not consider this a viable operating mode for the DEMO.

Instead, we assume density is held constant, and we examine the increase in δt associated with an increase in resistivity ($\alpha > 1$) during Δt. While neoclassical resistivity could be changed if dynamic control of Z_{eff} or T_e were possible, we note that REB injection automatically raises α without affecting the macroscopic plasma condition (n, T_e, Z_{eff}). In fact, a large bulk of theoretical and experimental analysis[21,23-25] suggests α may greatly

exceed ten during REB injection; this is evidently due to the nonlinear behavior of the two stream instability, which acts to enhance the return current's momentum transfer to the ions.

For purposes of illustration let us suppose $\alpha >> 1$. Then, provided I_{d0} significantly exceeds I_0, we see from Eq. 2-21 that $\delta t >> \Delta t$, and substitution of Eq. 2-20 into Eq. 2-15 shows the general result

$$\langle P_d \rangle = \frac{\mathscr{E}_d/(L/R)}{\Delta I/I_0} \quad . \tag{2-22}$$

If expression 2-19 is used for ΔI, this becomes

$$\langle P_d \rangle = \frac{\mathscr{E}_d/\Delta t}{\alpha[(I_{do}/I_0) - 1]} \quad . \tag{2-23}$$

If the resistance is greatly amplified during Δt ($\alpha >> 1$) then the average power can be small indeed.

The reduction in time-averaged current drive power may be explained physically. By increasing α during Δt the reverse current (driven by the reverse emf) is more strongly retarded. Thus, $\dot{I}$ (total current increase) is larger, and more of the driver energy, $\mathscr{E}_d$, is stored inductively in the ΔI increment. As α is increased, a greater proportion of $\mathscr{E}_d$ can be transferred without dissipation (plasma heating) to poloidal field energy. Then, after $t = \Delta t$, α returns to unity and the inductive energy drives a forward emf, sustaining the decaying current I for a period δt. We note that this inductive current drive phase ($\Delta t < t$) enjoys an extremely low power requirement, i.e. that due to ohmic dissipation. Consequently the average power input over the whole cycle, $\langle P_d \rangle$, can also be quite low.

There is a lower limit to $\langle P_d \rangle$. Taking the extreme case in which

$$\alpha >> (L/R)/\Delta t \ ,$$

we note the expression 2-19 is not an accurate evaluation of Eq. 2-18. Instead, we obtain the upper bound for ΔI:

$$\mathscr{E}_d = \Delta\left[\frac{1}{2} LI^2\right] = LI_0\Delta I \ , \tag{2-24}$$

which states that, in this limit, the driver energy is transferred completely to the poloidal magnetic fields. Then, substitution of this relation directly into Eq. 2-22 shows

$$\lim_{\alpha\Delta t/(L/R)\to\infty} \langle P_d \rangle = I_0^2 R \ .$$

Thus, this resistance oscillation always results in $\langle P_d \rangle$ greater than the equivalent ohmic power needed to sustain I_0.

We now proceed to calculate $\langle P_d \rangle$ more accurately in the $\alpha >> 1$ limit. Thus, we need to replace Eq. 2-16 with a better formulation for the beam current. The dynamics of relativistic beam electrons are given by[26]

$$\frac{d\gamma}{dt} = \frac{eEU}{m_e c^2} - \frac{\nu_e \gamma}{(\gamma^2 - 1)^{1/2}}$$

$$\frac{dU}{dt} = \frac{eE(1 - U^2/c^2)}{m_e \gamma} - \frac{\nu_t \gamma U}{(\gamma^2 - 1)^{3/2}} \ ,$$

where $\gamma m_e c^2$ is the total electron energy and U is the electron toroidal velocity. In terms of these variables the beam current density is $(n_d eU)$, where n_d is the density of the beam (driver) electrons. Terms proportional to E represent energy and momentum changes due to the emf. The term with ν_e represents beam energy loss due to collisions with thermal electrons, and ν_t accounts for parallel momentum loss due to slowing down and pitch angle scattering on the thermal electrons and ions. For the special case in which $\alpha \to 1$, i.e., for no enhancement of the return current's resistivity, the collisional terms dominate the emf; the REB problem for this situation is solved in Appendix A. For the more interesting case, $\alpha >> 1$, we will find that E is large enough to neglect the collisional drag. We assume the REB is injected completely parallel to the magnetic field, without a perpendicular velocity component. Under these circumstances the equations governing relativistic electron dynamics reduce to

$$\dot{\gamma} = eEU/m_e c^2 \qquad (2\text{-}25)$$

$$|U| = c(1 - \gamma^{-2})^{1/2} \ . \qquad (2\text{-}26)$$

We close this system of equations by computing E from Eqs. 2-9 and 2-10; we set $I = I_0$ in the result, since $\tau \ll 1$.

$$E = \alpha R\left[I_0 - I_d\right]/2\pi R_0 \ , \qquad (2\text{-}27)$$

or

$$E = \alpha R\left[I_0 - I_{do}|U|/|U_d|\right]/2\pi R_0 \ .$$

U_d is the initial value of U, immediately after injection.

We add to our list of definitions with the following normalizations: $x = |U|/c$ and $b \equiv I_0|U_d|/(I_{do}c)$. For the sake of illustration let us assume I_0 and I_d are positive quantities . Then, from Eq. 2-27 we find $E < 0$ (retarding the REB motion) as long as $I_d > I_0$, i.e. for $x > b$. Thus, $I_{do} > I_0$ is a prerequisite for driving currents with the REB. In the DEMO a circulating beam current exceeding 9 MA is necessary. This can be achieved, for example, with a cathode current, I_c, of 26 kA, operating for $t_{t-o} = 100$ μs. For 1.5 MeV (kinetic energy) electrons, the initial values of γ and $|U|$ are respectively $\gamma_d = 4.0$ and $|U_d| = 0.968$ c. Thus the toroidal transit time for one of these electrons is $t_{tr} = 2\pi R_0/|U_d| = 0.112$ μs, and the total, stacked current is $I_{do} = I_c t_{t-o}/t_{tr} = 23.2$ MA. As a service to the reader, Table 2-6 collects the myriad definitions introduced in this section.

Combining Eqs. 2-25 - 2-27 we get the equation

$$\dot{x} = -(\alpha/\sigma)(1 - x^2)^{3/2}(x - b) \ , \qquad (2\text{-}28)$$

where

$$\sigma \equiv \left[2\pi R_0 m_e U_d/(eRI_{do})\right] \ .$$

Recalling that $E = 0$ once $x = b$, we note that our neglect of Coulomb collisions is not valid once $x = b$, regardless of the magnitude of α. So Eq. 2-28 only applies when $x > b$. This REB equation, 2-28, is utilized to obtain explicit expressions for

$$\tau = \int_0^t \alpha(t')\ dt'/L/R = \int_{x_d}^{x} \alpha(t')\ dx/(dx/dt')/(L/R)$$

Table 2-6. REB Definitions

Symbol	Meaning	Value for DEMO
m_e	Electron rest mass	9.1×10^{-31} kg
c	Speed of light	3.0×10^{8} m/s
γ	Total relativistic electron energy normalized to $m_e c^2$	
U	Relativistic electron toroidal velocity	
x	$\lvert U/c \rvert$	
n_d	Density of relativistic electrons in plasma	5.9×10^{16} m^{-3}
e	Electron charge	-1.6×10^{-19} C
t_{tr}	Initial toroidal transit time; $2\pi R_0/\lvert U_d \rvert$	0.112 μs
t_{t-o}	Period of diode operation	100 μs
Δt	Period when $I_b > 0$ (slowing downtime for REB)	< 50 ms
δt	Period of forward emf; $\approx \Delta I(L/R)/I_0$	3.7 s
σ	$\lvert 2\pi R_0 m_e U_d/(eRI_{do}) \rvert$	401 ms
τ	Time normalized to $L/R\alpha$	
L	Self-inductance of toroidal current	10.6 μH
R	Neoclassical one-turn resistance	5.80×10^{-9} Ω, (16 keV)
R_0	Major radius	5.2 m
V	Loop voltage	
E	emf; $V/2\pi R_0$	
n_e	Plasma electron density	1.03×10^{20} m^{-3} (16 keV)
v_d	Thermal electron drift speed	2.0×10^{5} m/s
ν_m	Momentum transfer frequency from thermal electrons to ions	2.7×10^{3} s^{-1}
α	Ratio of resistivity to neoclassical value	
I_0	Equilibrium toroidal current; initial value of I	9.01 MA
I_c	Instantaneous cathode current during diode operation	26 kA
I_d	REB current in the plasma; $I_{do}U/U_d$	
I_p	Plasma current due to thermal electrons	
I	$I_p + I_d$	
ΔI	Maximum increase in I	18.2 kA
γ_d	Initial value of γ	4.0
U_d	Initial value of U	2.90×10^{8} m/s
x_d	$\lvert U_d \rvert/c$	0.968
I_{do}	Initial value of I_d; $I_c t_{t-o}/t_{tr}$	23.2 MA
b	$I_o \lvert U_d \rvert / (I_{do} c)$	0.376
$\mathscr{E}_d$	REB kinetic energy delivered by one diode pulse $(\gamma_d - 1)m_e c^2 I_c t_{t-o}/e$	4.0 MJ
$\langle P_d \rangle$	Time-averaged diode power; $\approx \mathscr{E}_d/(\Delta t + \delta t)$	

and for

$$\int_0^{\tau} d\tau' \, I_d(\tau') = \left(I_{do} c/U_d L/R\right) \int_{x_d}^{x} \alpha(t') x \, dx/(dx/dt') \quad ,$$

where

$$x_d \equiv \left|U_d/c\right| \, .$$

These two quantities are then inserted into the current equation, 2-13, evaluated in the $\tau << 1$ limit:

$$I(\tau) = I_0[1 - \tau] + \int_0^{\tau} d\tau' I_d(\tau') \, .$$

We find

$$I(\tau) = I_0 + I_0 \frac{\sigma/b}{L/R} \left[\frac{y}{(1 - y^2)^{1/2}}\right]_x^{x_d} \, . \qquad (2\text{-}29)$$

This last expression is a major result and deserves some comments. The function in brackets is evaluated in terms of the instantaneous value of x = U/c as the beam slows down. In particular, once x = b the electric field changes sign and I has reached its largest value. Our interests will focus on this maximum value of ΔI, when x = b, and we will be unconcerned with the eplicit time behavior of I. Notice, from this equation, ΔI is not sensitive to α in this $\alpha >> 1$ limit; this independence of α was anticipated by the upper limit on ΔI predicted by Eq. 2-24. In fact, ΔI depends crucially on the parameter σ/b. The ratio σ/b is not a function of the REB parameters, and, for the example cited in Table 2-5, σ/b = 1.07 s and L/R = 1830 s, so we find ΔI = 18.2 kA by setting x = b in Eq. 2-29. Consequently, $\Delta I/I_0$ = 0.2%, a very small current ripple, and we expect pulsed REB current drive to negligibly perturb plasma characteristics such as the MHD equilibrium. On the other hand, ΔI for this $\alpha >> 1$ case is much larger than the special case (α = 1) in which collisions dominate the REB dynamics. We can approximately order ΔI for these two limiting cases from Eq. 2-29 and Appendix A:

$$\frac{\Delta I}{I_0} \approx \begin{cases} \gamma_d (c/v_d)\nu_m^{-1}/(L/R) , & \alpha >> 1 \\ \gamma_d \nu_e^{-1}/(L/R) , & \alpha = 1 \end{cases} .$$

For the example of Table 2-5, ΔI is larger by a factor $c\nu_e/(v_d\nu_m) \approx 40$ when $\alpha \ll 1$ compared to the $\alpha = 1$ case. This translates, of course, into relatively lower values of $\langle P_d \rangle$ when α is large.

Another useful expression for ΔI obtains in the limit $\gamma_d >> 1$ and $b << 1$:

$$\Delta I \approx \frac{\gamma_d m_e c^2 2\pi R_0}{ecL} .$$

If we write the toroidal current's inductance as $L \approx \mu_0 R_0[\ell n(8A) - 1.75] \approx (1.4)\mu_0 R_0$, then we have $\Delta I = I_A[2(1.4)]$, where, in REB parlance, the Alfven current is $I_A \equiv 4\pi\varepsilon_0 m_e c^3 x_d \gamma_d / e \simeq 17000\, x_d \gamma_d$ amp. Thus, ΔI is always less than a few times the Alfven current.

The current increase, $I - I_0$, is plotted in Fig. 2-9 as a function of the beam velocity, U, for the case $\gamma_d = 4.0$ and $\mathcal{E}_d = 4.0$ MJ. The REB initially has $x_d = 0.968$ and U remains close to c even while most of the REB kinetic energy is lost, i.e., $x \gtrsim 0.9$ while $(\gamma - 1)$ decreases from 3.0 to 1.3. Most of the increase in $I - I_0$ occurs in this early phase when $U \approx c$. As the beam slows, the bump on the tail of the electron distribution moves toward the thermal electrons; the thermal distribution has a half width $v_e/c = 0.18$ for $T_e = 16$ keV. Thus, when x gets sufficiently small the two stream instability can no longer be excited, and α will most likely return to unity. Referring to the figure, we see b is sufficiently small that α will be close to one after the electric field changes sign (at $x \lesssim b$). Moreover, the evaluation of ΔI at $x = b$ is reasonable since $I - I_0$ is insensitive to a premature disappearance of the two-stream instability, provided $\alpha >> 1$ at least for the period $x_d \gtrsim x \gtrsim 0.7$.

For emphasis we reiterate a caveat on the validity of the theory. We assume once E changes sign the beam has slowed sufficiently that the two-stream mode ceases to exist. Thus, we assume $\alpha = 1$ for all times when $x < b$, so classical collisions dominate beam slowing until $U \approx v_e$. This means our theory is valid only for cases in which b is small [~ 0.1 to 0.4, such that $(\gamma - 1)m_e c^2 \sim$ 5-50 keV, and the beam has coalesced with bulk plasma electrons]. Another case, which we do not consider, exists if b is large. Here

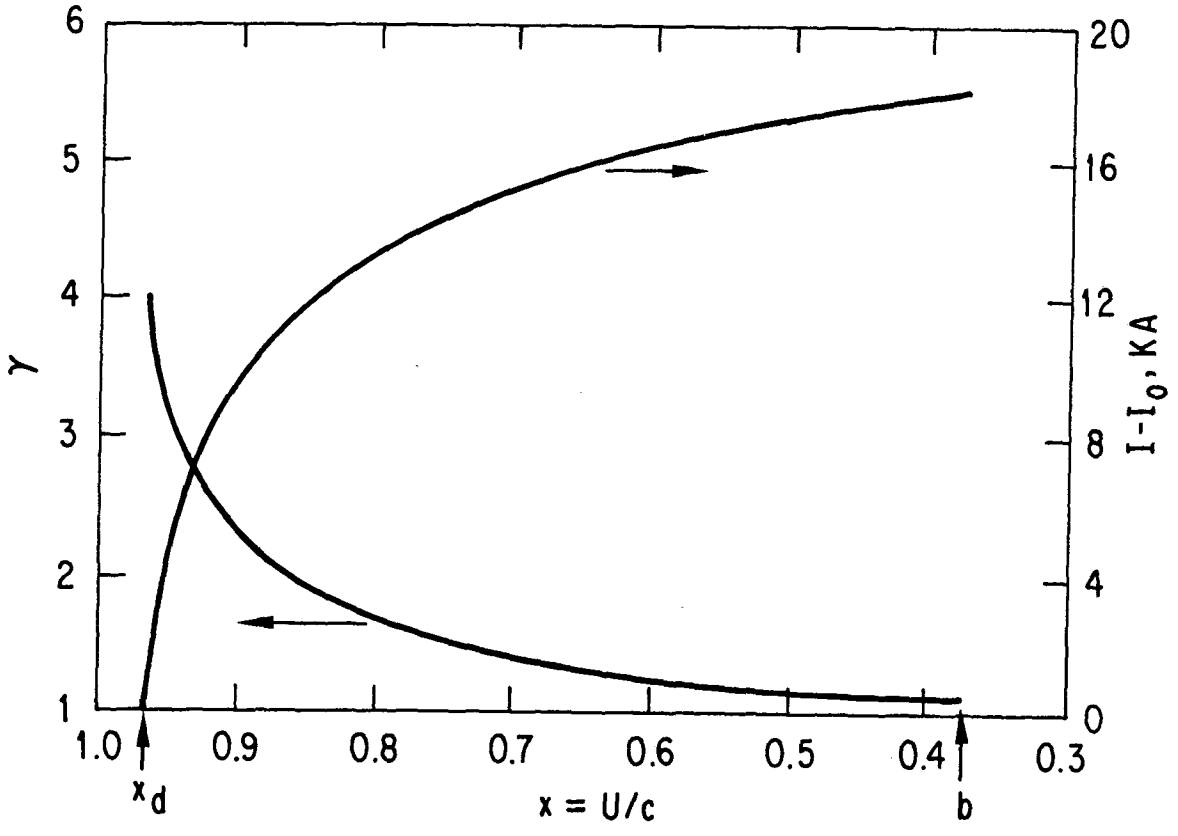

Fig. 2-9. γ_d = 4.0, $\mathscr{E}_d$ = 40 MJ, DEMO with R_o = 5.2 m, I_o = 9.01 MA, L = 10.6 μH.

the two-stream mode may exist with a large $\alpha >> 1$ after E changes sign. Then a "runaway" situation exists, the forward emf sustaining the beam population.

In the period for $x < b$ when collisions dominate the REB slowing down a small increase in I also occurs. However, using the methods of Appendix A it is straightforward to show that this increase is negligible compared to ΔI calculated from Eq. 2-29.

In the final period, $t > \Delta t$, the beam driver current has vanished so I must decrease. By our assumptons $\alpha = 1$ so the forward emf maintains an (ohmic) current for a period δt, given by Eq. 2-20. Once $t = \Delta t + \delta t$ the cycle is complete, $I = I_0$, and a new REB pulse is required. The period between pulses is thus $\Delta t + \delta t$ (recall $t_{t-0} << \Delta t$). The period Δt is much less than the collisional slowing down time, $\gamma_d \nu_e^{-1} \approx 50$ ms (see Appendix A), hence $\Delta t << \delta t$. Thus, combining Eqs. 2-20 and 2-29, the time-averaged REB power is

$$\langle P_d \rangle = \mathcal{E}_d/\delta t = {}_d(b/\sigma) \left\{ \left[\frac{y}{(1 - y^2)^{1/2}} \right]_b^{x_d} \right\}^{-1} , \qquad (2\text{-}30)$$

where $\mathcal{E}_d b/\sigma = (\gamma_d - 1) I_0^2 R/b$. The only beam variables entering this expression are γ_d and $\mathcal{E}_d$, b being a function of these variables.

Figure 2-10 displays $\langle P_d \rangle / I_0^2 R$ for the DEMO. Values of $\mathcal{E}_d$ yielding $b > 0.4$ are indicated by the dotted portions of the curves, and we recall that our theory is not applicable in this regime. Values of $\mathcal{E}_d$ corresponding to $b = 0.1$ are denoted with open circles; such low values of b may suffer from a premature disappearance of the two-stream instability and reduction in α, so $\langle P_d \rangle / I_0^2 R$ may be somewhat larger than shown in the figure. We also note that if γ_d approaches unity the beam is not highly relativistic $(U_d << c)$ and the two-stream mode is likewise unlikely to appear, so we focus our interest on cases with $\gamma_d \gtrsim 1.3$.

A noteworthy feature of Fig. 2-10 is the linear variation of $\langle P_d \rangle$ with $\mathcal{E}_d$ for a fixed γ_d in the range $b \lesssim 0.4$. In all cases, the minimum $\langle P_d \rangle$ approaches but is always larger than $I_0^2 R$, as predicted earlier. For the example $\gamma_d = 4.0$ we illustrate the energy flow during the current drive cycle Energy conservation demands that the return current ohmic heating plus the increase in inductive energy be equal to the work done by the REB against the reverse emf:

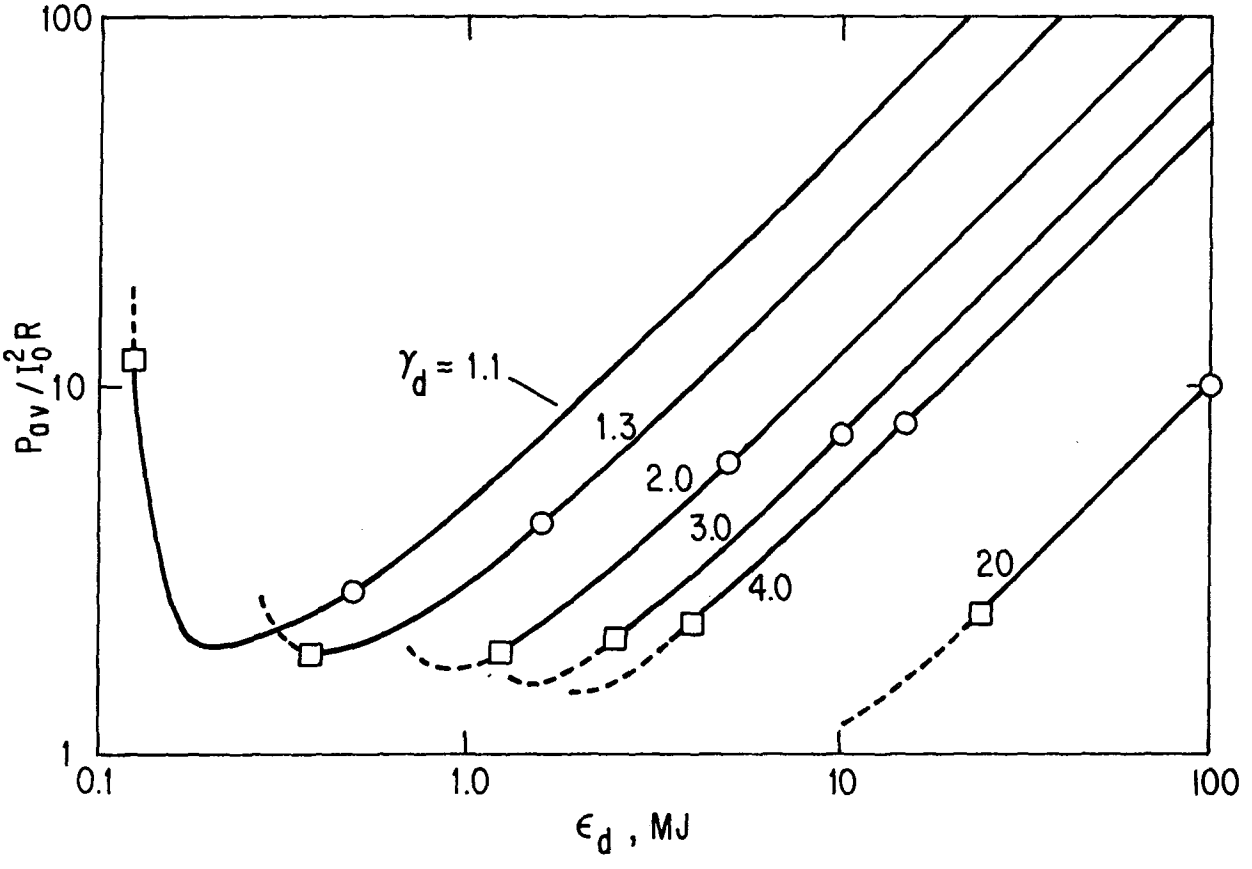

Fig. 2-10. DEMO with R_o = 5.2 m, I_o = 9.01 MA; dotted curve has b > 0.4, and open circle denotes b = 0.1.

$$\dot{W}_E = \dot{W}_\Omega + \frac{d}{dt}(LI^2/2)$$

or

$$-I_d V = I_p V + \frac{d}{dt}(LI^2/2)$$

$$= (-I_d + I)V + LI\dot{I} .$$

Substituting Eqs. 2-13 and 2-27 for I and V, respectively, and using Eq. 2-11 to perform the time derivative, the right-hand side of this equation explicitly reduces to $-I_d V$, verifying the accuracy of our formulation of the behavior of I. Thus, in Fig. 2-11 we display the energy split over a range of $\mathscr{E}_d$ values; the REB energy loss as x is reduced from x_d to b is

$$W_E = \mathscr{E}_d[1 - (\gamma_b - 1)/(\gamma_d - 1)] ,$$

where $\gamma_b \equiv (1 - b^2)^{-1/2}$; the inductively stored energy is $\Delta(1/2\ LI^2) = LI_0\Delta I$; and the return current heating is $W_\Omega = W_E - LI_0\Delta I$. We find that for $\mathscr{E}_d \gtrsim 4$ MJ the value of ΔI and, hence, the inductively stored energy is almost independent of $\mathscr{E}_d$, while the return current heating (the shaded portion in the figure) becomes the dominant energy sink. This demonstrates how, for a fixed γ_d, low $\mathscr{E}_d$ injection results in the most efficient current drive, wasting the least amount of energy on return current heating.

An alternative expression for $\langle P_d \rangle$, appropriate to the high γ_d, high $\mathscr{E}_d$ range where $\langle P_d \rangle \propto \mathscr{E}_d$, is

$$\langle P_d \rangle / I_0^2 R = 2\mathscr{E}_d / [I_A I_0 \mu_0 R_0] .$$

This can be rewritten in terms of the beam strength parameter, $\nu \equiv \gamma_d I_{do}/I_A$, as

$$\frac{\langle P_d \rangle}{I_0^2 R} = \frac{\nu}{\gamma_d} \frac{\mathscr{E}_d}{\mu_0 R_0 I_{do} I_0/2} .$$

In order to compare the normalized $\hat{j}/\hat{p}$ with other current drivers, we rewrite Eq. 2-30 as

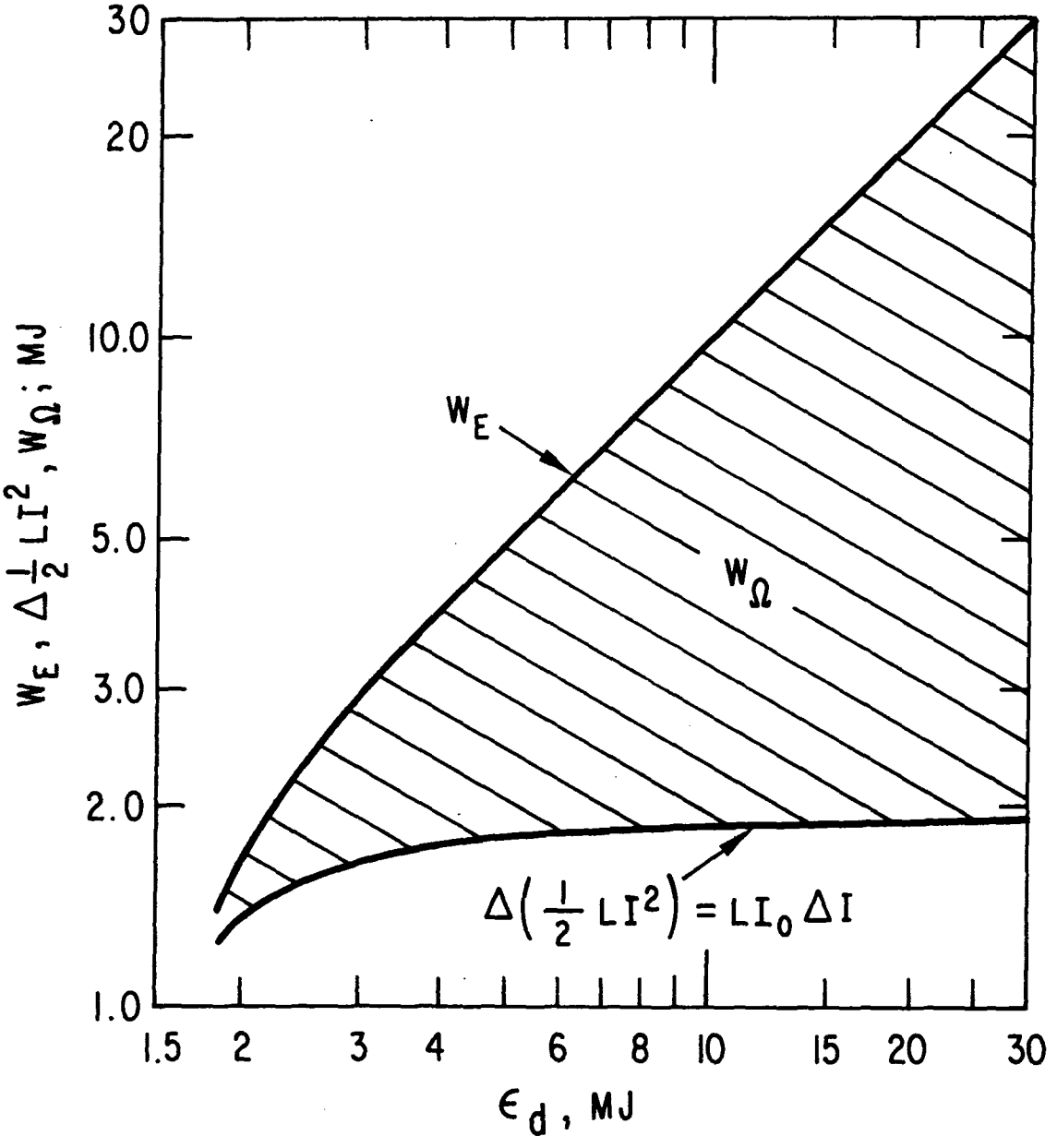

Fig. 2-11. DEMO beam energy losses for REB slowing down by reverse emf; $\gamma_d = 4.0$.

$$\frac{I_0}{\langle P_d \rangle} = \frac{n_e}{n_d} \frac{ce}{2\pi R_0 m_e c^2} \frac{\nu_m^{-1}}{(\gamma_d - 1)} \left[\frac{y}{\sqrt{1 - y^2}} \right]_b^{x_d} ,$$

assuming a uniform plasma and expressing R in terms of ν_m. Hirshman[27] relates the neoclassical ν_m to ν_o (defined prior to Eq. 2-3) as $\nu_m = K\nu_0$ where K is a function of Z_{eff} and the local aspect ratio. Then with $j/p = 2\pi R_0 I_0/\langle P_d \rangle$, we obtain

$$\hat{j}/\hat{p} = n_e V_p (m_e c^2/\mathscr{E}_d) \frac{(v_e/c)}{K} \left[\frac{y}{\sqrt{1 - y^2}} \right]_b^{x_d} , \qquad (2\text{-}31)$$

where V_p is the plasma volume. Figure 2-12 displays $\hat{j}/\hat{p}$ versus U_d/v_e for the DEMO with $\bar{T}_e$ = 16 keV, $n_e = 1.03 \times 10^{20}$ m^{-3} , Z_{eff} = 1.4, and an "average" ε = 0.125, for which K = 0.56; the case plotted has $\mathscr{E}_d$ = 4.0 MJ. In the figure values of $U_d/v_e \lesssim 4.8$ have $b \lesssim 0.1$ so $\hat{j}/\hat{p}$ may be smaller than indicated, as discussed earlier. Values of $U_d/v_e \gtrsim 5.5$ have $b \gtrsim 0.4$ and our theory is not applicable in this region. Consequently, for γ_d in the range ≈2-4 we find $\hat{j}/\hat{p}$ is very large (an order of magnitude higher than for CW power injection; cf. Appendix A), approaching the efficiency of inductively driven ohmic discharges. From Eqs. 2-3 and 2-31 we note that j/p is independent of n_e but is proportional to $T_e^{3/2}$; thus, as with other current drivers, high temperature (low density at fixed β) operation maximizes the current drive efficiency. It should be pointed out that $n_d/n_e \to 0$ as $\gamma_d \to \infty$ and that the two-stream instability vanishes[25] if $n_d/n_e \ll 10^{-3}$. Consequently, there is additional concern that α is not greatly enhanced at very large γ_d; already $n_d/n_e < 10^{-3}$ at γ_d = 4.0. (Moreover, we find for $\alpha \lesssim 10^2$ the collisional terms in the REB dynamic equations begin to be significant.)

To assess the impact of smaller values of α on the REB problem the REB equations were solved numerically, including collisions as well as the emf. The result for $\langle P_d \rangle$ is given in Fig. 2-13 for the DEMO for several values of α. Note that the solid curves are the limiting cases which have been derived in this section and in Appendix A.

We can estimate the enhancement of α for the DEMO. There are several instabilities which can increase the collision frequency between the plasma return current electrons and background plasma ions. The collective interactions which have received the most attention and which correlate well with experimental

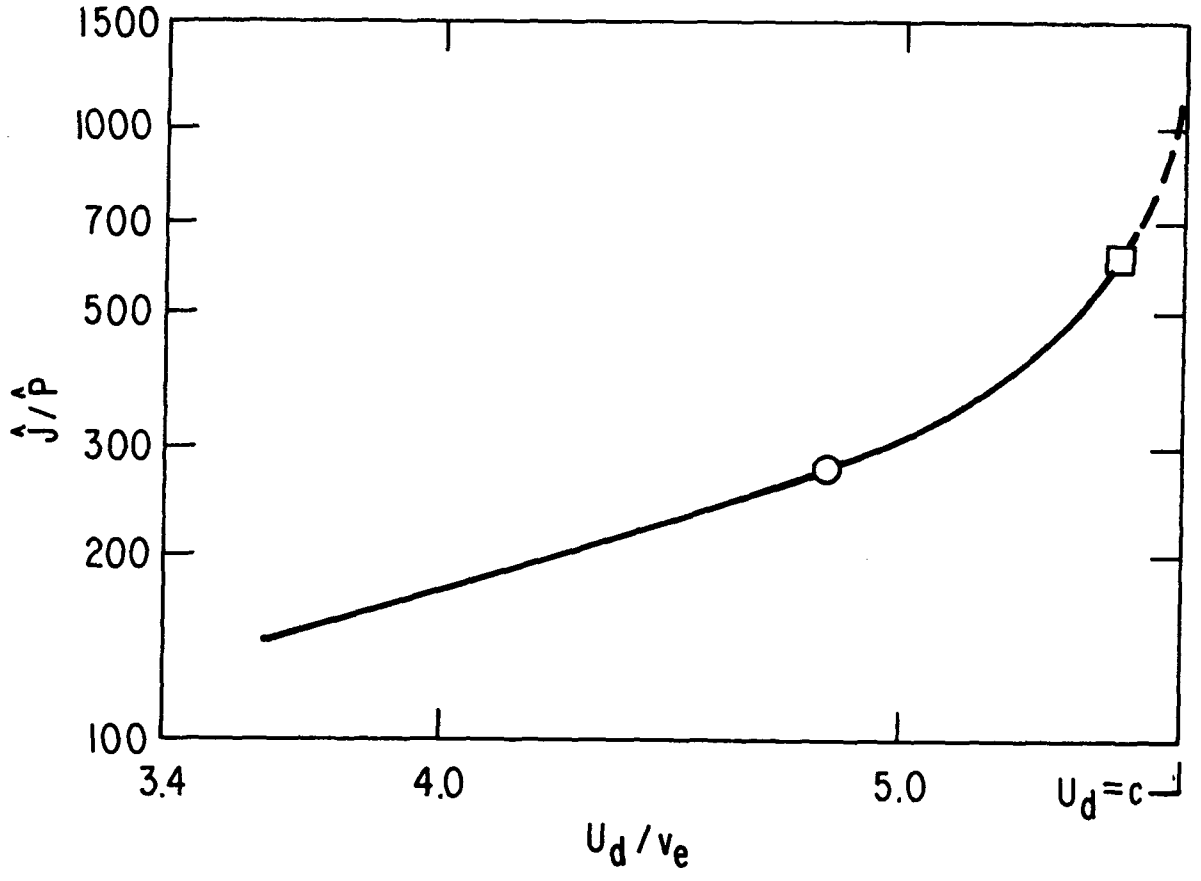

Fig. 2-12. REB with T_e = 16 keV, $\bar{n}_e = 1.03 \times 10^{20}$ m^{-3}, Z_{eff} = 1.4, ε = 0.125, V_p = 272 m^3, $\mathscr{E}_d$ = 4.0 MJ; the open circle corresponds to $\gamma_d \approx 1.7$; the box corresponds to γ_d = 4.0.

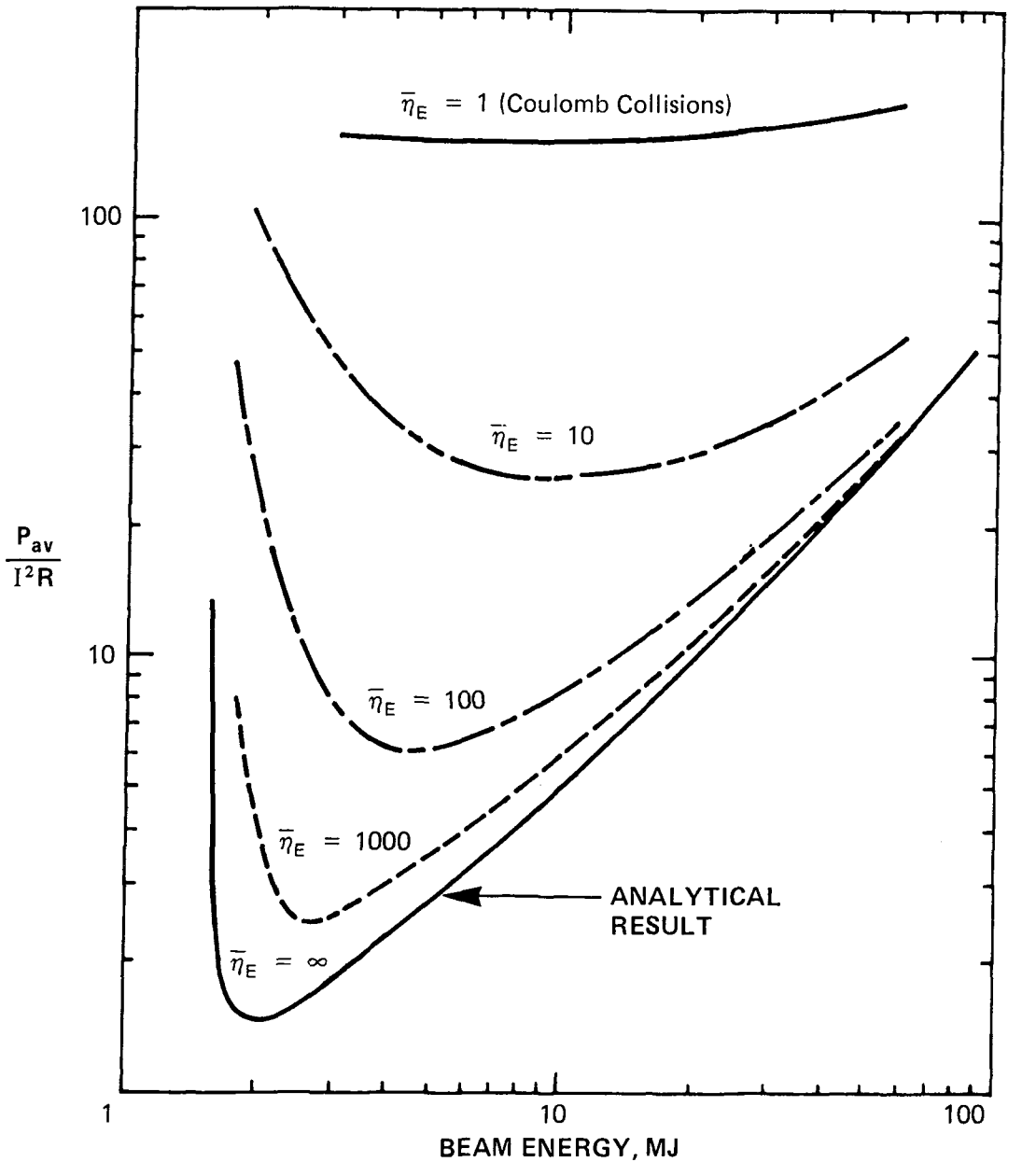

Fig. 2-13. Effect of beam-induced enhanced resistivity on the ratio of the average REB power to the I^2R plasma dissipation for DEMO (I^2R = 0.575 MW; $\bar{\eta}_e \equiv \alpha$); γ_d = 4.0.

data[23] are the Buneman, ion-acoustic[24], and the kinetic phase of the beam-plasma two-stream instability.[21,25] For the DEMO plasma and beam parameters the return current drift velocity, v_d, is much less than the electron thermal velocity, v_e, or the ion-acoustic velocity. Thus, the Buneman and ion-acoustic modes are stable and are not expected to increase the effective collision frequency.

Papadopoulos[21,25] has developed a full nonlinear treatment of the beam-plasma electron two-stream instability in the kinetic regime which predicts that the two-stream waves excite finite amplitude ion waves which can produce an effective d.c. resistivity. The corresponding effective collision frequency is $\nu_m^* = \overline{k\lambda_D}\, 2\delta$, where $\overline{k\lambda_D}$ is the characteristic wavenumber Debye length product for the ion waves and δ is the linear growth rate of the two-stream instability in the kinetic regime. The theory includes both analytical models and numerical simulations and is in agreement with experimental data.[23]

For the DEMO plasma and beam parameters the ratio of the beam number density, n_d, to the plasma electron number density, n_e, is $n_d/n_e = 4.8 \times 10^{-4}$. Assuming that the average angle of the beam, $\bar{\theta}$, is greater than 15 deg $(\bar{\theta} > 1/\gamma)$ and $(\Delta n/n_d) < 0.15$, the two-stream instability is in the kinetic regime.* The quantity $\Delta n/n_d$ is the fraction of the beam which can be considered as mono-energetic.

The average angle $\bar{\theta}$ can be controlled by shaping the cathode or injecting the beam at a non-zero angle with respect to the tokamak magnetic field. The ratio of $\Delta n/n_d$ depends on the kinetic energy of the injected beam and thus is also controllable.

The linear growth rate,[25] δ, for the two-stream instability for the DEMO plasma and beam parameters $(\gamma_d = 4,\ n_d/n_e = 4.8 \times 10^{-4},\ \bar{\theta} = 17$ deg, $n_e = 1.2 \times 10^{20}\ m^{-3})$ is $\delta = 6.8 \times 10^8\ s^{-1}$. The corresponding electron-ion Coulomb collision frequency is $\nu_m = 3 \times 10^3\ s^{-1}$. Since the growth rate exceeds the Coulomb collision frequency the two-stream instability is unstable and an enhanced collision frequency is expected in DEMO while the beam is present.

---

*The qusasihydrodynamics phase of the beam plasma mode is not considered since $\bar{\theta} > 1/\gamma$.

The effective collision frequency can now be determined. The analytic approximation for $\overline{k\lambda_D} = 0.03\text{-}0.3$ depending on the initial noise level of the secondary waves. The numerical simulations,[25] when scaled to the DEMO parameters, predict $\overline{k\lambda_D} = 0.1$, which lies within the range of the analytical predictions. The effective collision frequency is $\nu_m^* = 4 \times 10^7\text{-}4 \times 10^8\ s^{-1}$. Thus, the effective d.c. resistivity is enhanced by a factor of 10^4 to 10^5 over the d.c. resistivity based on Coulomb collisions alone.

We next study the DEMO performance at various temperatures with the REB driver. We assume $\alpha > 1000$, so by referring to Fig. 2-13 we expect $\langle P_d \rangle \approx 2.5\ I^2R_0$. In addition, we take a conservative position that α may return to unity prematurely and increase $\langle P_d \rangle$ still further; as a consequence we adopt the ratio $\langle P_d \rangle / I_0^2 R \equiv 5$ for the power balance calculations which follow. The fusion power and I_0^2R were computed over the range 6 keV $\leq \bar{T}_e \leq$ 18 keV, and the net power, from Eq. 2-1, is plotted in Fig. 2-14 for two different REB system efficiencies. The REB system, described in Appendix B, has several sources of uncertainty in estimates of its power efficiency, η_{REB}. In the best case all the electrons leaving the cathode are successfully trapped in the torus. On the Macrotor experiment, however, about 50% of the beam returned and hit the back of the diode.[20] Another source of concern is the initial pitch angle spread of the REB in the plasma. If the perpendicular velocity moment of the REB distribution is negligible compared to c then the two-stream mode is most strongly excited,[25] while an isotropic phase space distribution will tend to reduce the mode amplitude and the magnitude of α. We thus display P_n for optimistic and pessimistic estimates of η_{REB}. The quantity I_0^2R is so small compared to the DEMO's fusion power that P_n is close to the plant's gross electric output, $0.36 \times P_f$, regardless of the REB efficiency. We conclude from this power balance that the pulsed REB is indeed attractive for driving tokamak currents.

2.2.3 Other Current Drive Methods With Particle Injection

Here we consider tokamak currents driven by "automatic" means such as the bootstrap effect or the anisotropic loss of fusion alpha particles, as well as the intentional injection of momentum from ionized beams.

The bootstrap current is a diamagnetic response of the plasma to density and temperature gradients and is an artifact produced by the single particle guiding center excursions away from flux surfaces in a tokamak.[28] The

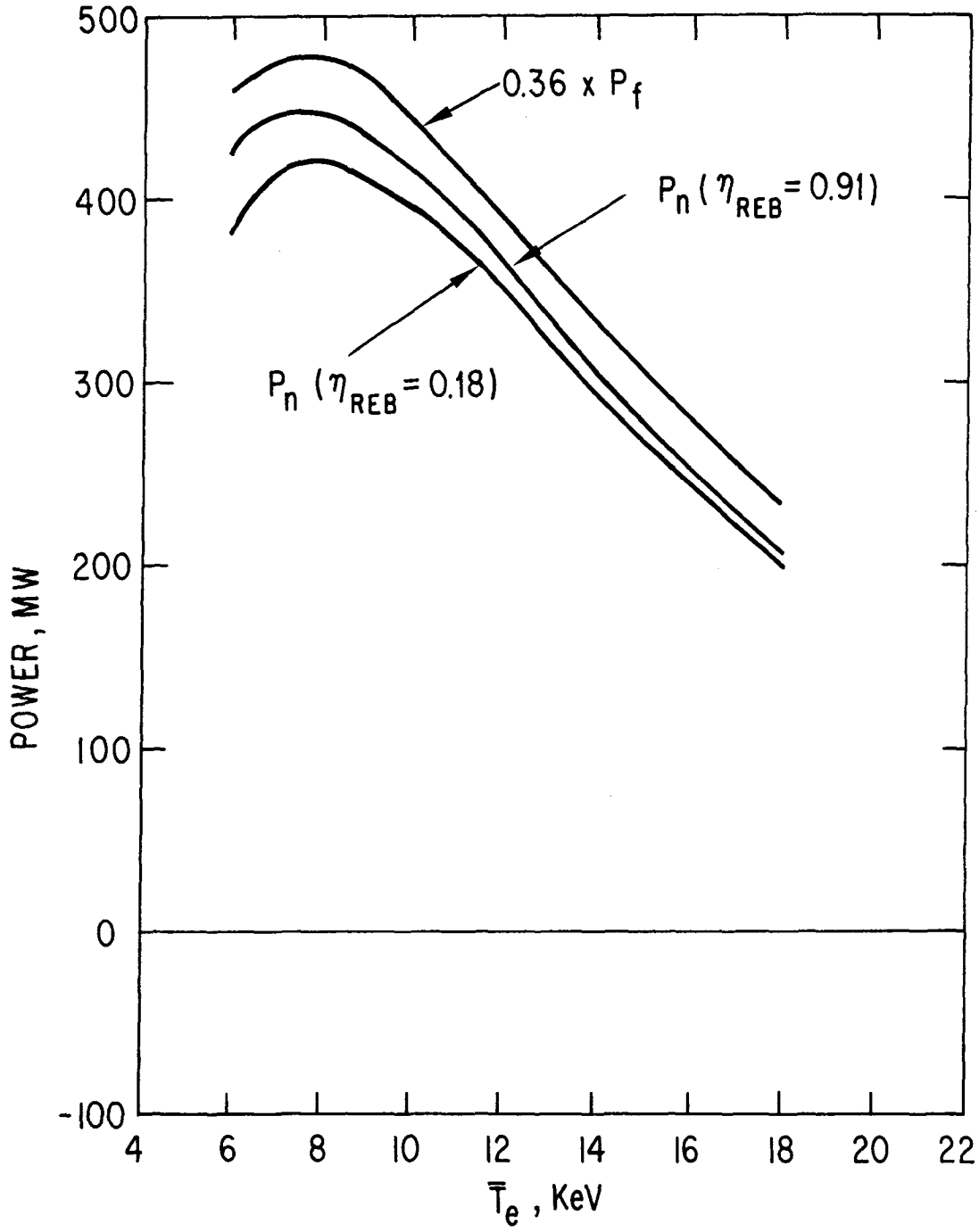

Fig. 2-14. Gross and net electric power from DEMO with REB driver (γ_d = 4.0, $\mathscr{E}_d$ = 4 MJ) and different driver efficiencies.

bootstrap current was proposed for maintaining steady-state operation of the MARK-I tokamak reactor designed by the Culham group, although no theoretical analysis of the plasma behavior was attempted in that study. In the neoclassical theory this current flows along the magnetic field, provided only that the proper, peaked pressure profile is maintained. Thus, the maintenance of a peaked density profile, for example, must be accomplished against the plasma's tendancy to flatten in density due to neoclassical particle diffusion. In the steady state this determines the rate that canonical angular momentum must be supplied, e.g. via central fueling of the plasma, in order to create the desired toroidal current.

One drawback according to the bootstrap theory is the tendancy to generate current density only where the pressure gradients are large, away from the magnetic axis.[28,29] Thus, hollow current densities are most likely to occur in the absence of an additional central current source; on these grounds the bootstrap current by itself does not satisfy the DEMO equilibrium requirements.

A more serious challenge to the credibility of this driver is the complete dependence on purely neoclassical effects. If, for example, turbulence severely destroys flux surface uniformity on a scale the order of a thermal electron poloidal Larmor radius, $\approx v_e m/eB_p$, then neoclassical theory is no longer a correct description of the plasma's behavior. There is ample evidence, of course, that electrons do not behave neoclassically. In a thorough analysis of the ISX-B experiment by Hogan[29] there is seen to be no evidence of the bootstrap current at all, despite the fact that $\beta_p \gtrsim \sqrt{A}$, which theoretically should allow measurable effects.

Another natural source of toroidal current, requiring only particle fueling, is the preferential loss of fusion alpha particles in a tokamak reactor, due to the asymmetry of co-streaming and counter-streaming neoclassical ion orbits, an effect first considered by McAlees.[30] A convenient analytic expression for the toroidal current of alpha particles is provided by Kolesnichenko:[31]

$$I_\alpha = 10^{-18}\, \tilde{n}_\alpha \left[1 - (v_c/v_\alpha)\right] \frac{a^2}{A} \left(\frac{3.82}{\sqrt{A}\, I}\right)^{\mu+1} Q_\mu H \,, \qquad (2\text{-}32)$$

where SI units are assumed, except for currents, which are in MA. This current is proportional to the density of suprathermal alpha particles, defined as

$$\tilde{n}_\alpha = n_{DT}^2 \langle \sigma_f v \rangle (\tau_s/4) \ , \tag{2-33}$$

where $\langle \sigma_f v \rangle$ is the fusion reactivity, and where we denote the alpha particle slowing down time as

$$\tau_s = \frac{0.21\ T_e^{3/2}}{\ell n\ \Lambda \times n_e \times 10^{-20}} \ . \tag{2-34}$$

At the center of the DEMO plasma example in Table 2-4, the density $\tilde{n}_\alpha$ is substantial, $\tilde{n}_\alpha = 3.7 \times 10^{18}\ m^{-3}$. Below a critical speed, v_c, Coulomb collisions isotropize the alpha particle distribution in velocity space; it is only at higher speeds that an anisotropy occurs which yields the toroidal current. The critical velocity is determined by alpha slowing on electrons and is

$$v_c = \sqrt{2}\ (m_e/m_\alpha)^{1/3}\ v_e \ . \tag{2-35}$$

For our example, the alpha current is proportional to $[1 - (v_c/v_\alpha)] = 0.57$. In Eq. 2-32 there appears the factor $\mu \equiv \alpha_n + 7\ \alpha_T/2$; an approximation to the DEMO profiles, with $\alpha_n = 0.3$ and $\alpha_T = 1.2$, yields $\mu = 4.5$, for which[31] $Q_\mu = 3.55$. Now, it is well known that alpha particle collisionless orbits become better confined as the product IA increases, and this is the downfall of this current drive option since the DEMO has such a large current and aspect ratio. We find, from Eq. 2-32, $I_\alpha = 94\ H$ amperes, where H is a factor (≈ 0.5) accounting for the nonuniformity of the current density profile. In addition, the electrons pushed by the alphas reduce the total current. By analogy with Eq. 2-2, since I_α flows parallel to I,

$$I = I_\alpha \left\{ 1 - \frac{Z_\alpha}{Z_{eff}} \left[1 - 1.46\sqrt{\epsilon} \left(1 + \frac{0.7}{Z_{eff}} \right) \right] \right\} \ . \tag{2-36}$$

For an average $\varepsilon = 0.125$ and $Z_{eff} = 1.4$, we find $I = 0.68\ I_{\alpha} \approx 32A$. We conclude, thus, that this natural alpha particle driven current is far too small to contribute to the steady-state current required for the DEMO.

Suggestions related to the proposals above would establish seed currents, driven by neutral beams[28] or by the natural alpha particle current,[31,32] which would be amplified by the bootstrap effect to establish the total toroidal current. Due to the experimental failure to observe the bootstrap current[29] we must conclude that these proposals do not present reliable options upon which to design the DEMO reactor.

In another recent suggestion Dawson and MacKenzie[33] pointed out that heavy ion beams could, in principle, supply energy and momentum to a tokamak. As an example, singly charged sodium ions, Na^{+}, are relatively easy to produce (compared to negative ions, like D^{-}, considered in Sec. 2.2.1), and, since no beam neutralization is required prior to injection, there would be no need to develop highly efficient neutralization systems (such as the photodetachment system for a D^{-} beam). One difficulty with this scheme is charged-particle transport through the strong toroidal field, including the complicated fringing field in the vicinity of the blanket, shield, and TF coils. This problem is severely compounded by the requirement for inboard (high field side) injection of the beam when $Z_b > Z_{eff}$, in order to drive currents. This follows from Eq. 2-2 where it is evident that counter-injection $(j_b \not\parallel j)$ is necessary to produce toroidal currents in the proper direction whenever $Z_b \gg Z_{eff}$ with small values of ε. Examination of collisionless orbits shows counter-injected ions are uncontained if launched on the outboard edge of a flux surface. Hence, the ions must be injected further inboard in order to assure additional ionization and capture instead of following a simple trajectory into the first wall. (Injection of He^{+} can, of course, avoid this requirement, provided $Z_{eff} \gg 2$.)[34]

In order to assess the current drive efficiency of this method the same Monte Carlo simulation was done as described in Sec. 2.2.1 for neutral beam driven currents. Generally speaking, the results indicate that ion injection may prove competitive with neutral beams for heating.[13] However, ion injection cannot be tangential to the toroidal field if centrally peaked power deposition is demanded, and, in consequence, it is not practical to inject toroidal momentum with this driver.

We conclude this section with a discussion of a potential current driver which has many attractions, namely the pulsed injection of intense, charge-neutralized ion beams. Intense ion beams have several attributes. In the first place, the last half decade has seen the rapid development of very high intensity ion sources, including the reflex triode and an improved device, the reflex tetrode.[35,36] These tubes, which we shall term ion diodes, effectively prevent electrons from being accelerated across the high voltage electrode gaps and thus very efficiently deliver energy from the pulsed power supply to the ion beam. This use of pulsed, megavolt diodes produces very high currents and efficient beam acceleration compared to the sources and rf accelerators proposed in Sec. 2.2.1 for CW ion beams. In addition, since the high energy ions do not require neutralization, there is no need to develop the highly efficient (photodetachment) neutralizers which plague neutral beam systems!

How does this ion beam miraculously penetrate the strong toroidal field into the plasma interior? The answer lies in the fact that the ions pull along electrons from the plasma in the vicinity of the anode so the propagating beam is space-charge neutralized. Dozens of experiments have demonstrated that such a beam propagates unimpeded through magnetic fields due to the $\underline{E} \times \underline{B}$ polarization drift[37] established by charge separation in the beam along the direction normal to $\underline{B}$. The best demonstration and analysis of this effect is by Robertson's group,[38] who establish the requirement $\omega_{pb}^2/\Omega_b^2 >> \sqrt{m_i/m_e}$ for beam penetration of the vacuum field. Ion diodes can readily satisfy this criterion, and experiments with plasma guns[39] also confirm that the rotational transform of field lines in a plasma-filled torus do not short the $\underline{E}$ field or inhibit beam propagation.

Manheimer and Winsor[40,41] have suggested several mechanisms which could be employed to trap the intense ion beam for heating a tokamak and initiating the toroidal current. The most attractive mechanism, requiring no external field changes or density oscillations, would invoke beam induced ion acoustic turbulence which would yield an anomalous plasma resistivity, analogous to that encountered with REB injection (Sec. 2.2.2). The resulting large reverse emf would act to retard the forward momentum of the beam ions, settling them on contained orbits as circulating ions. We note that the success of intense ion beam current drive would then rely on nonlinear plasma effects, as does

the REB current drive proposal. However, it may be that ion beam penetration is superior to REB penetration since the ion orbits are less determined by collective effects, such as eddy currents in the first wall.

We point out here that the proposal of Manheimer and Winsor can be extended to consider fully steady-state, pulsed current drive, quite similar to the REB system analyzed already. The electrons injected along with the beam will have energies negligible compared to that of the plasma target electrons, so they, in fact, can be assumed to be a part of the thermal distribution and to contribute to the plasma current, I_p, as governed by Eq. 2-7. (We note, however, an additional term should be added to Eqs. 2-6 and 2-7 to account for momentum transfer from the beam to the plasma electrons.) Thus, the work of Sec. 2.2.2 applies to ion beam injection as well as to the REB problem. (We note that the equations in Refs. 40 and 41 are similar to those presented here.) One obvious difference from the REB situation is the opposite direction of beam injection, as depicted in Fig. 2-15. As evident from Eq. 2-27 the beam current must exceed I_0 in order to achieve $\dot{I} > 0$. This will be a demanding requirement for intense ion beams since the pulse length is quite short; typically $t_{t-o} < 1\ \mu s$[41] so beam stacking will not occur. However, beams at MeV energies have been produced at MA current levels,[36] so we feel hopeful that 10 MA beams could be developed in the DEMO time frame. Since beam current densities are of the order 1 kA/cm^2 we expect diodes with areas of one square meter will be required. (We note, though, that high current densities may incidentally inject a substantial fraction of nonhydrogen species in the beam,[36] which may be undesirable. In addition, repetitive operation at about one Herz may be a difficult goal to achieve at high current densities.)

An intense ion beam also differs from an REB in that the beam is not "stiff"; i.e., the ions are not relativistic, so the driver current decreases in linear proportion with the decrease in driver momentum. Consequently, Eq. 2-16 would not accurately model $I_d(t)$. In addition, the momentum loss terms for the beam ions will be different from those of relativistic electrons, and the resistivity anomaly, α, may be less than that associated with REB injection. All these effects can be expected to produce quantitatively different results than for the REB case. In any event, $\langle P_d \rangle$ will exceed $I_0^2 R$, perhaps by a large factor. Detailed study of the intense pulsed ion driver must be

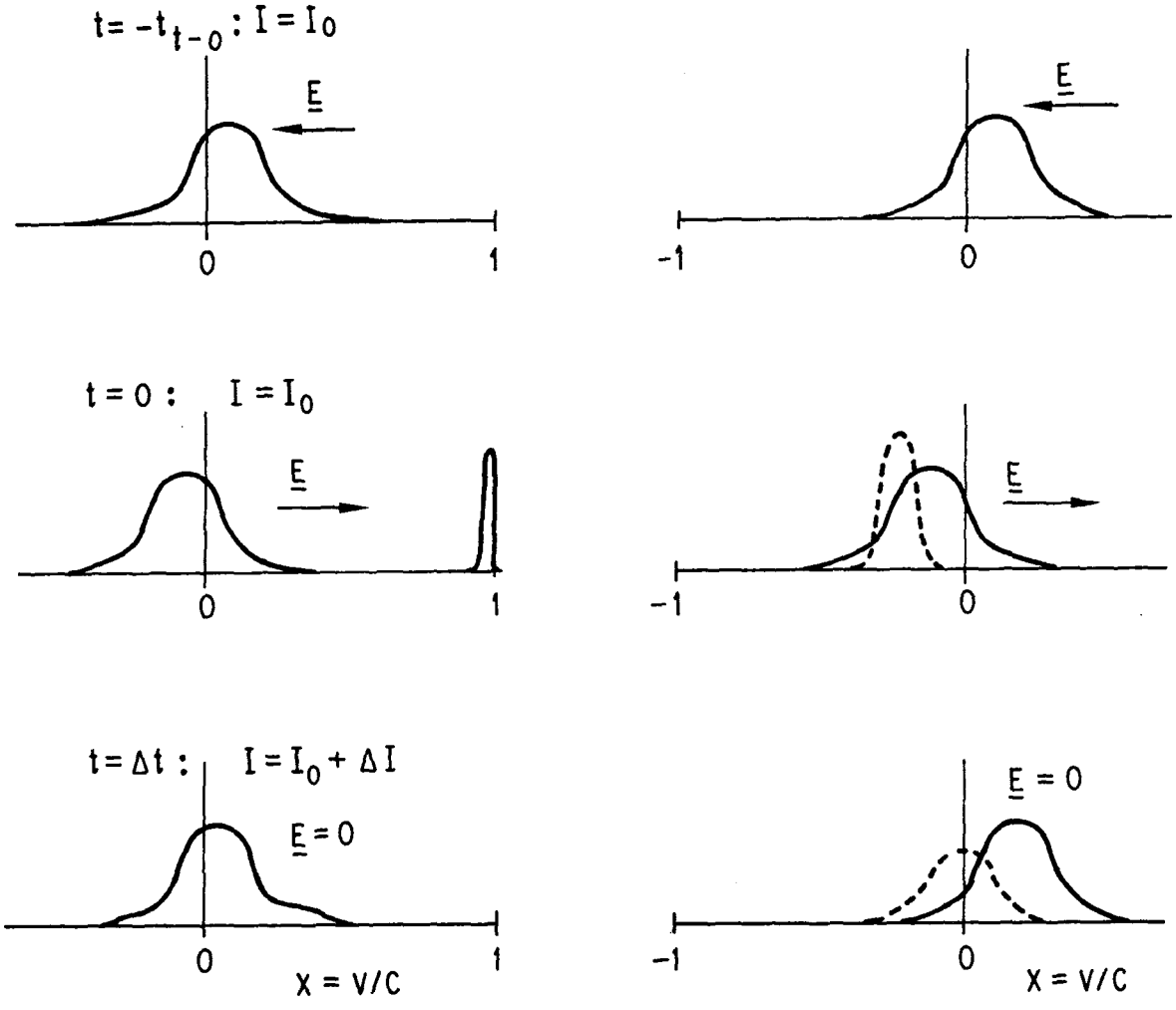

a. REB: ELECTRON DISTRIBUTION FUNCTION

b. INTENSE ION BEAM: ELECTRON DISTRIBUTION FUNCTION (SOLID); BEAM ION DISTRIBUTION (DOTTED).

Fig. 2-15. Comparison of particle distribution functions during pulsed REB and intense ion beam injection.

deferred at this point, but we conclude that it promises certain features which may recommend it as a serious contender for the DEMO current driver.

2.3 Wave Drivers

2.3.1 Wave Classification

We adopt the wave driver classification introduced in Ref. 42, namely, indirect current drive methods (e.g. anisotropic heating) which do not directly transfer momentum from waves to electrons, and indirect momentum transfer techniques. The latter drivers are further divided into high speed and low speed waves, referring to the parallel wave phase velocity normalized to the electron thermal speed, $\omega/k_{\parallel} v_e$. This is an important parameter since $\hat{j}/\hat{p}$ in Eq. 2-3 displays qualitatively different behavior in the two limits for $\omega/k_{\parallel} v_e$.

2.3.2 Indirect Wave Driven Currents

2.3.2.1 Minority Cyclotron Damping

The first, indirect means of generating current with waves which we consider is minority heating via the fundamental cyclotron resonance. This method, proposed by Fisch,[43] establishes a circulating ion beam, with $Z_b \neq Z_{eff}$, and this beam transfers momentum to electrons, the total current then resulting from ion and electron drifts. Physically the effect is the same as discussed in Sec. 2.2.1, but it is unnecessary to inject a beam or any significant amount of momentum. A traveling fast wave is simply launched into the plasma, and, provided it is strongly damped on one side of the minority cyclotron layer, only minority ions traveling in the preferred direction are heated. This anisotropic heating lowers the collision frequency of these preferred ions, allowing them to retain a greater momentum content than their counterparts streaming in the opposite direction.

A distinct advantage of minority heating is the ability to closely control the spatial damping profile. Experiments on tokamaks such as PLT[44,45] confirm the linear damping theory and suggest that this driver may reliably enable external control of the wave's spatial damping. Both the local wave power dissipation, $p(r)$, and the normalized $\hat{j}/\hat{p}$ depend on the quantity $w \equiv (\omega - \Omega_I)/k_{\parallel} v_I$, which is the Doppler shifted parallel velocity of resonance normalized to the minority thermal speed. In his development of this

problem Fisch assumes straight field lines and takes the $\varepsilon = 0$ limit of Eq. 2-2, viz $j = j_I(1 - Z_I/Z_{eff})$. Then he finds

$$\hat{j}/\hat{p} \approx \frac{3(1 - Z_{eff}/Z_I)}{1 + m_I/m_i} \frac{w^2}{(1 + Y w^3)^2} , \qquad (2\text{-}37)$$

where $Y = 0.266\sqrt{m_e/m_I}\,[1 + (m_I/m_i)]^{-1}$, and where the subscripts I and i refer respectively to the minority and majority (DT) species. We performed ray tracing calculations for the DEMO in order to evaluate p(r) and then to estimate the total power required to generate $I_0 = 9$ MA. Both Be, a naturally occurring minority species, and ^{3}He were considered, but we present only the ^{3}He results, which appear more attractive. We studied a plasma with $\bar{T}_{DT} = \bar{T}_{^3He} = 19$ keV, $\bar{n}_e = 1 \times 10^{20}$ m^{-3}, $\bar{n}_{^3He} = 4 \times 10^{18}$ m^{-3} , and $Z_{eff} \simeq 1.2$.

In order to provide ^{3}He cyclotron resonance along the whole minor radius, from $R_0 = 5.2$ m out to the outboard edge at 6.5 m, a tunable source, ~ 40-50 MHz is needed. At these frequencies, a phased array of re-entrant waveguides[46] could provide an attractive launcher. Such a launcher, located at the outboard plasma midplane, would span approximately one meter vertically, effectively subtending a poloidal angle of ±0.24 radians. Such a localized source results in a broad poloidal mode spectrum, and we selected test rays with a variety of mode numbers, m = 0, ±1, ±2, and ±4. The toroidal mode spectrum is determined by the waveguide phasing as well as the number and toroidal dimensions of the waveguide sources; we followed rays with n = 2, 12, and 22. In the first series of calculations, with a wave frequency $f = \omega/2\pi = 48.97$ MHz, about 65% of the incident power is absorbed by ^{3}He, all at a localized region in minor radius, $0 \lesssim r \lesssim 0.15$ m. However, a large portion of the power is dissipated by rays with $w \lesssim 4$. In the next set of runs, f = 45.47 MHz and about 80% of the power is absorbed by ^{3}He, all in the vicinity of $0.33\ \text{m} \lesssim r \lesssim 0.55$ m. Again much the power is absorbed by ^{3}He ions with $w \lesssim 4$. Now, $\hat{j}/\hat{p}$ has a maximum for ^{3}He of 13.7 when w = 6.7, as seen from Eq. 2-37. From our calculations we have found considerable rf power is absorbed at $w < 4$, so we feel it is more appropriate to evaluate Eq. 2-37 at w = 4, for which we find $\hat{j}/\hat{p} = 9.1$. Reference to Fig. 2-5 shows this ^{3}He minority current drive efficiency to be comparable with that for neutral beam driven currents when $\varepsilon = 0$.

However, since $Z_{^3He} > Z_{eff}$, we see from Eq. 2-2 that the ^{3}He current flows opposite to the net current and neoclassical effects (electron trapping) reduce the value of j and, hence, $\hat{j}/\hat{p}$. Fokker-Planck evaluations of $\hat{j}/\hat{p}$ for non-zero ε by Chiu, et al.[47] confirm this conclusion; in fact, their results indicate that near the plasma surface ($\varepsilon \gtrsim 0.1$) reversed current density may occur. Thus, based on the relatively modest $\hat{j}/\hat{p}$ values predicted and the unimpressive coupling to ^{3}He (65% near the magnetic axis), we are not optimistic regarding the prospects of this driver for the DEMO. For comparison with neutral beam-driven currents we computed P_n versus $\bar{T}_e$ from the approximate relationship $I/P_{ICRH} = 0.079\ (\bar{T}_e/18\ \text{keV})\ \left(0.84 \times 10^{20}\ m^{-3}/\bar{n}_e\right)$ (cf. Eq. 2-5). Our results, for two values of η_{aux}, are shown in Fig. 2-16. The curvès are dotted to indicate that neoclassical effects are not included; their inclusion leads to even worse performance for ^{3}He minority current drive.

2.3.2.2 Alpha Particle Landau and Transit Time Damping

A drawback of the ^{3}He minority current drive method described in the previous section is the fact that ^{3}He is relatively expensive; it is not a naturally occurring isotope. Some will be consumed by D-^{3}He fusion, and the remainder will require separation from the exhaust gas and reinjection with the fuel. Alpha particles, on the other hand, are copiously produced in the plasma and can serve as an ion beam current driver provided $Z_\alpha \neq Z_{eff}$. This is difficult to imagine with anisotropic ion cyclotron (ICRH) heating of the alphas because the alpha and deuteron cyclotron resonances are spatially coincident, $\Omega_\alpha = \Omega_D$. It may be possible to preferentially heat the alphas, however, by selecting a wave which is principally damped via alpha particle Landau damping.

This idea consists of using rf power to prohibit the alpha particles from slowing down isotropically and in pushing the alpha particles in a preferential direction to form the alpha particle beam. In a reactor, new alpha particles are born isotropically in velocity space and slow down via Coulomb interactions with the background plasma particles. In the absence of rf power the alpha particle distribution function remains isotropic during the slowing down, and there is no net current. In order to generate current, the alpha particle distribution function has to be made asymmetric. In the following, we consider the d.c. current driven by traveling fast waves. This wave seems particularly suitable for producing a beam when one notices that the phase

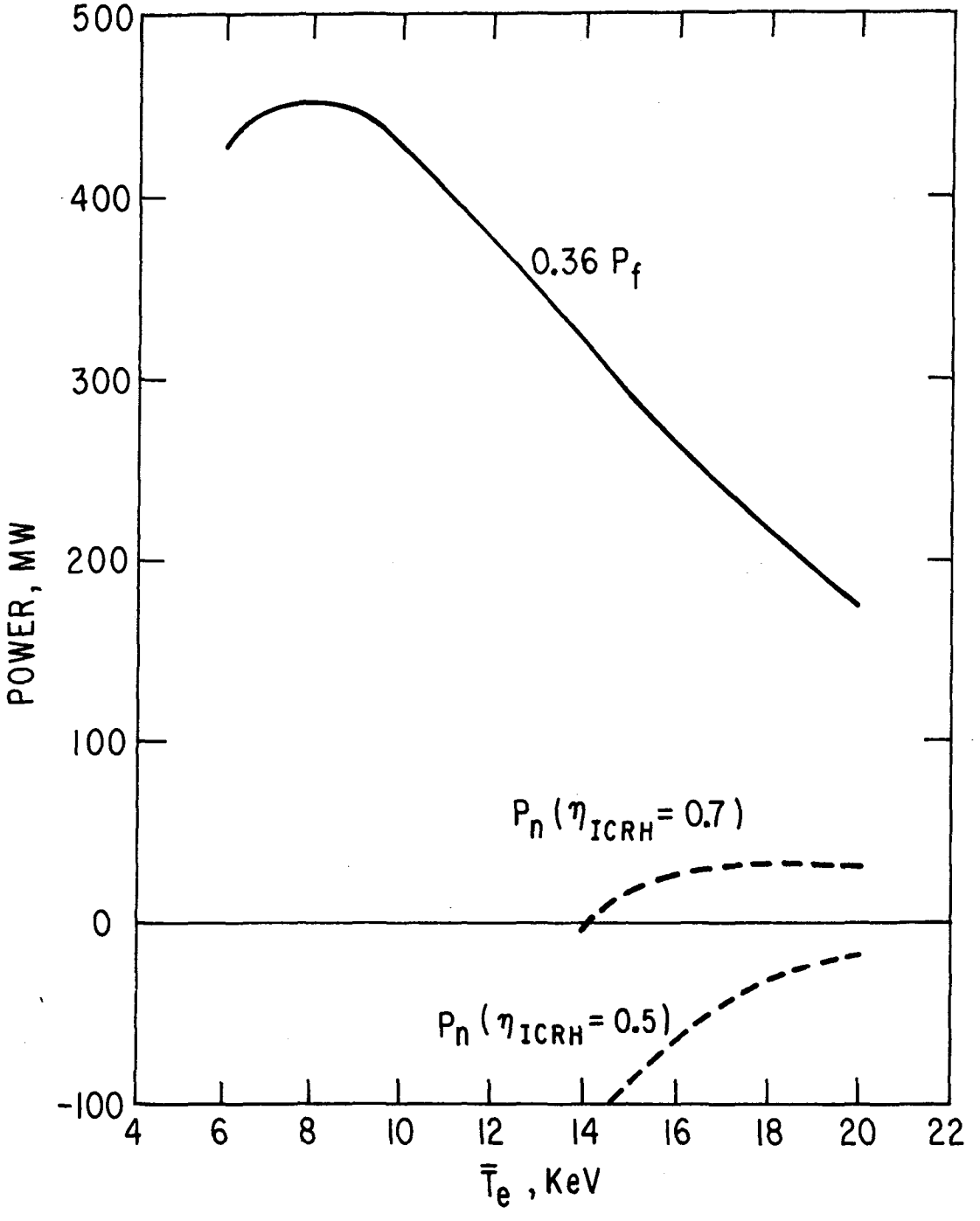

Fig. 2-16. Gross and net electric power from DEMO with ^3He minority ICRH (40-50 MHz, $Z_{eff} \approx 1.2$) and different efficiencies; dotted curves indicate that neo-classical effects are neglected.

speed of such waves is of the order of the Alfven speed, which, in a reactor-type plasma, is roughly the same as the speed of the alpha particles.

The fast wave is an electromagnetic mode in which the electric field is primarily perpendicular to the d.c. magnetic field, and because of this property it can propagate in a plasma over a wide frequency range from below the ion cyclotron frequency Ω_i all the way up to the electron cyclotron frequency Ω_e. One of the particular advantages of the fast wave is that, with appropriate frequencies which depend on the magnetic field strength and plasma density, it can be a waveguide eigenmode in tokamaks and therefore the coupling to external rf power sources can be very efficient.

The fast wave eigenmode structures of a bounded plasma are calculated by solving the coupled wave equations

$$\nabla \times (\nabla \times \underset{\sim}{E}) = \frac{\omega^2}{c^2} \underset{\sim}{K} : \underset{\sim}{E} , \qquad (2\text{-}38)$$

with appropriate boundary conditions, where $\underset{\sim}{K}$ is the plasma dielectric tensor. The geometry is assumed to be a metallic chamber with a rectangular cross section of width 2a and height 2b and a length L which lies along the z-axis.

For situations where the wave electric field $E_\parallel$ in the direction of the confining magnetic field is small, the perpendicular electric field $E_\perp$ and the associated eigen-wave number can be evaluated using the cold plasma dielectric tensor.[48] The solution for $E_\perp$ is obtained numerically from a computer code MOTHRA.[49] The wave magnetic field is calculated through the relation

$$\omega \underset{\sim}{B} = -i\nabla \times \underset{\sim}{E}_\perp .$$

Through an iterative scheme, the small parallel electric field $E_\parallel$ is then determined from the parallel wave magnetic field $B_\parallel$ by introducing some hot plasma effects. The details of the calculation are available in Ref. 49. It is convenient to plot the the parallel magnetic field $B_\parallel$ as a representation of the mode structure.

For the parameters given in Table 2-1 and for profiles given by Eq. 2-4 the fast wave with frequency $\omega \gtrsim \Omega_i$ can easily fit into the machine for $n_0 \gtrsim 10^{18}\ m^{-3}$. [We do not perform calculations for the case of $\omega \ll \Omega_i$, although the fast (compressional Alfven) wave can also propagate at these low

frequencies. In principle this low frequency wave can also drive current via the alpha Landau damping mechanism.] With a given frequency, the numerical solution of the coupled wave equations leads to a number of eigenmodes with discrete $k_{\parallel}$ values. A general trend of these eigenmode structures is that as $k_{\parallel}$ increases, not only the structures in the plane of the plasma cross section become simpler, but also the right-hand polarized electric field and the parallel magnetic field become more concentrated near the central part of the plasma. Examples are shown for the case of a plasma with $\bar{n}_e = 1.23 \times 10^{20}$ m^3, $\bar{T}_e = 14$ keV, and with $\omega \approx 1.25\ \Omega_{Do}$ and also $\omega \approx 5\ \Omega_{Do}$, in a DT plasma; the subscript zero indicates evaluation at $B = B_0$. The lower frequency case, viz, $\omega \approx 1.25\ \Omega_{Do}$, is more suited to ion heating through cyclotron damping as compared to that at the higher frequency, viz., $\omega \approx 5\ \Omega_{Do}$, which is more suited for current drive. The typical mode structure for $\omega \approx \Omega_{Do}$ is depicted in Fig. 2-17, which shows the wave B_z-field in the rectangular cross section, straight ("cylindrical") plasma. Figure 2-18 depicts the contours of the wave B_z-field for the case where $\omega \approx 5\ \Omega_{Do}$.

The effect of toroidicity is simulated in the MOTHRA code by including an inverse radial dependence of the magnetic field. Figure 2-19 shows the corresponding result for $\omega \approx 5\ \Omega_{Do}$.

The rate of momentum input from the traveling wave to the alpha particles has been calculated in Ref. 50. The current density generated may be obtained as:

$$j_\alpha = \frac{e_\alpha}{m_\alpha} \dot{P}_\alpha \tau_s \ , \qquad (2\text{-}39)$$

where $\dot{P}_\alpha$ is the momentum transfer rate and τ_s is given by Eq. 2-34. The total current including the electron "return" current is then given by Eq. 2-2 with $j_b \equiv j_\alpha$. The ratio of current generated to power dissipated by alpha Landau damping was estimated in the reference, and we merely give the results for the specific DEMO cases.

Figures 2-20a and 2-20b show the d.c. current generated (in arbitrary units) due to a traveling wave whose mode structure is shown in Fig. 2-17; Fig. 2-20a displays the contours for constant current in the plasma cross section and Fig. 2-20b gives the current distribution profile along the

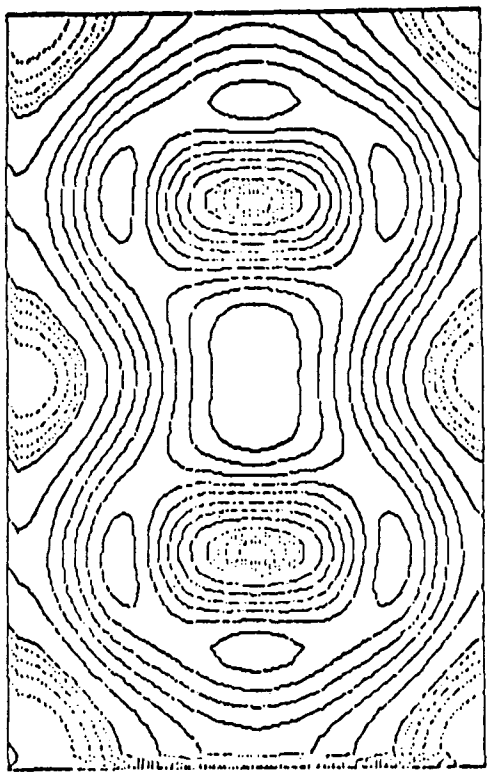

Fig. 2-17. The contour plot of constant parallel wave magnetic field $|B_{\parallel}|^2$ for $\omega \approx \Omega_D$.

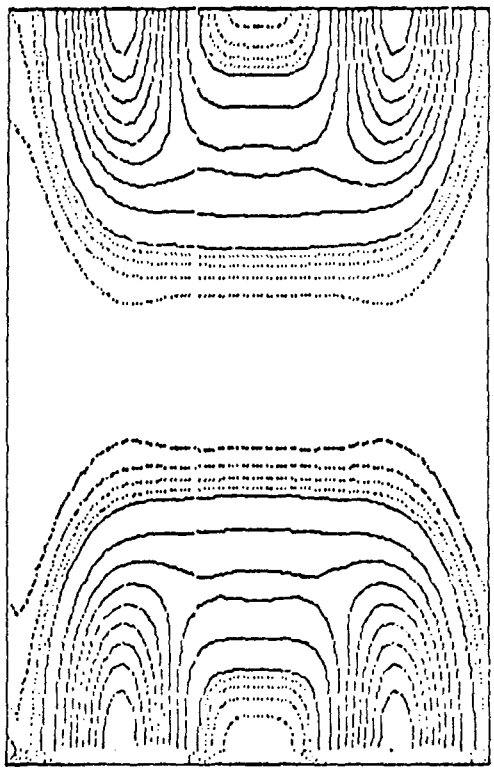

Fig. 2-18. The contour plot of constant parallel wave magnetic field $|B_{\parallel}|^2$ for $\omega \approx 5\ \Omega_D$.

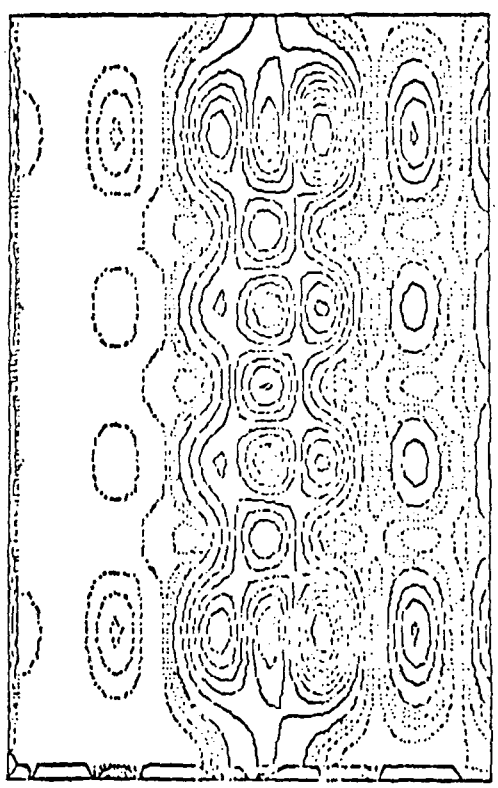

Fig. 2-19. The contour plot of constant parallel wave magnetic field $|B_{\parallel}|^2$ for $\omega \approx 5\ \Omega_D$, including radial dependence of the magnetic field.

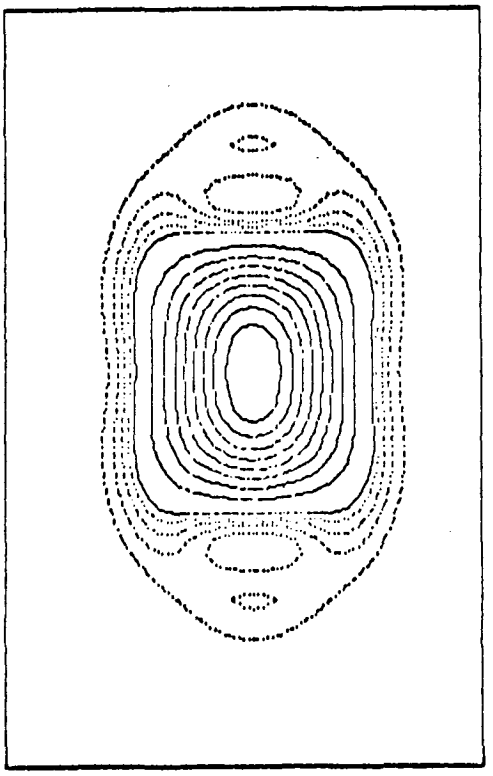

Fig. 2-20a. The d.c. current profile due to traveling wave corresponding to the mode shown in Fig. 2-17.

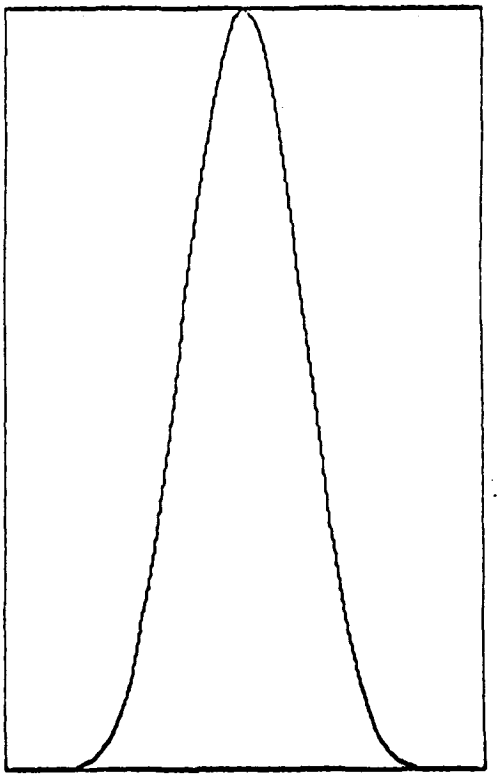

Fig. 20-b. The d.c. current distribution profile along the midplane corresponding to the mode shown in Fig. 2-17.

midplane. The I/P_α ratio is about 0.3 A/W for the case where $Z_{eff} = 1.4$. The current density is centrally peaked, as required for the DEMO. The fatal flaw at this low frequency, $\omega \approx 1.25\ \Omega_{Do}$, however, is that over 99% of the rf power is consumed by deuteron and triton cyclotron damping, i.e. $P_\alpha < 0.01\ P_{rf}$. In effect the rf current drive efficiency is reduced to $I/P_{rf} < 0.003$ A/W.

Operation at higher frequencies reduces the cyclotron damping relative to the Landau damping. The alpha-driven current density contours for the case $\omega \approx 5\ \Omega_{Do}$ are shown in Fig. 2-21. In this particular case, corresponding to the mode structure in Fig. 2-18, the wave fields are not concentrated near the plasma center, so centrally peaked current density does not appear. We compute $I/P_\alpha \approx 0.15$ A/W.

For the case with the mode structure shown in Fig. 2-19 (which includes the effect of toroidicity), the current was calculated with a non-zero (constant) value of ε in Eq. 2-2. The current profiles are shown in Figs. 2-22a and 2-22b, the I/P_α ratio being -0.6 A/W. However, we estimate the power absorption by alphas to be less than 25% of the rf power, the remaining 75% being absorbed by transit time electron damping. In consequence, the effective current drive efficiency is $I/P_{rf} \lesssim 0.15$ A/W. Moreover, this current flows opposite to that generated by direct momentum transfer to the electrons via the transit time pumping mechanism (see Sec. 2.3.3.2), so the net current may be smaller still. As with ^{3}He minority driven currents,[47] regions of reversed current density may occur.

In conclusion, we have shown the feasibility of a current-drive scheme using rf damping on the alpha particles which are produced in a burning DT plasma. Traveling fast waves, generated as waveguide modes for the plasma, are found to be particularly suitable for implementing such a scheme. The current profiles obtained for such a scheme are found to have considerable spatial structure. The gross stability of the plasma to such current profiles needs to be studied.

In addition, the wave power absorption by the alphas and the resulting j_α need more detailed analysis. In Ref. 50 the alpha particles were assumed to have a delta function distribution in velocity space, at their birth velocity. A more accurate representation of their distribution function would be in terms of a solution of the Fokker-Planck equation, which shows the effect of slowing-down in velocity space, similar to calculations in Refs. 31 and 47.

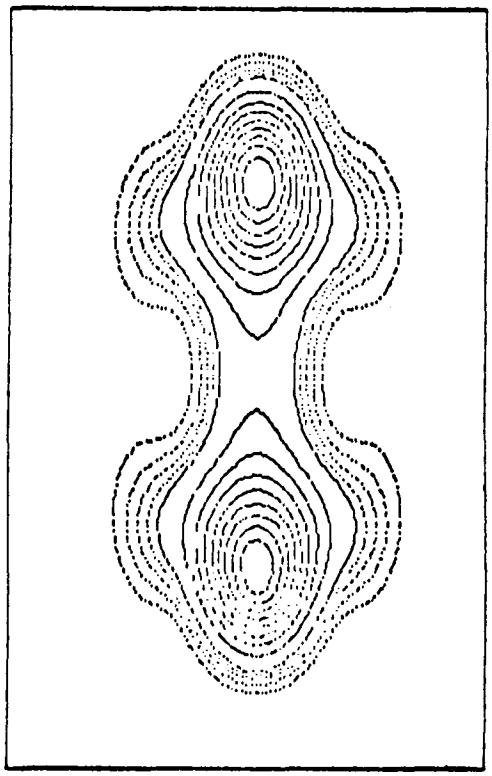

Fig. 2-21. The d.c. current profile due to traveling wave corresponding to the mode shown in Fig. 2-18.

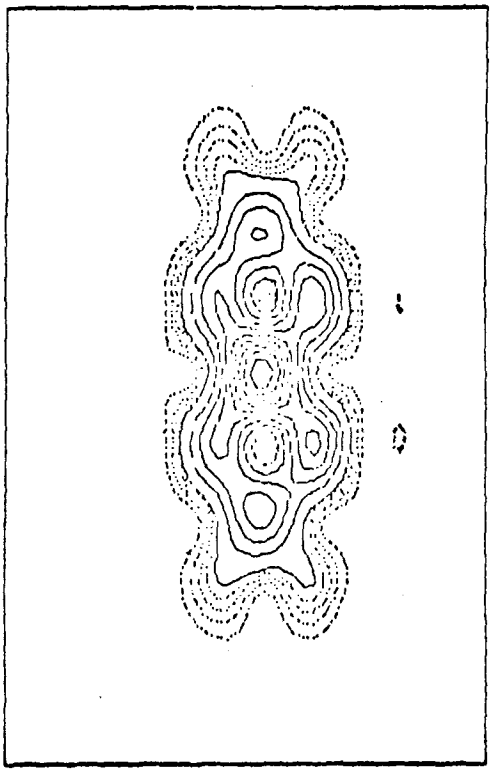

Fig. 2-22a. The d.c. current profile due to traveling wave corresponding to the mode shown in Fig. 2-19.

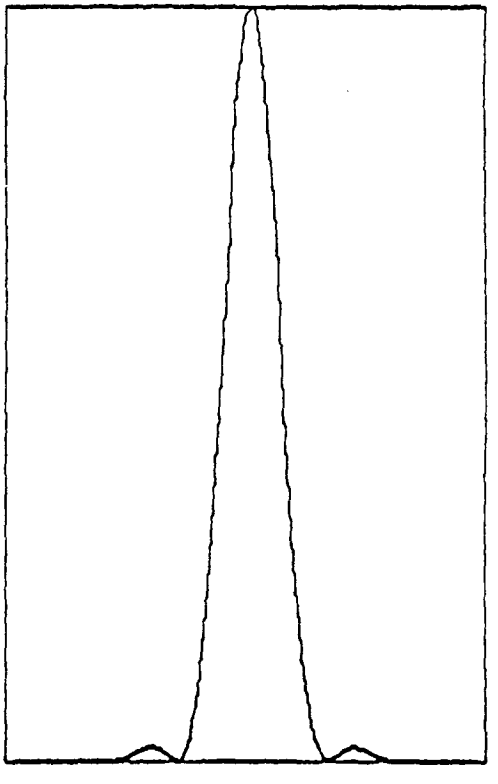

Fig. 2-22b. The d.c. current distribution profile along the midplane corresponding to the mode shown in Fig. 2-19.

2.3.2.3 Electron Cyclotron Resonance Heating (ECRH)

An alternative indirect current drive method to the ion heating proposed above is simply heating the electrons alone. This would be accomplished by ECRH, which is highly species selective. The efficiency of this method was first evaluated by Fisch and Boozer,[51] who pointed out that for most wave-driven currents the magnitude of $\hat{j}/\hat{p}$ derives mostly from heating and only to a minor degree from momentum input. Subsequent numerical work[12,52] has substantiated the earlier analysis, and experimental verification of this effect was achieved on the Culham Levitron.[53]

For comparison with other current drives we have displayed in Fig. 2-23 various calculations of fundamental harmonic ECRH $\hat{j}/\hat{p}$ as a function of $w = (\omega - \Omega_e)/k_\parallel v_e$ with $Z_{eff} = 1.0$, compiled from Refs. 12 and 52. The solid curve shows $\hat{j}/\hat{p} = w^2$ (we assume narrow wave spectra, $\Delta w \ll w$), without electron toroidal trapping. The dashed curve treats the same case but utilizes a truncated form of the electron distribution function[12] which tends to overestimate $\hat{j}/\hat{p}$. The virtue of the latter treatment is that the calculation is readily extended to include neoclassical effects. For example, the dotted curve is the same calculation except $\epsilon = 0.1$; we see there is a modest reduction in $\hat{j}/\hat{p}$ for DEMO-type aspect ratios, even at fairly large values of w. The curves in the figure were calculated in the linear regime (small wave electric fields) while the isolated point with $\hat{j}/\hat{p} = 37$ corresponds to the nonlinear limit,[52] which shows that $\hat{j}/\hat{p}$ may be doubled if the heating is sufficiently intense.

A number of factors conspire to make ECRH current drive unattractive for the DEMO reactor. In the first place, it is desirable to have the cyclotron waves damped at large w ($\gtrsim$ 4-5) since it is only in this regime that $\hat{j}/\hat{p}$ is substantial. In addition, the waves must be launched at a critical angle (with small tolerances) which assures damping on only one side of the cyclotron layer. Indeed, the Levitron experiment[53] showed the tendancy to generate bi-directional current density. Additional ray tracing calculations and experimental effort are needed to assess the difficulty of achieving one-sided absorption at high w.

The extraordinary mode is accessible to the plasma interior for the relatively low plasma densities we consider [$\omega_{pe}(0) < 2\Omega_{eo}$], but high power sources at 135 GHz are required. For CW operation at this high frequency,

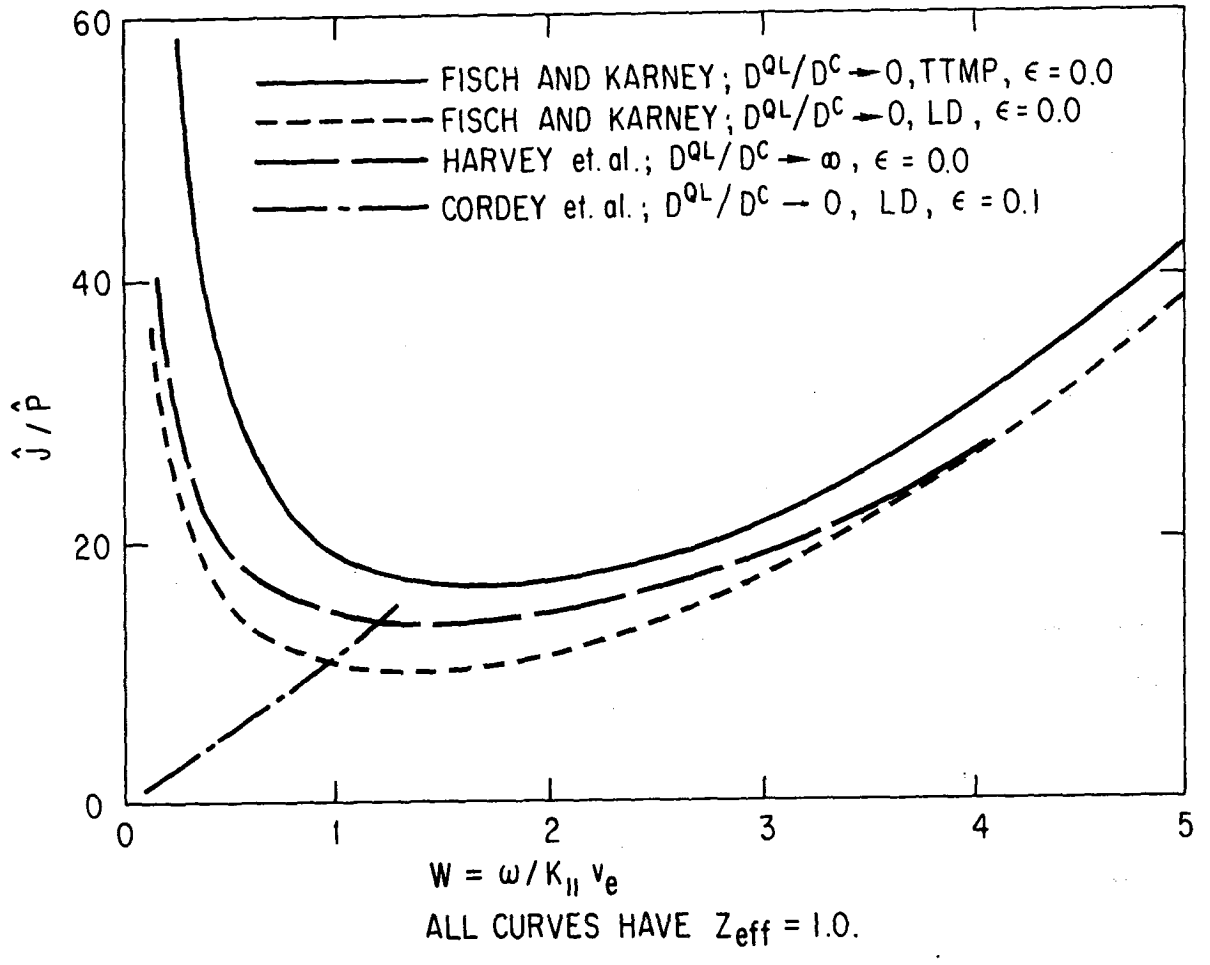

Fig. 2-23. Fundamental ECRH; curves are for linear limit, $D^{QL}/D^{C} \to 0$; all calculations use $Z_{eff} = 1.0$.

optimistic estimates of gyrotron tube efficiencies are $\eta_T = 0.6$; overmoded waveguide runs may have $\eta_{WG} \approx 0.8$; the highly regulated gyrotron power supplies may operate at $\eta_{PS} \approx 0.7$. Thus, the overall system efficiency would only be $\eta_{ECRH} \approx 0.34$. Thus, if minimizing the circulating electric power is of paramount concern, ECRH will not be as attractive as other current drive options. Moreover, individual gyrotron tubes may be limited to low power output. At present there is a 150 GHz source in the U.S.S.R. which generates 22 kW CW (22% efficiency), and MIT is designing a 100-kW tube at 150 GHz. It appears likely that new concepts must be developed if a megawatt source is desired at these very high frequencies. The quasioptical klystrogyrotron is one such promising approach; a 1-MW tube at 150 GHz ($\lesssim$ 26% efficiency) is being developed at the National Research Laboratory. It is evident, however, that both the poor projected system efficiencies and the short tube development time period assumed prior to the actual DEMO design will argue against selecting ECRH as the driver system.

2.3.2.4 Other Indirect Wave-Driven Current Proposals

A number of suggestions have been made to employ ECRH to increase the magnetic trapping/detrapping frequency or change the relative populations of trapped and untrapped electrons.[54-56] We point out that a simple increase in the $v_\perp$ moment of electrons (e.g., those resonant with $w = +1$) without supplying parallel momentum does not change the $v_\parallel$ moment of the electron distribution, even though the untrapped electron population may be depleted. However, ECRH can increase the fraction of trapped electrons, which have large banana widths, increasing the neoclassical diffusion rate and theoretically enhancing the bootstrap current. These approaches to current drive face several difficulties. In the first place, the bootstrap effect produces an undesirable hollow current density. Secondly, electrons do not behave neoclassically in a tokamak, and, as disucssed in Ref. 29, there is experimental evidence that the bootstrap effect is much weaker than neoclassical theory predicts. Finally, ECRH current drive generally suffers from the tube development problem in that high power sources may be unavailable in the short time period assumed prior to the actual DEMO design.

A novel approach to steady-state current generation, proposed by Dawson and Kaw,[57] would utilize the high frequency synchrotron radiation naturally emitted by the plasma. These incoherent waves are emitted at frequencies

which are harmonics of Ω_e, and, if they are anisotropically reflected at the first wall, their radiation pressure can transfer their net momentum to the electrons on reabsorption, creating a toroidal current. This proposal effectively circumvents the need for a millimeter source development program for current drive in the DEMO, but it suffers from other problems. The current generated is a very strong function of the electron temperature:

$$I = 1.4 \times 10^{-2} \left(T_e/m_e c^2\right)^{2.5} T_e^{2.75} a^{1.5} n_e^{0.75} \sqrt{1 - \tilde{\Gamma}}\, \alpha_s Z_{eff}^{-1} \beta^{-1.25} ,$$

where $\alpha_s \approx 5$. Substitution of values for high temperature operation of DEMO ($\bar{T}_e = 16$ keV, $\bar{n}_e = 1.03 \times 10^{20}$ m^{-3}), assuming an average wall reflectivity of $\tilde{\Gamma} = 0.9$, we find $I \approx 38$ kA/Z_{eff}, which, of course, is far too small to be useful. Even using the peak values ($T_{eo} = 33.6$ keV, $n_{eo} = 1.34 \times 10^{20}$ m^{-3}) only yields $I \approx 0.76$ MA/Z_{eff}. Moreover, this strong T_e dependence in the formulation of I will lead to an extremely localized current density profile; the concentration of j(r) near the magnetic axis is not compatible with the broad profile needed for the DEMO high beta equilibrium. Also, we note the anisotropic reflectivity of the first wall will degrade due to pitting and erosion; frequent maintenance would loom as a serious detrimental feature of this method.

2.3.3 Low Speed Waves

2.3.3.1 Compressional Alfven Wave (CAW) Current Drive

The use of low-phase speed traveling waves ($\omega/k_\parallel < v_e$) for current generation was originally proposed by Wort.[58] Subsequently, numerical calculations by Fisch and Karney[59] have supported Wort's idea. Similar Fokker-Planck calculations by Harvey[60] have clarified the role of electron-electron collisions in determining $\hat{j}/\hat{p}$, and a study by Cordey[12] has shown the reduction of $\hat{j}/\hat{p}$ caused by trapped electrons in the $w \lesssim 1$ regime.

Figure 2-24 summarizes the results of several calculations of $\hat{j}/\hat{p}$; our discussion concentrates only on the region $w \lesssim 1$ in this subsection. Fisch and Karney pointed out that in the linear regime electron transit time magnetic pumping (TTMP) can generate larger $\hat{j}/\hat{p}$ than Landau damping (LD), provided $w < 1$. This arises from the tendancy of TTMP to interact with higher $v_\perp$ electrons, which are less collisional. The solid and dotted lines in the figure bear this out. In consequence, in a (cylindrical) plasma the

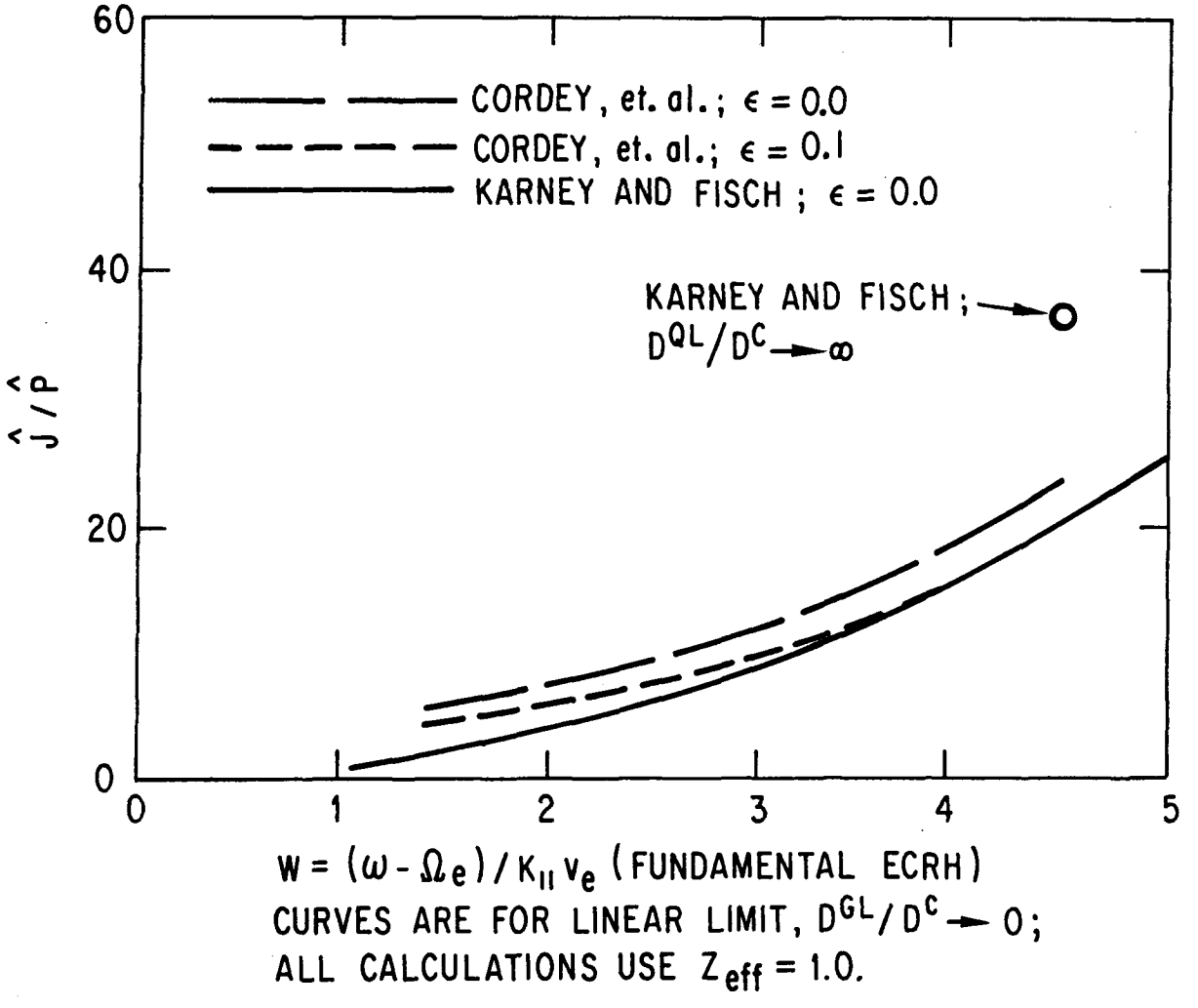

Fig. 2-24. Momentum transfer via Landau damping (LD) and transit time magnetic pumping (TTMP); all curves have $Z_{eff} = 1.0$.

compressional Alfven wave (CAW), which has a very small $E_\parallel$, is a more efficient current driver than the shear Alfven wave (SAW), which is principally Landau damped. If, however, the wave amplitudes are so large $(D^{QL}/D^{C} >> 1)$ that the electron distribution is flattened at all $v_\perp$ values then $\hat{j}/\hat{p}$ is reduced essentially to the Landau damping value, regardless of the wave type, as shown by the dashed line in the figure. For our calculations with the CAW we use the following fit to the solid curve:[59]

$$\hat{j}/\hat{p} = 5 + 13\ w^{-1} . \qquad (2\text{-}40)$$

We perform a simplified calculation of CAW current drive, assuming only the lowest order perpendicular eigenmode fits into the torus; the poloidal mode number is $m = 0$, the radial $k_r = \pi/(Sa)$, and the toroidal $k_\parallel = N/R_0$. For low frequencies $(\omega << \Omega_D)$ the approximate dispersion relation is[48,59]

$$\omega/k_\parallel v_i = 2\beta^{-1/2}\left[1 + (\pi R_0/SNa)^2\right]^{1/2} .$$

By increasing N the phase speed decreases, which generates higher $\hat{j}/\hat{p}$. A practical upper limit might be $N = 20$, which, for $\bar{T}_e = \bar{T}_i \approx 20$ keV, yields $\omega/k_\parallel v_i = 7.8$, $f = \omega/2\pi = 5.3$ MHz, and $\lambda_\parallel = 2\pi/k_\parallel = 1.64$ m. We see ω is sufficiently low that ion cyclotron damping is negligible, and $\omega/k_\parallel$ is high enough to ignore ion Landau damping. Having estimated ω and $k_\parallel$ from the global dispersion relation we proceed to evaluate $w = \omega/k_\parallel v_e$ from the radial profile of $v_e(r)$, given by Eq. 2-4; for $\bar{T}_e = \bar{T}_i$ we obtain

$$w(x) = 0.08(1 - x^2)^{-0.55} , \qquad (2\text{-}41)$$

where $x = r/a$. Assuming now that electron TTMP is the sole damping mechanism[61] we utilize this expression for the radial CAW power density absorbed:[62]

$$p(r) \propto n_e(r)\ T_e(r) w\ e^{-w^2/2}\ b_\parallel^2 ,$$

where $b_\parallel$ is the wave's parallel magnetic field. Taking $b_\parallel$ = constant, we rewrite this as

$$p(x) = p_0(1 - x^2)^{0.85} . \qquad (2\text{-}42)$$

For high Q cavity modes we can ignore wall losses, so the total power investment is the volume integral of Eq. 2-42,

$$P = V_p p_0 / 1.85 \ . \tag{2-43}$$

The current density profile is gotten by multiplying Eq. 2-3 by Eq. 2-42 and substituting Eq. 2-40 and Eq. 2-41:

$$j(x) = 1.6 \times 10^{18} \ p_0 (\bar{T}_e / \bar{n}_e)(1 - x^2)^{1.65} [5 + 13/w(x)] \ .$$

We display j(x) and w(x) in Fig. 2-25. The current profile is centrally peaked; however, if $b_{\|}$ is centrally peaked, then j(x) would have a narrower profile. Integrating j(x) over the plasma cross section, the total current, I, is obtained in terms of p_0. Then substitution of Eq. 2-43 yields

$$I/P = 1.03 \ \frac{(\bar{T}_e / 18 \text{ keV}) \ A/W}{(\bar{n}_e / 0.84 \times 10^{20} \ m^{-3})} \ . \tag{2-44}$$

Comparison with other drivers suggests the CAW yields quite favorable results in this limit which ignores neoclassical electron trapping. Figure 2-26 plots the net electric power production for the DEMO, assuming $\eta_{aux} = 0.71$. It appears that only a small ($\approx$ 10%) portion of the gross electric output would be circulated to sustain steady-state operation.

However, this favorable result may be deceiving. Since the CAW is resonant with trapped electrons ($w < 1$), these momentum recipients are not free to circulate toroidally, so it is unclear how large a toroidal current can actually be generated. Fokker-Planck calculations were done in Ref. 12 for Landau damping on trapped electrons. The result for $\varepsilon = 0.1$ is included in Fig. 2-24 as a chain-dashed line. The calculation was done in the Lorentz limit, which overestimates $\hat{j}/\hat{p}$,[12] and it is apparent that $\hat{j}/\hat{p}$ vanishes as $w \to 0$. If this calculation accurately models toroidal effects then the CAW is not nearly as attractive as Fig. 2-26 suggests. Nevertheless, the input of canonical angular momentum to the trapped electrons forces their banana centers inwards, towards the magnetic axis, analogous to the Ware pinch. This effectively fuels the central plasma region, creating a density gradient. Fisch and Karney[59] then invoke the bootstrap effect to create toroidal current. As discussed in Sec. 2.2.3, electrons do not behave neoclassically in tokamaks,

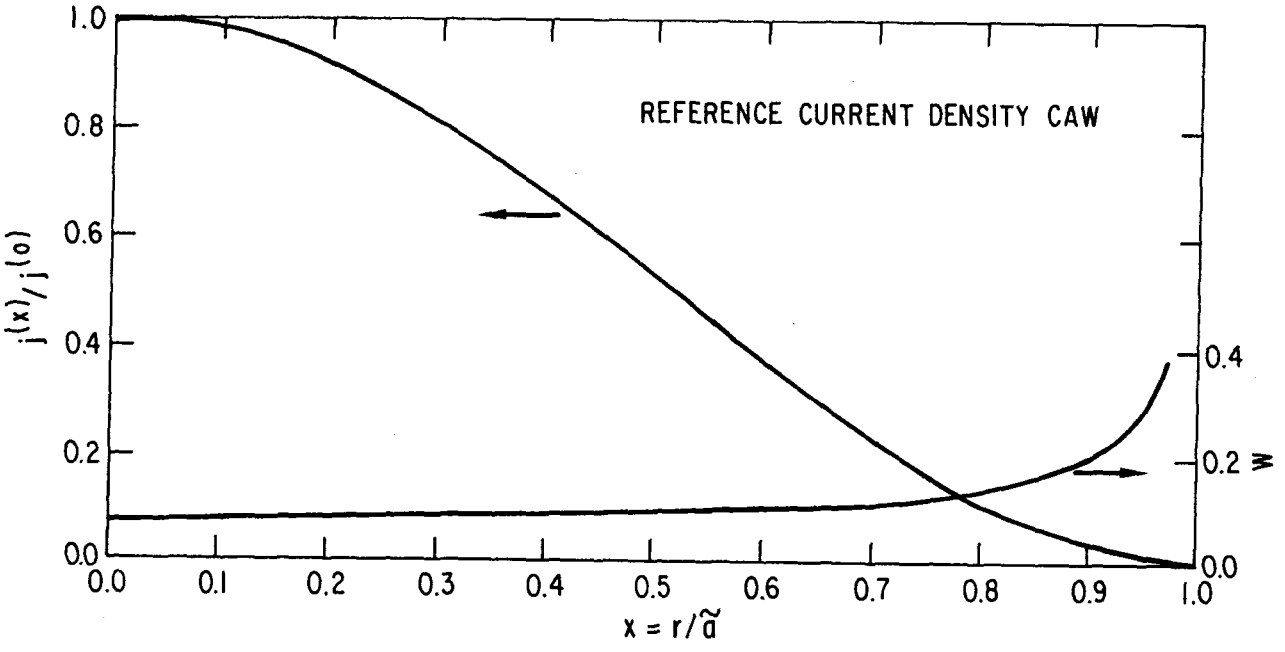

Fig. 2-25. Current density profile for compressional Alfven wave (5.3 MHz, $\lambda_{\|}$ = 1.6 m).

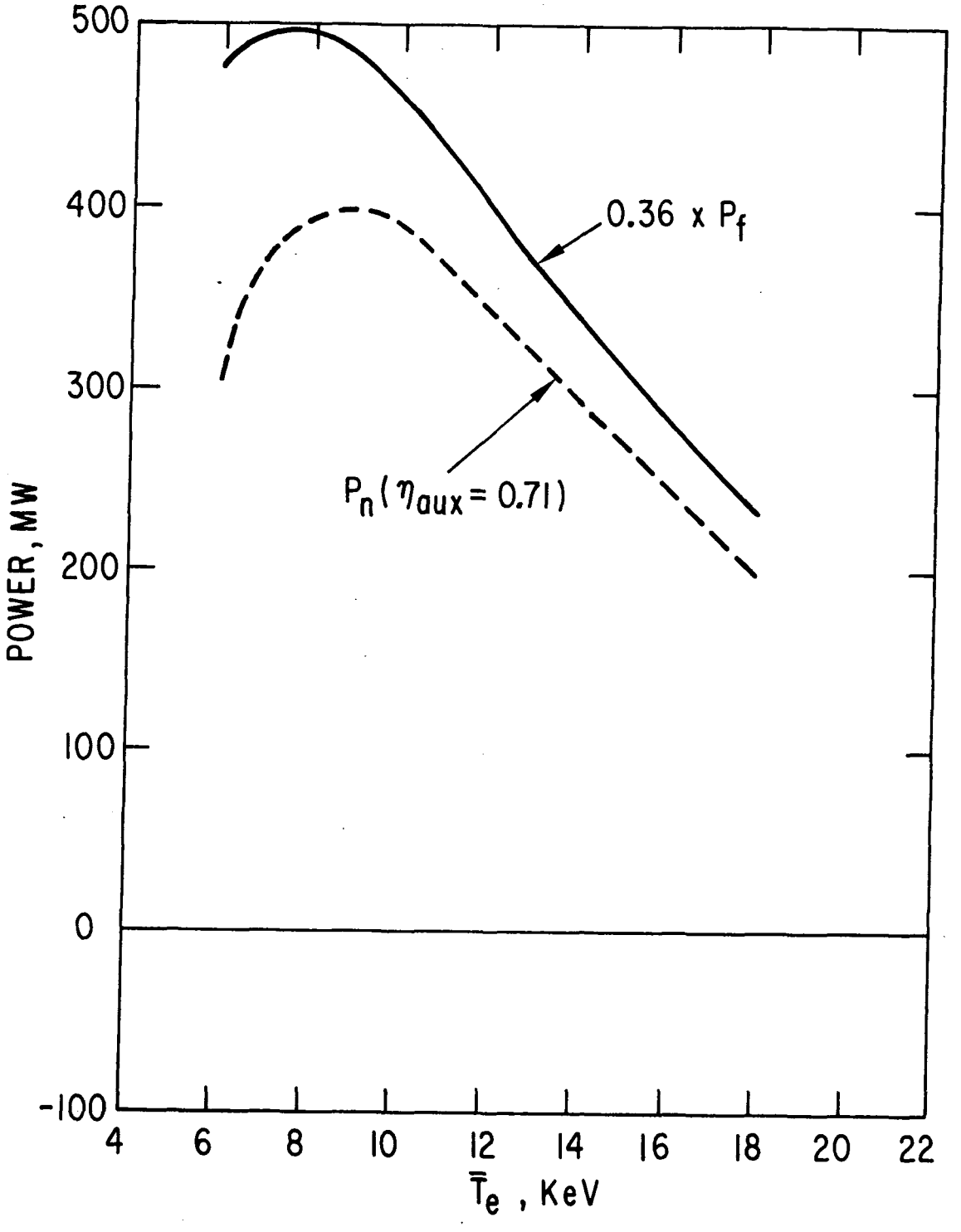

Fig. 2-26. Gross and net electric power for CAW; dashed line indicates neglect of neoclassical trapping.

so we are unable to reliably calculate toroidal currents based on these notions. Therefore, the P_n curve in Fig. 2-26 is left dashed as a reminder of our inability to quantify neoclassical effects.

2.3.3.2 Low Speed Magnetosonic Wave (LSMS) Drive

It is also possible to use the compressional (or "fast") wave at $\omega > \Omega_i$ to achieve electron TTMP with $w \lesssim 1$. As discussed in Sec. 2.3.2.2 this wave can exist as a high Q toroidal cavity mode with negligible ion damping, provided ω is at least four or five times Ω_i. Extensive experimentation by Fukuda[63,64] has verified that this mode can propagate and drive current in a torus, although his work has been limited to low $\bar{T}_e$ plasmas in which the wave damping is due to collisional dissipation, not TTMP.

Our method uses the same calculation as described in Sec. 2.3.2.2, except we ignore alpha particle Landau damping and use $\hat{j}/\hat{p}$ values taken from Fig. 2-24 (with $\varepsilon = 0$) to compute the current density. Our calculation is done for $\bar{T}_e = 14$ keV, $\bar{n}_e = 1.24 \times 10^{20}$ m^{-3}, and f = 184 MHz, such that $\omega/\Omega_{Do} = 5.0$. For a given frequency and $k_\parallel$ the dispersion relation determines the perpendicular wave structure.[49] Generally speaking, the shortest parallel wavelengths yield the simplest perpendicular structure, and we search for the mode near cutoff which has centrally peaked wave energy density. We find there is only one mode with a centrally peaked current density, which has $N \approx 411$, or $\lambda_\parallel = 2\pi R_0/N = 7.95$ cm. The two dimensional j is shown in Fig. 2-27. For this model

$$I/P = \frac{0.19\ (\bar{T}_e/18\ \text{keV})\ \text{A/W}}{(\bar{n}_e/0.84 \times 10^{20}\ \text{m}^{-3})},$$

which appears competitive with the value obtained with other drivers.

There are, however, serious problems with this wave. For one, it is difficult to design a traveling fast wave antenna with such a short $\lambda_\parallel$. A greater objection to this approach is that the very large mode density will make it impractical to couple to the unique mode which has a centrally peaked current density.[48] There are many eigenmodes with $\lambda_\parallel \approx 8$ cm, and our investigation showed that only one has a centrally peaked j. (Even in the collisional experiments the current density is hollow.)[65] We conclude this LSMS wave will not satisfy the DEMO criteria, even though hollow current profiles may ultimately be acceptable for reactors.[3,4]

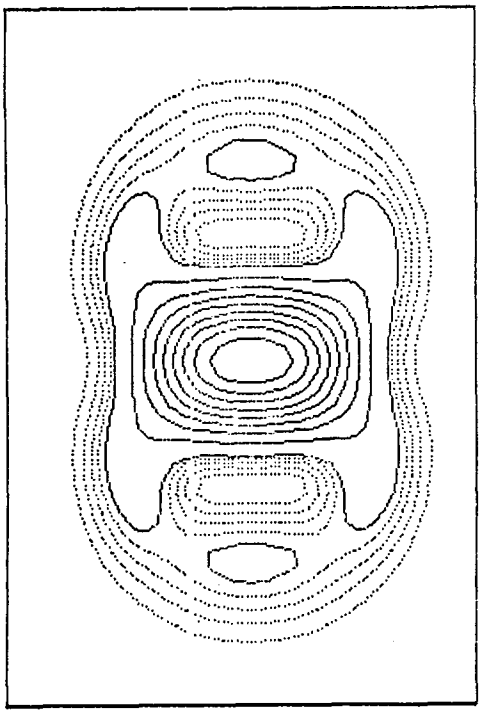

Figl 2-27. Current density contours for fundamental radial eigenmode of LSMS (184 MHz, $\lambda_{\parallel}$ = 7.95 cm), due to electron TTMP.

2.3.3.3 Shear Alfven Wave Drive

In contrast to the fast ("magnetosonic") wave, which is an electromagnetic mode damped by TTMP, the electrostatic slow wave can generate current. This wave, which is termed the shear Alfven wave (SAW) when $\omega << \Omega_i$ is known as the ion cyclotron wave when $\omega \approx \Omega_i$; it does not propagate at higher frequencies. Hasegawa[66] has considered this wave for driving currents. We do not dwell on this candidate but will simply indicate two serious defects it suffers. First, if the wave is absorbed by Landau damping then we note from Fig. 2-24 that $\hat{j}/\hat{p}$ will be very small when $w < 1$, since $\varepsilon \neq 0$. Secondly, if the SAW is converted to a kinetic Alfven wave[59,66] at a narrowly localized region in minor radius, then this may lead to highly local current density. The current drive prospects are not conclusive at present for the SAW, but the outlook is not promising.

2.3.4 High Speed Waves

2.3.4.1 Lower Hybrid Wave Drive

The electrostatic, slow wave will propagate at sufficiently high frequencies such that $\omega \gtrsim 2\,\omega_{LH}$, provided the accessibility criterion is satisfied.[3] Here $\omega_{LH}^2 \equiv \omega_{pi}^2\left[1 + \omega_{pe}^2\Omega_e^{-2}\right]^{-1}$, and the wave is known as the lower hybrid (LH) wave. Extensive current drive calculations have been performed in Ref. 3 for this driver, and we summarize the relevant conclusions below.

Typical LH wave frequencies are ~ 1-2 GHz, and the wave resonants naturally in the $w > 1$ region of phase space. Reference to Fig. 2-24 shows $\hat{j}/\hat{p} = 1.4\ w^2$. In the limit of very intense wave heating $\left(D^{QL}/D^{C} > 1\right)$, the values are even higher,[67] $\hat{j}/\hat{p} = 1.7\ w^2$. Moreover, as confirmed in Ref. 12, the reduction in $\hat{j}/\hat{p}$ due to electron trapping is small since so few electrons are magnetically trapped in the region $w >> 1$. The strategy for maximizing $\hat{j}/\hat{p}$ thus is to use the highest phase speeds possible to increase w. The accessibility criterion, however, demands a lower limit to $n_\parallel = ck_\parallel/\omega$ in order to avoid reflection of the wave. It is precisely this constraint which forces a compromise between wave penetration into the plasma interior and the choice of low $n_\parallel$, high w waves for maximum $\hat{j}/\hat{p}$ values.[4] Consequently, it is difficult to achive high I/P values with the LH driver if centrally peaked current profiles are demanded for the DEMO. Moreover, it is difficult to

design antennas to launch waves with $w \ll 1$ since, at these frequencies, $\lambda_\parallel$ is quite short; electrical breakdown limits $\lambda_\parallel$ to $\sim$ 10 cm.

Based on the difficulty of achieving centrally peaked current density the LH option can be ruled out for this DEMO study. We must keep in mind, though, that hollow current densities may ultimately be acceptable for commercial reactors.

2.3.4.2 Ion Cyclotron Wave Drive

In the range $\omega \lesssim \Omega_i$ the electrostatic slow wave, termed the ion cyclotron wave (ICW), propagates, and it is straightforward to achieve $w > 1$ with convenient parallel wavelengths of a meter or more. Electrostatic couplers (see, e.g., Ref. 68) could be employed to launch waves from the inboard (high field) side, and the Landau damping process would determine $\hat{j}/\hat{p}$. Laboratory demonstration of ICW current drive was achieved in the Model C.[69]

Preliminary calculations suggest I/P values from this driver are in the range of interest for the DEMO. Further studies need to be done to examine ray trajectories in a torus in order to determine if centrally peaked currents can be achieved. We have not fully assessed the ICW potential, but we note that the fast wave should yield larger $\hat{j}/\hat{p}$ than this slow wave, since the former is damped by TTMP while the latter suffers only Landau damping (cf. Fig. 2-24).

2.3.4.3 High Phase Speed Magnetosonic Wave (HSMS) Drive

By selecting long parallel wavelengths, it is not possible to obtain the high Q fast wave eigenmodes considered in Sec. 2.3.3.2. Instead, strong Landau damping will occur, and the $w \gtrsim 1$ regime will dictate the current drive physics. This electromagnetic wave, which we refer to as the high speed magnetosonic (HSMS) wave, has several features which recommend it for the DEMO over the slow waves (LH and ICW). First of all, the TTMP mechanism results in larger theoretical $\hat{j}/\hat{p}$ values than Landau damping,[59] as shown in Fig. 2-24. Also, the wave is not constrained to low densities by the accessibility condition, and the rays are not confined to localized resonance cones. In addition, considerable experience has been gained with HSMS experiments,[44,45] including successful high power antenna operation.

We calculate toroidal ray trajectories launched from an antenna of finite extent. Figure 2-28 shows the actual plasma cross section and, superimposed

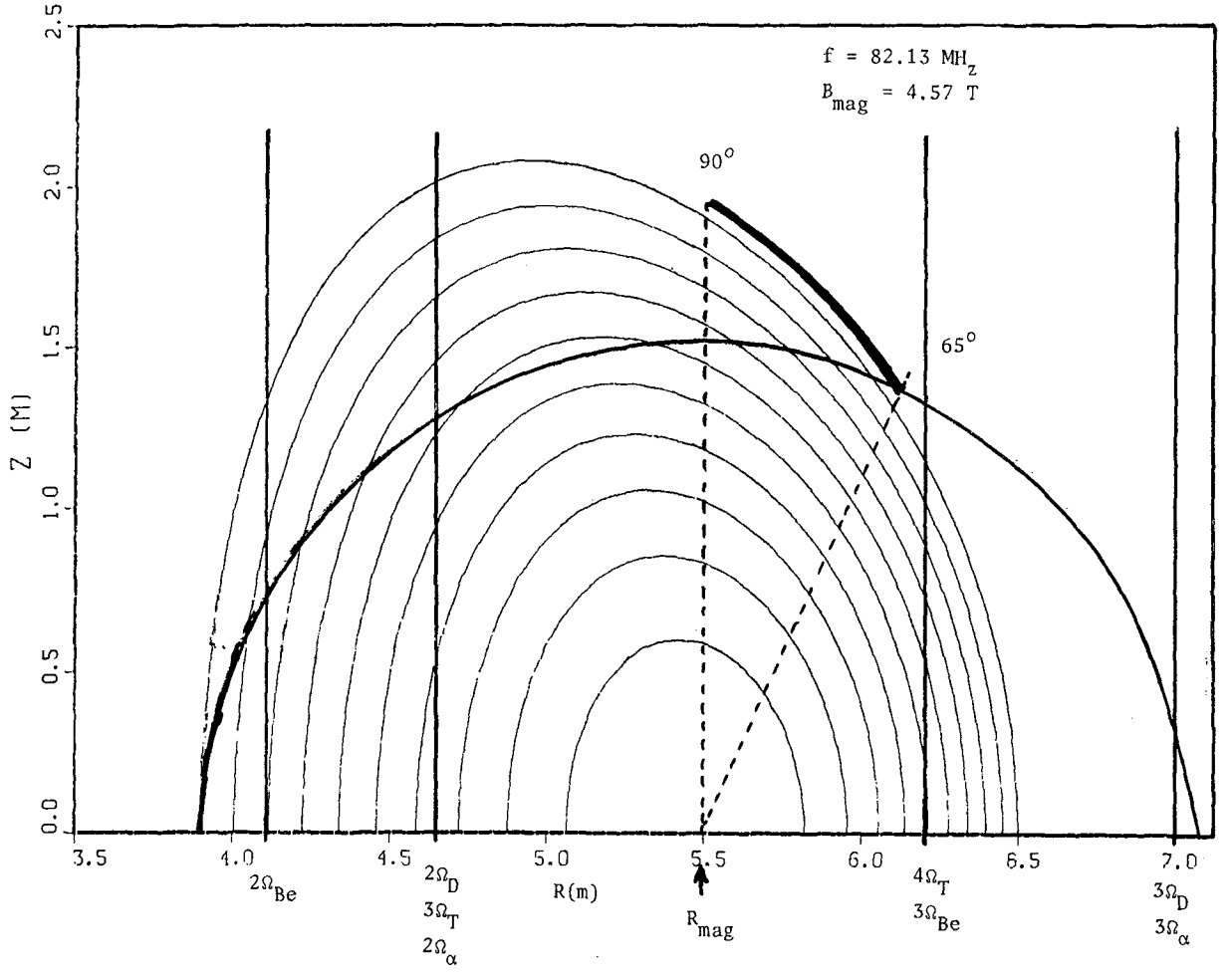

Fig. 2-28. Geometry for ray tracing calculation (HSMS).

on this, the circular boundary we use in our model. The circular model employs concentric flux surfaces, centered at the true magnetic axis, R_{mag} = 5.47 m. The circular boundary radius, $\tilde{a}$ = 1.59 m, is chosen so the volume $2\pi^2 R_{mag}\tilde{a}^2$ equals the actual DEMO plasma volume. In the figure we see the location of the cyclotron resonances for the sundry plasma constituents, D, T, α, and Be ($B = B_0 = 4.81$ T at $R = R_0 = 5.2$ m) at a frequency f = 82.13 MHz. By locating an antenna as shown, subtending the angles 65 deg to 90 deg on the circular model boundary, it is possible to shine the waves vertically into the plasma, and ion cyclotron damping can be almost completely avoided. We aim to identify a wave spectrum which is absorbed to a great degree in one pass.

The design of the HSMS antenna is in App. C. Properly constructed, the antenna should define a fairly narrow spectrum of $k_{\parallel} = n/R_0$, but the short poloidal extent of the antenna dictates a rather broad spectrum of poloidal mode numbers, m. In all our calculations we use test rays with m = 0, ±4, and ±15 to simulate the spectrum, and the rays are launched from the ends and center of the antenna (θ = 65, 77.5, and 90 deg); thus, fifteen rays (of equal amplitude) are followed for each case studied. We focus on current generation in two specific plasmas, one with $\bar{T}_e$ = 16 keV, $\bar{n}_e = 1.05 \times 10^{20}$ m^{-3} and one with $\bar{T}_e$ = 12 keV, $\bar{n}_e = 1.50 \times 10^{20}$ m^{-3}. In both cases $\bar{T}_i \gtrsim \bar{T}_e$, and the alpha and Be densities are $\approx 10^{18}$ m^{-3} .

A series of N values ($k_{\parallel}$) were tried for each plasma; the choice of N determines the damping profile since Landau damping is sensitive to $w = \omega/k_{\parallel} v_e$. Generally, large N, slow phase speed, waves are strongly absorbed on the plasma exterior. Decreasing N causes the wave to be absorbed near the higher temperature, central region. Further decreases in N place the phase speed well beyond the central v_e, which weakens the damping and requires reflections with multiple passes to absorb the wave energy. For both ($\bar{T}_e$ = 16 keV and $\bar{T}_e$ = 12 keV) plasmas studied we found N = 42 gives a broad absorption profile and results in 86-90% power absorption in one pass.

Figure 2-29 shows the ray trajectories for $\bar{T}_e$ = 12 keV, calculated from the warm plasma fluid equations. The power dissipation for a typical ray (m = 0, θ = 65 deg) is displayed in Fig. 2-30, which shows almost complete absorption before reflection takes place. Damping is calculated from Landau, fundamental, and harmonic cyclotron damping with quasilinear diffusion in isotropic velocity space,[70] and the electron distribution function is

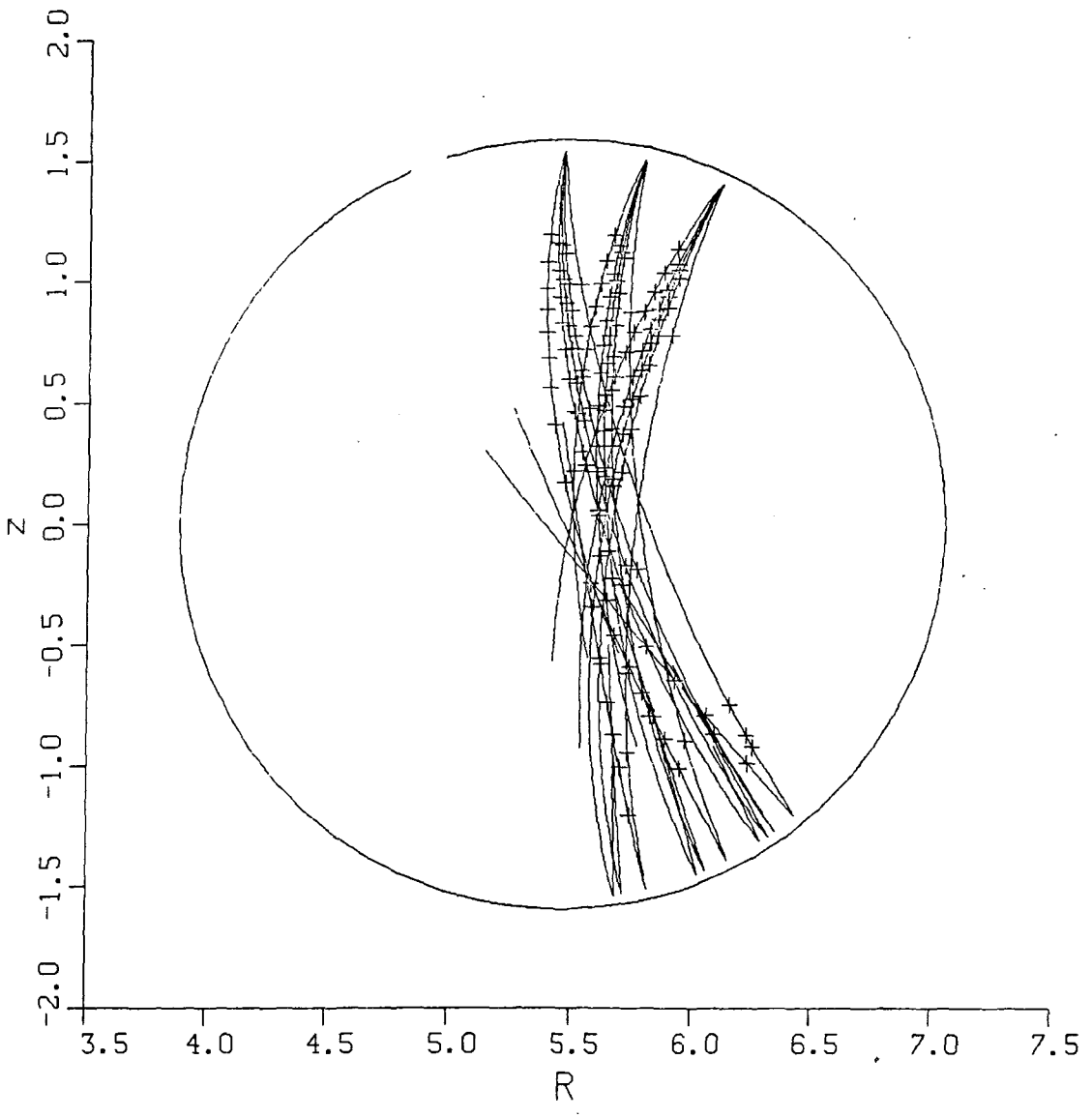

Fig. 2-29. Sample ray trajectories.

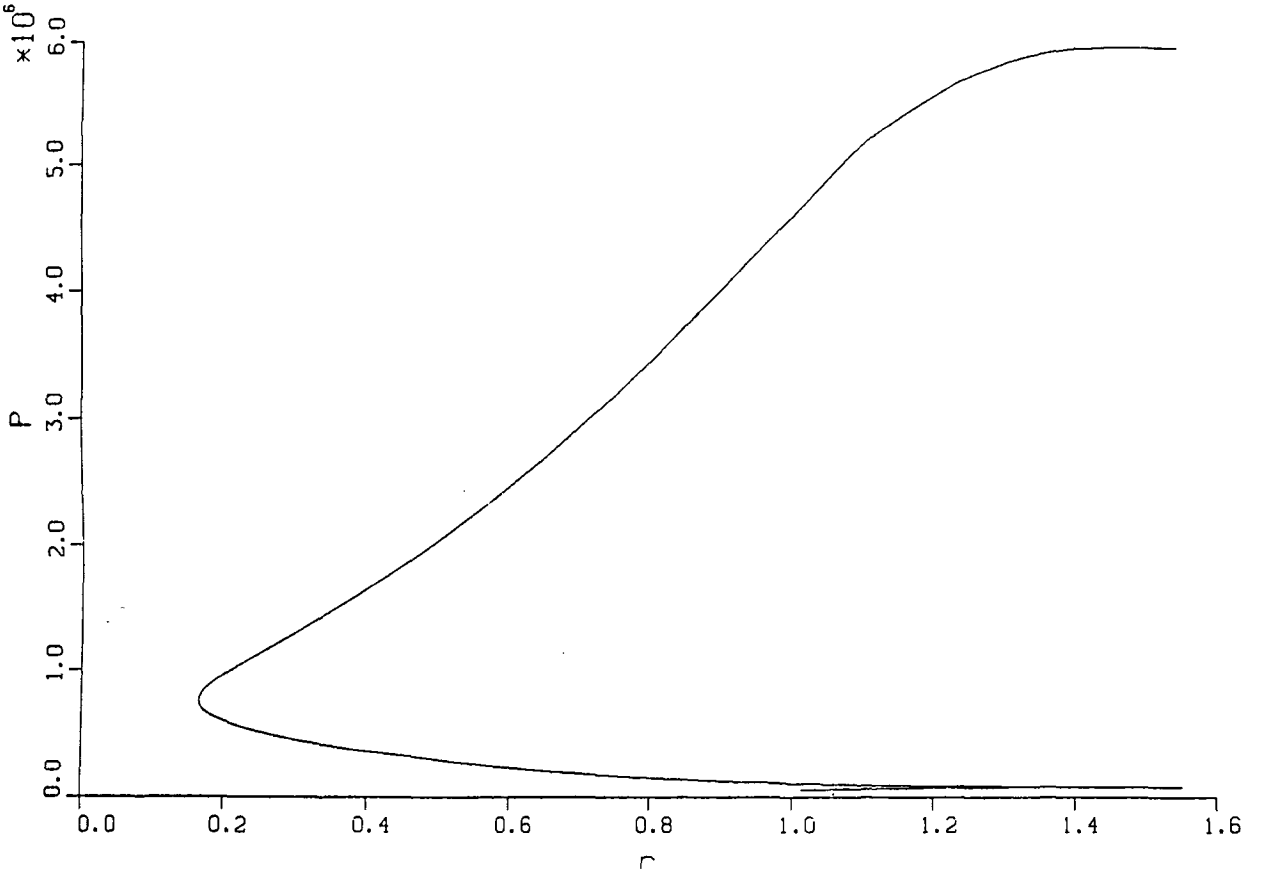

Fig. 2-30. Typical ray's power vs. minor radius.

computed from the coupled quasilinear-Fokker-Planck equation. The spatial wave power deposition is shown in Fig. 2-31; the bottom curve is power deposited on the electrons, the remaining small increments arising mostly from triton and Be damping where the rays cross the resonance at R = 6.2 m. The electron damping is in the linear regime $(D^{QL}/D^{C} \ll 1)$, and the electron distribution is only mildly non-Maxwellian. Thus, we can use the solid curve in Fig. 2-24 to compute $\hat{j}/\hat{p}$ at different minor radii once the local $k_{\parallel}$ spectrum is known. The wave vector $k_{\parallel}$ evolves along the ray path, the m = 0, θ = 65 deg example being shown in Fig. 2-32. By sampling the various rays in our spectrum the average w, prescribed in Ref. 59, is computed at each value of r. Over the bulk of the plasma we find w ranges from one to two, hence $\hat{j}/\hat{p} \approx 17$. With the use of Eq. 2-3 we construct the current density profile. The result for $\bar{T}_e$ = 16 keV is given by Fig. 2-33. The profile is centrally peaked but would need further optimization (larger N) to conform closely with the broad profile assumed for our high beta equilibrium.

By numerically integrating the current and power densities we find the general result for HSMS current drive,

$$I/P = \frac{0.11\ (\bar{T}_e/18\ \text{keV})\ \text{A/W}}{(\bar{n}_e/0.84 \times 10^{20}\ \text{m}^{-3})}\ , \qquad (2\text{-}45)$$

where the total power P includes the small amount ($\sim$ 3.3%) lost to direct ion heating. Using Eqs. 2-45 and 2-1 we compute the necessary wave power absorbed and the net electric power production for the DEMO plant; see Fig. 2-34. The antenna coupling and transmission losses have not been calculated, and the value η_{aux} = 0.7 used is only an estimate. We recall that the range 13 keV $\lesssim \bar{T}_e \lesssim$ 17 keV results in the desirable range of neutron wall loads for DEMO, and, from the graph, we would expect roughly the same P_n over this range. However, the capital cost for the rf driver at 13 keV is almost double that at 17 keV (P_{rf} = 180 MW vs. P_{rf} = 95 MW), so the higher temperature extreme would be more desirable.

We conclude the HSMS discussion with an epitome of several points favoring its selection as the DEMO driver. A comparison of the HSMS approach with neutral beam drive (cf. Figs. 2-5 and 2-7) shows the HSMS to generally have slightly inferior $\hat{j}/\hat{p}$ values and thus higher power requirements. However, MeV neutral beams may require extensive development in order to attain η_{aux} as

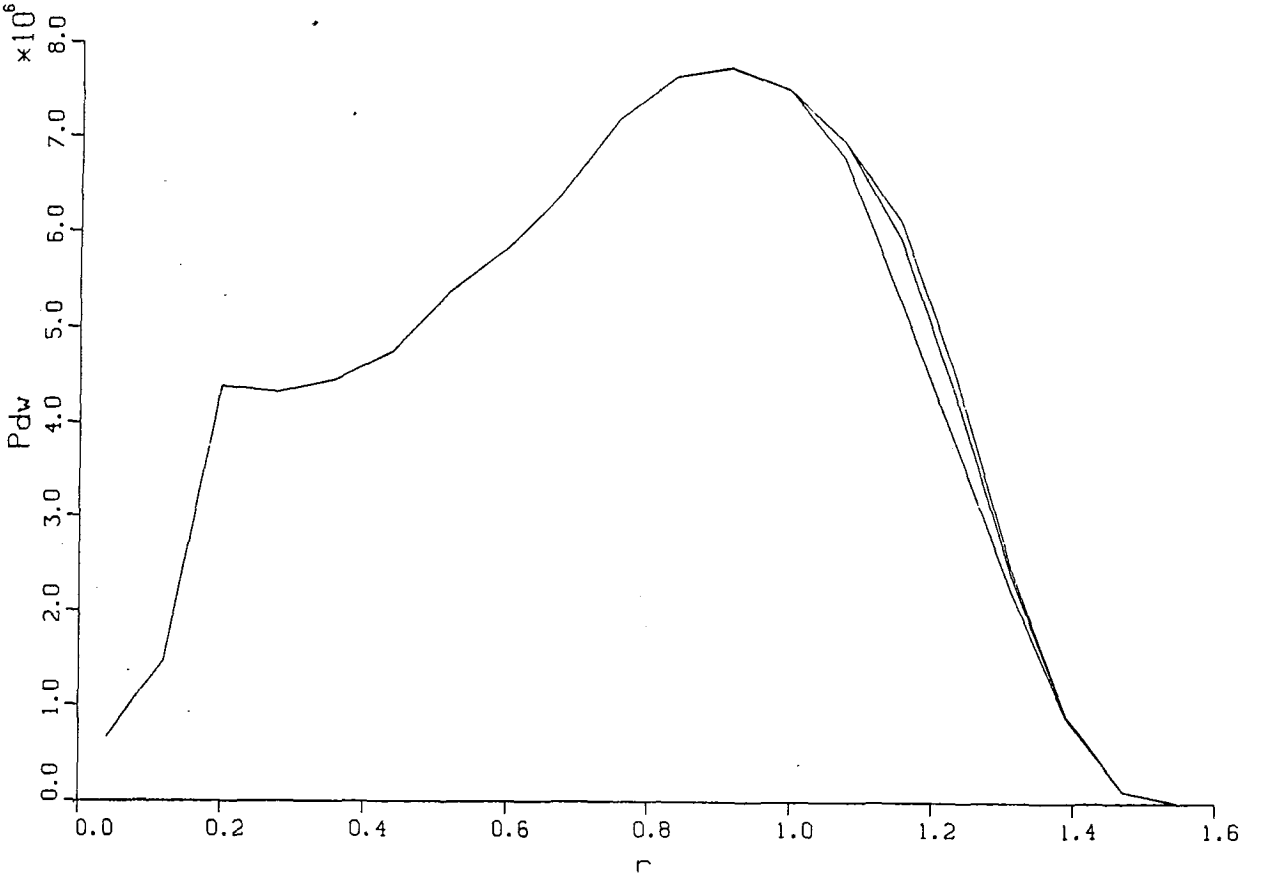

Fig. 2-31. Wave radial power dissipation; bottom curve is power absorbed by electrons, remaining increments are to tritium and beryllium.

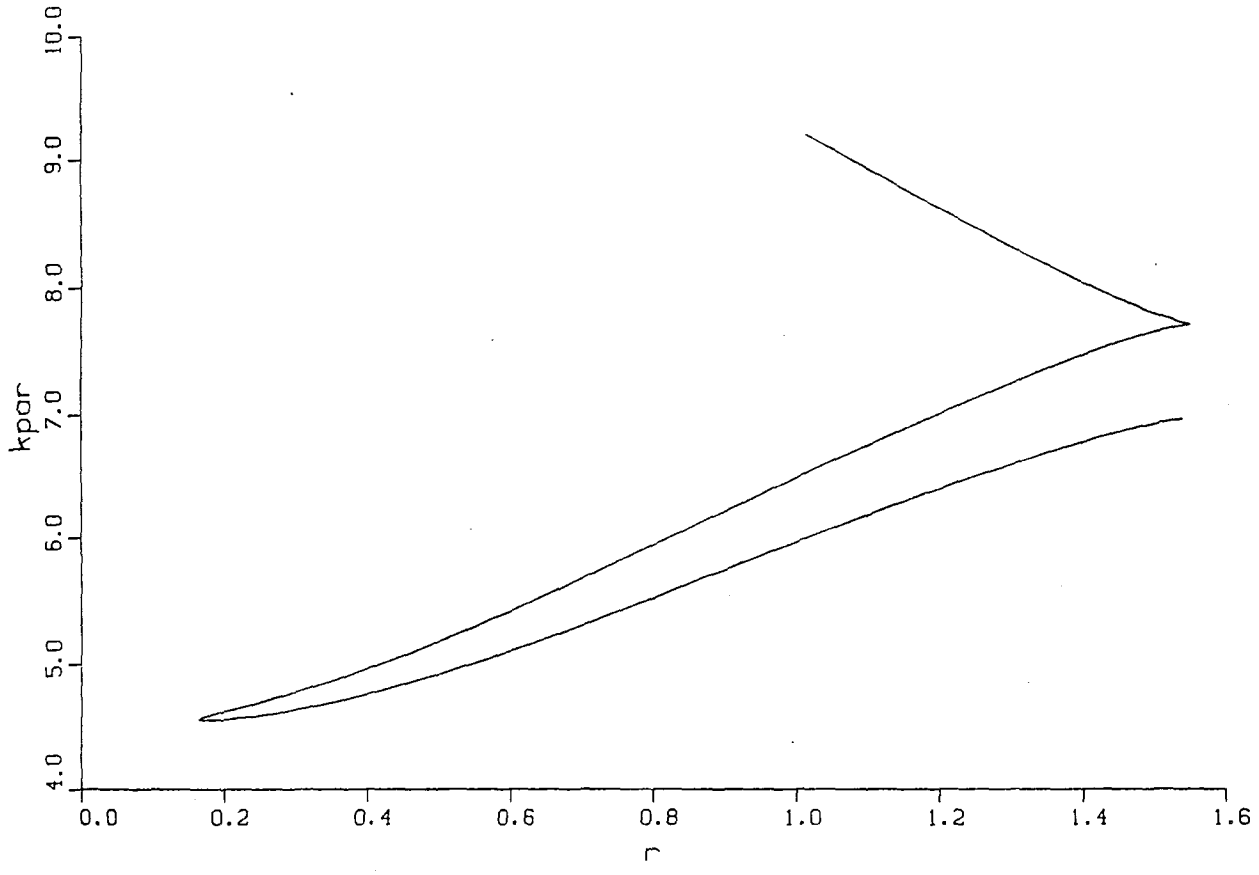

Fig. 2-32. Evolution of $k_{\parallel}$ along ray trajectory.

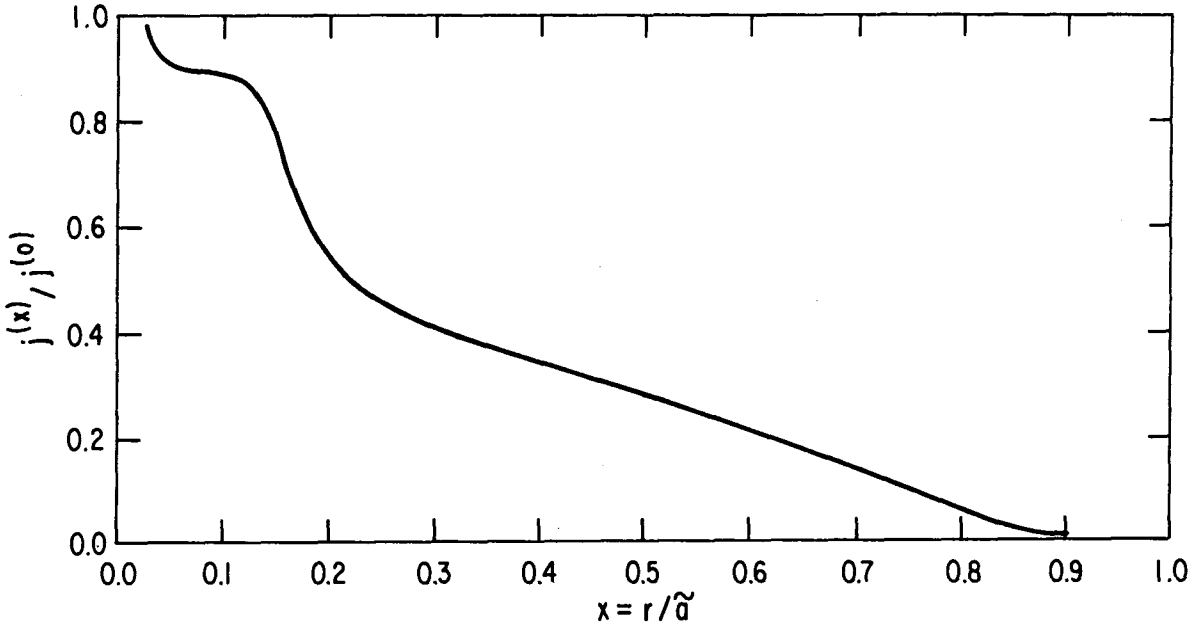

Fig. 2-33. Current density profile for HSMS at 82 MHz and $\lambda_{\parallel} \approx 0.8$ m.

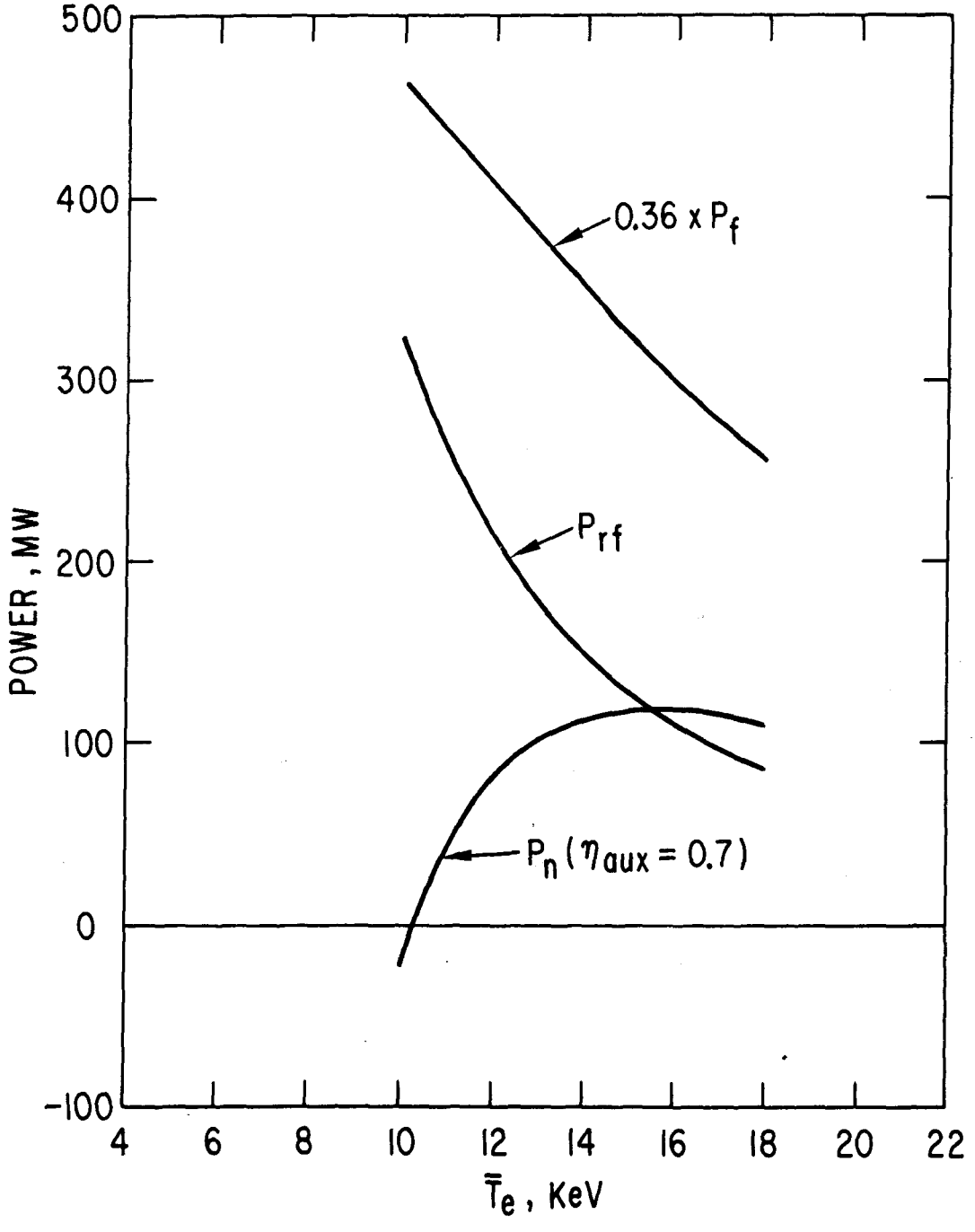

Fig. 2-34. Gross and net electric power for HSMS (82 MHz); capital cost of driver scales with the power absorbed in the plasma, P_{rf}.

high as the values achievable with present-day rf systems. Among wave driver schemes, the HSMS approach probably yields higher $\hat{j}/\hat{p}$ (lower P_{rf}) than other drivers which can supply centrally peaked current profiles. The only exception would be the CAW, but we reiterate that neoclassical trapping may reduce $\hat{j}/\hat{p}$ considerably from the values predicted in Ref. 59. Pulsed charged particle beams, such as the REB, promise the highest $\hat{j}/\hat{p}$ by far, but beam penetration is an unsettled question for the REB. Hence, the HSMS driver with its promise of deep plasma penetration and acceptable power requirements, must be considered a probable backup option to the REB driver.

References for Chapter 2

1. C. A. Flanagan, D. Steiner, and G. E. Smith, "Initial Trade and Design Studies for the Fusion Engineering Device," Oak Ridge National Laboratory, ORNL/TM-7777 (1981).

2. M. A. Abdou, et al., Proc. 8th Intern. Conf. on Plasma Physics and Controlled Nuclear Fusion Research, 1980, Brussels, Vol. 2 (IAEA, Vienna, 1981), p. 119.

3. D. A. Ehst, et al, "Lower Hybrid Heating and Current Drive System for a Tokamak Reactor," J. Fusion Energy (to be published).

4. D. A. Ehst, Nucl. Fusion, 19, 1369 (1979).

5. W. M. Stacey, Jr., et al., U.S. INTOR Conceptual Design, Vol. I, Ch. 3 (1981).

6. J. C. Wesley, et al., Proc. 8th Intern. Conf. on Plasma Physics and Controlled Nuclear Fusion Research, July 1-10, 1980, Brussels, Vol. 1 (IAEA, 1981), p. 35.

7. T. Ohkawa, Nucl. Fusion, 10, 185 (1970).

8. J. G. Cordey, et al., Nucl. Fusion 19, 249 (1979); D. F. H. Start, et al. Plasma Phys., 22, 303 (1980).

9. D. F. H. Start, J. G. Cordey, Phys. Fluids, 23, 1477 (1080).

10. D. F. H. Start, et al., Phys. Rev. Lett., 40, 1497 (1978).

11. K. B. Axon, et al., Proc. 8th Intern. Conf. on Plasma Physics and Controlled Nuclear Fusion Research, July 1-10, 1980, Brussels, Vol. 1 (IAEA, 1981), p. 413.

12. J. G. Cordey, et al., Culham Laboratory, CLM-P636 (1981); also, Plasma Phys. (submitted).

13. L. R. Grisham, et al., Princeton Plasma Physics Laboratory, PPPL-1839 (1981).

14. TRW, Inc., "Final Report, A Design Analysis of Supplemental Heating Systems," (1981); J. L. Orthel, et al., Bull. Am. Phys. Soc., 26, 1016 (1981).

15. S. Yoshikawa, Phys. Rev. Lett., 26, 295 (1971); S. Yoshikawa and N. C. Christofilos, Proc. 4th Intern. Conf. on Plasma Physics and Controlled Nuclear Fusion Research, 1971, Madison, Vol. 2 (IAEA, Vienna, 1972), p. 357.

16. K. Ikuta, Japan J. Appl. Phys., 11, 1684 (1972).

17. J. Benford, et al., Phys. Rev. Lett., 31, 346 (1973); J. Benford, J. Guilory, and C. Stallings, J. Appl. Phys., 45, 1657 (1974); D. W. Swain, P. A. Miller, and M. M. Widner, Sandia Laboratories, SAND75-0214 (1975); T. R. Lockner and B. R. Kusse, J. Appl. Phys., 49, 2357 (1978); A. Mohri, K. Ikuta and M. Masuzaki, J. Phys. Soc. Japan, 42, 1025 (1977).

18. J. Benford, B. Ecker and V. Bailey, Phys. Rev. Lett., 33, 574 (1974); P. Gilad, B. R. Kusse, and T. R. Lockner, Phys. Rev. Lett., 33, 1275 (1974); A. Mohri, et al., Phys. Rev. Lett., 34, 574 (1975); M. Masuzaki, et al., Japan J. Appl. Phys., 14, 1413 (1975).

19. A. Mohri, et al., Proc. 6th Intern. Conf. on Plasma Physics and Controlled Nuclear Fusion Research, 1976, Berchtesgaden, Vol. 3 (IAEA, Vienna, 1981), p. 395; A. Mohri, et al., Proc. 8th Intern. Conf. on Plasma Physics and Controlled Nuclear Fusion Research, 1980, Brussels, Vol. 1 (IAEA, 1981), p. 511; A. Mohri, et al., Proc 7th Intern. Conf. on Plasma Physics and Controlled Nuclear Fusion Research, Innsbruck, 1978, Vol. 3 (IAEA, Vienna, 1979), p. 311.

20. V. Bailey, et al., Proc. 4th Intern. Conf. on High-Power Electron and Ion-Beam Research and Technology, Palaiseau, France (1981) (to be issued).

21. D. A. Hammer and K. Papadopoulos, Nucl. Fusion, 15, 977 (1975).

22. N. J. Fisch, Princeton Plasma Physics Laboratory, PPPL-1772 (1981); also Proc. 4th Top. Conf. on RF Plasma Heating, Austin, Texas (1981).

23. D. A. Hammer, et al., Phys. Fluids, 21, 483 (1978); M. A. Greenspan, et al., Phys. Fluids, 23, 205 (1980).

24. R. V. Lovelace, R. N. Sudan, Phys. Rev. Lett., 27, 1256 (1971); R. Z. Sagdeev, Magneto-Fluid and Plasma Dynamics, H. Grad, Ed., Vol. 18, Am. Math. Soc., Providence, R.I. (1967), p. 18.

25. K. Papadopoulos, Phys. Fluids, 18, 1769 (1975); H. P. Freund, et al., Phys. Fluids, 23, 518 (1980); L. E. Thode, Phys. Fluids, 19, 831 (1976).

26. D. Mosher, Phys. Fluids, 18, 846 (1975).

27. S. P. Hirshman, R. J. Hawryluk, and B. Birge, Nucl. Fusion, 17, 611 (1977).

28. R. J. Bickerton, J. W. Connor, and J. B. Taylor, Nature, Phys. Sci., 229, 110 (1971); D. J. Sigmar, Nucl. Fusion, 13, 17 (1973).

29. J. T. Hogan, Nucl. Fusion, 21, 365 (1981).

30. D. G. McAlees, Oak Ridge National Laboratory, ORNL-TM-4661 (1974).

31. Y. I. Kolesnichenko, S. N. Reznik, and V. A. Yavorskij, Nucl. Fusion, 20, 1041 (1980).

32. J. R. McNally, Jr., Oak Ridge National Laboratory, ORNL-TM-6492 (1978).

33. J. M. Dawson and K. R. MacKenzie, Center for Plasma Physics and Fusion Engineering, UCLA, PPG-470 (1980).

34. F. L. Hinton and J. C. Wiley, Proc. Sherwood Theory Meeting, Austin, Texas (1981), Paper 1B16.

35. E. Ott and W. M. Manheimer, Nucl. Fusion, 17, 1057 (1977).

36. S. Humphries, Jr., Nucl. Fusion, 20 1549 (1980).

37. D. A. Baker and J. E. Hammel, Phys. Fluids, 8, 713 (1965).

38. F. Wessel and S. Robertson, Phys. Fluids, 24, 739 (1981); S. Robertson, et al., Phys. Rev. Lett., 47, 508 (1981).

39. E. J. Strait and J. C. Sprott, Nucl. Fusion, 18, 1595 (1978).

40. W. M. Manheimer and N. K. Winsor, Comments on Plasma Phys. and Controlled Fusion, 6, 53 (1980).

41. W. M. Manheimer and N. K. Winsor, Naval Research Laboratory, NRL-Memorandum Report 4213 (1980).

42. D. A. Ehst, "Wave Driver Options for Low Aspect Ratio Steady-State Tokamak Reactors," J. Fusion Energy, 1 (1981) (to be issued).

43. N. J. Fisch, Nucl. Fusion, 21, 15 (1981).

44. J. Hosea, et al., Phys. Rev. Lett., 43, 1802 (1979).

45. J. Hosea, et al., Proc. 8th Intern. Conf. on Plasma Physics and Controlled Nuclear Fusion Research, July 1-10, 1980, Brussels, Vol. 2 (IAEA, 1981), p. 95.

46. F. W. Perkins, Proc. 4th Top. Conf. on RF Plasma Heating, Austin, Texas (1981), Paper B-13.

47. S. C. Chiu, et al., General Atomic Co., GA-A16353 (1981); also, Nucl. Fusion (submitted).

48. H. Stix, Nucl Fusion, 15, 737 (1975).

49. C. Chu and J. L. Sperling, General Atomic Co., GA-A15027 (1978).

50. D. K. Bhadra and C. Chu, General Atomic Co., GA-A16326 (1981).

51. N. J. Fisch and A. H. Boozer, Phys. Rev. Lett., 45, 720 (1980).

52. C. F. F. Karney and N. J. Fisch, Princeton Plasma Physics Laboratory, PPPL-1808.

53. D. F. H. Start, et al., Culham Laboratory, CLM-P644 (1981).

54. T. Ohkawa, General Atomic Co., GA-A13847 (1976).

55. R. Prater, et al., General Atomic Co., GA-A15229 (1978).

56. P. B. Parks and F. B. Marcus, Nucl. Fusion, 21, 1207 (1981).

57. J. M. Dawson and P. Kaw, Bull. Am. Phys. Soc., 26, 866 (1981).

58. J. D. H. Wort, Plasma Phys., 13, 258 (1971).

59. N. J. Fisch and C. F. F. Karney, Phys. Fluids, 24, 27 (1981).

60. R. W. Harvey, K. D. Marx, and M. G. McCoy, Nucl. Fusion, 21, 153 (1981).

61. C. F. F. Karney, F. W. Perkins, and Y.-C. Sun, Phys. Rev. Lett. 42, 1621 (1979).

62. J. M. Dawson and M. F. Uman, Nucl. Fusion, 5, 242 (1965).

63. M. Fukuda and K. Matsuura, J. Phys. Soc. Japan, 41, 1376 (1976).

64. M. Fukuda and K. Matsuura, J. Phys. Soc. Japan, 44 1344 (1978).

65. W. N. Hugrass, Nucl. Fusion, 21, 1326 (1981); M. Fukuda, J. Phys. Soc. Japan 45, 283 (1978).

66. A. Hasegawa, Nucl. Fusion, 20, 1158 (1980).

67. C. F. F. Karney and N. J. Fisch, Phys. Fluids, 22, 1817 (1979).

68. C. P. Moeller, V. S. Chan, General Atomic Co., GA-A14836 (1978).

69. S. Yoshikawa and H. Yamato, Phys. Fluids, 9, 1814 (1966).

70. C. F. Kennel and F. Engelmann, Phys. Fluids, 9, 2377 (1966).

71. N. J. Fisch, Princeton Plasma Physics Laboratory, PPPL-1739 (1981).

72. W. F. Weldon, et al., Proc. 2nd IEEE Intern. Pulsed Power Conf., Lubbock, Texas (June, 1979), pp. 76-82.

73. I. Langmuir, Phys. Rev., 38, 954 (1929).

74. P. A. Miller, J. W. Poukey, and T. P. Wright, Phys. Rev. Lett., 35, 940 (1975).

75. M. Widner, et al., Phys. Fluids, 13, 2531 (1970).

76. M. M. Widner and J. W. Poukey, Phys. Fluids, 19, 1838 (1976).

77. G. N. Glasoe and J. V. Lebacqz, Pulse Generators, Dover Publications, New York, NY (1965), pp. 464-465.

78. W. L. Bird and H. H. Woodson, University of California, UCRL-15213 (1980).

79. J. H. Gully, et al., Proc. 2nd IEEE Intern. Pulsed Power Conf., Lubbock, Texas (June, 1979), p. 385-391.

80. M. Brennan, et al., ibid., pp. 392-397.

81. M. Pichot, et al., ibid., pp. 398-401.

82. B. M. Canter, et al., Proc. 14th Pulse Power Modulator Symp., (June 3-5, 1980), pp. 259-263.

83. J.-M. Noterdaeme, R. R. Weynants, and A. M. Messian, Proc. 9th IEEE Symp. on Engr. Problems of Fusion Research, Chicago, Illinois (October 26-30, 1981).

84. J. Jacquinot, et al., Proc. 11th Symp. on Fusion Technology, Oxford (1980).

85. A. H. Bohr, Proc. 9th IEEE Symp. on Engr. Problems of Fusion Research, (October 26-30, 1981).

86. J. Jung and M. Abdou, Nucl. Technol., 41, 71 (1978)

CHAPTER 2

APPENDIX

Chapter 2 Appendix

List of Figures

Chapter 2 Appendix

List of Tables

APPENDIX 2A

REB CURRENT DRIVE IN COLLISIONAL LIMIT

In situations for which the return current resistivity is not anomalous ($\alpha \equiv 1$) we find that the terms due to the emf in Mosher's REB equations[26] (see Sec. 2.2.2) are small compared to the collisional terms. In this limit the relativistic electron dynamics are governed by

$$\frac{d\gamma}{dt} = \frac{-\nu_e \gamma}{(\gamma^2 - 1)^{1/2}}$$

$$\frac{dU}{dt} = \frac{-\nu_t \gamma U}{(\gamma^2 - 1)^{3/2}} ,$$

where the energy loss frequency, due to electron drag, is $\nu_e = (1/2)(v_e/c)^3 \nu_0$, and the momentum loss rate, due to electrons and ions, is $\nu_t = \nu_i + 2\nu_e = (Z_i + 2)\nu_e$. The other quantities are defined in Sec. 2.2.2. Mosher provides the following solutions to these equations:

$$\nu_e t = \left\{ \left[\sqrt{\gamma^2 - 1} - \cos_\alpha^{-1} (\gamma^{-1}) \right] - \left[\sqrt{\gamma^2 - 1} - \cos^{-1}(\gamma^{-1}) \right] \right\} ,$$

$$U/U_d = \left(\frac{\gamma_d + 1}{\gamma_d - 1} \right)^{\nu_t/2\nu_e} \left(\frac{\gamma - 1}{\gamma + 1} \right)^{\nu_t/2\nu_e} .$$

Thus, the time required for the REB to dissipate all its energy, which is the period of reversed emf, is given by $\Delta t = \left[\sqrt{\gamma_d^2 - 1} - \cos^{-1}(\gamma_d^{-1}) \right] \nu_e^{-1}$. We note

$$\lim_{\gamma_d >> 1} \Delta t = \gamma_d \nu_e^{-1} . \qquad (2A\text{-}1)$$

As discussed in Sec. 2.2.2, the period of forward emf until I decays to its original value, I_0, is

$$\delta t = (L/R)\, \Delta I / I_0 . \qquad (2A\text{-}2)$$

Provided $\gamma_d \gtrsim 2$, the current increase during the short period of diode operation, t_{t-o}, is negligible, and ΔI is gotten from Eq. 2-13 in the $\tau << 1$ limit:

$$\Delta I = \frac{-I_0 \Delta t}{L/R} + \int_0^{\Delta t} \frac{dt' \; I_{do} U/U_{do}}{L/R} .$$

Combining this with Eq. 2A-2 we find the total interpulse time is

$$\Delta t + \delta t = \frac{I_{do}}{I_0} \int_0^{\Delta t} \frac{dt' \; U(t')}{U_{do}} .$$

Thus, since the energy injected at each pulse is $\mathscr{E}_d = I_{do} t_{tr} (\gamma_d - 1)\, mc^2/e$, the time averaged power requirement is $\langle P_d \rangle = \mathscr{E}_d / (\Delta t + \delta t)$, and we find

$$\frac{I_0}{\langle P_d \rangle} = \frac{\sqrt{1 - \gamma_d^{-2}}\; e}{(\gamma_d - 1) 2\pi R_0 m_e} \int_0^{\Delta t} dt' \; \frac{U(t')}{U_{do}} . \qquad (2A\text{-}3)$$

We note $I_0/\langle P_d \rangle$ is independent of the beam energy $\mathscr{E}_d$; γ_d is the only beam parameter which explictly enters the expression. Beam energy limitations only arise from the constraint (discussed in Sec. 2.2.2) that I_{do} exceed I_0. Examination of Eq. 2A-3 shows $I_0/\langle P_d \rangle$ increases monotonically with γ_d, but we shall find there is an upper bound as $\gamma_d \to \infty$.

It remains to evaluate the integral in Eq. 2A-3. This can be performed numerically with the aid of Mosher's solution for U/U_d, but it suffices here to recall that $U/U_d \approx 1$ for $0 < t < \Delta t$ if γ_d is large. We find

$$\frac{I_0}{\langle P_d \rangle} = \frac{\sqrt{1 - \gamma_d^{-2}}}{(\gamma_d - 1)} \; \frac{e}{2\pi R_0 m_e c} \; \frac{\Delta t}{1 + g(\gamma_d)} , \qquad (2A\text{-}4)$$

where $g \approx 1$ at $\gamma_d = 2$ and decreases as γ_d increases. For $\gamma_d = 4$ we have $\Delta t = 2.55\, \nu_e^{-1}$ and $g = 0.70$, and, for an average density $\bar{n}_e = 1.0 \times 10^{20}\ m^{-3}$ we find $\nu_e = 71\ s^{-1}$. Thus, for the DEMO plasma of Table 2-5, we find $I_0/\langle P_d \rangle = 0.127$ A/W. Also,

$$\lim_{\gamma_d \to \infty} I_o/\langle P_d \rangle = \frac{e}{2\pi R_o \nu_e m_e c} \quad . \tag{2A-5}$$

For the DEMO example, $I_0/\langle P_d \rangle \to 0.253$ as $\gamma_d \to \infty$. These values of $I_0/\langle P_d \rangle$ compare favorably with those obtained with wave driven currents. We notice $I_0/\langle P_d \rangle \propto \nu_e^{-1}$, so current drive efficiency increases with lower density, a result shared by the other current drive schemes.

Finally, we compute the normalized quantity $\hat{j}/\hat{p}$ with the relationship $j/p = 2\pi R_0 (I_0/\langle P_d \rangle)$. Then we find in the interesting $\gamma_d \to \infty$ limit that

$$\lim_{\gamma_d \to \infty} \hat{j}/\hat{p} = 2(c/v_e)^2 \quad .$$

This is identical with the result found by Fisch for steady state (CW) relativistic currents driven, for example, by ECRH.[71] Thus, for $\bar{T}_e \approx 20$ keV we would get the upper limit of $\hat{j}/\hat{p} \approx 50$, which, of course, is competitive with values obtained for other drivers. We conclude with the observation that $\hat{j}/\hat{p}$ can be much larger than 50 if the plasma resistivity increases due to REB injection, as discussed in the text. Thus, the pulsed REB appears at least as attractive as other drivers, and it may prove vastly superior.

APPENDIX 2B

PRELIMINARY DESIGN OF AN REB STARTUP AND CURRENT DRIVE SYSTEM FOR DEMO

2B.1 Introduction

The function of the relativistic electron beam system is to: (1) startup and maintain the toroidal current during steady state operation; and (2) heat the plasma to ignition during startup.

This appendix describes the electron beam apparatus including the generators, transmission lines, and diodes that generate the beam.

Because of the size of the pulsed power equipment and the need for periodic maintenance, the pulsed power generators that produce the high power electrical pulse are housed outside the reactor containment building. A transmission line transports the energy from the pulse generator to the diode within the tokamak first wall.

2B.1.1 Rationale for Selection of Beam System Parameters

Physical and technological constraints must be considered in choosing desirable beam parameters. Scaling of the average REB power, P_{av}, to the I^2R plasma dissipation for steady state operation of DEMO is shown in Sec. 2.2. As kinetic energy of the beam is increased, injected beam energy per pulse increases and the pulse repetition rate decreases.

For the most efficient current drive where P_{av}/I^2R is a minimum for a given beam kinetic energy, the injected charge $Q_{INJ} = I_B \tau_{INJ}$ (injected current times the injection time) remains approximately constant. For DEMO this is on the order of 1 to 3 C per pulse. Thus, a 1 μs injection time requires a 1 to 3-MA injected beam, while a 100 μs injection time gives a 10 to 30 kA injected beam.

In the diode design section in this appendix, it is demonstrated that injected electron current density depends primarily on the plasma parameters and is only a weak function of beam kinetic energy. Injected electron beam current density for the DEMO plasma parameters in the shadow of the limiter is $J_e \approx 13 \times 10^4$ A/m^2. The cathode area for a 1 μs injection time is 8 to 19 m^2 while a 100 μs injection time requires a much smaller cathode area of 0.08 to 0.19 m^2.

Since the cathode is within the first wall at the edge of the plasma, it is desirable to minimize the cathode area. This arrangement reduces the cooling requirement for the diode structure, lowers the level of impurities caused by plasma impinging on the diode, and reduces the probability of a portion of the injected beam striking the diode structure. Thus, longer injection times which require smaller diode structures are preferable.

Pulse duration selection is also important for the pulsed power system. In the range of a few 100 ns to 1 μs, both the lumped component pulse-forming network (PFN) and the distributed component pulse-forming line (PFL) systems must be considered (see Fig. 2B-1). For pulse durations less than 0.5 μs, the pulse-forming line approach is probably preferable despite the fact that PFLs require that energy be stored twice--once in the Marx generator and again in the liquid pulse-forming line. The PFL output switch must pass all energy in the system at high voltage.

PFNs obviate the second pulse charged energy store and have no output switch because the Marx is an element of the network. Each Marx does have a switch that must pass large currents at high voltages. The PFN approach is appropriate in the range of 1 μs to a few 100 μs. The PFN approach becomes more difficult as the pulse duration is shortened.

For pulse durations greater than 50 μs a new type of rotating machine, the compulsator[72], which is explained in more detail later in this appendix, becomes a viable alternative. Since the compulsator is a low voltage, high current source, it is generally used with a pulse transformer to increase voltage. The compulsator/transformer system is inherently a repetitive, pulsed power system.

The compulsator/transformer system is small and straightforward compared to the PFL and PFN systems. The PFL and PFN systems must store several megajoules in a Marx while the compulsator/transformer system will store at most 4% of the energy in a capacitor bank. Switches for the compulsator/transformer system are simpler and closer to present technology, and output efficiency is comparable to that of the PFL and PFN systems. Since the compulsator/transformer pulsed power system offers several engineering and technological advantages over the PFL and PFN systems, longer pulse durations that can utilize the compulsator/transformer are preferable.

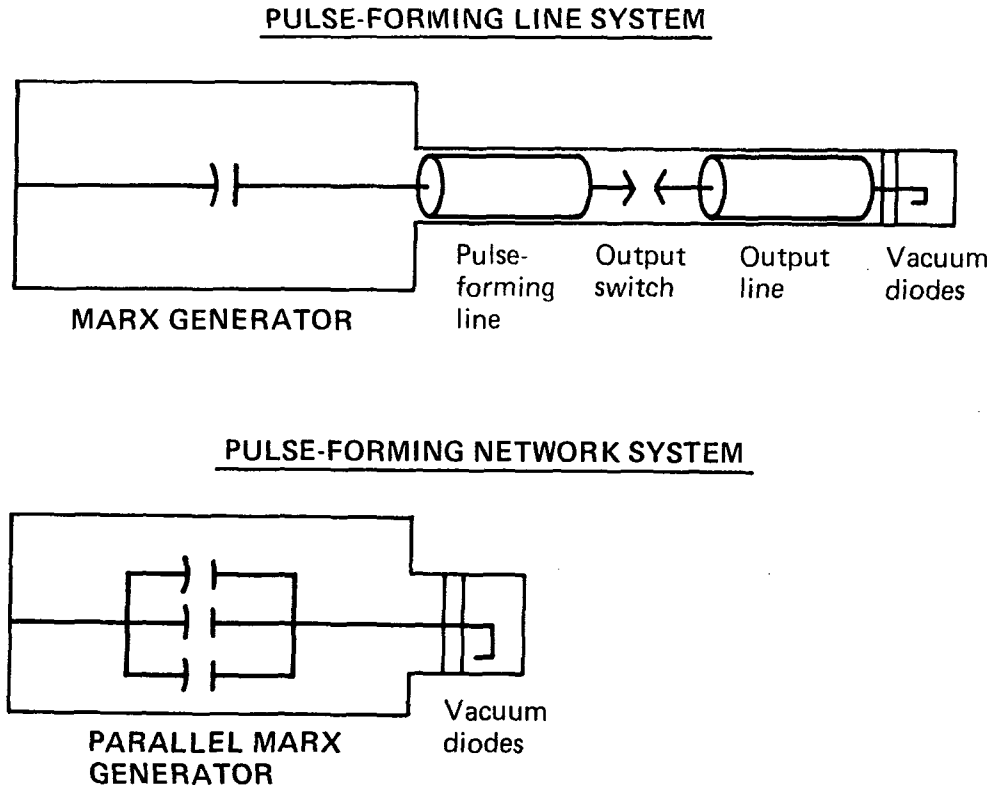

Fig. 2B-1. Basic elements of two pulsed power systems.

As the kinetic energy of the injected beam (or equivalently the voltage of the pulsed power system) increases, the efficiency of the current drive increases, but larger amounts of energy per pulse must be injected. The increase in current drive efficiency does not offset the increased difficulty for the pulsed power system in providing the larger energies per pulse.

Smaller kinetic energies for the beam translate into reduced transmission line dimensions. Since the transmission line dimensions determine the blanket, shield, and first wall penetration area for the beam line, smaller beam kinetic energies are preferable to reduce neutron streaming.

The ability of the beam to cross magnetic flux surfaces in the tokamak is a function of injected beam kinetic energy. If injected beam kinetic energy is small the beam will remain on the injected flux surface and eventually be re-incident on the diode structure. Thus, beam injection and trapping considerations provide a lower limit on the kinetic energy of the injected beam.

2B.1.2 Summary of Beam System for DEMO

The kinetic energy of the injected beam was established at 1.533 MeV, corresponding to a relativistic factor, γ, of $\gamma = 4$. This kinetic energy is a compromise between lower voltages where beam injection and trapping are predicted to be inefficient, and higher voltages where the first wall penetrations are large.

Minimum beam power for a $\gamma = 4$ beam occurs when the total injected beam energy per pulse, E_B, is 2 MJ (for an infinitely enhanced collision frequency). Since this value will not be achieved in a real reactor, a value of $E_B = 4$ MJ was used in the design. Estimates of the enhanced collision frequency suggest that this is conservative.

A beam pulse duration of 100 μs was chosen for the DEMO design study. This longer beam duration reduces the cross-sectional area of the diode structure and facilitates use of rotating machinery for the pulsed power systems.

To allow for periodic maintenance of the pulsed power equipment and to provide for redundancy, the beam system is composed of two identical beam lines (cathode, transmission line, and pulsed power generator).

Two cathodes are at the edge of the plasma in the shadow of the limiter. Each provides an electron current of 13,046 A for 100 μs. Each cathode, which does not have to be circular, measures 1,035 cm^2.

A transmission line transports energy from the pulsed power generator to the diode within the tokamak first wall. From the generator to the outside of toroidal field coils, the transmission line is a coaxial oil-insulated transmission line. An oil-insulated transmission line avoids the radiation shielding necessary to protect against an accidental shorting of a high voltage vacuum transmission line which can produce significant quantities of bremsstrahlung radiation. The outer conductor of the transmission line remains at ground and the inner conductor is pulsed negative.

From outside the toroidal field coils to the diode, the transmission line is a vacuum transmission line, which penetrates the blanket, shield, and first wall in a radial direction. The wall penetration area is 0.2 m^2. Once inside the first wall the transmission line turns until it is parallel with the toroidal magnetic field. The vacuum transmission line also is convoluted from circular to rectangular after it penetrates the first wall. Two ceramic insulators serve as the vacuum/oil interface. Two insulators are used for safety and to take up the bending stresses of the cantilevered inner portion of the vacuum transmission line.

From Sec. 2.2, the ratio of the average beam power, P_{av}, to the I^2 plasma dissipation for $\gamma = 4.0$ and $E_B = 4.0$ MJ is 2.31, yielding an average beam power of $P_{av} = 1.33$ MW for a plasma electron temperature of $T_e = 14$ keV. The interpulse period is 3 s, or the repetition rate is 0.33 Hz. To be conservative (by a factor of two) the pulsed power system is designed for $P_{av} = 2.67$ MW and an interpulse period of 1.5 s (0.67 Hz).

The compulsator/transformer pulsed power system has been chosen for the design. Each beam line has six compulsators in parallel driving one transformer.* This is the "parallel compulsator/series output approach." Each compulsator is driven by an electrical motor that must provide 605 HP for normal steady-state operation. This value includes the inefficiencies in the compulsator, transformer, transmission line, and diode.

During startup the beam system must heat the plasma to ignition while simultaneously increasing the toroidal current to the steady state value. Average beam power level required for this is 60 to 100 MW for 6 min. During

*See Sec. 2B.4.4 for a detailed explanation of the circuit.

this high power operation additional power sources will have to be coupled to the compulsator. An accumulator could, in principle, provide the additional power required during startup. The capital costs are relatively small for the power output.

Overall efficiency (power delivered to the plasma divided by power from external electrical source) of the beam system is expected to be 48%. The beam system thus requires 5.6 MW to maintain the current. This includes a safety factor of two in determining average required power. Capital cost of the beam system without the startup option is estimated to be $4.5 M, and with the startup option $9.6 M.

2B.2 Diode Design

The DEMO diode is a plasma diode. The cathode can be made from almost any conducting material including graphite, and the plasma serves as the anode.

Ion current density, J_i, drawn from a plasma diode neglecting relativistic and edge effects, is given by the Langmuir[73] expression for bipolar flow

$$J_i = \frac{1.86\ (4\epsilon_0/9)(2eZ/M_i)^{1/2}\ V^{3/2}}{x^2}\ , \qquad (2B\text{-}1)$$

where

ϵ_0 = permittivity constant,

e = electronic charge,

Z = average ion charge,

M_i = average ion mass,

V = diode voltage, and

x = effective anode and cathode spacing.

The electron current density, J_e, is then

$$J_e = \left[\frac{M_i}{Z\ m_e}\right]^{1/2} J_i\ ,$$

where m_e is the rest mass of an electron.

Initially, when a negative voltage is applied to the cathode, electrons are expelled from the cathode region and ions are drawn to the cathode. If the diode draws enough current the diode gap will open with a velocity[74]

$$\frac{dx}{dt} = \frac{J_i}{Z\, n_i\, e}\,, \qquad (2B\text{-}2)$$

where n_i is the ion number density.

As the diode spacing opens up, the ion current density decreases as $1/x^2$ (Eq. 2B-1) for a constant voltage source. As long as dx/dt given by Eq. 2B-2 is greater than the ion-acoustic velocity, diode spacing continues to open up with the velocity given by Eq. 2B-2. When $J_i/(Z\, n_i e)$ falls below the ion-acoustic velocity, a rarefaction wave is sent into the plasma and plasma ions flow into the gap.[75,76]

A Langmuir-type sheath develops in which the rarefaction wave causes ions to be accelerated and flow into the sheath. The ions flow into the sheath with a velocity given by the ion-acoustic velocity, v_{ia}, and density at the edge of the sheath of $0.368\ n_i(o)$ where $n_i(o)$ is the background ion plasma density in the undisturbed plasma.

The cathode-anode spacing increases at a rate given by

$$\frac{dx}{dt} = \frac{J_i}{Z\, n_i e} - 0.368\ v_{ia}$$

until the impedance of the diode increases enough to drop J_i to

$$J_i = 0.368\ e\ Z\ n_i(o)\ v_{ia}\,. \qquad (2B\text{-}3)$$

If the driving source has a constant voltage, the spacing will remain constant and steady state operation, in which V, J_i, J_e, and x are constant, is obtained.

We have numerically solved the transient sheath opening for a voltage source with the following characteristics: 10-μs linear rise to 1.533 MV, 100 μs at 1.533 MV, and a 10-μs linear fall to 0 voltage. Plasma parameters were taken from the DEMO parameters and a 10-m, 61-Ω vacuum transmission line was assumed to connect the voltage source with the diode. The parameters are

characteristic of the beam system being designed. The calculation determined that the sheath opens up to its steady state value during the risetime of the voltage source and then the diode has a constant impedance such that the ion current density is given by Eq. 2B-3.

The equations have been derived using the non-relativistic formulas. To first order, the correction for relativistic effects is

$$J_e = \left(\frac{M_i}{Z\, m_e}\right)^{1/2} J_i \frac{2.72 \times 10^3 \left[\sqrt{\frac{eV}{m_e c^2} + 1} - 0.8471\right]^2}{2.33 \times 10^{-6}\, V^{3/2}},$$

where c is the speed of light.

Since the effective anode-cathode spacing opens to its steady-state value on a time scale which is short compared to the full pulse length, the procedure for determining the diode area is as follows:

(1) Determine the γ and total beam energy, E_B, requirements for current drive.

(2) Determine the pulse length, τ_B, and number of diodes N_D from pulse power and reactor considerations.

(3) Calculate the electron current/diode, I_e, which is required.

$$I_e = \frac{E_B}{N_D \tau_B (m_e c^2/e)(\gamma - 1)}.$$

(4) Using the plasma parameters at the diode position, calculate the steady state ion current density

$$J_i = 0.368\, Z\, n_i(o) v_{ia}.$$

(5) Calculate the corresponding electr current

$$J_e = J_i \left(\frac{M_i}{Z\, m_e}\right)^{1/2} \frac{2.72 \times 10^3 \left[\sqrt{\frac{eV}{m_e c^2} + 1} - 0.8471\right]^2}{2.33 \times 10^{-6}\, V^{3/2}}.$$

(6) The cathode area is then

$$A = I_e/J_e \ .$$

Applying this to the beam system for DEMO with $\gamma = 4.0$, $E_B = 4$ MJ, $N_D = 2$ gives $I_e = 13{,}046$ A/diode. Using the plasma parameters at the edge of the plasma in the shadow of the limiter ($T_e = T_i = 340$ eV, $Z\ n_i(o) = n_e(o) = 2 \times 10^{17}\ m^{-3}$) the ion and electron current densities are $J_i = 0.27\ A/cm^2$ and $J_e = 12.6 A/cm^2$, respectively. Each cathode then has an area of $A = 1{,}035\ cm^2$. The average energy flux on the cathode from the backstreaming ions is $0.27\ MW/m^2$ Peak flux occurs during beam injection and is $4{,}050\ MW/m^2$. The diode structure also has a thermal flux incident due to the burning plasma.

Data on long-life field emission cathodes are minimal, especially for a plasma diode. However, active programs are investigating both the uniformity and the lifetime of surfaces such as blades, carbon felt, plasma surface flashover, etched metals, and other cathode materials. Programs in the DOD laser community are now investigating erosion rates, debris, and other engineering problems for field emission cathodes at repetition rates up to 100 pps. Data will be available in a timescale short compared to that of the DEMO facility we address. It is probable that reliable field emission cathode materials will be found with lifetimes in excess of 10^6 shots; these materials might be appropriate for the DEMO requirements. Other diode alternatives exist. One of these is the use of thermionic cathodes. The current densities required ($\sim 13\ A/cm^2$ have been achieved experimentally. However, thermionic cathodes are very sensitive to poisoning by ion bombardment.

2B.3 Transmission Line

A transmission line transports the energy from the pulsed power generator to the diode within the tokamak first wall. From the generator to the outside of the toroidal field coils the transmission line is a coaxial oil-insulated transmission line with an outer radius of the inner conductor of $r_i = 14.7$ cm and an inner radius of the outer conductor of $r_o = 40$ cm. The length of this portion of the line is expected to be between 10 and 15 m.

Two ceramic insulators at the outer edge of the toroidal field coils provide the vacuum/oil interface for the transition from an oil- to vacuum-insulated transmission line. The radius of the inner conductor is $r_i = 36.8$ cm and the radius of the outer conductor is $r_o = 1$ m at the insulator.

From the insulators to the diode the transmission line is a vacuum transmission line with a cantilevered inner conductor. The radius of the inner conductor is r_i = 9 cm and the outer conductor radius is r_o = 25 cm. The length of the vacuum transmission line is approximately 4.5 m.

The vacuum transmission line penetrates the blanket, shield, and first wall in a radial direction. The cross-sectional area of the wall penetration is 0.2 m^2. Once inside the first wall the transmission line turns until it parallels the toroidal magnetic field. The vacuum transmission line is also convoluted from circular to rectangular after it is inside the first wall.

A sketch of the transmission line and insulators is shown in Fig. 2-3. The convoluted section of the transmission line is sketched in Fig. 2B-2.

This section discusses energy losses in the transmission line and the electrical and structural design of the line.

2B.3.1 Energy Losses

When a transmission line carries current there is an inflow of energy into the solid conductor. The energy appears in two different forms

(1) Magnetic field energy density ($B^2/2\mu$), where B is the magnetic field and μ is the permeability.

(2) The standard joule heating (J^2/σ), where J is the current density and σ is the conductivity.

For the beam pulse lengths of interest, the magnetic skin depth is small or comparable to the thickness of the metal, and magnetic diffusion must be included in the estimates of the energy lost in the transmission line. We first obtain the magnetic diffusion equation in cylindrical coordinates and then show that for most cases of interest a one-dimensional rectangular coordinate approximation is valid.

Cylindrical geometry in which the current flows in the z direction is assumed. Since the frequency is on the order of 10^4 Hz, the displacement currents are neglected. All fields are assumed to be z and θ independent and the radial component of the magnetic field intensity $H_r \equiv 0$. Ampere's and Faraday's Laws then reduce to

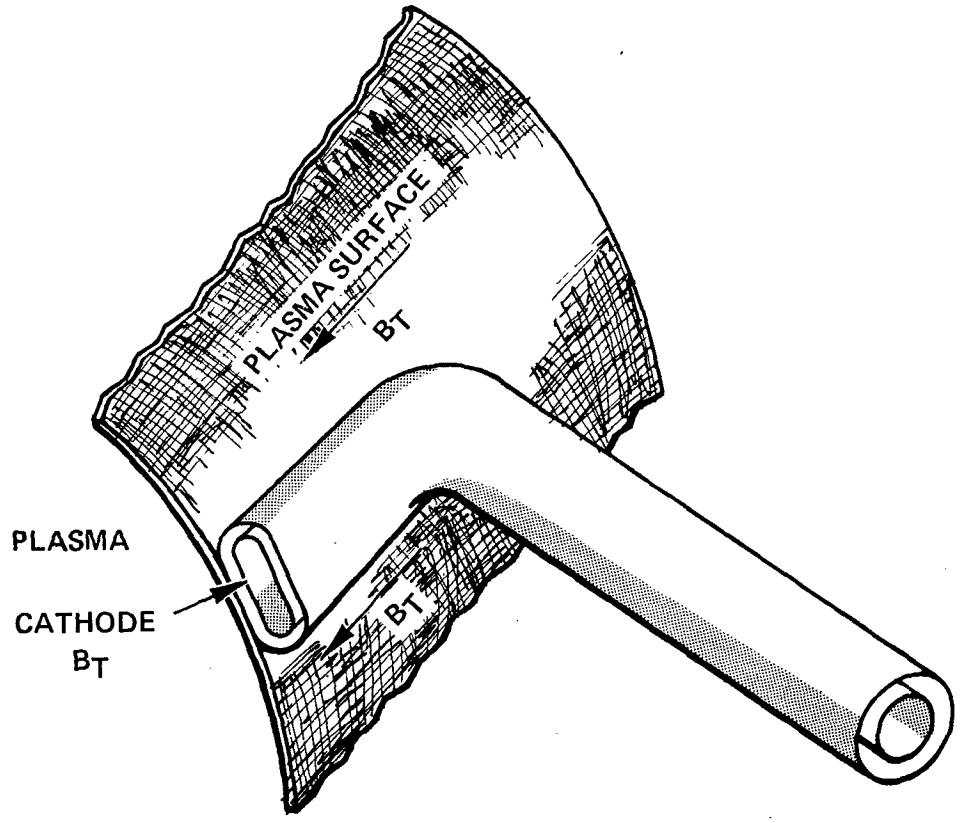

Fig. 2B-2. Sketch of vacuum transmission line. The vacuum transmission line penetrates the blanket, shield, and first wall in a radial direction. Once inside the first wall, the transmission line turns until it is parallel with the toroidal magnetic field. The transmission line is also convoluted from circular to rectangular after it is inside the first wall. The diode structure is tangential to the plasma.

$$-\frac{\partial H_z}{\partial r} = J_\Theta$$

$$\frac{1}{r}\frac{\partial (rH)_\Theta}{\partial r} = J_Z \qquad (2B\text{-}4)$$

$$\frac{\partial E_z}{\partial r} = \frac{\partial B_\Theta}{\partial t}$$

$$\frac{1}{r}\frac{\partial (rE_\Theta)}{\partial r} = -\frac{\partial B_z}{\partial t} ,$$

where E is the electric field strength. For the case under consideration, $J_\Theta = B_z = 0.0$.

Using the relations $E_z = J_z/\sigma$ and $B_z = \mu H_z$ and combining, the magnetic diffusion equation is obtained

$$\frac{\partial}{\partial r}\frac{1}{r}\frac{\partial rB_\Theta}{\partial r} = \sigma\mu\frac{\partial B_\Theta}{\partial t}$$

or

$$\frac{\partial^2 B_\Theta}{\partial r^2} + \frac{1}{r}\frac{\partial B_\Theta}{\partial r} - \frac{B_\Theta}{r^2} = \sigma\mu\frac{\partial B_\Theta}{\partial t} . \qquad (2B\text{-}5)$$

The current in the transmission line and thus B_θ at the surface of the conductor is assumed to be a specified function of time. Equation 2B-5 can then be solved for the magnetic diffusion in the metal.

The total energy per unit surface area which flows into the conductor is obtained from the Poynting vector at the surface

$$W_T = \int_0^t \vec{E} \times \vec{H}\, dt \ W/m^2 .$$

Usin Eq. 2B-4,

$$E_z = \frac{1}{\sigma\mu}\frac{1}{r}\frac{\partial rB_\Theta}{\partial r} ,$$

and $H_\theta = B_\theta/\mu$, the energy per unit area is

$$W_T = -\frac{1}{\sigma\mu^2} \int_0^t \frac{1}{r} \frac{\partial r B_\Theta}{\partial r}\bigg|_{r=b} B_\Theta\bigg|_{r=b} dt ,$$

where b is the radius of the transmission line.

The full solution of Eq. 2B-5 is given by an infinite series of Bessel functions. A simplified answer can be obtained by dimensionally examining the left hand side (LHS) of Eq. 2B-5:

$$LHS \approx \frac{B_\Theta}{r_{SD}^2}\left[1 + \frac{r_{SD}}{b} - \frac{r_{SD}^2}{b^2}\right],$$

where r_{SD} is the skin depth $r_{SD} = 2\sqrt{\tau/\sigma\mu}$ and τ is the beam duration. Thus, if $r_{SD} \ll b$, a one-dimensional planar approximation is valid. For the DEMO beam system the error will be < 15% if the planar approximation is used rather than the full cylindrical diffusion problem.

The coordinate system for the planar problem is shown in Fig. 2B-3. The magnetic diffusion equation is

$$\frac{\partial^2 B_y}{\partial x^2} = \mu\sigma \frac{\partial B_y}{\partial t} . \qquad (2B\text{-}6)$$

and the energy per unit area which has flowed into the conductor is

$$W_T = -\frac{1}{\mu\sigma^2} \int_0^t \frac{\partial B_y}{\partial x}\bigg|_{x=0} B_y\bigg|_{x=0} dt' .$$

The magnetic field at the surface of the conductor is $B_y(o,t) = -B_o$ during the beam pulse $o < t < \tau$ and zero after $[B_y(o,t) = o,\ t > \tau]$.

The solution of Eq. 2B-6 with the above boundary conditions is

$$B_y(x,t) = -B_0 \operatorname{erfc} \frac{x}{2\sqrt{kt}} \qquad 0 < t < \tau$$

$$B_y(x,t) = -B_0 \operatorname{erfc} \frac{x}{2\sqrt{kt}} + B_0 \operatorname{erfc} \frac{x}{2\sqrt{k(t-\tau)}} \qquad t > \tau$$

where erfc s is the complimentary error function

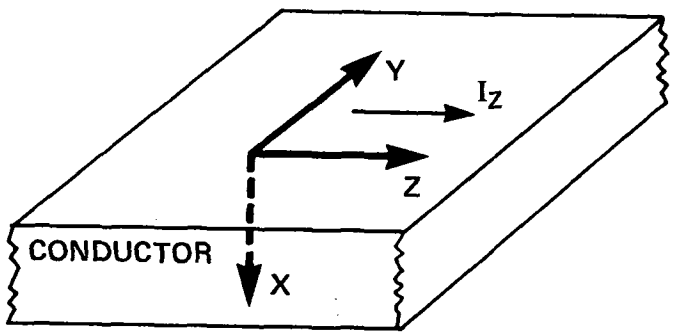

Fig. 2B-3. Coordinate system for planer magnetic diffusion problem.

$$\text{erfc } s = 1 - 2/\pi \int_0^s e^{-\xi^2} d\xi$$

and $k = 1/\sigma\mu$. The energy per unit area dissipated in the conductor is then

$$W_T = \sqrt{\frac{2}{\pi}} \frac{B_0^2}{\mu^{3/2}} \sqrt{\tau/\sigma} ,$$

where B_0 is the magnetic field at the surface and τ is the beam injection time. If the conductor is a circular cylinder or bar with constant radius then the total energy dissipated in the conductor is

$$E_{DIS} = \frac{I^2 \ell}{\pi^{3/2} b} \sqrt{\mu\tau/\sigma} ,$$

where I is the current carried by the conductor, ℓ the length, and b the radius of the conductor.

A worst-case example for the DEMO beam system transmission lines assumes that the radius of the inner coaxial conductor is 9 cm for the full length of the transmission line ($\ell \approx 10$ M) and the line is made of stainless steel (AISI 304) with an electrical conductivity of $\sigma = 1.4 \times 10^6$ mho/m. A current of 13.3 kA is carried by the line for 100 μs. The total energy dissipated in the inner conductor is 67 J and 24 J is dissipated in an outer conductor which has a radius of 25 cm. Since the line transmits 2 MJ of energy, the 91 J of energy which is dissipated in the conductors of the coaxial transmission line is insignificant.

This analysis assumes that there is no particle flow from the inner to the outer conductor of the transmission line. If particle flow does occur, the energy dissipated may significantly increase.

2B.3.2 Electrical Design

The oil-insulated coaxial transmission line has an outer radius of the inner conductor of $r_i = 14.7$ cm and an inner radius of the outer conductor of $r_o = 40$ cm. The maximum electric field occurs at the surface of the inner conductor and is 104 kV/cm for the design voltage of 1.533 MV on the transmission line. This electric field is below the federal specification (118 kV/cm) for the dielectric strength of insulating oils. Physics International has conducted insulating oil breakdown studies for pulse lengths as long as

60 μs and areas as large as 3600 cm^2 and found that the observed breakdown strength was greater than 130 kV/cm for the cases investigated.

Two ceramic insulators provide the vacuum/oil interface for the transition from an oil- to vacuum-insulated transmission line. At the insulator the radius of the inner conductor is r_i = 36.8 cm and the radius of the outer conductor is r_o = 1 m. The maximum electric field at the surface of the insulator is 42 kV/cm when no special attempts are made to uniformly grade the field.

Present-day high power generators can operate with insulators which have a peak electric field as large as 100 kV/cm. The pulse length of these generators is generally on the order of 100 ns. As the pulse length increases the peak electric field which the insulator can withstand decreases. Data on insulator breakdown strength for long pulse lengths and repetitive pulses are minimal. The 215WR generator, built by Physics International, has operated for over 10^6 shots at a rate of 1 pps with electric fields comparable to or larger than the design fields for the DEMO transmission lines. However, pulse length and total output energy are much less than the beam system for DEMO.

Shaping of the inner and outer conductors near the insulator can reduce the peak electric field near the inner conductor. Peak electric fields as low as 30 kV/cm could be obtained with the proper shaping of the inner and outer conductor.

The vacuum-insulated coaxial transmission line has an inner radius of r_i = 9 cm and an outer radius r_o = 25 cm. The maximum electric field at the surface of the inner conductor is 167 kV/cm for the design voltage of 1.533 MV. In short pulse experiments on field emission cathodes and magnetically insulated transmission lines, the electric field required for emission from the negative electrode is 250 to 300 kV/cm. We expect the electric field required for emission to decrease as the pulse length increases.

There was no attempt in these experiments to maintain a clean surface, and, in fact, the surfaces were most likely contaminated with pump oil. The Soviets have used a glow discharge to clean the surfaces and found that much larger electric fields could be maintained in a vacuum without field emission.

The assumption that the vacuum transmission line can withstand electric fields of 167 kV/cm is an optimistic design value. This value may be appropriate if the proper surface preparation is used.

2B.3.3 Structural Design

The structural design of the oil-insulated transmission line is straightforward. The inner coaxial line is suspended from the outer coaxial line by an insulator (see Fig. 2B-4). This technique is in common use in the industry and represents no extension of present engineering practice. However, once again we find that insulator design criteria are not well established for the case of long pulse lengths (> 60 μs) and repetitive pulses.

The most difficult structural problem occurs in the vacuum transmission line at the root of the cantilevered inner coaxial line. Since the inner line carries a current and crosses toroidal magnetic field it experiences an $\ell(I \times B)$ force during the beam pulse. Since the vacuum transmission line penetrates the blanket, shield, and first wall in a radial direction, the current, I, carried by the line is perpendicular to the toroidal magnetic field. For a current (I = 13.3 kA*), toroidal magnetic field (B_T = 5 T), and length of transmission line (ℓ = 4.5 m), which are characteristic of DEMO beam line parameters, the total force is $F = 3 \times 10^5$ N upward, or approximately 34 tons.

There is an equal but opposite force on the outer conductor. Since the outer coaxial conductor can be easily supported over its length, the outer conductor is not a problem mechanically.

The total force of 3×10^5 N (or equivalently, a uniform load of 6.66×10^4 N/m) would produce large stresses and deflections if the force were applied statically. However, the load is applied impulsively (6.66×10^4 N/m for 100 μs) and the maximum stresses and displacements are not given by the standard formulas for the static case. We now obtain an estimate of the maximum stresses and displacements for the impulsive load which is applied to a solid 9-cm-radius, 4.5-m-long inner conductor made of stainless steel.

The impulse given to the inner conductor is

$$\text{Imp} = F\tau = 30 \text{ N-s}$$

where the current, toroidal magnetic field, length of transmission line, and pulse length are I = 13.3 kA, B_T = 5 T, ℓ = 4.5 m, and τ = 100 μs, respectively.

*This includes both electron and ion current.

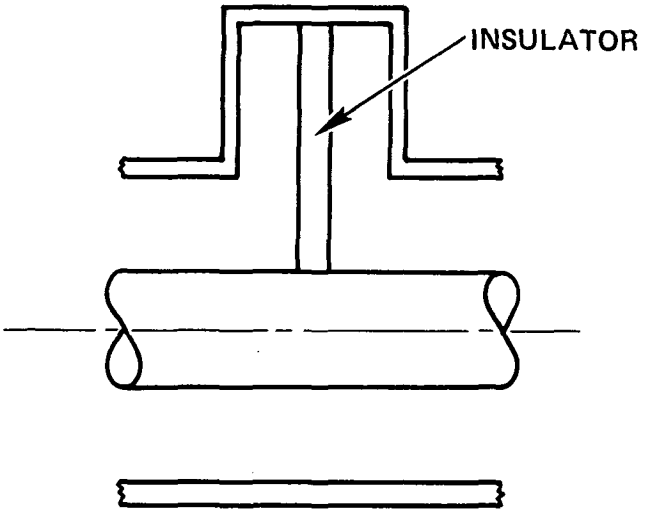

Fig. 2B-4. Suspension of the inner co-axial line in the oil-insulated transmission line.

The impulse is also the change in momentum of the inner conductor

$$Imp = \Delta(m_L\ v_L) = 30\ N\text{-}s,$$

where m_L is the mass of the inner conductor and v_L is the velocity of the inner conductor. If the inner conductor moves as a rigid body then the velocity imparted to the inner conductor during the current flow is

$$v_L = \frac{\Delta(m_L v_L)}{m_L} = 0.034\ m/s,$$

where we have assumed a solid inner conductor made of stainless steel. The total kinetic energy imparted to the line is

$$E_{KE} = \frac{1}{2}\ m_L v_L^2 = 0.51\ J.$$

As the inner conductor moves upward, shearing forces and bending moments build up to retard the motion of the cantilevered inner conductor. When the inner conductor reaches its largest deflection, all the kinetic energy has been transformed into elastic strain energy.

The ratio of the maximum shear stress, τ_{smax}, to the stress, σ_x, due to the bending moment for a uniform load is $\tau_{smax}/\sigma_x = 2r/(3\ell)$ or $\tau_{smax}/\sigma_x = 0.013$ for the inner conductor. The strain energy then is due mainly to the bending moment stress.

The strain energy due to a uniform load, q, is

$$V_{SE} = \frac{q^2\ell^5}{40EI_z},$$

where E is the modulus of elasticity, I_z is the moment of inertia, and ℓ is the length of the cantilevered section. Setting the strain energy equal to the kinetic energy and solving gives

$$q_{EFF} = \frac{\sqrt{40EI_z\ E_{KE}}}{\ell^5},$$

an effective force/unit length for the impulsive load. This effective uniform load is then used to calculate the approximate values for the maximum stresses and displacements when all the kinetic energy has become strain energy.

The effective uniform load for the DEMO case is

$$q_{EFF} = 3.37 \times 10^2 \text{ N/m} .$$

This represents an upper bound since the strain energy due to the shear stress, though small, has been neglected. The maximum shear stress for a solid circular cross section of radius r is

$$\tau_{smax} = \frac{4}{3} \frac{q_{EFF}\ell}{\pi r^2} ,$$

which is $\tau_{smax} = 7.94 \times 10^4 \text{N/m}^2 = 11.5$ psi for the DEMO example. The maximum tensile or compressive stress due to the bending moment is

$$\sigma_x = \frac{2q_{EFF}\ell^2}{\pi r^3} ,$$

which is $\sigma_x = 5.97 \times 10^6 \text{N/m}^2 = 866$ psi for the DEMO example.

The yield point of stainless steel varies, but a yield strength in tension (or compression) of 120,000 psi is not uncommon. The corresponding yield point in shear is 72,000 psi. Thus, the maximum stresses in the inner conductor due to the impulsive I x B uniform load are small compared with the yield stresses of stainless steel.

The maximum displacement at the cathode end of the inner conductor is

$$\delta^{max} = \frac{q_{EFF}\ell^4}{8EI_z}$$

which for the DEMO design $\delta^{max} = 1.67 \times 10^{-3}$ m. The displacement, δ, during the beam pulse is more important than the maximum displacement since a large displacement during the beam pulse can change the electrical characteristics of the transmission line. The displacement at the end of the beam pulse is small, 1.7×10^{-6} m, and the inner conductor remains approximately fixed during the beam pulse.

The force/unit length due to the weight of the inner conductor is larger than the effective force due to the impulsive force. Including the weight of the inner conductor and the impulsive load gives a maximum shear stress of $\tau_{smax} = 4.62 \times 10^5$ N/m^2 = 67 psi and a maximum tensile stress of $\sigma_x = 3.47 \times 10^7$ N/m^2 = 5,035 psi. Both of these stresses are small compared to the corresponding shear and tensile yield strengths for stainless steel.

Since the outer coaxial line can be designed to compensate for the displacement due to the static weight of the inner coaxial line, the relevant displacement is the additional displacement due to the impulsive load. This additional displacement is $\Delta\delta$ (t = 100 μs) = 1.7×10^{-6} m.

In summary, a 9-cm-radius inner conductor which is cantilevered at the outside edge of the toroidal field coils is mechanically sound for use in the DEMO beam system. The outer coaxial line can easily be supported over its length and, thus, is not a problem mechanically.

The stresses can be lowered further by using a hollow inner conductor since the force/unit length due to the weight of the transmission line decreases faster than I_z as the inner conductor is hollowed out. This will decrease the bending stresses, keep the shear stresses approximately constant, and decrease displacement. There are, of course, limits to how thin one can make the shell.

An optimized design (minimum stresses) will have a tapered wall thickness such as that shown in Fig. 2B-5. The stresses are expected to be much lower for an optimized design than for the solid inner conductor considered in detail in this section.

2B.4 Beam Generator

2B.4.1 REB Power Conditioning System

The pulsed power conditioning system (PPCS) for the REB current drive system converts wall plug energy into the pulse delivered to the transmission line feeding the plasma diode. PPCS consists of all equipment from the wall plug to the transmission line, including controls and support systems such as cooling and monitors. The output requirements of PPCS are shown in Table 2B-1 for one line, steady state performance. The startup requirements for PPCS are shown in Table 2B-2 for one line.

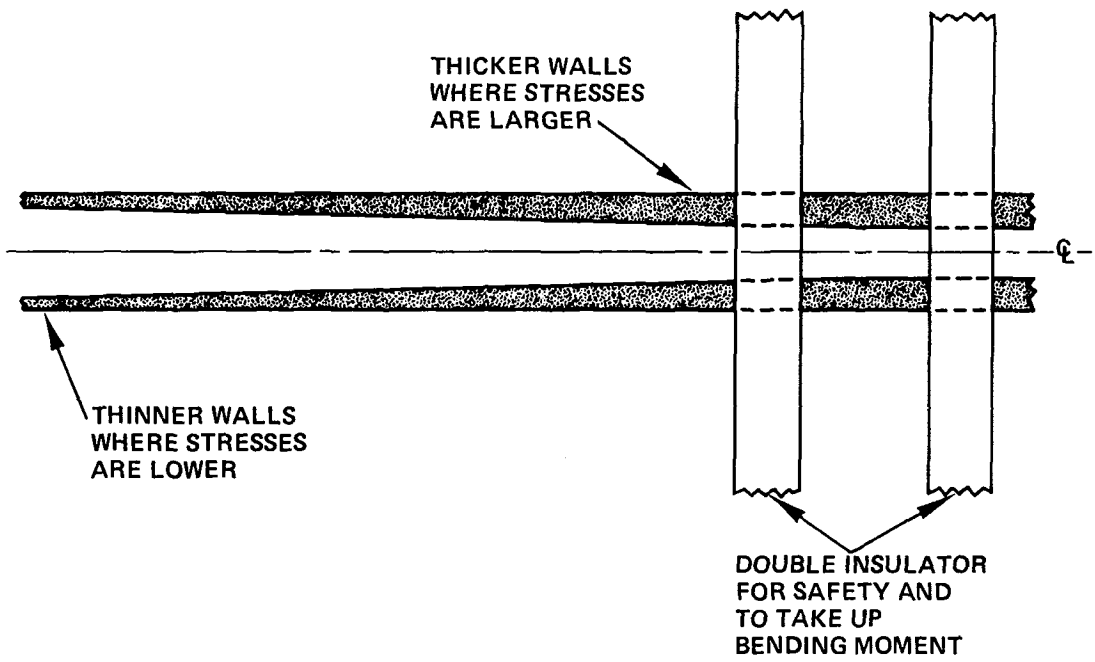

Fig. 2B-5. An inner conductor of the vacuum transmission line with tapered wall thickness to reduce peak stresses.

Table 2B-1 PPCS Steady-State Requirements for One Line

V_{out}, MV	1.53
E (> 90% V_{out}), MJ	2
f, Hz	2/3
Z, Ω	117

Table 2B-2 PPCS Startup Requirements for One Line

V_{out}, MV	1.53
E (> 90% V_{out}), MJ	2
f, Hz	20
Z, Ω	117

An additional requirement for PPCS is reliability, with system and component lifetimes on the order of 10^8 shots.

A block diagram of a typical pulsed power system is shown in Fig. 2B-6. The modulator converts dc power into pulsed power. The modulator voltage is then transformed to the required load voltage. Typical methods of voltage transformation use transformers and/or Marx generators. The output pulse is produced by means of a pulse-shaping network. The pulse-shaping network may be in the low voltage or the high voltage section of PPCS, or pulse shaping may be included in the method of voltage transformation, as in a PFN-Marx (Sec. 2B.4.3).

A typical modulator consists of filter capacitor, charging inductor, blocking diode, command charge switch, intermediate storage capacitor, intermediate switch, and output transformer, as shown in Fig. 2B-7. Initially, the command charge switch is open. When the command charge switch is triggered, the filter capacitor, C_F, charges the intermediate cap, C_I. The charging diode prevents the charge on C_I from ringing back into C_F and the power

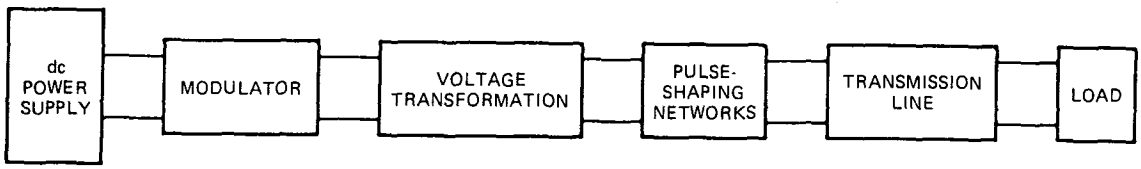

Fig. 2B-6. Block diagram of a conventional pulsed power conditioning system.

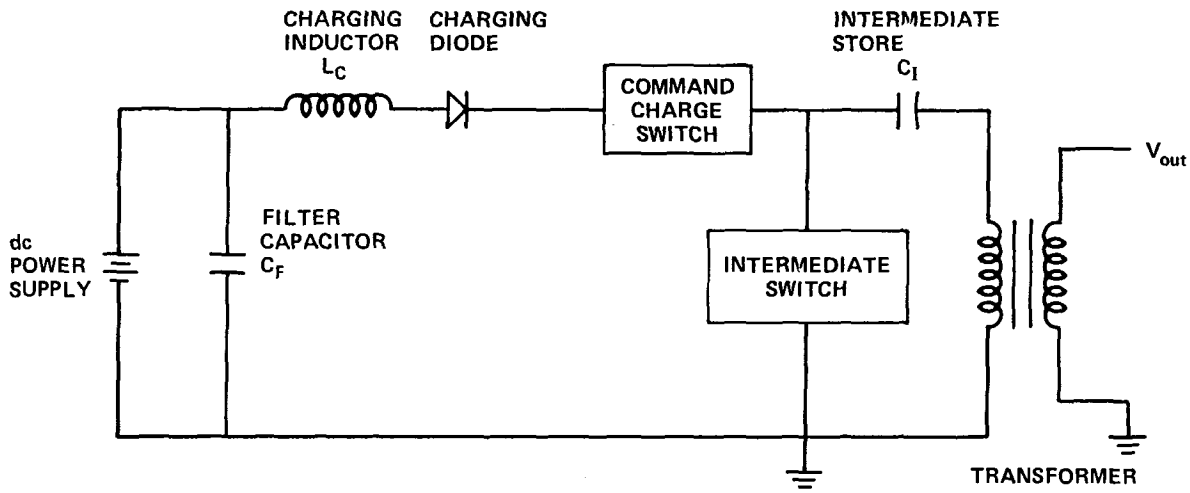

Fig. 2B-7. Circuit diagram for typical pulsed power modulator.

supply. After C_I has charged to full voltage, the intermediate switch is triggered, allowing C_I to discharge through the transformer into the PFN. When the PFN is fully charged, the output switch is fired, and the PFN discharges into the load.

The PFN voltage divides between the PFN impedance and the load impedance. If the PFN impedance is matched to the load, then the PFN charge voltage must be twice the load voltage. To apply 1.5 MV to the load, the PFN must be charged to 3 MV. The output switch, transformer secondary, and all PFN components must be designed to hold off 3 MV reliably, for 10^8 shots. Since transformers and switches carry a high degree of risk at 2 MJ and 3 MV, a desirable power conditioning method would provide 1.5 MV to the load, while stressing individual components at 100 to 500 kV.

Several pulsed power systems were analyzed for feasibility and performance in this application. The most promising standard technology systems use a modulator to charge a Darlington network (Fig. 2B-8) or a PFN-Marx (Fig. 2B-9). These systems are discussed in detail in Secs. 2B.4.2 and 2B.4.3. A better, but less standard, approach using compensated pulsed alternators (compulsators) to provide the output pulse is presented in Sec. 2B.4.4.

2B.4.2 Darlington Approach

A Darlington network[77], shown in Fig. 2B-8, will reduce the voltage stress on the transformer secondary, the output switch, and the PFN components. The impedance of each PFN is given by

$$Z_i = Z_L \frac{i(i+1)}{n^2} .$$

where i refers to the i^{th} PFN, n is the total number of PFNs, and Z_L is the load impedance. If all of the networks have the same delay time and phase characteristics, then one pulse of width τ will appear across the load (n-1) $\tau/2$ s after the switch is closed. Each PFN interacts with its neighbor such that the output pulse adds to (n/2) V_{PFN}, while the reflections cancel. For a charging voltage of 500 kV, n = 6; the impedance of each PFN is shown in Table 2B-3.

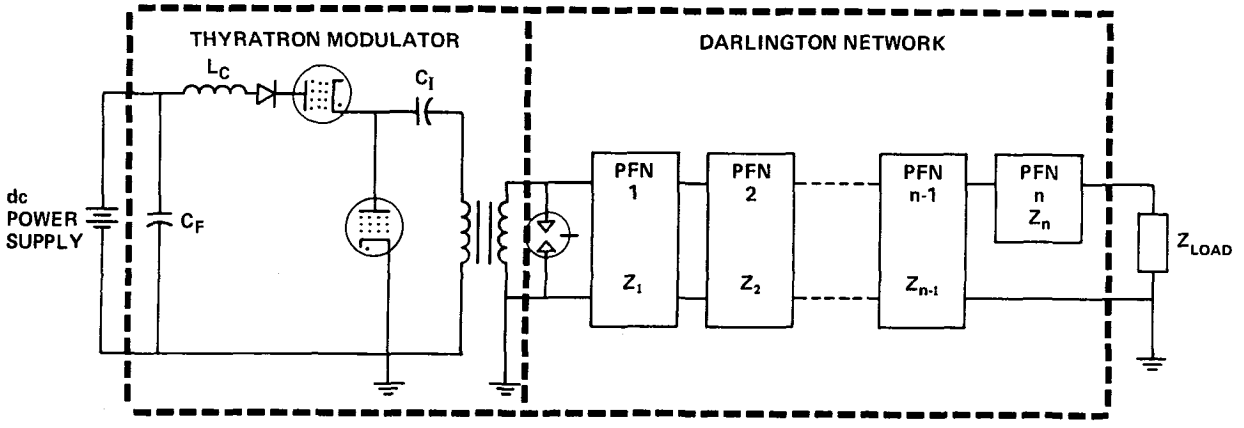

Fig. 2B-8. Darlington network and thyratron modulator.

Table 2B-3. Impedance of Darlington PFNs with Respect to the Load Impedance

PFN	Impedance Ratio (Z_i/Z_L)
1	2/36
2	6/36
3	12/36
4	20/36
5	30/36
6	6/36

The Darlington approach offers several advantages. The transformer and switch voltage have been reduced from 3 MV to 500 kV. Only one output switch is required. Voltage multiplication is achieved by impedance mismatching between the PFNs.

The disadvantages of this approach involve PFN, transformer, and switch designs. Each PFN has a different impedance, which complicates design and assembly of the PFNs. The PFNs must have four terminals; standard PFNs are designed with two terminals. Therefore, a design procedure must be developed to produce a suitable four-terminal PFN.

Even at a reduced voltage of 500 kV, the transformer and switch will require developmental effort. With sufficient funding, the voltage grading, inductance, and cooling problems of the transformer may be overcome. The switch will be more difficult to design than the transformer. The switch will require some form of electrode feeding due to electrode erosion. Assuming that the switch must transfer the total charge of each pulse, the electrodes will lose 8 kg of material over a life of 10^8 shots. A mechanical feeding device further complicates system design since the feeding device must operate in the high voltage portion of the circuit, and either be floated to 500 kV or insulated from 500 kV. An alternate to the electrode-fed switch would be a switch with some form of recyclable electrode material; the design of this type of switch has not been developed at this time.

In addition, the startup power of 40 MW required per side will be difficult to achieve with this system. Each component must be sized to handle the

startup power at steady state, even though 40 MW is required for only a few minutes. Many thyratrons will be required in parallel in the modulator to handle the average and rms current load. The dc power supply must be sized to accommodate peak demand of 40 MW. This implies that in case of a fault, large fault currents based on the 40 MW rating of the power supply can be drawn. The fault current under worst case conditons for a 40-MW power supply with a 13.5 kV, 3 ϕ input would be approximately 90 kA per phase. A typical circuit breaker would interrupt the fault within 1-1/2 cycles at 60 Hz, or 25 ms. The energy dumped into the system during this time would be $\sim$ 35 MJ. Accommodating this size of fault while maintaining the reliability of the system presents a difficult design problem.

2B.4.3 PFN-Marx Approach

The circuit schematic for a PFN-Marx is shown in Fig. 2B-9. The PFNs are charged in parallel and discharged in series to obtain the output pulse. When discharged, each PFN halves the charge voltage. For a charge voltage of 100 kV and an output voltage of 1.5 MV, at least 30 stages, or PFNs, will be required. The switch for each stage must hold off 100 kV, and conduct a charge of 2.1 C.

The PFN-Marx approach offers several advantages. Each switch must withstand 100 kV, as opposed to 3 MV for a conventional approach or 500 kV for the Darlington approach. A 100 kV switch is inherently easier to design, construct, and operate than a 500 kV switch. As shown in Fig. 2B-9, no transformer is required to step up the modulator voltage. Each PFN is identical, which is advantageous when designing and assembling 30 PFNs. Also, each PFN halves its charge voltage, implying that no place in the circuit will have an applied voltage of more than 1.5 MV; a conventional approach would charge to 3 MV.

While using 30 stages reduces the charge voltage, it also decreases system reliability by requiring 30 switches. Since each switch must conduct 2.61 C of charge for 10^8 shots, 2.61 kg of electrode material will erode away. As in the Darlington approach, the electrodes must be either mechanically fed into the switch to keep up with electrode wear, or a new type of switch with recyclable electrodes must be developed.

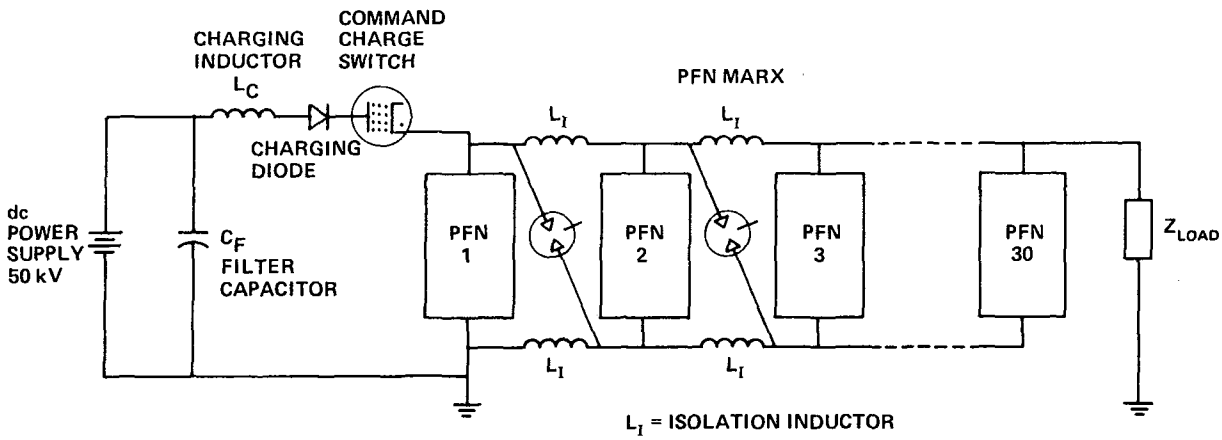

Fig. 2B-9. PFN Marx approach.

A mechanical feed for 30 switches is not a simple task. In addition, the startup power for this system is as difficult to achieve as in the Darlington system.

2B.4.4 Compulsator Approach

A less standard, but more viable, pulsed power conditioning approach than either the Darlington or PFN-Marx approaches uses compensated pulsed alternators (compulsators) to provide the 1.5 MV, 2 MJ, 100 μs pulse to the plasma diode. The performance and operating characteristics of compulsators are discussed in Refs. 78-81. Figure 2B-10 shows a block diagram of the compulsator configuration. The compulsators each feed a transformer; the transformer secondaries are connected in series to achieve 1.5 MV. The output voltage of each compulsator is limited to about 12 kV due to insulation and inductance limitations.[78] Since a reasonable limitation on the transformer turns ratio is 20:1, each transformer would provide about 250 kV. Therefore, six compulsator/transformer units would be required to provide a pulse of 1.5 MV.

The major advantage to this system is that no high voltage output switch is necessary. Each compulsator is switched individually at 12 kV with a standard ignition. Compulsators are reliable and long-lived. Because the energy is stored in rotating machinery rather than capacitors, the system is relatively small and inexpensive. The startup power is comparatively easy to achieve by increasing the repetition rate from 0.67 to 20 Hz. The motors driving the compulsators will have to be sized to provide the rotational energy necessary to produce 40 MW of power. However, increasing the size of these motors does not affect fault modes or fault currents.

Critical issues for this system involve the transformers, the pulse shape of the compulsator output, and the problems of operating machines in parallel. The transformers of this system must be designed to match the compulsator source and plasma diode characteristics. The University of Texas Center for Electro-Mechanics (UTCEM) believes they can develop such a transformer. The transformers must also be designed with adequate voltage grading so that the secondaries withstand 1.5 MV under fault conditions.

The compulsator does not produce a square pulse. The pulse shape depends to an extent upon load characteristics.[82] UTCEM currently estimates they

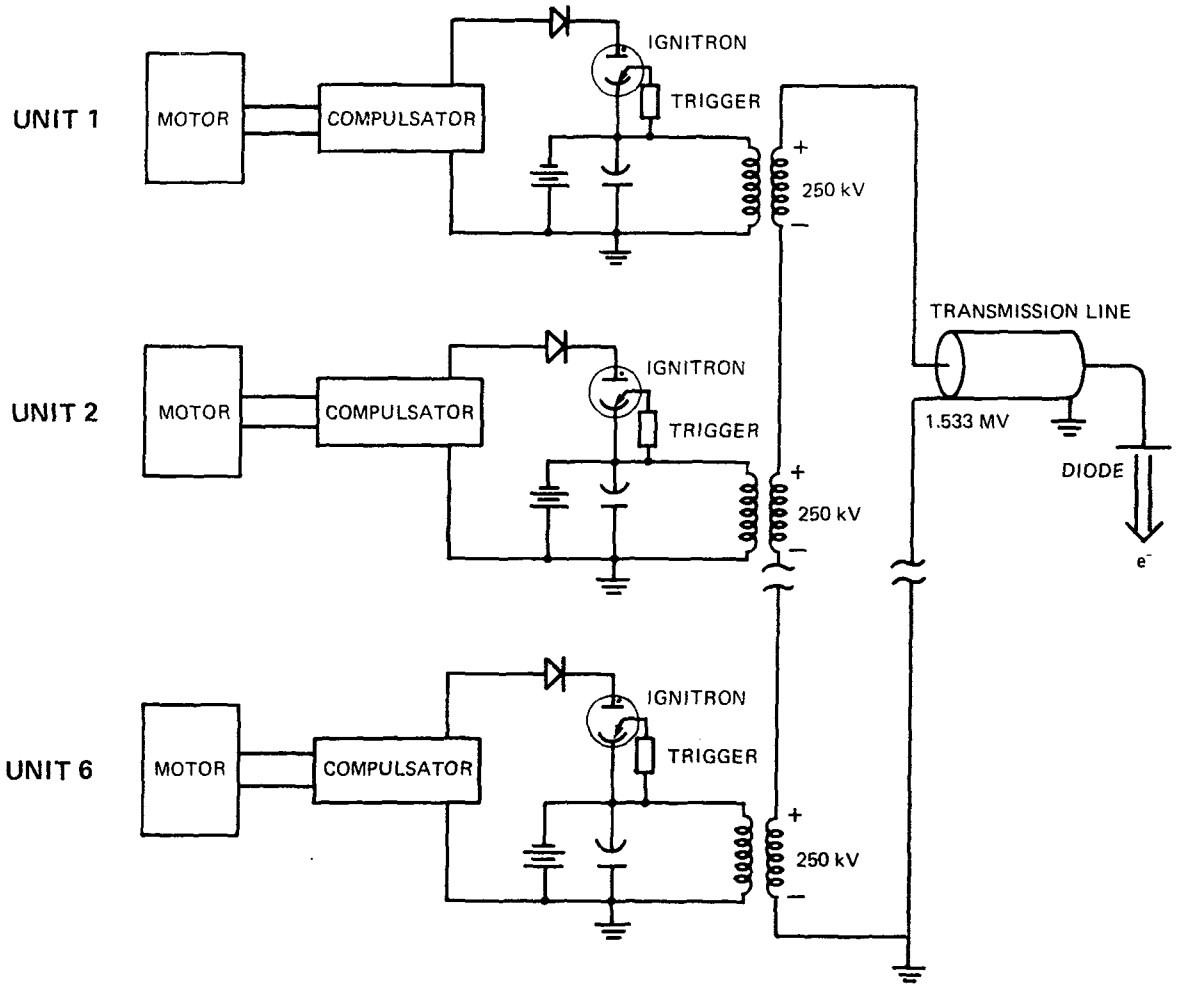

Fig. 2B-10. Parallel-compulsator series-output approach. Switching is provided for each compulsator by the ignitron.

can achieve a 150 μs pulsewidth above two-thirds load voltage. Pulse shaping compensating networks may be added to the circuit if a better pulse shape is desired.

Operating compulsators in parallel may induce circulating currents. If one machine provides more voltage than the others, current will flow from the higher voltage machine to the lower voltage machines. There are three solutions to this problem:

1. Allow the current to circulate and increase the compulsator brush size.
2. Add blocking diodes to the output of each compulsator to prevent current from circulating.
3. Add precision control for each compulsator, varying the rotor speed to maintain constant and equal pulse voltages.

The best approach for the REB application can be determined by analyzing the extent of the circulating currents and their effect on compulsator and system performance.

2B.4.5 System Efficiency

An efficiency diagram for the compulsator system is shown in Fig. 2B-11. Each diode requires 2 MJ/pulse to drive the current. An additional 400 kJ/pulse is supplied to the diode during the rise and fall of the voltage pulse. Since the kinetic energy of the beam will be less than 1.533 MeV during the rise and fall, we assume, conservatively, that this energy does not contribute to current drive. The transmission line and diode combination are approximately 90% efficient. The pulsed power conditioning system must then provide 2.67 MJ/pulse to the transmission line. The output of each of the six compulsator/transformer units must be 444 kJ/pulse. Based on estimates of the component efficiency, each compulsator/transformer unit is 64% efficient. The transmission line/diode combination efficiency, including energy lost in the rise and fall of the voltage pulse, is 75%. The total system efficiency from electrical power from an external source to electron beam for current drive is 48%.

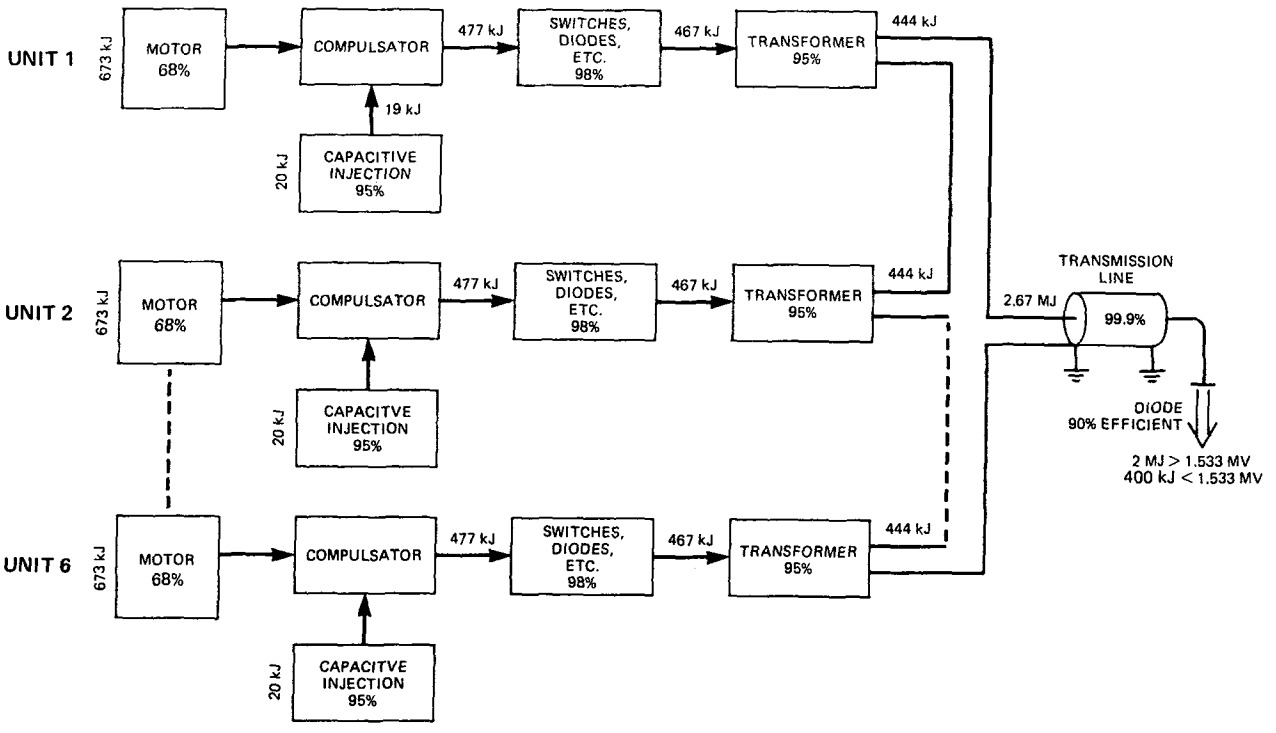

Fig. 2B-11. Efficiency diagram for compulsator approach. The efficiency for the motor-compulsator unit is shown with the motor.

2B.4.6 System Costs

The pulse power of 673 kJ at 2/3 Hz per motor translates to 450 KW, or 605 HP. There are many different types of motors capable of providing 605 HP of rotational energy to the compulsator. However, we need a system that is also capable of providing 13.5 MW or 18,000 HP for a startup duty of 6 minutes every 6 months. One method of achieving this performance would use a hydraulic drive for the compulsator. An induction motor would drive a hydraulic pump which supplies the hydraulic drive compulsator for steady state operation. A variable displacement pump power averages by pumping low volumes of oil at low pressure and low demand, and high volumes of oil at high pressure and high demand, thus keeping the load on the induction motor approximately constant. We would use an accumulator to provide startup power. An accumulator is a pressure tank with a bladder of compressed nitrogen. Oil is pumped into the tank to a pressure of 5000 psi, compressing the bladder. When the startup power is required, the oil is released from the tank to drive the compulsator. The bladder maintains constant pressure. To produce 18,000 HP for 6 minutes, the volume of the accumulator would be 40,000 gal, or a cube of 5.33 M on a side. Six of these systems will be required, one for each compulsator. The six compulsators will power one diode at 1.33 MW average steady-state power.

The estimated cost of this system is shown in Table 2B-4. The cost for each component is indicated, along with the cost to power one diode (six compulsator units), and the total cost for both diodes.

Table 2B-4. Rough Order of Magnitude Cost

Device	Cost/Unit (steady state)	Cost/Unit (with startup)
605 Hp hydraulic motor	$27K	$27K
40,000 gallon accumulator	--	420K
Compulsator, capacitor, with controls	82K	82K
Diodes, ignitron, etc.	50K	50K
Transformer	30K	30K
Cost/Compulsator Unit	$189K	$609K
PPCS cost/beam line	$1.134M	$3.654M
Transmission line/diode	1.140M	1.140M
Cost/beam line	$2.274M	$4.794M
TOTAL SYSTEM COST	$4.548M	$9.588M

APPENDIX 2C

WAVE LAUNCHER PRELIMINARY ENGINEERING

The electrical design of a loop antenna is decribed in Ref. 83, which we follow. Generally, the antenna conductor should be as close as possible to the plasma edge, located behind the leading edge of the Faraday shield. We assume a 1-cm thick coolant tube bank serves as the screen and allow a gap s = 1 cm between the screen and the antenna, so the antenna is a distance a = 2 cm from the plasma. We assume the antenna averages a distance d = 15 cm from the first wall (see Fig. 2-3), and we take the antenna conductor width (in the toroidal direction) to be $2w$ = 12 cm. The specific antenna capacitance is approximately given by $C = \varepsilon_0(2w)/s = 1.1 \times 10^{-6}$ F/m, and we estimate its specific inductance to be[83] $L \approx 9 \times 10^{-7}$ H/m, so its characteristic impedance is $Z_0 = \sqrt{L/C} = 91\ \Omega$. With a phase velocity $(LC)^{-1/2} = 1.0 \times 10^8$ m/s, we see the propagation constant is $\beta = \omega\sqrt{LC} = 5.0\ m^{-1}$ at the 82 MHz frequency proposed in Sec. 2.3.4.3. A three-quarter wavelength antenna has favorable characteristics, so we select a length $\ell_A = 3\pi/(2/\beta) = 0.95$ m.

To estimate the maximum antenna power, which is limited by breakdown at high electric fields, we need to know the antenna's radiation resistance. This is a difficult calculation, which is treated in depth in Ref. 83. We estimate $R \approx 250\ \Omega/m$. For a given antenna power, P_A, the maximum antenna voltage is $V_A = Z_0 P_A^{1/2}/(0.28\ R\ \ell_A)^{1/2}$ for a $3\ \lambda/4$ antenna. In particular, P_A = 10 MW results in V_A = 35 kV and an electric field across the antenna to Faraday screen gap of E_A = 35 kV/cm. These values have already been achieved in TFR experiments[84] without evidence of breakdown, so we feel confident these values are realistic for the DEMO. The success of this high voltage operation is evidently due to the very low free electron density in the antenna vicinity, the Faraday screen very effectively preventing plasma accumulation.

The vacuum feedthrough, from the coax transmission line to the antenna strip line, is usually the location where breakdown is most likely. We calculate the complex antenna input impedance,

$$Z_A = \left[\frac{R - i\omega L}{-i\omega C}\right]^{1/2} \tanh\left\{\left[-i\omega C(R - i\omega L)\right]^{1/2}\ell_A\right\} = -(107 + i38)\Omega\ .$$

If an unmatched system is used, with a $Z_{o,f} = 50\ \Omega$ feeder, the reflection coefficient would be

$$|\Gamma| = \left[\frac{Z_A - Z_{o,f}}{Z_A + Z_{o,f}}\right] = 0.42 .$$

The resulting VSWR could be significant,

$$s = \frac{1 + |\Gamma|}{1 - |\Gamma|} = 2.5 .$$

The maximum voltage on the antenna feed is $V_L = (2P_A Z_{o,f} s)^{1/2}$, which would be 35 kV for $P_A = 10$ MW. For a 9-in. 50-Ω coax the field is $E_L = 8.3$ kV/cm, which is also below the TFR value. To reduce the VSWR it is standard procedure to install two or three motor-driven stubs in the circuit, spaced at $\lambda/8$ intervals.(85) Beyond the ceramic vacuum windows it is possible to reduce the coax diameter to 6 in. since the line can be pressurized.

We feel the antennas can each handle 10 MW or more. This is higher than achieved in present machines for two reasons. First, the antenna is separated by a larger distance ($d \approx 15$ cm) from the return currents in the wall, so its radiation resistance is higher (more power is radiated for a given voltage). In addition, the extra room in a reactor permits reasonably large separations between the antenna and the Faraday screen ($s = 1$ cm) which accordingly keeps E_A fairly low. Thus, only ten antennas would be needed to provide the requisite current drive power for the HSMS wave. The choice of a toroidal mode number $N = 42$ (Sec. 2.3.4.3) dictates a $\lambda_{\|} = 2\pi R_{mag}/N = 0.82$ m at the magnetic axis. It may be possible to space the antennas with $\lambda/4$ separation on centers, so the whole phased array will be 2-1/4 toroidal wavelenths, spanning 19.3 deg toroidally. (See Figs. 2-3 and 2-4.)

The antenna and Faraday screen should be in proximity to the plasma, yet not so close that normal heat fluxes or disruptions might jeopardize a long, maintenance-free life of the assembly. A distance 4 cm into the shadow of the limiter is proposed.

We conclude this discussion with comments on the materials used for the antenna construction. The antenna conductor and Faraday screen are actively cooled tube structures, fabricated from the structural steel used in the DEMO

blanket. Electrical conductivity is a secondary consideration, although a special surface treatment may be needed to minimize breakdown problems. Use of a slotted, overlapping screen will permit an all-metal design within the vacuum chamber.[84] The only vulnerable insulator is the vacuum feedthrough in the coax. We note that the narrow diameter of the 9-in. coax is beneficial in reducing the neutron dose away from the first wall.[86] A ceramic insulator (BeO, e.g.) will be required for this window, but further studies need to be done to determine the best location.

CHAPTER 3

IMPURITY CONTROL AND EXHAUST

Chapter 3

Table of Contents

Table of Contents (continued)

Chapter 3

List of Figures

Chapter 3

List of Tables

List of Tables (continued)

3.1 Introduction

3.1.1 Scope of Work

Impurity control and exhaust represents a crucial area in the design of STARFIRE/DEMO. The impurity control system must ensure long pulse and, possibly, steady state plasma operation, must be reliable enough to achieve multiyear lifetimes, and should not adversely affect the other reactor systems. Besides having a major influence on the plasma, the impurity control system interacts with other reactor systems including the first wall, the vacuum system, the blanket, and possibly the magnet system. The system may also have a significant impact on the tritium fueling and breeding and reactor maintenance.

Most impurity control systems devised to control plasma impurities can be divided into two groups - divertors and limiters. A divertor system employs modifications to the magnetic field such that ionized particles escaping the plasma are swept out of the plasma chamber and into the divertor where they are neutralized when they strike the divertor collector plates. Most neutralized particles are then pumped into the vacuum system. The limiter projects directly from the first wall and serves to intercept ionized particles escaping the plasma. These particles strike the limiter surface and are neutralized. The pumped limiter has holes or slots where a small fraction (about 10%) of the incident particles are captured and neutralized. Most of the captured particles then enter the vacuum duct and are pumped.

Recent reactor design studies[1-3] have selected either a pumped limiter or poloidal divertor for the impurity control system, and the present study has focused on the generic issues of these concepts. A pumped limiter similar to that used in STARFIRE[1] has been selected as the baseline design for limiters, and a poloidal divertor similar to that used in INTOR[2] has been selected as the baseline divertor system. Most of the work at this point in the study has been on issues related to the pumped limiter. Work on the poloidal divertor is in progress.

The issues examined for the pumped limiter are shown in Table 3-1. Emphasis has been placed on the plasma edge-materials surface interactions. Codes have been developed to model the plasma edge conditions and to model the anticipated sputtering and redeposition of material on the first wall and limiter. Details of the plasma edge and sputtering calculations are given in

Sections 3.3.2 and 3.3.4 respectively. The materials selection, presented in Section 3.4, is based upon the results of the plasma and sputtering calculations. The possible structure of redeposited materials has also been examined. The design engineering issues for the limiter consist of trade-off considerations for the limiter placement, and parametric studies of the temperatures and stresses at the leading edge of the limiter. Initial trade-off considerations for the poloidal divertor are also presented.

Table 3-1. Issues Examined for Pumped Limiter Systems

ISSUE	AREAS CONSIDERED
Plasma Edge Physics	Heat Load Edge Conditions
Redeposition and Sputtering	Low Z Materials High Z Materials Limiter Geometry Plasma Edge Temperature
Configuration and Maintenance	Disruptions Tritium Breeding Replacement Procedures
Material Selection	Structural Materials Coating/Cladding Materials Redeposited Materials
Operating Temperatures	Coating-Structural Material Combinations Coating Thickness
Stresses	Thermal Stresses Magnetic Forces During Disruptions

3.1.2 Baseline Designs

The limiter baseline design is a blade type of limiter similar to the STARFIRE design shown in Fig. 3-1.[1] The front surface of the limiter extends about 20 cm into the plasma chamber, and the blade is about 1 m in height. The leading edge of the limiter is recessed from the plasma edge to reduce the heat flux to a reasonable level. The limiter blade is continuous in the toroidal direction. The vacuum duct is placed in back of the limiter to pump the particles entering the limiter slot. Three limiter configurations

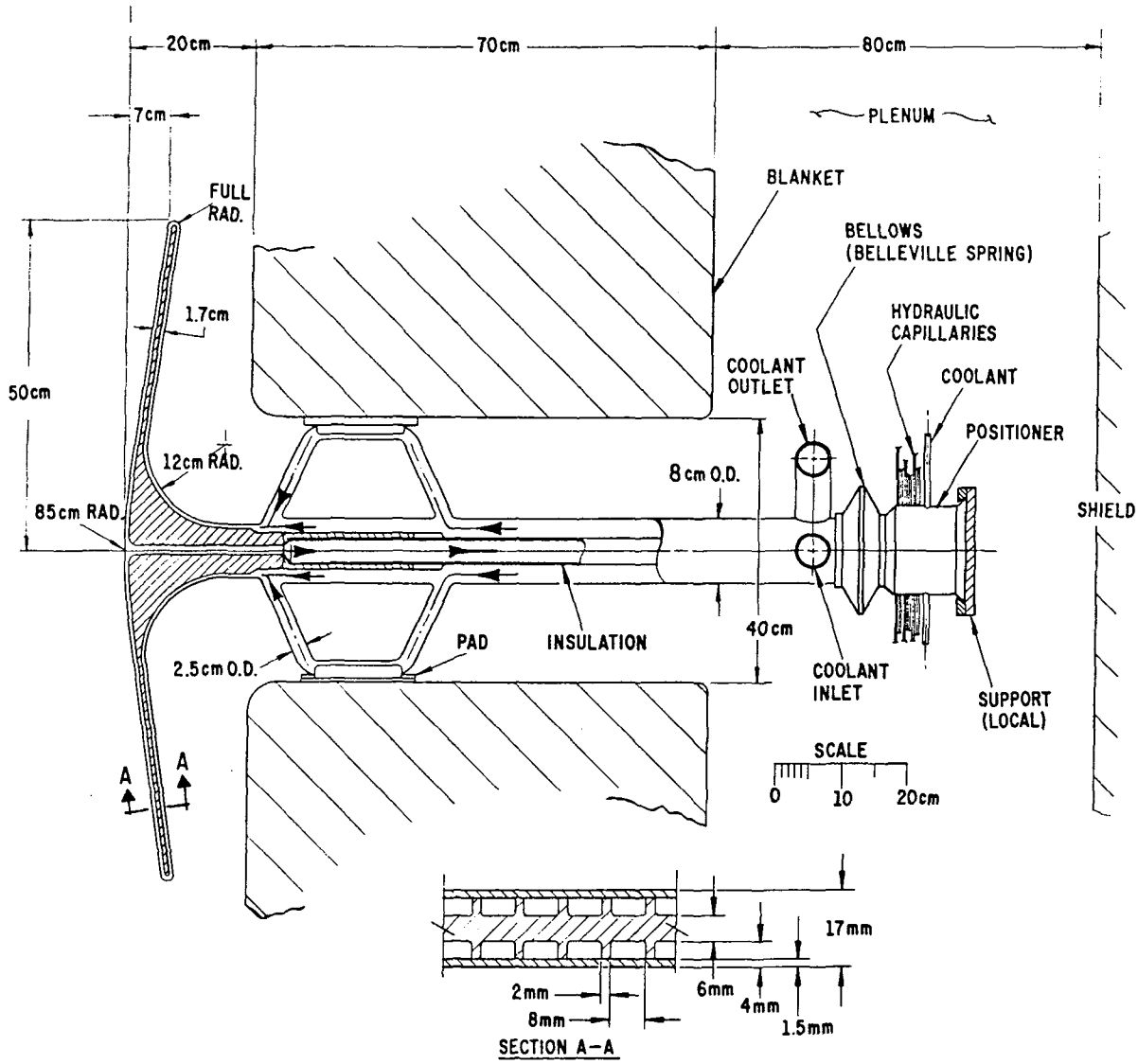

Figure 3-1. Cross Section of the STARFIRE Limiter Design.

have been considered: the outer midplane (Fig.3-2a), the bottom of the plasma chamber (Fig.3-2c), and midway in between (Fig.3-2b). The bottom limiter design is a single blade design similar to the FED limiter[3]. The three limiter configurations are designed to be removed independently of the rest of the blanket and shield to allow for the limiter's reduced lifetime compared with the other components. Tradeoff considerations for the limiter placement are given in Section 3.2.

The baseline design for the divertor is a single null poloidal divertor similar to the INTOR design shown in Fig. 3-3. A single null divertor has been selected over a double null divertor because a single null divertor is easier to maintain and occupies less blanket space than a double null divertor. Ionized particles entering the divertor first strike the divertor collector plates. These plates are thus subjected to high heat fluxes and potentially high sputtering rates similar to the limiter. The plates are designed to be removed independently of the rest of the blanket and shield. The baseline design of the collector plates is expected to be similar to the U.S. INTOR design, shown in Fig. 3-4. The plate design consists of a low-sputtering protection plate that is mechanically attached to a water cooled heat sink. Additional divertor engineering considerations are given in Section 3.2.

3.1.3 Limiter Impurity Control Options

An effort was made to study the limiter impurity control options over a wide range of operating parameters. The primary variables are those related to the plasma edge conditions with the baseline limiter design and the reactor power characteristics remaining constant. A summary of the cases considered is given in Table 3-2. Three plasma edge temperatures have been selected for detailed study. The edge temperatures of ~1000 eV, ~100 eV, and ~10 eV are designated as high, medium, and low temperature cases respectively. Other parameters, such as particle fluxes, charge exchange neutral energy, and surface heat fluxes, are expected to change as the edge temperature is changed. The parameters shown for the high and medium edge temperatures have been determined based on the analysis discussed in Section 3.3. The parameters for the low edge temperature case are assumed values. The low temperature regime is not well understood at this time, and additional work is required. The assumption of a 10 eV edge temperature is sufficient for design

Figure 3-2.

OPTIONS FOR PUMPED LIMITER CONFIGURATIONS IN STARFIRE/DEMO

- o ALL LIMITER MODULES REMOVABLE RADIALLY, SEPARATELY FROM SHIELD AND BLANKET SECTOR
- o MAGNETIC DIVERTOR AND NEUTRAL BEAM HEATING ARE NOT OPTIONS
- o VACUUM PUMPS LOCATED BELOW REACTOR

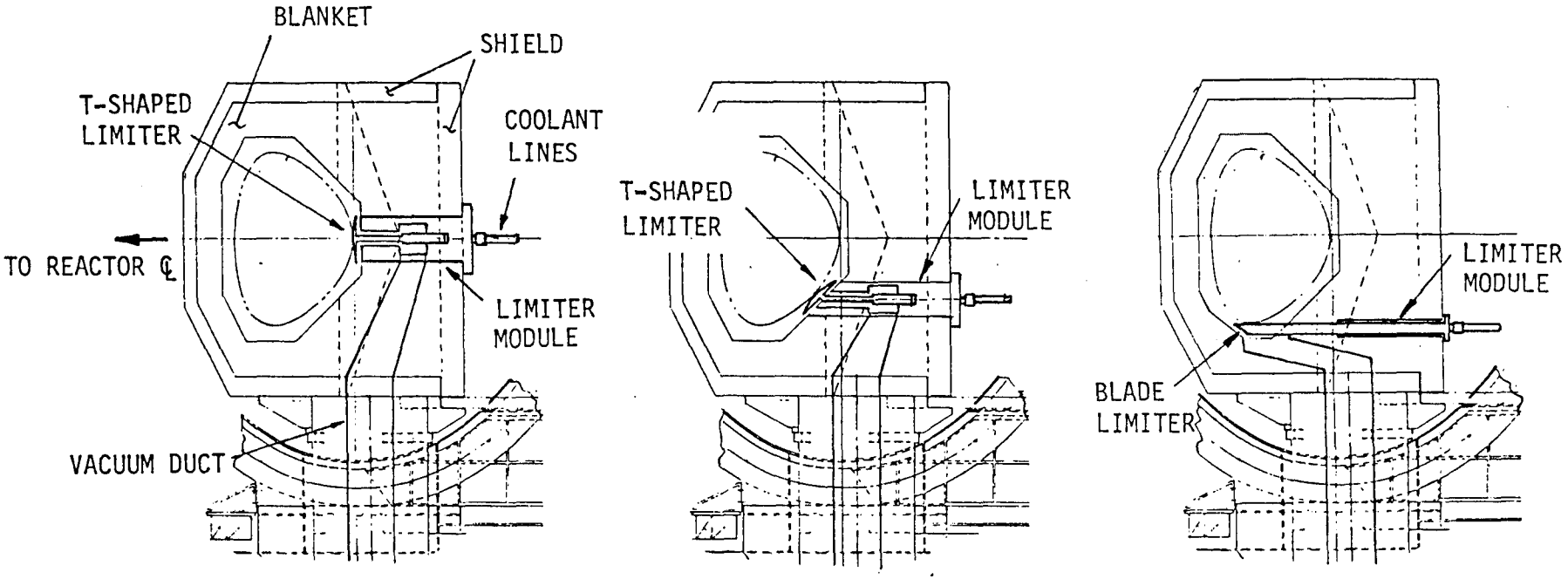

(A) LIMITER AT OUTER MIDPLANE

(B) LIMITER AT LOWER 45° SEGMENT

(C) LIMITER AT BOTTOM SEGMENT

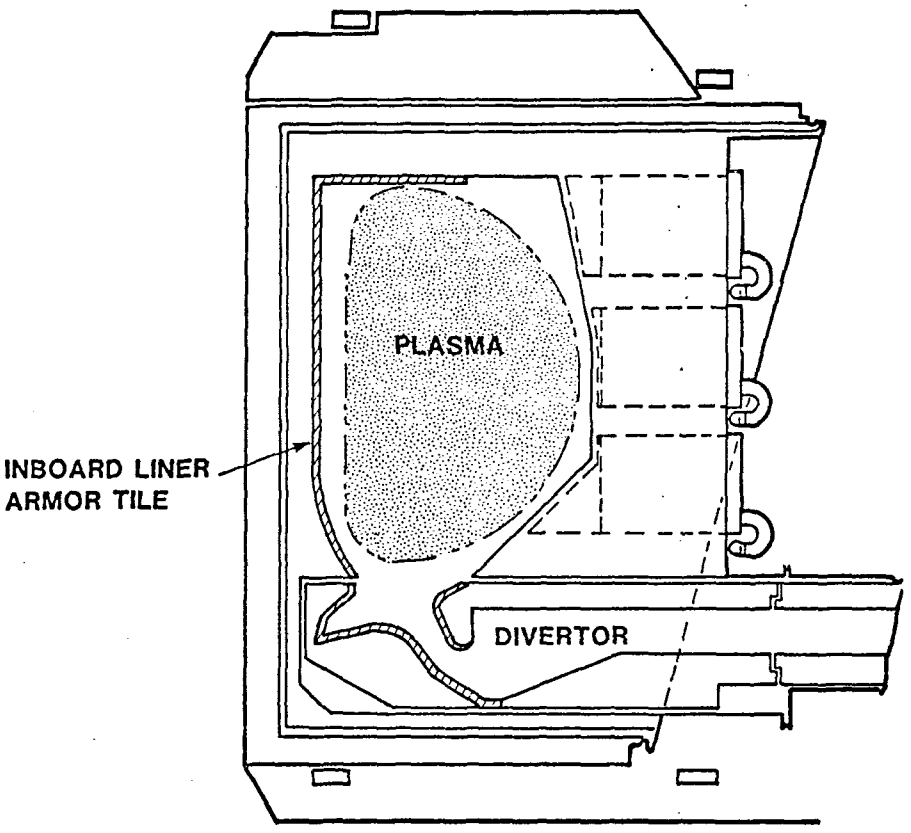

Figure 3-3. Poloidal Divertor Configuration of INTOR.

Table 3-2. Limiter Operating Conditions

Edge Temp.	Average Electron Temp.	Average[a] C-X Energy	D-T Current[a] to Limiter	C-X Current[a] to 1st Wall	Transport power to Limiter
HIGH	1.5 KeV	3.0 KeV	$7.60 \times 10^{22} s^{-1}$	$1.0 \times 10^{23} s^{-1}$	100 MW
MEDIUM	100 eV	200 eV	$1.14 \times 10^{24} s^{-1}$	$1.0 \times 10^{23} s^{-1}$	100 MW
LOW	10 eV	--	--	--	--

[a] C-X ≡ Charge Exchange

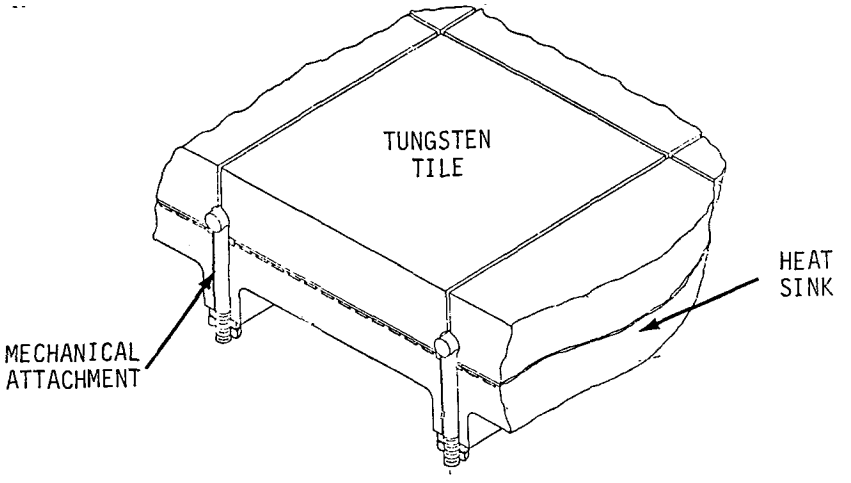

Figure 3-4. Divertor Collector Plate Design for INTOR.

purposes, however. The changes in these parameters affect the materials selection and the detailed limiter design is likely to be different for each of the cases considered.

At present, a single option for the divertor is being examined. The operating conditions are similar to those in INTOR[2], but the parameters will be modified to account for the different reactor geometry and power output in DEMO. The anticipated plasma edge temperature is about 100 eV, and the total ion flux to the divertor is expected to be about $5 \times 10^{23} s^{-1}$. The surface heat flux to the collector plate is anticipated to be 2-3 MW/m^2. The possible redeposition of material on the collector plates is now under investigation.

3.1.4 Summary of Results

At high edge temperature conditions, low-Z materials provide the most suitable materials facing the plasma. A higher concentration of low-Z impurities can be tolerated within the plasma, and the self-sputtering coefficient at high energies is less than unity. As shown in Table 3-3, beryllium is the preferred low-Z material. The average rate of sputtering of Be on the first wall is estimated to be ~ 1 mm/y, and the average rate of buildup on the limiter due to redeposition is estimated to be ~ 1 cm/y at 100% duty factor. This sputtering rate means that the beryllium layer on the first wall must be ~ 1 cm thick in order to achieve an extended lifetime. On the other hand, a relatively rapid buildup of material on the limiter could lead to high thermal stresses and may necessitate frequent replacement. The copper alloy AMAX-MZC has been chosen as the limiter structural material primarily because of its ability to withstand high heat fluxes. The major concerns of this design involve the fabrication and bond reliability of the two layered structures and the stability of the redeposited material or rapid erosion of low-Z materials. Details of the materials selection are given in Sec. 3.5.

Table 3-3. Edge Temperature Considerations

Edge Temperature	Materials	Advantages	Concerns
High	Be-Surface bonded to Cu-Structure	Low temperatures and stresses	Duplex fabrication and bond strength
		Minimum impurity effect in plasma	Properties of redeposited materials
Medium	W-Surface bonded to Cu-Structure	Thin limiter/first wall	Self-sputtering
		Very low sputtering	High-Z concentration in plasma
Low	Cu-Limiter	Thin limiter/first wall	Physics uncertainties
		No sputtering	
		Simplified engineering	

At medium edge temperatures, the choice of the first wall and limiter coating changes. At energies of ~ 100 eV, the high-Z materials exhibit the lowest DT sputtering rates while satisfying the requirement of self-sputtering coefficients < 1 on the limiter surface. Preliminary analysis using the computer code described in Sec. 3-3 indicates that at medium edge temperatures, high-Z materials may exhibit low net erosion and low concentrations within the plasma. These conditions would occur when sputtered high-Z atoms are ionized near the surface ($\gtrsim$ 1 cm) and then returned. Little or no sputtered material would be transported into the plasma. An edge temperature of $\gtrsim$150 eV is required to avoid a self-sputtering coefficient $\geq$ 1 . This edge temperature may be attainable by gas puffing of the D-T fuel. The analysis of redeposition of materials depends upon estimates of ionization cross sections, plasma profiles, sputtering coefficients, and momentum transfer effects, some of which are highly uncertain. Preliminary calculations are encouraging, but more detailed calculations are required. Tungsten has been chosen as the high-Z material and AMAX-MZC is again the limiter structural material. The principal advantage of tungsten is its high melting point, and its very low vaporization rates, as discussed in Sec.4-2. Calculations of plasma disruption effects on tungsten indicate that under most disruption conditions, tungsten will not reach its melting point. For a tungsten clad first wall, the sputtering rate of tungsen would ~ 0.2 mm/y and the average rate of buildup rate on the limiter is estimated to be about 1.5 mm/y at 100% duty factor if the entire first wall is coated with tungsten. The low sputtering rates mean that the first wall and possibly the limiter structure can be designed to be thin. A major concern is the fabrication and bonding of two layered materials.

At low edge temperatures (~ 10 eV) all materials exhibit low sputtering rates. Materials can be chosen independently of sputtering considerations. For this case, AMAX-MZC alone and austenitic stainless steel alone have been selected as the limiter and first wall materials, respectively. The major concern for this configuration is the uncertainty in achieving such low edge temperatures. Additional work is required to determine if this regime is attainable.

3.2 Engineering Tradeoff Considerations

3.2.1 Pumped Limiter

The toroidal belt pumped limiter was evaluated to determine the best location from the standpoint of plasma and reactor engineering. Three positions were considered: the outer midplane (Fig. 3-2a), the upper or lower 45° blanket segment (Fig. 3-2b), and the bottom of the plasma chamber (Fig. 3-2c). The assembly, maintenance, and repair (AMR) requirements, the effects on tritium breeding, and the effects of disruptions were considered.

The outer midplane limiter has advantages over the other locations from the standpoint of plasma engineering. First, the particle and heat fluxes are roughly uniform across the front face of the limiter, as described in Section 3.3.3, and second, this location is the least likely to be struck by the energy of a disruption. The disadvantages of this concept are that it can interfere with other penetrations, such as diagnostics and plasma heating components and that the limiter module occupies a significant fraction of the blanket volume. To facilitate maintenance, it may be preferable to design the limiter modules to be non-breeding. Therefore, the additional space occupied by the outboard limiter module compared with other positions could produce the largest reduction in the tritium breeding ratio.

The 45° limiter placement allows more space for other blanket penetrations. The particle and heat fluxes on the limiter are non-uniform, however, which presents additional engineering difficulties. This location is believed to be more prone to receiving disruptions than the midplane location.

The bottom single blade limiter penetration occupies the smallest fraction of the blanket and shield. It is less sensitive to plasma scrape-off parameter changes. The flux surfaces for a D-shaped plasma are further apart at the top and bottom, resulting in a larger scrapeoff zone. The increased zone size spreads the heat flux over a large area. The fraction of the particles pumped by the system can be changed by moving the limiter in or out. The disadvantages of the bottom limiter are increased vulnerability to disruptions, and reduced pumping (by 50%) capability compared with the 2-slot midplane design. However, the bottom limiter can be designed for pumping from both sides. It can also be shaped to receive uniform heat fluxes. These modifications to the FED type limiter, although desirable from a reactor standpoint, introduce additional design complexities.

The selection of the limiter position depends in part on the goals for the reactor. Since STARFIRE/DEMO must demonstrate both high fusion power production and high availability, the primary concerns are the effect of disruptions and the long-term reliability of the limiter system. These requirements are in contrast to an experimental device such as FED, where diagnostic space, test module space, and flexibility to changes in scrapeoff parameters are of primary importance. The first choice for the limiter placement in STARFIRE/DEMO is therefore the outer midplane, and the limiter analysis presented in the remaining sections are based upon the outer midplane placement. Modifications to the bottom limiter to make it more compatible with reactor applications are under investigation.

3.2.2 Poloidal Divertor

A poloidal divertor occupies a larger volume of the blanket and shield compared with the pumped limiter, and requires additional magnets to produce the desired magnetic field. The divertor collector plates are subjected to severe operating conditions and provision must be made to replace them independently of the rest of the blanket and shield. The single null poloidal divertor has been adopted for STARFIRE/DEMO since it requires less space and provides for easier maintenance than a double null divertor.

The primary engineering concerns of a divertor are directly or indirectly related to the large volume occupied by the divertor chamber. The toroidal and poloidal coil dimensions may need to be enlarged to accommodate the chamber. If the chamber is designed to be non-breeding to facilitate replacement, then the entire bottom segment of the blanket will be removed from tritium production. It is likely that this design would eliminate most solid breeders from consideration because of their marginal breeding characteristics. (See Chapter 4 for tritium breeder evaluations.) The other major concern is the design of the divertor collector plates, which must withstand high heat and particle fluxes. The conditions at the collector plates are similar to those at the limiter, but design and materials selection are more flexible since the plates are not adjacent to the plasma edge. In the case of the INTOR design, tungsten was selected as the surface material, since it offers the longest sputtering lifetime (about 2 y at 50% DF) in the absence of redeposition. The material selection could change when redeposition is considered, however.

The single null poloidal divertor will be studied in more depth during the remainder of the study to evaluate its potential as an alternative to the pumped limiter. Specific areas to be addressed are:

1) Magnet configuration
2) Materials selection for the collector plate, including the surface and heat sink material
3) Sputtering and redeposition of material on the collector plates
4) Configuration of the collector plates, detailed design, allowable coolant conditions, and lifetime analysis
5) Divertor system maintenance.

3.3 Plasma Engineering

3.3.1 Introduction

Impurity control studies for DEMO have focused on the pumped limiter concept with more work planned for a poloidal divertor design. The major plasma engineering areas under investigation are 1) the plasma equilibrium and edge conditions for a DEMO type reactor, 2) high vs. low edge temperature operation, and 3) low Z coatings vs. uncoated structural materials for the first wall and limiter. The most critical area of concern for a limiter, and the divertor as well, is believed to be erosion and the associated lifetime of the limiter surface. We have continued the work begun in this area for STARFIRE through the use of a code[4] that models the sputtering and redeposition of the limiter and wall material back on the limiter. Analysis of the plasma equilibrium and edge conditions has been done with a modified version of the WHIST 1-D transport code. A code (DSPUT)[5] has also been developed to predict sputtering coefficients on the limiter and first wall. Work is also in progress in examining the physics of the sheath region for the type of oblique incidence boundaries encountered in a toroidal limiter and poloidal divertor impurity control system.

Based on the work performed to date, the following conclusions can be made about a limiter impurity control system. 1) The plasma edge conditions in DEMO can apparantly be controlled to give either a high or low edge temperature by selecting the appropriate combination of pumping efficiency and plasma fueling method. 2) Plasma operating regimes can be identified where low Z coatings are absolutely required or where medium or high Z materials may be acceptable. 3) In most cases, the limiter surface grows with time due to a transfer of wall sputtered material to the limiter. The growth rates predicted imply multi-year operation before removal of the limiter is necessary. All of these conclusions are subject to uncertainties in both plasma physics and materials considerations. An ongoing effort, both in the theoretical and experimental areas is needed to resolve these uncertainties.

3.3.2 Plasma Equilibrium and Edge Conditions

Part of the DEMO work in impurity control has been to study the expected plasma equilibrium and edge conditions and to explore ways of controlling the edge. This analysis made use of a one-dimensional, time-dependent plasma transport code adapted from the code WHIST, which has been developed for the last several years at Oak Ridge National Laboratory. Given an initial set of plasma profiles and suitable boundary conditions, WHIST advances the profiles in time, using specified plasma diffusion laws and appropriate source terms. Because this study concerns the steady-state phase of the burn, the plasma behavior was calculated with the code until a time-independent configuration developed. Additional details of this work are given in Reference 6.

As in STARFIRE, a high-Z impurity, iodine, is used to enhance the plasma radiation, in order to maintain thermal equilibrium during the burn and to minimize the transport power to the limiter. Since the diffusion properties and source term are even less well understood for high-Z impurities than for hydrogenic species, the iodine profile and concentration were kept fixed during a run. Various iodine profiles were considered, and in each case the concentration was adjusted to yield the same overall plasma parameters. The iodine content was always less than 0.1% of the fuel content.

The following basic recycling/refueling strategy was investigated:

(a) A fraction, ε, of the plasma ions which, according to the code, strike the limiter, is considered to be pumped by the vacuum system and the remaining fraction is recycled as cold neutral gas from the tip of the limiter, with an energy of 10 eV.

(b) All neutrals which strike the wall are recycled as cold neutral gas, again at 10 eV. (Ions striking the wall are also recycled as neutrals but their number is insignificant.)

(c) Helium neutrals are considered to undergo ionization only and are recycled from the tip of the limiter.

(d) The pumped and burned fuel is replenished by either of two mechanisms: pellet injection (the reference case), or additional gas puffing from the tip of the limiter.

Four recycling/refueling cases were considred, three corresponding to pellet injection with various choices of the pumping efficiency, and the fourth corresponding to refueling with gas puffing:

1) $\varepsilon = 0.25$; pellet injection;

2) $\varepsilon = 0.10$; pellet injection;

3) $\varepsilon = 0.05$; pellet injection; and

4) $\varepsilon = 0.10$; gas puffing.

Deuterium and tritium pellets were treated separately in the code.. The pellet radius was 1.5 mm, so that a single pellet represented a 7% perturbation in the plasma density for that species. The pellet injection speed was 2 km/s, and the injection rate varied from 25 s^{-1} (case 1) to 9 s^{-1} (case 3) for each species.

Profiles of the electron temperature, the ion temperature, and the deuterium density in case 2 are shown in Fig. 3-5. The average electron temperature $\bar{T}_e = \langle n_e T \rangle \langle n_e \rangle^{-1}$ and the average ion temperature, $\bar{T}_i = \langle n_i T_i \rangle \langle n_i \rangle^{-1}$ are 19.0 keV and 20.2 keV, respectively. (The averages without the density weighting factor are 16.9 keV and 18.0 keV, respectively.) The total fusion power, without blanket multiplication, is 753 MW. As shown, the deuterium density profile is nearly flat over most of the discharge and sightly hollow in the center. The hollow feature is believed to be a nonequilibrium effect which would flatten out over longer running times. The tritium density is generally within a few percent of the deuterium density.

The loads on the limiter and first wall and the plasma edge temperatures, for the cases defined above, are summarized in Table 3-4. Table 3-5 summarizes the plasma power balance for these cases. As Table 3-4 indicates, the confinement time τ decreases steadily with decreasing pumping efficiency (here τ is defined as the total number of ions of a species, divided by the loss rate to the limiter; τ_{dt} denotes the average of τ_d and τ_t, with the former exceeding the latter by a few percent). At the same time, however, the edge temperatures drop because of the increased recycling, so that the heat load on the limiter remains relatively constant. This heat load represents about 70% of the α heating power to the plasma, which is an acceptably low value for this design. (In STARFIRE, which had a much larger margin of ignition, the load on the limiter was 17% of the α-heating power.)

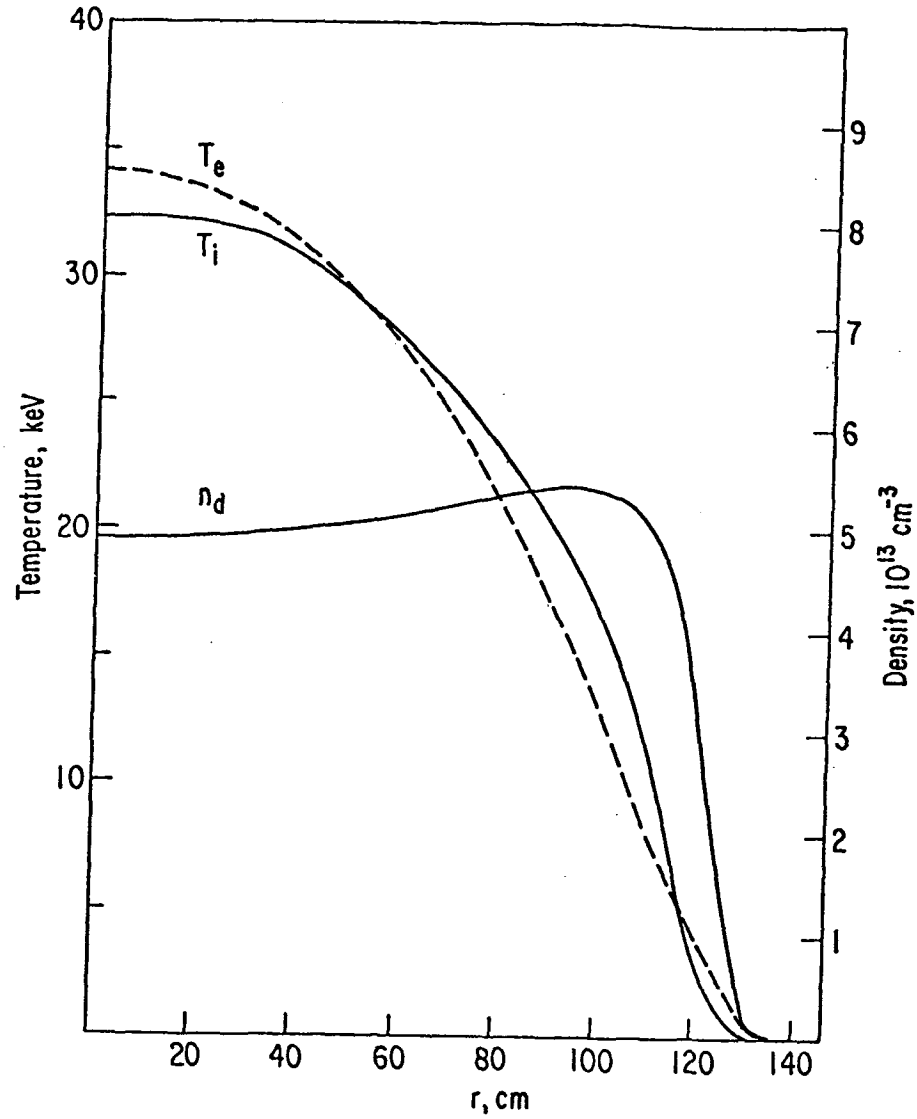

Figure 3-5. Radial profiles of the electron temperature, ion temperature, and deuterium density for the reference case 2. In this figure, r is the distance along the horizontal midplane.

Table 3-4. Loads on the Limiter and Wall for Cases 1 - 4

	(1)	(2)	(3)	(4)
Removal efficiency, ε	.25	.10	.05	.10
Method of fueling	pellet	pellet	pellet	puffing
τ_{dt}, ms	176	125	101	50
τ_{α}, ms	1081	472	266	449
I_{dt}, 10^{23} s^{-1}	1.43	2.02	2.51	5.03
I_{α}, 10^{21} s^{-1}	1.16	2.85	5.68	2.16
Power to limiter, MW	107	103	105	105
T_e at limiter tip, eV	805	560	455	235
T_i at limiter tip, eV	262	182	173	129
Charge-exchange current to wall, $10^{23}s^{-1}$	1.08	1.38	1.57	1.88
Charge-exchange power to wall, MW	24	23	21	12
Fractional iodine concentration, N_I/N_{DT}	2.9×10^{-4}	2.9×10^{-4}	2.1×10^{-4}	0

Table 3-5. Power Balance for Cases 1 - 4

(Power in units of MW)

	(1)	(2)	(3)	(4)
Fusion (to α's)	155.8	150.6	146.2	115.1
Ohmic	11.9	11.9	10.8	9.5
Transport-electron	96.0	92.3	92.7	86.9
Transport-ion	11.5	11.0	12.8	18.6
Charge-excahnge and ionization	24.6	22.0	21.5	12.1
Radiation-atomic	23.1	24.9	18.6	---
Radiation-other	12.5	12.3	11.4	7.0

While the code computes the density and temperature at the start of and in the scrapeoff region, these must be viewed as particularly uncertain due to poor knowledge of diffusion coefficients and loss mechanisms in this region. Adding to the uncertainty are the steep gradients near the limiter as well as 2-D effects not taken into account. Preliminary runs have been made to assess the sensitivity to scrapeoff physics. It has been found that there is a substantial decoupling of the scrapeoff region from the rest of the plasma so that even if the scrapeoff parameters change substantially, the transport power to the limiter, and the core parameters remain nearly constant. The general trend found in all cases considered is that a fair degree of control of edge temperature is possible, noted in Table 3-4, through the measures described. More work is planned to examine other ways of varying edge conditions, and to better estimate the conditions.

The ratio of τ_α to τ_{dt}, as noted from Table 3-4, represents an important consideration. The fact that this ratio considerably exceeds unity means that adequate helium removal would involve a higher hydrogen gas load and/or a higher concentration of helium than for the case with τ_α equal to τ_{dt}. Apparently while helium recycles faster than hydrogen at the plasma edge (mostly due to the lack of helium charge exchange), helium takes longer to diffuse to the edge, due to its centrally peaked birth profile. This effect is not governed by the emission energy of neutral helium (here taken as 10 eV), since a run with an emission energy of 0.3 eV gave only a 10% reduction in the alpha confinement time. An effect which would be expected to reduce τ_α, and which has not been taken into account in the code, is the enhancement of transport within the $q = 1$ surface due to MHD activity (the current profile in the present runs was taken to have a fixed form because of uncertainties in the REB current drive model). Other variations in plasma transport could also influence the result, and this issue needs further analysis.

Notwithstanding the issue of helium and hydrogen containment times, an interesting tradeoff exists between sputtering and impurity control, as shown in the data of Table 3-4. In going from a pumping efficiency of 0.05 to 0.25 (cases 3 and 1, respectively), the hydrogen flux to the limiter decreases by nearly a factor of two. Together with a doubling of particle energies, this would reduce sputtering by roughly a factor of four for low-Z materials. On the other hand, the rate of hydrogen removal, which scales as ε/τ_{dt}, increases

by nearly a factor of three. Therefore, a higher removal efficiency reduces sputtering of low-Z coatings considerably but correspondingly increases the gas load to the pumps.

For a medium- or high-Z limiter surface, an entirely different tradeoff strategy might be required. For higher Z materials it is crucial to minimize self-sputtering and therefore to maintain low plasma edge temperatures. Based on the trends found here, one way of accomplishing this would be to use a combination of low removal efficiency and refueling via gas puffing, both of which increase recycling and decrease the edge temperatures. The results are summarized under case 4. Possible difficulties associated with this approach are inadequate core refueling and an excessive hydrogen flux to the limiter. More work is needed to explore this subject.

The sensitivity to the assumed impurity profile was also examined. The cases discussed above had a fixed impurity which was flat in the plasma and which dropped off in the scrapeoff region in the same manner as the deuterium. To assess the sensitivity of the results to the assumed impurity profile, runs were made with recycling and refueling as in case 2 but with other choices of the profile. These cases were:

(5) $\varepsilon = 0.10$; pellet injection; impurity profile identical to the deuterium profile across the entire discharge.

(6) $\varepsilon = 0.10$; pellet injection; impurity profile proportional to a Gaussian, $\exp[-4(r/a)^2]$.

In each case the impurity content was adjusted to yield the same fixed average electron temperature.

For case 5, the edge conditions differ by less than 7% from those of the reference case 2. The power balance values are also very similar. The changes are somewhat more pronounced in case 6, in which the centrally peaked impurity profile leads to substantially less enhanced radiation. In this case the edge becomes about 15% hotter, the charge-exchange flux intensifies, and the transport power increases by 8%. These last changes do not represent large departures from the reference edge conditions. It appears, therefore, that there is some latitude in the choice of the impurity profile.

3.3.3 Reference Design

Although there has been, to date, more emphasis on general tradeoff studies, an initial reference limiter concept has been developed, to serve as a framework for studies of materials, thermal hydraulics, etc., as well as for plasma engineering calculations. The reference concept is a pumped limiter located at the torus midplane. We have subdivided the plasma edge temperature into three regimes denoted "high", "medium", and "low" as discussed earlier. The limiter design for the high temperature case is shown in Fig. 3-6 and key design parameters are summarized in Table 3-6. The limiter is of the same general geometry as in STARFIRE but has been shaped to spread the heat flux uniformly over the front surface. The limiter slot regions, between the leading edges and the first wall, lead through a series of vacuum ducts to compound cryopumps where helium and hydrogen are removed. The limiter is designed to remove 10% of the incident DT and He flux. For this design, the transport power to the limiter, and other plasma core parameters, were taken from the 1-D runs described above. The edge temperature and other scrapeoff parameters however, were taken as higher than the runs indicated, because of substantial uncertainties in the transport code scrapeoff model. The uncertainties will be exaimined in future work for DEMO.

An important design parameter for the limiter is the particle and energy e-folding distances in the scrapeoff zone. The particle e-folding distance was estimated using the following equations:

$$\bar{\delta}_p = \sqrt{D\tau}$$

$$\delta_{p_o} = \bar{\delta}_p \frac{\sqrt{\langle |\nabla\psi|^2 \rangle}}{|\nabla\psi_0|} \qquad (3\text{-}1)$$

where $\bar{\delta}_p$ is the average e-folding distance (averaged over a poloidal flux surface), δ_{p_o} is the e-folding distance at azimuthal location $\phi = \phi_o$, D is the perpendicular diffusion coefficient, τ is the particle flight time in the scrapeoff region, and ψ is the poloidal flux function. The terms involving the gradient of the flux function represent the effect of non-circularity. For the low q DEMO design, this term is approximately equal to 0.75 at the

Table 3-6. Reference Limiter Impurity Control System Parameters for High Edge Temperature operation.

Parameter	Unit	Value
Impurity Control Scheme	—	pumped limiter located at torus midplane
Surface Coating	—	Beryllium
Pumping System	—	Cryopumps
Plasma Edge Temperature	keV	1.5
DT Particle removal efficiency	—	0.10
α particle removal efficiency	—	0.10
Transport Power to Limiter	MW	100
Heat Flux on Front Surface (before leading edge)	MW/M^2	2.25
Peak heat Flux to Leading Edge	MW/M^2	2.33
Particle e-folding distance	cm	4.0
Energy e-folding Distance	cm	2.6
DT Particle Containment Time	sec	0.30
Helium Particle Containment Time	sec	0.60
DT Current to Limiter	ions/sec	8.0×10^{22}
Charge Exchange Current to First Wall	atoms/sec	1.0×10^{23}
DT Gas Load to Vacuum Pumps	molecules/sec	4.0×10^{21}
Helium Gas Load to Vacuum Pumps	atoms/sec	3.2×10^{20}
Helium Concentration in Plasma	—	~ 0.08

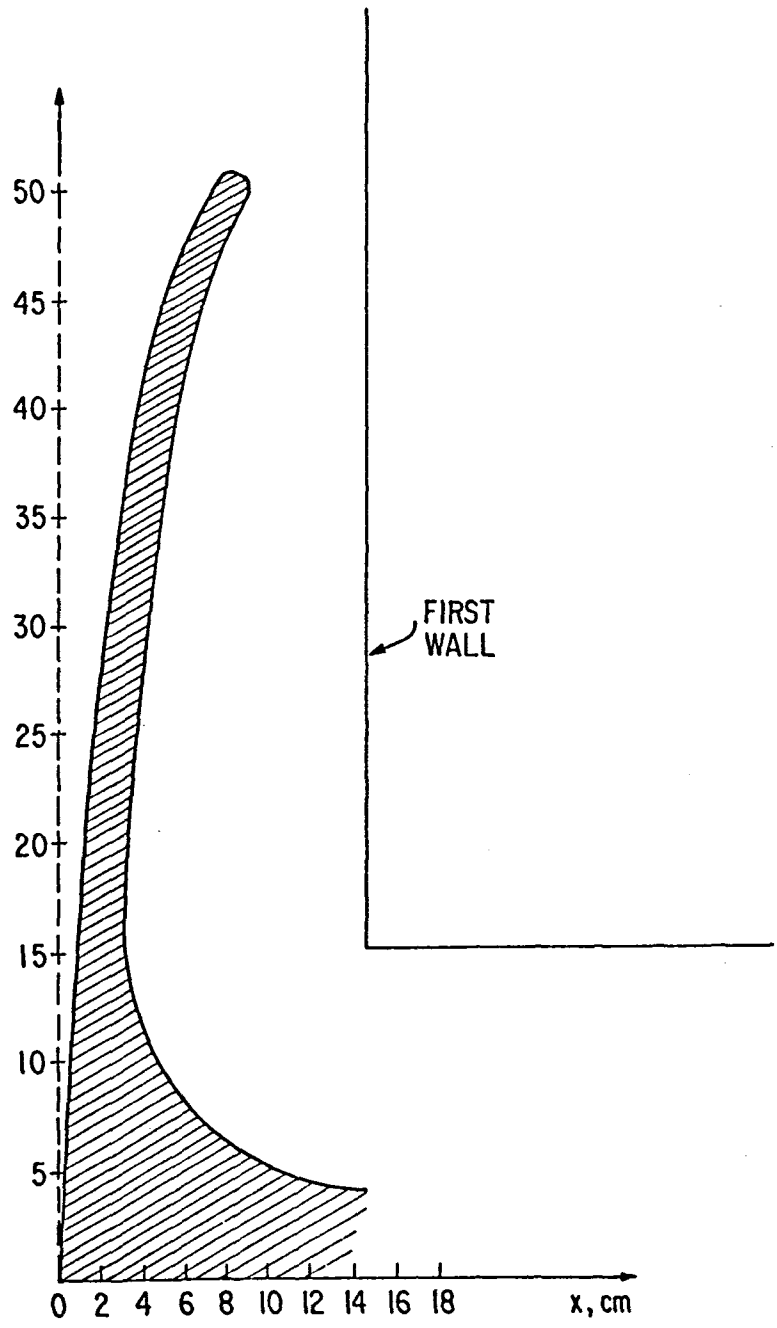

Figure 3-6. A Schematic of the Shape of the Reference Limiter for the High Edge Temperature Case.

midplane, i.e., $\delta_{p_o} \simeq .75\ \bar{\delta}_p$. The flight time can be expressed $\tau = \frac{2\pi Rq}{V}$ where V is the flow velocity. For the typical choice of Bohm diffusion, flow at the sound speed, and for parameters R = 5.2 m, q = 2.0, and B = 4.8T, the midplane particle e-folding distance is:

$$\delta_p \simeq 4\ (T_e/1500\ \text{eV})^{1/4},\ \text{cm} \tag{3-2}$$

where $T_e = T_i$ has been assumed for simplicity.

Thus $\delta_p \simeq 4$ cm for edge temperatures in the keV region, and falls to $\delta_p = 2$ cm at $T_e = 100$ eV. The value of δ_p depends on uncertain values of diffusion coefficient and flow velocity but this is a second order (square root) dependence. The behavior of plasma temperature in the scrapeoff region is somewhat less clear. For a choice of $\delta_T = 2\delta_p$ the reference energy e-folding distance is $\delta_E = (\frac{1}{\delta_p} + \frac{1}{\delta_T})^{-1} = 2.67$ cm.

The front face of the limiter was shaped to yield a constant heat flux, up to the vicinity of the leading edge where the flux becomes non-uniform. In general, the heat flux is given by the expression:

$$q(x) = \frac{q_m \exp -x/\delta_E}{\sqrt{1 + (dy/dx)^2}} \tag{3-3}$$

where x and y are the coordiantes defined in Fig. 3-5, and q_M is a constant given by:

$$q_M = \frac{P_{TR}^{LIM}}{4\pi R_L \delta_E} \tag{3-4}$$

where P_{TR}^{LIM} is the transport power to the limiter and R_L is the limiter major radius. (The shape of the poloidal field lines does not enter into Eq. (3-3) because the lines are all nearly vertical at the location of the limiter). For a constant heat flux q_o, q(x) is set equal to q_o in Eq. (3-3), giving a solution as follows:

$$y = \left\{ S_E \ \text{SEC}^{-1}\left(\frac{q_M}{q_o} e^{-x/S_E}\right) - \text{SEC}^{-1}\left(\frac{q_M}{q_o}\right) + \sqrt{\left(\frac{q_M}{q_o}\right)^2 - 1} + \sqrt{\left(\frac{q_M}{q_o} e^{-x/\delta_E}\right)^2 - 1} \right\} \tag{3-5}$$

Table 3-7. Sensitivity of Midplane Limiter Design to Scrapeoff Parameters δ_p = particle e-folding distance, δ_T = temperature e-folding distance, δ_E = energy e-folding distance, x_L = location of leading edge midpoint, y^{MAX} = limiter half-height.

δ_p	δ_T	δ_E	x_L	y^{MAX}
4 cm	8 cm	2.67 cm	8.0cm	51 cm
2	4	1.34	5.0	53
8	16	5.33	12.5	47
4	4	2.0	6.6	52
2	2	1.0	4.0	54

For DEMO, the transport power to the limiter is P_{TR}^{LIM} = 100 MW giving a value of q_M = 46.6 MW/m^2. For the choice of a moderate heat flux of q_0 = 2.25 MW/m^2, the limiter has the shape shown in Fig. 3-6, with a half height of $y^{MAX} \simeq$ 50 cm and a leading edge centered at x_L = 7.5 cm from the limiter tip. The peak heat load on the leading edge, for this design, is actually very close to the value on the front face. For a plasma with a fixed value of transport power, but different e-folding distances, this type of limiter design would have constant area, but different height and width parameters. The sensitivity of these parameters to changes in the scrapeoff parameters are shown in Table 3-7 for a variety of values of δ_p and δ_T. As shown, the limiter height is insensitive to scrapeoff parameter changes but the limiter width does vary. These differences do not seem to significantly affect the surface erosion, according to initial analysis, but may affect the mechanical performance.

3.3.4 Limiter Sputtering Calculations

Sputtering is probably the most critical unresolved issue for both limiter and divertor impurity control systems. Previous studies[4] of the STARFIRE and FED limiters showed that the surface coatings are likely to grow with time, due to a transfer of wall sputtered material back to the limiter surface. However, coating growth may be as much of a problem as erosion if the coating becomes too thick. For DEMO, a major focus of the work on impurity control has been in the analysis of sputtering and redeposition. As mentioned in the introduction, we have begun an investigation of a broad range of plasma edge temperatures and materials for the first wall and limiter. To date, an analysis has been made for the "reference" limiter concept with a Be coating, at a "high" edge temperature of 1500 eV. An analysis has also been made for a W coated limiter at a "medium" edge temperature of 100 eV. Edge plasma parameters for these cases such as heat transport power, particle flux, etc. were scaled from the transport code results. The resulting parameters are listed in Table 3-2. Additional work is planned to characterize the scrapeoff zone conditions and other techniques needed to obtain these edge temperatures.

The analysis of sputtering was done primarily with a computer code, "REDEP", which attempts to model the phenomena involved in limiter and divertor sputtering in a tokamak. The code requires as input the specification of hydrogen ion flux, temperature and density in the scrapeoff zone, and neutral hydrogen charge exchange flux to the first wall. The code first calculates the sputtering yield at each point along the limiter surface using the DSPUT code to compute sputtering coefficients and using a given sheath potential ($e\phi/KTe = 3$ for this study). The code than follows the sputtered neutral atoms ejected from the surface. A 2-D geometry is used with the neutrals launched at 30 different angles, corresponding to a cosine distribution from the normal, and at an energy given by one-half of the surface binding energy. For each angle, the code computes the attenuation of the neutral flux due to electron impact ionization along the path length. Ionized atoms in the scrapeoff zone tend to return to the limiter (because of momentum transfer with the incoming plasma and pre-sheath electric field acceleration) and this is followed in the code. The returning ions hit the limiter following a trajectory with guiding center motion along the field line passing through the point where the ionization occurred. (Diffusion of the

returning ions can also be treated but was assumed zero for simplicity in the present calculations. Cross field diffusion will affect redeposition profiles and will be examined in the future). Near the limiter surface the returning ions gain energy when accelerated across the sheath. Upon impacting the limiter surface, the ions cause additional sputtering by the self-sputtering process. In addition, surface material sputtered from the first wall can be ionized in the scrapeoff zone and impinge on the limiter, and sputtering from this source is calculated. Finally wall sputtered, and limiter sputtered material, that is not ionized in the scrapeoff zone, and does not flow in the direction of the wall, ends up in the plasma. This material is then assumed to impinge on the limiter at a rate and with a profile similar to the hydrogen flux, and with a charge state given by the coronal-equilibrium value. This causes yet more self-sputtering. The code iterates on these effects until convergence is established with fixed values of (a) surface erosion or growth rate and (b) plasma impurity content. A necessary condition for convergence is that the self sputtering coefficient, for impurity atoms ionized in the scrapeoff zone, be less than unity over most of the limiter surface. This severely restricts the range of edge temperatures where the medium and high Z materials can operate.

The results of this calculation for the cases mentioned are shown in Fig. 3-7. The Be case is for the reference design shown in Fig. 3-6. The W case is for this same limiter design scaled down so that the leading edge is centered at 5.0 cm, because of the reduction in e-folding distances at the lower edge temperature.

For the Be case, the coating is seen to grow everywhere on the limiter. The maximum growth rate is approximately 0.35 cm/yr for the DEMO at 50% duty factor. This level of growth is basically due to a transfer of wall sputtered material to the limiter. The Be concentration in the plasma is predicted to be 2.6% of the DT density. This penalty is judged to be acceptable.

Lower edge temperatures would give worse performance for a Be or other low Z coated limiter. This performance is due to two effects: 1) the particle flux to the limiter scales inversely with temperature since the transport power appears to be constant, and 2) both DT and self-sputtering coefficients increase for lower temperature.

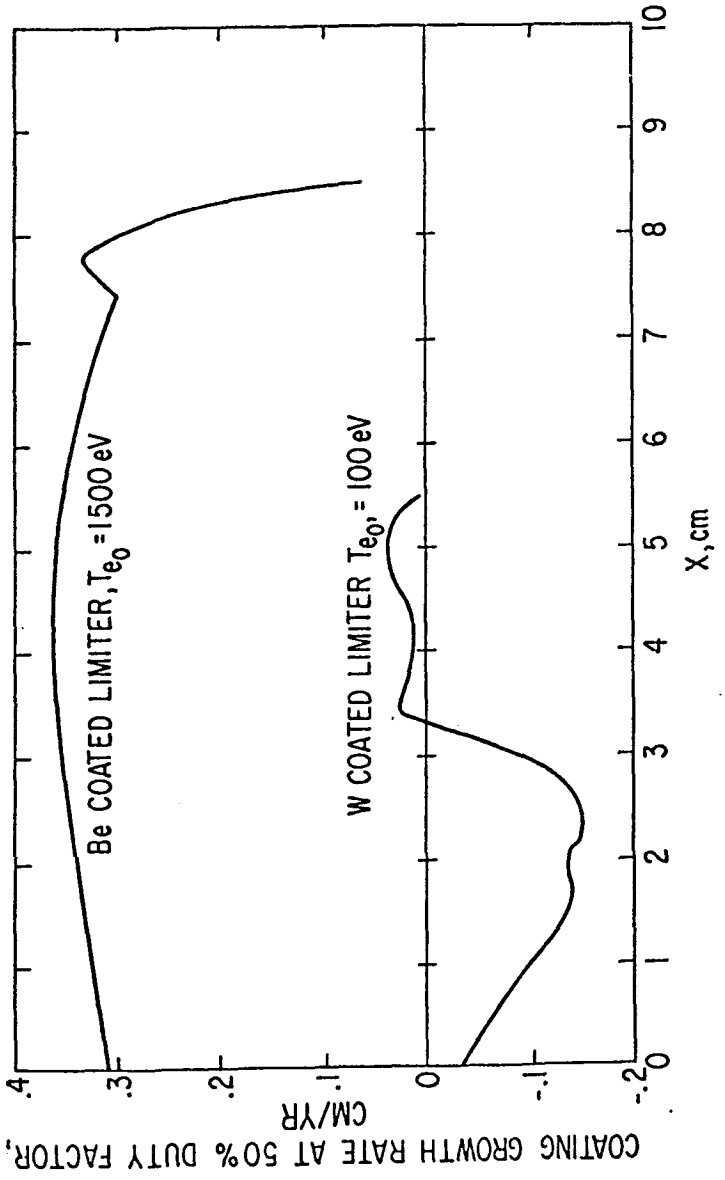

Figure 3-7. Predicted Limiter Redeposition Rates

As an example of the effect of lower edge temperatures, a preliminary run was made for T_{e_o} = 500 eV. A growth rate in excess of 2 cm/yr on some portions of the limiter is predicted. However the plasma Be concentration was still an acceptable 2.8%. The converse of this is that higher edge temperatures would reduce surface erosion/growth from the reference value. Some means to achieve higher edge temperatures might be the direct heating of the edge region with rf heating.

The W coated limiter results shown in Figure 3-6 are for an edge temperature of 100 eV and for a limier of width 5.5 cm, corresponding to the smaller e-folding distances at this edge temperature. As for the Be case the particle fluxes, densities, etc., used for this calculation were taken from the transport code results, extrapolated to this temperature. There are a number of critical uncertanties associated with the W calculation. For example electron impact ionization cross sections are almost unknown experimentally and uncertain theoretical estimates had to be used[7]. The results however are indicative of a possible regime where very low surface growth/erosion may be possible. This is due primarily to low DT sputtering coeffcients for W (in fact, the lowest of any possible surface material) and high redeposition rates. The W concentration in the plasma, for this case, is about .01%, an acceptable value. Essentially, all wall sputtered W is predicted to be deposited on the limiter due to complete ionization in the scrapeoff zone. Most limiter-sputtered material redeposits immediately but some does get into the plasma. For W, plasma edge temperatures lower than 100 eV would result in even less erosion. However, the edge temperature could not be much higher than 100 eV if a runaway sputtering cascade is to be avoided. Further work is planned to examine the W option in detail as well as medium Z materials such as vanadium.

3.4 Vacuum System

The vacuum system interacts directly with the impurity control system, since the gas loads to the vacuum pumps are determined by the plasma edge characteristics and the limiter design. The vacuum pumps should be capable of operating over a range of gas pressures down to about 1×10^{-7} Pa, have a relatively high helium capture probability, be compatible with the fusion environment, and have high reliability and maintainability. Several pumping systems have been evaluated to determine the most suitable system for the STARFIRE/DEMO limiter design.

The systems evaluated are liquid helium cryopumps, turbomolecular pumps, evaporable and non-evaporable getter systems, diffusion pumps, and differential ion pumps. A summary of the advantages and disadvantages of the pumping systems is shown in Table 3-8. The comparison indicates that liquid helium cryopumps are the preferred vacuum pumps. They have the highest helium capture probability, are very reliable and clean, and should be available in the sizes required. Since cryopumps must operate at liquid helium temperatures, they have strict limitations on the allowable heat input. This limitation means that the pumps must be placed at a reasonable distance from the plasma and must be properly shielded to reduce the internal neutron heating. The details of the engineering requirements and analysis for the cryopump system are given in Section 5.4.2.

Table 3-8. Vacuum Systems Comparison

System	Advantages	Disadvantages
Turbomolecular Pumps	Good tolerance to thermal heating	Low H and He capture probability Components susceptable to radiation damage Organic liquids required Size limitations
Liquid Helium Cryopumps	Highest He capture probability (~0.2) High reliability Clean system (no organics) Available in large sizes	Regeneration required Low tolerance to thermal heating Liquid He system required
Getters	High radiation and thermal tolerance Clean system Available in large sizes	Will not pump He Evaporable getters require frequent filament replacement Non-evaporable getters require fore-pumps for regeneration
Diffusion Pumps	Acceptable H and He capture probability Good tolerance to thermal heating	Working fluids can produce system contamination Organic components susceptable to radiation damage
Differential Ion Pumps	Good tolerance to irradiation and thermal heating Clean system	Low He capture probability Not regenerable Potentially high tritium inventory Magnetic compatibility

3.5 Materials

3.5.1 Structural Materials

3.5.1.1 General Considerations

The operating conditions for limiter structural materials are severe, as shown in Table 3-9. Most of the conditions are similar to the conditions experienced by the first wall, and the requirements for limiter materials are therefore similar to the first wall requirements. The material should have adequate structural strength, it should be resistant to radiation damage, it should be compatible with the coolant (and coating/cladding, if used), and it should have low hydrogen permeability and retention. The high heat flux to the limiter places an additional restriction on the materials selection. In order to minimize thermal gradients and stresses, the limiter material should have a high thermal conductivity, a low coefficient of thermal expansion, and a low elastic modulus. In addition, it is desirable that the material have a high specific heat and melting point to increase the safety margin during off-normal events such as loss of coolant or disruptions.

The high heat flux reduces the number of potential limiter materials. In particular, both austenitic and ferritic stainless steels are unacceptable because of their relatively poor thermophysical properties.

Table 3-9. Limiter Operating Conditions

Surface heat flux	2.3 MW/m^2
Neutron wall loading	1.8 MW/m^2
Burn cycle	continuous
Coolant	H_2O at $\sim 100^0C$
Duty factor	50%
Particle energies	10 eV (low) 100 eV (medium) 1.5 keV (high)
Desired lifetime	$\gtrsim$ 2 y

The classes of materials which can meet the high heat flux requirements are copper alloys, aluminum alloys, and refractory metal alloys, all of which have high thermal conductivities. Copper alloys are preferred over aluminum alloys because they have higher thermal conductivities and higher allowable operating temperatures. Several refractory metals which are capable of withstanding the high heat fluxes are not generally considered to be adequate structural

materials. The high-Z refractory metals (tungsten, tantalum, and molybdenum), fall into this class. Tungsten is difficult to fabricate and is prone to severe radiation embrittlement. Tantalum is very expensive, has a high rate of transmutation to tungsten, and has a negative effect on tritium breeding. Molybdenum is difficult to fabricate and is also prone to severe radiation embrittlement. The other candidate refractory metals are titanium, vanadium, niobium, and their alloys. These materials have all been considered for the Alloy Development for Irradiation Performance Program, and thus, a substantial data base exists.

Four candidate alloys have been selected for further evaluation. They are AMAX-MZC (copper), V-15Cr-5Ti, FS-85 (niobium), and Ti-6242. AMAX-MZC is a commercial copper alloy which combines high strength with a high thermal conductivity[8]. The high strength results from cold working plus a thermal aging process. The vanadium alloy was originally developed for the fast breeder reactor program, and it combines high temperature strength with excellent resistance to radiation damage. The niobium alloy has good high temperature strength and favorable thermophysical properties. Ti-6242 is a commercial titanium alloy which has adequate thermophysical characteristics. A summary of the major advantages and disadvantages of the candidate alloys is given in Table 3-10. In the following sections, the major concerns for each material will be discussed in detail. A reference and a backup material will then be selected.

3.5.1.2 Thermophysical Properties

The thermophysical properties at room temperature and 773 K of the candidate alloys are shown in Table 3-11[8-13]. The copper alloy has the highest thermal conductivity and would be expected to exhibit the lowest operating temperatures. It also has the lowest melting point, and thus has the lowest permissible operating temperatures. Ti-6242 has the lowest thermal conductivity and would be expected to exhibit the highest operating temperatures.

3.5.1.3 Tensile Properties

The tensile properties of the candidate limiter materials are shown in Table 3-12[8,10,12-15]. Also shown is the calculated thermal stress parameter which combines the material strength and the thermophysical properties and

Table 3-10. Structural Material Comparisons

Alloy	Advantages	Disadvantages
Copper (AMAX-MZC)	Excellent thermophysical properties	Operating temperature limited to ~ 300^0C
	Commercial availability	Potentially large radiation effects
	Fabricability	Not compatible with liquid metals
	Good tritium barrier	
Titanium (Ti6242)	Commercial availability	High tritium retention
	Fabricability	Relatively poor thermo-physical properties
Vanadium (V-15Cr-5Ti)	Excellent resistance to radiation damage	Not commercially available
	Compatible with liquid metals	High oxidation rates if exposed to air
	High temperature capability	Potentially difficult fabrication
	Low activation	High tritium permeability
		Potentially high H_2O corrosion at T > 100°C
Niobium (FS-85)	Good thermophysical properties	High activation
	Compatible with liquid metals	High oxidation rates if exposed to air
	High temperature capability	High tritium permeability
		Potentially difficult fabrication
		Potentially high H_2O corrosion at T > 100°C

Table 3-11. Thermophysical Properties of Candidate Limiter Materials

Materials	Melting Point K	Density Kg/m^3	Thermal Cond. W/m K		Thermal Exp. x 10^{-6}/K		Elastic Mod. GPa		Specific Heat		Poissons Ratio
		300 K	300 K	773 K	300 K	773 K	300 K	773 K	300 K	773 K	
AMAX-MZC	1356	8930	320	300	16.7	20.4	137	75	392	435	.34
V-15Cr-5Ti	2161	6160	24	28	9.3	10.4	124	117	475	572	.36
FS-85	2743	10,600	45	48	5.6	7.1	140	135	215	230	.38
Ti-6242	1923	4500	7.2	12	7.2	9.5	115	85	465	725	.32

and which indicates the relative heat load capability of the materials. The superiority of AMAX-MZC is clearly evident. The niobium alloy follows and the vanadium and titanium alloy have roughly equivalent thermal stress parameters. The relatively high thermal stress parameter of Ti-6242 is due to its high strength compared with the other materials. All four of these alloys appear to be capable of withstanding a heat flux of ~ 2 MW/m^2 (1).

Table 3-12. Tensile Properties of Candidate Limiter Materials.

Material	.02% YS MPA		UTS MPa		Elongation %		Thermal Stress[a] Parameter x 10^4	
	300 K	773 K	300 K	773 K	300 K	773 K	300 K	773 K
AMAX-MZC	475	401[b]	551	416[b]	12	9[b]	4.38	5.19[b]
V-15CR-5Ti	507	350	600	510	26	14.5	.675	.515
FS-85	485	375	600	380	23	18	1.72	1.16
Ti-6242	950	600	1025	775	11	10.5	.561	.480

a $\frac{0.2\%\ YS \times (1 - \nu) \times k}{E \times \alpha}$

b 663 K

3.5.1.4 Irradiation Effects

Neutron irradiation is known to induce swelling, accelerate creep, alter the strength, decrease the ductility, and produce compositional changes in structural materials. All of these changes can potentially affect the heat load capability and lifetime of the limiter materials. Unfortunately, the information available on irradiation effects on the candidate alloys is sparse. The next few paragraphs will focus on radiation swelling and embrittlement.

Swelling in metals is caused by the segregation of radiation produced vacancies into voids during irradiation at temperatures from 0.3 to 0.5 of the absolute melting temperature, T_m. Several factors, including temperature, neutron flux, total neutron fluence, helium generation rate, cold work, grain size, and precipitate structure can influence the amount of swelling. Pure copper exhibits a peak swelling at ~ 325°C (0.44 T_m) and the rate of swelling is high (~ 1%/dpa)[16]. Alloying the copper can reduce the observed swelling[17], but it is not known what, if any, reduction in swelling will be observed in AMAX-MZC. Pure niobium and vanadium exhibit swelling peaks at ~ 600°C (0.32 T_m) and 550°C (0.38 T_m), respectively[10,14]. The observed peak swelling rates are considerably below that of pure copper. Alloying can significantly reduce the swelling in refractory metals. In the case of V-20Ti, no swelling has been observed up to a fast fluence of 8.4×10^{22} n/cm^2 (~ 42 dpa) and between temperatures of 470 and 780°C[14,18,19]. Addition of molybdenum, vanadium, titanium, zirconium, and hafnium have been shown to reduce void swelling in niobium[20]. Irradiation of Nb-Zr to a fast fluence of 5.4×10^{22} m/cm^2 at 650°C resulted in practically no swelling[19]. Swelling of this alloy has been observed at temperatures between 700 and 900°C[21]. Titanium alloys have recently been irradiated with heavy ions and neutrons. Ion irradiation of Ti-6Al-4V and Ti-14.4 a/o Al have resulted in void production at 670°C. No voids have been observed at temperatures below 630°C[22,23]. Voids have been observed in Ti-6242S irradiated with neutrons to ~ 31 dpa at 550°C, but the total swelling was low[24]. In summary for the low anticipated limiter operating temperatures only AMAX-MZC might be expected to exhibit significant void swelling. Swelling in refractory metals is generally low and has not been observed at temperatures < 500°C.

Neutron irradiation is known to reduce the ductility of metals. Since the limiter is designed to operate in the elastic range, residual ductility is only necessary to prevent catastrophic failure during an off-normal event. The amount of ductility required will depend upon the severity of the event, and cannot be realistically estimated at this time. Unfortunately, there is only a limited amount of data on the materials of interest. The irradiation data for copper is restricted to low fluences (< 1 dpa), but there are indications that neutron irradiation can severely embrittle cold-worked copper [25]. Vanadium alloys appear to retain the greatest amount of ductility. V-20Ti shows only a relatively small decrease in uniform elongation, from 15% to

~ 10%, after EBR-II irradiation at 525°C to a neutron fluence of 2.5×10^{26} n/m^2 (E > 0.1 MEV). Low fluence irradiations of V-15Ti-7.5Cr at 600°C resulted in an increase in the uniform elongation[14,18]. Pure niobium retains ~ 5% uniform elongation at temperatures from 400 to 600°C after irradiation at 450°C to a fluence of 3.7×10^{26} n/m^2 (E > 0.1 MEV)[26]. Nb-1Zr, however, retains almost no uniform ductility under the same conditions. Recently, Ti-6242S, which was irradiated at ~ 550°C to a damage level of 24 dpa, has been tensile tested. Little change in ductility was observed at 400°C, but there was a 75% decrease (to 3.3%) in the total elongation at 500°C [27]. Additional experimental effort is required to adequately determine the influence of radiation on these materials.

3.5.1.5 Compatability

Compatibility of the limiter materials with the reactor environment is also a concern. The limiter must be compatible with the water coolant as well as the deuterium and tritium from the plasma. The corrosion rate of the materials will depend upon the temperature, coolant flow rate, alloy composition, and water chemistry. Since the water outlet temperature is $\leq 100^0$C , corrosion is expected to be low. The refractory metals are generally more reactive to water than copper, but the corrosion rates should remain within acceptable limits. Additional work is needed to determine the best coolant chemistry to minimize corrosion.

Protium, deuterium and tritium introduced into the limiter materials are a concern because of the potential for hydrogen embrittlement and increasing the tritium inventory in the limiter structure and coolant. Copper and copper alloys can become embrittled by hydrogen if there is a significant amount of oxygen dissolved in the metal[12]. Reduction of the oxygen concentration to low levels should eliminate this concern, however. The other candidate materials are susceptible to hydrogen embrittlement due to the formation of a brittle hydride phase at low temperatures. Both vanadium and niobium have high hydrogen solubilities (~ 10 a/o at 100^0C)[1], and thus it is unlikely that hydrides would form during reactor operation. Titanium alloys have a much lower solubility for hydrogen, and hydrides may be present at temperatures < 150°C. The solid solution solubility of α-titanium is only 0.1 a/o at room temperature[28]. Therefore, there is a concern that titanium alloys could easily be embrittled by hydrogen. The penetration of tritium

into the coolant is dependent upon the permeability of the structural material. Copper has a low hydrogen permeability and refractory metals have high hydrogen permeabilities, giving copper a significant safety advantage. The candidate refractory metals may, in some cases, be unacceptable with water coolant because of rapid tritium permeation into the coolant.

In summary, the copper alloy, AMAX-MZC, offers significant advantages in terms of thermal gradients and stresses, fabricability and availability, and hydrogen embrittlement and permeation. The primary uncertainty is the response of this material to an irradiation environment. The vanadium alloy, V-15Cr-5Ti is considered the first choice of the refractory metals due to its superior resistance to radiation damage. High hydrogen permeability is a concern for all refractory metals. AMAX-MZC is, therefore, proposed as the reference material. It is strongly recommended that irradiation experiments be performed in the near future to determine if AMAX-MZC has acceptable properties at high neutron fluences.

3.5.2 Low-Z Materials

At high plasma edge temperatures, low-Z materials provide the most suitable surface material for the first wall and limiter. Relatively high concentrations of a low-Z material can be tolerated within the plasma, and the self-sputtering coefficient of low-Z particles striking the limiter is always less than unity. Three materials, Be, B, and C, have been considered for limiter applications. None of these materials have the mechanical properties required for a structural material, and therefore they will have to be bonded to a standard structural material. This section will briefly discuss the properties of low-Z materials and recommend a reference material.

The thermophysical properties of the three materials are shown in Table 3-13[9,12]. It is desirable that the material has a high thermal conductivity to reduce the thermal gradients and stresses. In addition, it is desirable to have a high specific heat, a high melting point, and a high heat of

Table 3-13. Thermophysical Properties of Low-Z Materials.

Material	Th. Exp.* x 10^{-6}/K	Th. Cond.* W/m K	Sp. Heat* J/Kg K	MP K	BP K	Heat of Vap. J/g
Be	16	100	2250	1557	3243	24,790
B	5.5	15	2090	2573	2823(s)	46,740
C	4.5	104	1880	----	4000(s)	59,356

*500°C

vaporization in order to minimize the effects of plasma disruptions. The thermal expansion coefficient should match that of the structural material as closely as possible to minimize the differential expansion between materials. Carbon and beryllium both have high thermal conductivities. Carbon also has a low coefficient of thermal expansion which gives it an excellent thermal shock resistance. The thermal expansion coefficient of beryllium most closely matches that of most structural metals. The low thermal conductivity of boron will result in a high thermal gradient through the material.

The reactor environment is expected to have a large effect on low-Z materials. Neutron irradiation will produce large quantities of hydrogen and/or helium in all three materials. In order to accommodate the resultant gas swelling, the material should be fabricated with ~ 30% porosity. The porosity will decrease the thermal conductivity and reduce the mechanical strength. Neutron irradiation will also produce lattice displacement damage. In the case of graphite, the thermal conductivity is reduced to ~ 30 W/m K, the strength decreases, and the material shows high swelling rates at radiation levels equivalent to 1-2 MW-y/m^2 [29]. Chemical sputtering is also a concern for carbon and boron, since both materials are known to chemically react with hydrogen at temperatures which may be achieved during reactor operation. Beryllium has a lower hydrogen solubility and permeability than the other materials, and it will provide a superior barrier to tritium permeation.

There is still only a limited data base for the low-Z materials which makes the selection of a reference material difficult. Beryllium is tentatively selected as the reference material based upon its relatively good thermophysical properties, its low hydrogen permeability, and the expected lack of chemical sputtering.

3.5.3 High Z Materials

High-Z materials offer potential advantages as the material facing the plasma edge temperatures of ~ 100 eV . First, the sputtering of the first wall will be low compared with other materials, and the first wall thickness can be considerably reduced. Second, several high-Z materials have high thermal conductivities and high melting points which will reduce the impact of disruptions. The two high-Z materials that have been considered are tantalum and tungsten. The sputtering characteristics of the two materials are similar. For INTOR like conditions, the calculated sputtering rate of the first wall is only ~ 0.1 mm/y at a 50% duty factor. The buildup rate on the limiter is ~ 1 mm/y. Tungsten has superior thermophysical properties (see Table 3-14), and is more likely to survive intact during a disruption. Tungsten has therefore been selected as the reference material for the limiter/first wall coating for plasma edge temperatures of ~ 100 eV.

Table 3-14. Thermophysical Properties of Tungsten and Tantalum at 500°C.

Material	Th. Exp. $x10^{-6}/K$	Sp. Heat J/Kg K	Th. Cond. W/m K	Melting Point K
Ta	6.7	150	54	3270
W	4.4	160	90	3650

3.5.4 Redeposited Material

Plasma-wall interaction models predict that material that is sputtered from the first wall will be directed to the limiter. Along with the wall particles, a high flux of energetic plasma particles will also strike the limiter. The interactions of the incoming particles with the limiter surface represent a complex set of phenomena. The incoming particles may be reflected from the surface, become trapped within a thin surface layer, produce lattice displacement damage, or sputter additional particles from the limiter. As

long as the sputtering coefficient of the incoming first wall particles is less than unity, there will be a buildup of material at some locations on the limiter surface. For STARFIRE/DEMO like conditions, the buildup rate for low-Z materials is predicted to be ~ 10 mm/y and the buildup rate for high-Z materials is predicted to be ~ 1 mm/y. The structure and properties of this redeposited material is likely to be quite different from the original material, as will be described below.

Helium, deuterium and tritium particles have been observed to become trapped in metals when they are injected at energies typical of plasma edge conditions[30-32]. As the total dose of particles increases, the trapping will reach a saturation level. This level depends upon the incoming particle energy, the type of material being bombarded, and the material temperature. The saturation level corresponds to the point where gas bubbles have formed and have produced interconnected pathways to the surface, allowing the injected gas to escape. The important materials properties that determine the degree of trapping are the gas solubility and permeability. Helium has essentially zero solubility in metals, and has a low permeability because it is easily trapped at lattice defect sites. Therefore, injected helium is easily trapped in metals. Hydrogen solubility and permeability varies significantly from one material to another, and these properties usually have a large temperature dependence. In addition, some metals, like titanium, vanadium, or niobium, form stable hydrides, so when the solubility is exceeded, the hydrogen will become trapped as a hydride. The hydrogen can be released only when the temperature is increased to the point where the hydrides are unstable and dissolve. The differences in trapping between helium and hydrogen imply that some materials will trap both species, and other materials will trap helium alone.

Trapping of hydrogen and helium has been studied in several materials over a range of temperatures. Deuterium trapping and release has been investigated for 304 stainless steel, Inconel 625, TZM, and Ti-6Al-4V[30]. For particle energies of 3.3 KeV, ~ 20% of the incident particles were directly reflected. The trapping of deuterium in 304 stainless steel, Inconel 625, and TZM was relatively low and decreased rapidly with temperature. The trapping coefficient for these materials implanted at room temperature ranged from 10^{-1} to 10^{-2}, and the trapping coefficient dropped by approximately an

order of magnitude when the implantation temperature was raised to 450-500 K. Ti-6Al-4V, on the other hand had a trapping coefficient of unity for implantation temperatures up to 675 K, due to the formation of hydrides. The trapping coefficient dropped to ~ 0.5 at 775 K. The low Z materials, TiC, TiB_2, VB_2, B_4, B, Si, and graphite have been bombarded with hydrogen and deuterium at room temperature, and the saturation concentration of retained gas atoms to host lattice atoms has been calculated[32]. The saturation concentrations varied from 16% in VB_2 and TiB_2 to ~ 50% in graphite, Si, B, and B_4. The temperature range for hydrogen release in these materials is 100-500°C. Helium trapping in Ni and Be has been studied with and without coinjection of hydrogen[33]. Both materials trapped helium alone at injection temperatures of 300 and 675 K. When hydrogen was co-injected with helium, the helium trapping was relatively unaffected in Ni but was significantly reduced in Be. The reduced trapping in Be was attributed to the much lower diffusivity and solubility of hydrogen in Be compared with Ni. At high particle injection rates, the hydrogen would be expected to compete for trapping sites in Be, but would be expected to simply diffuse out of the Ni.

The structure of metals that contain trapped helium has been investigated. The effect of helium on the microstructure of Ni at room temperature has been studied as a function of dose[34]. For a dose level of $10^{20}/m^2$, defect clusters, and dislocation loops and tangles have been observed. At higher dose levels, helium bubble lattices are observed which are preferentially aligned along crystal planes. At very high doses, the bubbles are observed to coalesce and form into channels to the surface. As the implantation temperatures were raised, the bubbles became more randomly distributed and grew to larger sizes. At doses of $10^{22}/m^2$ the calculated swelling was 29%. Helium bubble lattices have also been observed in copper, 321 stainless steel, and titanium[35]. Calculations indicate that most of the helium is retained in the lattice and not within the bubbles.

The results of the hydrogen and helium trapping experiments have several implications for the redeposited materials on the limiter. First, bubble formation will result in swelling of the materials. At high dose rates, the swelling can approach 30%. Second, as more material is deposited, helium, along with deuterium and tritium, can become trapped. If the tritium is permanently trapped, the redeposited layer could have a high tritium inventory. Third, the materials properties are likely to be substantially

different from the original material. The swelling will result in a lower thermal conductivity, and the lattice damage will result in altered mechanical strength. At this time there is insufficient information to make accurate predictions. Since the implications on limiter operation are significant, additional experimental effort in this area is recommended.

3.5.5 Tritium Inventory and Migration

Tritium inventory and migration in the limiter have safety implications for the reactor operation, particularly if water coolant is used. The magnitude of the inventory and migration rates have been computed for several material combinations. The input parameters used for the calculations are:

Surface area	40 m^2
Thickness	1 mm (single materials)
	2 mm (dual materials)
Average Temperature	300°C (V, Cu)
	700°C (Be, W)
Tritium Pressure	0.4 Pa

Under these conditions the amount of tritium dissolved in the wall is negligible for beryllium and tungsten, is ~ 0.01 mg for copper and about 10 g for vanadium. If the average temperature were lower, the tritium solubility in vanadium would increase for a given pressure.

The migration rates were calculated using both the Hickman model and a standard permeation model. These models are described in detail in Section 4.2.3. The steady state migration rates are shown in Table 3-15. When tritium is injected into the candidate materials, the migration rate into the coolant for 100% dense material predicted to be very high (about 1 kg/d). The migration rate for beryllium is high because it is a low Z material and the ions can penetrate to a greater depth. However, the material on the surface of the limiter is expected to be porous as described in the previous section. Because of the low effective path length, tritium can easily migrate back to the plasma and migration through the wall is driven by simple permeation. Therefore, a permeation model should more realistically represent migration through porous materials. As shown in Table 3-15, the permeation model predicts greatly reduced tritium migration rates, although the rate for vanadium is still high. The presence of an oxide layer is needed to further reduce the migration rates. The permeation model has also been used to predict migration rates in dual material structures. The predicted rates are low.

The calculations indicate that copper has a significant advantage over vanadium in terms of tritium solubility. If simple permeation controls migration, then both the beryllium or tungsten coated structures appear to be acceptable.

Table 3-15. Tritium Migration in Limiter

Model	Material	Temp. (°C)	Ci/d	g/d
Hickman[a]	V		9.6×10^{6}	10^{3}
Hickman	Cu		9.6×10^{6}	10^{3}
Hickman	Be		9.6×10^{8}	10^{5}
Hickman	W		9.6×10^{6}	10^{3}
permeation	V	300	7×10^{5}	73
permeation	V (with oxide)	300	700	0.07
permeation	Cu	300	15	1.6×10^{-3}
permeation	Cu (with oxide)	300	1.5	1.6×10^{-4}
permeation	Be	700	2	2.1×10^{-4}
permeation	W	700	5	5.2×10^{-4}
permeation	Be/Cu	700/300	1.5	1.6×10^{-4}
permeation	Be/V	700/300	2	2.1×10^{-4}
permeation	W/Cu	700/300	1.5	1.6×10^{-4}
permeation	W/V	700/300	5	5.2×10^{-4}

[a]Hickman model is temperature independent.

3.6 Thermal Hydraulics

3.6.1 Introduction

Thermal hydraulic calculations have been performed for the leading edge of the limiter using a variety of material combinations and different coating/cladding thicknesses. The assumed operating conditions are shown in Table 3-16 along with the materials that were examined. As a starting point, the STARFIRE limiter geometry has been used,[1] but the addition of the coating/cladding has been included in the calculations. The purpose of this effort is first to determine if the temperature of the materials remain in an acceptable range during operation, and second to provide the required input for the thermal stress evaluation presented in the following section.

The leading edge is a half cylinder with a diameter of 19 mm including a 1 mm coating. As shown in Fig. 3-8, the heat flux is assumed to be 2.3 MW/m^2 and is uniformly distributed around the circumfrence. The temperatures were calculated using a 2-D model as shown in Fig. 3-8. Although the results are practically one-dimensional, the 2-D model was employed since it can easily be adopted to perform calculations for non-uniform heat flux cases in the future. The thermal-hydraulic computer code used is THTB[36]. This code is capable of performing three-dimensional, transient, heat transfer calculations for various geometries.

The results presented are for steady-state conditions. The leading edge is the most critical area of the limiter since it receives the highest heat flux. To be conservative, conduction between the leading edge and the rest of the limiter structure will be neglected. The parameters varied are listed in Table 3-17. The nomenclature used for the various parameters is listed in Table 3-18.

3.6.2 Results

The results are presented in the following manner. First, the temperature distributions in the coating and the strutural material are presented for a selected value for each parameter shown in Table 3-19. Values given in Table 3-11 represent the most reasonable estimates of these parameters and therefore will be refered to as the reference conditions. The second part of this section are the results of sensitivity calculations obtained by varying the parameters shown in Table 3-17 with a specific

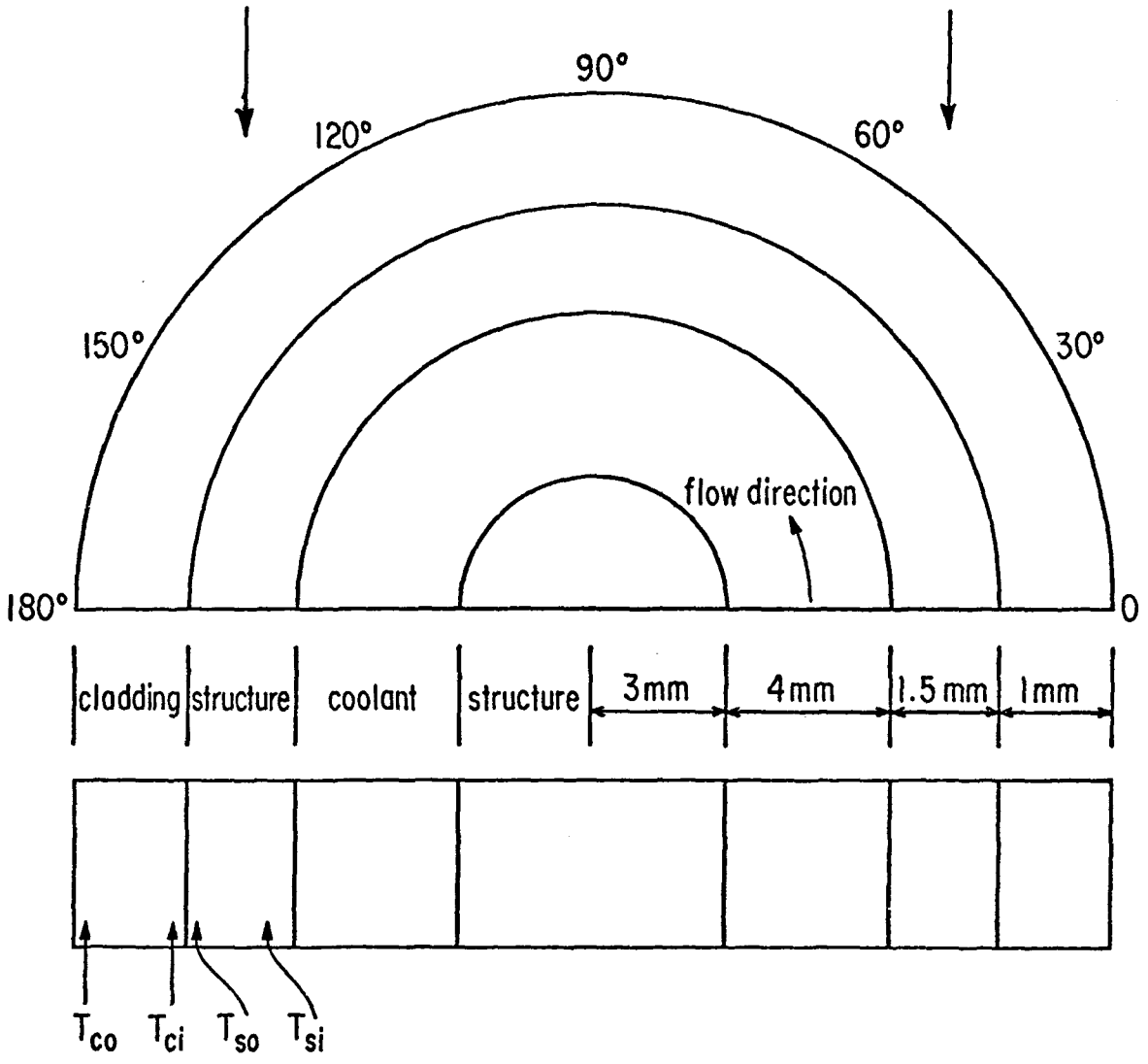

Figure 3-8. Geometry and Dimensions of the Leading Edge of the Limiter.

Table 3-16. Assumed Operating Conditions for the Limiter Thermal Hydraulics

heat flux:	2.3 MW/m^2, uniform over the circumference.
coolant: MPa	pressurized water at approximately 2.07 MPa (300 psia), coolant entering the leading edge at 90°C with a velocity of 8 m/s.
bulk nuclear heating for coating and structural materials, and coolant:	10 MW/m^3
geometry:	same as STARFIRE[1], see Fig. 1.
coating material:	Beryllium (Be), Boron (B), and Tungsten (W)
structural material:	AMAX-MZC (copper alloy), V-15 Cr-5 Ti (Vanadium alloy), Ti-6242 (Titanium alloy), and FS-85 (Niobium alloy)

Table 3-17. Parameters Varied for Thermal Hydraulics Calculations

Parameters	Range
coating thickness (mm)	1 - 10
heat transfer coefficient (h) between coolant and structural material (W/m^2 - K)	22700 - 34050
contact coefficient (h_c) between coating and structural materials (W/m^2 - K)	8512 - 17025
coating material density (ρ/ρ_0)	0.7 - 1.0
coolant temperature rise (°C)	5 - 15

Table 3-18. Nomenclature

h	=	heat transfer coefficient between fluid and structure.
h_c	=	contact coefficient of heat transfer between coating and structural material.
T_{CO}	=	temperature on the outer surface of the coating material.
T_{Ci}	=	temperature on the inner surface of the coating material.
T_{SO}	=	temperature on the outer surface of the structural material.
T_{Si}	=	temperature on the inner surface of the structural material.
ΔT_C	=	$T_{CO} - T_{Ci}$.
ΔT_S	=	$T_{SO} - T_{Si}$
ρ	=	actual density of the coating material.
ρ_O	=	nominal (reference) density of the coating material.

Table 3-19. Reference Conditions for the Results Shown in Table 3-20.

Parameter	Value
coating thickness (mm)	1
structural material thickness (mm)	1.5
h $(W/m^2 - K)$	29375
$(Btu/hr - ft^2 - °F)$	5000
h_c $(W/m^2 - K)$	17025
$(Btu/hr - ft^2 - °F)$	3000
coating density (ρ/ρ_O)	1.0
coolant temperature rise (°C)	5

combination of coating-structure material (e.g., Berylium-copper alloy). The uncertainties caused by the variations of these parameters on the temperature distribution can then be assessed.

The temperature distributions in the coatings and the structure materials for the reference conditions are shown in Table 3-20. The temperatures of the coating and the structural materials shown in Table 3-20 are well below the melting point of the respective materials. The temperature of Ti-6242 of about 530°C appears to be slightly above the allowable temperature range for this material, however. The temperature gradients ($T_{CO} - T_{Ci}$ and $T_{SO} - T_{Si}$) are proportional to the thermal stresses in the material. For all the structural materials evaluated in Table 4, AMAX-MZC has the lowest temperature gradient (about 6.7°C/mm) followed by FS-85 (about 40°C/mm), V-15Cr-5Ti (about 65°C/mm), and Ti-6242 (about 164°C/mm). The gradients are the result of differences in thermal conductivities for these alloys. For the cladding materials evaluated, Table 3-20 indicates that beryllium has the lowest temperature gradient (about 13°C/mm), followed by tungsten (about 17°C/mm) and boron (about 106°C/mm). Thus, copper and niobium alloys are the preferred structural material; and beryllium and tungsten are the preferred material for coating.

During the lifetime of the limiter, it is anticipated that some cladding material will be eroded from the first wall and deposited on the limiter. The thickness of the coating material will gradually increase with time. It is estimated that a thickness up to 10 mm coating material may be deposited on the limiter during its lifetime. Table 3-21 show the results of calculated temperature distribution in the coating and structural materials assuming that the thickness of the coating material equals 10 mm. The results in Table 3-21 indicate that the increase in coating thickness to 10 mm significantly increased the temperature of both the coating and the structural materials. The copper temperature is above allowable limits, and the berrylium temperature on the vanadium cladding is close to the melting point. A 10 mm deposit of berylium on the limiter is, therefore, not considered feasible for the assumed conditions. The increased temperature is due primarily to the limiter geometry. The radius of the leading edge is effectively doubled by increasing the coating thickness to 10 mm. Since the surface heat flux remains constant, the total heat load to the leading edge is doubled. The effect of additional nuclear heating in the 10 mm coating is relatively

Table 3-20. Temperature Distributions in Cladding & Structural Materials (°C)

Plasma Edge Temp.	Coating-Structure	T_{CO}	T_{Ci}	T_{SO}	T_{Si}
High	Be - Cu Alloy	392	380	220	211
	Be - V Alloy	527	514	334	236
	Be - Ti Alloy	756	740	531	285
	Be - Nb Alloy	471	458	286	225
	B - Cu Alloy	496	401	220	211
	B - V Alloy	655	539	335	237
Medium	W - Cu Alloy	398	381	220	211
	W - V Alloy	532	515	334	237
	W - Ti Alloy	758	740	531	285
	W - Nb Alloy	476	459	286	225
Low	Cu Alloy	*	*	207	197
	V Alloy	*	*	320	209
	Ti Alloy	*	*	515	232
	Nb Alloy	*	*	272	204

*No coating material.

Table 3-21. Temperature Distributions in Coating and Structural Materials with the Thickness of Coating Material Increased to 10 mm.

coating - structure	T_{CO}	T_{Ci}	T_{SO}	T_{Si}
Be - Cu	984	706	344	326
Be - V	1262	960	552	372

minor. The temperature gradient in both the coating (about 28°C/mm) and the structural material (about 12°C/mm for copper alloy and 120°C/mm for Vanadium alloy) are also doubled compared to the corresponding cases with 1 mm thick coating. The increased temperature gradient will adversely affect the thermal stresses in the structure. It is important to note that these results are considered conservative, because the leading edge will actually receive less heat energy than has been assumed. The heat flux will drop off rapidly with distance from the plasma such that only a small portion of the leading edge will receive the maximum flux of 2.3 MW/m^2. In addition, several design changes, such as placing the leading edge further from the plasma, will also reduce the heat flux. The influence of a non-uniform heat flux is presently being investigated.

The previous results are based on a given set of parameters, such as h, h_c, coolant ΔT, and beryllium density. Sensitivity calculations have been made to determine the influence of these parameters on the temperature of the leading edge. The combination of the coating and structural materials used for the sensitivity calculations are beryllium (1 mm) and AMAX-MZC (1.5 mm). The difference in temperature between the coating and structure interface is inversely proportional to h_c. For a value of h_c = 8500 W/m^2K, the temperature difference is 314°C, whereas for a value of h_c = 17,000 W/m^2K, the temperature difference is 157°C. This temperature difference should be minimized in order to reduce the differential thermal expansion between the coating and substrate, and thus a high value of h_c is desirable. Additional information of the effect of h_c on operating temperatures is given in Sec. 4.3. Similarly, the difference in temperature between the water and copper alloy interface is inversely proportional to h. For h = 23,000 W/m^2K, the temperature difference is 158°C, and for h = 34,000 W/m^2K the temperature difference is reduced to 111°C. The thermal gradients through the leading edge are relatively uneffected by the changes in these two parameters. Reducing the density of the beryllium coating will increase the temperature gradient. The temperature gradient for 100% dense Be is 12.7 K/mm, and the gradient for 70% dense Be is 21.1 K/mm. The influence on these temperature variations on the thermal stresses can be significant, and they will be examined in more detail.

Ongoing work includes evaluation of some other candidate coating materials (such as graphite) for the limiter and the effect of coating thickness (between 1 to 5 mm) on the temperature of the structure. Future effort will be directed towards studying the response of the cladding and structural materials under non-uniform heat flux and transient conditions.

3.7 Stress Analysis

The limiter is a critical component of the reactor and, consequently, a high degree of reliability is required. One aspect of assuring reliability is to show that the maximum stresses under normal operating conditions are below the allowable design stress for that temperature. In this section we compute, by means of prudent engineering assumptions and elementary calculations, the maximum stress and compare this stress with the allowable design stress. This provides a measure of the adequacy of the design and provides some guidance for more sophisticated numerical analysis.

Under steady-state conditions the maximum heat load (2.3 MW/m^2) occurs at the leading edge of the limiter. The approach adopted is to superimpose stresses due to three loading conditions. The first case is the membrane solution for internal pressure (1.4 MPa) which is low. Secondly, the stresses due to the radial thermal gradient are computed on the basis of a generalized plane strain analysis. Thirdly, the stresses due to the end constraints on the cylinder are computed on the basis of a thin shell theory. The purpose of this analysis is to compile the maximum stresses in the leading edge and then compare them with the stress allowables.

3.7.1 Requirements

The allowable design stresses and failure are basically the same for the limiter as for the first-wall/blanket components. Several design codes already exist which consider the allowable component stresses for various stress classifications, including primary stresses, secondary stresses due to sustained loads and temperature gradients, and peak stresses. The design code used for stress analysis of reactor components is ASME Code Case N-47 for Class 1 components in elevated temperature service, and it will be used here as a starting point for the stress analysis in the limiter. Code Case N-47 is intended to cover a wide variety of design configurations and service conditions, and the design criteria are therefore usually quite conservative. Since different stress classifications have different degrees of significance, the code assigns a different allowable stress for each classification. The allowable stresses are given in terms of the stress intensity, S_{mt}, which is calculated from the tensile and creep properties of the structural materials. At lower temperatures, the value of S_{mt} is either two-thirds of tensile yield or one-third of ultimate stress, and at high

temperatures, S_{mt} is the stress necessary to produce a given amount of thermal creep during the expected component lifetime. In the case of the reference limiter materials, S_{mt} is one-third of the ultimate stress for the normal operating temperatures. Code Case N-47 limits the primary mean stress (P_m), i.e., coolant stress, to a value of S_{mt}, and it limits the combined primary mean stress plus the primary local membrane stress ($P_L + P_B$) to a value of 1.5 S_{mt}. The combined primary local membrane plus bending plus secondary stress ($P_L + P_B + Q$) is limited to 3 S_{mt}.

Radiation effects are not considered in the present analysis. Since the STARFIRE/DEMO is basically a steady state machine, fatigue and interaction of creep-fatigue are assumed not to limit the life of the limiter. It is hoped that by comparing the elastically computed maximum stress intensities with the allowables, the present approach will identify the substrate-coating combinations that are likely to produce accpetable designs.

3.7.2 Stress Analysis Model

The basic configuration of the leading edge of the limiter is shown in Fig. 3-9. Since the outer wall forms a 180-degree segment, a reasonable model for determining the effects of pressure and temperature on wall stresses is to use the cylindrical model also shown in Fig. 3-8. The end of the cylinder, which correspond to the edges of a typical cooling channel, constrain the cylindrical wall from expanding axially as well as radially when the wall is subjected to a uniform axial and radial growth due to pressure, p, and temperature T. Although the radius to thickness ratio of the cylinder is about 4 which is not sufficiently large for thin shell theory to be strictly applicable, thin shell theory is used to obtain estimates of the bending stresses due to the mismatch in radial growth between the wall and the end plate. Future analysis should attempt to model the true geometry of the leading edge.

For the purpose of analysis, three structural materials, 1.5 mm thick, are considered. They are a copper alloy, a vanadium alloy and a titanium alloy. The analysis assumes that a 1 mm thick coating is initially deposited on the plasma side of the limiter. Three coating materials--beryllium, boron, and tungsten are considered. Because of its stiffness, the coating will significantly affect the stress in the substrate material if it is tightly bonded to the substrate. The stress analysis has therefore been conducted for

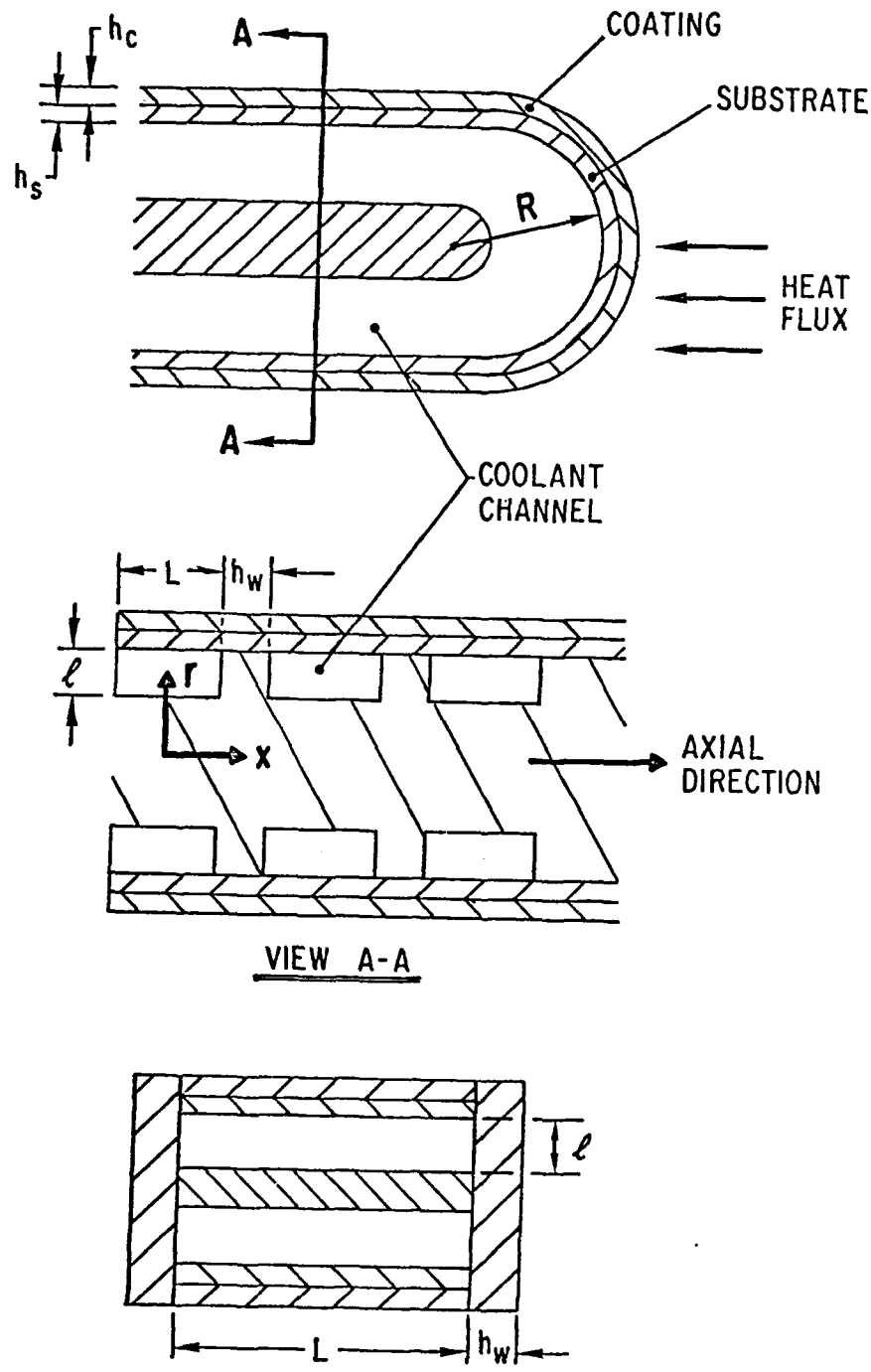

Figure 3-9. Leading Edge Geometry used for Stress Calculations.

two conditions. First, the coating is assumed to be uncracked and fully bonded to the substrate and second, the coating is assumed to be cracked so that it does not offer any constraint on the deformation of the substrate. Analyses with the coating thickness of 10 mm have been carried out to simulate the effects of redeposition. An important stress that has been neglected in the present analysis is the residual stress which is created because the coating will be deposited on the substrate at an elevated temperature. On subsequent cooling, residual stresses will develop because of the difference in the coefficient of thermal expansion between the coating and the substrate. Future studies should focus on the impact of the residual stress on the life of the limiter.

3.7.3 Results and Conclusions

The results are computed on the basis of the following geometrical constants:

$L = 8$ mm
$h_s = 1.5$ mm
$h_c = 1$ mm (or 10 mm)
$\ell = 4$ mm
$h_w = 2$ mm
$R = 8.5$ mm

The stresses have been computed using the equations given in the appendix at the end of the chapter. Table 3-22 summarizes the maximum stress intensities in the leading edge for various material combinations. Note that in all cases the primary membrane stress (P_m) due to pressure is small and is easily within the primary allowable stress S_{mt}. On the other hand, the elastically computed primary plus secondary thermal stresses ($P_L + P_B + Q$) are very large and strictly meet the 3 S_{mt} allowable criteria for both the substrate and coating for the cases of Cu-B, Cu-W, and V-W only. However, it may be argued that since the coating is not a structural material, it should not be designed on the basis of the conservative Code Case N-47 criteria which are meant for use in design of pressure boundary structural components. If the stress criteria for the coating is dropped, then the Cu-Be (with 1 mm Be thickness) is also acceptable. Note, however, that neither Cu nor V meets the allowable 3 S_{mt} stress criterion if the Be thickness increases to 10 mm because of redeposition.

A second set of calculations (Table 3-23) was run assuming that the coating is cracked and does not offer any resistance to the deformation of the substrate. A comparison of Tables 3-22 and 3-23 shows that the maximum stress intensities in the substrate are reduced by the added stiffness of the coating in some cases but not in others. In all cases, except the 10 mm thick Be case, both the primary and the primary plus secondary stresses are within the respective allowables. Such a design analysis should be acceptable provided it can be shown either by tests or by detailed analyses that a crack in the coating will not propagate into the substrate.

Table 3-22. Maximum Stresses in the Leading Edge of the Limiter

SUBSTRATE					COATING				
		Maximum Stress Intensity		Allowable Primary Stress			Maximum Stress Intensity		Allowable Primary Stress
Material	Thickness (mm)	P_m (MPa)	$P_L + P_B + Q$ (MPa)	S_{mt} (MPa)	Material	Thickness (mm)	Pm (MPa)	$P_L + P_B + Q$ (MPa)	S_{mt} (MPa)
Cu	1.5	3	372	150	Be	1	8	530	80
V	1.5	3	1107	200	Be	1	7	1393	71
Ti	1.5	3	1707	220	Be	1	8	2044	34
Cu	1.5	1	757	140	Be	10	1	3685	0[1]
V	1.5	1	2619	200	Be	10	1	5229	0[1]
Cu	1.5	2	166	150	B	1	9	606	528
V	1.5	2	740	200	B	1	8	1884	528
Cu	1.5	2	347	150	W	1	8	582	233
V	1.5	3	230	200	W	1	8	161	200

1 - Allowable stress obtained by extrapolating (linearly) data with temperataure.

Table 3-23.

Maximum Stresses in the Leading Edge of the Limiter
Assuming that the Coating is Cracked

SUBSTRATE					COATING	
		Maximum Stress Intensity		Allowable[a] Stress		
Material	Thickness (mm)	P_m (MPa)	$P_L + P_B + Q$ (MPa)	S_{mt} (MPa)	Material	Thickness (mm)
Cu	1.5	8	422	150	Be	1
V	1.5	8	413	200	Be	1
Ti	1.5	8	490	220	Be	1
Cu	1.5	8	862	140	Be	10
V	1.5	8	721	200	Be	10
Cu	1.5	8	371	150	B	1
V	1.5	8	413	200	B	1
Cu	1.5	8	371	150	W	1
V	1.5	8	413	200	W	1

[a]Total allowable stress $(P_L + P_B + Q) = 3S_{mt}$.

3.7.4 Electromagnetic Forces on the Limiter

An important consideration in the design of a limiter is its electromagnetic response to a plasma disruption. A disruption will induce eddy currents in the limiter, which will interact with the poloidal and toroidal magnetic fields to produce pressure, forces, and torques on the limiter. These effects are described here, using analytical models developed in the STARFIRE[1] study.

Four different limiters were studied, all with the same geometry, but with four different material specifications:

(1) Stainless steel limiter (electrical resistivity $\rho = 76\ \mu\ \Omega$ cm), with a 1 mm thick coating of Be (80% dense, equivalent $\rho = 55\ \mu\ \Omega$ cm).

(2) Stainless steel limiter with a 10 mm thick Be coating.

(3) Copper limiter ($\rho = 1.72\ \mu\ \Omega$ cm) with a 1 mm thick Be coating.

(4) Copper limiter with a 10 mm thick Be coating.

3.7.4.1 Pressure on Be Coating

One of the electromagnetic effects is a pressure acting on the Be coating, tending to pull it off the limiter. The pressure arises from the interaction of the induced currents and the poloidal field. For a plasma current of $I_p = 9.01$MA, and a minor radius of $a = 1.3$ m, the magnetic field at the limiter from the plasma is $B_p = 1.38$T. For the case of an instantaneous disruption, that field would disappear instantaneously outside the limiter, and currents would be induced in the Be coating to maintain the field inside the limiter. The pressure would be

$$p = B^2/2\ \mu_0 = 0.76\ \text{MPa} = 105\ \text{psi}. \qquad (3\text{-}6)$$

This is a modest force that would not be expected to detach the coating. For realistic disruption times, the pressure actually would be much reduced from the value. During a finite plasma disruption time, where τ_0 is long compared to the L/R time, τ, of the limiter coating, the pressure is reduced by a

factor τ/τ_0. For the 1 mm Be coating, the L/R time τ = 0.018 ms, τ_0 = 20 ms, and p = 0.09 psi. For the 1.0 cm coating, τ = 0.29 ms and p = 1.5 psi.

In this analysis, it does not matter whether the underlying material of the limiter is copper or stainless steel.

3.7.4.2 Torque about the Limiter Support Axis

The radial component of current in the limiter arms and support interact with the toroidal field to produce vertical forces. There is no net force, but those forces do produce a net torque about the support axis.

As in reference (1), we treat the two arms and support of the limiter as three rectangular loops, sharing a common side and neglect the (low) resistance of that common side. Each loop then has three sides, each with resistance

$$R = (\ell^2/2A)/[\omega_{base}/\rho_{base} + 2\ \omega_{Be}/\rho_{Be}] \qquad (3\text{-}7)$$

where ℓ is the length of the side, A the area of the triangle defined by the side and center of the loop[37], ω_{base} and ρ_{base} the thickness and resistivity of the (copper or stainless steel) base, and ω_{Be} and ρ_{Be} the thickness and resistivity of the Be coating. Table 3-24 gives the resulting resistances, $R_1 = R_3$ of the arms and R_2 of the support.

Table 3-24. Equivalent Resistances of the Limiter Arm and Support

Base and Coating	Arms: R_1R_3 ($\mu\ \Omega$)	Support: R_2 ($\mu\ \Omega$)
SS base, 1 mm Be Coating	388	67.1
SS base, 10 mm Be Coating	124	50.3
Cu base, 1 mm Be Coating	11.4	1.58
Cu base, 10 mm Be Coating	10.7	1.56

The inductance values and Eqn. 77 of reference (1) yield:

$$\tau^2 R_1 R_2 - \tau(1.119\ R_2 + 0.668\ R_1) + 0.6659 = 0 \qquad (3\text{-}8)$$

The torque analysis has been carried out for the two cases with 10 mm thick Be coatings, which have the larger torques.

Stainless Steel Base, 10 mm Coating

Equation (2) yields the two values τ_{Long} = 15.3 ms, τ_{Short} = 6.94 ms. The currents I_1 and I_2, for an instantaneous plasma disruption, then become

$$I_1 = 40.17\ \text{kA}\ \exp(-t/15.3\ \text{ms}) - 33.58\ \text{kA}\ \exp(-t/6.94\ \text{ms})$$

$$I_2 = 160.04\ \text{kA}\ \exp(-t/15.3\ \text{ms}) + 42.56\ \text{kA}\ \exp(-t/6.94\ \text{ms}) \qquad (3\text{-}9)$$

The torque tending to twist the limiter is given by the product of the current, the radial current path, the toroidal field, and the length of the limiter:

$$N = (2\ I_1 + 0.07\ \text{m} + I_2 \times 0.20\ \text{m})\ 3.85\text{T} \times 0.5\ \text{m} \qquad (3\text{-}10)$$
$$= (0.2695\ I_1 + 0.3850\ I_2)\ \text{kNm}.$$

With the substitution of Eqn. 3-9 into Eqn. 3-10, the expression for torque from an instantaneous disruption becomes

$$N = 72.44\ \text{kNm}\ \exp(-t/15.3\ \text{ms}) + 7.34\ \text{Knm}\ \exp(-t/6.94\ \text{ms}) \qquad (3\text{-}11)$$

and the peak torque is 79.78 kNm.

If we ignore the second term of Eqn. 3-11, we can use Eqns. 80 and 81 of reference (1) to find the peak torque with a finite plasma disruption time τ_0. For τ_0 = 20 ms, the peak torque occurs at time 17.44 ms, and has a value of 23.16 kNm.

Copper Base, 10 mm Coating

The times resulting from Eqn.3-8, τ_{Long} = 433 ms and τ_{short} = 90.0 ms, are both much longer than the plasma disruption time of 20 ms, so that the

analysis for an instantaneous disruption is adequate. The currents in the arm and in the support are given by

$$I_1 = 11.34 \text{ kA} \exp(-t/443 \text{ ms}) - 4.75 \text{ kA} \exp(-t/90 \text{ ms})$$

$$I_2 = 198.96 \text{ kA} \exp(-t/443 \text{ ms}) + 3.64 \text{ kA} \exp(-t/90 \text{ ms}) \quad (3\text{-}12)$$

Again ignoring the terms involving τ_{short}, we find that the torque is given by

$$N = 79.66 \text{ kNm} \exp(-t/443 \text{ ms}),$$

which taken on its maximum value 79.66 kNm at time zero. This value is very near the 79.78 kNm found for an instantaneous disruption with a stainless steel base for the limiter.

This calculation of torque and the calculation of force which follows assume a limiter length of 0.5 m. For a longer limiter, the torque and force would increase more than linearly with limiter length. A toroidally continuous limiter would have much larger forces, but no torque, because of its toroidally circulating induced current.

3.7.4.3 Equivalent Bending Force at Tip of Arm

The current flowing along the tips of the limiter arm interacts with the poloidal field to exert a radial force which tends to bend the limiter arm. The face per unit length of limiter arm can be expressed as a function of time t, for a specified plasma disruption time τ_0 and L/R time τ:

$$\frac{F}{\ell} = \frac{I_0 B_0}{2(1 - \tau/\tau)^2} [\exp(-2t/\tau) - (1 - 2\,\tau_0/\tau) \exp(-2\,t/\tau_0) - (2\,\tau_0/\tau) \exp\{-t(1/\tau + 1/\tau_0)\}] \quad (3\text{-}13)$$

where I_0 is the initial value of current and B_0 is the initial value of poloidal field, 1.38T. Eqn. 3-13 is a corrected version of Eqn. 83 of reference (1). It must be applied separately to the currents for τ_{Long} and τ_{Short}.

Stainless Steel Base, 10 mm Coating

The currents in the arm, I_1 for τ_{Long} = 15.3 ms and τ_{Short} = 6.94 ms, are given in Eq 3-9 with I_0 = 40.17 kA and -33.5 kA respectively. Equation 3-13 yields:

$$F/\ell = 293.72\ \text{kNm}^{-1}\ [\exp(-t/7.65\ \text{ms}) + 1.614 \exp(-t/10\ \text{ms})$$

$$-2.614 \exp(-t/8.669\ \text{ms})]$$

$$-6.54\ \text{kNm}^{-1}\ [\exp(-t/3.47\ \text{ms}) + 4.764 \exp(-t/10\ \text{ms})$$

$$-5.764 \exp(-t/5.152\ \text{ms})]$$

At time 15 ms, F/ℓ takes on its peak value of 6.06 kN/m; so that the peak force on the 0.5 m long limiter tip is 3.03 kN or 680 lb.

Copper Base, 1.0 cm Coating

Substituting from Eqn. 3-12 yields

$$F/\ell = 8.58\ \text{kNm}^{-1}\ [\exp(-t/222\ \text{ms}) - 0.9097 \exp(-t/10\ \text{ms})$$

$$-0.0903 \exp(-t/19.14\ \text{ms})]$$

$$-5.42\ \text{kNm}^{-1}\ [\exp(-t/45\ \text{ms}) - 0.5556 \exp(-t/10\ \text{ms})$$

$$-0.4444 \exp(-t/16.36\ \text{ms})]$$

The peak force on the tip of the limiter is 2.56 kN = 576 lb, and occurs at 65 ms.

3.8 Summary and Conclusions

The work performed to date has led to the following conclusions concerning pumped limiters.

1) The outer midplane is the first choice for the limiter location since disruptions are least likely to strike this area. If the midplane location must be used for other purposes, then the bottom location will be considered.

2) The plasma edge temperature can be controlled by varying the limiter pumping efficiency and the method of fueling. A high pumping efficiency coupled with pellet injection produces a high edge temperature, whereas a low pumping efficiency coupled with gas puffing results in a low edge temperature.

3) The choice of material facing the plasma depends upon its sputtering characteristics, which in turn depends upon the plasma edge conditions. At high edge temperatures, beryllium is recommended, at medium edge temperatures, tungsten is recommended, and at low edge temperatures, copper can be used. At high and medium edge temperatures, the surface materials will need to be bonded to the first wall and limiter structural materials.

4) A copper alloy (e.g., AMAX-MZC) is recommended as the limiter structural material. Copper alloys are capable of operating with high heat loads, are commercially available, are easily fabricated, and are compatible with water coolant. The major uncertainty is the response of copper alloys to high neutron fluences. Experiments should be initiated to examine the long term effects of neutron irradiation.

5) The presence of a relatively thick coating on the limiter will have a significant impact on its operating characteristics. The primary effect is the potentially

high thermal stresses that result from the differential thermal expansion between the coating and structural material. The structural materials, AMAX-MZC and V-15Cr-5Ti meet ASME allowable stresses with 1 mm coatings of Be, B, and W. A 10 mm coating appears to be unacceptable at the leading edge due to the resultant high temperatures and stresses. There are, however, major uncertanties in quantifying the influence of the coating due to uncertainties in the bonding characteristics and physical properties of the coating materials.

6) Copper exhibits a lower tritium inventory and migration rate than vanadium. Migration rates for single materials are unacceptably high if ion insertion is considered as the controlling mechanism. If standard permeation is controlling, then migration rates to the coolant will be low.

7) The viability of the pumped limiter concept depends upon the sputtering and redistribution of the surface material. At present, it is believed that sputtered first wall material will be redeposited on the limiter. The redeposited material is not likely to have the same properties and structure as the original material.

8) Major uncertainties exist in the understanding of plasma wall interactions, and work in this area will continue. In particular, the effects of the tungsten limiter on the plasma will be examined in more detail.

9) Little information exists on the plasma operating characteristics at low (about 10 eV) edge temperatures. There is an incentive to examine this plasma regime, since it would result in considerable simplification of the first wall and limiter designs.

References for Chapter 3

1. C. C. Baker, et al, "STARFIRE - A Commercial Tokamak Fusion Power Plant Study," Argonne National Laboratory, ANL/FPP-80-81 (1980).

2. W. M. Stacey, et al, "U.S. INTOR - The U.S. Contribution to the International Tokamak Reactor Phase-1 Workshop," INTOR/81-1 (1981).

3. FED Design Study - To be published.

4. J. N. Brooks and R. T. McGrath, "Redeposition of the Sputtered Surface in Limiters," presented at the 9th Symposim on Engineering Problems in Fusion Research," Chicago, October 26-29 (1981).

5. D. L. Smith, J. N. Brooks, and D. E. Post, "A Physical Sputtering Code for Fusion Applications," presented at the 9th Symposium on Engineering Problems in Fusion Research, Chicago, October 26-29 (1981).

6. C. D. Boley and J. N. Brooks, "Study of Plasma Edge Conditions for a Commercial Tokamak Reactor," presented at the 9th Symposium on Engineering Problems in Fusion Research, Chicago, October 26-29 (1981).

7. Yong-Ki Kim, Argonne National Laboratoary, personal communication.

8. P. W. Taubenblat, W. R. Opie, and Y. T. Hsu, Metals Engineering Quarterly, 12, 41 (1972).

9. Y. S. Touloukian, ed., Thermophysical Properties of High Temperature Solid Materials, The MacMillan Company, New York (1967).

10. L. I. Pionke and J. W. Davis, "Technical Assessment of Niobium Alloys Data Base for Fusion Reactor Applications," McDonnel Douglas Astronautics Company, COO-4242-2 (1979).

11. F. L. Yaggee, E. R. Gilbert, and J. W. Stiles, Journal of the Less Common Metals, 19, 39 (1969).

12. Metals Handbook, 9th ed., Vol. 2, (American Society for Metals, Metals Park, Ohio) (1979).

13. D. L. Smith, et al., "Fusion Reactor Blanket/Shield Design Study," Argonne National Laboratory, ANL/FPP-79-1 (1979).

14. R. E. Gold, et al., "Technical Assessment of Vanadium Base Alloys for Fusion Reactor Applications," Vol. 2, Westinghouse Electric Corp., COO-4540-1 (1978).

15. R. F. Mattas, et al., "Elevated-Temperature Tensile Properties of V-15Cr-5Ti Containing Helium Introduced by Ion Bombardment and Tritium Decay," Proc. 2nd Topical Meeting on the Technology of Controlled Nuclear Fusion, Vol. 1, CONF-760935-P1, 199 (1976).

16. M. Gomolinski and G. Bubee, J. Nucl. Mater., 43, 59 (1972).

17. D. E. Mazey and F. Menzinger, J. Nucl. Mater., 48, 15 (1973).

18. R. Carlander, S. D. Harkness and A. T. Samthanam, "Effects of Fast-Neutron Irradiation on Tensile Properties and Selling Behavior of Vanadium Alloys," Effects of Radiation on Substructure and Mechanical Properties of Metals and Alloys, ASTM-STP 529, 399 (1973).

19. J. A. Sprague, F. A. Schmidt, and J. R. Reed, J. Nucl. Mater. 85 & 86, 739 (1979).

20. B. A. Loomis, Argonne National Laboratory, personal communication.

21. H. Jang and J. Moteff, Radiation Effects and Tritium Technology for Fusion Reactors, CONF-750989, I-106 (1976).

22. R. A. Erck, D. I. Potter and H. Wiedersich, J. Nucl. Mater., 80, 120 (1979).

23. R. H. Jones and L. A. Charlot, J. Nucl. Mater., 91, 329 (1980).

24. D. T. Peterson, "Initial Observation of Voids in Neutron Irradiated Titanium Alloys," Alloy Development for Irradiation Performance, Quarterly Progress Report for Period Ending Dec. 31, 1980, DOE/ER-0045/5, 103 (1980).

25. Japanese INTOR Studies, Phase I (1981).

26. F. W. Wiffen, "The Tensile Properties of Fast Reactor Neutron Irradiated BCC Metals and Alloys," Nucl. Metallurgy 18, 176 (1973).

27. D. R. Duncan, R. J. Puigh and E. K. Opperman, "Titanium Alloy Tensile Properties After Neutron Irradiation," Alloy Development for Irradiation Performance - Quarterly Progress Report for Period Ending Dec. 31, 1980. DOE/ER-0045/5, 77 (1980).

28. G. W. Wille and J. W. Davis, "Hydrogen in Titanium Alloys," McDonnell Douglas Astronautics Co., DOE/ET/52039-2 (1981).

29. U.S. INTOR Conceptual Design, Phase I, USA-INTOR/81-1 (1981).

30. K. L. Wilson and A. E. Pontau, J. Nucl. Mater., 85 & 86, 989 (1979).

31. A. E. Pontau, et al., J. Nucl. Mater., 85 & 86, 1013 (1979).

32. W. R. Wampler, et al., "Retention, Isotopic Exchange and Thermal Release of Hydrogen in Candidate Materials for TFTR," Sandia National Laboratories, SAND-80-1184 (1981).

33. A. E. Pontau, W. Bauer, and R. W. Conn, J. Nucl. Mater., 93 & 94, 564 (1980).

34. W. Jager and J. Roth, J. Nucl. Mater., 93 & 94, 756 (1980).

35. P. B. Johnson and D. J. Mazey, J. Nucl. Mater., 93 & 94, 721 (1980).

36. G. L. Stephens and D. J. Campbell, "Program THTB, For Analysis of General Transient Heat Transfer Systems," General Electric #R60FPD647, April 1961.

37. L. Turner, IEEE Trans. Mag., Vol MAG-13, 119 (1978).

CHAPTER 3

APPENDIX

CHAPTER 3 APPENDIX

Stress-Strain Equations for the Limiter Leading Edge

Internal Pressures

Denoting the properties and dimensions of the substrate and coating (see Figure 3-9) by subscripts s and c respectively, the hoop and axial stresses due to internal pressure are given by

$$\sigma_{s_{hoop}} = \frac{pR}{h_s} \frac{1 - \nu_s\nu_s + (1 - \nu_c^2)\, E_s h_s/E_c h_c}{2(1 - \nu_s\nu_c) + (1 - \nu_c^2)\, E_s h_s/E_c h_c + (1 - \nu_s^2)\, E_c h_c/E_s h_s}$$

$$\sigma_{s_{Axial}} = \frac{pR}{h_s} \frac{\nu_s - \nu_c}{2(1 - \nu_s\nu_c) + (1 - \nu_c^2)\, E_s h_s/E_c h_c + (1 - \nu_s^2)\, E_c h_c/E_s h_s} \qquad (3A\text{-}1)$$

$$\sigma_{c_{hoop}} = \frac{pR}{h_c} \frac{1 - \nu_s\nu_c + (1 - \nu_s^2)\, E_c h_c/E_s h_c}{2(1 - \nu_s\nu_c) + (1 - \nu_c^2)\, E_s h_s/E_c h_c + (1 - \nu_s^2)\, E_c h_c/E_s h_s}$$

$$\sigma_{c_{Axial}} = -\frac{pR}{h_c} \frac{\nu_s - \nu_c}{2(1 - \nu_s\nu_c) + (1 - \nu_c^2)\, E_s h_s/E_c h_c + (1 - \nu_s^2)\, E_c h_c/E_s h_s}$$

In above E and ν denote the elastic modulus and Poissons ratio, respectively.

The average radial growth, $\bar{w}$ and axial growth $\bar{u}$ are given by

$$\bar{w} = pR^2 \frac{(1 - \nu_s^2)/E_s h_s + (1 - \nu_c^2)/E_c h_c}{2(1 - \nu_s\nu_c) + (1 - \nu_c^2)\, E_s h_s/E_c h_c + (1 - \nu_s^2)\, E_c h_c/E_s h_s} \qquad (3A\text{-}2)$$

$$\bar{u} = -pRL \frac{\nu_c(1 - \nu_s^2)/E_s h_s + \nu_s(1 - \nu_c^2)/E_c h_c}{2(1 - \nu_s\nu_c) + (1 - \nu_c^2)\, E_s h_s/E_c h_c + (1 - \nu_s^2)\, E_c h_c/E_s h_s}$$

Temperature Gradient Through the Wall

The average hoop and axial strain are given by

$$\bar{\varepsilon}_{hoop} = \bar{\varepsilon}_{Axial} = \frac{E_s\alpha_s/(1-\nu_s) \int T_s dh_s + E_c\alpha_c/(1-\nu_c) \int T_c dh_c}{E_s h_s/(1-\nu_s) + E_c h_c/(1-\nu_c)} \qquad (3A\text{-}3)$$

The hoop and axial stresses are given by

$$\sigma_{s_{hoop}} = \sigma_{s_{Axial}} = \frac{E_s}{1-\nu_s}[\bar{\varepsilon}_{hoop} - \alpha_s T_s]$$

$$\sigma_{c_{hoop}} = \sigma_{c_{Axial}} = \frac{E_c}{1-\nu_c}[\bar{\varepsilon}_{Axial} - \alpha_c T_c] \qquad (3A\text{-}4)$$

Shell Analysis

For the purpose of this analysis, the two-layered shell is replaced by an equivalent single layer shell of bending stiffness, D_{eff}, and membrane stiffness, K_{eff}, and poissons ratio, υ_{eff}

$$D_{eff} = \frac{1}{4}\frac{[E_s h_s^2/(1-\nu_s^2) + E_c h_c^2/(1-\nu_c^2)]^2 + 2E_s h_s h_c (h_s^2+h_c^2)/[(1-\nu_s^2)(1-\nu_c^2)]}{E_s h_s/(1-\nu_s^2) + E_c h_c/(1-\nu_c^2)}$$

$$- \frac{E_s h_s^3}{6(1-\nu_s^2)} - \frac{E_c h_c^3}{6(1-\nu_c^2)} \qquad (3A\text{-}5)$$

$$K_{eff} = \frac{E_s h_s}{1-\nu_s} + \frac{E_c h_c}{1-\nu_c}$$

$$\upsilon_{eff} = \frac{\nu_s E_s h_s/(1-\nu_s^2) + \nu_c E_c h_c/(1-\nu_c^2)}{E_s h_s/(1-\nu_s^2) + E_c h_c/(1-\nu_c^2)}$$

For a unit displacement (w = 1) at the edge (with axial stress resultant $N_x = 0$), the membrane stress resultant (N_ϕ), bending moments (M_x, M_ϕ) and radial displacements are given by [1]

$$M_x = 2\mu^2 D_{eff} [G(\delta)\text{Sin } \mu x \text{ Sinh } \mu x + F(\delta)\text{Cosh } \mu x \text{ Cos } \mu x]$$

$$M_\phi = \nu M_x, \; N_\phi = \frac{K_{eff}}{R}(1 - \nu_{eff}^2) W, \; N_x = 0 \qquad (3A\text{-}6)$$

$$W = G(\delta) \text{ Cosh } \mu x \text{ Cos } \mu x + F(\delta) \text{ Sinh } \mu x \text{ Sin } \mu x$$

where

$$\mu^2 = [(1 - \nu_{eff}^2)K_{eff}/(4 D_{eff} R^2)]^{1/2} \text{ and } \delta = \frac{\mu L}{2}$$

$$F(\delta) = (\text{Cos } \delta \text{ Sinh } \delta - \sin \delta \text{ Cosh } \delta)/H(\delta)$$

$$G(\delta) = (\text{Sin } \delta \text{ Cosh } \delta + \text{Cos } \delta \text{ Sinh } \delta)/H(\delta) \qquad (3A\text{-}7)$$

$$H(\delta) = \text{Sinh } \delta \text{ Cosh } \delta + \text{Sin } \delta \text{ Cos } \delta$$

The membrane stresses corresponding to the stress resultants are

$$\sigma_{c_{Axial}}^{(m)} = \frac{E_c(\nu_c - \nu_{eff})}{(1 - \nu_c^2)(1 - \nu_{eff}^2)} \frac{N_\phi}{K_{eff}}$$

$$\sigma_{s_{Axial}}^{(m)} = \frac{E_s(\nu_s - \nu_{eff})}{(1 - \nu_s^2)(1 - \nu_{eff}^2)} \frac{N_\phi}{K_{eff}} \qquad (3A\text{-}8)$$

$$\sigma_{c_{hoop}}^{(m)} = \frac{E_c(1 - \nu_c \nu_{eff})}{(1 - \nu_c^2)(1 - \nu_{eff}^2)} \frac{N_\phi}{K_{eff}}$$

(3A-9)

$$\sigma^{(m)}_{s_{hoop}} = \frac{E_s(1 - \nu_s \nu_{eff})}{(1 - \nu_s^2)(1 - \nu_{eff}^2)} \quad \frac{N_\phi}{K_{eff}}$$

The bending stresses corresponding to the bending moments are

$$\sigma^{(b)}_{c_{Axial}} = \frac{E_c}{1 - \nu_c^2} \quad \frac{M_x}{D_{eff}} \quad y$$

$$\sigma^{(b)}_{s_{Axial}} = \frac{E_s}{1 - \nu_s^2} \quad \frac{M_x}{D_{eff}} \quad y \qquad \text{(3A-10)}$$

$$\sigma^{(b)}_{c_{hoop}} = \nu_c \, \sigma^{(b)}_{c_{Axial}} \quad \text{and} \quad \sigma^{(b)}_{s_{hoop}} = \nu_s \sigma^{(b)}_{s_{Axial}}$$

The distances (y) from the neutral surfaces to the inner surface of substrate, interface between substrate and coating and outer surface of coating are respectively

$$-\frac{1}{2} \quad \frac{E_c h_c (h_c + 2h_s)/(1 - \nu_c^2) + E_s h_s^2/(1 - \nu_s^2)}{E_c h_c/(1 - \nu_c^2) + E_s h_s/(1 - \nu_s^2)}$$

and (3A-11)

$$-\frac{1}{2} \quad \frac{E_c h_c^2/(1 - \nu_c^2) - E_s h_s^2/(1 - \nu_s^2)}{E_c h_c/(1 - \nu_c^2) + E_s h_s/(1 - \nu_s^2)}$$

and

$$\frac{1}{2} \quad \frac{E_s h_s (h_s + 2h_c)/(1 - \nu_s^2) + E_c h_c^2/(1 - \nu_c^2)}{E_c h_c/(1 - \nu_c^2) + E_s h_s/(1 - \nu_s^2)}$$

The total axial displacement from end to end due to the unit radial displacement at the edges is given by

$$2 \int_0^{L/2} \varepsilon_x^{(m)} \, dx = - \frac{\nu_{eff} \, L}{R} \left[H/2(F^2 + G^2) \right] \qquad (3A\text{-}12)$$

where F, G, and H have been defined before. The axial strain mismatach (ε) between the central cool restraining region and the hot leading edge causes an axial stress in the leading edge walls and a shear deformation in the constraining end plates. These axial stresses are given by

$$\sigma_{s_{Axial}} = \frac{E_s \varepsilon}{1 + 2 (1 + \nu_s) \, \ell/L \, (h_s/h_w + E_c h_c / E_s h_c)} \qquad (3A\text{-}13)$$

and

$$\sigma_{c_{Axial}} = \sigma_{s_{Axial}} \times \frac{E_c}{E_s}$$

CHAPTER 4

FIRST WALL AND BLANKET

Chapter 4

Table of Contents

Table of Contents (continued)

Table of Contents (continued)

Chapter 4

List of Figures

List of Figures (continued)

List of Figures (continued)

List of Figures (continued)

Chapter 4

List of Tables

List of Tables (continued)

List of Tables (continued)

Chapter 4

List of Tables

4.1 Introduction and Strategy

The primary functions of the first-wall/blanket system of a tokamak demonstration reactor are to provide the first physical barrier for the plasma chamber, to convert the fusion energy into sensible heat and provide for adequate heat removal, to breed tritium and provide for tritium recovery, and to provide some of the shielding for the magnet system. The first wall must withstand energetic particle fluxes and heat fluxes from the plasma, high thermal and mechanical stresses, and elevated temperature operation. Also, the first wall must not be a source of excessive plasma contamination. The first wall of a power reactor is generally perceived to be an integral part of the blanket. The blanket must withstand high neutron fluences, elevated temperature operation, and thermal and mechanical stresses. The blanket materials must be compatible with each other and with the plasma.

Initial phases of the present first-wall design study have focused on critical issues related to plasma-wall interactions that impact materials selection and/or concept feasibility. These issues include (1) sputtering erosion of the first wall, (2) the impact of plasma disruptions on the erosion and integrity of the wall, (3) the impact of energetic tritium injected into the first wall surface on the permeation through the wall and the hydrogen (DT) inventory in the wall, and (4) the nuclear response. Important aspects of first wall design such as structural material selection, neutron radiation damage effects, mechanical properties, and operating temperature limits have been addressed extensively in previous studies such as STARFIRE,[1] INTOR,[2] UWMAK,[3-5] and Blanket Design Study[6]. Therefore, only general conclusions of these studies are summarized here. More quantitative lifetime analyses of the structure will be presented in the final design report.

Development of a viable blanket system is essential before the feasibility of fusion as a commercial energy source can be established. The importance of near-term blanket development is due partially to the recognition that breeding of tritium in the next-generation reactors may be necessary to supply tritium needed for projected operating scenarios. Near-term blanket development is also vital because of the impact on materials research and development requirements, and the need for testing in near term devices such as FED, which will require detailed definition of concepts. The blanket problems are quite complex because several components, such as the breeder, coolant, and structure must operate for extended lifetimes at

elevated temperature while exposed to severe radiation and chemical environments. Solutions to critical problems may be obtained by a combination of design options and by appropriate materials selection.

The present blanket design study is focused on selection of the tritium breeder material. Four types of breeder materials, two solid breeder concepts and two liquid metal breeder concepts listed in Table 4-1, are generally believed to offer the most potential. Within the scope of the present effort is is not possible to analyze all four concepts in depth. Therefore, the strategy for the present study is to focus on only two concepts, viz., the Li_2O breeder and the liquid Li-Pb breeder concepts. The recent STARFIRE design study[1] provides an in-depth analysis of the ternary ceramic ($LiAlO_2$) design. Most of the conclusions regarding the critical materials and design issues associated with the STARFIRE blanket concept are still considered valid. Therefore, a greater contribution can be made by defining the critical design and operating criteria for a Li_2O blanket. One can then compare the performance characteristics, design implications, and operating limits for the two types of solid breeder concepts.

Table 4-1. Candidate Blanket Concepts

SOLID BREEDER CONCEPTS
- Li_2O Breeder
- Ternary Ceramic ($LiAlO_2$) Breeder
LIQUID-METAL BREEDER CONCEPTS
- Li-Pb Alloy Breeder
- Li Breeder/Coolant

Two types of liquid metal breeder concepts must also be considered. Although no recent in-depth design study of a liquid lithium blanket concept has been made, earlier studies such as the UWMAK-I,[3] UWMAK-III,[5] ORNL/WEC Blanket,[7] and the ANL Blanket/Shield Study[6] provide a general basis for comparison. Therefore, the present study on liquid-metal concepts is focused on the lead-rich Li-Pb eutectic (17 at % Li- 83 at % Pb,

subsequently referred to as 17Li-83Pb) as the tritium breeder. The performance characteristics, design implications, and operating limits for this concept can then be compared with those of a liquid lithium system.

Critical issues related to the first wall-plasma interactions are presented in Sec. 4.2. Section 4.3 presents results of the Li_2O breeder blanket study and Sec. 4.4 contains results of the Li-Pb breeder blanket study. The two blanket sections present analyses related to materials selection, stress analyses, neutronics analyses, properties of the breeder, tritium recovery, thermal-hydraulic analyses, and materials compatibility considerations. Critical design issues are summarized and proposed blanket design configurations are presented for the two breeder concepts.

4.2 First Wall/Plasma Interactions

Studies related to the response of the first wall have been focused on two general areas. Those aspects such as sputtering erosion, response to plasma disruptions, tritium permeation, and nuclear response, which are generally insensitive to the blanket concept considered, are presented in this section. Bulk property effects and design related issues, which interface more closely with the blanket materials selection and configuration are presented in Section 4.3.3 and 4.4.3 for the Li_2O and Li-Pb blanket concepts, respectively. Those aspects of the first wall that impact impurity control in the plasma are included in Section 3.

A major consideration in the selection of the material for the first surface of the first wall relates to the predicted redistribution of this material as a result of sputtering during operation and potential vaporization during a plasma disruption. The redistribution of the first-wall material within the plasma chamber indicates that it is highly desirable, if not imperative, that:

- the surfaces of all components within the plasma chamber be of the same material
- this material be a single element.

Material eroded from the wall either by sputtering or vaporization during a disruption is expected to redeposit in other regions of the chamber, e.g. the limiter. If the material is originally a compound or alloy, uniform redeposition of different elements cannot be guaranteed. The composition of the first surface would thus be changed.

A second major consideration relates to conditions that lead to self sputtering yields in excess of unity. Wall material sputtered by energetic plasma particles eventually deposit somewhere. If the self sputtering yields are greater than unity, the increasing source term could lead to a propagating type effect, and hence, excessive erosion. (See Section 3.2.)

A third important consideration relates to chemical reactivity of the wall material with the hydrogenous plasma. This is a major concern with materials such as graphite and titanium.

Table 4-2 summarizes the materials considered for the first wall surface. These include the three candidate structural materials: austenitic stainless steel, ferritic steel and a vanadium-base alloy in addition to high- and low-z coatings/claddings that can be used on one or more of the structural alloys.

Table 4-2. Candidate Materials for First-Wall Surface

Structural Alloys
Austenitic Stainless Steel (PCA)
Ferritic Steel (HT-9)
Vanadium-Base Alloy (V-15 Cr-5Ti)
Coating/Cladding
Beryllium
Vanadium
Tungsten

4.2.1 Sputtering Erosion

Physical sputtering by the energetic charge-exchange neutrals (D,T) is predicted to be the primary erosion process for the first wall (see also Sec. 3.2). The erosion rates for the first wall are based on two operating scenarios: (1) a high edge energy of 1500 eV that produces a charge-exchange energy of 3000 eV, and (2) a low edge energy of 100 eV that produces a charge-exchange energy of 200 eV. Experimental data on the energy-dependent physical sputtering yields of most wall materials of interest have been reported for

normally incident deuterium and helium as well as for some higher mass particles, e.g., Ne, Ar, and Xe. Since data for sputtering by tritium have not been reported, analytical models must be used to predict erosion rates caused by tritium. The major contribution to the erosion comes from tritium since tritium has a higher mass than deuterium. Data for the angular dependence of physical sputtering are very limited. Available information indicates some type of cosine distribution with little effect at angles less than 45° from the normal. Higher angles up to about 85° give substantially higher yields. Table 4-3 summarizes the predicted erosion rates for candidate wall materials based on an average charge-exchange flux (50% D, 50% T) to the wall of 10^{23} s^{-1} and a duty factor of 50%. Calculated erosion rates are based on the DSPUT code[8] which generally gives good agreement with available experimental data. Figure 4-1 shows the calculated energy-dependent physical sputtering yields for deuterium incident on several candidate wall materials. Figure 4-2 shows a comparison of experimental data[9] with the calculated angular dependence of the physical sputtering yield for deuterium incident on nickel. For the case of beryllium the sputtering yields from the code are higher than the published experimental data. It is believed that the experimental data are affected by oxygen contamination and are more indicative of BeO sputtering. The erosion rate of tungsten at 200 eV is very sensitive to minor changes in energy since this value is near the threshold energy for sputtering. For example, an increase of only 50 eV to an energy of 250 eV would increase the predicted erosion rate by a factor of 8.

Table 4-3. Predicted Physical Sputtering Erosion Rates for Candidate First Wall Materials

Wall Material	Erosion Rate[a], mm/y	
	200 eV[b]	3000 eV[b]
Be	2.1	0.50
V	1.1	2.0
SS,FS	1.0	2.2
W	0.004	0.68

[a] charge exchange flux: 2.5×10^{16} cm^{-2} s^{-1}, 50% duty factor
[b] average charge exchange energy (50%D, 50%T)

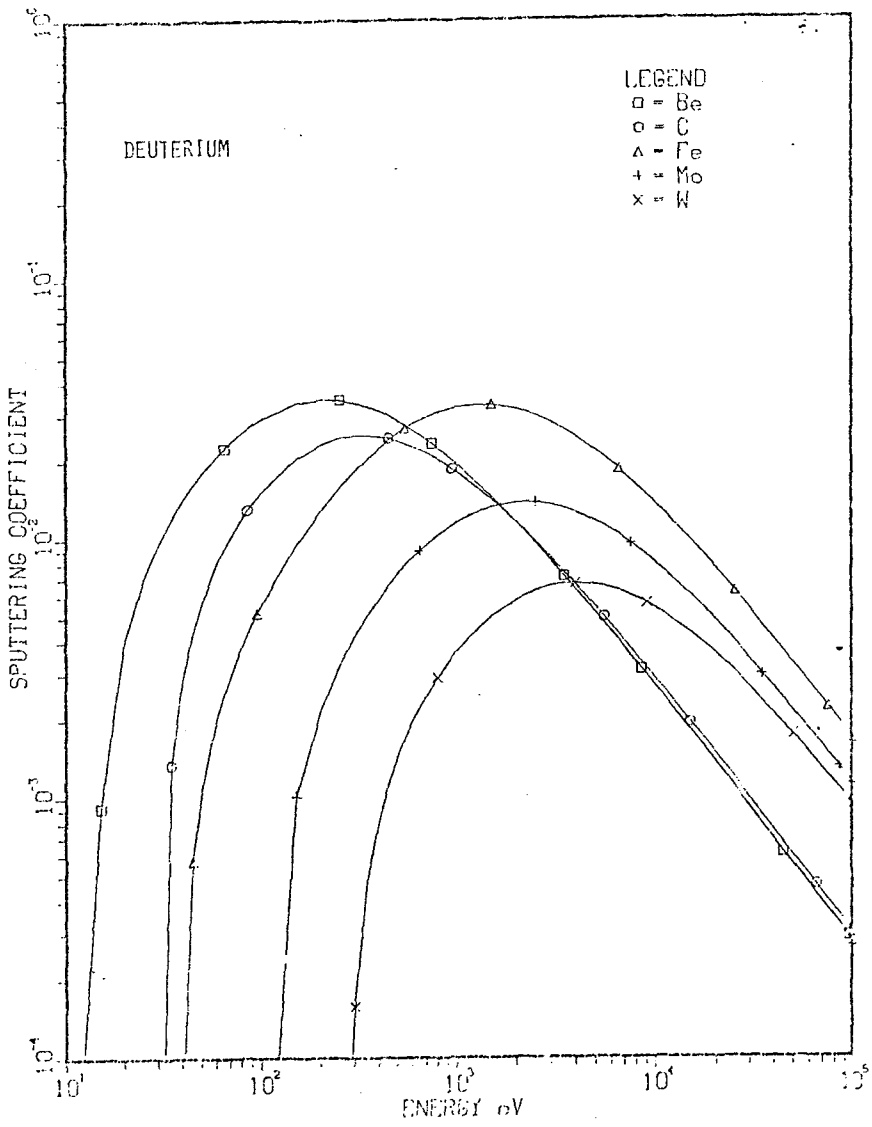

Figure 4-1. Calculated energy-dependent physical sputtering yields for candidate wall materials bombarded with normally incident monoenergetic deterium.[8]

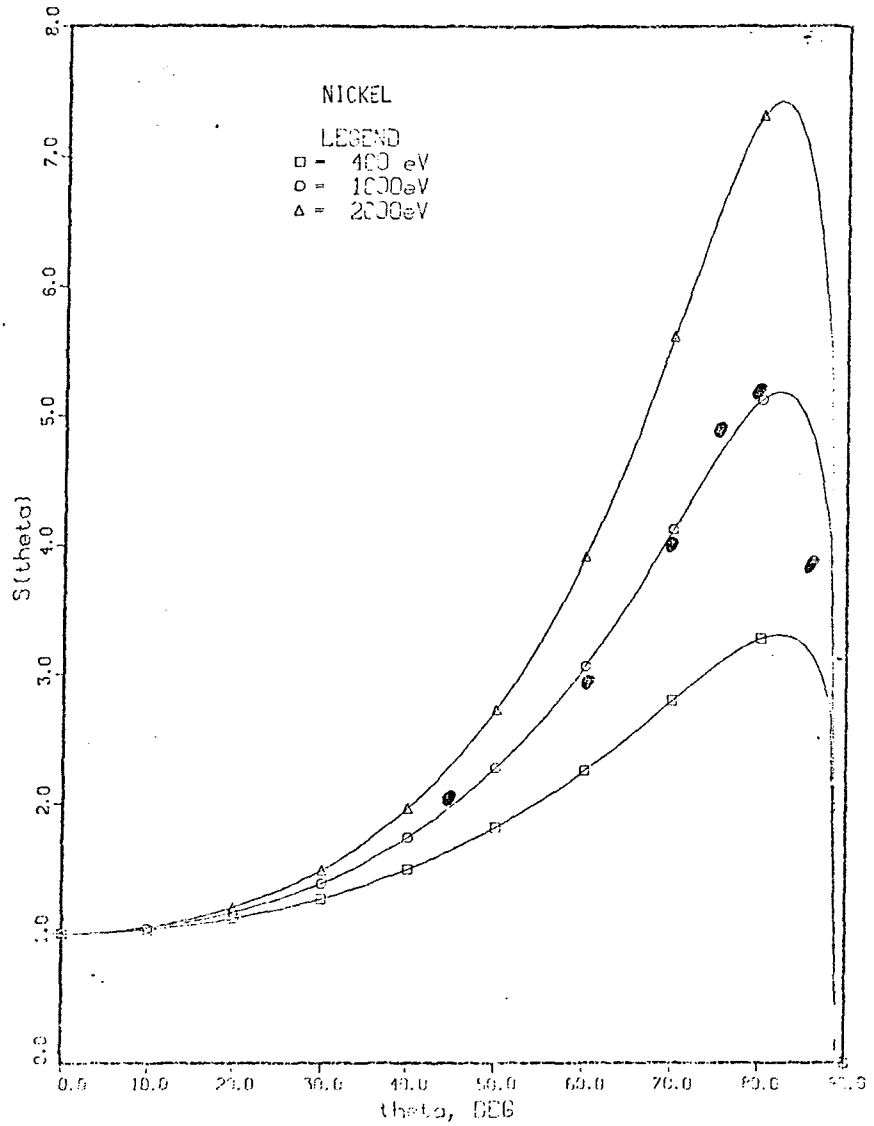

Figure 4-2. Calculated angular-dependent physical sputtering yields for 0.4, 1.0, and 2.0 keV deuterium incident on nickel (normalized to normal incidence).[8] (Solid symbols represent experimental data for 1 keV D.)

4.2.2 Plasma Disruption Effects

An important consideration in the design of the first wall relates to the effects of plasma disruptions. The present study has focused on the response of various candidate first wall materials to the high energy deposited on the first wall during a plasma disruption. There is a high degree of uncertainty as to the time of the disruption, the region or fraction of the first wall over which most of the energy is deposited (peaking factor), and the time dependence of the deposition rate. For the DEMO the plasma energy is ~ 300 MJ and the total first wall area is ~ 400 m^2. If the plasma energy were distributed uniformly over the entire first wall, the energy density would be 75 J/cm^2. It is generally believed that most of the energy will be deposited on the inboard region of the first wall. Uniform deposition over 20% of the wall (peaking factor of 5) would give 375 J/cm^2. The analyses presented are based on a uniform (time independent) deposition for times of 5, 20 and 60 ms. Values of 375 J/cm^2 (peaking factor of 5) during a 20 ms disruption are believed to be representative of the probable disruption scenario for the DEMO.

The energy deposited on the first wall during a plasma disruption can lead to vaporization of the surface regions, melting of the surface regions and conduction of heat into the bulk material. The analyses for the materials responses are based on analytical models developed by Merrill[2-10] and Hassanein[11]. Both models determine the extent of wall melting by solving equations which define the net energy content in the wall resulting from the plasma disruption. Merrill's model solves the following energy equation for the first wall material

$$\rho \frac{\partial E}{\partial t} = q + \nabla \times K \nabla T \qquad (4\text{-}1)$$

where

E = material energy (J/kg)
q = bulk heat rate density (W/m^3)
k = thermal conductivity (W/m-k)
T = material temperature (K)
ρ = material density (kg/m^3)

This equation defines the time and space dependent energy content of the wall material. Those wall regions predicted to have energies in excess of the amount required to melt the material represent the melt layer. A convective mass term is added to this equation to account for the moving boundary at the melt/vapor interface. Subsequent to each solution time interval, the node structure at the back of the wall is restructured. This procedure conserves both mass and energy during the evaporation process.

The Hassanein model solves separate conduction equations for the solid and liquid phases:

Solid Equation

$$\rho_s C_s \frac{\partial T_s}{\partial t} - \nabla \times k_s \nabla T_s = 0$$

Liquid Equation

$$\rho_\ell C_\ell \frac{\partial T_\ell}{\partial t} - \nabla \times k_\ell \nabla T_\ell = 0.$$

where

C = material specific heat (J/kg-K)

T = material temperature (K)

k = material conductivity (W/m-K)

ρ = material density

subscripts s, ℓ = solid, liquid phase.

Two interfaces exist for this model, the solid/melt and melt/vapor interfaces. The equations needed to specify the propagation of these interfaces are the following energy balances:

Solid/Melt

$$-k_\ell \frac{\partial T_\ell}{\partial x} = - k_s \frac{\partial T_s}{\partial x} + \rho_s L_f (W_s/m)$$

Melt/Vapor

$$q_s(t) = - k_\ell \frac{\partial T_\ell}{\partial x} + \rho_\ell \, (T_v) L_v \, V_{m/v} + \sigma(T_v^4 - T_o^4)$$

where

q_s = surface heat flux from plasma disruption
L_f = material heat of fusion (J/kg)
V = interface velocity (m/s)
L_v = material latent heat of evaporation (J/kg)
σ = Stefan-Boltzmann constant
subscripts s/m, m/v, v = solid/melt, melt/vapor, and vapor.

The solid/melt energy balance implies that the difference in the rate of energy conducted to the interface by the liquid phase and that conducted away from the interface by the solid phase must produce melting. The rate of melting is proportional to the material density and heat of fusion. The melt/vapor energy balance provides the boundary condition for the liquid conduction equation through the conductive term. The rate that energy from the plasma disruption arrives at this interface is equal to the rate that energy leaves the interface due to vaporization, conduction, and radiation. The last term on the right-hand side of the equation represents the energy radiated away from the surface; but it isn't apparent at this time why the material emissivity was not considered.

The Merrill and Hassanein models both consider the kinetics of surface evaporation. The Merrill model adopted the Schrage[12] modified phase change relationship.

$$j = \left(\frac{M}{2\pi R}\right)^{1/2} \left[\Gamma\sigma_c \frac{P_v}{T_v^{1/2}} - \sigma_e \frac{P_s}{T_s^{1/2}}\right]$$

where

j = vaporization mass flux (kg/m^2 x s)
M = vapor molecular weight (kg/mole)
$P_{v,s}$ = pressure (N/m^2) vapor, first wall surface
$T_{v,s}$ = temperature (K) vapor, first wall surface
R = universal gas constant (J/kg x mole K)
Γ, σ_c, σ_e = condensation or evaporation multipliers.

The terms of this equation predict the rate of condensation and evaporation respectively. The melt surface temperature and pressure of the evaporation term are determined from saturated relationships and the predicted surface energy. These same properties for the condensation term are obtained from a solution of the vaporized material transport equations. The boundary condition of surface heat flux for the first wall energy equation is the difference of the incident plasma flux and the convective vapor energy flux (the product of vaporization rate and latent heat of evaporation).

The Hassanein model solves a similar equation for the evaporation process

$$j_e\,(T_v) = (2\pi mkT_v)^{-1/2}\,\sigma_e P_s(T_v).$$

The condensation term is based on transport calculations[13] which indicate that the condensation rate asymptotically approaches 20% of the evaporation rate after 20 collision times. The resulting net vaporization rate is determined to be

$$j(t) = j_e\,[0.8 + 0.2\,\exp\,(-t/\tau_R)\approx.$$

Vaporized material transport is addressed differently in these models. The transport of the vaporized material away from the first wall surface for the Merrill model was determined by a solution of the continuum theory conservation equations:

Conservation of Mass

$$\frac{\partial \rho}{\partial t} + \frac{\partial \rho u}{\partial x} = 0,$$

Conservation of Momentum

$$\rho\,\left(\frac{\partial u}{\partial t} + u\,\frac{\partial u}{\partial x}\right) = \frac{\partial P}{\partial x} - \rho\,g_c\,\cos\,\theta$$

Conservation of Energy

$$\frac{\partial \rho E}{\partial t} + \frac{\partial \rho E u}{\partial x} = -P\,\left(\frac{\partial u}{\partial x}\right) + q,$$

where

u = vapor velocity (m/s)
P = vapor pressure (N/m^2)
E = vapor energy (J/kg)
q = vapor heat rate density (W/m^3)
ρ = vapor density (kg/m^3)

The solution of these equations provides the required vapor temperature and pressure for the condensation term of the vaporization equation.

For the Hassanein model, the influence of the vapor transport in the condensation term of the vaporization equation is through the relaxation time constant, τ_R. This time constant results in 98% of the asymptotic condensation flux after 20 collision times, and is given as

$$\frac{1}{\tau_R} = 1.6 \quad 2\pi^{1/3} \left(\frac{3}{4}\Omega\right)^{2/3} j_e$$

where Ω is the elastic scattering cross section.

The Hassanein model considers the effects of plasma attenuation by the vaporized material stream. The adopted approach for this attenuation was based on the premise that the vaporization of the quantity of material equivalent to the penetration depth of 10 keV ions in the solid phase will provide a vapor shield with an atom density sufficient to attentuate the incident plasma. As a result, the mechanism of wall heating changes from one of deposition of ions to radiation, and since this radiation is isotropic, the intensity of wall heating is one half the unattenuated value. The transition in intensity of heating was assumed to be linear with vaporized depth until the depth exceeds that of the original penetration depth of the ions.

Figures 4-3 and 4-4 compare the predicted melt layer thicknesses and vaporization depths for several materials as calculated with the Hassanein and Merrill models as functions of plasma energy density for disruption times of 5 and 20 ms. As can be noted, good agreement resulted for the case of no vapor shielding even though the modeling approaches differed. The predictions of melt layer thickness at 5 ms were in closer agreement than at 20 ms. The opposite was noted for vaporization depth. This would seem to imply that the different modeling approaches for vaporized material transport was a major

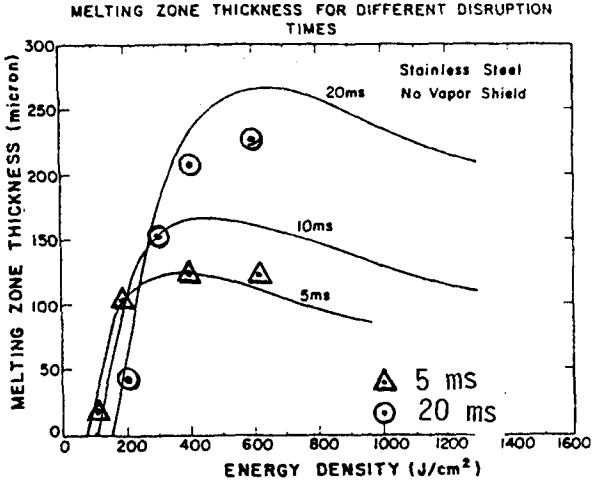

Figure 4-3. Stainless steel melting zone thickness with no vapor shield as a function of energy density (Curves - Hassanein model; symbols - Merrill model.)

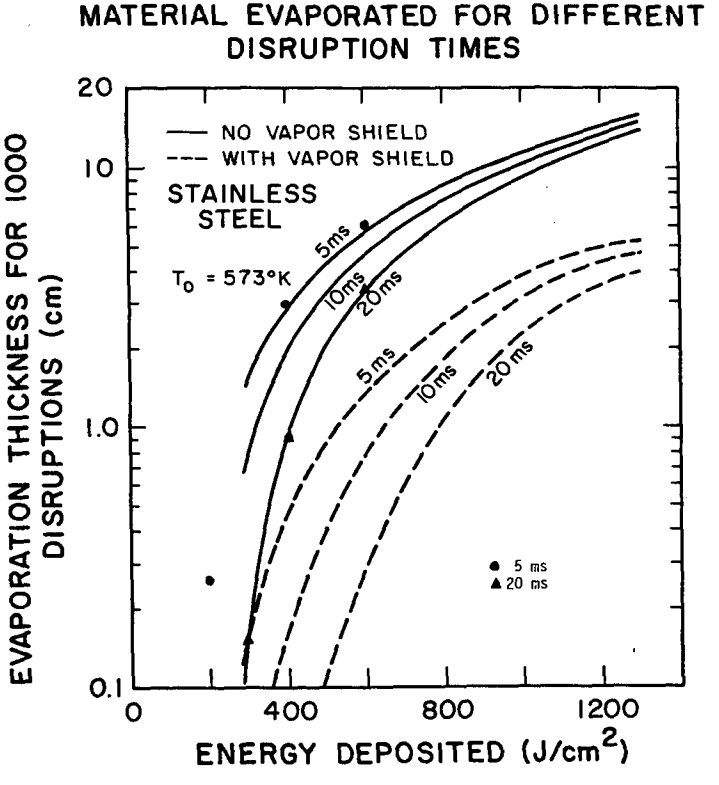

Figure 4-4. Evaporation thickness of stainless steel for 1000 disruptions for different energy deposited (Curves - Hassanein model; symbols - Merrill model.)

contributor to this difference. Figures 4-4 and 4-5 illustrate the impact of the vapor shield. For stainless steel, the vaporized depth decreased by approximately an order of magnitude whereas the melt layer thicknesses were affected only slightly.

Figures 4-6 through 4-12 contain predictions of melt layer thickness and vaporized depth for beryllium, molybdenum, tungsten, and carbon. The results for beryllium and tungsten are from the Merrill model and as a consequence do not include the effects of vapor shileding. The results for melt layer thickness, Fig. 4-6 through 4-8, suggest that a maximum value exists for a given disruption time. This characteristic is a consequence of vaporization becoming more predominant as energy density is increased. The vaporized depths, Fig. 4-4 and 4-9 through 4-12, indicate that increased vaporization occurs as a result of decreased disruption times at a given energy density. A transition to a linear dependence of vaporized depth with energy density was noted.

Table 4-4 summarizes the required energy densities to produce 1) melting, 2) one micron of vaporization, and 3) the maximum melt layer thickness for the case of no vapor shielding. These points have been interpolated or extrapolated from Fig. 4-3 through 4-12. The results for stainless steel and beryllium are fairly similar, with the difference becoming more pronounced at longer disruption times. This similarity was attributed to the face that the total energy change, the product of density and energy, from the initial value at 573 K to vaporization is practically identical for these materials. The energy thresholds for molybdenum and tungsten were significantly higher than either stainless steel or beryllium. The maximum melt layer thicknesses during a 5 ms disruption for molybdenum and tungsten were both ~ 220 μm, while those for stainless steel and beryllium were ~ 120 μm. This indicates that the latter materials are more volatile. On the basis of these results, tungsten would be the more resistant metal to erosion by disruption, due to 1) high total energy requirement to melt and vaporize, 2) high thermal conductivity, 3) moderate vapor pressure. Should the melt layer not be stable during this event, a metal with the same characteristics but higher vapor pressure would be more desirable. It is important to point out that the melt layer will exist for only a short time (of the order of the disruption time) and that much of the layer will be molten only a fraction of this time.

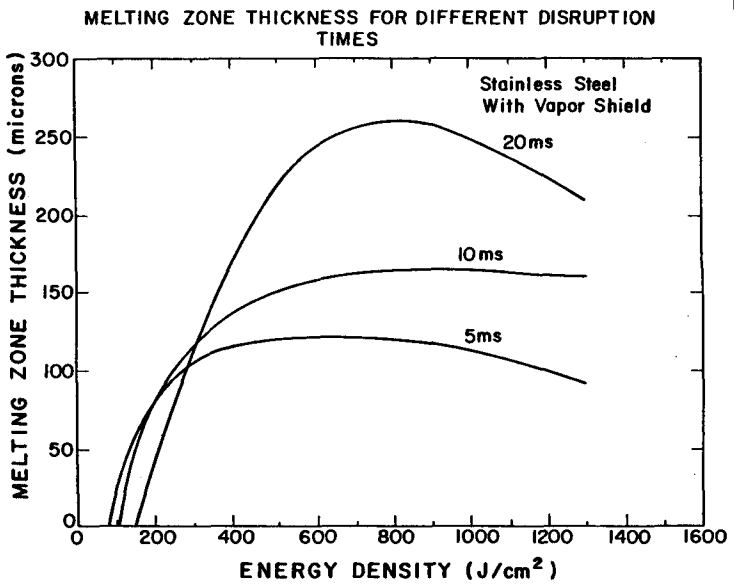

Figure 4-5. Stainless steel melting zone thickness with vapor shield as a function of energy density (Hassanein model).

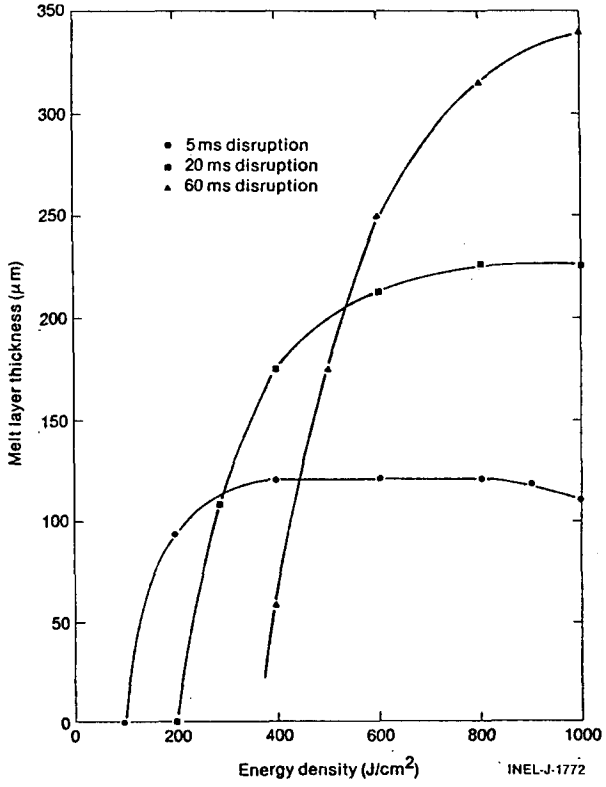

Figure 4-6. Beryllium maximum melt layer thickness for plasma disruptions of 5, 20, and 60 ms duration (INTOR model).

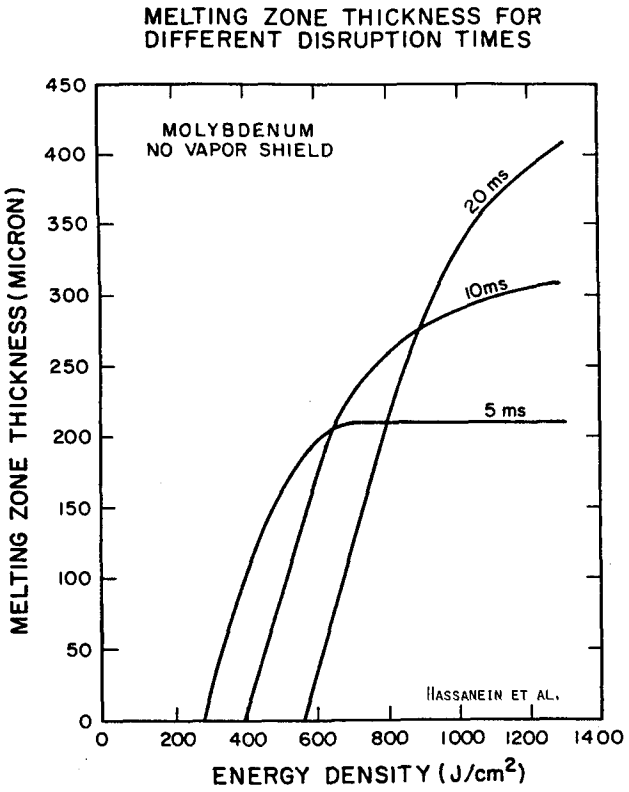

Figure 4-7. Molybdenum melting zone thickness with no vapor shield as a function of energy density (Hassanein model).

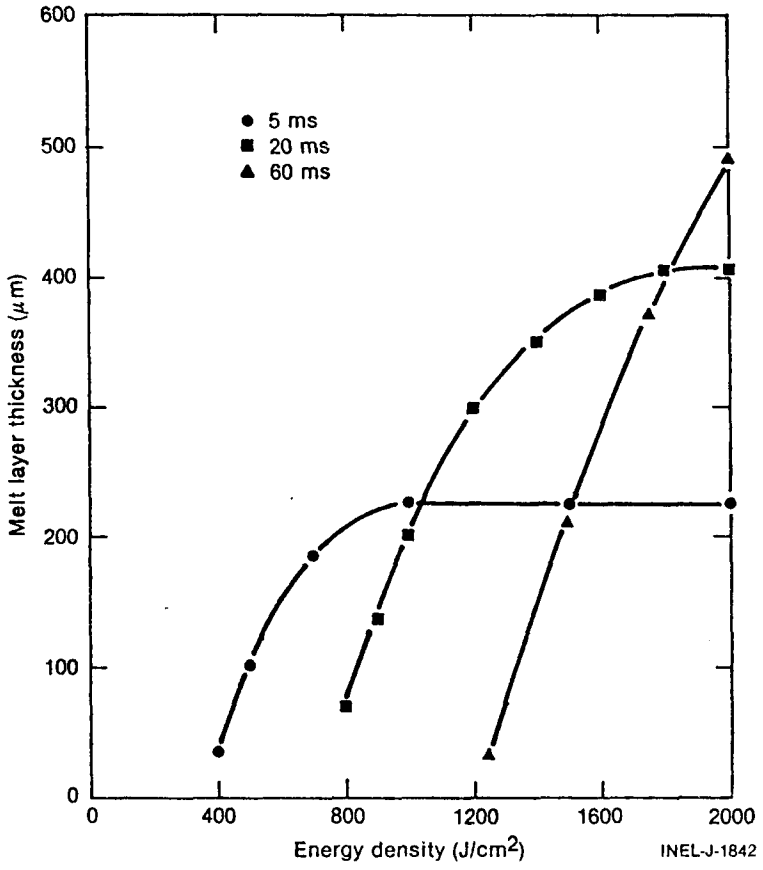

Figure 4-8. Tungsten maximum melt layer thickness for plasma disruptions of 5, 20, and 60 ms duration (Merrill model).

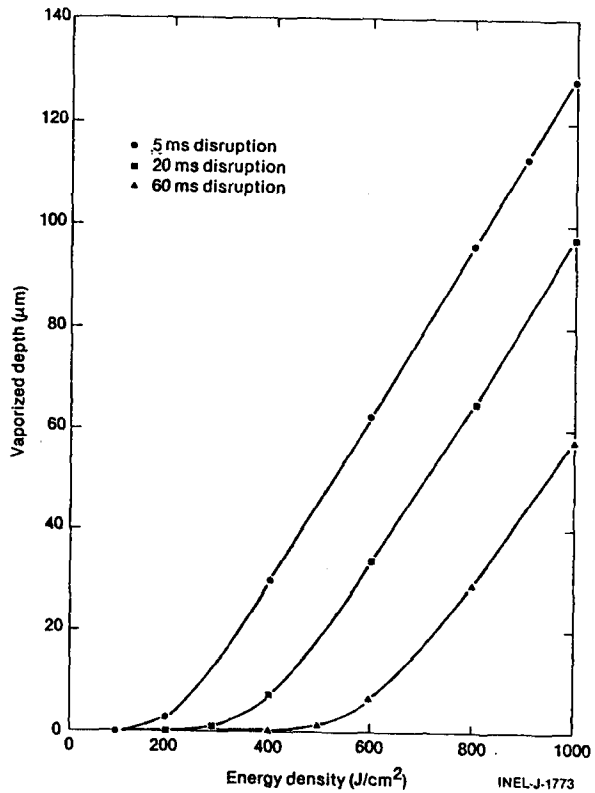

Figure 4-9. Beryllium vaporization depth for plasma disruptions of 5, 20, and 60 ms duration (Merrill model).

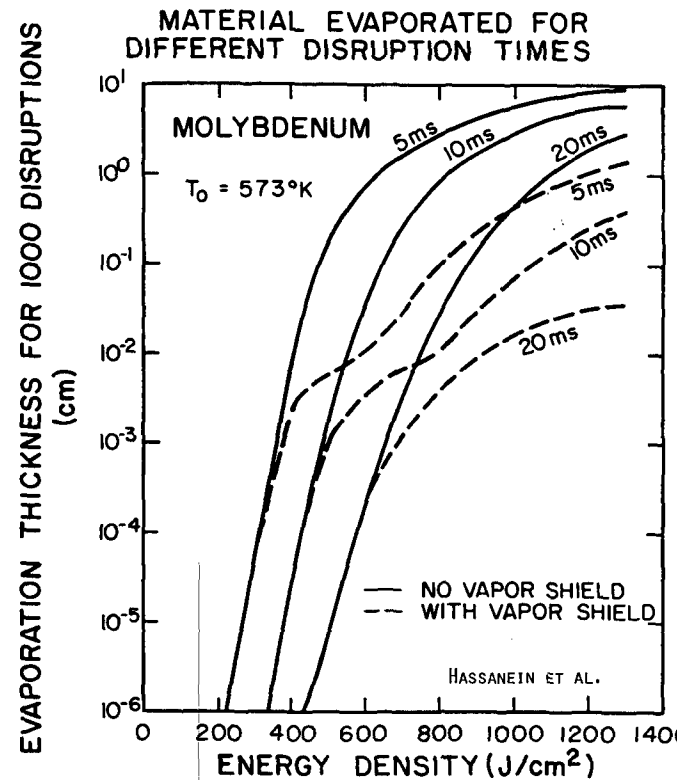

Figure 4-10. Evaporation thickness of molybdenum for 1000 disruptions as a function of energy density (Hassanein model).

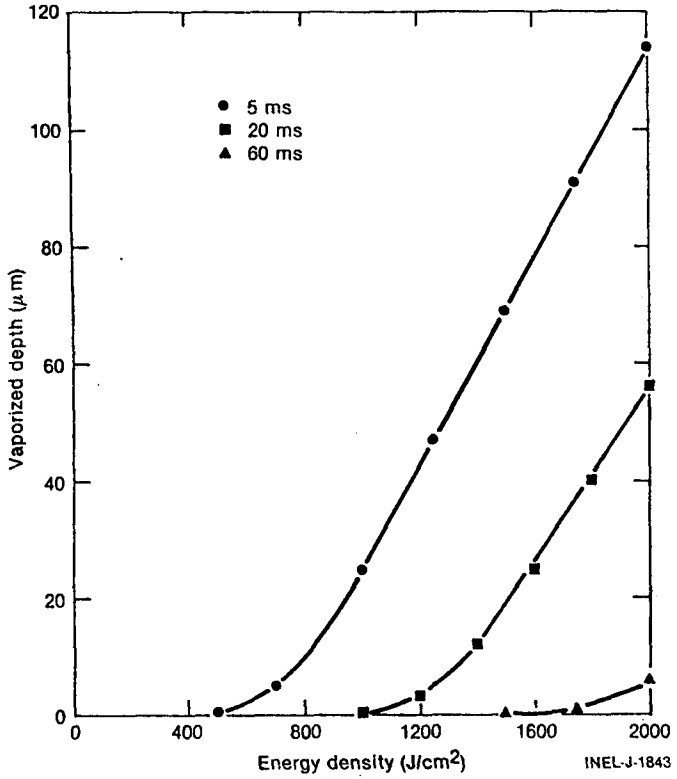

Figure 4-11. Tungsten vaporization depth for plasma disruptions of 5, 20, and 60 ms duration (Merrill model).

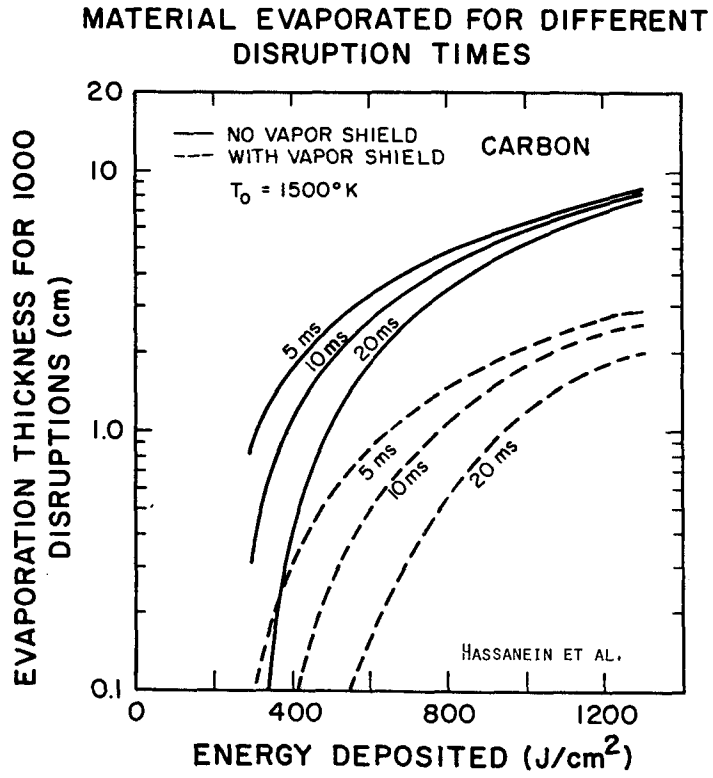

Figure 4-12. Evaporation thickness of carbon for 1000 disruptions as a function of energy density (Hassanein model).

Table 4-4. Required energy densities to produce melting, one micron of vaporization, and the maximum melt layer thickness.

Material	Disruption Time (ms)	Energy Density Required To Cause Melting (J/cm^2)	One Micron of Vaporization (J/cm^2)	Maximum Melt Layer Thickness (J/cm^2)
Stainless steel	5	90	150	290
	20	170	290	600
	60	300	480	-
Beryllium	5	100	150	350
	20	200	300	800
	60	360	500	-
Molybdenum	5	280	400	700
	20	560	750	-
	60	-	-	-
Tungsten	5	360	560	1000
	20	700	1080	1800
	60	1220	1750	-

- Not predicted

Results presented are for calculations without consideration of the effects of the vapor shield

Table 4-5 summarizes the estimated vaporization erosion thicknesses for the cases of 375 J/cm^2 and 750 J/cm^2 and with the vapor shielding. These values are used as a basis for specifying the first wall thickness and lifetime. Since there is a large uncertainty regarding both the disruption time and the area of the disruption (peaking factor), the impact of a few very severe disruptions is an important consequence. The integrity of the wall should not be lost in the event of a single or even a few very severe disruptions. For the case of a very short disruption (< 1 ms), nearly all of the energy from the plasma is dissipated by vaporization. The calculations indicate that an energy density of about 6000 J/cm^2 is required to vaporize 1 mm of beryllium (assumes no vapor shield). This energy corresponds to a peaking factor of 80 or an equivalent wall area of 5 m^2. The vapor shielding should be even more effective at the higher vaporization rates. An order of magnitude reduction in erosion provided by the vapor shield would correspond to a peaking factor of 800 or an area of 0.5 m^2 for the case above. As indicated by the tendency to saturate at very high energy densities with the vapor shield (see Figs. 4-4 and 4-12), the vapor shield may be even more protective for very severe (or concentrated) disruptions. These results indicate that it is very unlikely that the integrity of a beryllium-clad wall would be lost even under a very serios disruption. Since the probability is low that a very serious disruption would occur at the same small area, the wall should withstand a reasonable number of very concentrated disruptions.

Table 4-5. Vaporization Thickness for 20 ms Disruption Peaking Factors of 5 and 10

Wall Material	Vaporization Thickness, μm	
	5(375 J/cm^2)	10 (750 J/cm^2)
Beryllium	0.2[a]	8[a]
Stainless Steel	0.3	9
Tungsten	0	0

[a]Assume shielding effect similar to graphite.

Although the present models adequately predict the thermodynamic response of the first wall material, these models do not account for the melt layer dynamic behavior. Movement of the melt layer could significantly increase first wall erosion. The behavior of the melt layer could significantly increase first wall erosion. The behavior of the melt layer is affected by such phenomena as induced magnetic forces, plasma kinetic pressure and/or surface sputtering, and acceleration force of the vapor during evaporation. Plasma/vapor interactions should result in a change in the type and intensity of the energy deposition experienced by the first wall surface, through energy absorption and re-radiation by the vapor, ionization of the vapor, and increased plasma radiative losses. The Hassanein model has addressed this area, but both the theory of plasma vapor interaction and experimental verification of models are required.

4.2.3 Tritium Transport in the First Wall

Tritium migration in the first wall is an issue of considerble importance, particularly if water is used as the coolant. Recently this issue was highlighted by considerable controversy during the March 1981 INTOR meeting in Vienna at which results of Wienhold, Waelbroeck, Winter, and Ali-Khan[14] predicted tritium migration rates of the order of 10 Curies/day whereas Bartlit, Finn, and Abdou[15] predicted migration rates of 1 Curie/day -- a difference of five orders of magnitude. The differences resulted not only from the conditions assumed (surface condition at the first wall and at the coolant interface, wall temperature, wall thermal gradient, etc.) but more importantly from the models used to represent the transport processes that occur and the assumed boundary conditions. In this section, the following topics are discussed: (1) tritium transport models; (2) surface desorption; (3) deuterium transport experiments; and (4) tritium transport in the DEMO first-wall designs.

4.2.3.1 Tritium Transport Models

In Fig. 4-13, tritium migration processes in a fusion reactor first wall are illustrated. Energetic tritons ranging from 0-3 keV are injected to a mean depth, δ, of ~ 0.01 μm into the first wall at a rate, S. These particles can then migrate to the coolant at the rate, R_1, or back to the plasma at the rate R_2. The internal concentration of tritium will increase until steady-state levels are achieved and $S = R_1 + R_2$.

The rate R_1 is affected not only by bulk diffusion kinetics but also by the conditions at the coolant/structure interface. (If an oxide film is present at the interface, transport rates can decrease by from one to three orders of magnitude.[16]) It has been shown that for steels implanted with deuterium, the experimentally measured diffusion rates are highly dependent on surface treatment history.[17,18] For as received material:

$$D(cm^2/s) = 1.7 \times 10^{-3} \exp(-12{,}713/RT)$$

or about 10^{-11} cm^2/s at 400°C, whereas for electropolished material

$$D(cm^2/s) = 1.2 \times 10^{-1} \exp(-14{,}100/RT)$$

or about 10^{-10} cm^2/s at 400°C. Thus substantial variations (at least on order of magnitude) are predicted for different surface conditions.

The rate R_2 also depends on both diffusion and surface phenomena, e.g., recombinative desorption. The presence of an oxide film, trapped particles, or porous surfaces (produced by radiation damage) will affect both of these phenomena. The models which have been developed to predict tritium migration at the first wall generally assume that either bulk diffusion[19] or surface interactions[20,21] are rate limiting. The key issue is to establish which mechanisms are in control under conditions of interest. A critical review of the models developed and the experimental data base used to evaluate tritium migration through the first wall is presented.

The Hickman[19] insertion model assumes that the migration rate R_1 is proportional to the ratio between the implantation depth, δ, and the wall thickness, t,

$$R_1 = \phi(Ci/d) = S(\delta/t)(4.14 \times 10^{-15}).$$

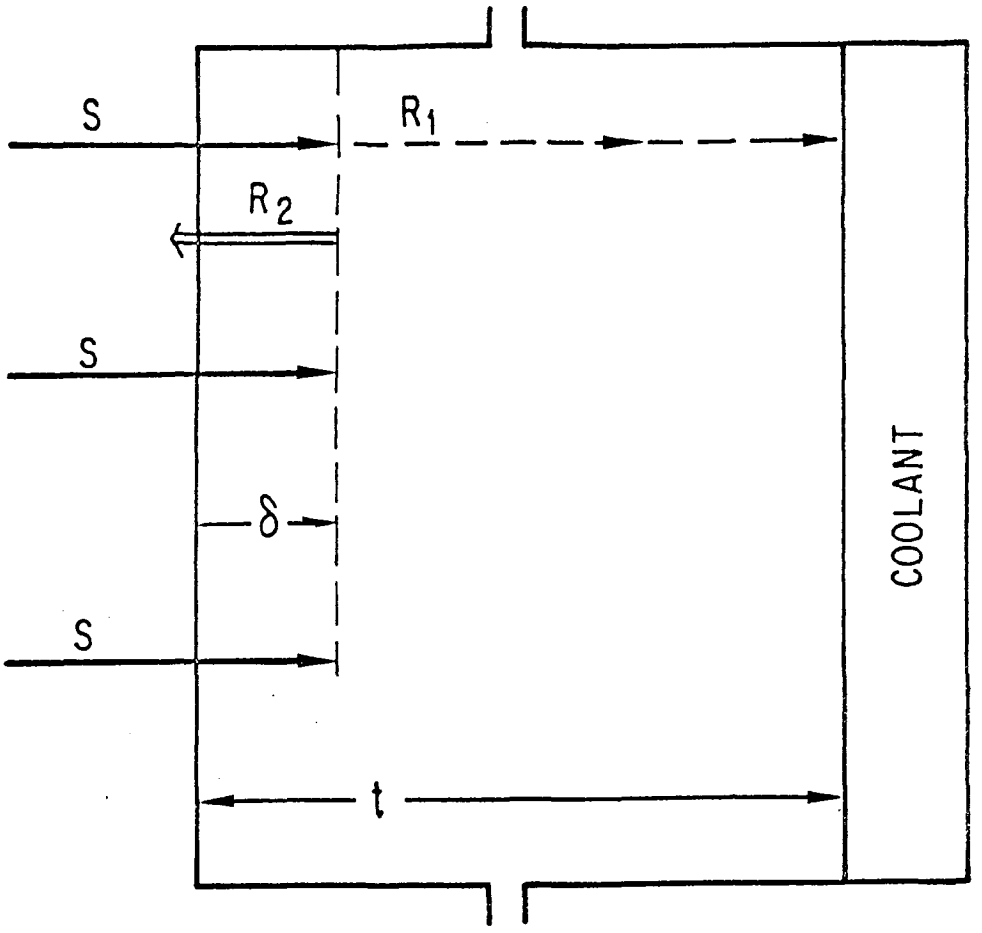

$S = R_1 + R_2$ -- S = Source, R_1 = Rate at which particles migrate to coolant, and R_2 = Rate at which particles migrate to first wall.

Figure 4-13. Tritium migration in a fusion reactor first wall.

The calculated steady-state migration rate (R_1) is not dependent on either pressure or temperature but increases as the particle energy increases, i.e., as the implantation depth, δ, increases. The creation of porosity near the plasma/wall interface would tend to decrease R_1, since the particle would have a shorter distance to diffuse to a surface. Since the mean injection depth[22] $\sim$ 0.01 μm is approximately equal to an oxide film thickness,[23] 0.003-0.02 μm, energetic particles in an environment with trace amounts of oxygen or water[24] could be trapped within or under an oxide film. Under these conditions, R_2 would decrease, the internal concentration would increase, and R_1 would therefore increase.

Another important effect is tritium trapping. It has been determined[25,26] that deuterium retention in the first 0.5 μm of a bombarded first wall saturates at $\sim 10^{17}/cm^2$. Increased implantation fluences have no further effect on the surface concentrations and the bulk retention is increased slightly. This could result in an initial increase in the migration rate followed by a decrease to steady state levels.

The simple gaseous permeation model, e.g. that

$$\phi = \frac{k_T A}{t} (P_2^{1/2} - P_1^{1/2})$$

has the best reference data[27] (k_T = permeation coefficient at temperature T, A = area, t = thickness of first wall, P_2 = hydrogen pressure at the plasma interface, P_1 = hydrogen pressure at coolant interface, assumed $\simeq 0$). This model may be the least acceptable representation of tritium migration at the first wall since the neutral pressure at the plasma interface is not quantitatively known. In practice, the driving pressure inside the wall could be used if it were known.

The model developed by Ali-Khan, et al.[20] assumes that at low hydrogen pressures, surface desorption at the plasma interface is the rate limiting step for R_2,

$$R_2 = k_r K_s^2 P_1,$$

where ϕk_r Π k_r = recombination rate constant, K_s = Sieverts' constant, and P_1 = hydrogen pressure. This process is temperature-dependent but independent of wall thickness. Although the values of k_r at the plasma/wall and at the coolant/wall interfaces can be substantially different, they have been assumed equal in most calculations. In addition, the k_r values used have been calculated from other experimental data and not directly measured.

The model developed by Baskes[21] assumes that the surface boundary conditions are of the form

$$R_2 = k_r C_s^2$$

(C_s is the near-surface tritium concentration). Although the effect of different k_r values at the plasma/wall and the coolant/wall interfaces has been examined, it has been acknowledged that the appropriate values of k_r are not known. A model developed for calculating k_r assumes that this parameter is proportional to the molecular sticking coefficient, α, which is equal to ~ 0.5 for a clean surface and ~5×10^{-5} for a "dirty" surface,[28] the dirty surface being representative of the existance of an oxide film. Any trapping at radiation-induced defects is neglected in this model.

4.2.3.2 Surface Desorption

In both models that include surface desorption, the rate-limiting step is recombinative desorption; therefore, a critical review of the available information on the recombination rate constant was conducted. Wilson[29] who presented a summary of the available data on k_r, noted that the data base for the recombination rate constant, and for surface desorption in general, was quite uncertain. The references cited in the summary plus additional references are given in Fig. 4-14. Some of the obvious conclusions are the following. At 400°C, the value of k_r can vary by six orders of magnitude.[20,30] Both Baskes[38] and Wienhold[39] used the data that Weinhold had collected on gas recycling to calculate k_r using their respective models. Good agreement between each model and the experiment resulted in values of k_r differing by two orders of magnitude. The data of Braun[30] had the caveat that the surface concentration could have been overestimated due to the presence of surface trapping centers, the presence of an oxide film or surface gas adsorption. At this time, it appears probable that the surface concentration was indeed overestimated. Several experimenters derived expressions for k_r, shown below, which are represented by the four curves in Fig. 4-14:

$$k_r = 5.4 \times 10^{-19} \exp(-15600/RT), \quad 150^0C < T < 400^0C \text{ (Ref. 30)}$$

$$k_r = 6.3 \times 10^{-14} \exp(-21400/RT), \quad 70^0C < T < 400^0C \text{ (Fe) (Ref. 33)}$$

$$k_r^{24} = 8.8 \times 10^{-18} \exp(-13600/RT), \text{ (Ref. 37)}$$

$$k_r^{23} = 4.5 \times 15^{-15} T^{-1/2} \exp(-11930/RT), \quad 25 < T < 100^0C \text{ (Ref. 36)}$$

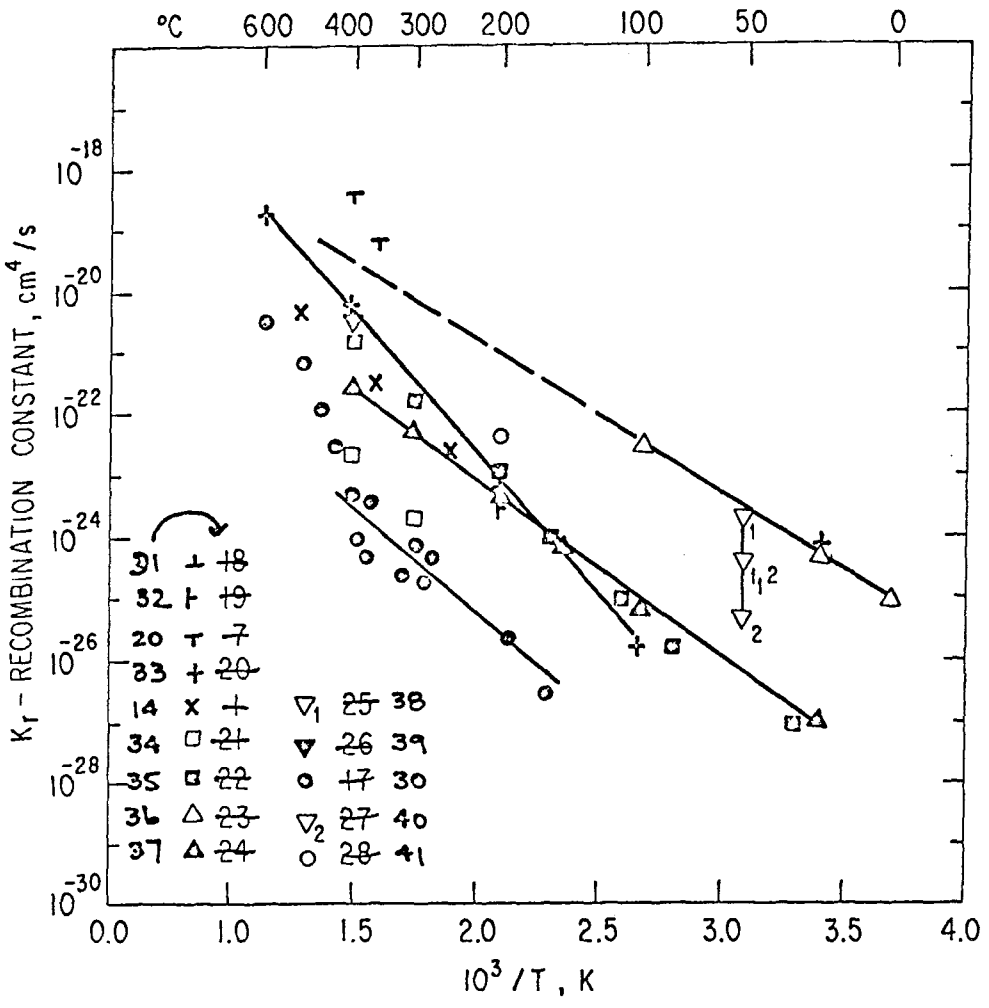

Figure 4-14. Temperature dependence of recombination constant (different investigators).

Baskes' model[36] (expression d) results in migration rates approximately an order of magnitude larger than that of the permeation model if a clean surface is assumed at the plasma/wall interface and a "dirty" one at the coolant/wall interface. Because the large variation in k_r suggests the presence of complicating factors (oxide film, etc.), actual conditions expected in a fusion reactor cannot be accurately modeled with existing data.

Some bombardment experiments with tungsten filaments have been reported. Tritium migration in iron held at 92°C[33] increased a factor of 5×10^4 when a tungsten filament was operated. Since the same rate was attained when the hydrogen pressure was increased a factor of 10^6, this may have been due to the

presence of an oxide film with a barrier effectiveness of 10^3. In an experiment with SS-4301 at 300°C[42] it was reported that increasing the hydrogen pressure by a factor of 10^4 achieved the same effect as operating a tungsten filament. If some oxygen or water were present, an oxide film with an effectiveness of $\sim 10^2$ would produce the same result.

4.2.3.3 Deuterium Transport Experiment

The data base for deuterium transport during ion implantation is very limited. However, the migration rate in both Type 316 stainless steel and nickel was measured[43] during deuteron (20 keV) bombardment ($9 \times 10^{18}/m^2s$). It was found that for Type 316 stainless steel the rate increased to a maximum and then decreased to a steady-state value, saturating at $\sim 10^{17}/cm^2$ as noted previously.[21,22] The difference between the maximum and steady-state values was approximately a factor of two. The maximum migration rate observed at 500°C was approximately four times greater than that predicted by a simple gaseous permeation model. It was ≈50% less than that predicted by the Hickman model. The decrease in the migration rate may have resulted from the formation of an oxide film; however, it would seem that this experiment is reasonably well explained using the Hickman model. The desorption models would have to assume a large k_r to explain the experimental results.

Another deuteron (15 keV) bombardment, this time of Type 304 stainless steel, was done at a fluence of $\sim 10^{18}/m^2s$ by Perkins and Noda.[44] The migration rate was ≈0.5 of Saitoh's.[43] Thus, for stainless steels the tritium migration at the first wall can be better approximated by the insertion model than the permeation model. For other materials, one would expect that the maximum tritium migration rate would be better predicted by the Hickman model, if the insertion effect is dominant.

Based on these conclusions, we have utilized both the Hickman model and the permeation model to predict tritium migration rates and the associated steady-state tritium concentration in the water coolant for several first-wall designs for DEMO. The tritium wall inventories are calculated assuming no radiation-induced trapping.

4.2.3.4 Tritium Transport in the DEMO First-Wall Designs

The first-wall designs considered were: (1) a beryllium-metal composite consisting of 10 mm beryllium and 5 mm ferritic, vanadium or stainless steel alloy; and (2) a metal wall of ferritic, vanadium, or stainless steel. (The thickness was varied from 15 to 5 mm to account for erosion losses during lifetime). The common parameters are listed in Table 4-6. The reference case approximates the thermal gradient in the wall by assuming an average temperature of 400°C. The average ion energy assumed was 1.2 keV. Ions at 3 keV would result in rates twice as high. The average hydrogen pressure was assumed to be 10^{-3} Pa; in the limiter slot pressures of $\sim 10^{-1}$ Pa could be generated. Some of the cases considered are shown in Table 4-7. The temperature dependence of the permeation constants for several materials is shown in Fig. 4-15. The reference cases are summarized in Table 4-8. The coolant was assumed to have a volume of 10^5 ℓ . In most cases it was found that tritium migration and decay rates would be equal in ∿20 y.

Table 4-6. Parameters for First Wall

Surface area, m^2	400
Thickness, mm	5-10-15
Volume, m^3	2-4-6
Temperature, °C	300-500
Average temperature, °C	400
Hydrogen pressure, Pa	10^{-5}-1
Average pressure, Pa	10^{-3}
Average energy of insertion, keV	1.2 (0-3 range)
Flux to wall, s^{-1}	10^{22}
Volume coolant, m^3	100 (water)
Tritium fueled, kg/d	2
Tritium burned, g/d	140

For the composite Be-M wall, transport rates are <20 Ci/d if no oxide barrier is assumed and <10 Ci/d if an oxide barrier is present at the coolant interface. In the case of vanadium, ~ 56 g of tritium is dissolved in the wall; for the ferritic or stainless steel <1 g is dissolved in the wall. For a structural metal wall, an oxide barrier is required for both vanadium and ferritic alloys to maintain tritium transport rates at <20 Ci/d. For stainless steel the transport rates are predicted to be <20 Ci/d without an oxide barrier. As discussed in Ref. 1, an oxide film will be present on these structural alloys when exposed to water under conditions of interest. For both ferritic and austenitic steels, wall inventories are predicted to be <1 g. For the vanadium alloy the inventory is predicted to be between 50 and 170 g.

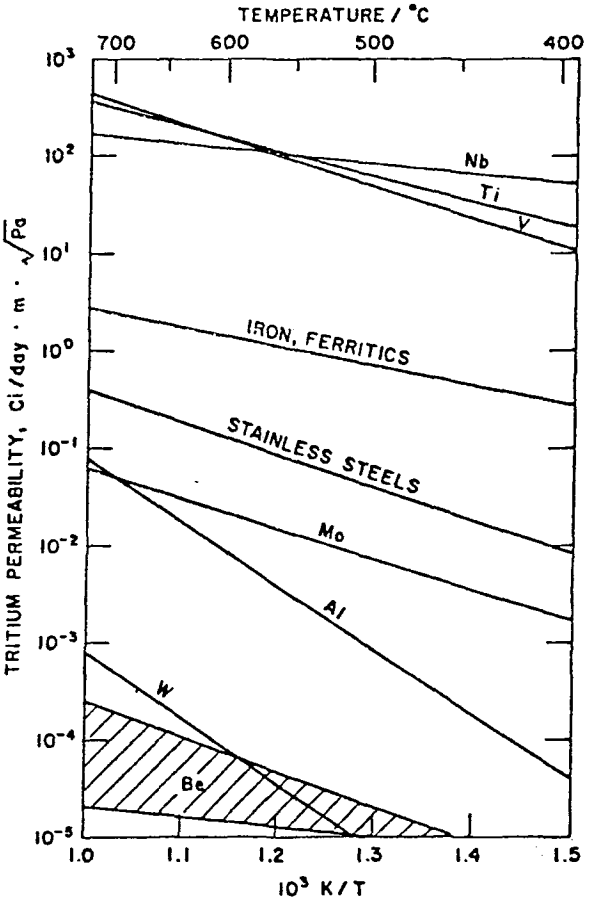

Figure 4-15. Tritium permeability of several materials as a function of temperature.

Table 4-7. Tritium Transport Rates for 400 m^2 First Wall

Material	Temp. (°C)	Permeabil. Constant[a]	Thickness. (mm)	Press. (Pa)	Transport Rate Ci/d) Simple Permeation	Transport Rate Ci/d) Insertion
Be, 100%[c]	500	10^{-5}	10	10^{-3}	7×10^{-3}	110
			5	10^{-3}	1.4×10^{-2}	220
			10	1	2.2×10^{-1}	110
Be, 60%	500	10^{-5}	10	1	2.2×10^{-1}	2.2×10^{-1}
			5	10^{2}	4.4	4.4
			5	10^{4}	44	44
Be, 100%	300	10^{-6}	10	10^{-3}	7×10^{-4}	110
			5	10^{-3}	1.4×10^{-3}	220
Be, 60%	400	8×10^{-6}	10	10^{4}	15	15
Ferritic[d]	500	1	15	10^{-3}	4.9×10^{2}	17
			5	10^{-3}	1.4×10^{3}	50
			15	1	1.5×10^{4}	17
Ferritic (10^2X)[e]	500	10^{-2}	15	10^{-3}	4.9	1.7×10^{-1}[f]
			5	1	4.4×10^{2}	5×10^{-1}
Ferritic	300	10^{-1}	15	10^{-3}	49	17
			5	10^{-3}	1.4×10^{2}	50
Ferritic (10^2X)	300	10^{-3}	5	10^{-3}	1.4	5×10^{-1}
Ferritic	400	4×10^{-1}	10	10^{-3}	2.9×10^{-2}	34
V[g]	500	80	15	10^{-3}	3.9×10^{4}	19
			5	10^{-3}	1.2×10^{5}	60
			15	1	1.2×10^{6}	19
V (10^3X)	500	8×10^{-3}	5	10^{-3}	1.2×10^{2}	6×10^{-2}
			5	1	3.8×10^{3}	6×10^{-2}
V	300	5	15	10^{-3}	2.4×10^{3}	19
			5	10^{-3}	7.2×10^{3}	60
			5	1	2.3×10^{5}	60
V (10^3X)	300	5×10^{-3}	15	1	7.6×10^{1}	1.9×10^{-2}
			5	1	2.3×10^{2}	6×10^{-2}
V	400	10	10	$10^{/3}$	7.3×10^{3}	40
V (10^3X)	400	$10^{/2}$	10	10^{-3}	7.3	4×10^{-2}
SS[h]	500	5×10^{-2}	15	10^{-3}	24	17
			5	10^{-3}	72	50
			5	1	2.3×10^{3}	50
SS	300	10^{-3}	15	10^{-3}	4.9×10^{-1}	17
			5	10^{-3}	1.4	50
			5	1	44	50
SS (10X)	300	10^{-4}	15	1	1.5	1.7
			5	1	4.4	5
SS	400	10^{-2}	10	10^{-3}	7.3	34
SS (10X)	400	10^{-3}	10	10^{-3}	7.3×10^{-1}	3.4

[a] Units = $Ci/(d \quad m \quad Pa^{1/2})$.

[b] 9.6×10^{3} Ci = 1 g tritium.

[c] Refers to percent theoretical density.

[d] For ferritics, iron atoms were used for insertion calculation.

[e] Presence of oxide coating at coolant wall assumed.

[f] Oxide coating at coolant wall should reduce effect of insertion.

[g] For vanadium alloys, vanadium atoms were used for insertion.

[h] For stainless steel, iron atoms were used for insertion calculations.

Table 4-8. Summary of Tritium Transport, Wall Inventory, and Coolant Concentation for First Wall, Average Temperature 400°C, 10^{-3} Pa

Design	Transport Rate (Ci/d)	Coolant Steady-State Concentration (Ci/∓)[a]	Hydrogen Solubility (ppm $Pa^{-1/2}$)	Tritium Inventory (g)
10Be[b]-5V	15	1.5	-,800	<56
10Be[b]-5Fe	15	1.5	-,0.1	<1
10Be[c]-5SS	15	1.5	-,0.5	<1
10Be-5V (10^3X)	15	1.5	-,800	<56
10Be-5Fe (10^2X)	5	0.5	-,0.1	<1
10Be-5SS(10X)	1	0.1	-,0.5	<1
15V(10^3X)[c]	5	0.5	800	168
5V(10^3X)	15	1.5	800	56
15Fe (10^2X)	2	0.2	0.1	<1
5Fe (10^2X)	6	0.6	0.1	<1
15SS (10X)	0.5	0.05	0.5	<1
5SS (10X)	2	0.2	0.5	<1
15V	4900	500	800	168
5V	15,000	~2000	800	56
15Fe	190	20	0.1	<1
5Fe	580	60	0.1	<1
15SS	5	0.5	0.5	<1
5SS	15	~2	0.5	<1

[a]Coolant volume = 10^5 ℓ, ~20 y for decay to equal migration rate if no processing is done.

[b]Porous beryllium with maximum hydrogen internal pressure 10^4 Pa.

[c]Oxide barrier at coolant wall, assumed effectiveness.

4.2.4 Nuclear Response

This section presents the nuclear analysis for the first-wall armor designs. The two armor materials studied are type 316 stainless steel (316 SS) for solid Li_2O breeder blanket designs and Fe9Cr1Mo ferritic steel for liquid 17Li83Pb breeder blanket designs. Both armors (flat portions of the first wall) are assumed to be 13.4 mm thick, and the Fe9Cr1Mo armor is cooled by the 90% ^6Li enriched 17Li83Pb breeder itself while the 316 SS armor is cooled by light water. Table 4-9 summarizes the nuclear response rates of the respective armor designs. The neutron wall load and the plant availability for the accumulated response rate calculations are assumed to be 1.8 MW/m^2 and 100%, respectively. The analysis was performed based on a one-dimensional infinite cylinder model in which the plasma center is taken as the cylinder axis and all sub-regions (e.g., first wall, blanket, etc.) are represented by concentric annuli about the plasma region. The plasma and armor surface radii are assumed to be 2.08 m and 2.245 m, respectively.

It is found that there exists a substantial difference in the response rates between the two armor designs. As shown in the energy breakdown of the neutron flux, the difference stems largely from the difference in the degree of the neutron spectrum softening as well as in the number of neutrons. Because of the large neutron multiplication in the Fe9Cr1MO armor/17Li83Pb breeder system (due primarily to the Pb (n,2n) reaction), the neutron population for energies above 1 MeV in this system, for instance, is about 30% higher than that in the 316 SS armor/Li_2O breeder system. As a result, the atomic displacement is almost proportionally increased in the Fe9Cr1MO armor. On the other hand, the gas production, exhibits larger rates in the 316 SS armor design due to the presence of nickel. Table 4-9 indicates that low-energy neutrons are more populated in the ferritic steel armor design. For example, in the neutron energy range of 0-1 Mev, the neutron flux in Fe9Cr1Mo is 9.9×10^{18} $m^{-2}s^{-1}$ compared to 3.1×10^{18} $m^{-2}s^{-1}$ in 316 SS. However the nuclear heating rate in the ferritic steel armor is lower than the corresponding 316 SS heating rate due to the strong absorption of secondary gamma rays in lead of the 17Li83Pb breeder.

The potential armor erosion does not seem to appreciably alter the nuclear performance of the armor design as the reactor operates. For example, the nuclear heating rate in the 316 SS armor varies from the start-up value of 19.5 MW/m^3 shown in Table 4-9 to 19.2 MW/m^3 after the first 10 mm thick region

Table 4-9. Nuclear Response of First-Wall Armor[a]

1.	Armor Material	316 SS	Fe9Cr1Mo
2.	Breeding Material	Li_2O[b]	17Li83Pb[c]
3.	Atomic Displacement (dpa/yr)	18.2	25.4
4.	Gas Production (appm/yr)		
	a. Hydrogen	935	785
	b. Helium	257	188
5.	Nuclear Heating (MW/m^3)	19.5	16.1
6.	Neutron Flux (m^{-2} s^{-1}) x 10^{-18}		
	a. E > 0	5.68	13.3
	b. E > 0.1 MeV	4.23	11.3
	c. E > 1.0 MeV	2.59	3.45
	d. E > 10.0 MeV	1.39	1.37
7.	Gamma Flux (m^{-2} s^{-1}) x 10^{-18}		
	a. E > 0	2.91	2.45
	b. E > 0.1 MeV	2.91	2.45
	c. E > 1.0 MeV	1.01	0.843
	d. E > 10.0 MeV	7.15×10^{-4}	7.06×10^{-4}

[a]Neutron Wall Load: 1.8 MW/m^2, Plant Availability: 100%, Armor: 13.4 mm, First Wall: 3.0 mm H_2O (for Li_2O System)/3.0 mm 17Li83Pb, followed by 3.0 mm 316 SS (for Li_2O System)/4.5 mm Fe9Cr1Mo.
[b]Li_2O: Natural Lithium: 70% of theoretical density.
[c]17Li83Pb: 90% ^6Li enrichment.

has eroded. The corresponding Fe9Cr1Mo heating rate at the 10 mm erosion results in about 14.6 MW/m^3 indicating a variation of 10% at most at the end of the armor life-time. The potential impact of the armor erosion, from the neutronics standpoint is the change of tritium breeding performance in the blanket region which surrounds the armor/first-wall region.

Figure 4-16 presents the possible variation of tritium breeding ratio (BR), based on full coverage one-dimension of calculations, with armor erosion. The Fe9Cr1Mo armor system analyzed employs 90% ^6Li enriched 17Li83Pb as a breeder as well as a coolant while the 316 SS armor system employs the Li_2O breeder of natural content. The variation of trituim BR with armor thickness is caused by different mechanisms for the two armor designs. In the case of the 316 SS/Li_2O system, the primary impact of the armor erosion is found in the increase of the $^7Li(n,n'\alpha)t$ reaction due to the relatively hard neutron spectrum characterized in this system as indicated in Table 4-9. On the other hand, the Fe9Cr1Mo/17Li83Pb system enhances the tritium production as the armor erodes, primarily through the ^6Li (n, α)t reaction induced by the increased number of secondary neutrons resulting from the more effective Pb(n,2n) reaction for thinner armor. The results of Fig. 4-16 indicate a

potential increase in BR amounting to 0.05 - 0.08 near the end of the armor life-time (about 10 mm armor erosion). However, uncertainties in the magnitude of wall erosion and the redistribution of eroded materials make it difficult to predict precisely the change of tritium breeding ratio with operating time.

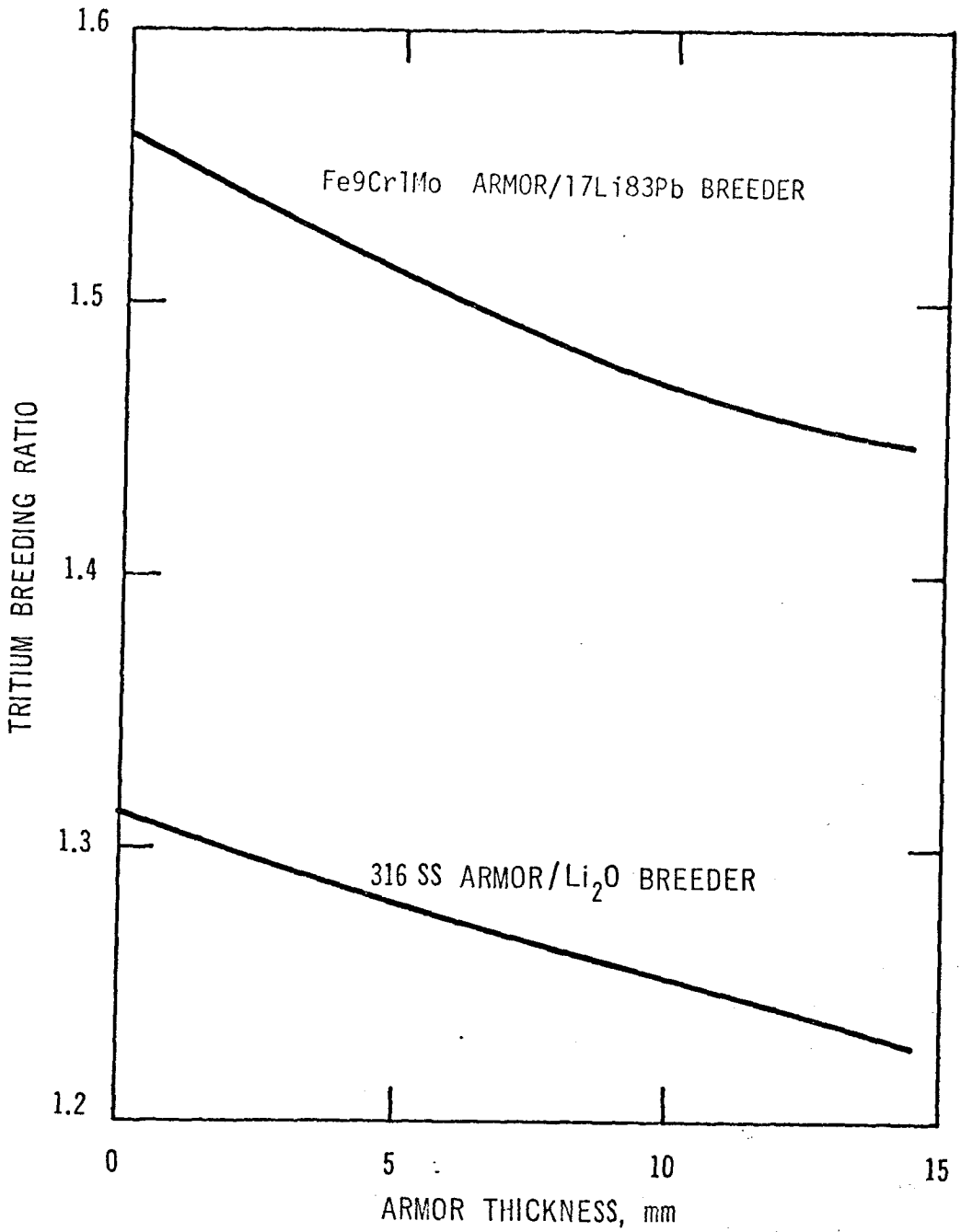

Fig. 4-16. Effect of armor erosion upon tritium breeding.

4.3 Li_2O Breeder Blanket

A summary of the analyses and evaluations performed in support of the Li_2O breeder first wall/blanket concept is presented in Section 4.3.1. The remaining subsections of 4.3 deal with specific related topics:

Section	Subject
4.3.2	Design Considerations
4.3.3	First Wall Materials, Analyses and Design
4.3.4	Neutronics Analysis
4.3.5	Li_2O Properties
4.3.6	Tritium Recovery
4.3.7	Blanket Thermal-Hydraulics
4.3.8	Blanket Materials Compatibility
4.3.9	First Wall/Blanket Design

4.3.1 Summary

The most important considerations related to first wall/blanket mechanical and structural design (Sec. 4.3.2) were (1) choice of breeder/coolant containment method, (2) Li_2O breeder temperature, and (3) the degree of first wall/blanket mechanical and structural integration. Small-diameter toroidally-oriented coolant tubes were chosen to contain the high pressure water coolant within the breeder zone. This approach is considered to have relative advantages over a radial flow (pressurized module) approach in structural efficiency, neutronics (because of lower volume fraction of structure and coolant), compatibility with first wall designs, and certain fabricability aspects (e.g., no separate helium purge piping system is required within the blanket). The method presently assumed for keeping breeder temperature at all points within minimum and maximum temperature limits is to use a ceramic insulator of controlled thickness on the outside of the coolant tubes. This is preferable to the use of only a helium-filled gap of specified width to control heat transfer at the breeder-to-tube interface, because of anticipated difficulties in achieving the very tight tolerances necessary for the gap both during fabrication and during blanket operation. The first wall and blanket coolant systems and structure were combined. This approach eliminates the need for an additional actively cooled front wall for the breeding zone, and enhances the tritium breeding by reducing the total

amount of structure and coolant. First wall/blanket maintainability and availability are considered equal to or better than those for a first wall and blanket which are mechanically and structurally separate.

Pressurized water (260-300°C) was selected for the first-wall and blanket coolant. Since the range of operating temperatures required for acceptable Li_2O performance is very limited, the low system ΔT characteristic of pressurized water systems appears necessary for a satisfactory design. The relatively low operating temperature is also advantageous for the stainless steel structural material, particularly with respect to the effects of radiation on the properties. Analyses indicate that pressurized water provides significant economic advantages over helium for tokamak reactor applications.[1] The use of water coolant permits a smaller reactor size or a higher fusion power for a given size compared to helium coolant, provides for much lower pumping power losses, and results in lower cost of the heat transport system. An advanced austenitic stainless steel (designated PCA in the alloy development program) similar to Type 316 was selected as the structural material for the DEMO. Both the mechanical properties and radiation damage resistance are considered acceptable for reasonable lifetimes at the projected operating temperatures. Structure temperatures in a water-cooled system can be maintained below the temperatures at which severe displacement damage embrittlement, helium embrittlement, and maximum swelling occur. Although data are limited for the projected operating conditions, acceptable chemical compatibility can probably be maintained at the low temperatures with appropriate design. Steady-state reactor operation is important for acceptable wall lifetimes because of the relatively high thermal stress factor associated with stainless steel. The fact that solid breeder materials also have a limited lifetime because of Li burnup reduces the incentive for a very long lifetime structure. As discussed in Sec. 4.2 and 3.0, one of the most promising design options utilizes a beryllium cladding bonded to the structural wall to prevent excessive limiter erosion and plasma contamination.

Structural analyses of various coolant channel geometries and sizes for actively-cooled first-wall panels were conducted to evaluate tradeoffs between thermal, pressure, and bending stresses. Results indicate that the corrugated panels with relatively small channels (< 20 mm wide) offer a good compromise solution. The semicircular cross sections provide the best combination of

higher allowable coolant pressures and higher thermal or bending stresses. However, the sinusoidal segment cross sections may provide a better choice when fabrication aspects are considered.

Neutronics analyses were performed to evaluate (1) the impact of ^{6}Li enrichment on the tritium breeding performance, (2) the potential for a nonbreeding inboard blanket design, (3) the tritium-breeding enhancement provided by a neutron multiplier, and (4) the geometrical dependence of the nuclear heating and the decay heat for a reference first-wall/blanket configuration. The 1-D neutronics calculations indicate that, in the absence of a neutron multiplier, the tritium breeding potential of a Li_2O blanket decreases significantly with ^{6}Li enrichment above that for natural lithium. The maximum breeding ratio (100% blanket) for a Li_2O blanket with stainless steel first wall (13.4 mm thick) is 1.23 compared to a breeding ratio of 1.41 for the reference design with a 10 mm thick beryllium cladding. Some breeding in the inboard blanket appears essential unless an effective neutron multiplier is used. Both breeding in the inboard blanket and a neutron multiplier may be required if a significant fraction of the outboard blanket is nonbreeding as in the case of a poloidal divertor. Beryllium is found to be the only effective neutron multiplier for a Li_2O blanket. In contrast to the STARFIRE design with $LiAlO_2$ as the breeder material, the beryllium multiplier is more effective when placed behind several centimeters of the Li_2O breeder material. The nuclear heating in the Li_2O varies by approximately two orders of magnitude from the front of the blanket to a depth of 60 cm. For the reference design the nuclear heating is 13.4 MW/m^3 at a distance 5 mm behind the first wall. Although the radioactive products (except tritium) generated within Li_2O completely decay within a minute, a significant fraction of the decay gamma's generated in the stainless steel structure are absorbed in the Li_2O resulting in significant decay heat for longer periods. The total decay power in the first-wall/blanket, which amounts to about 14.5 MW (1.6% of the total thermal power) at shutdown, decreased to about 3 MW within 7 h and tends to level off at about 2 MW for several weeks.

The physical properties, thermodynamic properties and the effects of radiation on the properties and behavior of Li_2O have been evaluated in detail. Fabrication and handling problems associated with Li_2O have also been assessed. The melting temperature of Li_2O has now been established as

1430°C[45] instead of the higher value of 1700°C given in the STARFIRE report. The temperature dependence of the thermal conductivity is given in Sec. 4.3.5.1 as a function of porosity. Uncertainties and variations in the data associated with grain size, purity, and radiation effects have not been studied in detail. Lithium oxide is known to be very hygroscopic, reacting readily with moisture to form LiOH. As a result, high purity Li_2O is not only difficult to obtain but is difficult to maintain during handling. Commercially available material typically contains at least 2% of LiOH and 2% of Li_2CO_3. Recent investigations[46] indicate that the solubility of LiOH in Li_2O is very low. Fabrication of Li_2O with small grain size and interconnected porosity, although difficult, appears feasible. However, the stability of this microstructure under anticipated thermal and radiation environments of a reactor blanket is a major concern. Large weight losses have been observed at 1000°C when Li_2O is exposed to vacuum or helium with very low moisture concentrations. This is generally attributed to mass transfer of LiOH. Also, chemical effects produced by burnup of lithium and displacement damage effects produced by energetic recoils (T and He) are predicted to cause sintering and pore closure under certain conditions. Preliminary data indicate substantial restructuring of Li_2O after irradiation at temperatures of 750°C and above.

Tritium recovery is considered to be the key feasibility issue regarding the viability of Li_2O as a tritium breeder material. Tritium generated within the Li_2O grains must diffuse to the surface of the grains, desorb as T_2O, and migrate through interconnected porosity to a helium purge stream where it is transported to the tritium processing system. Similar to the case for STARFIRE, a Li_2O microstructure with small grain size (< 1 μm) and a bimodal pore distribution is believed to offer the most potential for acceptable tritium recovery. The difficult design problems arise from the limited operating temperature range projected for Li_2O and the fact that the thermal conductivity, although higher than that of the ternary oxides such as $LiAlO_2$, is relatively low (about 4 W/m K at 500°C). Effects that result in a projected allowable operating temperature range between 410 and 670°C for Li_2O are summarized in Table 4-10. The critical concerns relate to the fact that some of the phenomena may cause irreversible propagating-type effects. For example, precipitation of LiOT could lead to enhanced sintering at low temperatures.

Table 4-10. Basis for Allowable Operating Temperature Range of Li_2O

Maximum Allowable Temperature	
Radiation-induced sintering	700°C
Mass Transport of LiOH (1% of T_2O)	670°C
Minimum Allowable Temperature	
Solid state diffusion (1 μm grain)	410°C
LiOT precipitation (160 Pa)	410°C

This in turn would produce higher tritium partial pressures, and hence, more LiOT precipitation and subsequently more sintering. The mass transport of LiOT leads not only to a loss of lithium from the blanket but to possible corrosion problems caused by precipitation of liquid LiOT in the tritium processing circuit. Analyses indicate that, in the absence of radiation effects, the blanket tritium inventory can be maintained at relatively low levels (< 50g in Li_2O). However, radiation effects are expected to substantially increase the tritium inventory, possibly to unacceptable levels. Additional experiments are required to more accurately predict the effects of irradiation.

Thermal-hydraulic analyses have been conducted to evaluate the sensitivities of the blanket design, particularly with respect to tritium recovery, to variations in breeder physical properties, geometrical parameters and power level. Calculations based on specified materials properties data and idealized operating conditions were used to determine coolant tube spacing, coolant flow rates, and other design specifications required to maintain the Li_2O breeder within the projected allowable temperature range. The sensitivity studies then provided an indication of the impact on design tolerances and operation of performance uncertainties, such as (1) variations in thermal conductivity of the breeder caused by density variations or radiation effects, (2) variations of coolant tube breeder gap conductances caused by thermal expansion effects, creep or fabrication tolerances, and (3) power level or coolant flow-rate fluctuations. It was concluded that the tolerances required for a designed helium gap conductance (tube-breeder) were

too small for use in a practical system. Also, significant variations in coolant tube spacing (and hence coolant, structure, and breeder fraction) are required to accommodate relatively small uncertainties. Normal effects such as thermal cycling during startup and shutdown, and lithium burnup have not been analyzed in detail but are a major concern. Preliminary analyses have also been conducted to evaluate the flow characteristics of the helium purge stream. Further analyses are required to evaluate effects caused by flow reductions in both the coolant and the helium purge gas.

The materials compatibility issues include breeder-structure, coolant - structure, and breeder-coolant compatibility. The first two issues involve normal operation whereas the breeder-coolant compatibility is of interest only in the event of off-normal conditions such as a coolant leak into the breeder region. Limited data from short-term (< 2000 h) sealed capsule experiments indicate that the reactivity of Li_2O with stainless steel is probably not excessive. However, no data exist under the more severe conditions of appropriate oxygen and moisture pressures. Potential approaches for reducing breeder-structure reactions include coating of the steel surfaces with nickel or an oxide such as Al_2O_3. The potential for stress corrosion cracking of cold-worked austenitic steel under attainable conditions should be assessed in more detail. The impact of tritium or hydrogen containment has not been evaluated in detail. In the event of a water leak into the breeder region, pressurization of the breeder region and formation of corrosive LiOH will occur. The combination of high pressure, significant heat of reaction, and potentially high velocity as a result of turbulence from a leak could lead to rapid corrosion of adjacent structural material with a potential for a propagating-type failure. More detailed analyses must be conducted to assess the severity of a coolant-breeder reaction that would result from a coolant tube leak.

The interim Li_2O breeder first wall/blanket design (Sec. 4.3.9) is illustrated in Fig. 4-17 and major parameters are listed in Table 4-11. The first wall and blanket are integrated mechanically and structurally into modules, which are assembled into eight blanket sectors identical except for local variations required for other reactor components (e.g., REB current drive launcher). The first wall is a beryllium-clad corrugated panel, with channels of circular segment cross section. The breeder and first wall are cooled by high pressure (11.0 MPa), high temperature (260°C inlet, 300°C

Figure 4-17. Li_2O solid breeder reference blanket design.

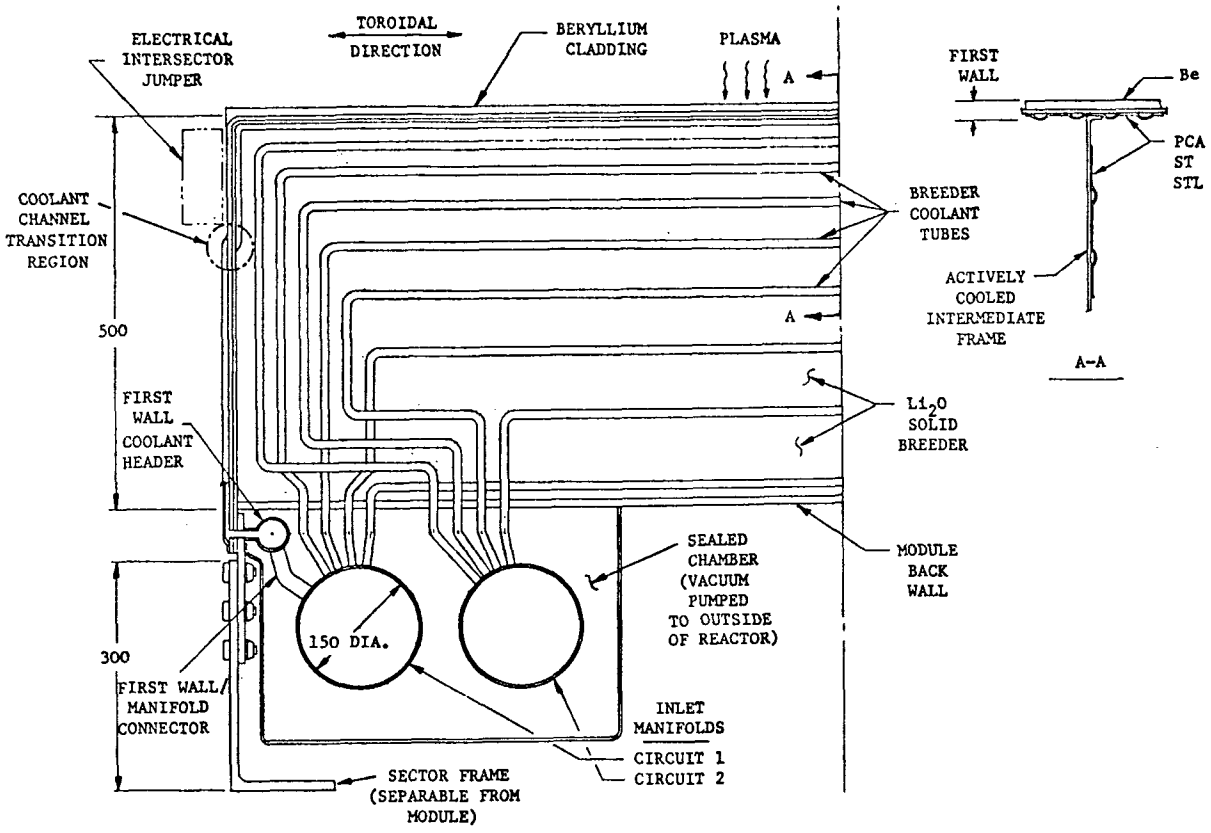

Table 4-11. STARFIRE/DEMO Li_2O Breeder Reference First Wall/ Blanket Concept Description

Selected Materials	
- Tritium Breeder	Li_2O (solid; 70% d.f.)
- Coolant	Pressurized H_2O (11.0 MPa)
	- Inlet temperature 260°C
	- Outlet temperature 300°C
- Tritium Processing Fluid	Low-velocity Helium (0.05 MPa)
- Structure	Titanium-modified Austenitic
	- Stainless Steel
Selected Design Options	
- First Wall	Be-clad Corrugated Panel
- Breeder Coolant Containment	Small-diameter Tubes
- Other	

- First wall and blanket mechanically and structurally integrated
- Coolant flow in toroidal direction
- Dual parallel primary coolant loops
- Maintenance by sector removal and replacement

outlet) water. The breeder coolant is contained in small-diameter tubes connected to inlet and outlet manifolds at the rear of the blanket. The Li_2O breeder is fabricated at 70% of theoretical density with bi-modal porosity to enhance tritium release. Helium purge gas at approximately 1 atm flows through 2-mm diameter holes in the breeder to remove tritium.

Dual parallel primary coolant loops are provided to effect safe removal of afterheat in the event of a coolant circuit failure. Maintenance of the first wall/blanket is performed by sector removal and replacement, to minimize downtime.

4.3.2 Design Considerations

Table 4-12 lists most of the principal considerations, issues or concerns, and candidate design detail options involved in the mechanical and structural designs of the Li_2O breeder first wall/blanket. Although many of these issues were previously addressed in the STARFIRE study for the $LiAlO_2$ breeder blanket; they have been reconsidered for the Li_2O breeder within the context of STARFIRE/DEMO objectives and parameters.

The information in the table assumes the selection of first-wall blanket materials: austenitic stainless steel structure (Sec. 4.3.8); pressurized water coolant (Sec. 4.3.3); helium purge gas (Sec. 4.3.6); and Li_2O breeder. Issues and options pertaining specifically to other materials are not shown.

The reasons for the importance of the listed issues, and the advantages and disadvantages of the various design detail options, are discussed in Sections 4.3.3 and 4.3.9 together with the rationale supporting the options selection for the reference first wall/blanket design configuration.

Table 4-12. Design Considerations for Li_2O Breeder Blanket

Consideration	Primary Issues or Concerns	Options
First wall design	o Plasma disruption loads o Reliability against leaks o Thermal-hydraulics	o Coolant containment method: - Tubes - Panels - Front wall of large pressurized blanket module
First wall/blanket coupling	o Effects on breeding ratio o Maintainability/availability	o Integrated with or separable from blanket - Structurally - Mechanically
Breeder temperature control	o Thermal conductance at breeder/coolant tube in interface	o Helium gap o Controlled-thickness ceramic insulation on coolant tubes o (Others to be determined)
Breeder coolant containment	o Reliability against leaks o Structural coolant volume minimization o Structure temperature limit o Coolant pressure, ΔT, T_{max}	o Coolant containment in breeder zone: - Small-diameter tubes - Panels - Large pressurized modules - Large-diameter tubes o Plenum location: - Module ends (toroidally) - Rear of blanket o Coolant flow direction
Energy conversion system	o Thermal energy recovery efficiency o Component capital costs o Pumping power losses	o Heat exchanger options: - Intermediate heat exchanger (IHX) - Steam generator: - Single wall tubes - Double wall tubes
Safety	o Effects of breeder/coolant contact in accident o Blanket afterheat removal	o Blanket protection methods: - Double walled coolant tubes - Relief (blow-out) plugs - Module walls designed for full coolant pressure o Afterheat removal: - Dual parallel coolant circuits - Emergency coolant circuit - Via radiation and conduction only

4.3.3 First Wall

Critical aspects of the first wall that relate to plasma-materials interactions, and hence are generally insensitive to the blanket concept, are presented in Sec. 4.2 above. Those aspects that relate more specifically to the blanket materials selection are presented in this section for the Li_2O breeder blanket concept. Many factors regarding solid breeder first-wall/blanket concepts were evaluated in considerable detail in the STARFIRE study[1]. Those factors that are relevant for the Li_2O blanket concept are only briefly summarized here. In particular, selection of the reference first-wall/blanket coolant for the DEMO is the same as for the STARFIRE design. A major focus of the present study is a more detailed thermal-hydraulic and stress analysis of proposed first-wall designs. Important aspects of the materials selection are summarized below and the proposed design configuration is presented.

4.3.3.1 Materials Selection

Coolant Selection

The choice of coolant has a major impact on the selection of other blanket materials, reactor operating parameters, the energy conversion system, shielding, maintenance and repair, tritium systems, and reactor building design. Although lithium, helium, water and molten salts have all been proposed as potential reactor coolants,[6] water and helium are considered to be the preferred candidates for solid breeder blanket concepts[1]. Pressurized water was selected for the STARFIRE design and is chosen for the Li_2O breeder concept. Important advantages associated with the choice of water coolant include:

- Operating temperature is compatible with Li_2O breeder requirements.
- Operating temperature is compatible with structural material requirements.
- First-wall heat fluxes can be accommodated.
- Sufficient radiation attenuation (no loss of shield space).
- Manifold sizes are tolerable.
- Recirculating power is minimal.

Since the range of operating temperatures required for acceptable Li_2O performance is very limited (see Secs. 4.3.5 and 4.3.6), the low system ΔT character-

istic of pressurized water systems appears necessary for a satisfactory design. The low operating temperature is also advantageous with respect to radiation damage effects of the structural materials.

The primary feasibility issue associated with water coolant relates to control of tritium permeation into the coolant. A critical design problem involves accommodating the high pressure coolant. The major penalty associated with pressurized water is the limited energy conversion efficiency attainable. The primary safety concern relates to pressure transients and formation of corrosive LiOH in the event of a coolant leak into the breeder zone.

Key factors in the elimination of helium as a candidate coolant include:

- Difficulty or inability to design within the temperature limits for Li_2O.
- Neutronic (shielding/breeding) penalty associated with helium, particularly the loss of inboard shielding efficiency.
- No satisfactory structural material for use in high temperature helium.
- Potential helium leakage into plasma chamber and difficult leak detection.
- Limited first-wall heat-flux capability.
- High pumping power requirement.
- High pressure/large manifold requirement.

Design of a functional helium-cooled Li_2O first-wall/blanket system within the proposed constraints is questionable. Probably the most severe criterion relates to the limited operating temperature range for Li_2O.

Structural Material Selection

The selection of candidate structural material for the first-wall blanket of solid breeder concepts has been extensively evaluated in several designs, particularly the STARFIRE[1], INTOR[2], and UWMAK-II[4] designs. Conclusions from these studies in addition to results generated in the fusion materials alloy development program indicate that austenitic stainless steel is the primary candidate structural material. Ferritic steels are considered as the backup structural material. Vanadium-base alloys, which are considered to be attractive structural materials for liquid metal blankets, may not be acceptable because of compatibility limitations with Li_2O and potentially excessive tritium permeation rates for water-cooled systems. Table 4-13 lists

Table 4-13. Alloy Systems That Have Been Eliminated as Prime Candidate First-Wall/Blanket Structural Materials.

ALLOY	PRIMARY LIMITATIONS
Aluminum	Poor mechanical properties at elevated temperature. Loss of ductility caused by high transmutation rates under irradiation (He, H). Compatibility with liquid metal breeder.
Molybdenum	Difficult fabrication/welding Effect of radiation on DBTT
Nickel	Loss of ductility under irradiation Compatibility with liquid metal breeder
Titanium	Hydrogen interactions Phase stability under irradiation Low thermal conductivity
Niobium	Generally less desirable than vanadium. Loss of ductility under irradiation. Long-term activation Resource limitations

other structural materials that have been considered or proposed in various designs and the primary reasons these alloys have been eliminated as candidate structural materials for the DEMO design. Table 4-14 summarizes the important favorable and unfavorable characteristics of austenitic stainless steel (primary candidate alloy - PCA) and the commercial ferritic steel (HT-9).

The radiation damage resistance of advanced austenitic stainless steel (PCA) appears to be adequate for the water-cooled solid breeder blanket concepts. Structure temperatures in a water cooled system are below the temperatures where severe displacement damage embrittlement, helium embrittlement and maximum swelling occur. Also, the mechanical properties are not substantially reduced at these temperatures. Steady-state reactor operation is im-

Table 4-14. Favorable and Unfavorable Characteristics of Prime Candidate First-Wall Structural Alloys.

ALLOY SYSTEM	FAVORABLE CHARACTERISTICS	UNFAVORABLE CHARACTERISTICS
Austenitic Stainless Steels (316, PCA)	Good fabricability/welding ability Extensive property data-base Availability/experience factor Compatible with H_2O, Air, H	Physical Properties (k,α) Limited operating temp-erature (radiation effect and mechanical properties) Requires thermomechanical treatment (cold-work)
Ferritic steels	Low radiation swelling Better physical proper-ties than austenitic steel Compatible with H_2O, Air, H	Effect of radiation on DBTT Welding difficulties (PWHT) Sensitivity to TMT Ferromagnetic property Limited radiation data base

portant for acceptable wall lifetimes because of the relatively high thermal stress factor associated with stainless steel. The fact that solid breeder materials also have a limited lifetime because of Li burnup reduces the incentive for a very long lifetime structure.

4.3.3.2 Stress Analysis

An important aspect of the first wall design with pressurized water coolant is the coolant channel configuration. Four options have been analyzed for stress in the present report: (1) grooved channel in the back of the first wall covered with a flat plate, (2) solid first wall with a corrugated panel in the shape of a sine wave, (3) solid first wall with a corrugated panel in the shape of an arc of a circle, and (4) solid first wall with a corrugated panel in the shape of a semi-circle.

The four configurations are compared for the same width (W). The sinusoidal panel and the circular arc panel are compared for the same width to height (W/h) ratio.

Analysis of a Flat Plate (thickness, h)

The maximum bending stresses for an internal pressure, p, are

$$\sigma_b = \mp \frac{p}{2} \left(\frac{W}{h}\right)^2 \qquad (4\text{-}1)$$

and the maximum primary shear stress is

$$\tau = \frac{3}{4} p \left(\frac{W}{h}\right) \qquad (4\text{-}2)$$

If the average temperature of the first wall exceeds that of the flat plate by ΔT, the membrane stress in the flat plate (assuming that the first wall is rigid compared to the plate) is

$$\sigma_m = E\alpha\Delta T \qquad (4\text{-}3)$$

where

E = elastic modulus of the plate, and

α = coefficient of thermal expansion of the plate.

Analysis of a Sinusoidal Panel

The sinusoidal panel has been analyzed in the same fashion as reported in [1] except that the contribution of shear strain energy which was neglected in [1] is taken into account in this report. Only the final results are given here. The maximum primary membrane stress (P_m) intensity due to internal pressure occurs at the midpoint (A) of the corrugation and is given by

$$\sigma_m^{(A)} = \frac{2pR}{h} (1 - \text{Cos } \beta) \frac{X}{Y} \tag{4-4}$$

where

$$\beta = \text{Cos}^{-1} \left[\frac{1 - 4 (H/W)^2}{1 + 4 (H/W)^2}\right],$$

$$R = \frac{W [1 + 4 (H/W)^2]}{16 (H/W)},$$

$$X = \frac{\beta - \text{Sin } \beta}{Eh} + \frac{3}{2} \frac{\beta + \text{Sin } \beta}{Gh} + \frac{12R^2}{Eh^3} (\beta + \text{Sin } \beta - 2\beta \text{ Cos } \beta)$$

$$Y = \frac{2\beta + \text{Sin } 2\beta}{Eh} + \frac{3}{2} \frac{2\beta - \text{Sin } 2\beta}{Gh} + \frac{12R^2}{Eh^3} (4\beta + 2\beta \text{ Cos } 2\beta - 3 \text{ Sin } 2\beta),$$

G = shear modulus of the panel.

The maximum primary membrane plus bending stress intensity ($P_L + P_B$) occur at the edges (C) where the panel is roll bonded to the first wall. The membrane stress is given by

$$\sigma_m^{(C)} = \sigma_m^{(A)} - \frac{2pR}{h} (1 - \text{Cos } \beta) \tag{4-5}$$

and the maximum bending stresses are given by

$$\sigma_b^{(C)} = \mp \frac{6pR^2}{h^2} \left[-1 + \frac{\text{Sin } \beta}{\beta} + 3 (1 - \text{Cos } \beta) - 2 (1 - \text{Cos } \beta)^2 \frac{X}{Y}\right] \tag{4-6}$$

The primary shear stress is given by

$$\tau^{(C)} = \frac{2pR}{h} \text{ Sin } \beta = \frac{1}{2} p \frac{W}{h} \tag{4-7}$$

If the average temperature of the first wall exceeds that of the panel by ΔT, the maximum thermal stresses occur at the edge and the center of the panel. However, the total primary plus secondary stress is maximum at the edge where the panel is roll bonded to the first-wall.

The membrane thermal stess is

$$\sigma_m = 4E\alpha\Delta T \frac{\text{Sin } \beta}{Eh}/Y \tag{4-8}$$

and the maximum thermal bending stress is

$$\sigma_b = \pm \sigma_m \frac{R}{h} (1 - \text{Cos } \beta) \tag{4-9}$$

Analysis of a Circular Arc Panel

As in the case of the sinusoidal panel the maximum primary membrane stress occurs at the center (A) of the panel and is given by:

$$\sigma_m^{(A)} = \frac{pR}{h} \left[1 - \frac{4 \text{ Sin } \beta}{Z}\right] \tag{4-10}$$

where

$$Z = 2\beta + \text{Sin } 2\beta \pm \frac{3}{2} \frac{E}{G} (2\beta - \text{Sin } 2\beta) + 12 \frac{R^2}{h^2} (2\beta + \text{Sin } 2\beta - \frac{4 \text{ Sin}^2 \beta}{\beta})$$

β is defined after Eq. 4 and R is the radius of the circular arc. The maximum primary bending plus membrane stress occurs at the edge (C) of the panel where it is bonded to the first wall. The primary membrane stress is given by

$$\sigma_m^{(C)} = \sigma_m^{(A)} \text{ Cos } \beta + \frac{pR}{h} (1 - \text{Cos } \beta) \tag{4-11}$$

and the primary bending stress is given by

$$\sigma_m^{(C)} = \mp \left[24p \frac{R^2}{h^2} \frac{\text{Sin } \beta \ (1 - \text{Sin } \beta/\beta)^2}{Z} + \frac{6pR}{h^2}(1 - \text{Cos } \beta) - 6 \sigma_m^{(A)} \frac{R}{h}(1 - \text{Cos } \beta)\right] \tag{4-12}$$

and the primary shear stress is

$$\tau^{(C)} = \frac{1}{2} p \frac{W}{h} \tag{4-13}$$

As in the case of the sinusoidal panel, the thermal membrane stress at the edge of the panel is given by

$$\sigma_m^{(C)} = 2E\alpha\Delta T \text{ Sin } 2\beta/Z \tag{4-14}$$

and the bending stress at the edge of the panel is

$$\sigma_b^{(C)} = \mp 24E\alpha\Delta T \frac{R}{h} \left[\text{Sin } \beta \left(1 - \frac{\text{Sin } \beta}{\beta}\right)/Z - \text{Sin } \beta \ (1 - \text{Cos } \beta)/Z\right] \tag{4-15}$$

and the maximum shear stress at the edge due to thermal loading is

$$\tau^{(C)} = 6E\alpha\Delta t \text{ Sin}^2 \beta/Z \tag{4-16}$$

Analysis of a Semicircular Panel

All the stresses for this case are obtained by substituting $\beta = \pi/2$ in Eqs. 10-16.

Results and Conclusions

The maximum stress intensity at any point is defined by twice the maximum shear stress at that point. The maximum primary stress intensity (P_m) as a function of the panel wall thickness for unit pressure is plotted in Fig. 4-18 for the four geometries and for three values of the width (W). The width to height ratio of (W/h) for the sinusoidal and circular arc panels are taken as 4.0. Note that the lowest primary membrane stress occurs for the semicircular case. For widths greater than 10 mm and thicknesses less than 4 mm the primary membrane stress in the circular arc is less than that in either the flat plate or the sinusoidal panel. For small widths ($W \lesssim 5$ mm) the difference between the four geometries is small. Since the maximum coolant pressure p = 15 MPa, the primary membrane stresses are rather small particularly for widths $\leq$ 10 mm, and the primary stress intensities are less than the allowable S_m values for either annealed or cold-worked type 316 SS. Fig. 4-19 shows a plot of the maximum primary local membrane plus bending stresses for the various cases. For small widths ($\sim$ 5 mm) both the flat plate and the sinusoidal panel have the minimum stress. However, the difference between the various geometries is not large. For larger widths and smaller thicknesses, bending predominates, and as expected, the semicircular panel provides the lowest stress intensity and the flat plate the highest stress intensity. The 5 mm width panels of all four geometries satisfy the 1.5 S_m requirement of either annealed or cold worked type 316 SS for all thicknesses considered. The same is true for 10 mm wide panels provided the thickness is greater than 2.5 mm.

Fig. 4-20 shows the variation of maximum thermal stress for a difference of ΔT in the average temperatures of the first wall and the panel. Again, as expected the semicircular panel provides the lowest stress followed by the flat plate and the sinusoidal panel. The circular arc panel experiences the largest thermal stess at the points of attachment to the first wall due to bending. Fig. 4-21 gives a plot of the total primary plus secondary stress for panels of width 10 mm and for $\Delta T = 100^0C$ and $\Delta T = 50^0C$. The figure also shows the allowable 3 S_m limits for both annealed and cold- worked type 316 SS. Note that whereas the 3 S_m limit for the cold-worked material is satisfied by all geometries at both temperatures, the annealed material is acceptable only for the semicircular panel. For a ΔT of 50°C the flat plate

and sinusoidal panels also satisfy the 3 S_m limit of annealed 316 SS for all thicknesses considered. Although from the viewpoint of stress the semicircular panel is the most desirable, consideration of cooling efficiency and cost of fabrication might indicate the sinusoidal panel to be the optimum choice.

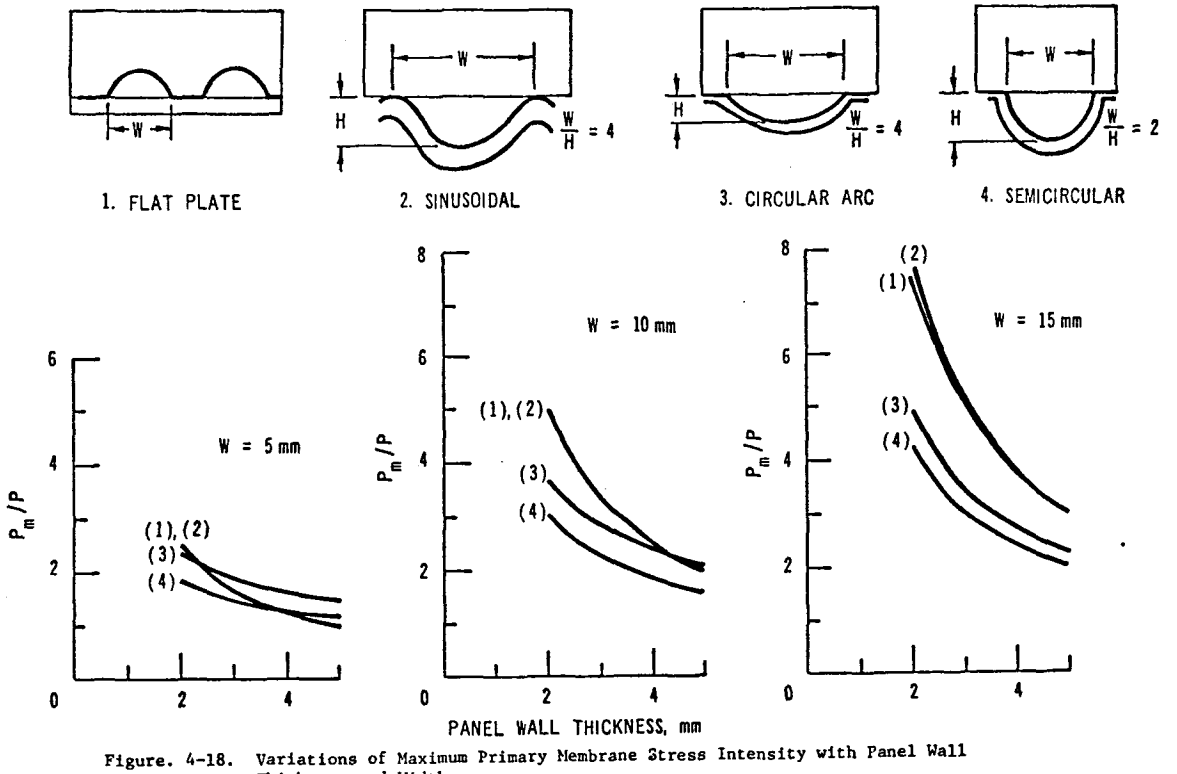

Figure. 4-18. Variations of Maximum Primary Membrane Stress Intensity with Panel Wall Thickness and Width.

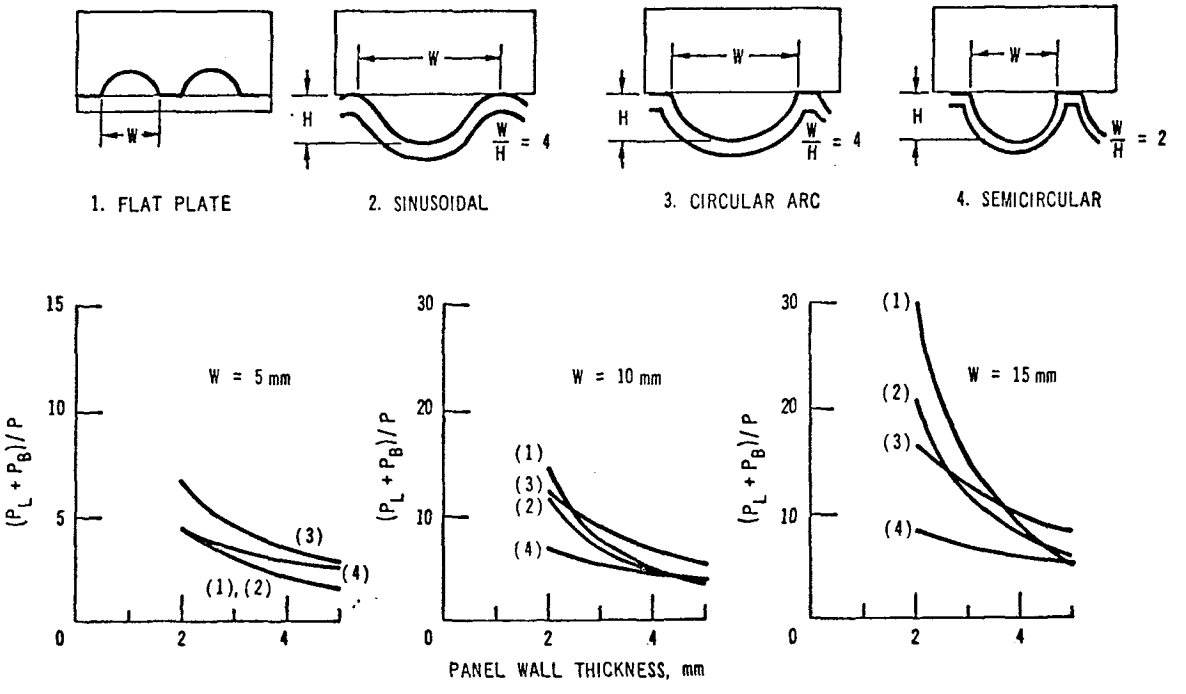

Figure 4-19. Variation of Maximum Primary Membrane Local Plus Bending Stress Intensity with Panel Thickness and Width.

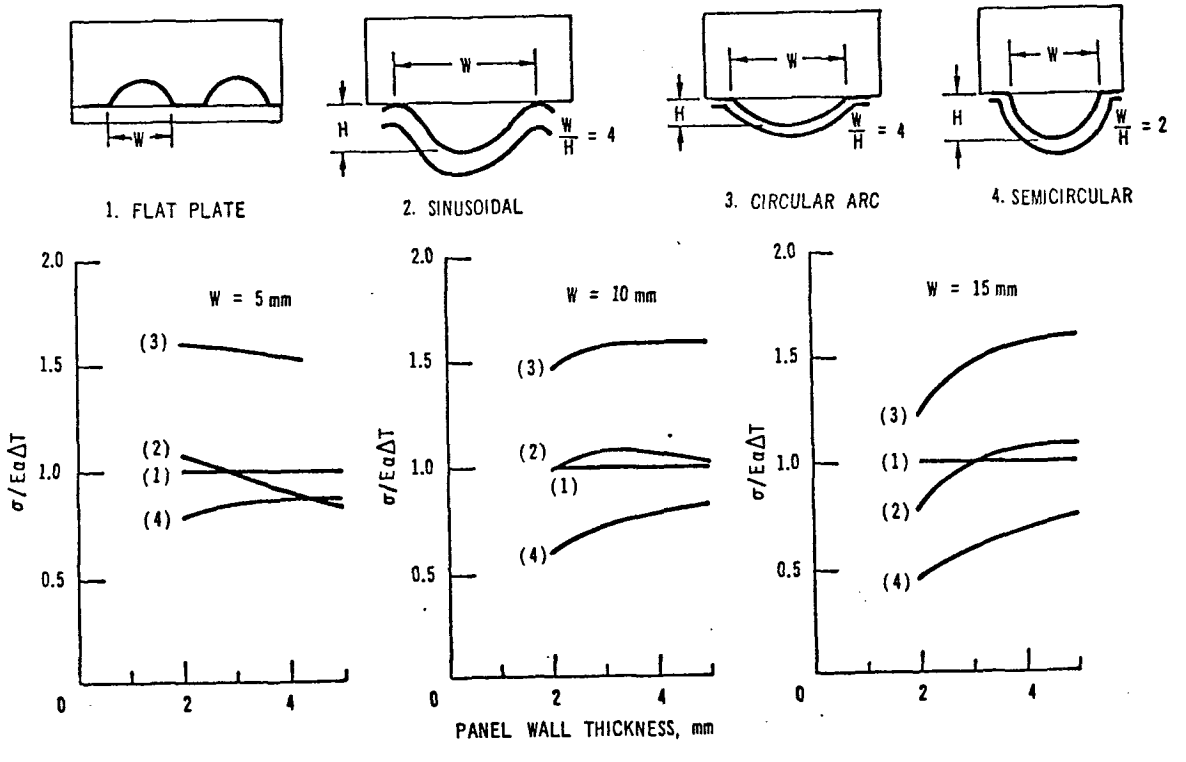

Figure 4-20. Thermal Stress in the Panels as a Function of Panel Width and Thickness.

4.3.3.3 Thermal Hydraulics Analysis

The first wall design is based on the use of coolant panels as shown schematically in Fig. 4-22. It may be noted that in contrast to STARFIRE [1] design studies, the corrugated surface of the coolant panels are assumed to face away from the plasma direction. This makes thermal hydraulic modeling of the high flux region (essentially a flat plate) simpler and, possibly, the application of a low-Z coating (e.g., Be) easier. To evaluate the design problems associated with pressure stresses and thermal stresses (for steady-state operation), a detailed thermal hydraulics analysis was not necessary. For an operating range of coolant temperatures (T_{in} = 260°C, T_{out} = 300°C) and pressure (10.34 MPa, 1500 Psia), the internal conditions of the coolant panels (e.g., temperature) are fixed. The temperature gradient across the coolant panels can be estimated based on ~ 50°C/MW/mm for PCA stainless steel as the structural material.

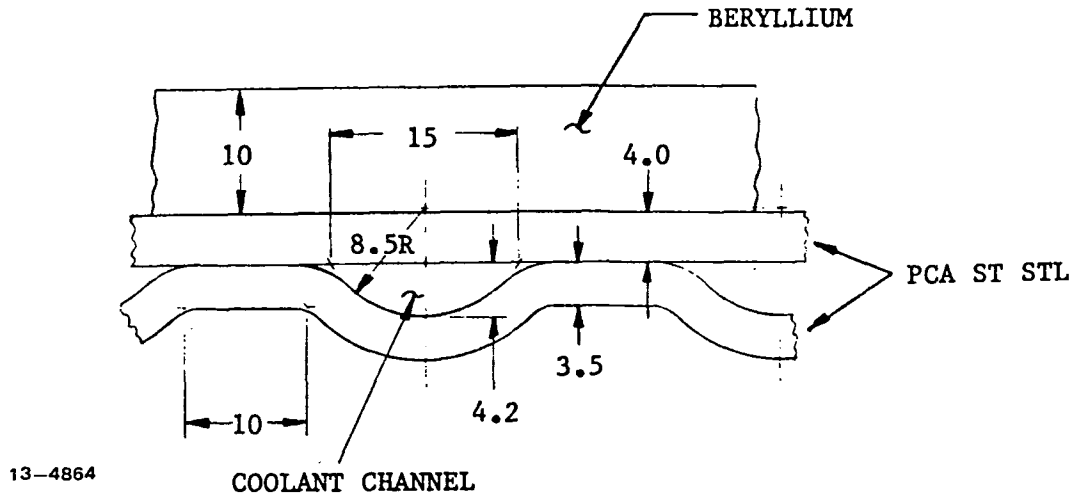

Figure 4-22. First wall configuration for Li_2O solid breeder reference blanket design. (All dimensions are in mm.)

4.3.3.4 Design Configuration

The first wall design configuration for the Li_2O solid breeder reference blanket is illustrated in cross section in Figure 4-22. It consists of two elements: (1) a 10-mm thickness of beryllium clad; and (2) a coolant panel consisting of a 4-mm flat plate welded to a 3.5-mm corrugated plate. The first wall is mechanically and structurally integral with the breeding blanket. First wall support and manifolding are included in the blanket description given in Section 4.3.9.

The coolant panel concept selected is very similar to that chosen for the STARFIRE reference design[1]. The rationale for its selection over other configurations parallels that for STARFIRE and will not be repeated here.

The beryllium clad, together with the protective beryllium coating in the limiter, acts as part of the impurity control system for STARFIRE/DEMO. It provides a single low-Z material covering all surfaces inside the plasma chamber which may undergo physical sputtering. Application of the beryllium to the flat stainless steel plate would be accomplished by plasma spraying or by explosive bonding of beryllium blocks to the panel. Both methods appear feasible, but further work is required. Grooving of the beryllium to relieve thermal stresses during normal operation does not appear to be necessary because the steady-state nature of STARFIRE/DEMO operation will subject the first wall to only a low number ($<10^4$) of thermal stress cycles. However, grooving may be desirable to reduce eddy currents and induced stresses during a plasma disruption.

The coolant channels are formed by resistance seam welding the corrugated and flat sheets together. The cross section of each channel is a circular chord segment, which provides adequate strength to contain the 11.0 MPa (1600 psi) coolant, while minimizing the amount of water coolant present in the first wall to keep tritium breeding as high as possible. The resistance weld which joins the sheets is considered to be the best weld type in terms of maintaining the radiation damage resistance level of the 20% cold worked PCA stainless steel.

4.3.4 Neutronics Analysis

4.3.4.1 Tritium Breeding

The solid lithium oxide (Li_2O), which has been one of the most extensively studied breeder materials for fusion reactor applications, possesses several salient advantages in comparison with other candidate tritium breeding materials. The high potential for tritium production, the possible elimination of neutron multiplier because of the high breeding capability, and low neutron-induced activation are among those favorable features associated with the use of Li_2O in fusion reactor designs. It should be noted, however, that whether blanket designs based on the use of Li_2O could eliminate the need of any additional neutron amplification for sufficient tritium production depends strongly upon the overall reactor design concept. The design considerations that must be taken into account in this regard include: (1) whether the inboard blanket is used for tritium breeding; (2) how much of the outboard blanket volume must be set aside for the impurity control system (e.g., divertor or limiter) and the plasma heating system, and (3) first wall/blanket design details such as the thickness of the first wall and amount of structure and coolant in the blanket. The neutronics effort in this section is, therefore, devoted to scoping the tritium breeding capability of Li_2O blanket designs so that one can identify the impact or constraints on these pertinent design considerations.

The neutronics model used for the analysis is the same as that described in Section 4.2.4; namely, a full coverage, one-dimensional model. The 13.4 mm-thick 316 SS-base armor is cooled by light water (3-mm thick region) which is separated from the breeding blanket by a 3-mm thick corrugated 316 SS panel. The breeding blanket is neutronically represented by a homogeneous mixture, (90 V/O Li_2O + 5 V/O 316SS + 5 V/O H_2O). Li_2O is assumed to be 70% of the theoretical density including the design porosity for tritium extraction. Fig. 4-23 displays the tritium BR as a function of ^6Li enrichment for two armor designs; (1) 13.4 mm thick bare 316 SS armor; and (2) 3.4 mm thick 316 SS armor coated by 10 mm thick beryllium. It is found that for both armor designs in the absence of a neutron multiplier, the natural lithium systems result in the highest BR's. The substantial decrease in the ^7Li (n, n'α)t reaction with fewer ^7Li atoms is the reason for lower BR at higher ^6Li enrichment. The result shown in Fig. 4-23 is consistent with the

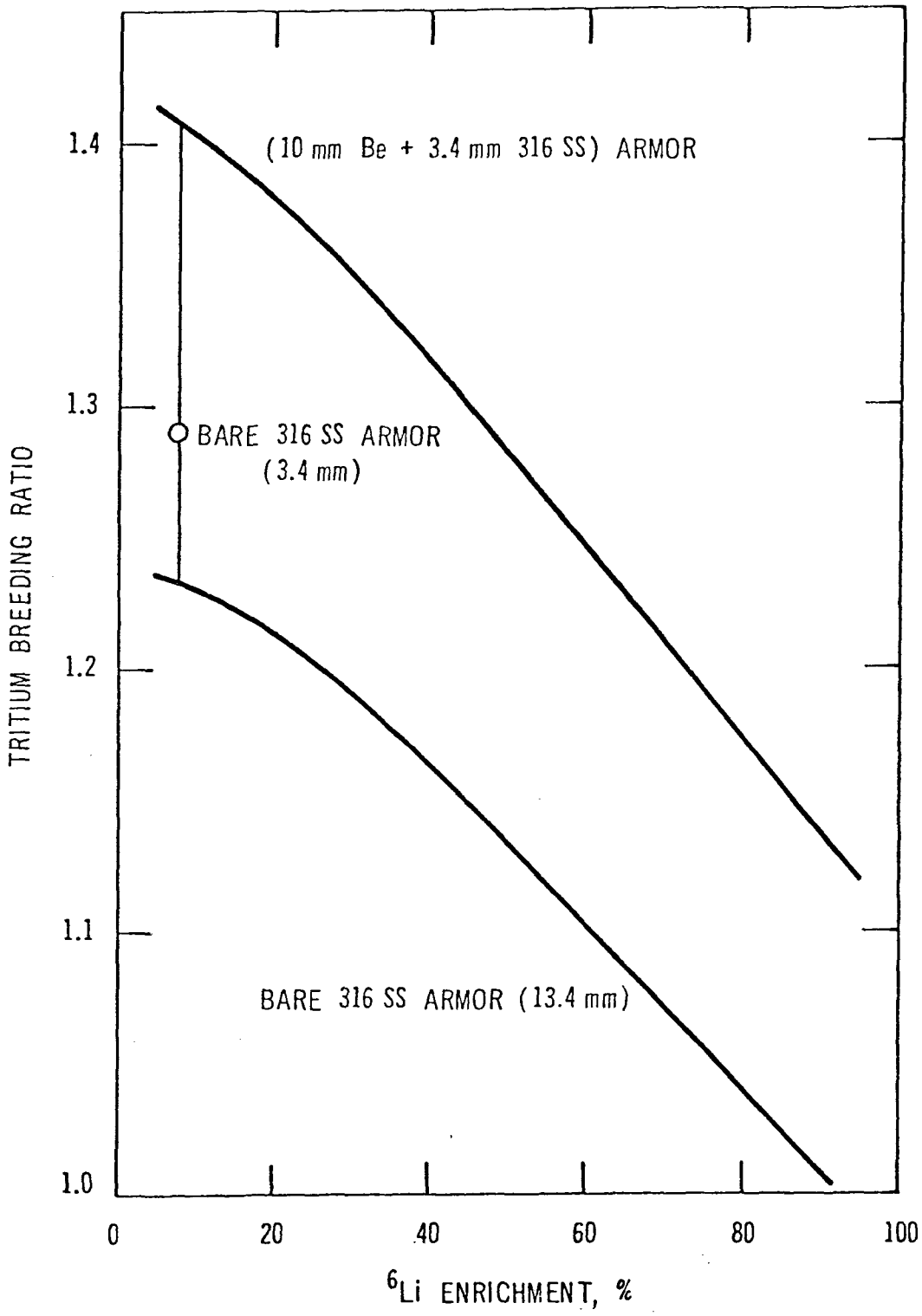

Figure. 4-23. Effect of ^{6}Li Enrichment Upon Tritium Breeding for Li_2O Breeder Blanket Designs.

analysis of Ref. 77B. At the reactor start-up, the bare-armor system can yield a BR of about 1.23 which would increase to about 1.29 after the first 10 mm thickness of 316 SS has eroded. In the case of the Be armor design, the initial BR is significantly higher than the bare-armor case (1.41 vs. 1.23), but the BR will eventually drop significantly as the beryllium is eroded. The breeding gain in the Be-coated system results from (1) an increase in the $^{7}Li(n,n'\alpha)t$ reaction rate due to the thinner 316 SS armor and (2) an increase in the $^{6}Li(n,\alpha)t$ reaction rate due to the neutron amplification by the Be(n,2n) reaction. For example, the Be(n,2n) reaction rate for the case with natural lithium shown in Fig. 4-23 amounts to about 0.18 per fusion neutron.

The impact of a non-breeding inboard blanket design upon the tritium production rate was examined by replacing the inboard blanket composition by (95 V/O 316 SS + 5 V/O H_2O). The result is shown in Table 4-15 and compared to the case of the full breeding blanket design. The analysis is based on a one-dimensional infinite cylinder model in which the toroidal axis of the reactor is taken as the cylinder axis, and the inboard and outboard sub-regions as well as the central plasma region are represented by concentric annuli about the axis. The plasma major and minor radii are assumed to be 5.2 m and 1.3 m, respectively, and the plasma scrapeoff region size is taken to be 0.165 m on both sides of the plasma region.

Table 4-15 indicates that the reduction in the BR caused by the placement of the non-breeding inboard blanket amounts to about 26% relative to the full breeding coverage case. Although the analysis shown is based on a very approximate model, it is very likely that the net BR becomes less than unity with a complete lack of tritium production in the inboard blanket. In fact, the INTOR analysis[77D] which has been performed for a similar Li_2O blanket design by making use of a three-dimensional Monte-Carlo model shows that the complete elimination of the inboard breeding results in a BR of only about 0.97 compared to a BR of 1.28 for the 100% breeding surface coverage. The effect of partial tritium breeding in the inboard blanket is examined in Fig. 4-24 which shows the relationship between the fraction of non-breeding zone in the outboard blanket and the required inboard breeding zone thickness. The relationship is shown for several net BR's of practical interest. The nonbreeding fraction shown in Fig. 4-24 is defined as the ratio of a nonbreeding zone volume (or its area at the armor surface) to the total

Table 4-15. Effect of Inboard Tritium Breeding for DEMO/Li_2O Breeder Blanket Designs[a]

		Case A	Case B
(1)	Inboard Blanket		
	Structure	316 SS (5%)	316 SS (95%)
	Coolant	H_2O (5%)	H_2O (5%)
	Breeder	Li_2O[b] (90%)	--
(2)	Tritium Breeding		
	T_6	0.927	0.693
	T_7	0.293	0.209
	Total BR	1.220	0.902
		(1.234)[c]	

[a]Armor: 13.4 mm 316 SS

First Wall: 3.0 mm H_2O
3.0 mm 316 SS Plate

Outer Blanket: 666 mm (90% Li_2O[b] + 5% 316 SS + 5% H_2O)

[b]Li_2O: Natural lithium; 70% of theoretical density

[c]One-dimensional infinite-cylinder calculation without toroidal curvature effect

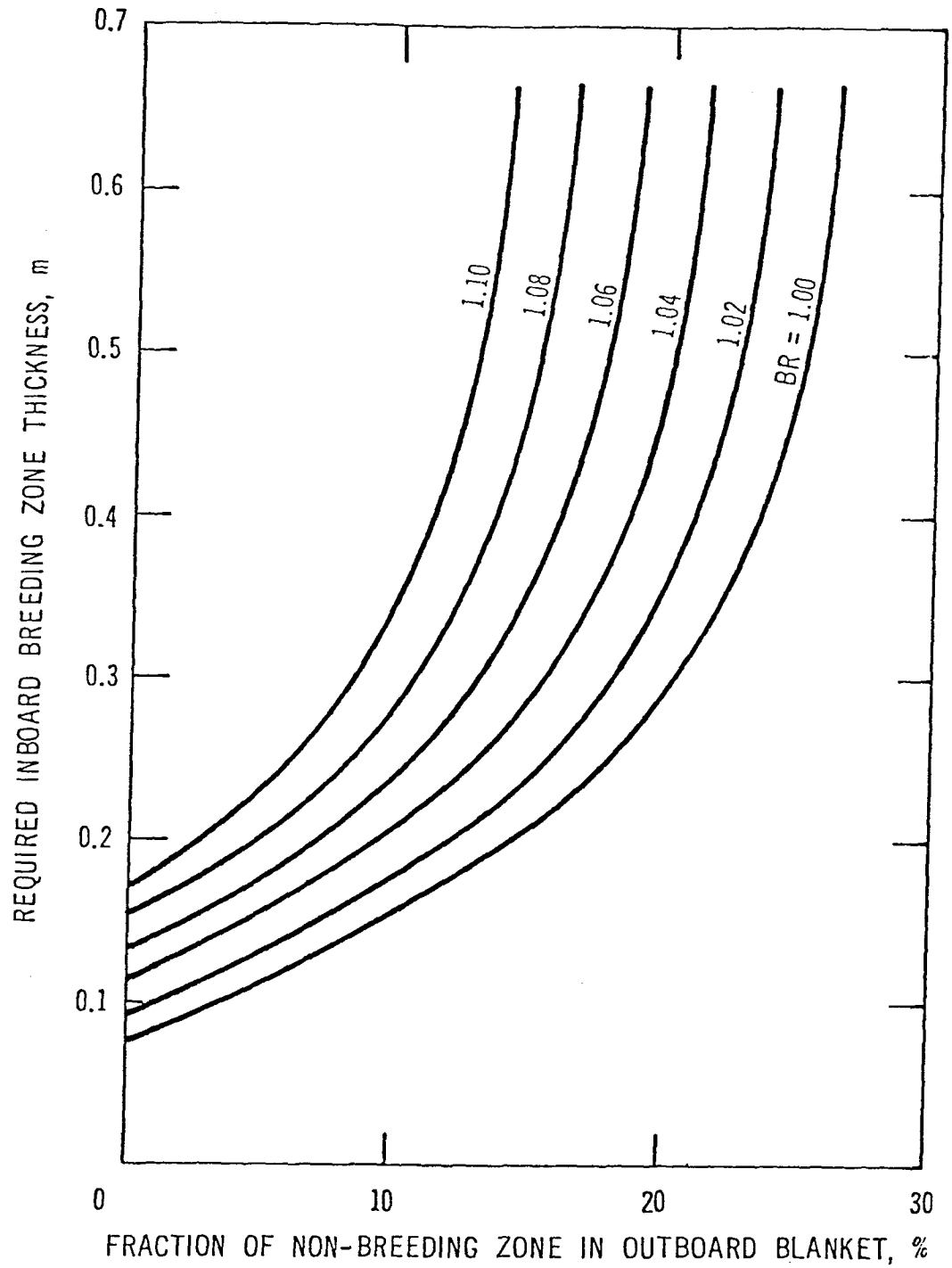

Figure 4-24. Impact of Non-Breeding Zone in Outboard Blanket Upon Inboard Breeding Requirement for Li_2O Breeder Blanket Designs.

outboard volume (or its surface area). The non-breeding zones considered include several major penetrations such as the limiter opening (or divertor slot) for impurity control and the REB duct for plasma heating. The result of Fig. 4-24 indicates that the non-breeding fraction must be less than 15-25% at most for a wide range of the net BR requirement. The implication is that it is quite difficult for self-sufficient fuel production, and in the absence of a neutron multiplier, to implement too large an outboard space allowance, e.g., an allowance for a divertor system which could take up about 20-30% of the outboard region. In the case of accommodation of a limiter opening as well as an REB duct, which is expected to result in a nonbreeding fraction of about 15%, the inboard breeding zone thickness required for a net BR criterion of 1.0 to 1.08 is estimated to be about 0.2 m to 0.65 m. It appears that such a thick inboard breeding blanket has a non-trivial impact on the required thickness for the inboard radiation shielding. The increase in the inboard distance from the first wall to the magnet, Δ^{i}_{BS}, will be roughly 40% of the breeding blanket thickness. This is a large penalty since the fusion power decreases by ~ 1% for every one centimeter increase in Δ^{i}_{BS} assuming fixed maximum magnetic field and plasma beta.

The tritium breeding can be enhanced by use of neutron multipliers. The breeding enhancement has two obvious impacts on the design: (1) the potential for a complete elimination or substantial curtailment of the inboard breeding, and (2) a substantial reduction of breeder material inventory as well as the associated tritium inventory. Table 4-16 shows the effect of a beryllium multiplier on tritium breeding for two different blanket material layouts. System B is regarded as a more or less conventional design in which the multiplier is placed in front of the Li_2O breeder zone. In System A the beryllium multiplier zone is sandwiched by two Li_2O regions as studied in the UWMAK-II design.[4] Both Systems A and B employ an 80 mm thick Be zone (100% of the theoretical density) without internal coolant and a Li_2O breeder with 30% enriched ^{6}Li. System B yields a BR of about 1.36, which is about 0.13 greater than the case without a multiplier, whereas System A enhances the tritium production by more than 0.32. The substantial breeding enhancement in System A stems largely from the blockage of neutron reflection into the armor/first-wall region thereby drastically decreasing the parasitic neutron loss in this pre-blanket region. In fact, the BR in the first bank alone (40 mm thick) in System A amounts to about 0.71, which is slightly below one-half

Table 4-16. Effect of Blanket Material Selection Near the First Wall upon Tritium Breeding

	System A	System B
(1) Material Layout		
Bank 1 (4 cm)	Li_2O[a]	Be[b]
Bank 2 (4 cm)	Be[b]	Be[b]
Bank 3 (4 cm)	Be[b]	Li_2O[a]
Bank 4 (54.56 cm)	Li_2O[a]	Li_2O[a]
(2) Tritium Breeding		
T_6	1.410 (0.646[c])	1.249
T_7	0.146 (0.068)	0.109
Total BR	1.556 (0.714)	1.358
(3) Neutron Balance/DT		
Net Current into Blanket	0.997	0.652
Reflection at Interface[d]	0.549	0.812
Net Loss in Pre-Blanket	0.003	0.348
Neutron Multiplication in Be	0.520	0.727
Leakage to Shield	0.0057	0.0057

[a] Li_2O: 5% SS + 5% H_2O + 90(63)% Li_2O [30% ^6Li enrichment]

[b] Be: 100% Be

[c] Bank 1 BR only

[d] J^-/J^+ at the interface between the first wall and blanket

of the total BR. In the case of System B, a majority of the secondary neutrons generated by the Be (n,2n) reaction, which are more than in System A, tend to be lost in the preblanket region due to the strong neutron back-flow. As shown in Fig. 4-25, the blanket designs based on the concept of System A can yield a continuously increasing BR with thicker multiplier while the conventional designs based on the System B configuration show a maximum BR at a beryllium thickness of about 50mm. The breeding performance of the blanket designs based on the former concept is not significantly influenced by the material choice in the region following the second Li_2O breeder zone. Table 4-17 compares the tritium BR for five material choices (primary constituents of (1) Li_2O breeder itself, (2) graphite, (3) silicon dioxide, (4) stainless steel, and (5) a combination of graphite and stainless steel) in this deep blanket region. The result of Table 4-17 along with the result of Fig. 4-26 which displays the accumulation of bred tritium, indicates that the required breeding blanket thickness can be substantially reduced by making use of any of these material compositions. For example, the system of Case 5, which has a graphite reflector followed directly by a 316 SS-base shield, can yield a BR of about 1.35 with a breeder zone thickness of only 120 mm. Assuming a full breeding blanket coverage and a first wall surface of about 400 m^2, this system has a breeder (Li_2O) inventory of about 60 MT and a pure lithium (30% ^6Li enriched) inventory of about 18 MT. These figures are compared to the α-$LiAlO_2$ inventory of about 605 MT and the lithium (60% ^6Li enriched) inventory of about 64 MT in the STARFIRE [1] design which yields a net BR of 1.04 (1D-BR of 1.21). The surface area of the first wall in STARFIRE is about a factor of two larger than that in the DEMO; therefore, the difference in the blanket concept alone results in more than 40% reduction in the lithium inventory.

One of the concerns associated with the use of a Be multiplier is the possibility of tritium production in Be because the threshold energy for the Be (n,t) reaction is 11.6 MeV and the cross section amounts to about 20 mb around the source neutron energy. The relatively long half-life (approximately 12.3 yr) of tritium leads to a continual increase of tritium inventory in the multiplier region without saturation, over the entire life-time of the DEMO plant. For example, at an integral wall load of 10 MW-yr/m^2 after reacter start-up, the tritium inventories become ~1.6 Kg, ~2.5 Kg, and and ~3.1 Kg for beryllium thicknesses of 40 mm, 80 mm, and

Table 4-17. Effect of Material Selection in Deep Blanket Region upon Tritium Breeding

Bank 1 (4 cm)	Li_2O[a]
Bank 2 (8 cm)	Be
Bank 3 (8 cm)	Li_2O[a]
Bank 4 (46.56 cm)	X

	Material in Bank 4				
	Li_2O[a]	C[b]	SiO_2[c]	Shield[d]	C[c,e]/Shield[d]
(1) Tritium Breeding					
T_6 BR	1.410	1.250	1.242	1.209	1.243
T_7 BR	0.146	0.108	0.107	1.106	0.107
Total BR	1.556	1.358	1.349	1.315	1.350

[a] 90% Li_2O + 5% SS + 5% H_2O

[b] 90% C + 5% SS + 5% H_2O

[c] 90% SiO_2 + 5% SS + 5% H_2O

[d] 90% SS + 10% H_2O

[e] 12 cm C[b] + 34.56 cm Shield[d]

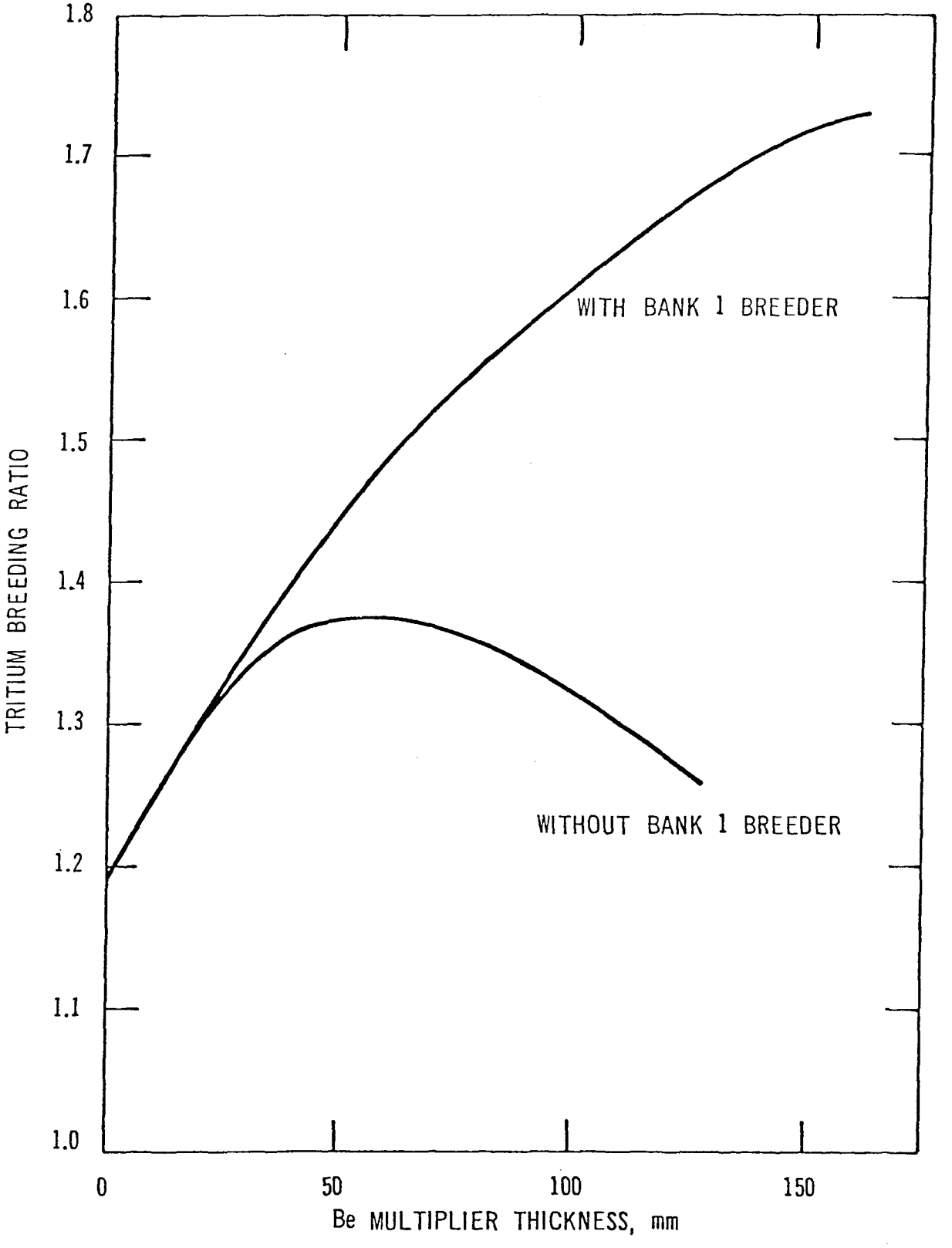

Figure 4-25. Effect of First-Bank Material Selection Upon Tritium Breeding for Be Multiplier/Li_2O Breeder Blanket Designs.

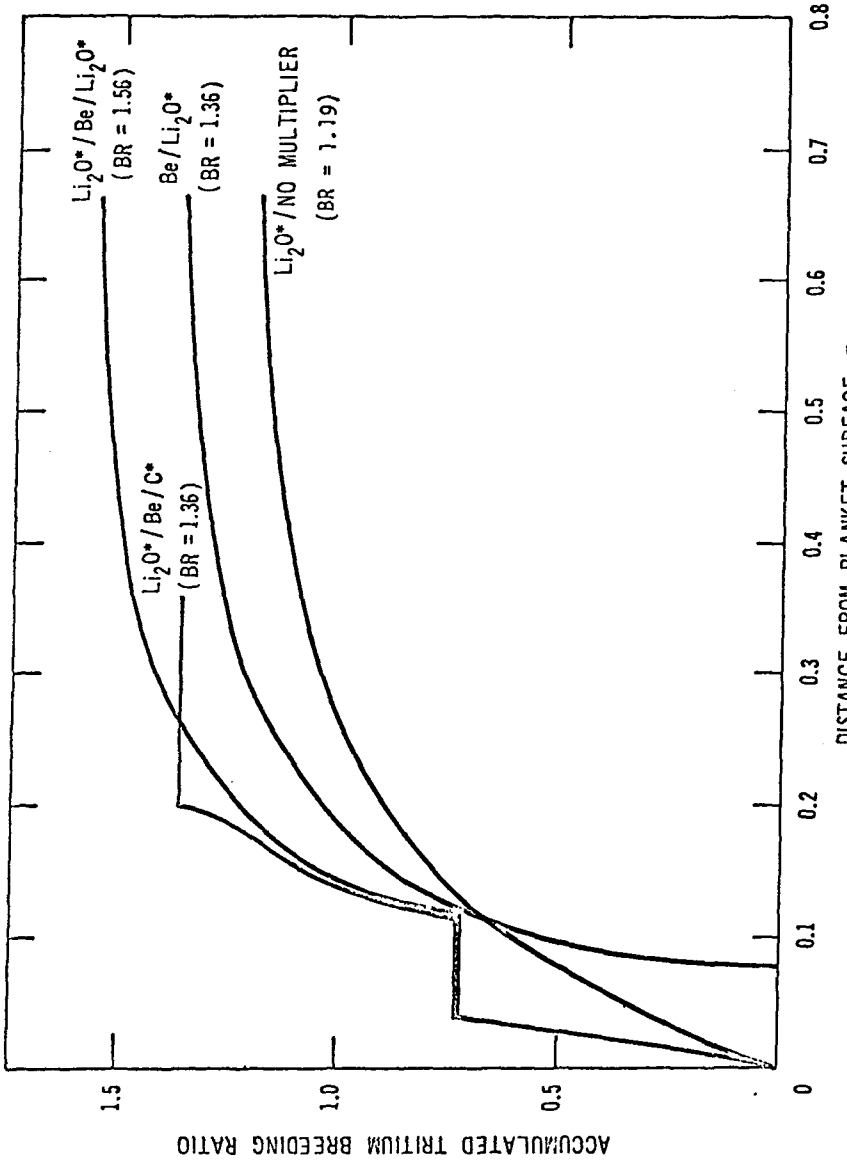

Figure 4-26. Accumulation of Tritium Breeding Ratio in Li_2O Breeder Blanket Designs.

Li_2^*: 90% Li_2O + 5% SS + 5% H_2O

C*: 90% C + 5% SS + 5% H_2O

Li_2O: 70% of theoretical density; 30% ^6Li enrichment

Be: 100% of theoretical density

120 mm, respectively, in a System A blanket design described in Table 4-15. The estimate is based on a total fusion power of 900 MWth. The inventory shown is expected to be on the same order of magnitude as the anticipated steady-state tritium inventory in the Li_2O blanket. Provisions for removal of the tritium from the beryllium region are, therefore, warranted in such a design. Another concern with the use of beryllium, and neutron multipliers in general, is the substantial increase in the heating rates and lithium burnup in the Li_2O regions adjacent to the multiplier.

Use of lead as a neutron multiplier was also considered during the course of the present study. However, the low melting point (327°C) of lead is of particular concern with its use in the high nuclear radiation environment. Based on a recent INTOR[2] study, the maximum temperature rise in a 50 mm-thick lead multiplier, for instance, is estimated to be about 190°C relative to the inlet coolant temperature for a given steel/lead gap conductance. Note that the neutron wall load and the outlet coolant temperature of the INTOR design are 1.3 MW/m^2 and 100°C, respectively, compared to 1.8 MW/m^2 and 300°C of the DEMO design. As a result the allowable lead thickness for DEMO is expected to be appreciably smaller than 50 mm unless a molten multiplier is assumed. From the neutronics standpoint, use of such a thin multiplier provides little incentive for enhancement of tritium breeding because the possible increase in BR by a lead multiplier is estimated to be only ~ 0.04 for every centimeter of lead.

4.3.4.2 Nuclear Heating and Activation Afterheat

Table 4-18 lists the zone averaged nuclear heating rate in each component of the preblanket region and the spatial variation of the Li_2O blanket heating. It is noted that the heating rate in most of the Li_2O breeder is less than that in the 316 SS structure and the H_2O coolant because of the low material density factor used (70% of the theoretical density) and the sizable amount of the endothermic ^7Li $(n,n'\alpha)t$ reaction rate. In addition, the heating rates are reduced by a factor of 100 or less for all the components, over the entire breeding blanket region. Note that the result shown in Table 4-18 does not account for the geometrical effects arising from the system toroidal curvature[77e] and the shifted neutron source distribution due to the MHD plasma equilibrium. According to the result of a recent INTOR work,[2] the nuclear heating shows a variation of more than 25% in the

Table 4-18. Spatial Variation of Nuclear Heating Rate (MW/m^3) for Li_2O Breeder System Design[a]

		316 SS	H_2O	Li_2O[b]
Armor (13.4 mm)		18.2	-	-
First Wall				
Coolant (3 mm)		-	16.7	-
Structure (3 mm)		16.5	-	-
Blanket				
At depth:	5 mm	15.5	15.0	13.4
	10 mm	15.0	14.3	12.4
	30 mm	13.0	12.1	9.84
	50 mm	11.4	10.4	8.33
	100 mm	8.20	7.07	5.79
	200 mm	4.31	3.33	2.94
	300 mm	2.29	1.55	1.49
	400 mm	1.23	0.715	0.739
	500 mm	0.670	0.329	0.365
	600 mm	0.382	0.154	0.187

[a]Neutron Wall Load: 1.8 MW/m^2

[b]Li_2O: 70% of theoretical density; natural lithium

poloidal direction due to these geometrical effects. It is likely that the outboard heating deep in the blanket region tends to be higher than what is predicted by the one-dimensional analysis shown here. A detailed three-dimensional analysis remains to be done for more precise evaluation of the nuclear heating rate as it affects the thermal hydraulic design.

After reactor shutdown, the 316 SS structure becomes the major source of the decay heating. Li_2O itself generates only a few short-lived radioactive isotopes such as ^{6}He (decay half-life of 0.8s; β- emmission), ^{8}Li ($\sim$ 0.8s; α and β-) and ^{16}N ($\sim$7s; α, β-, and γ) with the emission of the most dominant 6.1 MeV gamma ray. Although the radioactivities in the Li_2O breeder completely decay within a minute, some of the decay gamma rays generated in and transported from the 316 SS structure are deposited in Li_2O. Figure 4-27 presents the total decay power in the armor/first-wall/blanket region as well as the accumulated decay energy release in the blanket region as a function of post-shutdown time. The total decay power amounts to about 14.5 MW_{th} (approximately 1.6% of the total fusion power of 900 MW_{th}) at shutdown, being rapidly reduced to 2-3 MW_{th} within several hours after shutdown. It is found that the accumulation of the energy release exceeds 100 GJ at about 11 hr after shutdown. The maximum decay heating rates are about 0.7 MW/m^3 and 0.14 MW/m^3 in the 316 SS armor and the blanket, respectively. These figures are compared to the respective operating nuclear heating rates of 18.2 MW/m^3 and 13.6 MW/m^3 indicating that the maximum decay heating rate is only about 4% or less relative to that at normal operation. The analysis shown here will provide a useful information basis for the future safety analysis.

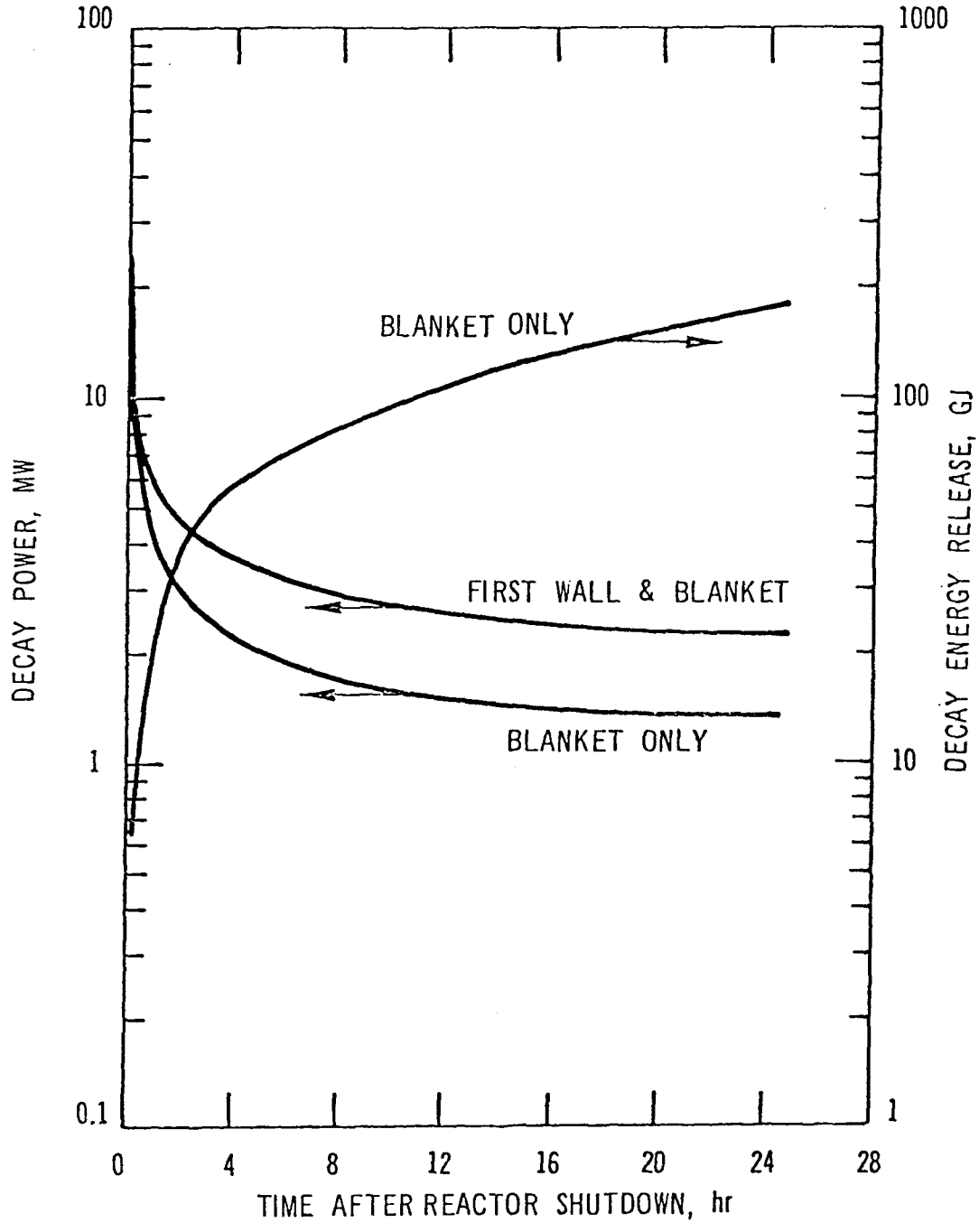

Figure 4-27. Activation Afterheat for Li_2O Breeder Blanket Design.

4.3.5 Properties of Li_2O

Lithium oxide and certain ternary lithium oxides are considered potentially viable tritium breeding materials. These materials have been the subject of a number of recent reviews [1, 47-50]. The materials property data base for Li_2O, although far from being sufficient for the needs of fusion, is rather extensive compared to that of other solid breeders. An excellent summary of the data base for Li_2O, with 31 references, was complied by Nasu [51] in late 1979. Recently, experimental programs at ANL [46, 52-54] and General Atomic Company [55] have generated a number of results which have significant implications regarding the use of Li_2O in fusion reactor blankets. Summarized below is an assessment of the current data base for Li_2O, with emphasis on certain key feasibility concerns: (1) physical properties, (2) fabrication, (3) thermochemical properties, and (4) radiation effects.

4.3.5.1 Physical Properties

As noted above, the data base for Li_2O has been summarized previously [51]. Selected properties of lithium oxide are listed in Table 4-19. Lithium oxide has a high lithium atom density and, therefore, has good tritium breeding capability. The operating temperature range, as discussed for STARFIRE [47-48] is estimated to be 410-660°C. In addition, Li_2O reacts exothermically with water to form LiOH. A key property with regard to blanket design is the thermal conductivity. Thermal conductivity for Li_2O of 70-93% theoretical density is shown in Fig. 4-28 [56].

Table 4-19. Selected Properties of Li_2O

Density, g/cm^3	2.01
Li atom density, g/cm^3	0.93
Melting point, °C	1430
Heat capacity, J/g K	2.6 @ 500°C
Enthalpy of hydrolysis, KJ/g	-3.9 @ 500°C

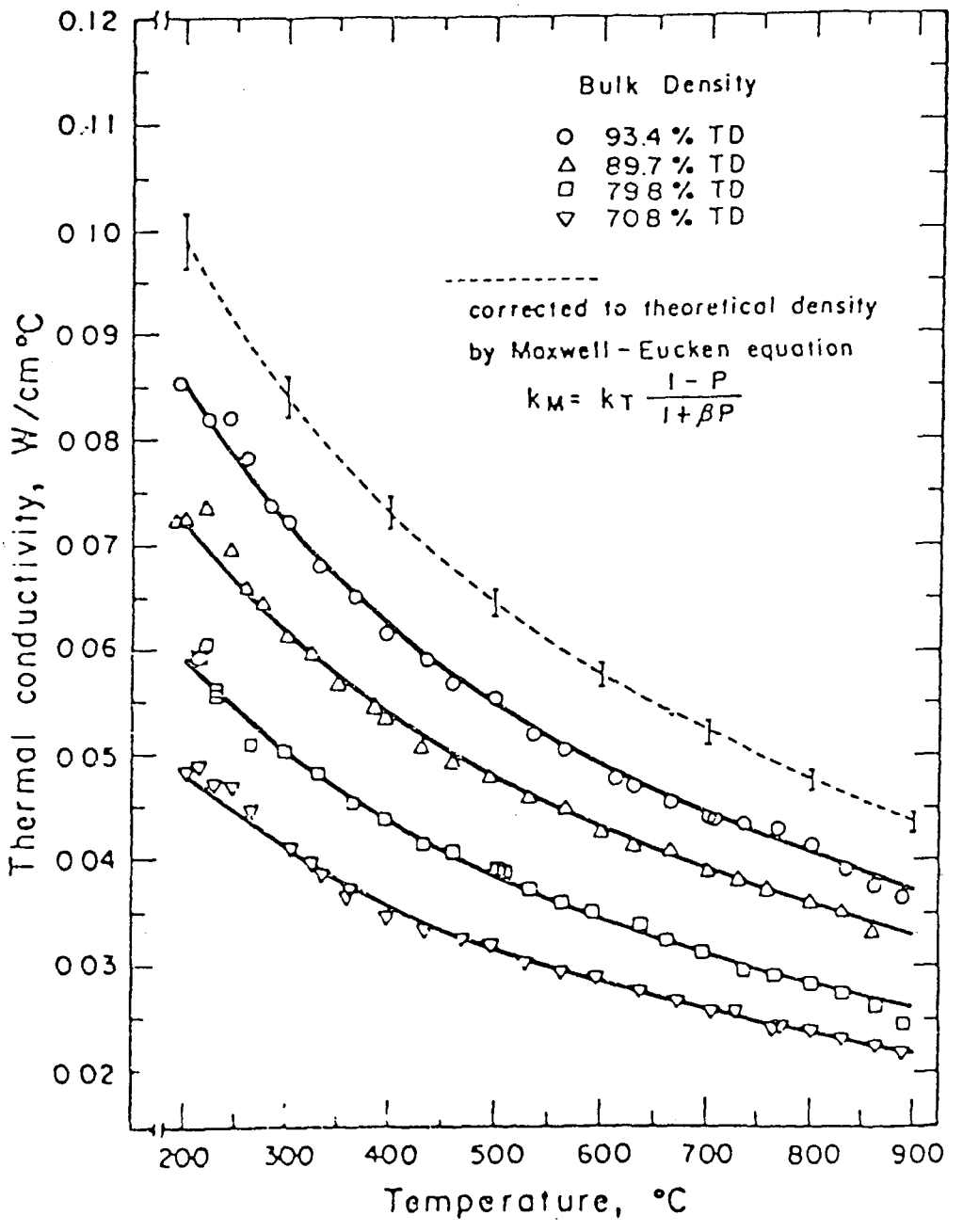

Figure 4-28. Thermal conductivity of Li_2O.[56]

4.3.5.2 Preparation/Fabrication

Preparation and fabrication of high purity Li_2O on a large scale for fusion reactor blanket applications is an important feasibility issue. One must not only be able to prepare high purity material but one must avoid contamination during handling, storage, and blanket assembly since the properties of Li_2O are very sensitive to material purity. This appears to be feasible on a laboratory scale but may be quite difficult on a large scale because of the high hygroscopicity of Li_2O and the fact that very small grain size with substantial porosity is essential for tritium recovery.

Either sintering or hot pressing are probably acceptable fabrication methods. Arons, et al [46] have demonstrated that sintered pellets of high purity Li_2O can be fabricated. However, the purity and microstructure of the pellets are quite sensitive to minor variations in procedures. Sintering in vacuum at ~ 1000°C for 4 h resulted in large weight loss of the pellet whereas heating in vacuum at 950°C prior to sintering in oxygen 4-6 h at 1050°C gave a density of ~ 80%. A reverse procedure, i.e., sintering in O_2 at 1050°C prior to heating in vacuum at 950°C, gave >95% dense material. Moisture pickup during handling or storage at room temperature is significant unless extreme precautions are taken. Because of these sensitivities, microstructure control in Li_2O may be difficult to achieve in practice, particularly on a large scale. Also, sintering temperatures may be quite low (possibly as low as 450°C) if significant amounts of LiOH are present. As a result, in-reactor sintering and grain growth may be a serious problem for Li_2O.

4.3.5.3 Chemical Properties of Li_2O

Lithium oxide is very hygroscopic, reacting readily with moisture to form LiOH. Li_2O also reacts with CO_2 in air to form Li_2CO_3. In addition, Li_2O reacts with a large number of metal oxides to form ternary oxides, e.g., $LiCrO_2$. Thus, samples of Li_2O obtained from commercial vendors or samples prepared in laboratories without the utmost care are likely to contain significant quantities of LiOH, Li_2CO_3, and cationic impurities. Reported chemical analysis of a number of Li_2O samples are given in Table 4-20. Commercially available material appears to have at least 2% by weight of each of LiOH and Li_2CO_3. Careful laboratory preparation has achieved rather pure material with 0.25% by weight of Li_2CO_3 and <0.1% by weight of LiOH [46].

Table 4-20. Impurity Content of Li_2O Samples

	wt % Li_2CO_3	wt % LiOH	Wppm Cations	Ref.
Vendor A[a]	12.6	6.9	--	57
Vendor B	2.1	--	--	57
Vendor C	4.8	--	--	57
Vendor D	--	1.8	--	46
Prep A[b]	--	--	1000 (Pt)	46
Prep B[c]	--	2.4	--	46
Prep C[d]	--	0.5	~ 10	46
Prep D[e]	0.25	--	~ 10	58
Prep E[f]	--	<0.1	--	59

[a]Exposed to air

[b]Decomposed Li_2CO_3 in Pt at 880°C - dark grey

[c]Decomposed Li_2CO_3, some exposure to air

[d]Decomposed Li_2CO_3, minimal exposure to air

[e]Decomposed Li_2CO_3, 21 days at 700°C plus 14 days at 750°C

[f]Heat treated impure Li_2O in dry (<5 ppm H_2O) flowing He stream, 600°C, ~ 2 hr.

Exposure of pure Li_2O to air will increase both the carbonate and hydroxide levels to about 2% by weight. Because of the corrosive nature of LiOH and Li_2CO_3 at elevated temperatures, preparation can introduce significant levels of metallic impurities, e.g., Prep A in Table 4-20 [46]. It appears that it is possible to obtain samples with cation impurities of less than 10 ppm [46, 58].

A key question regarding Li_2O is the tritium "solubility." As discussed in 1980 [1, 47-50], it was presumed that there is an equilibrium of the bred tritium between the solid and gas phases:

$$2\ LiOT(s) \rightleftharpoons T_2O(g) + Li_2O(s) \qquad (4\text{-}1)$$

and

$$K_p = \frac{P(T_2O)}{a^2_{LiOT}} \qquad (4\text{-}2)$$

where a_{LiOT} = the activity of LiOT. Previously, it was assumed that a_{LiOT} was equal to the concentration of tritium in the solid phase (Raoult's Law). However, recent experiments [52, 60] have shown that LiOH (also LiOT) is nearly insoluble in Li_2O, and thus a_{LiOT} in Eq. 4-2 is close to unity. Thus, the tritium "solubility" previously calculated to result in very high tritium inventories for Li_2O blankets is in fact low, so that tritium inventories due to "solubility" are no longer a major concern. Some experimental results of Tetenbaum [52] are given in Table 4-21.

Table 4-21. Tentative Values for the Solubility of LiOH in Li_2O (from Tetenbaum)

T,°C	ppm H_2O in He Carrier Gas	Wt. % LiOH		wppm H in Li_2O	
		Cooling	Reheating	Cooling	Reheating
650	500	*	*	*	*
850	65	0.0029	0.0024	1.2	1.0
950	110	0.0057	0.0053	2.4	2.2
980	500	0.0290	0.0310	12.3	13.1
990	285	0.0200	0.0120	8.4	4.9
995	40	0.0021	0.0038	0.9	1.6

*Moisture peaks not observed

Two trends (Table 4-21) were observed: (1) solubility of H_2O decreases with decreasing temperature, and (2) solubility appears to be proportional to the concentration (pressure) of H_2O in the gas phase. In a separate experiment by Nasu, an irradiated Li_2O sample in equilibrium with 48.5 Pa T_2O at 650°C had a tritium content of ~ 0.4 wppm [60]. For hydrogen, this would correspond to 0.1 wppm in the solid with 480 ppm H_2O in the gas phase. This appears to be consistent with the first trend noted above. This result also supports the assumption by Tetenbaum [52] that upon cooling a lithium oxide sample to

650°C, the observed moisture evolved is equal to the amount in solution at 850-995°C (Table 4-21). It is evident that tritium "solubility" in an Li_2O blanket will be small (<1 ppm).

Another important consequence of these results follows. Since LiOH (also LiOT) is nearly insoluble in Li_2O, the phase field can be represented in a manner previously described [61]. The curved line in Fig. 4-29 separating Li_2O from LiOH is the dissociation pressure of LiOH. During operation, the Li_2O breeder must be maintained at temperature and pressure conditions to the left of and below the LiOH dissociation pressure curve in Fig. 4-29. This criterion implies significant temperature and pressure constraints upon blanket operation. For example, if the T_2O pressure in any part of the blanket is 160 Pa (1.2 torr), a separate LiOT phase will form at temperatures below 410°C. In addition, it is evident that whenever the blanket is cooled to room temperature, the tritium in solid solution will precipitate out as a separate phase of LiOT.

Another important consideration relates to vaporization of LiOH (LiOT), which has been studied by Tetenbaum [52]. The results of that study (Table 4-22) show the effects of moisture on Li_2O vapor phase transport. The blanket purge stream has a T_2O partial pressure of about 1 Pa or 10 ppm. It is evident that at the high temperatures in Table 4-22 (1100 K and higher), the LiOT pressures are ≥1 Pa. Vapor phase transport of lithium under these conditions would be excessive, ≥750 g per day, or ≥0.36% of the blanket per year. The data in Table 4-22 are in very good agreement with JANAF [62], which are based on the work of Berkowitz, et al [63]. Using the JANAF data for the equilibrium

$$H_2O(g) + Li_2O(s) \rightleftarrows LiOH(g) \qquad (4\text{-}3)$$

and setting $P(H_2O)$ = 1 Pa, the pressure of T_2O in the purge stream, the pressure of LiOH (LiOT) was calculated, as shown in Fig. 4-30. It is suggested as a design criterion that the LiOT pressure should not exceed 1% of the T_2O pressure. Thus, for $P(T_2O)$ = 1 Pa, P(LiOT) must not exceed 10^{-2} Pa. This corresponds to a maximum allowable Li_2O temperature of 660°C.

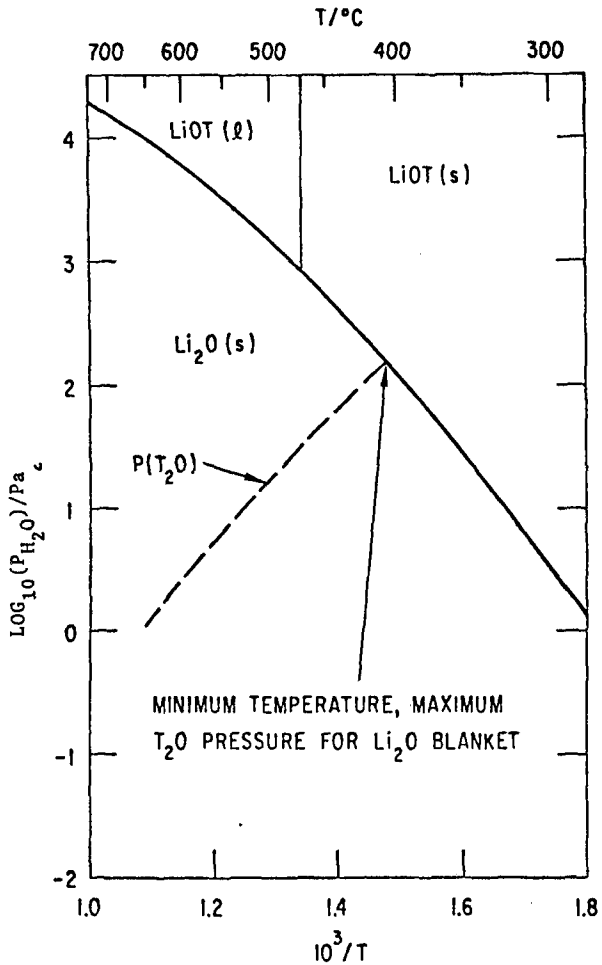

Fig. 4-29. LiOH-Li_2O phase diagram showing operating temperature limits for Li_2O blanket.

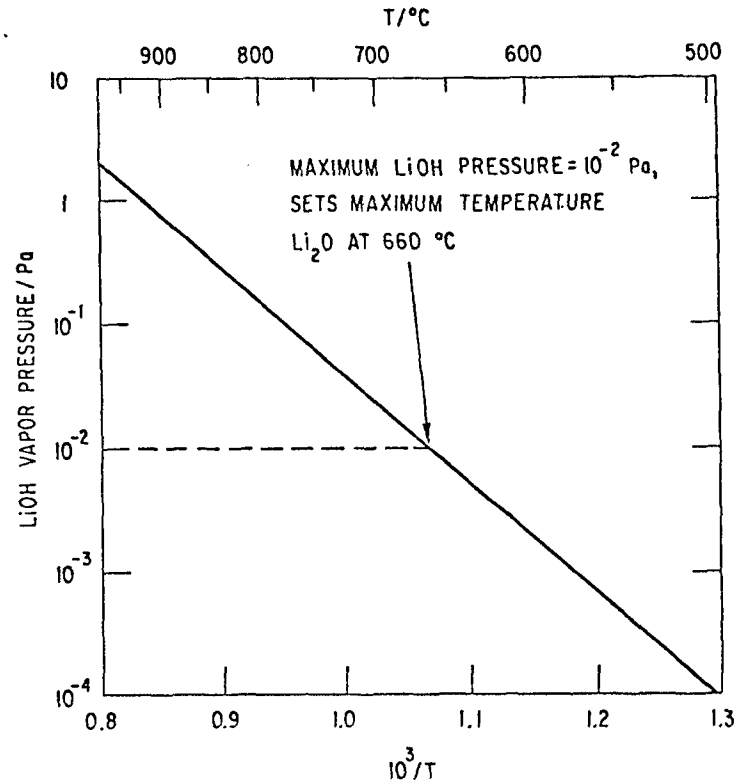

Fig. 4-30. Vapor pressure of LiOT above Li_2O with $P(T_2O)$ equal to 1 Pa. The maximum temperature limit is ~660°C.

Table 4-22. Vaporization Behavior of Lithium Oxide [59]

T K	Carrier Gas Flow Rate, ml/min	ppm H_2O	-log p[a] ANL Work	-log p[a] Calc. via JANAF	Kudo et al.	-log k ANL Work	-log k Calc. via JANAF
1073	158	105	5.62	5.35	9.81	7.25	6.71
1123	220	4	5.94	5.70	9.06	6.48	6.00
1123	175	65	5.19	5.13	9.06	6.19	6.08
1128	150	105	5.08	4.99	8.99	6.19	6.02
1173	142	420	4.43	4.40	8.35	5.49	5.42
1223	225	110	4.36	4.37	7.71	4.76	4.80
1258	225	110	4.33	4.18	7.29	4.70	4.41
1263	157	440	4.00	3.35	7.22	4.64	4.34
1268	143	115	4.18	4.10	7.16	4.42	4.28
1268	158	45	4.45	4.31	7.16	4.57	4.28

[a] p in atmospheres: 1 atm = 101.325 kPa

4.3.5.4 Radiation Effects

Fabrication of Li_2O with small grain size and uniform interconnected porosity, although difficult, appears feasible. However, the stability of this microstructure under the anticipated thermal and radiation environments of a reactor blanket is a major concern. Large weight losses have been observed at 1000°C when exposed to vacuum conditions or helium with very low moisture concentrations [46, 64]. This is generally attributed to mass transfer of LiOH. Although experimental data are quite limited, chemical effects produced by burnup of lithium and displacement damage effects produced by the high energy recoils (several MeV T and He) could cause enhanced sintering which would lead to pore closure and a buildup of T or LiOT. A buildup of LiOT would also enhance sintering as discussed in Sec. 4.3.5.2. A maximum temperature of 0.6 T_m, which corresponds to ~ 750°C for Li_2O, was suggested in the STARFIRE study [1, 48].

Scoping studies by L. Yang, et al [55] tend to support the predicted results. Small capsules containing ~ 70% dense Li_2O were irradiated in ORR to fluences of ~ 2 x 10^{21} n/cm^2 at temperatures of 750, 850, and 1000°C. The

samples were depleted to 0.05% ^{6}Li to more nearly approximate tritium generation rates projected for fusion reactor blankets. Therefore, the maximum lithium burnup was only 0.05%. This compares to an estimated burnup of ~ 0.4%/Y near the first wall of the DEMO (or equivalent to about one-month's operation). Post irradiation examination revealed that the pores became completely closed in samples irradiated at 850 and 1000°C. Although some interconnected porosity remained after the 750°C irradiation, significant changes were observed in the microstructure after irradiation. The grain size of the test samples was <47 μm. One would predict more extensive sintering in the small grain size (<1 μm) proposed for reactor applications and for the much higher burnup required for a practical system. These results indicate that Li_2O must be operated at temperatures considerably below 750°C if the desired open microstructure is to be stable. Obviously additional experimental investigations are required to more accurately determine the temperature limits. A maximum temperature of 650-700°C is proposed for the current study.

4.3.6 Tritium Recovery

The proposed method of tritium recovery from the Li_2O blanket is basically the same as that proposed for the STARFIRE study.[1,48] The Li_2O is in the form of a low-density (70% theoretical density) hot-pressed or sintered product with a tailored bimodal pore distribution, i.e., a small grain size (<1 μm) and a fine porosity within larger particles (~1 mm diameter) with a more coarse porosity between particles. The Li_2O is perforated with ~2 mm diameter holes through which low-pressure (0.1 MPa) helium passes to recover the tritium from the breeder. Tritium generated within the grains must diffuse to the surface of the grains, desorb as T_2O, and migrate (percolate) through the interconnected porosity to the helium purge stream where it is transported to the tritium processing system. Further analyses of the migration (percolation) of T_2O through the interconnected porosity have been conducted in an attempt to define the optimum particle-to-grain size ratio and the amount of porosity required. An assessement of the tritium inventory in the Li_2O blanket is presented for two cases. The first idealized case for which a more accurate estimate can be made because of a better data base neglects any effects of radiation on the release characteristics. Although the effects of radiation on the tritium inventory are highly uncertain, estimates of possible impacts of various radiation effects are presented.

4.3.6.1 Percolation Analysis of T_2O Transport

The tritium inventory in the grain matrix of a fusion blanket material (e.g., $LiAlO_2$ or Li_2O) is a sensitive function of the partial pressure of tritium (T_2) in the interconnected porosity between the grain surfaces and the helium purge stream. Calculations were performed to determine the steady-state T_2O concentrations and partial pressures in the interconnected porosity of both monolithic and bimodal pore structures.

The geometric parameters assumed for this study are: helium purge stream radius of 1.0 mm, unit cell outer radius of 13.6 mm, grain radius of 0.25 μm, particle radius for the bimodal structure of 500 μm, average radius of fine porosity of 0.05 μm, and an average radius of the large pores of 100 μm. Porosity fractions of 0.1 to 0.4 were investigated. For the bimodal structure, the fine porosity fraction and the large porosity fraction were assumed equal (e.g., $\varepsilon_f = \varepsilon_L = 0.106 \rightarrow \varepsilon = 0.2$).

The assumed operating conditions are a temperature at the cell outer radius of $T_o = 500°C$ and inner-radius temperatue of $T_i = 850°C$. The tritium generation rate is taken from calculations of values for the Row-1 coolant tube position in STARFIRE:[1]

$$Q_A' = 4.34 \times 10^{-10} \text{ g } T_2O/\text{s-cm}^3$$

$$= 1.97 \times 10^{-11} \text{ moles } T_2O/\text{s-cm}^3 ,$$

where Q_A' is per unit of solid volume. To convert Q_A' to a value per unit of pore volume, we have

$$Q_A = (1/\varepsilon - 1)Q_A' .$$

For the case of T_2O diffusion and convection through the large porosity of the bimodal structure, the mean-free path for the T_2O-helium collisions is small compared to the average pore radius ($\lambda/r_p < 0.01$) and ordinary diffusion models apply. The POROUS code,[65] which inclues models for ordinary diffusion and convecton, was used. The results are shown as Cases 35-40 in Table

4-23. The porous equations were also solved approximately to give the following analytical expressions which agree to within 10% of the POROUS results for the maximum rise in total pressure ΔP_{max} and the maximum rise in T_2O partial pressure $(\Delta P_{T_2O})_{max}$:

$$\Delta P_{max} = (1 + 0.5\ \Delta P_{max}/P_i)^{-1}\ \frac{\varepsilon \mu_i Q_A}{4\kappa\rho_i}\ (r_o^2 - r_i^2)\ f(r_o/r_i)$$

and

$$(\Delta P_{T_2O})_{max} = (1 + \Delta P_{max}/P_i)\ \frac{RT_i}{W_A}\ \frac{Q_A}{4KD_i'}\ (r_o^2 - r_i^2)\ g(r_o/r_i),$$

where the subscript "i" refers to conditions in the purge stream:

ε = large porosity fraction (0.106 to 0.225)

μ_i = helium purge stream viscosity = $3.65 \times 10^{-4}\ (T_i/T_o)^{0.64}$ (Ref. 66)

ρ_i = helium purge stream density at T_i and P_i

κ = permeability = $4 \times 10^{-10}[2(\varepsilon - \varepsilon_0)\bar{r}_p]^{1.8}$, cm^2 (Ref. 67)

$\bar{r}_p$ = average pore radius in μm

ε_0 = fractional porosity that is isolated = 0 for large porosity

$Q_A = (1/\varepsilon - 1)\ 4.34 \times 10^{-10}$ g $T_2O/s\text{-}cm^3$

D_i' = ordinary diffusion coefficient for T_2O-He mixture at T_i, P_i
= $3.50 \times 10^{-6}\ (T_i^{2.334}/P_i)$ cm^2/s, where $[T_i]$ = ^0K, $[P_i]$ = atm (Ref. 66)

K = factor to account for tortuous diffusion path (~1 for this case)

r_o = 1.36 cm

r_i = 0.1 cm

$$f(r_o/r_i) = 2(1 - r_i^2/r_o^2)^{-1} \int_1^{r_o/r_i} (T/T_i)^{3/2}[1/\eta - (r_i^2/r_o^2)\eta]\, d\eta$$

$$g(r_o/r_i) = 2(1 - r_i^2/r_o^2)^{-1} \int_1^{r_o/r_i} (T/T_i)^{-1.334}[1/\eta - (r_i^2/r_o^2)\eta]\, d\eta$$

For the cases of T_2O transport through the fine pores in the monolithic pore structure and the particles of the biomodal structure, the mean-free path for T_2O-He collisions is large ($\lambda/r_p \sim 0$) compared to the average pore radius. ordinary convection and diffusion models no longer apply. Collisions between the T_2O and the walls of the pore dominate, and the Knudsen models[68] apply. The diffusion coefficient becomes independent of the helium and is given by

$$D_{KA} = KD'_{KA},$$

where

$$K = \varepsilon$$

$$D'_{KA} = \frac{2}{3} r_p \left(\frac{8RT}{\pi W_A}\right)^{1/2}$$

W_A = molecular weight of T_2O

R = universal gas constant.

The solution to the Knudsen diffusion problem for $(\Delta P_{T_2O})_{max}$ is

$$(\Delta P_{T_2O})_{max} = \frac{3Q_A}{8r_p K} (\pi W_A R T_o/8)^{1/2} (r_o^2 - r_i^2) f(r_o/r_i)$$

where

$$f(r_o/r_i) = 2(1 - r_i^2/r_o^2)^{-1} \int_1^{r_o/r_{i(T/T_o)^{1/2}}} [(1/\eta) - (r_i^2/r_o^2)\eta]\, d\eta.$$

For the monolithic structure with r_o = 1.36 cm, r_i = 0.1 cm, T_o = 773°K, and T_i = 1123°K, we have

$$(\Delta P_{T_2O})_{max} = 0.037\left(\frac{1-\varepsilon}{r_p \varepsilon K}\right), \quad \text{Pa} \cdot \mu\text{m} .$$

For the fine pore particles in the bimodal case, r_o = 1.36 cm, r_i = 1.26 cm, $T_o = T_i \sim 773$°K, and

$$(\Delta P_{T_2O})_{max} = 1.1 \times 10^{-4}\left(\frac{1-\varepsilon}{r_p \varepsilon K}\right), \quad \text{Pa} \cdot \mu\text{m} .$$

The results of these calculations are presented in Table 4-23 and Fig. 4-31. Clearly, there is no significant buildup (<1 Pa) of T_2O in either the fine or large porosity of the bimodal structure as long as the porosity remains interconnected ($\varepsilon_f > 0.1$ and $\varepsilon > 0.2$). These results assume that the average pore radii of the two types of pores are maintained constant as the porosity is decreased. However, for the monolithic structures consisting of fine pores only, the T_2O partial pressure builds up to ~67 Pa for the limiting case of ε = 0.1.

In generating the results in Table 4-23 and Fig. 4-31, it was assumed that the average pore radius is 20% of the grain diameter and insensitive to the total porosity fraction. This crude model can be improved by appealing to sintering models. However, it would be more informative to make samples of the bimodal and monolithic structure and measure the average pore radius. Also, the assumption that the effective diffusion coefficient is KD where $K = 1/\tau = \varepsilon$ needs to be tested.

Table 4-23. Increase in T_2O Partial Pressure in the Interconnected Porosity of Monolithic and Bimodal Pore Structures

Case	Description	ε	K	r_p (μm)	$(\Delta P_{T_2O})_{max}$ (Pa)	P_{He}
31	Monolithic	0.4	0.4	0.05	2.80	5.05×10^4
32	Monolithic	0.3	0.3	0.05	5.80	5.05×10^4
33	Monolithic	0.2	0.2	0.05	14.80	5.05×10^4
34	Monolithic	0.1	0.1	0.05	66.60	5.05×10^4
35	Fine bimodal	0.225	0.225	0.05	0.034	5.05×10^4
36	Fine bimodal	0.163	0.163	0.05	0.069	5.05×10^4
37	Fine bimodal	0.106	0.106	0.05	0.176	5.05×10^4
38	Large bimodal	0.225	0.225	100	0.0135	5.05×10^4
39	Large bimodal	0.163	0.163	100	0.0205	5.05×10^4
40	Large bimodal	0.106	0.106	100	0.0343	5.05×10^4

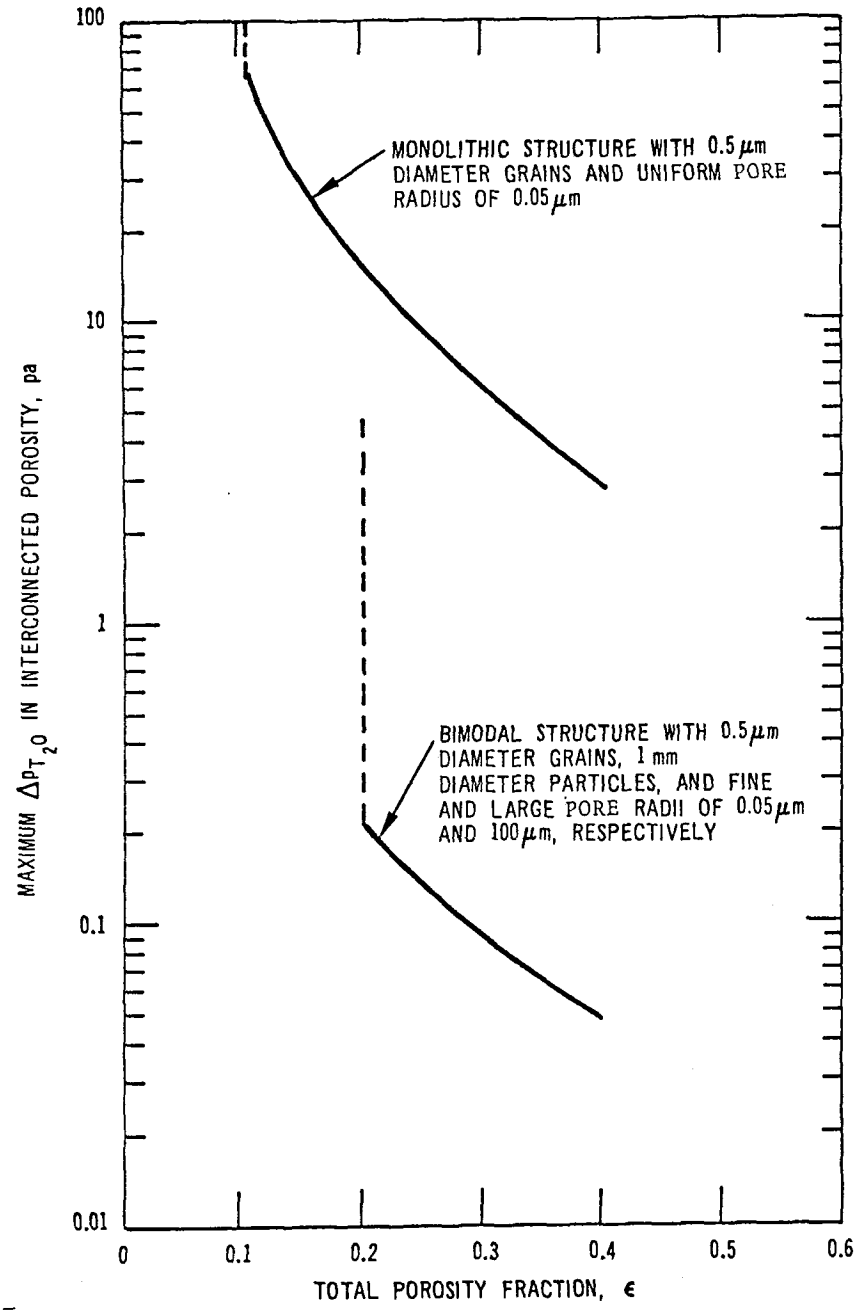

Fig. 4-31. Maximum increase in T_2O partial pressure from the helium purge stream to the outer radius of a unit blanket cell as a function of total porosity fraction and pore distribution (monolithic vs. bimodal).

4.3.6.2 Tritium Inventory

The methodology used to estimate tritium inventory in the blanket follows the procedures used for STARFIRE.[1,4,7,48] Tritium generated within the solid must diffuse to the surface, desorb as T_2O, and percolate through the interconnected porosity to a purge stream where it is transported to the processing system. Selected blanket parameters are summarized in Table 4-24. In the absence of radiation effects, the tritium inventory is assumed to be the sum of the "diffusive" inventory and the "solubility" inventory. Estimates of the tritium inventory, and the effects of irradiation are summarized below.

The diffusive inventory was estimated by the methods discussed previously.[1,4,7,48] The approximate temperature distribution was estimated from a thermal calculation using pure conduction with cylindrical geometry.[1] The breeder region is divided into 22 regions of equal volume, represented by nodes numbered 3 to 24 (Table 4-25). The total diffusive inventory is estimated to be about 20 g, over 80% of which is in the regions of lowest temperature, i.e., below 470°C.

Table 4-24. Selected Li_2O Blanket Parameters

Blanket, Li_2O inventory, Mg	54
T_{min}, °C	410
T_{max}, °C	660
Tritium generation rate, g/s	1.74×10^{-3}
Purge stream T_2O pressure, Pa	1.0
Purges stream LiOT pressure, Pa	1.0×10^{-2}
T_2O generation rate, Pa-liters/s @ 650°C	2.2×10^{3}
Tritium breeding rate, g/day	150
Purge stream helium pressure, atm	1 (1.013×10^{5} Pa)
Purge stream flow rate (total), liters/s	2.2×10^{3}
Purge stream volume, liters	1000[a]
Purge stream velocity, m/s	12

[a] 2% of blanket volume.

Table 4-25. Diffusive Tritium Inventory

Node	T/°C	Tritium Inventory (g)	% of Inventory	Cumulative Inventory (g)	Cumulative (%)
3	430.1	11.3	59.2	11.3	59.2
4	465.4	4.1	21.5	15.4	80.7
5	494.8	1.5	7.9	16.9	88.6
6	519.6	0.70	3.7	17.6	92.2
7	540.9	0.40	2.1	18.0	94.3
8	559.2	0.24	1.3	18.24	95.6
9	575.1	0.16	0.8	18.40	96.4
10	589.0	0.12	0.6	18.52	97.0
11	601.1	0.09	0.5	18.61	97.5
12	611.5	0.07	0.4	18.68	97.9
13	620.6	0.06	0.3	18.74	98.2
14	628.4	0.05	0.26	18.79	98.5
15	635.2	0.04	0.21	18.83	98.7
16	640.9	0.04	0.21	18.87	98.9
17	645.7	0.03	0.16	18.90	99.1
18	649.7	0.03	0.16	18.93	99.2
19	653.1	0.03	0.16	18.96	99.4
20	655.7	0.03	0.16	18.99	99.5
21	657.7	0.03	0.16	19.02	98.6
22	659.1	0.02	0.10	19.04	99.8
23	660.1	0.02	0.10	19.06	99.9
24	660.5	0.02	0.10	19.08	100.0

Cyl. model: $q''' = 12.94\ w/cm^3$.

$h_g = (430\ Btu/ft^2\text{-}hr\text{-}°R) = 0.244\ W/m^2 \cdot K$.

Tritium generation rate = 1.74×10^{-3} g/s.

Total tritium inventory = 19.1 g.

The solubility inventory can be estimated from preliminary experimental data. Assuming that the solubility is proportional to pressure, the results of Tetenbaum[59] extrapolate to 7×10^{-3} wppm tritium at 410°C and 0.12 wppm tritium at 650°C for a T_2O pressure of 1.0 Pa. For comparison, the results of Nasu[60] translate to a tritium solubility of 0.008 wppm at 650°C, for $P(T_2O)$ = 1.0 Pa. In the blanket, the T_2O pressure will increase at regions away from the purge channel, but this effect is compensated for by decreasing solubility at lower temperature. Thus, a reasonable estimate of the solubility is on the order of 0.1 wppm. This translates to a solubility inventory of about 5 g. Thus, in the absence of radiation effects, the total tritium inventory in the blanket is estimated to be about 25 g.

As discussed in STARFIRE[1], radiation effects (sintering, restructuring, and trapping) can significantly increase tritium inventories in solid breeders.

Radiation-induced sintering could result in some pore closure, thereby increasing the T_2O pressure and solubility. A two order of magnitude increase in the T_2O pressure would give a tritium concentration of 500 g. Restructuring leading to increased grain size could increase the diffusive inventory an order of magnitude to 200 g. Although the degree of radiation-induced tritium trapping is highly uncertain, estimates[1,48] based on results from ion bombardment studies indicate that tritium concentrations of the order of 1 at % may occur. Concentrations of this order of magnitude would lead to unacceptably high tritium inventories of ~50 kg. The results of estimates of tritium inventory with and without predicted radiation effects are given in Table 4-26.

Table 4-26. Estimated Tritium Inventory in Li_2O

	Without Radiation Effects (g)	Predicted Radiation Effects (kg)
Diffusion	25	0.2-50
Solubility	5	0.5
TOTAL	25	0.7-50

Several factors, such as surface desorption of LiOT, that could influence tritium inventory have not been accounted for. Also, chemical effects such as LiOH/LiOT formation and gas phase transport could promote restructuring and sintering, therby increasing tritium holdup in the blanket. In addition, formation of LiOH or LiOT layers on the surfaces of particles could inhibit the release of T_2O from within the particles.

4.3.7 Thermal Hydraulics Analysis

The thermal hydraulics design problems associated with solid breeders are complex due to the fact that: (1) solid breeders are susceptible to thermal, chemical, and neutron environments and (2) the tritium release rates are highly dependent upon the temperature distribution in the solid breeder. Since the operating temperature limits of the solid breeders are influenced by the design and operating conditions, a series of parametric investigations were carried out to study the effect of (1) geometric variables, (2) thermal conductivity of solid breeders, (3) interfacial contact resistance, and (4) operating power level on the design characteristics. In addition, an assessment of the overall design in terms of (1) coolant and structural material fractions, (2) pumping power losses, and (3) purge gas flow rates and pressure losses was carried out based on the following design requirements.

Design Requirements

As discussed in Sec. 4.3.2 and Sec. 4.3.9.1, the design is based on modular blanket cells consisting of Li_2O solid breeder and light water as the heat-transfer and thermodynamic fluid. The temperature limits and coolant operating conditions are summarized in Table 4-27.

Table 4-27. Summary of Blanket Parameters Used in Thermal Hydraulics Calculations

Maximum operating temperature for Li_2O	660°C
Minimum operating temperature for Li_2O	410°C
Coolant inlet temperature	260°C
Coolant outlet temperature	300°C
Coolant pressure	10.34 MPa (1500 Psia)
Operating power level (steady-state)	100%
Neutron heating rate in Li_2O:	
Near first wall	12.94 W/cc
Near reflector/shield	0.47 W/cc

4.3.7.1 Geometric Variables

Since the nuclear heating rate in the blanket is not uniform with respect to depth into the blanket, the temperature distribution is greatly influenced by the spatial distribution of coolant channels. Two geometric models (see Fig. 4-32), as discussed below, are used to estimate the steady-state temperature distribution.

Cylindrical Blanket Cell Model

A cylindrical blanket-cell model, shown schematically in Fig. 4-32a, has been used for scoping studies. Although the temperature distribution in the breeding blanket is three-dimensional, the cylindrical blanket cells provide mathematical simplifications based on assumed uniform internal heat generation and invariant material and fluid properties. With uniform nuclear heat and constant properties of the materials, the governing equations can be solved in closed form. Thus, a large number of parametric investigations to study the effect of heat flux levels, coolant inlet and outlet conditions, variations in material properties, temperature limitations, and design variations can be studied with only a limited amount of effort.

Three separate blanket regions were selected for the parametric investigation. The first region with the maximum nuclear heating rate was taken near the first wall/multiplier region. The second region was taken within the breeder where the nuclear heating has decreased to ~ 25% of the maximum value. The third region was taken near the reflector/shield region where the volumetric heating rate has decreased to ~ 4% of the peak value. For each region, the zone-averaged values of neutron heat flux were used. Since the angular variation (poloidal direction) of neutron heat flux has not been calculated, constant heat flux values were used for the cylindrical cells. The important geometrical variables and the operating parameters are listed in Table 4-28. The results of thermal hydraulics analyses, for the cylindrical model, are given in Table 4-29. An examination of the cylindrical cell concept shows that a significant fraction of the blanket volume lies outside the isothermal boundaries indicated by the dotted lines in Fig. 4-32a. The optimum tube spacing cannot be accurately determined from the cylindrical cell model because of the multidimensional heat transfer near the isothermal boundaries.

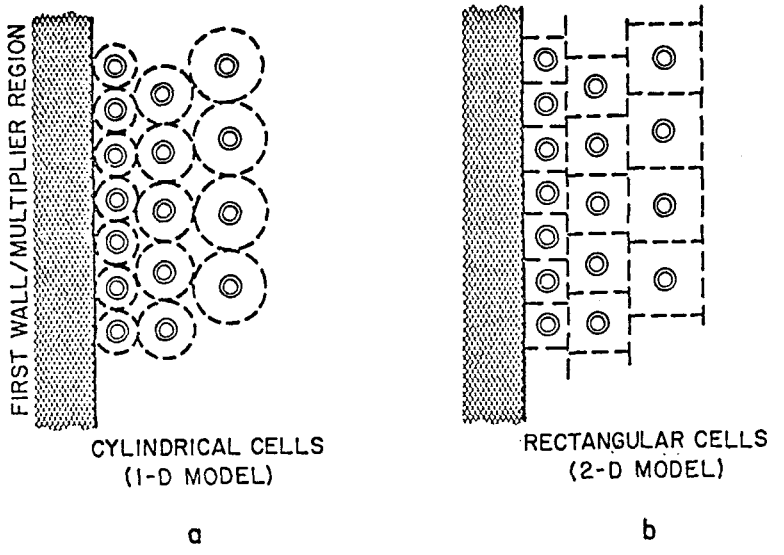

Fig. 4-32. Schematics of cylindrical and rectangular cell models.

Table 4-28. Geometrical Parameters and Results of Thermal Hydraulics Calculations for Li_2O Breeding Blanket (1-D Cylindrical Blanket Cells)

	Region 1	Region 2	Region 3
Average nuclear heating rate, W/cc	12.94	3.33	0.47
Coolant tube inside diameter, mm	10.2	10.2	10.2
Coolant tube outside diameter, mm	12.7	12.7	12.7
Coolant inlet temperature, °C	260	260	260
Coolant outlet temperature, °C	300	300	300
Coolant channel length, m	3	3	3
Breeder cell diameter, mm	31.4	47.4	94.0
Maximum breeder temperature, °C	660	660	660
Minimum breeder temperature, °C	410	410	410
Coolant velocity, m/s	2.6	1.5	1.0
Pressure drop across coolant channel, KPa	4.7	1.8	0.6
Ratio of pumping power to thermal power (for coolant channels only), %	<1	<1	<1

Rectangular Blanket Cells

Figure 4-32b schematically shows the rectangular blanket cell concept that can be used to study multidimensional heat transfer effects. An examination of the typical blanket cell (either with a square or rectangular cross section) shows that the heat transfer in the blanket modules is three-dimensional, even when the heat generation in the blanket cells is uniform. A three-dimensional conduction code capable of using temperature-dependent material properties, non-uniform heat flux, convective heat transfer in the coolant channels, and contact resistance between dissimilar materials was used for thermal hydraulic analysis. Coolant temperature variations were limited to ~ 1°C so that the problems analyzed were essentially two-dimensional. The geometric models of the blanket cells are shown in Fig. 4-32b. It can be seen from this figure that, unlike the cylindrical cells, there are no breeder regions outside the cell boundary. Hence, there are no uncooled regions and all of the breeder volume can be accounted for by the individual blanket cells. The helium purge gas channels can be located appropriately to accommodate tritium extraction. For analytical simplicity, the coolant channels are assumed to be square. The cross section of the coolant channels and the clad thickness are assumed to be the same for both models (see Fig. 4-33). As discussed further in Sec. 4.3.7.3, the outer boundary of each blanket cell (denoted by dashed lines) is assumed to represent an insulated boundary (i.e., no heat transfer between modules). (This is discussed further in a later section.) In comparing the temperature distribution for the two models, the volume of breeder material for both cases was assumed to be the same. In addition, the nuclear heating rates for the three regions of the rectangular cells were assumed to correspond to the three regions of the cylindrical cells. Based on constant nuclear heating rates in each region, the temperature distributions within the cylindrical cells and the rectangular cells were calculated. The radial and diagonal temperature distributions in equal volume cylindrical and square cell models for a typical set of operating conditions near the first wall (i.e., Region 1) are plotted in Fig. 4-34. It can be seen that the maximum temperature at the corners of the square cell is ~ 60-70°C higher than that in the cylindrical cell. Hence, the design of the rectangular cells must be based on a smaller breeder volume to keep the maximum temperature within the allowable limit.

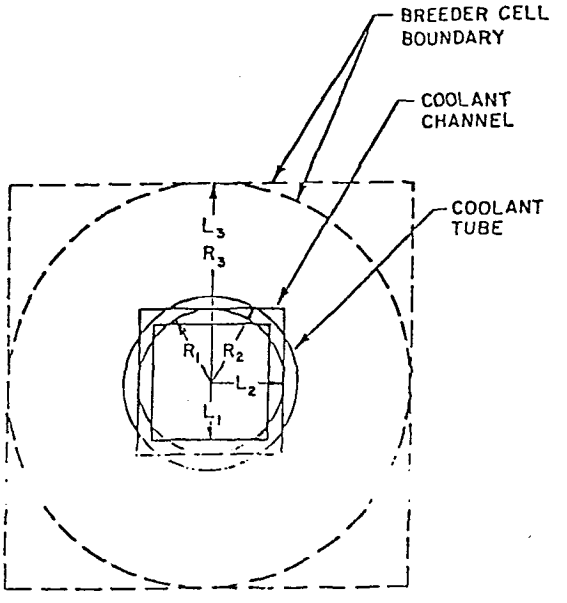

Fig. 4-33. Geometrical parameters for cylindrical and rectangular blanket cells.

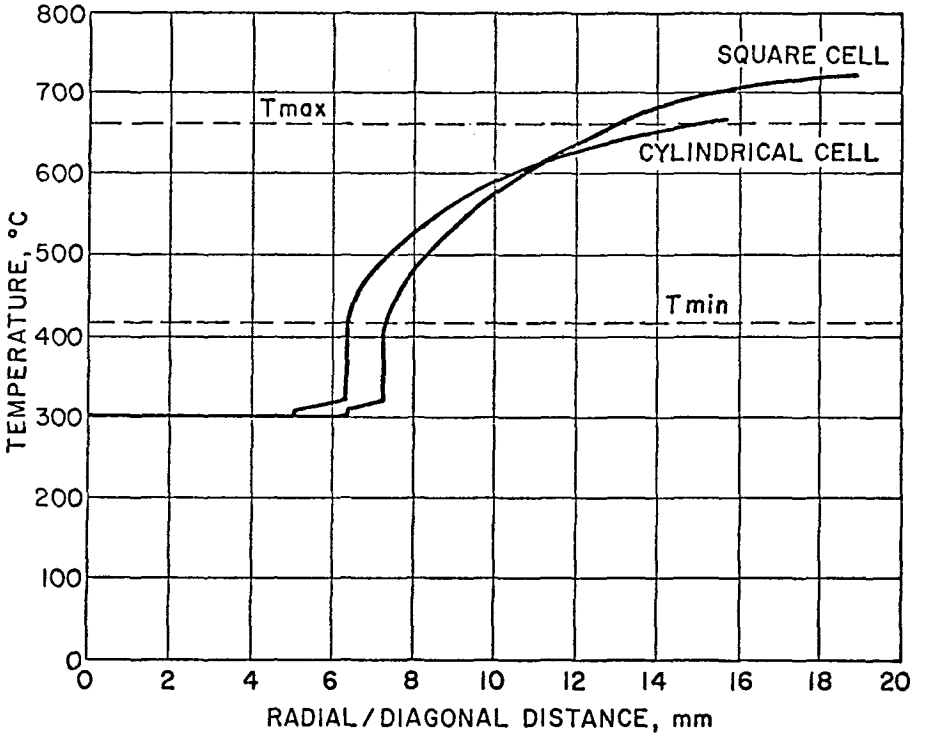

Fig. 4-34. Comparison of temperature distribution in equal volume cylindrical and rectangular blanket cells.

Figure 4-35 shows a typical mathematical model of a rectangular blanket cell. The square cell with L_4 as one of the sides represents boundaries of a blanket cell which has the same breeding material volume as its cylindrical counterpart. The cell with L_5 and L_6 as its sides represents the modified blanket cell of lesser breeder volume. For the modified rectangular cell model, the variation of the nuclear heating rate in each cell was considered. The dimensions of the rectangular cell (L_5 and L_6) were calculated by an iteration process for each of the three regions. The geometrical parameters for the three regions and the results of the thermal hydraulic calculations are summarized in Table 4-29. The effect of the non-uniform heating rate is to slightly offset the coolant channel towards the side of the cell nearest the plasma. This is due to the slightly higher heating rates in the breeder nearer the plasma in each cell as compared to the rates in the breeder further away from the plasma. It can be seen frim Fig. 4-36 that there would be transfer of heat between adjacent cells although the analytical studies assume that the individual blanket cells are thermally isolated from their neighbors. Further thermal hydraulics analyses are planned which will incorporate multiple cells, both poloidally and depthwise, and which will account for heat flow between adjacent cells. The results of these analyses will provide more realistic guidance for determining blanket thermal hydraulics parameters, in particular, coolant tube spacing and breeder temperature distribution.

4.3.7.2 Sensitivity to Thermal Conductivity

One of the important thermophysical properties that affects the blanket design is the thermal conductivity of the solid breeder. Since the thermal conductivity plays such a dominant role in temperature distribution, and hence, tritium extraction and tritium inventory, this subject is divided into two parts. In the first part, rather modest variations in the thermal conductivity values were taken into account. A series of parametric analyses were carried out using: (1) temperature dependent thermal conductivity values as given in Sec. 4.3.5 for Li_2O (for 70% theoretical density) over the temperature range of 410-660°C, (2) a constant value of thermal conductivity corresponding to the average breeder temperature (535°C)$\frac{}{}$ and (3) variations in thermal conductivity values corresponding to $\pm$ 10% of the reference values. The results, summarized in Table 4-30, indicate that the temperature

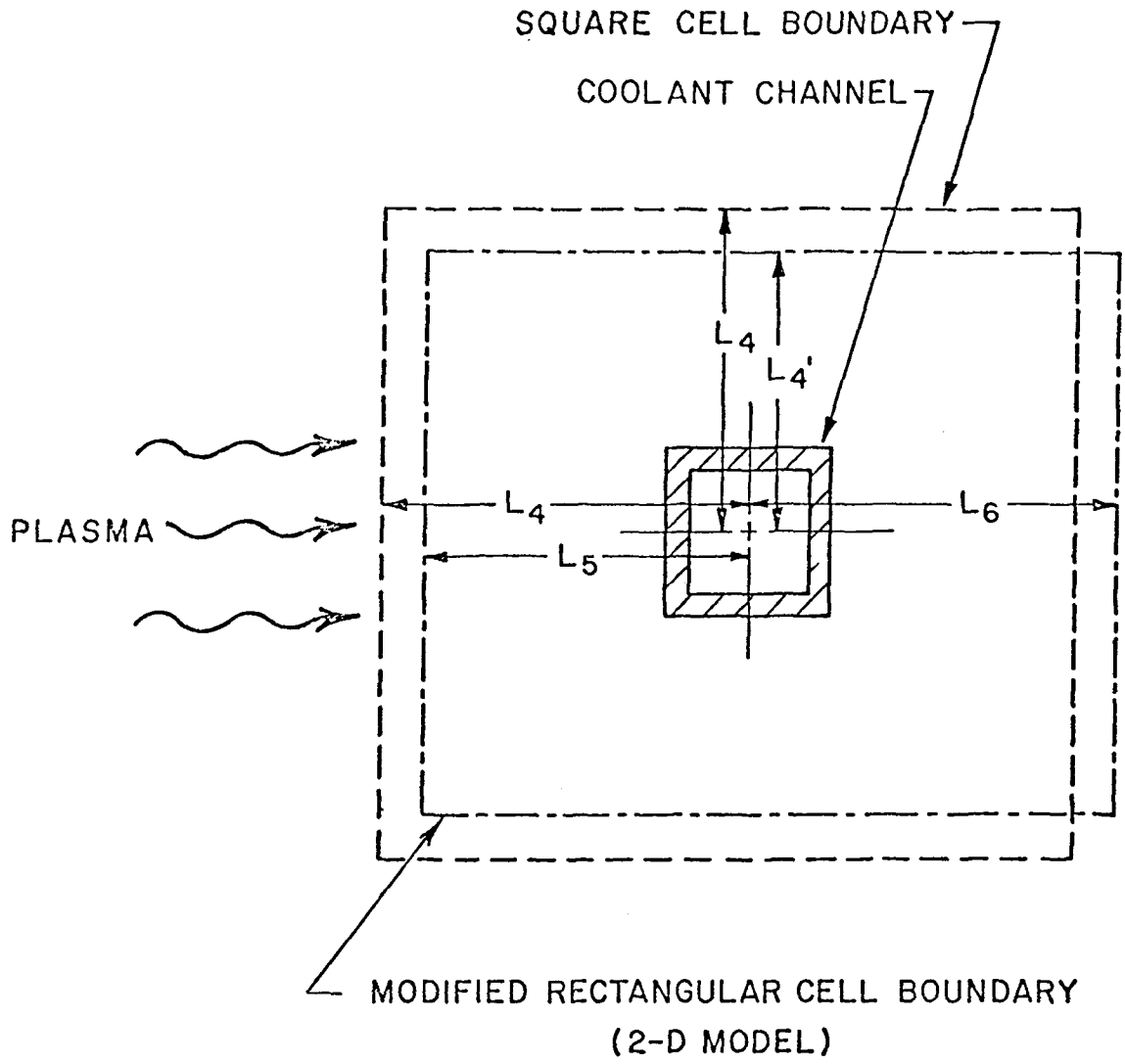

Figure 4-35: Schematics of square and modified rectangular cell models.

Table 4-29. Summary of Parametric Investigations for Li_2O Breeding Materials for Three Separate Breeder Blanket Regions

Geometrical & Physical Parameters	Breeder Cell Model								
	Cylindrical Cell[a,b]			Square Cell[a,b]			Modified Rectangular Cell[c]		
	Regions			Regions			Regions		
	1	2	3	1	2	3	1	2	3
R_1, $2L_1$, mm	5.1	5.1	5.1	9.08	9.08	9.08	9.08	9.08	9.08
R_2, $2L_2$, mm	6.35	6.35	6.35	11.54	11.54	11.54	11.54	11.54	11.54
R_3, mm	15.7	23.7	47.0	-	-	-	-	-	-
$2L_4 \times 2L_4$, mm	-	-	-	27.94 x 27.94	42.08 x 42.08	83.34 x 83.34	-	-	-
$2L_5 \times 2L_6$, mm	-	-	-	-	-	-	25.65 x 26.96	39.54 x 41.57	78.26 x 78.26
Vol. % Coolant	10.6	4.6	1.2	10.5	4.1	1.2	11.8	5.0	1.3
Vol. % Clad	5.8	2.5	0.7	6.6	2.9	0.7	7.4	3.1	0.9
H_g Inlet, W/m^2-K	1704	994	596	1334	852	454	1278	795	443
H_g Outlet, W/m^2-K	2442	1420	852	1874	1193	653	1846	1136	625
T_{max}, °C	661	660	661	721	728	725	660	662	661
T_{min}, °C	415	416	415	410	402	413	407	404	401

[a]Heating rates assumed constant for each region.

[b]Cylindrical cell volume equal to square cell volume for each region.

[c]Heating rates assumed to vary with depth throughout each region.

NOTE: The length parameters are the appropriate radii for the cylindrical model and the sides of the rectangle for the slab model. (See Figs. 4-33 and 4-35.)

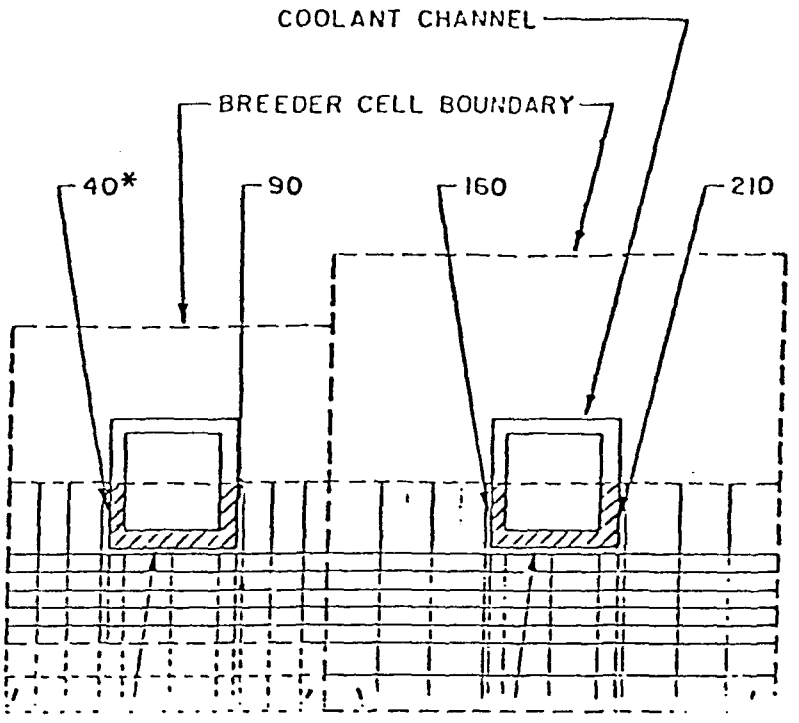

2-CELL BLANKET SEGMENT

(2-D MODEL)

* 1, 40, etc. REFER TO NODE NUMBERS USED IN THE COMPUTER PROGRAM

Figure 4-36. Schematic presentation of two adjacent cells for computer modeling.

variations between cases with constant thermal conductivity and thermal conductivity as a function of the operating temperature are only of the order of 10°C. However, thermal conductivity variations of $\pm$ 10% from the reference case results in temperature variations of 25-35°C. This indicates the importance to the blanket design of achieving a high degree of predictability and repeatability in thermal conductivity values of fabricated breeder.

In the second part, the effects on blanket designs of even wider variation in average thermal conductivity for candidate solid breeders was assessed. A parametric investigation was carried out covering a range of thermal conductivity (K) values, from 3 W/m-K for the higher conductivity solid breeders such as Li_2O to K = 1 W/m-K for the lower conductivity solid breeders such as Li_2ZrO_3. Conditions assumed for these calculations are summarized in Table 4-31. The breeder region radius and the required gap conductance values for various power factors (100% to 5%) were calculated using a cylindrical cell model for three values of thermal conductivities (K = 1, 2, and 3 W/m-K). The results are summarized in Fig. 4-37. The volume fraction of the coolant plus the coolant tube structural material are plotted against breeder thermal conductivity for various power factor values. There is a maximum decrease of 11% in breeder volume at the first wall (i.e., 100% region) as K varies from 3 to 1 W/m-K; this decrease is only ~ 2% near the back of the blanket. Thus, when the thermal conductivity of the breeder is decreased from 3 to 1 W/m-K, the overall breeder volume is expected to decrease on the average of about 7%. If the results of the previous ANL studies [1] can be used as a guide, the reduction in the tritium breeding ratio that would be predicted at the lower breeder fraction may be within tolerable limits. The breeder-to-tube gap conductance values required in the blanket vary by approximately a factor of three (see Fig. 4-38) from the region near the first wall to the region near the reflector/shield. This result holds for values of K from 1 to 3 W/m-K. However, the absolute values of required gap conductance at a given power level decrease sharply with conductivity, which reflects the reduced heat flux across the breeder/tube interface resulting from the smaller breeder cell sizes (diameters) permitted for the lower conductivities.

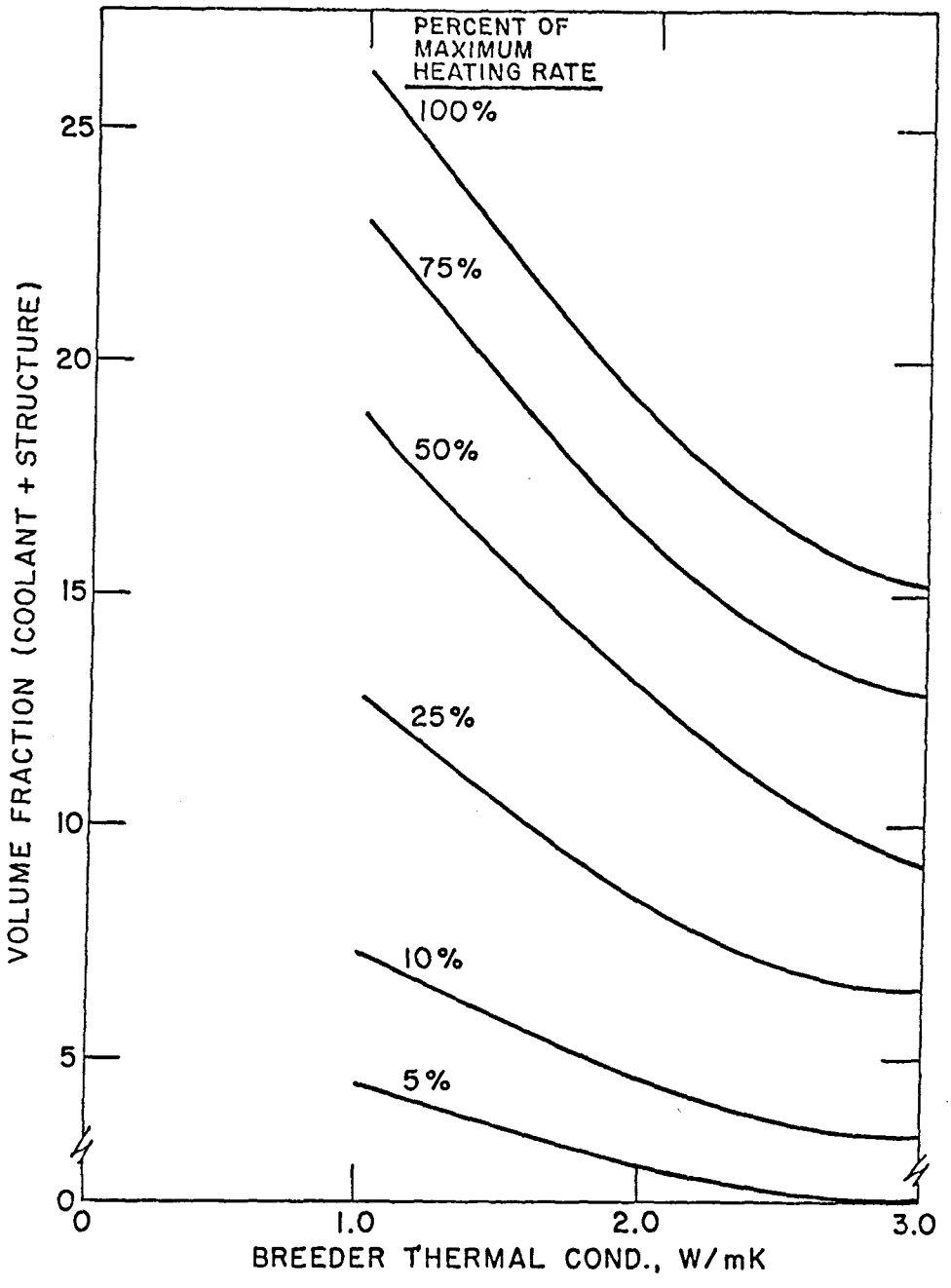

Fig. 4-37. Coolant and structure volume fraction as a function of breeder thermal conductivity.

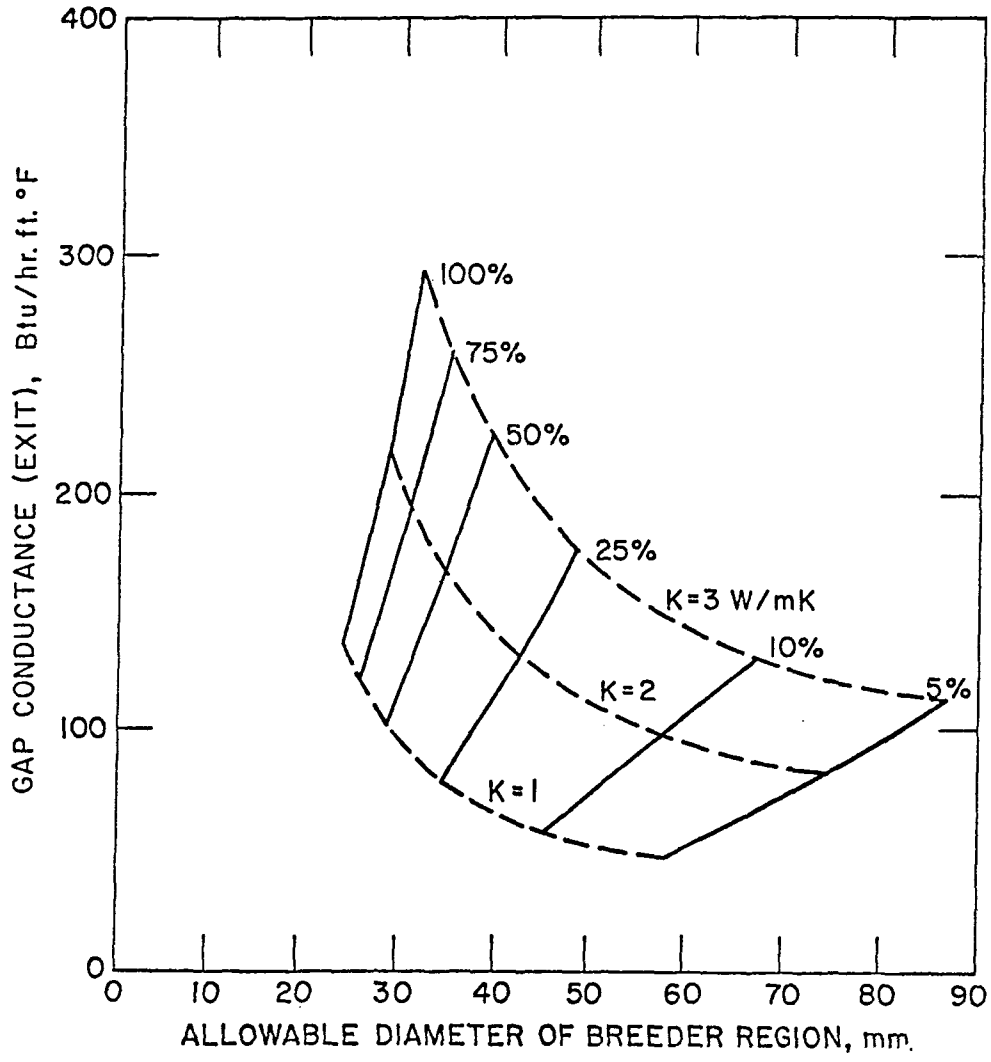

Fig. 4-38. Gap conductance as a function of breeder region diameter, breeder thermal conductivity, and power factor.

Table 4-31. Summary of Parameters Used for Thermal Conductivity Sensitivity Analysis

	Coolant tube wall thickness	1.25 mm
γ-$LiAlO_2$	Breeder module length	3.0 m
	Coolant (H_2O) inlet temperature	260°C
	Coolant outlet temperature	300°C
	Minimum breeder temperature	500°C
	Maximum breeder temperature	850°C
	Nuclear heating in breeder (maximum value)	15.9 W/cc

The actual helium gap widths required to produce typical required conductance values are indicated in Fig. 4-39. No breeder-to-tube contact across the gap is assumed; heat is transferred only by radiation and conduction through the helium. The gap widths shown are those required to obtain the ~ 1700 W/m^2-K (~ 300 Btu/hr-ft^2-°R) conductance corresponding to a 100% power level and a 3 W/m-K breeder conductivity (Fig. 4-38). The required gap widths vary linearly along the tube from 0.195 mm (~ 0.08 in.) to 0.157 mm (~ 0.06 in.), a change of only 0.038 mm (~ 0.02 in.). It is not considered feasible to fabricate blankets which requires such close control of a helium gap, and it is considered impossible (based on present knowledge of breeder fabrication methods) to guarantee the control of such gap widths during reactor operation within tolerances acceptable for reliable breeder temperature control. This further illustrates the need for additional analysis and experimental work in the area of breeder/tube heat transfer control.

4.3.7.3 Tube/Breeder Gap Conductance

One of the greatest challenges in the solid breeder blanket design is the maintenance of the solid breeder within the upper and lower temperature bounds. Since the the breeder minimum allowable temperature is significantly higher than the coolant inlet and outlet temperatures, an artificial thermal barrier between the coolant-carrying channels and the solid breeder is necessary to modify the temperature distribution within the solid breeder. The interfacial contact resistance provides this needed thermal resistance.

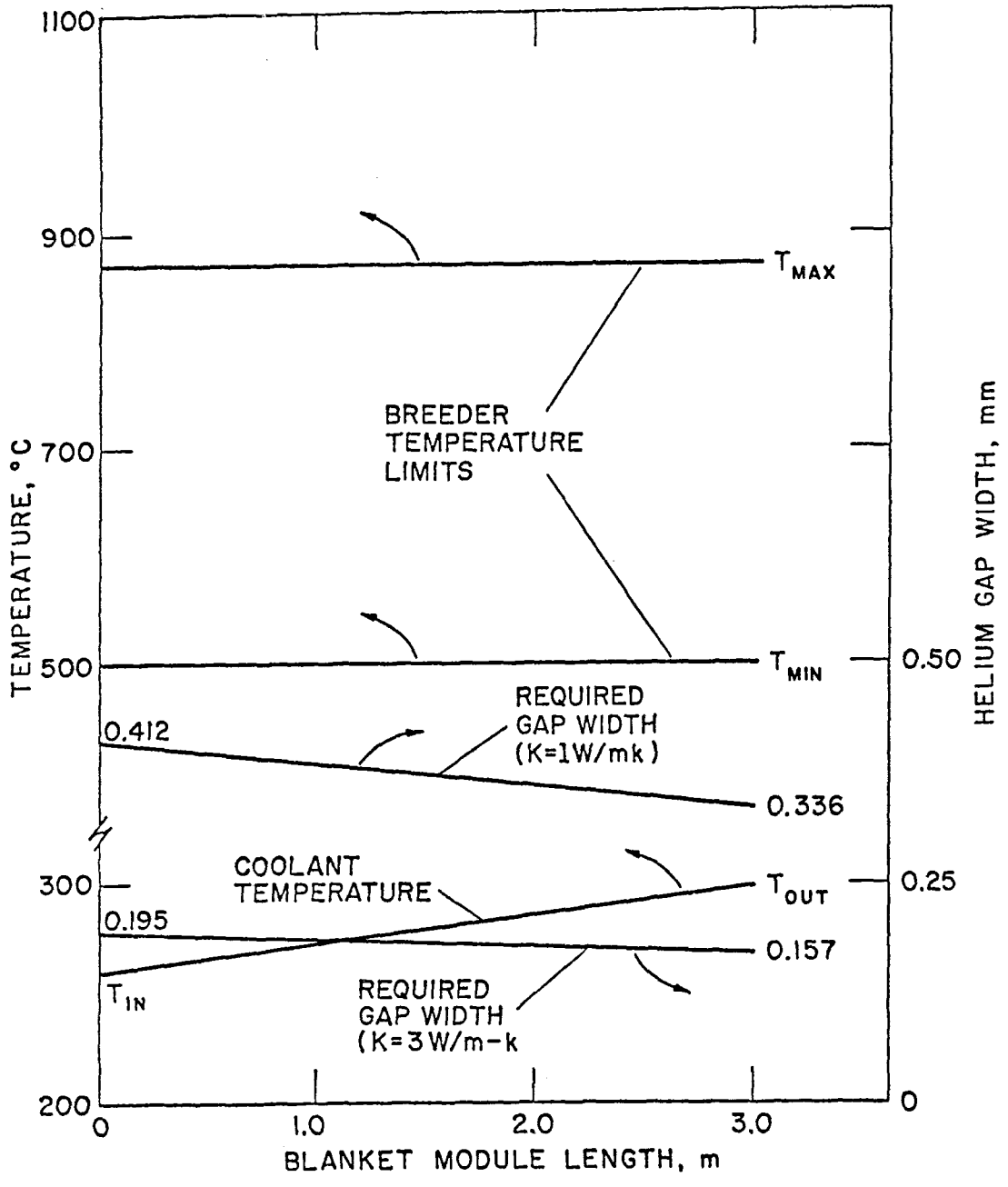

Fig. 4-39. Reproduction of temperature and helium gap width as a function of blanket module length.

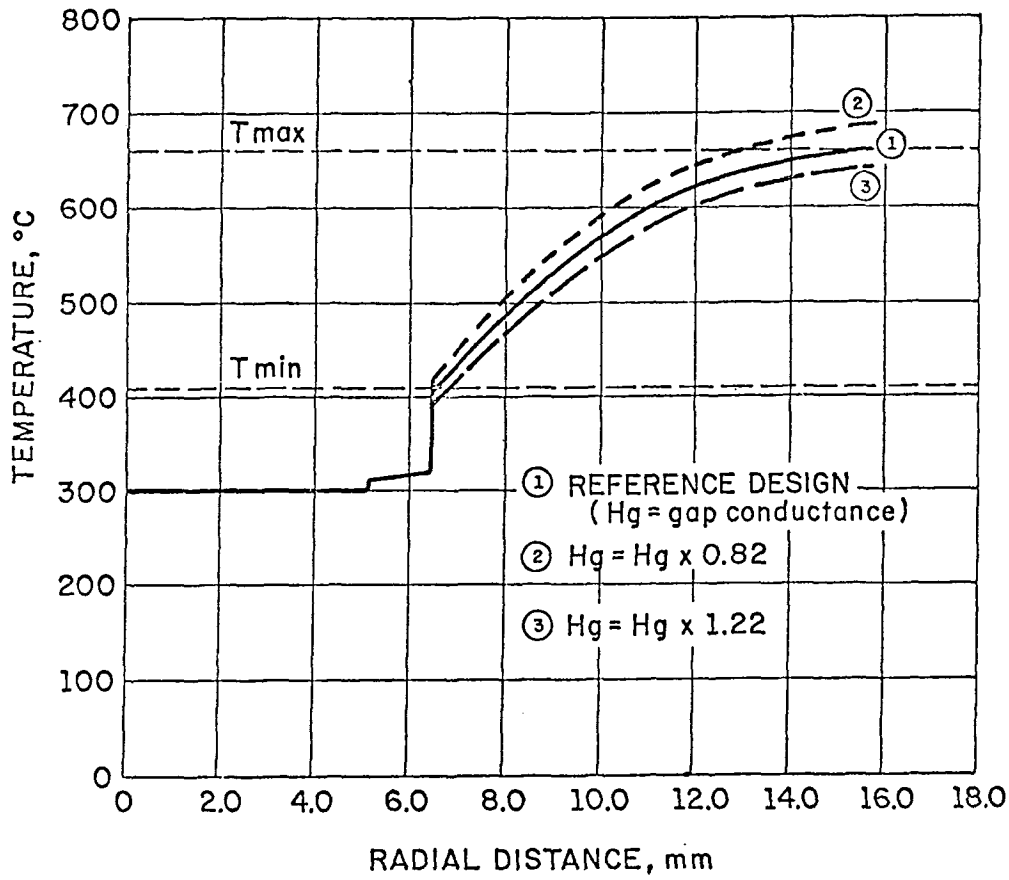

Fig. 4-40. Temperature distribution in breeder by a function of gap conductance.

However, the exact prediction and control of this thermal barrier presents a formidable task. Although there are no experimental data on the interfacial contact resistance between the ceramic breeding material and the structural material, the experimental data for mixed oxide fuels and cladding materials (fission reactor studies) may provide some guidelines regarding the gap conductance for the solid breeders. In this study, an overall gap conductance value was selected for each case that led to the desired temperature distribution.

Table 4-29 shows that the required gap conductance values vary between 2442 and 596 W/m^2-K (430 and 105 Btu/hr-ft^2-°R) for the cylindrical blanket cells. For the rectangular blanket cells, the variations in the gap conductance values range between 1846 and 443 W/m^2-K (325 and 78 Btu-hr-ft^2-°R). The variations in the gap conductance values between the coolant inlet and coolant outlet ends of the breeder are due to the fact that the coolant temperature rises by 40°C.

One approach to breeder temperature control would be to coat the coolant tubes with a ceramic material (either breeding or non-breeding type). Since the coolant temperature rises essentially linearly along the length of the coolant channels, the coating thickness can be varied linearly. However, the mechanics of controlling the overall gap conductance (coating plus contact resistance between the coated tube and breeding blanket) is not clear. An alternate approach to modifying the breeder temperature examined during the STARFIRE and INTOR studies was to consider a helium gas gap between the coolant and the breeder. As discussed in Sec. 4.3.7.2, temperature control through the use of a gaseous helium gap alone is not practical. There are several reasons for this. Because of the low thermal conductivity of helium, the required thickness of the He gas gap is small. In addition, control of the gap conductance between the coolant inlet and coolant outlet ends is not practical due to the very small differences in the gap thickness values at the coolant inlet and exit ends. The helium gap will require double-wall tubes, which will not only lead to added manufacturing cost, but also reduce the breeder volume fraction by introducing more structural material. However, the use of a ceramic insulating material between the cladding and the breeder to control the interfacial contact resistance appears feasible. The ceramic insulating materials have thermal conductivity values which are higher by more than an order of magnitude compared with the thermal conductivity of helium.

Hence, the required coating thicknesses are larger and, thus, the ceramic insulators provide a larger latitude in the manufacture of ceramic-coated tubes.

The overall resistance between the breeder and the outer surface of the coolant channel may be thought of as consisting of three resistances in series: (1) interfacial resistance between the clad and the coating, (2) resistance across the coating, and (3) interfacial resistance between the coating and the breeder. It is reasonable to assume that the gap conductance (Hg_1) between the cladding and coating is of the same order of magnitude as have been measured for oxide fuel and zircolloy cladding ($Hg_1 \simeq 1$ W/cm^2-K). For carefully designed coated tube and ceramic breeder, the gap conductance (Hg_2) may also be assumed to be ~ 1 W/cm^2-K, although there is considerable uncertainty in this number. With these values of gap conductances, the thickness (L) of the ceramic coating (with thermal conductivity K = 1 W/m-K) corresponding to the lowest and highest values of the overall gap conductances (i.e., 443 and 1846 W/m^2-K, see Table 4.29) was estimated to be 1.9 mm and 0.25 mm. In order to estimate the effect of gap conductance on the temperature distribution, the uncertainty in Hg_1, Hg_2, and L values was assumed to be $\pm$ 20%. It may be noted that an uncertainty value of $\pm$ 20% may be an acceptable upper limit as the data below indicates. With these values, the worst combination of Hg_1, Hg_2, and L for the case corresponding to Hg = 1846 W/m^2-K leads to variation of Hg values amounting to -18% and +22%. Table 4-30 shows the maximum and minimum temperatures corresponding to the above values of gap conductances. A comparison of the temperature distributions for these two cases with the reference design is made in Fig. 4-40. The temperature difference between these two cases and the reference design is found to be $\sim$ +30°C and -26°C, respectively. From the temperature distribution calculations, it was observed that only a very small volume fraction of the cell is below the minimum temperature. However, from Fig. 4-40, one can observe that a significant fraction of the breeder region is above the upper temperature limit. This indicates that even uncertainties of the order of $\pm$ 20% can have adverse effects on the breeder design. Hence, the uncertainties in the gap conductance and coating thicknesses need further study.

The other problems that might arise for the solid breeder are the effects of thermal cycling, restructuring of the breeder due to thermal and neutron environment and lithium burnup, swelling, and slumping of breeder, manufacturing tolerances, etc., which might lead to further variations in the gap between the ceramic and the breeder (in the form of a He gas gap). It was found that even 0.1 mm He gas gap can reduce the gap conductance by 25%, with the resultant large uncertainty in the temperature distribution. Obviously, large gaps between the breeder and the coated tubes are unacceptable.

4.3.7.4 Sensitivity to Operating Power Levels and Other Factors

While sensitivity to large power excursions such as plasma disruptions will not be treated in this section, a case of modest power fluctuations of the order of $\pm$ 10% from the reference power levels was analyzed under steady-state operating conditions. The results are presented in Table 4-30. It can be observed from this table that even a modest fluctuation in power levels can lead to rather large variations (40-50°C) in the maximum operating temperature. Therefore, fluctuations in the operating power levels, even $\pm$ 10%, may have detrimental effects on the solid breeder.

As discussed in Sec. 4.3.5, for Li_2O, both the lower temperature limit (to prevent hydroxide precipitation) and the upper temperature limit (to prevent mass transfer) are important. Hence, the worst combination of physical constants and operating power levels would be those that result in temperatures outside the temperature window (i.e., T_{min} = 410°C, T_{max} = 660°C). Two such cases [e.g., (1) 10% lower thermal conductivity and gap conductance and 10% higher power level, and (2) 10% higher thermal conductivity and gap conductance and 10% lower power level) were analyzed, and the results are included in Table 4-30. For the first case, the temperature range was found to be 758°C and 427°C. The temperature extremes for the second case were found to be 587°C and 338°C. For the reasons discussed in Sec. 4.3.5, both cases would be unacceptable if they prevailed for extended periods of time.

4.3.7.5 Coolant and Clad Fractions

Table 4-29 summarizes the coolant and clad fractions for all of the cell designs included in this investigation. The coolant and cladding fractions for the cylindrical and square cell models do not vary significantly.

Table 4-30. Summary of Parametric Investigation (Data Represent Conditions Corresponding to Breeder Region Near First Wall)

	a	b	c	d	e
	Reference Design $Q''' = f(x)$ $K = f(T)$ $Hg = const.$	$Q''' = f(x)$ $K = f(T) \times 1.1$ $Hg = const.$	$Q''' = f(x)$ $K = f(T) \times 0.9$ $Hg = const.$	$Q''' = f(x) \times 1.1$ $K = f(t)$ $Hg = const.$	$Q''' = f(x) \times 0.9$ $K = f(T)$ $Hg = const.$
T_{max}, °C	661	635	693	710	613
T_{min}, °C	407	404	404	418	390

f	g	h	i	j
$Q''' = f(x)$ $K = f(T)$ $Hg = Hg \times 1.1$	$Q''' = f(x)$ $K = f(t)$ $Hg = Hg \times 0.9$	$Q''' = f(x) \times 0.9$ $K = f(T) \times 1.1$ $Hg = Hg \times 1.1$	$Q''' = f(x) \times 1.1$ $K = f(T) \times 0.9$ $Hg = Hg \times 0.9$	$Q''' = f(x)$ $K = f(T) \times 0.9$ $Hg = Hg \times 0.9$
651	674	587	758	707
398	415	388	427	415

K = Thermal Conductivity

Hg = Gap conductance

Q''' = Volumetric heat generation rate

f(x) = Function of Length, x

f(T) = Function of temperature, T

However, there are large variations between these fractions from region to region. The modified rectangular cells are based on slightly smaller breeder volumes and with no change in the coolant channel geometry. This leads to breeder volume reduction of the order of 9-13% for the three regions. This means that the total breeder volume may need to be increased by slightly more than the above percentages in order to maintain the same tritium breeding ratio. To keep the breeder temperature within the established limits, this would require that more cells be added to the rear of the breeding zone (i.e., thicker blankets).

4.3.7.6 Pressure Drop in Coolant Channels and Pumping Power Losses

Since the heat fluxes on the coolant channels are quite modest for low power fusion reactors such as DEMO, the coolant velocities in the blanket coolant channel are only of the order of 3 m/s. The pressure drop across the coolant channels for one of the longest (3 m) blanket modules is estimated to be ~ 7 kPa (1 Psi). This pressure loss in the blanket results in pumping power losses much less than 1%. The thermal hydraulic performance of the blanket modules can be improved slightly (e.g., higher heat transfer coefficient) by using smaller coolant channels than the ones used in these analyses. The use of smaller coolant channels (e.g., 5.1 mm diameter coolant channels instead of 5.1 mm radius coolant channels) will lead to larger pressure losses, but would still be less than 1% of the thermal power. The coolant velocities for the three blanket regions and the pumping power loss were summarized in Table 4-28.

4.3.7.7 Purge Stream Thermal Hydraulic Analysis

Some of the design considerations for the helium purge gas system are the total number of purge gas channels, flow rate through each channel, and the resultant pressure losses across each channel. Since the purge does not provide any cooling function for the breeder, the amount of purge gas and the total number of purge channels are based on considerations of adequate removal of the bred tritium and the processing needs for the purge gas stream. Based on 150 g/day tritium production, two cases were analyzed. The desired partial pressure of tritium (as T_2O) for the two cases was assumed to be 10^{-2} torr to 10^{-1} torr. After a few iterative calculations, the problem was approached indirectly for the conditions presented in Table 4-32.

Table 4-32. Parameters Used for Purge Gas Flow Analysis

Purge gas channel diameter, mm	2.0
Number of purge gas channels	30,000
Purge gas flow velocity, m/s	10.0, 1.0
Purge gas inlet pressure, atm	1.0
Purge gas inlet temperature, °C	200
Purge gas channel length, m	2.5
Desired tritium partial pressure, torr	10^{-2}, 10^{-1}

The above set of data leads to tritium partial pressures of 0.0091 torr and 0.091 torr, respectively, for the two cases. These values are very close to the design goals. The pressure across the purge gas channels was found to be 14 kPa and 1.4 kPa (2.0 psi and 0.2 psi). These pressure loss values for the purge channels are considered acceptable.

4.3.7.8 Summary and Conclusions

The results of the two-dimensional thermal hydraulics analyses show that the use of rectangular blanket cells of appropriate dimensions to account for the variation in the nuclear heating rate results in a viable design concept. Based on the conservative analytical assumption of no intercell heat transfer, the dimensions of the cell modules in relation to the coolant channel dimensions and the location of the coolant channel within the blanket block will keep all the breeder within the allowable temperature limits. The thermal hydraulics parameters in Table 4-28 and the geometric parameters for the three blanket regions summarized in Table 4-29 (modified rectangular cell model) may be used as the interim design basis for the blanket. The major problem is assuring the overall gap conductance values required for the specific blanket regions. However, an experimental program is needed to develop methods (e.g., insulated coatings) for gap conductance control.

The results of the parametric studies shows that combined uncertainties in power levels and thermal conductivities, each amounting to $\pm$ 10%, may lead to unacceptable temperature distribution. Individual uncertainties in gap

conductance or thermal conductivity values of $\pm$ 10% may be acceptable. Power level uncertainties of $\pm$ 10% over an extended period of time would probably be unacceptable for Li_2O breeder. The pressure losses for the coolant and purge gas system are quite small, and the pumping power losses for the blanket coolant as a fraction of the thermal power are negligible.

Although the thermal conductivity of the solid breeder plays a prominent role in the design of solid breeder blankets, appropriate changes can be incorporated into the blanket design to account for low thermal conductivity of a specific solid breeder. There is some loss of tritium breeding ratio when a solid breeder having low thermal conductivity is used. In such cases, appropriate design changes (such as neutron multipliers and/or thicker blankets) may be sufficient to achieve an acceptable tritium breeding ratio.

4.3.8 Materials Compatability

Materials compatibility is an important consideration in the development of a viable blanket design. Primary areas of concern for the Li_2O breeder concept include: breeder/structure, coolant/structure, breeder/purge stream, and breeder/coolant compatibility. The first three issues involve normal operation whereas the breeder/coolant compatibility is of interest only in the event of off-normal conditions such as a coolant leak into the breeder region.

4.3.8.1 Breeder-Structure Compatibility

The compatibility of solid breeder materials with candidate structural materials is an important consideration in the development of a solid breeder blanket. Chemical interactions between the structure and the breeder could impact the mechanical integrity of the structural material and the tritium release characteristics of the breeder. Limited experimental data are available on the compatibility of candidate structural materials with Li_2O. Also, most of the data are from short term tests ($\leq$1000 h) and relatively high temperatures ($\geq$ 600°C). Temperatures of interest in the present design are approximately 400°C. In general, tests have been conducted in a closed system, i.e., sealed capsules. Results will probably be significantly different under more realistic conditions where the oxygen and moisture partial pressures are controlled by the tritium recovery system.

Much of the experimental work on the compatibility of Li_2O with structural alloys has been reported by Chopra,[54] Finn,[53], and Kurasawa.[70,71] Observations from these studies on 316 stainless steel, HT-9 alloy and Inconel 625 exposed to Li_2O and several ternary ceramics, such as $LiAlO_2$ and Li_2SiO_3, are summarized as follows:

- Li_2O is much more reactive than the ternary ceramics under similar conditions.
- Nickel and high nickel alloys are more compatible with all ceramics than are 316 SS and HT-9.
- Although the reaction zones of 316 SS and HT-9 exposed to Li_2O are significantly different, the reaction zone thicknesses do not differ greatly.
- The reaction products Li_5FeO_4 and $LiCrO_2$ are observed after exposure of both 316 SS and HT-9 to Li_2O.
- Li_5FeO_4 is predominant in the outer scale next to the Li_2O whereas $LiCrO_2$ is present near the alloy.
- Significant amounts of Fe and Cr are detected in the Li_2O scale after exposure to 316 SS and HT-9.
- Sealed capsule tests tend to indicate a significant decrease in reaction rate with time.
- These reaction products, Li_5FeO_4 and $LiCrO_2$, are quite volatile at the higher test temperatures (700°C).
- Total scale thicknesses of $\sim$ 50 μm were observed after 1000 h exposure of Li_2O to 316 SS.

The data base on the compatibility of Li_2O with Type 316 stainless steel and HT-9 alloy is insufficient to evaluate the importance of this problem area for the conditions of interest, viz., temperature and oxygen and moisture pressure. Potential approaches for reducing the reaction rates include coating the steel surfaces with nickel or an oxide such as Al_2O_3 or $LiAlO_2$. The impact of these solutions will require further neutronic and thermal-hydraulic analyses.

4.3.8.2 Coolant-Structure Compatibility

Austenitic stainless steels, in general, have good corrosion resistance to degassed high-temperature water. The corrosion resistance is attributed primarily to the formation of an adherent protective spinel film of the type M_3O_4. The corrosion rate under well controlled conditions is about 5 mg/dm^2.month or about 0.75 μm/y.

The major concerns regarding compatibility of stainless steel and water relate to effects of water purity, stress, and steel microstructure. Sensitization, i.e., precipitation of chromium carbides at grain boundaries that occurs after certain heat treatments, appears to have little effect on the corrosion rate of stainless steels in pressurized water with a pH of 7 to 11. However, intergranular attack has been observed in both Types 304 and 316 stainless steel exposed to water with a pH of 3.5.[72] Stress corrosion cracking can occur in stainless steel structural components particularly under heat transfer conditions where steam blanketing can occur or at liquid-vapor interfaces which provide alternate wetting and drying. The principal problems in this area relate to boiling-water reactor or steam-generator applications where chlorides or free caustic in water become sufficiently concentrated to produce cracking. If there is a concentrating mechanism present, chloride and caustic concentrations of the order of ppm in the bulk water can cause cracking. It is generally agreed that some oxygen is required to cause chloride cracking whereas none is required for caustic cracking.

Hydrogen additions to water reduce the tendency for corrosion cracking. The most susceptible areas are welds and the heat affected zones where microstructural changes have occurred and a residual stress is often present. The microstructural effects in the heat-affected zones can be minimized by either reducing the carbon content or adding stabilizers such as Ti, Nb or Ta to the stainless steel. The cold-worked materials are generally regarded as more susceptible to stress-corrosion effects than solution-annealed material.

Since the DEMO application is quite severe in that it includes: (1) high thermal stresses, (2) radiation that can cause hydrolysis of the water and microstructural changes in the steel, and (3) cold-worked material; attention must be given to these compatibility problems. Further analyses should be conducted to evaluate the impact of tritium control requirements on the water chemistry and subsequently on the compatibility effects.

4.3.8.3 Breeder-Purge Stream Compatibility

The stability of Li_2O in the helium purge stream proposed for tritium recovery is a major concern. Two key issues include: (1) the potential for mass transfer of lithium in the form of LiOT in the purge stream, and (2) the potential liquid phase (molten LiOT) sintering of the Li_2O if the tritium (or T_2O) pressure is high enough to precipitate LiOT. The assessment of these effects is given in Sec. 4.3.5.3. A secondary effect which must be evaluated relates to the potential problems that could arise as a result of LiOT precipitation on the down-stream structural wall.

4.3.8.4 Breeder-Coolant Compatibility

During normal operation the coolant will not come in contact with the Li_2O breeder material. However, the potential problems resulting from leakage of high pressure (12 MPa) water coolant into the breeder region are of concern since the blanket will contain on the order of 50,000 tubes with possibly twice as many weld joints. Two key issues relate to (1) high pressure release into the breeder region and (2) formation of highly corrosive LiOH upon contact of the water with Li_2O.

Thermodynamic analyses presented in Sec. 4.3.5.3 indicate that LiOH will form if water leaks into the Li_2O region. The kinetics of the reaction have not been analyzed; however, the reaction is known to be exothermic (ΔH = 8.4 KJ/g Li). The corrosion rates of austenitic steels in LiOH have not been measured for conditions of interest; however, the alkali metal hydroxides are known to be highly corrosive. The combination of high pressure, significant heat of reaction, and potentially high velocity as a result of turbulence from a leak could lead to rapid corrosion of adjacent structural material with a potential for propagating effects. More detailed analyses must be conducted to assess the severity of a coolant-breeder reaction that would result from a coolant tube leak.

4.3.9 Design Configuration

This section provides a description of the conceptual design for the Li_2O solid breeder reference blanket (Sec. 4.3.9.1) and the related energy conversion system (Sec. 4.3.9.2). Rationale for blanket design detail choices is given in Sec. 4.3.9.3, and operational and safety considerations are discussed in Sec. 4.3.9.4.

4.3.9.1 Design Description

The interim reference first wall/blanket design for the Li_2O solid breeder concept is illustrated schematically in Figure 4-17. Materials and design option selections and major operating parameters are listed in Table 4-11. The reference blanket has only Li_2O in the breeding zone; an alternate design (Figure 4-41) adds a neutron multiplier of solid beryllium and a second coolant panel (second wall) between the first wall and the solid breeder to increase tritium breeding. The reference and alternate design concepts are being further developed and analyzed to ensure that design requirements are satisfied and to determine how well they satisfy the overall STARFIRE/DEMO project objectives. The designs will subsequently be compared and the final choice made for the reference Li_2O first wall/blanket materials combination and mechanical design.

Reference Design

Both the reference and alternate designs use the concept of individual first wall/blanket modules configured as parallelepipeds. These modules are assembled into sectors; eight of these identical sectors comprise the first wall/blanket system for the reactor. Final module dimensions will be determined later in the study. This sector/module approach was adapted from the STARFIRE reactor design. Its principal advantages compared to other approaches and the rationale for its selection apply as well to STARFIRE/DEMO, and the related discussions from Reference 1 will not be repeated here.

The first wall is an actively cooled panel made of PCA austenitic stainless steel. Details of the first wall design configuration were presented in Section 4.3.3.4. The basic concept is common to both the reference and alternate Li_2O first wall/blanket concepts. The plasma-facing portion of the first

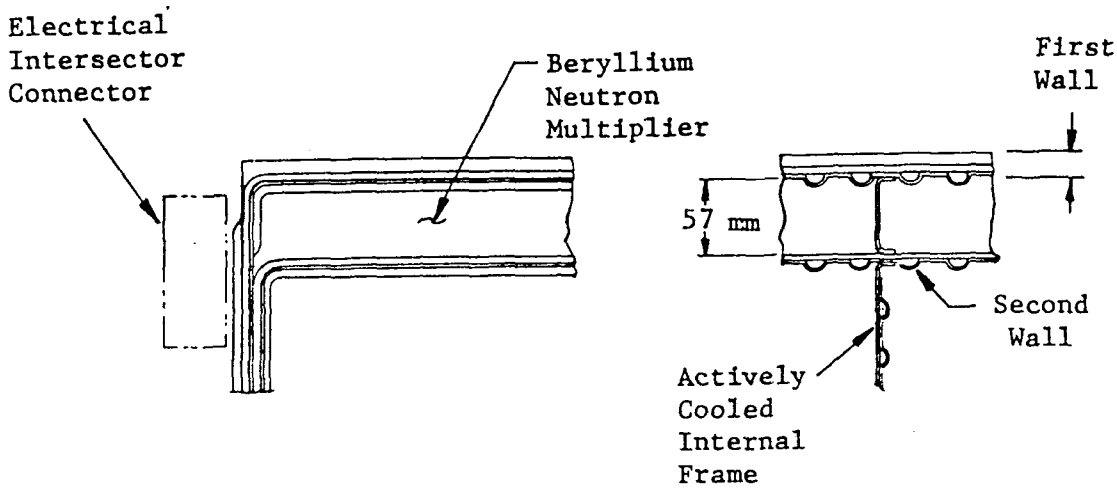

Fig. 4-41. Neutron multiplier/second wall zone for alternate Li_2O breeder blanket design.

wall consists of a 14-mm thick flat plate (10-mm of Be on 4-mm of PCA structure) with a corrugated 3.5-mm sheet of PCA resistance seam welded to the plate's rear face. The 10-mm layer of beryllium is eroded away during the blanket design life; the remaining 4-mm PCA plate thickness together with the corrugated sheet act as first wall structure and contain the water coolant. This structural panel continues down both sides of the modules to the rear of the breeding zone, but the 10-mm Be thickness ends at the edges of the plasma-facing first wall surface. The inlet and outlet ends of the panel terminate in headers in the manifold zone.

The first wall is mechanically and structurally integrated with the blanket. Intermediate, actively cooled frames within the breeding zone are welded to the back side of the first wall and to the rear wall of the breeding zone.

The Li_2O breeder is contained within the boundary formed by the six sides of the module. The toroidally-oriented coolant tubes in the breeder zone are arrayed in banks as shown in Figure 4-17. Each tube makes a single pass

through the breeder. Each tube is fabricated from seamless PCA tubing in the CW condition; inside diameter is 10 mm for each tube, and wall thickness is 0.625 mm. Tube spacing radially and poloidally through the breeding zone is graded in proportion to the local nuclear heating rate, to ensure breeder minimum and maximum temperatures of 410°C and 660°C respectively at all points. Coolant temperature is raised from 260°C at the inlet to 300°C at the outlet by using the proper combination of flow rate and flow velocity produced by orificing at each tube entrance.

The breeder coolant tubes are U-shaped and terminate in the inlet and outlet manifolds located immediately behind the back wall of the breeder zone. As in the STARFIRE design, these manifolds connect all first wall/blanket modules within a sector. There are two inlet and two outlet manifolds, one of each for each of the two separate cooling circuits. The first wall and all even-numbered coolant tube banks are connected to the first circuit; the first coolant tube bank and all other odd-numbered banks are connected to the second circuit. Manifold segments are joined by welding to seals of omega-shaped cross section which accommodate misalignment and any differential thermal expansion between segments.

Helium purge gas is used to remove tritium from the breeder. The low-pressure (~ 1 atm), low flowrate gas is introduced into the pressure-tight breeding zone at one end (in the toroidal direction) of the module through the rear wall. The gas flows through narrow channels (~ 2 mm dia.) formed in the breeder, and exists through the rear wall at the other end of the module. The Li_2O breeder is fabricated in the form of sintered or hot pressed blocks, which are fitted around the U-bend tubes during assembly of the blanket.

Alternate Design

The alternate design approach to the Li_2O solid breeder blanket, shown in Figure 4-41, adds a neutron multiplier and a second actively cooled panel (second wall) to the reference design. The neutron multiplier is solid beryllium, 5.7-cm thick at a 70 percent density factor. The second wall is constructed of two PCA sheets, one flat (facing the breeder) and the other corrugated as for the first wall. The second wall removes part of the nuclear heat from the beryllium and from the first few centimeters of Li_2O breeder. Inter-

costals join the first wall and second wall; these intercostals are aligned with and fastened to frames which extend through the breeding zone to its rear wall. The result is an efficient, integral structural unit which reacts all loads applied to the first wall/blanket module. Addition of the second wall requires that the first wall and all odd-numbered breeder coolant tube banks be connected to the first coolant circuit; the second wall and even-numbered banks are connected to the second loop.

4.3.9.2 Energy Conversion System

Based on the choice of H_2O as the first-wall and blanket coolant for the Li_2O blanket concept (see Section 4.3.3), the basic energy conversion system selected for STARFIRE has been adopted for this blanket concept in STARFIRE/DEMO. Therefore, only a brief description of the system will be given here. The rationale for selection of this system is similar to that for STARFIRE.

Separate heat removal systems operating at different pressure and temperature levels are used for the first-wall/blanket and for the limiter. Dual parallel primary coolant loops cool the eight first-wall/blanket sectors. It is assumed that the power deposited in the limiter will be removed by the limiter/feedwater loop and used for feedwater heating in the steam power conversion system. Thermal energy from other reactor components (e.g., shield, REB) is at such low temperature that it cannot feasibly be used in the power conversion system.

A simplified schematic of the primary coolant system is shown in Figure 4-42. A residual heat removal loop similar to that for STARFIRE is included. Supporting systems are not shown since they will have little if any impact on other reactor systems. Major parameters of the primary coolant system are listed in Table 4-33. Two independent circuits provide water coolant to each blanket sector through dual inlet and outlet headers (ring manifolds). From the outlet header the hot coolant passes through a steam generator and then to the pumps from which it is returned to the inlet ring manifold. The pressurizers (one per loop) are connected directly to the inlet manifolds. The residual heat removal loop connects directly across the two ring manifolds. Because STARFIRE/DEMO operates steady-state, a thermal storage system is not required.

An intermediate heat exchanger is not considered to be required for this system to protect against tritium permeation into the steam side. If an intermediate loop is later shown to be necessary, an economic penalty would result for the Li_2O breeder/H_2O coolant approach because of a significant reduction in thermal energy conversion efficiency.

4.3.9.3 Rationale for Design Detail Selection

The key features of the Li_2O breeder reference first wall/blanket design are listed in Table 4-34, together with the primary reasons for their selection. These features in general are similar to those for the STARFIRE reference design blanket, and the rationale for their selection is likewise similar. The reasons for the changes made from the STARFIRE blanket, primarily in the first wall and manifold zones, are discussed in the following

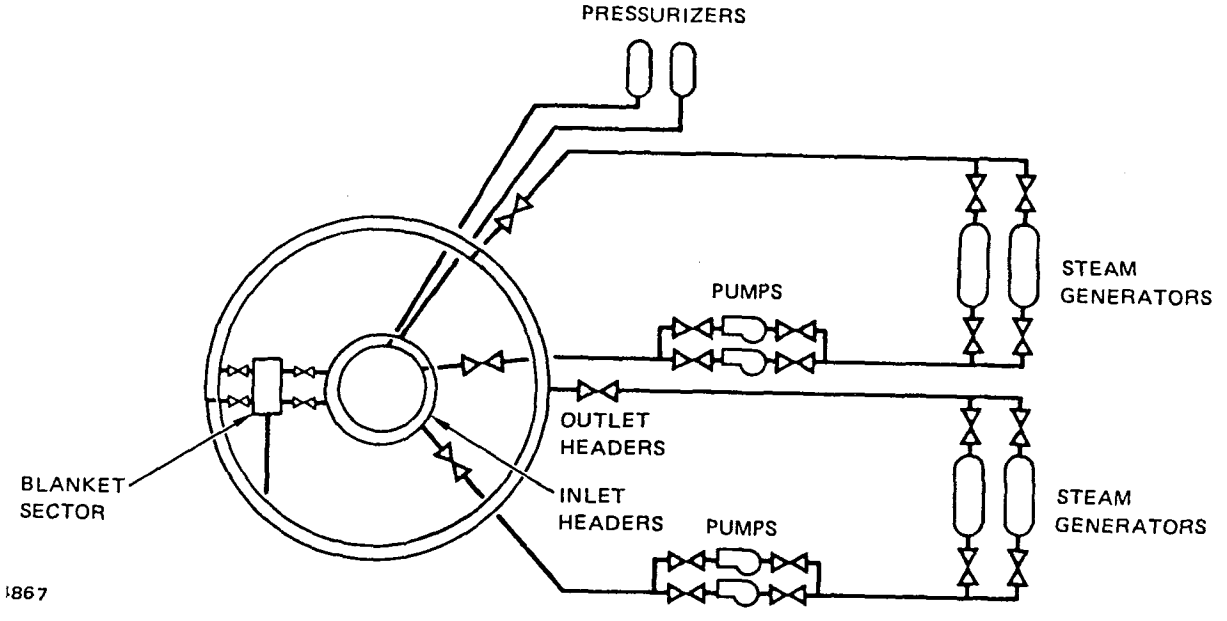

Fig. 4-42. Schematic of energy conversion system for Li_2O solid breeder blanket.

Table 4-33. Major parameters for primary loop (Li_2O breeder blanket)

Coolant	Water
Heat Load	850 MW
Blanket Outlet Temperature	300°C
Blanket Inlet Temperature	260°C
Operating Pressure	11.0 MPa (1600 psig)
Number of Independent Loops	2
Maximum Pipe Size	~ 1.0 m I.D.
Maximum Velocity	~ 20 m/s
Pumping Power	7 MW
Coolant Volume	~300 m^3 (excluding pressurizers)
Number of Steam Generators	2 per loop
Number of Pumps	2 per loop
Pump Capacity	50% of total required capacity

Table 4-34. Key features of selected design details for Li_2O solid breeder reference first wall/blanket concept

First Wall: Be-clad Panel

- Minimum number of pressure boundary welds
- Separates structural and surface-related requirements
- All plasma chamber components coated with same material (Be)
- Low structure temperature (<400°C)
- Mechanically and structurally integrated with blanket

Breeding Zone: Sintered Ceramic with Coolant in Tubes

- All tube welds located outside of breeder zone in low-fluence region
- High pressure coolant contained in small-diameter tubes
- Coolant tubes oriented toroidally
- Tube spacing graded to conform to energy deposition profile
- Reduced density ceramic (70% d.f.with biomodal porosity) to facilitate tritium recovery
- Low pressure He purge stream for tritium recovery
- Coolant outlet temperature and pressure reduced (from STARFIRE) to increase reliability

Manifold Zone: Tubular Manifolds

- Most coolant system welds located within vented secondary containment to accommodate minor leakages while reactor continues to operate
- Steel and water, together with shield, serve as neutron reflectors

Dual Independent Primary Coolant Loops

- Dual loops throughout each module and sector to provide adequate after-heat removal even if only one loop is operable

and water is not included. The total amount of structure required for the first wall is also reduced because no separate first-wall-to-blanket-wall connections or structure are required. Maintainability and availability are not affected, since downtime for changeout of an integrated module would be equal to or less than downtime) for changeout of a separate first wall or a separate breeding blanket.

Neutron Multiplier/Second Wall Zone (Alternate Concept Only)

The primary motive for the use of Li_2O as the tritium breeding material in a power reactor blanket is the anticipated achievement of a net breeding ratios >1 without using a separate neutron multiplier. However, the addition of a neutron multiplier to a Li_2O blanket can produce much higher breeding ratios (1-D basis) than can Li_2O alone. This can permit significant improvements in the reactor design, primarily the reduction in capital costs resulting from reducing the reactor geometric envelope as a result of not requiring a breeding blanket on the inboard wall.

The choice of beryllium as the neutron multiplier is clear, for the STARFIRE/DEMO alternate design Li_2O blanket. Table 4-35 lists the applicable physical properties of beryllium. Table 4-36 presents the comparative advantages and disadvantages of the two primary candidates, beryllium and lead. The principal disadvantage of lead as a neutron multiplier in a power reactor relate to its low melting point (327°C) and potential corrosion concerns. Cooling the lead with primary coolant — whether with internal coolant tubes or with coolant panels at the front and back faces — results in lead temperatures well above the melting point. This leads to long-term corrosion problems for the austenitic stainless steel structure which must contain the lead. The principal advantages of beryllium are higher neutron multiplication, high melting point, and good thermal conductivity, all of which are important to the performance and safety of STARFIRE/DEMO. Swelling of beryllium caused by internal generation of helium can be accommodated by incorporating significant porosity (20-30%) into the microstructure. Toxicity, although a concern, does not appear to be prohibitive either before reactor operation — since fabrication methods have been developed — or subsequent to reactor operation, because fully remote maintenance or

Table 4-35. Properties of solid beryllium

Property[1]	Value
Density, g/cm^3	1.85
Melting Point, °C	1278
Specific Heat, J/g-K	
@ 25°C	2308
@ 300°C	2583
@ 700°C	2983
Thermal Conductivity[2], W/m-K	
@ 25°C	98
@ 300°C	76
@ 700°C	57
Vapor Pressure, Pa	
@ 25°C	2.9×10^{-27}
@ 300°C	9.4×10^{-18}
@ 700°C	1.8×10^{-7}

[1]At 25°C unless otherwise specified

[2]For material at 70% of theoretical density

Table 4-36. Comparison of beryllium and lead as neutron multiplier materials for STARFIRE/DEMO

Category	Beryllium	Lead
Advantages	Very good neutron multiplier. Good thermal conductivity. Low density. High heat capacity. Solid at operating temperature. Good electrical conductivity. Low decay heat after shutdown.	Good neutron multiplier. Low decay heat after shutdown. Availability.
Disadvantages	Resource concern for large fusion reactor economy. Toxicity. Radiation damage (Helium generation).	Highly corrosive. Volume increase, solid to liquid. High density. Low electrical conductivity. Low thermal conductivity.

disassembly operations would be required in any event. Beryllium resources are certainly not a concern for STARFIRE/DEMO, and were shown in Appendix C of Reference 1 to be adequate for a reasonable number (>80) of STARFIRE-sized commercial reactors.

The second wall design is similar to that used for the STARFIRE design, and the rationale for its selection will not be repeated here.

Tritium Breeding Zone

The breeding zone configuration of the Li_2O solid breeder reference design blanket is similar to that for STARFIRE. The primary difference is the absence of the neutron multiplier and second wall. Elimination of the neutron multiplier automatically removes the need for a second wall because the first wall serves as the actively cooled front wall of the breeding zone. This simplifies the blanket design and the connections into the inlet and outlet manifolds.

The toroidal coolant flow direction was selected over the radial flow direction, because radial flow results in a number of important relative disadvantages for concepts using solid breeders and pressurized water coolant. An example of a radial flow blanket design is described in Reference 73. This blanket, designed for a field-reversed mirror device (FRM), uses helium coolant to cool Inconel-clad plates of Li_2O. The choice of water coolant over helium was discussed in Sec. 4.3.3. The primary disadvantages of the radial flow blanket approach (as described in Reference 73) may be briefly summarized as follows:

- Pressurized modules with flat walls are less desirable than small-diameter tubes to contain high pressure coolant. (Such modules would be needed for tokamaks; a more efficient large cylindrical module as used for the RFM[73].)
- The Li_2O plates (2.1 cm average width have average centerline temperatures of ~ 800-1000°C or higher, which are considered to be excessively high (see Sec. 4.3.5). The analysis[73] assumes perfect contact between clad and Li_2O (i.e., no temperature increase at interface) which has not been demonstrated.

- The concept relies on very closely controlled 1-mm constant width gaps between adjacent plate surfaces. The much lower Li_2O temperature range allowed for STARFIRE/DEMO would require gap widths which vary significantly with depth into the blanket, which would compound tolerance control difficulties.
- A helium purge gas piping system is required within the blanket. Separate inlet and outlet connections must be made to each Inconel-clad Li_2O bar.
- An auxiliary cooling system for the blankets was identified[73] as necessary to remove afterheat in the event of a LOCA, but the design and method of operation of such a system were not described.

For these reasons, the toroidal flow concept was judged to be preferable overall to radial flow for the STARFIRE/DEMO Li_2O blanket.

Control of the breeder temperature range is aided by use of a ceramic insulator applied to the coolant tube outer surface. The insulator thickness is varied such that breeder minimum temperature is maintained at 410°C; this is achieved by matching the thermal drop through the tube, insulator, and insulator/breeder contact interface so that the effects of increased coolant temperature along the tube length are compensated. This approach to breeder temperature control is preferable to the use of helium-filled gaps between coolant tube and breeder. There are other considerations which affect breeder temperature control, among which are the effects of: (1) variations in breeder thermal conductivity; (2) variations in nuclear heating rate during operation; and (3) non-uniform gaps due either to tube sag or to compression of the breeder at the breeder/tube interface under thermal cycling. Some of these effects were examined in Section 4.3.7. Further work is needed to define other methods of minimizing variations in, and controlling the magnitude of, the temperature difference between the breeder and coolant tube surfaces.

The selected coolant outlet temperature of 300°C for STARFIRE/DEMO is 20°C lower than for STARFIRE, although the coolant inlet-to-outlet temperature difference of 40°C is the same. The lower outlet temperature will result in a lower thermal energy conversion efficiency, but it permits a reduction in

nominal coolant pressure from 2200 psi to 1600 psi. The reduction in coolant temperature and pressure should lead to increased blanket and coolant system reliability for STARFIRE/DEMO, and on this basis the reduction in efficiency is acceptable.

Manifold Zone

The U-shaped breeder coolant tubes connect to the large-diameter inlet and outlet manifold tubes to permit dual parallel coolant circuits which assures safe cooldown of all the first-wall/blanket modules in the event of the loss of one coolant circuit. The manifold segments are joined together by welding to intermediate seal rings of omega-shaped cross section. These rings accommodate initial misalignment during either blanket sector assembly or module replacement, and differential thermal expansion during operation. The seals simplify removal of the modules during operations in the hot cell, since far fewer module replacement connections need to be cut and rewelded compared to the small-diameter heaters placed between the U-bend tubes and manifolds in the STARFIRE reference blanket. Connecting the tubes to manifolds at the rear of the blanket is considered preferable to using end plenums (as in INTOR[2]) primarily because it avoids difficulties in integrating the high-pressure coolant plenums of the first wall with those of the blanket. Additional work is needed, however, to determine whether the use of seal rings is preferable overall to the header/manifold system in STARFIRE. Further neutronics analyses will help determine whether a separate additional reflector is required, as used for the STARFIRE design.

4.3.9.4 Operation/Safety Considerations

The most important considerations in the operation of a Li_2O solid breeder blanket are (1) the importance of maintaining breeder temperature within the desired range, (2) safe removal of blanket (and first wall) after-heat, and (3) the consequences of breeder/coolant contact in an accident situation. These considerations and the reasons for their importance are summarized in Table 4-37.

The importance of maintaining the breeder between 410°C and 665°C was addressed in Section 4.3.5. The concerns regarding (1) excessive vapor trans-

Table 4-37. Principal operation/safety considerations for Li_2O breeder reference blanket

Concern	Importance	Remarks
o Maintaining breeder temperature within limits	o Temperatures exceeding T_{max} = 665°C lead to excessive transport of LiOH vapor in purge stream o Temperatures below T_{min} = 410°C lead to precipitation of LiOH, and possible low-temperature sintering which tends to inhibit tritium release	o Further work required: - Combined effects on breeder temperature of local variations in breeder properties and wall loading - Conditions which can produce low-temperature sintering - Methods of controlling breeder/tube thermal conductance
o Safe removal of blanket afterheat following a coolant loop accident	o Temperature increases in blanket can lead progressively to annealing of structure and breeder thermal sintering, which preclude reuse	o Dual parallel coolant loops nearly eliminate possibility of unacceptable temperature increases
o Breeder/coolant contact as result of smaller large coolant leak	o Pressure pulse created can rupture module wall o Corrosive LiOH resulting from breeder/coolant reaction can damage other blanket areas, coolant system, or other components	o Further work required to determine consequences to system from LiOH corrosion o Blow-out plugs in module walls vent over-pressures without rupturing module

port of LiOH from the blanket via the purge stream at breeder temperatures above ~ 665°C and (2) the precipation of LiOH as a second phase at temperatures below ~ 410°C, are both considered to be potentially serious problems for Li_2O as a breeder which require further investigation.

The safe removal of afterheat from the Li_2O breeder reference or alternate design blanket is assured by the use of dual parallel coolant circuits, either of which is adequate to safely remove the heat energy even at very low coolant flowrates. Total blanket decay heat is ~ 14.5 MWth at shut-down, decreasing to ~ 2-3 MWth several hours after shutdown. This coolant system arrangement provides the maximum capital investment protection for the plant by keeping all blanket sectors and modules reusable except for any initially failed module.

The pressure pulse created when the high-pressure, high-temperature water coolant leaks from a coolant tube and contacts the hot solid breeder will be safely vented from the blanket by a system of blow-out plugs in the module walls at the end of channels which are in line with the axes of the longest portions of the coolant tubes. This concept requires further analytical investigation, however. Of perhaps even more importance, in terms of protecting plant capital investment, is the LiOH formed in large quantities upon the occurrence of such an accident. The LiOH could enter both the coolant system and purge system, with unknown consequences of increased corrosion. Further work is required to define the severity of such LiOH releases.

4.4 Li-Pb Alloy Breeder Blanket

A summary of the work performed in support of the Li-Pb alloy breeder first wall/blanket concept is presented Section 4.4.1. The remaining subsections of 4.4 deal with specific related topics:

Section	Subject
4.4.2	Design Considerations
4.4.3	First Wall
4.4.4	Neutronics Analysis
4.4.5	Properties of Li-Pb
4.4.6	Tritium Recovery
4.4.7	Thermal-Hydraulics Analysis
4.4.8	Materials Compatibility
4.4.9	Design Configuration

4.4.1 Summary

Liquid Li-Pb alloys have several attractive properties for use as a tritium breeder in a fusion reactor, particularly neutronics properties. The neutron multiplication by the lead provides excellent tritium breeding performance and the neutron attenuation properties of the alloy are attractive for radiation shielding. The 17Li-83Pb eutectic alloy, which has a relatively low melting temperature of 235°C, is selected as the reference breeding material for the liquid breeder portion of the present study. Although the 10Li-50Bi-40Pb alloy has a melting temperature approximately 100°C lower than the Li-Pb binary alloy, the polonium generation from the bismuth and the poorer compatibility of bismuth (compared to lead) with structural materials make this ternary alloy less desirable.

The most important initial consideration for the blanket design is whether to use Li-Pb as both breeder and coolant, or to use a separate gas or liquid coolant. Economics-related issues (e.g., pumping power losses, energy conversion system component design, and efficiency), safety, and blanket and coolant system design complexity are of primary concern. The most important materials-related concerns pertinent to the design evaluations are: the high density of Li-Pb -- which increases blanket structural requirements (and pumping power requirements if used as a coolant); the maximum allowable structural temperature -- about 450°C for ferritic steel because of compatibility concerns; and the low solubility of tritium in Li-Pb -- which

impacts both tritium containment and tritium recovery. For separate coolant concepts, additional important design considerations are breeder/coolant compatibility, control of tritium permeation into the coolant, breeder containment approach, and coolant containment approach (e.g., pressurized module or small-diameter tubes). Induced MHD forces are also important concerns for Li-Pb breeder/coolant concepts and for liquid-metal coolant (i.e., sodium) concepts. Both design concepts (i.e., with and without a separate coolant) were analysed. Conclusions presented for the Li-Pb first-wall/blanket are based on preliminary analyses. More in-depth analyses will be performed to verify these conclusions and to better quantify the design constraints and operating limits.

Helium, pressurized water, and liquid sodium have been considered as potential coolants for the separate-coolant concepts. Primary disadvantages of helium relate to: (1) shielding problems, particularly in the inboard blanket; (2) design constraints imposed by the use of a high pressure coolant in a liquid metal system; (3) lack of a structural material that is compatible with both helium and Li-Pb at acceptable operating temperatures, and (4) economic penalties associated with high pumping power requirements and a more expensive heat transport and energy conversion system. Pressurized water is considered to have two serious disadvantages: (1) perceived safety problems, in terms of a large-scale expulsion of Li-Pb breeder from the blanket as the result of Li-Pb/water contact; (2) high tritium permeation rates through coolant containment structure into the water. Sodium, on balance, is considered at present to be the best separate coolant, primarily because of its good thermal-hydraulic characteristics, its low reactivity with Li-Pb, and its potential to serve as a tritium-recovery medium without requiring Li-Pb circulation. However, MHD effects and reactivity of sodium with water and air are major concerns with sodium coolant.

Ferritic steel appears to be the most appropriate choice for the structural material, primarily because of compatibility considerations. It is questionable whether stainless steel can be used with Li-Pb because of poorer compatibility that results from the higher nickel concentration. Vanadium alloys probably have better compatibility with Li-Pb because of lower solubilities in lithium and lead; however, no experimental data are available. Also, compatibility with the separate coolants would be a major consideration for these concepts.

The first wall of the sodium-cooled Li-Pb blanket is cooled by sodium, and has the same general configuration as the first wall of the Li_2O blanket concepts. The channel size and spacing are modified to account for the lower sodium coolant pressure ($\lesssim$ 0.5 MPa) and differing thermal-hydraulic characteristics. For the Li-Pb breeder/coolant blanket concept, the first wall is formed by the semi-elliptical heads of the elongated radial flow cell which forms the first wall/blanket module. The first wall surface for both concepts can be clad with 10-mm thick beryllium for purposes of plasma impurity control.

Neutronics analyses for the Li-Pb breeder blanket indicate that breeding ratios of about 1.5 to 1.6 (1-D basis) are attainable for blankets with full coverage and 70-cm depth, depending on first wall materials and thicknesses. However, the Li-Pb must be highly enriched (~ 60-70% of ^6Li) to achieve these breeding ratios. A Li-Pb blanket with natural lithium will provide a breeding ratio of only 1.2-1.3 for otherwise similar conditions.

Key properties of 17Li-83Pb that have major impact on the design include melting temperature (235°C), relatively high density (9.4 g/cm^3), and its relatively low solubility for hydrogen (tritium). For a relatively high tritium pressure of 1 Pa, the amount of tritium dissolved in the alloy is only about 4.4 weight parts per billion at projected operating temperatures. This low solubility has important implications regarding tritium recovery, tritium inventory and tritium containment. Tritium permeation rates at this pressure are quite high for most structural materials. The heat of reaction of the 17Li-83Pb alloy with air and water is lower than that of liquid lithium by a factor of ten when compared on a unit volume basis.

Tritium recovery and containment problems associated with the Li-Pb breeder have been evaluated for the separately cooled concepts as well as the Li-Pb breeder/coolant concept. Because of the low solubility of tritium in 17Li-83Pb, fairly high tritium pressures (about 1 Pa) are required for acceptable flowrates if Li-Pb is used as the tritium recovery fluid. These high tritium pressures create tritium containment difficulties in the ex-reactor system, e.g., the steam generator and piping. An intermediate heat exchanger or a double-walled steam generator would be required to reduce leakage of tritium to acceptable levels. Tritium permeation in a water-cooled blanket concept would also be excessive unless a double-walled coolant containment is employed in the blanket. For the case of sodium as the

coolant, permeation rates into the sodium appear to be sufficient to use the sodium as the tritium recovery fluid. Recovery of tritium from the sodium by cold-trapping appears to be an attractive method. The molten salt extraction process is considered the most appropriate method for direct recovery of tritium from Li-Pb.

Compatibility with the structural material is a key feasibility question for the Li-Pb breeder blanket concept. The maximum blanket operating temperature will probably be limited by corrosion/compatibility criteria. Since the data base for 17Li-83Pb is very limited, the compatibility assessment is based extensively on extrapolations of results from similar types of systems, e.g., pure lead and pure lithium and limited static Li-Pb compatibility tests. Critical issues include (1) corrosion/mass transfer effects, and (2) stress corrosion effects. Because of the high solubility of nickel in both lithium and lead, structural alloys containing significant amounts of nickel are subject to extensive mass transfer at higher temperatures. Corrosion of austenitic steels in a large heat transport system are believed to be excessive at acceptable operating temperatures (> 400°C). Those ferritic steels with no nickel should be more resistant to mass transfer effects; however, low temperature (about 350°C) liquid metal embrittlement phenomena are of concern for structures under high stress. Additional experimental data are required to more accurately define the operating limitations of the candidate structural alloys.

Design details of the first wall/blanket for both the sodium-cooled and self-cooled Li-Pb breeder blanket concepts remain to be developed, subsequent to further structural and thermal-hydraulic and analyses. The configurations described indicate the general design features projected from the preliminary analyses. The conceptual sodium-cooled first wall/blanket design (Sec. 4.4.9) is illustrated in Figure 4-43; major parameters are listed in Table 4-38. The module/sector approach used for the Li_2O breeder blanket was adopted for the Li-Pb breeder blanket also. The first wall and blanket are integrated mechanically and structurally. The first wall consists of a beryllium-clad corrugated panel. The breeder zone and first wall are cooled by low pressure ($\lesssim$ 0.5 MPa), high temperature (~ 275° inlet, ~ 400°C outlet) liquid sodium, contained in small-diameter toroidally-oriented tubes or channels which are connected to inlet and outlet manifolds at the rear of the blanket. Tritium permeates through the coolant tube walls from the Li-Pb into

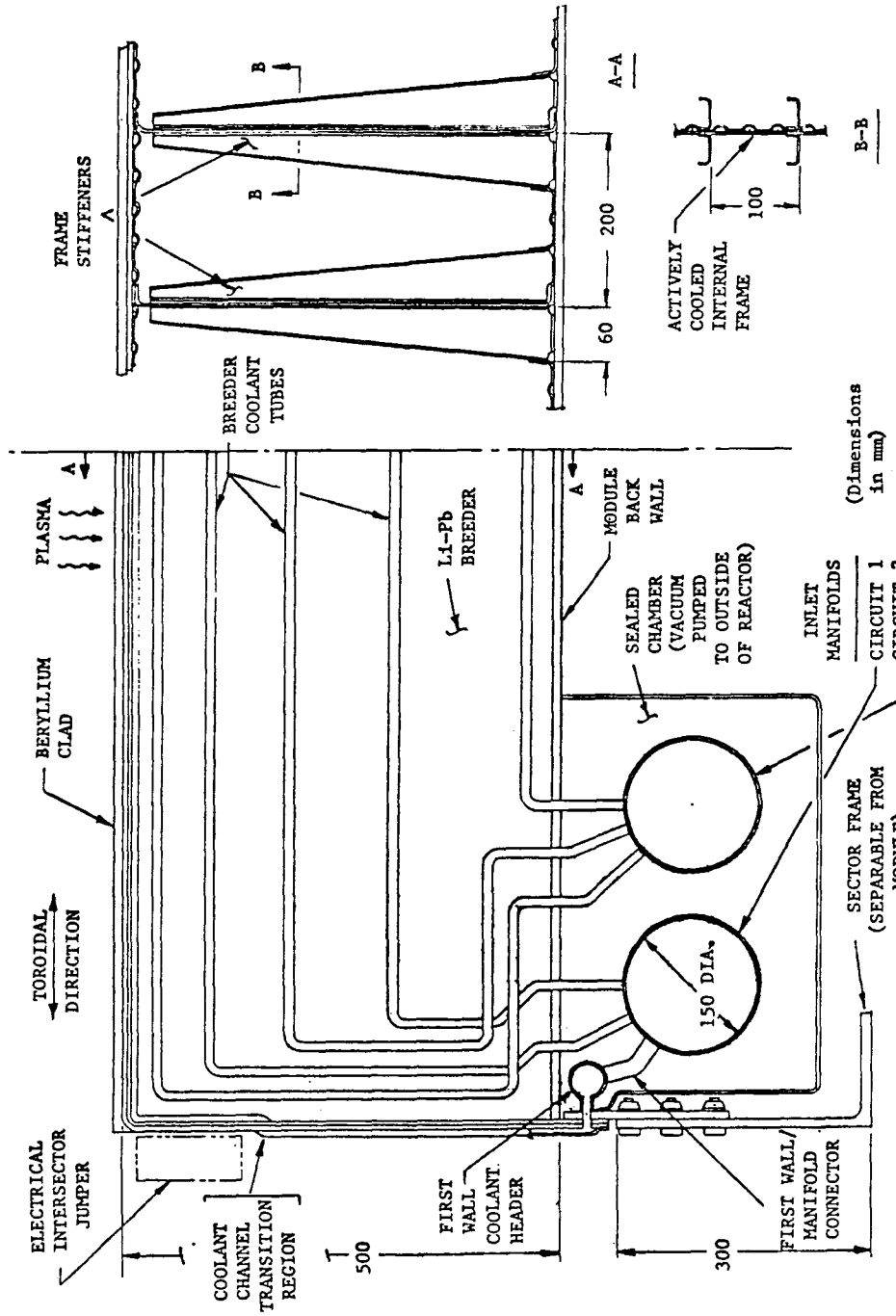

Fig. 4-43. Sodium-cooled lithium-lead breeder reference blanket design.

Table 4-38. STARFIRE/DEMO Lithium-Lead Alloy Breeder Reference Design Description

Selected Materials	
- Tritium Breeder	Liquid 17Li-83Pb Alloy
- Coolant	Liquid Sodium ($\lesssim$ 0.5 MPa)
	- Inlet temperature $\sim$300°C
	- Outlet temperature $\sim$400°C
- Structure	Ferritic Stainless Steel
Selected Design Options	
- First Wall	Be-clad Corrugated Panel
- Breeder Coolant Containment	Small-diameter Tubes
- Other	
	- Toroidal direction for coolant flow
	- Dual parallel primary coolant loops
	- Maintenance by sector removal and replacement

the sodium; a small percentage of the flow rate is processed externally by cold trapping to remove the tritium. Module internal pressure is minimized by using the internal frames to form a series of pressure-tight compartments within the module. For the vertical and slanted outboard modules, most of the gravity load acting on these frames is reacted to the module rear wall through closely-spaced frame stiffeners. Dual parallel primary coolant loops are provided to effect safe removal of afterheat in the event of a coolant loop failure. First wall/blanket maintenance is performed by sector removal and replacement, to minimize reactor downtime.

The conceptual first-wall/blanket design for the Li-Pb breeder/coolant concept is similar to a design proposed for liquid lithium.[6] The blanket module cross section has the form of a double cusp; the beryllium-clad first

wall is formed by the semi-ellipsoidal domes which comprise the front face of the module. The flat side walls of the module are stiffened by internal frames which self-react loads due to internal pressure (~ 1-2 MPa) and which react the gravity loads of the Li-Pb from the side walls and first wall to the back wall and sector structure. The Li-Pb enters the blanket through radial standpipes at about 300°C and is channeled directly behind the first wall at a velocity of about 3 m/s. The liquid metal then slowly circulates toward the back of the blanket to the outlet manifold. A fraction of the coolant is diverted to a tritium processing system for tritium recovery. An intermediate heat exchanger is located as close to the reactor as possible to minimize the amount of Li-Pb required. First wall/blanket maintenance is performed by sector removal and replacement.

4.4.2 Design Considerations

The most important initial consideration in the design of the Li-Pb breeder blanket is whether to use a separate coolant for the Li-Pb breeder, or to use the Li-Pb as both breeder and coolant and to circulate it into and out of the reactor. The two approaches are discussed in Sections 4.4.2.1 and 4.4.2.2 respectively; Section 4.4.2.3 presents a comparison of the two approaches.

Table 4-39 lists the principal considerations, issues or concerns, and candidate design detail options involved in the mechanical and structural design of the Li-Pb alloy breeder first wall/blanket. Where appropriate, distinction has been made between areas applicable to only the separate coolant approach or to the Li-Pb breeder/coolant approach.

The issues presently considered most important to blanket designs using Li-Pb breeder area:

- Effects of breeder/separate coolant contact in an accident
- Structure temperature limit
- Control of tritium permeation into separate coolant
- Pumping power basis
  - MHD effects (sodium or Li-Pb as coolant)
  - High coolant mass flow rate (Li-Pb as coolant)
- Breeder containment approach

Most of the design issues listed in Table 4-39 as well as those above, are related to specific characteristics of the Li-Pb alloy:

- o Relatively high corrosivity to structural materials
- o High density
- o Low tritium solubility

The reasons for the importance of the issues, and the advantages and disadvantages of the various options for design details, are discussed in the following three subsections, as well as in Sections 4.4.3 and 4.4.9. The rationale for selection of the details for the Li-Pb breeder reference first wall/blanket design is also presented in Sec. 4.4.9.

Table 4-39. Design considerations for Li-Pb alloy breeder blanket (separate coolant concept and Li-Pb breeder/coolant concept)

Consideration	Primary Issues or Concerns	Options
Breeder temperature control	o Structure temperature limit o Breeder movement due to E-M forces and thermal gradients	(Separate coolant) o Actively-cooled structure
Breeder containment	o High gravity loads and hydrostatic pressures due to high density	o Containment method: - Compartmentalization with modulator (separate coolant only) - Large modules
Coolant containment	o Reliability against leaks o Coolant pressure and temperature o Structure temperature limit o MHD effects (liquid metal coolants)	(Separate coolant) o Containment method: - Bottle (cylinder) - Small-diameter tubes - Coolant panels o Plenum location: - Module ends (toroidally) - Rear of blanket (Li-Pb breeder/coolant) o Containment method: - Bottle (cylinder) - Pressurized module - Large-diameter tubes
Tritium removal	(Separate coolant) o Permeation into coolant	(Separate coolant) o Removal methods: - Permeation into coolant - Li-Pb circulation for out-of-reactor processing - Double wall coolant tubes with purge helium in annulus
Energy conversion system	o Thermal energy recovery efficiency - Coolant ΔT, T_{max} o Component capital costs o Pumping power losses: - MHD effects (liquid metal coolant) - High mass flowrates (Li-Pb breeder/coolant)	o Heat exchanger options: - Intermediate heat exchanger (IHX) - Steam generator: - Single wall tubes - Double wall tubes
Safety	o Effects of breeder/separate coolant contact in accident o Blanket afterheat removal o Tritium inventory in breeder and coolant	o Blanket protection methods: - Double wall coolant tubes (separate coolant) - Module walls designed to full coolant pressure o Afterheat removal - Dual parallel coolant circuits (separate coolant) - Emergency coolant circuit (separate coolant) - Via radiation and conduction

4.4.2.1 Separate Coolant Concepts

This section describes the definition and evaluation of design concepts featuring Li-Pb breeder blankets cooled by a different fluids. The rationale for selection of sodium as the best separate coolant for a STARFIRE/DEMO Li-Pb blanket is discussed.

Candidate Coolants and Design Concepts

The three separate coolants considered were helium, pressurized water, and sodium. Design concepts and major operating parameters for the coolant were selected to show each coolant to best advantage. Figure 4-44 illustrates the concepts and lists the parameters. Rationale for concept and parameter selection is discussed below as part of the evaluation of concepts.

Comparison of Approaches

The criteria of primary importance for selection of the best Li-Pb breeder/separate coolant concept were (1) extrapolability to commercial reactor conditions in terms of economic competitiveness, (2) safety during accidents, and (3) protection of capital investment during an accident.

The results of the comparative evaluation of the three candidate coolants for Li-Pb breeder blankets are shown in Table 4-40. On balance, cooling with molten sodium appears the best approach of the three, particularly because of its combination of perceived advantages in economics and in safety relative to the other coolants.

The design concept selected for the helium coolant is that of the ORNL/Westinghouse helium-cooled lithium cylinder (Reference 7). This concept eliminates the possibility of large-scale rupture of the Li-Pb container due to a pressure pulse, since the Li-Pb cylinder is designed to withstand the full coolant pressure level. The radial coolant flow approach also takes maximum advantage of the relatively low allowable helium outlet temperature, by (1) cooling the first wall before cooling the breeder, and (2) enabling coolant outlet temperature to be as close as possible to the maximum allowable structural temperature. Tritium is assumed to be recovered by processing the helium coolant stream to remove tritium which permeates through the cylinder

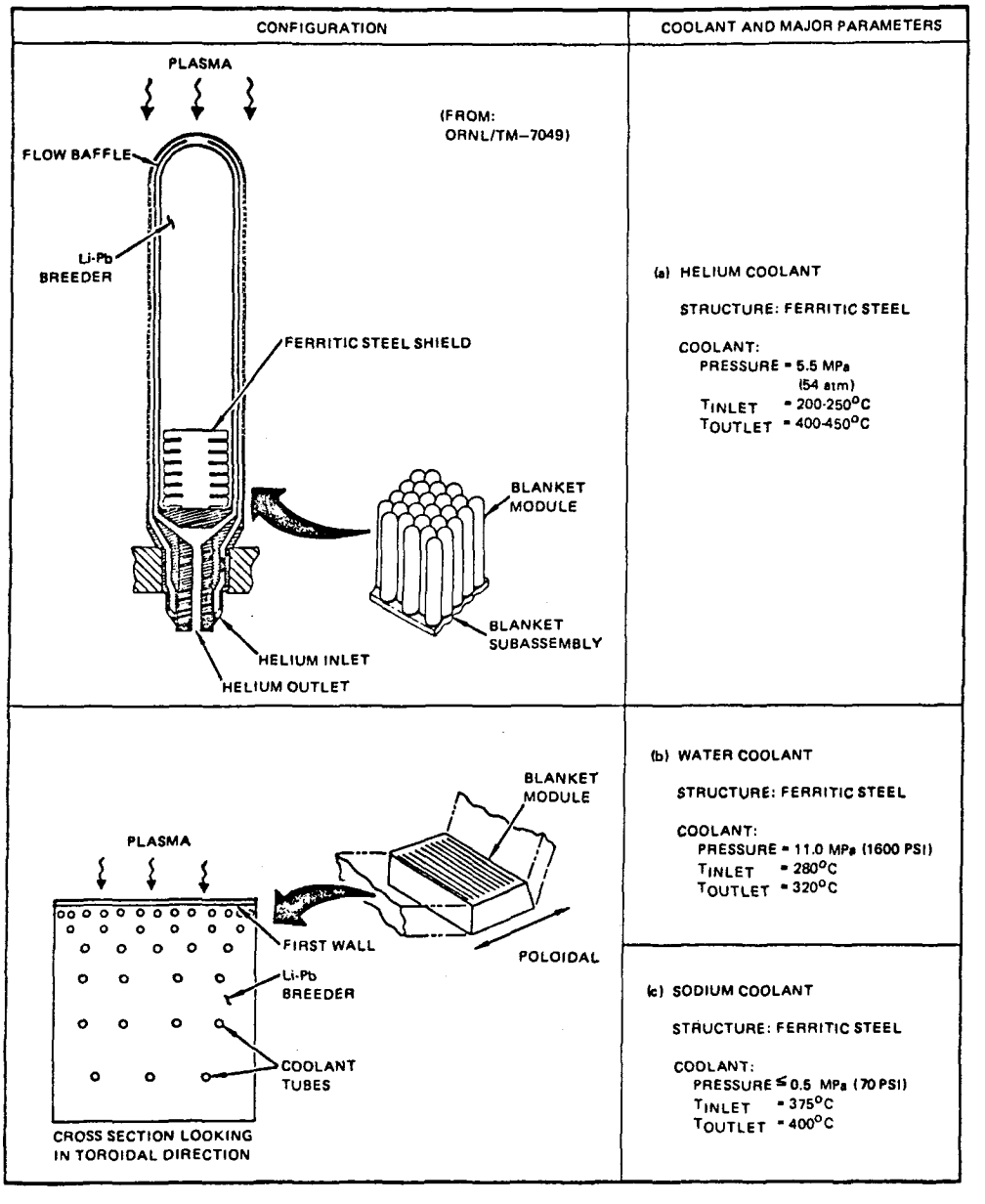

Figure 4-44. Blanket design for candidate separate coolants.

Table 4-40. Comparison of separate coolant approaches for Li-Pb breeder blanket

Consideration	Helium	Water	Sodium
Blanket design	o Bottle	o Slab	o Slab
Tritium breeding	o 15-20% voids	o More than adequate	o More than adequate
Tritium removal	o Permeation into helium coolant	o Processing of low-flowrate Li-Pb stream	o Cold trapping of sodium coolant
Safety			
o Afterheat removal following coolant system accident	o Dual circuits not possible; emergency circuit(s) needed	o Dual parallel circuits	o Dual parallel circuits
o Tritium permeation	o High permeation rate into coolant; used for tritium recovery	o High permeation rate into coolant requires costly processing or double wall containment	High permeation rate into coolant; used for tritium recovery
o Consequences of Li-Pb/coolant contact	o Possible pressurization of breeder region	o Possible expulsion of Li-Pb o H_2 formed by chemical reaction	o No severe consequences; minimal chemical reaction
o Consequences of coolant contact with air, water, or concrete	o None	o None	o Highly reactive
Economics			
o Inboard blanket thickness	o Moderate	o Minimum	o Minimum
o Thermal conversion efficiency	o Low due to reduced coolant T_{max}	o Reduced if double walled tubes required in blanket or if IHX is required	o Acceptable
o Intermediate heat exchanger	o None required	o Not acceptable (economic penalty)	o Possibly required for tritium containment

wall. This means that the Li-Pb cylinders can be individually sealed and that circulation of Li-Pb is not required, a distinct advantage.

The primary drawback of helium coolant, as discussed in Section 5.4.2 of Reference 1, is its economic disadvantages when extrapolated to commercial reactor conditions (e.g., 3.5-4.0 MW/m^2 neutron wall loading). These disadvantages fall into the categories of gross thermal efficiency and pumping power requirements.

An added handicap for helium is the relatively low allowable coolant outlet temperature. The ferritic stainless steel assumed here for construction of the cylinder concept has a maximum temperature limit of 450°C, which is 29°C lower than the structural T_{max} reported in Reference C for austenitic stainless steel for the ORNL/ Westinghouse design (10-cm cylinder o.d. at 4 MW/m^2 wall load). Reducing that T_{max} to the 450°C limit would reduce the helium outlet temperature by approximately the same temperature difference, i.e. from 421°C to 392°C. (The comparison of helium and water coolants in the STARFIRE report assumed a helium outlet temperature of 475°C, and PCA austenitic stainless steel as structure.) Since gross thermal efficiency was only 30% initially for the 421°C helium outlet temperature ($\sim$ 6% less than STARFIRE's gross thermal efficiency), the further temperature reduction is considered to place the economics of a helium/Li-Pb blanket in a poor competitive position at commercial reactor conditions.

The design concept for the water coolant is the slab module shown in Figure 4-44. It has several relative advantages for water coolant over the bottle approach. First, the high percentage of lost breeding volume for the bottle approach is reduced to a low value. Second, first wall and breeder can each be cooled by separate flows, each of which uses the full coolant ΔT. Third, these coolant flows would be contained within small-diameter channels or tubes, which are structurally more efficient than large-diameter cylinders. In addition, dual coolant circuits can be incorporated easily into the design for safe removal of afterheat in the event of a coolant circuit accident.

The use of high-temperature, high-pressure water coolant with 17Li-83Pb appears to have two serious disadvantages. The first is the possibility of reactor damage resulting from breeder/coolant contact. If water coolant contacts the Li-Pb in a leak situation -- pressurization of the module will occur. This pulse propagates to the module walls at the sonic velocity for Li-Pb. Since there is a relatively large amount of coolant present, the energy of the pulse is far greater than the module walls can withstand. It is postulated that the result could be a large-scale rupture a module wall with ejection of a large fraction of the contained Li-Pb into the vacuum chamber. This type of accident could perhaps be precluded by use of the bottle concept rather than the slab concept. The probability of its occurrence in the slab module could be minimized by using a double wall tube construction with an annulus between tubes for detection of a leak from either the breeder or the coolant. (This approach is used for double wall tubes for LMFBR steam generators, as described in Reference 73.) Additional analyses are necessary to properly quantify the results of a water/Li-Pb contact. Engineering tests simulating realistic blanket designs and conditions should also be performed to help determine the validity of the accident scenario.

The second serious disadvantage of the water coolant is the very high level of tritium permeation through single wall tubes into the water (see Sec. 4.4.6). Processing of substantial amounts of tritium from the water coolant is currently considered economically prohibitive. Excessive accumulation of tritium in the water coolant would have important safety implications in the event of a leak. Possible solutions to this problem -- double walled coolant tubes with helium purge gas in the annulus, an IHX, or a steam generator with double walled tubes -- may lower the overall thermal recovery efficiency to levels that are economically unacceptable on a commercial scale. The use of double walled tubes for water coolant requires further investigation.

On balance, sodium appears at present to be the best choice as a separate coolant for an Li-Pb breeder blanket. It retains the desirable qualities of water as a separate coolant while either eliminating or making use of its undesirable qualities. Table 4-41 summarizes the relative advantages and disadvantages of the sodium separate coolant approach. The risk of large-

Table 4-41. Advantages and disadvantages for sodium-cooled Li-Pb breeder blanket relative to other coolants

Advantages
- Low pressure (< 0.5 MPa); nonreactive with Li-Pb
- Good thermal conversion efficiency
- Proven tritium recovery method (cold-trapping)
- Tritium permeation into coolant provides a method for tritium recovery
- LMFBR primary coolant system component technology is directly applicable
- Dual parallel coolant circuits for safe afterheat removal
Disadvantages
- Small volume (<5 vol. %) of chemically reactive liquid metal introduced into blanket
- Relatively corrosive coolant
- MHD effects introduce pumping power losses
- May require IHX or double-walled steam generator for tritium containment

scale module rupture is negated since contact between Li-Pb and the low-pressure sodium in an accident will not cause a vapor explosion or pressure pulse. Tritium permeates readily from the Li-Pb through the ferritic steel blanket coolant tubes into the sodium, from which it is recovered using cold trapping. Tritium inventories are kept at acceptably low levels in the Li-Pb and in the sodium. The energy conversion system can utilize either an intermediate heat exchanger (IHX), or a liquid metal steam generator with double-wall tubes of the type being developed for the Liquid Metal Fast Breeder Reactor (LMFBR) program (Reference 73). The major concerns regarding the use of sodium coolant relate to its reactivity with air, water, and concrete and potential design constraints imposed by MHD effects.

The sodium-cooled Li-Pb blanket concept is discussed in more detail in Section 4.4.9.

4.4.2.2 Li-Pb Alloy Breeder/Coolant Concepts

This section describes the development and evaluation of design concepts which use Li-Pb alloy as both tritium breeder and coolant. Rationale for selection of the elongated radial-flow cell as the reference Li-Pb breeder/coolant concept is presented.

The process of developing and evaluating candidate design concepts for Li-Pb breeder/coolant approach relied heavily on the results of similar efforts for liquid lithium blankets in the joint Argonne/MDAC study reported in Reference 6. Based on these results, two concepts were given serious consideration in the present study: (1) the bottle-type cell concept; and (2) the elongated radial-flow cell concept. These are described in Figure 4-45. Ferritic steel is assumed to be the structural material for both, with vanadium alloy V-15Cr-5Ti as an alternate material.

A variation of the tube bank approach illustrated in Figure 4-45 (a) was adapted for the WITAMIR-I tandem mirror reactor (TMR) Li-Pb breeding blanket (Reference 75). It is a logical blanket concept for a TMR, but is not a feasible concept for a tokamak because its use has two severe disadvantages which do not apply to a TMR: (1) a separate, additional first wall is required which can take surface heat loads equal to 25% of the neutron wall load value; (2) it is very difficult to incorporate a pump limiter for impurity control, and virtually impossible to incorporate a poloidal divertor.

The bottle-type, or cylindrical, cell has a first wall which is formed by the cell's dome (see Figure 4-45(b)) and cooled from the back side by flowing Li-Pb. This is a relatively simple design mechanically and structurally, and adapts readily to non-uniform plasma chamber regions such as the limiter zone. However, the void space enclosed by contiguous bottles would average 15% to 20% of available breeding volume. In addition, these spaces should be occupied by some material such as graphite to avoid neutron streaming problems. This presents an added complexity to the blanket design since these regions must be cooled in some way and protected from the plasma. This concept would also require a large number of individual bottles -- probably 10,000 to 20,000 -- for a STARFIRE-sized commercial tokamak. (Bottle diameter and quantity would be a function of induced E-M forces during a disruption.)

The elongated radial-flow cell shown in Figure 4-45(c) is similar to the STARFIRE backup lithium blanket concept (Reference 76 and to the lithium-cooled module concept in Reference 6. The semi-ellipsoidal heads form the first wall, which is cooled from the back side by flowing Li-Pb. The Li-Pb enters the blanket through a standpipe, flows from a manifold through the gap between a baffle and the first wall, then reenters the chamber from which it is withdrawn through holes in the cell's rear wall. This concept minimizes voids in the regions which are available for breeding and also minimizes associated neutron streaming problems. It is thus a lower risk in assuring that the STARFIRE/DEMO blanket would produce a net breeding ratio > 1 in actual practice. The module walls are pressurized internally to ~ 1-2 MPa, however, because of (1) the interconnection of the blanket modules combined with the high density of the Li-Pb, and (2) the pressure head required to pump the Li-Pb through the primary coolant system. This requires internal frames spaced relatively close together to break up the large-area flat walls into smaller panels.

Although the choice is not clear-cut, the elongated radial-flow cell approach is considered overall to be superior to the bottle cell, and has been adopted for the present as the reference design concept for the Li-Pb alloy breeder/coolant blanket.

4.4.2.3 Comparison of Separate Coolant and Breeder/Coolant Approaches

Comparison of the sodium-cooled (Section 4.4.2.1) and self-cooled (Section 4.4.2.2) design concepts for Li-Pb breeder blankets for STARFIRE/DEMO indicated significant differences important to selection of a Li-Pb breeder reference design in four areas. The results of the comparison are summarized in Table 4-42. They indicate that, on the basis of the work performed to date on both approaches, cooling the Li-Pb breeder with sodium coolant appears preferable to using the Li-Pb as both breeder and coolant.

Of the issues listed in Table 4-42, the one considered ultimately most important to the feasibility of any Li-Pb breeder blanket is compatibility with structure. As discussed in Section 4.4.8, on the basis of available data, austenitic stainless steel is not acceptable for use with Li-Pb in power reactor blankets. It is also questionable whether Li-Pb is adequately compatible with ferritic steel at temperatures $\gtrsim$ 375°C for continuous use. The

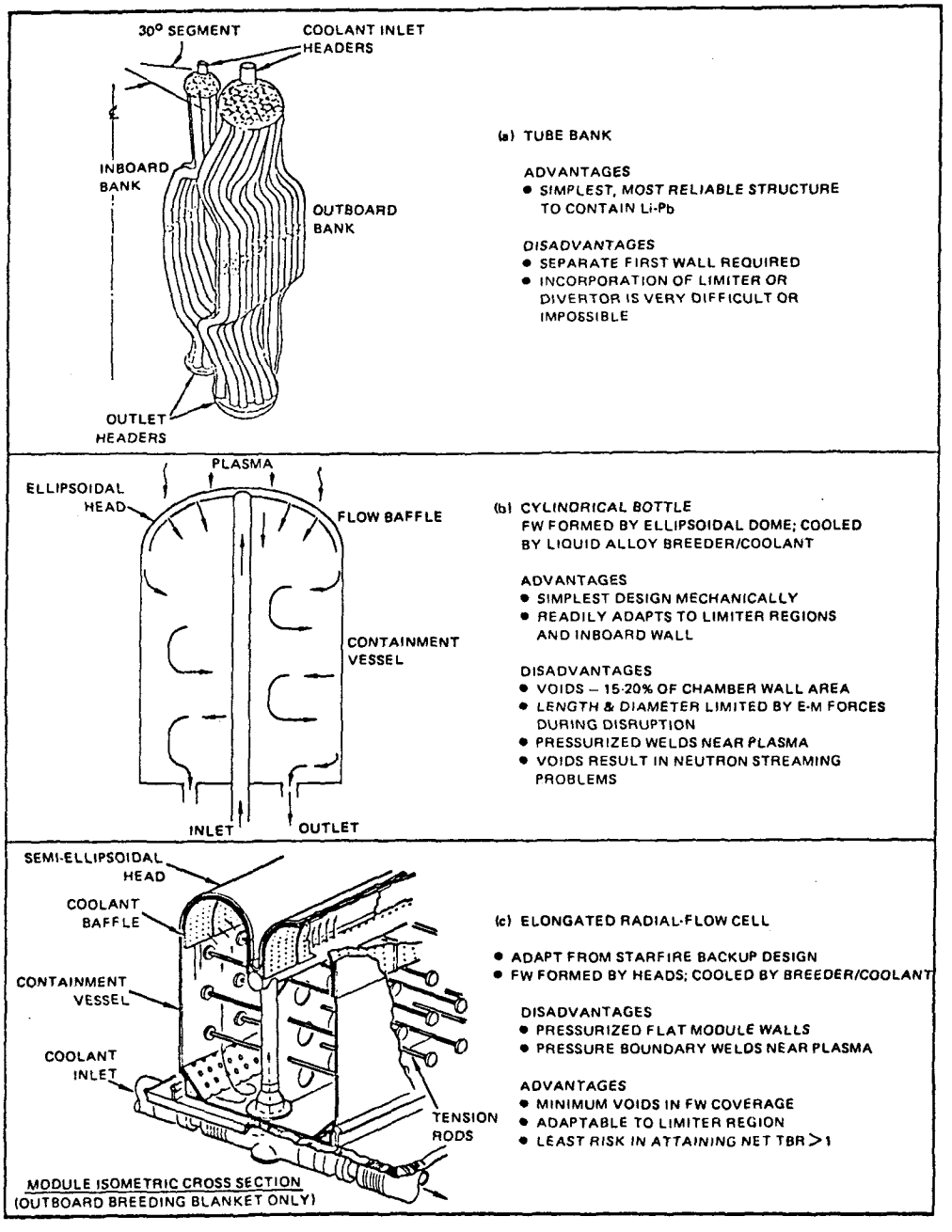

Figure 4-45. Candidate blanket design approaches for Li-Pb breeder/coolant concept.

Table 4-42. Comparison of sodium-cooled to self-cooled Li-Pb alloy breeder blanket

Category	Advantage: Sodium Cooled	Advantage: Li-Pb Cooled	Remarks
Li-Pb Structure Compatibility	✓		Structure T_{max} limit for corrosion expected to be lower for system with flowing Li-Pb
Chemical Reactivity		✓	~ 5 volume % of reactive liquid metal added to blanket
Afterheat Removal following coolant loop accident	✓		Dual parallel coolant circuits for sodium-cooled blanket
Primary Coolant Loop Component Development	✓		LMFBR technology available for sodium-containing components
Blanket module internal pressure	✓		Low Li-Pb static head and no pump pressure head within sodium-cooled module

alternate vanadium alloys may ultimately be shown to be the only acceptable candidate structure material; however, ferritic steel is presently the reference structural material for STARFIRE/DEMO for Li-Pb blankets. The discussion in Section 4.4.8 also indicates that compatibility problems are likely to be significantly greater for systems in which Li-Pb is pumped through the blanket than for systems with "stagnant" Li-Pb (i.e., where Li-Pb is not pumped or moved by other than induced electromagnetic forces). The 450°C structural temperature limit is specified for ferritic steel in the sodium-cooled blanket where the Li-Pb is essentially stagnant is expected to be lower for the self-cooled blanket, which will make it less attractive from an economic standpoint.

Blanket safety is an important concern for both concepts. The sodium-cooled concept introduces a small amount of a more reactive liquid metal (< 5% of the blanket volume) into the reactor. However, the blanket and shield construction results in at least three separate structural barriers between the sodium and any source of water (e.g., shield coolant). The double-wall construction of the steam generator, using LMFBR technology being developed (Reference 73), minimizes the risk of sodium/water contact in that component;

the sodium-cooled blanket has dual parallel coolant circuits (similar to the arrangement for the Li_2O solid breeder blanket) which ensure safe removal of blanket afterheat in the event of failure of one coolant circuit. Such an arrangement is not possible with the self-cooled Li-Pb blanket. In the event of failure in the primary coolant circuit or a significant leak from a blanket module, the coolant circuit must be shut down. Consequently, blanket afterheat is removed only by radiation and conduction to regions away from the blankets. Whether this is possible without exceeding the safe reuse temperature for ferritic steel ($\sim$ 650°C), with or without draining of the Li-Pb from the modules, remains to be determined.

The availability and applicability of LMFBR steam generator and coolant pump technology from the LMFBR program appears to be a relative advantage for the sodium-cooled blanket. Because of the much higher mass flow rate required for Li-Pb ($>$ 8X higher than for sodium at the same ΔT) and higher corrosivity of Li-Pb, the development of high-rate Li-Pb pumps and Li-Pb steam generators is considered to be more difficult than for sodium coolant. This development would have to be accomplished prior to STARFIRE/DEMO final design. Li-Pb energy conversion system component costs are likely to be higher, also. As an example, the twelve Li-Pb pumps for WITAMIR-I had total projected costs of 112 M$ (Reference 75). Using the same cost equation, sodium pumps required for the same reactor thermal power level and coolant temperature differences (blanket inlet to outlet) would be $\sim$ 22 M$, a reduction of 90 M$. Operating parameters for the energy conversion systems for separately-cooled and self-cooled Li-Pb blankets remain to be determined.

Blanket module internal pressure levels are much lower for the sodium-cooled concept, $\lesssim$ 0.5 MPa as compared to $\sim$ 1-2 MPa for the self-cooled concept. This low pressure level is the result of (1) not requiring the interconnecting of the Li-Pb zones of blanket modules within a sector, and (2) the absence of any pumping pressure head applied to the Li-Pb. The low internal pressure levels are perceived as a distinct advantage in reduced stress levels and reduced risk of leaks for the module walls.

4.4.3 First Wall

Critical aspects of the first wall that relate to plasma-materials interactions, and hence are relatively insensitive to the blanket concept, are presented in Sec. 4.2 above. Those aspects that relate more specifically to the blanket materials selection are presented in this section for the lithium-lead breeder blanket concept. The focus in this section is on the thermal-hydraulic and stress analysis of the lithium-lead first wall and the impact on design configuration. The important area of materials compatibility is presented in Sec. 4.4.8.

4.4.3.1 Materials Selection

For the analyses presented, ferritic steel (HT-9) is considered as the primary candidate structural material and the vanadium alloy (V-15Cr-5Ti) is considered as the backup material. Table 4-43 summarizes the important favorable and unfavorable characteristics of these two candidate first-wall structural alloys. Compatibility with lithium-lead is an area of great uncertainty and is a key feasibility issue for the lithium-lead breeder/coolant system. Poor compatibility (see Sec. 4.4.8) is the primary reason austenitic stainless steel is not proposed as a candidate structural material.

4.4.3.2 Stress Analysis

The lithium-lead cooled blanket module shown in Fig. 4-46 has a design pressure of 2 MPa. The hoop stress due to such a pressure on the semicircular first wall of thickness 5 mm is only of the order of 50 MPa. This stress will be further reduced to about 10-20 MPa if advantage is taken of the stiffness of the 10-mm thick beryllium cladding. There is about a 110°C temperature gradient through the first wall. The additional stresses due to this temperature gradient have to be computed in the future. Each blanket module is stiffened by a series of frames with a 5-mm thick web (Fig. 4-46) spaced at an interval of S (cm) whose magnitudes are to be determined. The maximum bending stress in the sidewall due to the internal pressure is $\sigma_b = 6\ S^2$.

The maximum allowable bending stress is 1.5 S_m, which at 450°C, is 275 MPa for HT-9 and 300 MPa for vanadium. Thus, the maximum allowable spacing (S) for the frame is 6 cm for HT-9 and 7 cm for vanadium. The membrane stress created in the frame web because of the pressure acting on the side walls is 12 MPa for HT-9 and 14 MPa for vanadium which are small.

Table 4-43. Favorable and Unfavorable Characteristics of Prime Candidate Alloy Systems

Alloy System	Favorable Characteristics	Unfavorable Characteristics
Austenitic Stainless Steels (316, PCA)	Good fabricability/weldability Extensive property data base Availability/experience factor Compatible with H_2O, Air, H	Physical properties (k, α) Limited operating temperature (radiation effect and mechanical properties) Requires thermomechanical treatment (cold-work) Radiation creep properties
Ferritic Steels	Low radiation swelling Better physical properties than austenitic steel Compatible with H_2O, Air, H Low radiation creep	Effect of radiation on DBTT Welding difficulties (PWHT) Sensitivity to TMT Ferromagnetic properties Compatibility limitations
Vanadium Alloys	Good radiation damage resistance Low long-term activation Properties insensitive to composition variations Good physical properties (k, α)	Compatibility with Air, H_2O, He Fabrication requirements (environment) High hydrogen permeability/solubility Not commercially available

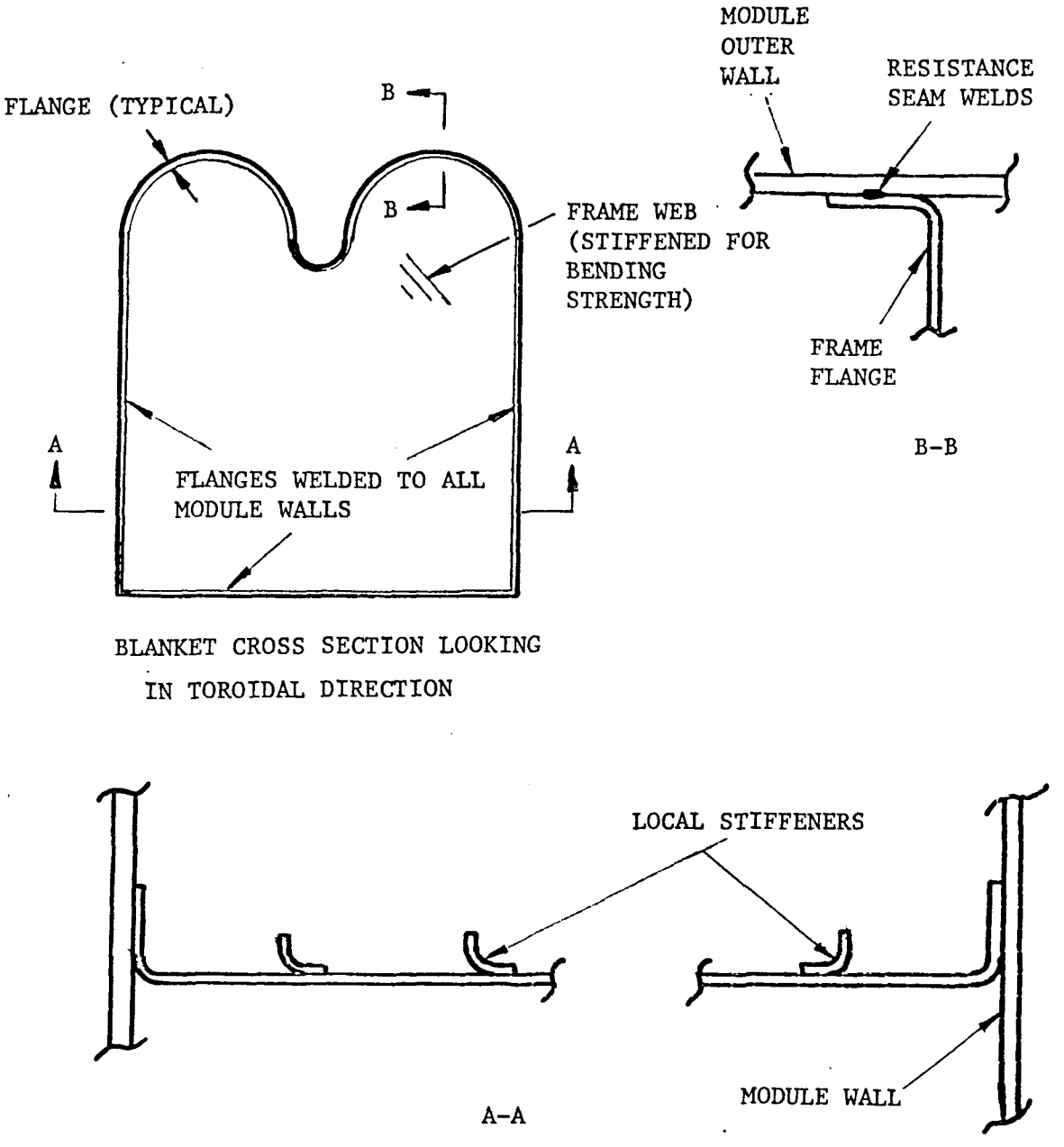

Fig. 4-46. Schematic of first-wall for lithium-lead self-cooled breeder blanket concept.

An additional purpose served by the stiffening frame for the blanket modules is to allow a more efficient load path for the dead weight of the lithium-lead in each module to the back wall. The most critical module from this viewpoint is the one that is horizontal in which case, if the stiffening frames were absent, the total dead weight of the lithium-lead would have to be transferred by the bottom side wall to the back wall, causing very large bending stresses in it. The stiffening frames act as shear panels and provide a major load path for the dead weight to the back wall. The maximum stress in the side wall due to the dead weight is reduced to 5 MPa for HT-9 and 7 MPa for vanadium which are very small. A further source for stress in the blanket module is the temperature difference between the first wall and the back wall which could cause additional stresses in the side walls and the stiffening frames. This has to be analyzed in the future.

4.4.3.3 Thermal-Hydraulic Analysis

Thermal-hydraulic analyses were performed for the first wall of the lithium-lead module to determine if the temperatures of the structural materials are within the acceptable range and to provide necessary input for calculations described previously. The first wall and the coolant channels of the lithium-lead blanket module consist basically of two half-cylindrical shells as shown in Fig. 4-46. By symmetry, the temperature distributions in the two half-cylindrical shells should be very close and it is only necessary to calculate the temperature distribution in one of the cylindrical shells. Figure 4-47 shows the two-dimensional geometrical model used for calculating the temperature distributions of the first wall. As shown in Fig. 4-47, in an exaggerated manner, the first wall consists of a 10 mm thick coating material and a 5 mm thick structural material. Coolant channel is located inside the structural material. The cladding, the structural material, and the coolant are divided into a total of 66 cells as shown in Fig. 4-47. As a first approximation, the thermal interactions between the half-cylindrical shell and the rest of the blanket module are neglected. Temperature distributions of the cladding and the structural materials were obtained by using the computer code THTB[77], which is capable of performing 3-dimensional, transient, heat transfer calculations for various geometries.

The operating conditions along with the materials examined for the first wall are listed in Table 4-44. In addition to the operating parameters listed

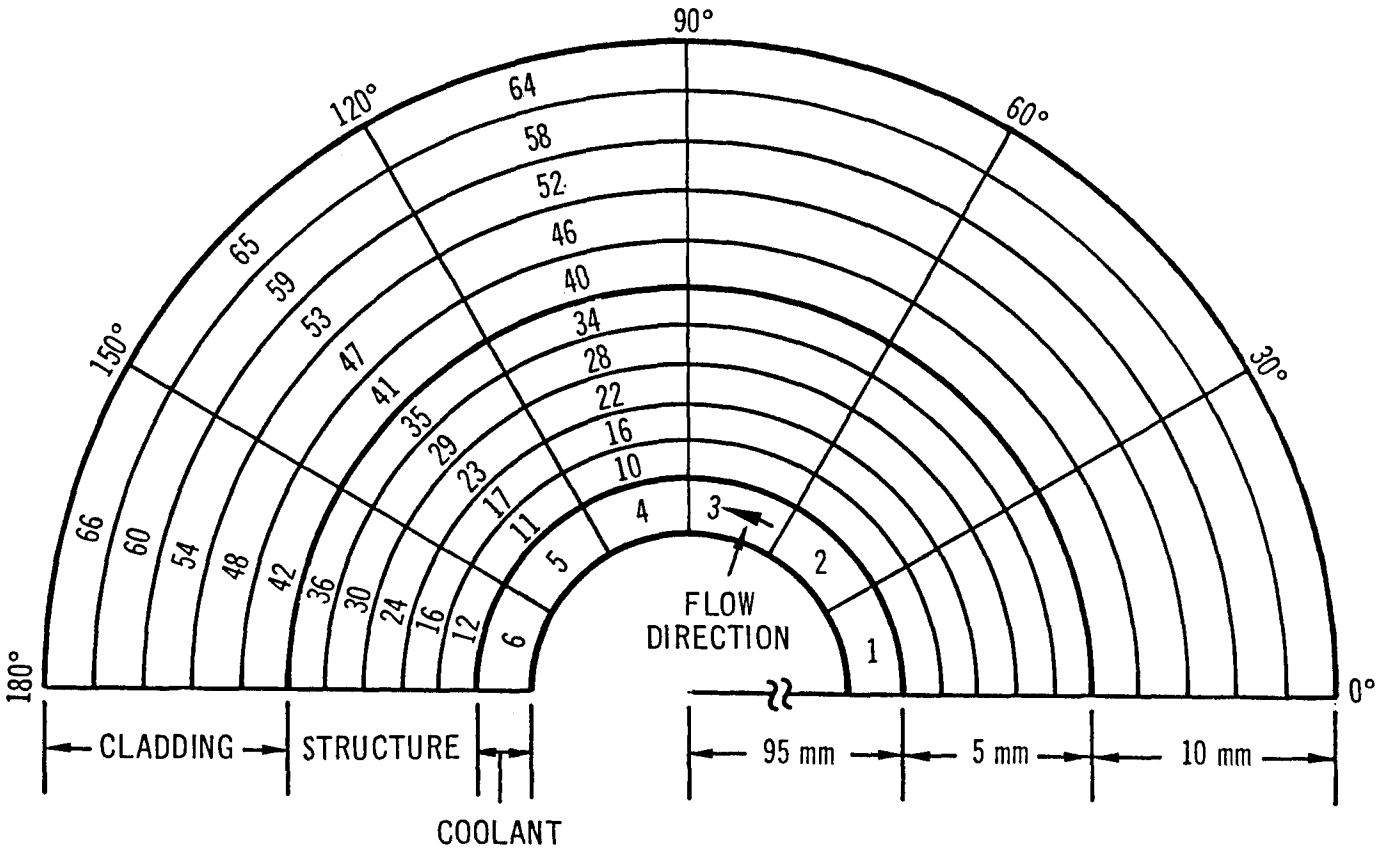

Fig. 4-47. Geometrical model and dimensions of the first-wall-coolant system for the lithium-lead blanket module.

Table 4-44. Operating Conditions and Materials Used for the First Wall of the Li-Pb Blanket Module

Surface Heat Flux:	40 W/cm^2 with a cos ξ distribution away from the plasma (vertical) axis
Bulk Nuclear Heating (cladding, structural material, and coolant):	20 W/cm^3
Coolant (Li-Pb) Inlet Temperature:	600 K
Cladding Material (10 mm):	Beryllium
Structural Material (5 mm):	Ferritic Steel (HT-9) and Vanadium alloy (V-15Cr-5Ti)
Coolant Pressure:	2 MPa

in Table 4-44, several other parameters required as the input to the calculations include: (1) the heat transfer coefficient between the coolant and the structural material (h); (2) contact coefficient between the cladding and the structural materials (h_c); (3) coolant temperature rise (ΔT); (4) coolant velocity (V); (5) and thermodynamic properties of coolant, structural, and cladding materials. Table 4-45 is a list of the values assumed for some of these parameters used in the calculations.

Table 4-45. Assumed Values for h, h_c, ΔT,

h	=	$56750 \frac{W}{m^2 - K}$ $(10000 \frac{Btu}{hr\text{-}ft^2\text{-}^oF})$
h_c	=	$17025 \frac{W}{m^2 - K}$ $(3000 \frac{Btu}{hr\text{-}ft^2\text{-}^oF})$
ΔT	=	15^o C

Results of steady state calculations for beryllium-ferritic steel combinations are shown in Table 4-46. Only temperatures in half of the calculation domain are shown in Table 4-46. The other half of the first wall showed similar temperature distribution. The maximum temperature of 537°C

Table 4-46. Temperature Distribution in the First Wall (Beryllium-Ferritic Steel) of the Li-Pb Blanket Module

	Node	Temp(°C)	Node	Temp(°C)	Node	Temp(°C)
Coolant	4	335.1	5	337.9	6	340.6
	10	361.1	11	360.1	12	356.8
	16	385.8	17	380.9	18	371.9
	22	409.2	23	400.7	24	386.0
Structure	28	431.9	29	419.8	30	399.4
	34	453.8	35	438.0	36	411.9
	40	504.8	41	480.1	42	440.3
	46	513.8	47	493.9	48	444.8
	52	522.1	53	493.9	54	448.6
Cladding	58	529.8	59	499.8	60	451.7
	64	536.7	65	504.9	66	454.0

is well below the melting points of the materials used. The circumferential temperature gradient is quite small (<1°C/mm) compared to the radial temperature. This is because the resistance to heat transfer is predominantly in the radial direction. The largest temperature gradient (~ 22°C/mm) occurred in the structural material in the radial direction. Similar results were obtained for the beryllium-vanadium alloy combination.

There are two places in the radial direction where temperature jump occurs. These are located at the interfaces between the coolant and the structural material and between the structural material and the cladding. Of particular interest is the ΔT across the struture-cladding interface, since differential thermal expansion between the two materials may cause excessive thermal stress at the interface. The ΔT across the structure-cladding interface is determined mainly by the contact coefficient (h_c). Table III (h_c = 17025 W/m^2-K) shows that a ΔT of 51°C occurred between nodes 34 and 40. The

temperatures shown in Table 4-46 are located at the center of each node. By extrapolating linearly to the interface, the ΔT at the interface is $35.5^{o}C$ between nodes 34 and 40. It is important to find out how ΔT across the interface varies with the value of h_c since an accurate determination of h_c is not likely from existing data at this time (h_c depends on such parameters as interface flatness, joint pressure, mean interface temperature, etc.). Figure 4-48 shows the variation of ΔT across the beryllium-ferritic steel interface with h_c obtained by extrapolation described previously. It can be observed that ΔT decreases with increasing values of h_c and appears to asymptotically approach some constant value. The value of h_c (1.7×10^4 W/m^2-K) used in the calculations described previously is believed to be a reasonable estimate. The selection of this particular value of h_c is based on the assumption that good contacts are maintained between the cladding and the structural materials during fabrication of the first wall. This should also be the minimum requirement for the first wall in general, otherwise the first wall will not be expected to last through its required lifetime. However, in view of the uncertainty associated with the value of h_c (particularly, the lack of data in the relatively high temperature range which is of interest here), it becomes necessary to conduct further research in this area.

4.4.3.4 Design Configuration

Design details of the first wall for both the sodium-cooled and self-cooled lithium-lead breeder blanket concepts remain to be developed, subsequent to further structural and thermal-hydraulic analyses. The configurations described below for the two concepts were selected based on qualitative evaluations and on the results of preliminary analyses described in the foregoing sections.

The first wall for the sodium-cooled lithium-lead blanket has the same configuration as that for the water-cooled Li_2O solid breeder blanket described in Section 4.3.3.4. The principal differences in design details for the sodium-cooled first wall are (1) changed flow channel cross section areas to account for the differences in thermal-hydraulic characteristics compared to water coolant, and (2) additional structural attachments connecting the first wall to the blanket structure, to help react lithium-lead gravity loads acting on the wall in the modules at the top and sides of the blanket sector.

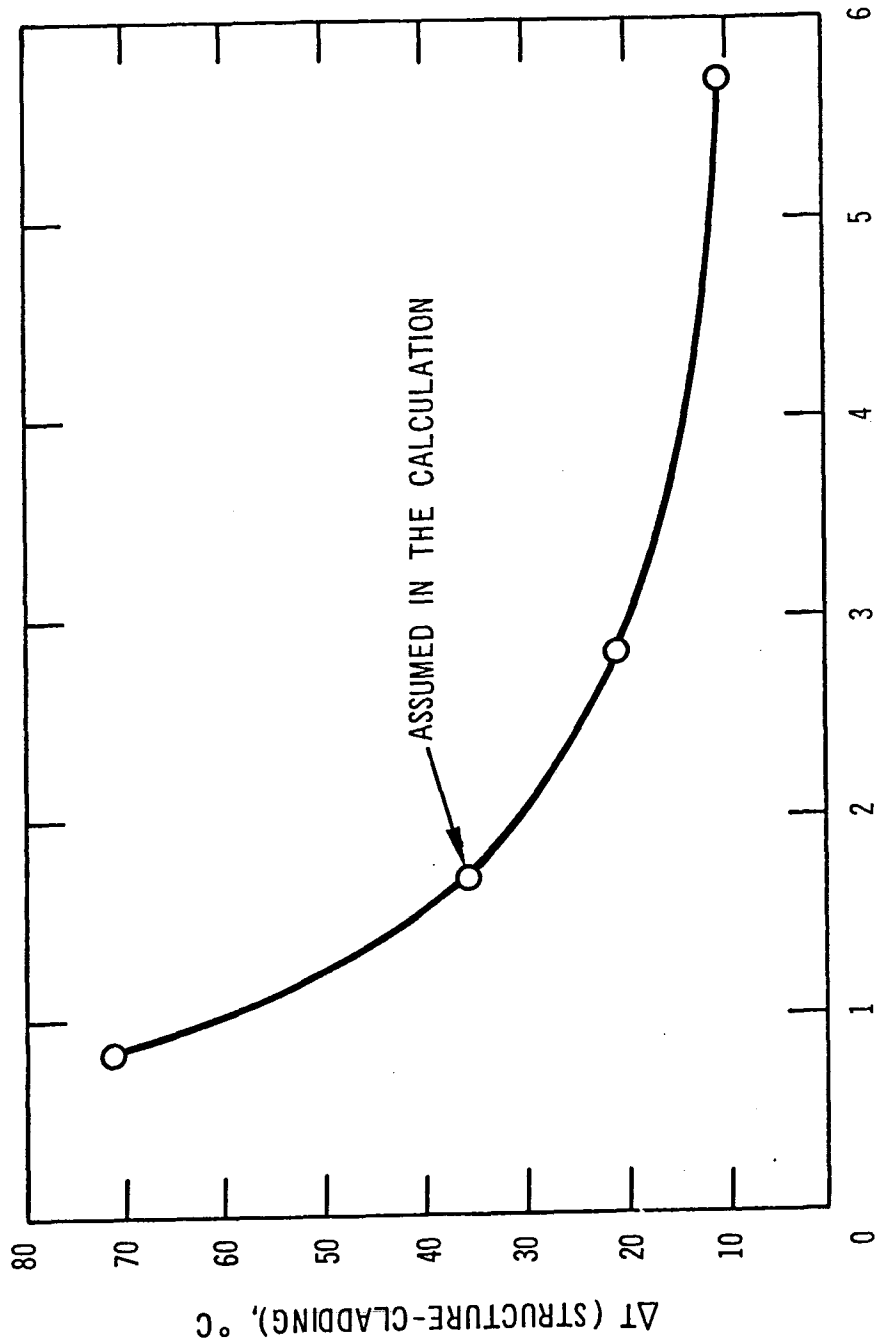

Fig. 4-48. Effect of h_c on the ΔT across the beryllium-ferritic steel interface.

The first-wall configuration selected for the self-cooled lithium-lead blanket is formed by the heads of the two semi-ellipsoidal portions of the blanket module. The outside surfaces of the heads are beryllium-clad for protection from erosion. Wall thickness and head radius will be determined as a function of: (1) module internal design pressure (maximum hydrostatic head plus pumping losses); (2) temperature gradient through the structural wall and beryllium clad; and (3) internal frame spacing. Gravity load of the lithium-lead will also affect the structure requirements for all but the bottom modules in each sector.

4.4.4 Neutronics Analysis

4.4.4.1 Tritium Breeding

Liquid 17Li-83Pb is one of the most attractive tritium breeding materials in that a substantial neutron multiplication can take place in the breeder itself through the Pb(n,2n) and Pb(n,3n) reactions. The resultant neutron spectrum is generally quite soft, implying great potential for tritium production by the $^{6}Li(n,_{\alpha})t$ reaction. The atomic number density of lithium in 17Li-83Pb is, however, only ~ 5.6×10^{21} atoms/cc (at density of 9.4 gr/cc) compared to 8.1×10^{22} atoms/cc in Li_2O for instance. As a result, the content of ^{6}Li or the enrichment of ^{6}Li in 17Li-83Pb plays the most important role in the tritium breeding performance in 17Li-83Pb breeder blanket designs. Figure 4-49 shows the variation of tritium BR with ^{6}Li enrichment in the 17Li-83Pb breeder for two possible armor designs: (1) 13.4 mm bare Fe9Cr1Mo ferritic steel armor and (2) 3.4 mm Fe9Cr1Mo armor coated by 10 mm-thick beryllium. Also shown in the figure is the case with only a 3.4 mm-thick Fe9Cr1Mo armor in order to account for the effect of armor erosion during reactor operation. The one-dimensional neutronics model used for the analysis is similar to the one used in Sec. 4.3.4.1. The 13.4 mm-thick armor region is cooled by the 17Li-83Pb breeder itself (3-mm thick) which is followed by a 4.5-mm thick Fe9Cr1Mo region. The blanket region immediately following this ferritic steel region is neutronically represented by a homogeneous mixture, 85% 17Li-83Pb + 5% coolant + 10% Fe9Cr1Mo considering a bottle-type liquid breeder blanket design [6]. Based on the result of Fig. 4-49, one finds a very strong incentive for ^{6}Li enrichment in 17Li-83Pb. The increase in BR from the natural lithium to 90% ^{6}Li enrichment amounts to more

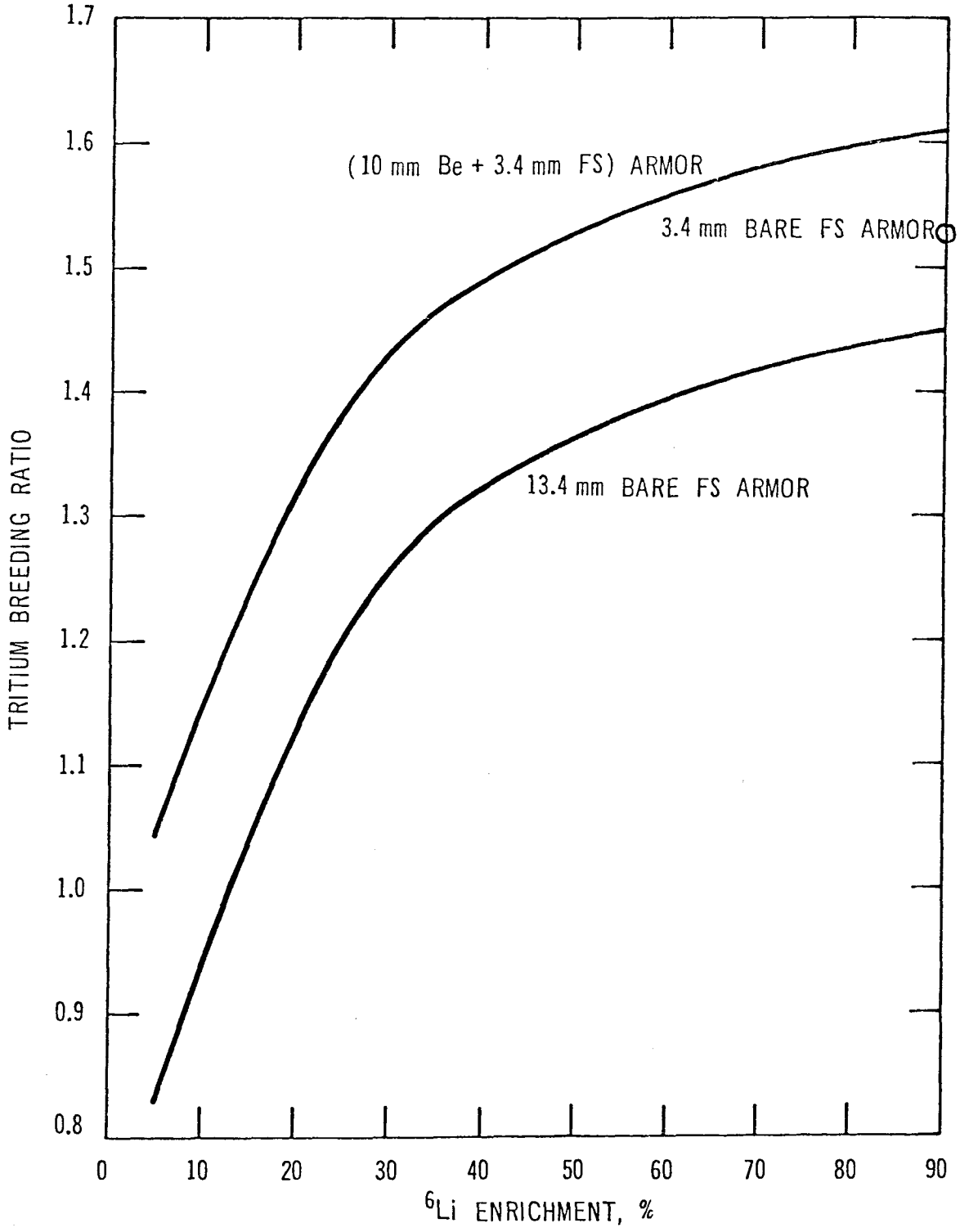

Figure 4-49. Effect of ^{6}Li Enrichment Upon Tritium Breeding for 17Li-83Pb Breeder Blanket Designs.

than 0.5, compared to the Li_2O case shown in Fig. 4-23 where the BR monotonically decreases with ^6Li enrichment. As the neutron spectrum in 17Li-83Pb is intrinsically soft, the increase in BR with ^6Li enrichment solely comes from the increase in the $^6Li(n,\alpha)t$ reaction. In fact, the isotopic BR's for the 13.4 mm-thick bare armor system with 90% ^6Li enrichment, for example, are 1.450 [$^6Li(n,\alpha)t$] and 0.002 [$^7Li(n,n'\alpha)t$] indicating that more than 90% of the total tritium production is made by the soft neutron reaction of ^6Li $(n,\alpha)t$. Such an extremely unbalanced tritium production by ^6Li may yield a high lithium burn-up rate in 17Li-83Pb. However, in the case of 90% ^6Li enrichment of the bare armor design, the average ^6Li burn-up in the 17Li-83Pb blanket is $\sim 1.32 \times 10^{-5}$ atom/cc/DT-burn, which results in only $\sim$ 10% of ^6Li burn-up over an integral wall load of 18 MW-yr/m^2.

Vanadium-base alloys are very attractive structural materials for application to liquid breeder blanket designs because of the well-known corrosion resistance against the breeder. In addition, as shown in an in-depth study carried out for a blanket/shield design[78] in which a vanadium-base alloy is employed along with a liquid lithium, blanket designs based on vanadium alloy structure have substantial potential for minimization of long-term activation induced in fusion reactors. The major concerns regarding the use of vanadium alloys are the lack of information on fabricability, particularly welding, and the effects of atmospheric environment during fabrication and operation[6]. A second-generation research alloy, V15Cr5Ti, is expected to alleviate the swelling and fabrication problems. Table 4-47 shows the tritium breeding performance of a V15Cr5Ti/17Li-83Pb blanket design along with a comparison with the case in which the V15Cr5Ti structural material is replaced by ferritic steel. Again, the two cases of armor design, with and without beryllium coating, are considered. It is found that the V15Cr5Ti structural systems can yield consistently higher BR's than the corresponding ferritic steel structural systems. This results from the less parasitic absorption and the greater probability for the (n,2n) reaction in the V15Cr5Ti alloy. The difference becomes greater with lower ^6Li enrichment.

So far the coolant has been assumed to be the 17Li-83Pb breeder itself. There are several other candidate coolant materials that are considered for use with the liquid breeder material. They include sodium, light water, and helium. Table 4-48 lists the tritium BR's for the 17Li-83Pb breeder blanket designs using these coolants for three different ^6Li enrichment cases, 7.5%

Table 4-47. Effect of Structural Material Selection upon Tritium Breeding for 17Li-83Pb Breeder Blanket Designs[a]

Lithium Enrichment of 17Li-83Pb	Total Tritium Breeding Ratio			
	Structural Material			
	Fe9Cr1Mo		V15Cr5Ti	
	Bare Armor[1]	Be-Coated Armor[2]	Bare Armor[1]	Be-Coated Armor[2]
(A) Natural Lithium	0.881	1.093	1.064	1.227
(B) 50% ^{6}Li Enrichment	1.364	1.529	1.473	1.604
(C) 90% ^{6}Li Enrichment	1.452	1.611	1.551	1.671

[a]Armor: (1) 13.4 mm Structure; (2) 10 mm Be + 3.4 mm Structure

First Wall: 3.0 mm 17Li83Pb
4.5 mm Structure

Blanket: 664 mm (90% 17Li83Pb + 10% Structure)
15.0 mm Structure

Table 4-48. Effect of Coolant Selection upon Tritium Breeding for 17Li83Pb Breeder Blanket Designs[a]

	Tritium Breeding Ratio			
	Coolant			
	Helium	H_2O	Sodium	17Li-83Pb
(A) Natural Lithium				
T_6	0.822	1.231	0.834	0.862
T_7	0.018	0.017	0.018	0.019
Total BR	0.840	1.248	0.852	0.881
(B) 50% ^{6}Li Enrichment				
T_6	1.322	1.410	1.316	1.354
T_7	0.010	0.009	0.010	0.010
Total BR	1.332	1.419	1.326	1.364
(C) 90% ^{6}Li Enrichment				
T_6	1.425	1.448	1.417	1.450
T_7	0.002	0.002	0.002	0.002
Total BR	1.427	1.450	1.419	1.452

[a]Armor: 13.4 mm FS (Fe-9Cr-1Mo Ferritic Steel)

First Wall: 3.0 mm Coolant
4.5 mm FS

Blanket: 664 mm (85% 17Li-83Pb + 10% FS + 5% Coolant)
15.0 mm FS

(natural lithium), 50%, and 90%. In all the cases examined, the increase in ^6Li enrichment always results in a substantial improvement of the breeding performance. It is noticed that the presence of a small amount of light water (only 5% in the present case) affects the breeding to a very appreciable degree. Obviously, the breeding improvement is offered by the neutron energy moderation due to neutron collisions with the water coolant leading to a significant enhancement in the $^6Li(n,\alpha)$ reaction. This is, in fact, the reason that the breeding enhancement is notable, particularly with the natural lithium case, as the atomic number density of ^6Li in 17Li-83Pb is quite low. As ^6Li is highly enriched, the choice of coolant becomes less important in terms of tritium production. For instance, the difference in BR among the four candidate coolants studied, reduces to only ~ 2% in the case of 90% ^6Li enrichment. The selection of coolant, therefore, can be made for such a high enrichment system, based on design considerations other than the neutronics performance, and, hence, a great degree of design flexibility can be afforded to the relevant technical areas such as the thermal hydraulics and mechanical designs. It should also be noted that the BR's for high ^6Li enrichment shown in Table 4-48 are much greater than those for Li_2O blanket designs without neutron multipliers. As the volumetric lithium content in 17Li-83Pb is more than a factor of 10 lower than that in Li_2O, there is a possibility of a drastic reduction in the required lithium inventory in 17Li-83Pb blanket designs. Even compared to the Li_2O blanket design with the Be multiplier presented in Sec. 4.3.4.1, 17Li-83Pb blanket designs are expected to result in a much smaller lithium inventory. Based on a breeding accumulation analysis performed for the 17Li-83Pb breeder/coolant design, a BR of 1.35 for the 100% breeding coverage requires a blanket thickness of ~ 0.5 m. This blanket contains ~ 1600 MT of 17Li-83Pb and ~ 9.6 MT of pure lithium (at 90% ^6Li enrichment). These figures are compared to the respective inventories of ~ 60 MT and ~ 18 MT for the Li_2O blanket design with the 80-mm thick Be multiplier, indicating a factor of two reduction in the lithium inventory in the 17Li-83Pb blanket.

In order to identify the impact of non-breeding inboard blanket designs, three different inboard systems are studied, with an approximate model, and the resultant BR's are summarized in Table 4-49. These three systems are: a) full inboard plus outboard tritium breeding, b) outboard breeding along with 17Li-83Pb coolant flow in the non-breeding inboard blanket, and c) outboard breeding only along with H_2O coolant flow in the non-breeding inboard

Table 4-49. Effect of Inboard Tritium Breeding for 17Li-83Pb Breeder Blanket Designs[a]

	Case A	Case B	Case C
(1) Inboard First Wall			
Coolant	17Li-83Pb	17Li-83Pb	H_2O
(2) Inboard Blanket			
Coolant	17Li-83Pb (5%)	17Li-83Pb (5%)	H_2O (5%)
Breeder	17Li-83Pb (85%)	--	--
Structure	FS (10%)	FS (95%)	FS (95%)
(3) Tritium Breeding			
T_6	1.431	1.116	0.879
T_7	0.002	0.001	0.001
Total BR	1.433 (1.452)[b]	1.117	0.880
Inboard BR	0.467	0.094	--
Outboard BR	0.967	1.023	0.880

[a]Armor: 13.4 mm FS (Fe9CrlMO Ferritic Steel)
First Wall: 3.0 mm Coolant
4.5 mm FS
Outer Blanket: 664 mm (90% 17Li-83Pb + 10% FS)
15.0 mm FS
17Li-83Pb: 90% ^{6}Li enrichment

[b]One-dimensional infinite-cylinder calculation without toroidal system curvature.

blanket. The coolant for the outboard breeding blanket is always assumed to be 17Li-83Pb. The one-dimensional neutronics model used for this analysis is identical with that used for the Li_2O system analysis shown in Table 4-12. The results of Table 4-49 indicate that: 1) it is impossible to obtain a BR greater than unity with the complete elimination of the inboard breeding (Case C); 2) the use of 17Li-83Pb as an inboard coolant substantially increases the outboard breeding (Case B); and 3) the case of full breeding coverage yields a net BR of 1.4 (Case A). An INTOR neutronics analysis [81] which was done by the three-dimensional Monte-Carlo method for a similar 17Li-83Pb blanket design shows BR's of 1.396 and 0.9248 for the full breeding blanket coverage and the outboard breeding only, respectively. This result leads to the same conclusion as item 1) above as to the impact of the complete elimination of inboard tritium breeding. The system of Case B in Table 4-49, which is a semi-non-breeding inboard blanket design, can yield a net BR greater than unity. However, there seem to be several questions posed in this type of blanket design. One question is whether the BR in excess of unity is sufficient for implementation of outboard penetrations such as limiter (or divertor) and REB ducts. Another question is whether the pumping power requirement for the 17Li-83Pb coolant flow inside the inboard blanket, where the magnetic field is high, is tolerable from the practical design standpoint.

It is noticed in Table 4-49 that the difference in the inboard blanket design strongly affects the outboard breeding performance. For example, the outboard breeding in Case A, which amounts to ~ 67% of the total breeding reduces to ~ 61% when the inboard blanket is replaced by the non-breeding blanket, 95% Fe9Cr1Mo + 5% H_2O as Case C. Table 4-50 compares the neutron balance of Cases A and C. It is observed that the significant decrease in the outboard BR of Case C is driven by two factors. First, the neutron current into the inboard region is increased in Case C compared to Case A because of the larger gradient in the neutron distribution caused by the one-sided neutron amplification through the Pb(n,2n) reaction in the outboard blanket. Secondly, neutrons reflected from the inboard region to the outboard region are substantially degraded in energy after they have experienced collisions, particularly with the water coolant in the inboard region. As a result, these reflected neutrons have higher probabilities of parasitic capture by the outboard structure, preferably by the outboard armor structure.

A solution for attaining an adequate tritium BR without introducing too much design complexity can be obtained by a partial inboard breeding

Table 4-50. Neutron Balance in DEMO 17Li-83Pb Breeder Blanket Designs[a]

	With Inboard Breeding	Without Inboard Breeding
(A) Inboard		
Net Current to Armor/DT	0.3550	0.3990
Neutron Gain/DT	0.1808	0.0403
Neutron Loss/DT	0.0692	0.4393
Tritium BR	0.4666	0.0000
(B) Outboard		
Net Current to Armor/DT	0.6450	0.6010
Neutron Gain/DT	0.4676	0.4671
Neutron Loss/DT	0.0963	0.1439
Tritium BR	0.9666	0.8805
Leakage to Blanket Jacket/DT	0.0497	0.0439

[a]In the case with the inboard breeding, both the inboard and outboard designs are as follows:

Armor: 13.4 mm FS

First Wall: 3.0 mm 17Li-83Pb
4.5 mm FS

Blanket: 664 mm (90% 17Li-83Pb + 10% FS)

Blanket Jacket: 15 mm FS

In the case without the inboard breeding, the inboard first-wall coolant is H_2O and the inboard blanket is represented as follows:

Blanket: 664 mm (95% FS + 5% H_2O)

The rest of the system is the same as the case with the inboard breeding. In all cases, 17Li-83Pb contains 90% enriched ^6Li.

blanket. The pumping power problem for the inboard 17Li-83Pb breeder/coolant mentioned earlier will be much alleviated by an effort to minimize the required thickness of the breeding blanket. Figure 4-50 illustrates the relationship between the fraction of non-breeding zone in the outboard region and the requirement of the inboard breeding zone thickness for several net BR criteria. It is assumed that in all the cases studied, the total outboard thickness including the pre-blanket region is fixed at 0.7 m. Figure 4-51 shows that as the required net BR varies from 1.0 to 1.1, approximately 10% variation is allowed in the non-breeding fraction of the outboard blanket for a given inboard breeding thickness. On the other hand, the required breeding zone thickness is substantially altered depending upon the magnitude of net BR for a given fraction of non-breeding zone in the outboard region. The steep rise in the required inboard blanket thickness beyond certain non-breeding fraction reflects the fact that the tritium breeding accumulation approaches to the saturation level deep in the blanket region. By comparing the result of Fig. 4-50 with that for the Li_2O blanket design presented in Fig. 4-24, one finds that the 17Li-83Pb systems can incorporate a much larger space allowance for the major penetrations not usable for breeding in the outboard region. Non-breeding zone fraction of ~ 15%, for instance, requires an inboard breeding zone of only 0.1 m to 0.2 m for a net BR range of 1.0 to 1.1. This range of net BR requirement needs an inboard breeding thickness of 0.2 m to 0.65 m in the Li_2O blanket design. It is, therefore, expected that the choice of impurity control method (limiter or divertor) as well as the plasma heating method is of less constraint in the 17Li-83Pb breeder blanket designs from the standpoint of self-sufficient tritium production.

The above analysis assumes that all of the inboard blanket (vertical height is several meters) is removed. It should be noted, however, that the critical space in the inboard region is the area located close to the horizontal midplane. To minimize the breeding loss without using a breeder in the critical space region, one can eliminate the breeder blanket from only the portion around the midplane (e.g., 0.5 m above and 0.5 m below the midplane).

4.4.4.2 Nuclear Heating

Table 4-51 shows the spatial variation of nuclear heating rate in an 17Li-83Pb blanket design for a neutron wall load of 1.8 MW/m^2. A 13.4 mm-thick bare ferritic steel armor is assumed. The first wall and the blanket

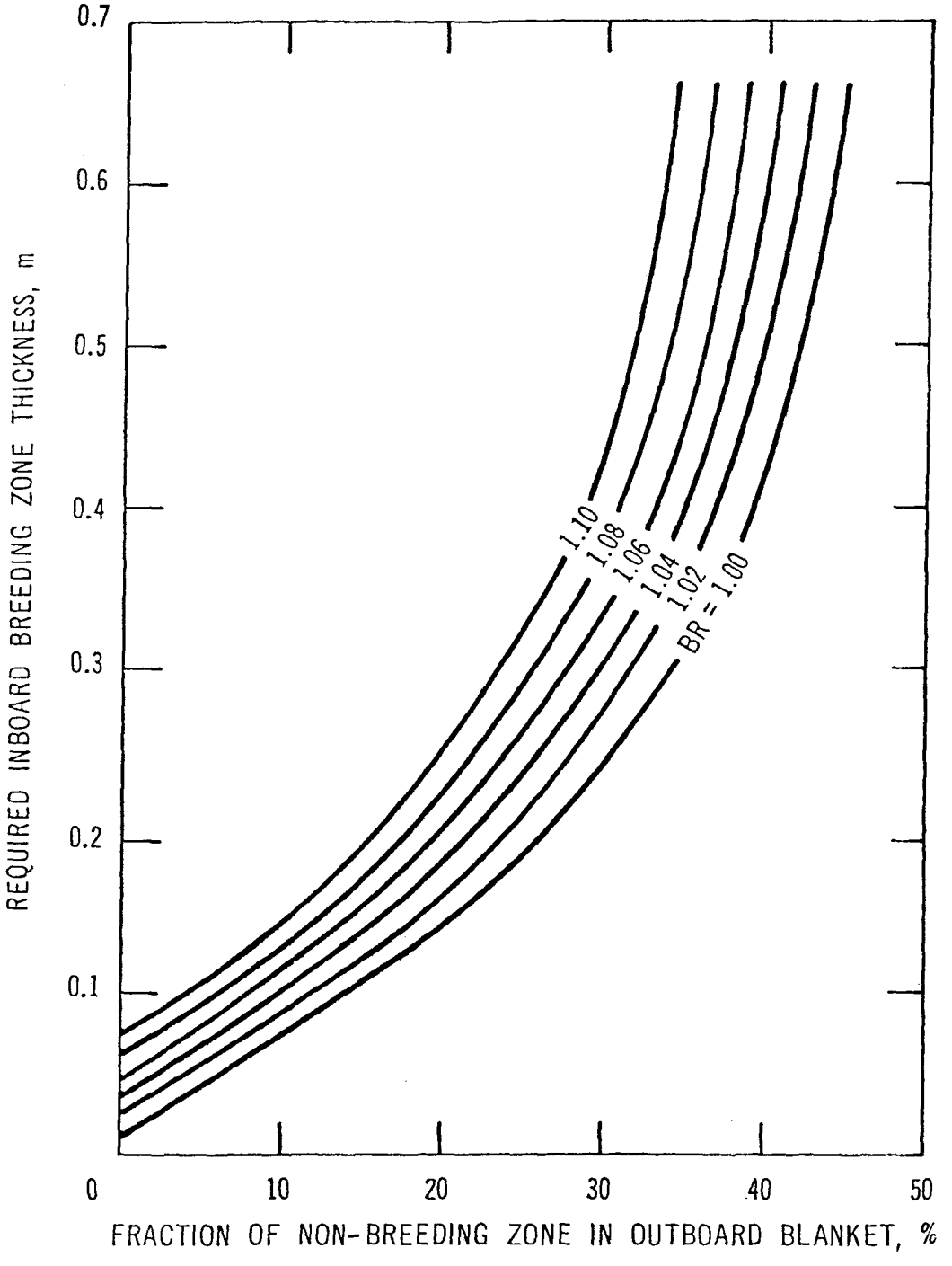

Figure 4-50. Impact of Non-Breeding Zone in Outboard Blanket Upon Inboard Breeding Requirement for 17Li-83Pb Blanket Designs.

Table 4-51. Spatial Variation of Nuclear Heating Rate (MW/m^3) for 17Li-83Pb Breeder System Design[a]

	Fe9Cr1MO	17Li-83Pb[b]
Armor (13.4 mm)	16.1	-
First Wall:		
Coolant (3.0 mm)	-	22.2
Structure (4.5 mm)	11.5	-
Blanket:		
At Depth: 5 mm	9.30	14.8
10 mm	8.29	13.1
30 mm	5.81	9.32
50 mm	4.49	7.68
100 mm	2.61	5.30
200 mm	1.02	2.88
300 mm	0.443	1.66
400 mm	0.206	0.976
500 mm	0.100	0.573
600 mm	0.0549	0.364

[a]Neutron Wall Load: 1.8 MW/m^2

[b]17Li-83Pb: 90% ^6Li enrichment

are cooled by the breeder itself. Assuming a bottle-type blanket design, the blanket composition is represented by a homogeneous mixture of 90% 17Li-83Pb + 10% Fe9Cr1Mo with 90% ^{6}Li enrichment in 17Li-83Pb. Due to the strong capture of gamma rays in the 17Li-83Pb breeder/coolant, the nuclear heating in the ferritic steel structure is substantially lower than the corresponding 316 SS structure heating in the Li_2O blanket designs. The maximum nuclear heating in 17Li-83Pb apparently takes place in the first-wall coolant region, amounting to ~ 22 MW/m^3. The maximum 17Li-83Pb heating in the blanket region is substantially lowered, and amounts to only ~ 15 MW/m^3 which is comparable to the maximum Li_2O breeder heating rate at 70% of the theoretical density, shown in Table 4-15.

4.4.5 Properties of 17Li-83Pb

The materials property data base for liquid 17Li-83Pb and its use as a tritium breeding medium for fusion reactors have been recently reviewed.[83,84] Therefore, the information previously reported will not be reiterated here. Selected properties of the alloy are summarized in Table 4-52. Rather, emphasis is placed on key information relating to use of 17Li83Pb and more recent data, with the focus on two key areas: safety and tritium recovery.

One of the reasons that 17Li83Pb is of interest is that it is believed to be relatively non-reactive with oxidizing media such as air and water. An experiment at Argonne National Laboratory[85] in which the alloy was heated to 500°C and then dropped into water at 90°C, minimal evidence of chemical reaction was observed. Also, measurements of activity coefficients by Saboungi, et al,[86] showed that the lithium activity in the 17Li83Pb eutectic was about 1×10^{-3}, which is three orders of magnitude lower than that of pure lithium. However, it is reported that a Li-Pb alloy (approximately 17Li83Pb) burns in air with very high flame temperature (1200°C) when heated to about 300°C.[87] It would appear that experimental results to date have not fully resolved the issue of chemical reactivity. Additional experiments more nearly simulating potential reactor situations are needed.

It is useful to quantify the potential exothermicity of reactions of air and water with 17Li83Pb and compare the results with those of other breeder materials. Using available thermochemical data,[86,62] the heats of reaction (ΔH_R, enthalpy change) with water and air were calculated for various breeder materials (Table 4-53). It can be seen that per gram of lithium, the enthalpy of reaction of the alloy with water and with air is not significantly

different than that of lithium. In fact, per mole of alkali metal, the exothermicity of the alloy is about the same as sodium. However, on a unit volume basis, since it has a low lithium density, the alloy appears to be much less reactive than lithium. Overall, the alloy is expected to be less reactive than lithium, although exothermic reactions with oxidizing media, such as water and air, are possible. In addition, since the alloy is to be used as a liquid, reactions potentially could have severe consequences.

Another area of key interest for this material is the Sieverts' constant, which defines the partitioning of tritium between the gas phase (square root of pressure) and the liquid metal. Preliminary measurements of K have been reported.[89] Also, the Sieverts' constants were estimated from a model.[89] More recently the Siverts' constants for hydrogen in 17Li83Pb have been measured by Veleckis.[90] It was found that $K_s = 7.1 \pm 1.5 \times 10^3$ $atm^{1/2}$ per atom fraction of H, in the range 400-600°C. As predicted by the model,[89] the constant was found to be independent of temperature. Assuming that, as is the case for Sieverts' constants in lithium,[91] the isotopic effect is approximately proportional to the square root of mass, K_s for tritium is higher by a factor of $\sqrt{3}$. Thus, for tritium in 17Li83Pb, $K_s = 12.3 \pm 2.6 \times 10^3$ $atm^{1/2}$ per atom fraction of T. This expression can be converted into units more convenient for blanket design: $K_s = 4.4 \pm 0.9$ wppb/ Pa. Thus, for a relatively high tritium pressure of 1 Pa, the amount of tritium dissolved in the alloy is only 4.4 parts per billion. It is clear that any tritium extraction method will result in a very low tritium inventory in 17Li83Pb. However, tritium pressure will be quite high and permeation rates could be excessive. Design solutions to keep tritium permeation low represent additional cost and complexity.

Table 4-52. Selected Properties of 17Li83Pb

		Reference(s)
Composition, Atom Fraction Li	0.17	78, 79
Melting Temperature, °C	235	78, 79
Density at 500°C, g/cm^3	9.4	79
Volumetric Coefficient of Thermal expansion	7×10^{-4}	78, 79
Li atom density, g/cm^3	0.064	
Electrical Conductivity, $\Omega^{-1}\ cm^{-1}$	8000	78, 79
Heat Capacity, J/g-K	0.17[a]	
Li Vapor Pressure at 500°C, Pa	0.5	78

[a]averaged from Li and Pb data.

Table 4-53. Heat of Reaction (ΔH_R) of Breeders with Water and Air

Breeder	ρ_{Li}, g/cm^3	Reaction with Water KJ/gLi	Reaction with Water KJ/cm^3	Reaction with Air (O_2) KJ/gLi	Reaction with Air (O_2) KJ/cm^3
Li	.48	-34.3	-16.5	-25.9	-12.4
17Li83Pb	.064	-28.4	- 2.4	-20.0	- 1.8
Li_2O	.93	- 8.4	- 7.8	0.0	0.0
$LiAlO_2$	.24	- 0.9	- 0.2	+10.5	+ 1.8
Li_2SiO_3	.36	+ 2.1	+ 0.8	+10.5	+ 3.8

4.4.6 Tritium Recovery, Inventory and Leakage

4.4.6.1 Tritium Recovery

It has previously been shown (4.4.5) that 17Li83Pb has a low tritium solubility which results in a high tritium overpressure. This makes tritium control difficult. The high overpressure drives the design for any blanket/coolant/tritium recovery system. The 17Li83Pb blanket could conceivably use sodium, helium, water or 17Li83Pb as the coolant. To determine which tritium extraction system and which coolant is most advantageous, an assessment was done in which permeation rates, inventories and release paths were identified for each design. For each system, steady state was assumed, i.e., the extraction system processed the tritium at the rate at which it was bred, 182 g/d at BR = 1.3.

The first requirement was to determine the tritium permeation rates between the blanket and each coolant. A summary of the tritium permeation rates and tritium inventories for the two reference alloys, vanadium and ferritic steel are listed in Table 4-54. For both alloys permeation could be used for tritium recovery (i.e., sodium, helium). However it also serves as a major tritium leak (i.e., water, 17Li83Pb). The permeation rates could be decreased by factors of 10-1000 by an oxide barrier.

Assuming an oxide barrier, the reduced permeation rate for water with a ferritic steel would be ~0.1 g/d which is unacceptably high. Drastic measures would have to be employed to reduce permeation to acceptable levels. Double-walled coolant tubes would have to be used. The plenum would be vacuum pumped or would contain slowly flowing helium and ~1.4 Pa oxygen. The oxygen is necessary for conversion of T_2 to T_2O which is scrubbed from the helium. An added tube wall would reduce coolant temperatures because of the thermal gradient across it; this would in turn reduce thermal conversion efficiency. Therefore, water does not appear to be an attractive coolant to use with 17Li83Pb. For helium, the permeation rate for ferritic steel with an oxide barrier would be reduced to ~2 g/d if oxygen were added to the coolant. This would eliminate using the helium coolant as the primary tritium recovery route. However, it would still be necessary to process the helium since it is a major tritium leak pathway.

Table 4-54. Tritium Permeation Rates and Inventories within the 17Li83Pb Blanket

Alloy/ Coolant	Pressure (Pa)	Area (m^2)	Permeation Rate[a,b] (g/d)	Structure Volume (m^3)	Tritium Inventory (g)	
					Alloy[c]	17Li83Pb
V/Na	10^{-1}	2052	156	10	440	6
V/He	10^{-1}	3970	302	20	890	6
	10^{-3}	3970	30	20	90	1
V/17Li83Pb	10^{-1}	5317	404	27	1200	10
Fe/Na	10^{2}	2052	123	10	5	193
Fe/He	10^{2}	3970	239	20	10	193
Fe/17Li83Pb	10^{2}	5317	320	27	13	340
	10^{4}	3970	2390	20	100	1930

[a]No oxide barriers, 5 mm thick wall, 450°C.

[b]Permeability:[87] K_V= 20 Ci/d•m•$Pa^{1/2}$; K_{Fe} = 0.5 Ci/d•m•$Pa^{1/2}$

[c]Solubility[87]: S_V = 400 ppm $Pa^{-1/2}$; S_{Fe} = 0.1 ppm $Pa^{-1/2}$.

[d]Tritium Solubility = 4.42 wppb $Pa^{-1/2}$.

Table 4-55. Practical Tritium Extraction Methods for 17Li83Pb

Coolant Method	Molten Salt	Cold Trap	Oxidize Mol. Sieves	Gas Sparge	Getter
17Li83Pb	A,P	N.A.	N.A.	A	A
Na	N.A	A, P	N.A.	A	A
He	A,P	N.A.	A[b]	N.A.	A
H_2O	A,P	N.A.	N.A.	A	A

[a] A = appropriate, N.A. = not appropriate, P = Preferred.

[b] Method used to control tritium permeation.

If one compares the amount of tritium dissolved in the candidate structural materials (vanadium and ferritic alloys, Table 4-54), then from a tritium inventory standpoint, the ferritic would be the alloy of choice with 17Li83Pb. This choice is assumed for the remainder of this section.

The tritium recovery methods considered are shown in Table 4-55. With 17Li83Pb as the coolant molten salt extraction[93,94] is the preferred method. With sodium, a cold trap[95] is the preferred method. With helium, a small fraction of the static blanket could be processed by molten salt extraction[75] or a portion of the helium flow could be passed over getter beds.[95] The preferred method is to process the blanket so that there is a reduced possibility for tritium leakage to the steam generator. In Fig.4-51, the preferred tritium extraction systems are shown for the coolants. Selected parameters are presented in Table 4-56. For systems using either sodium or 17Li83Pb coolant, approximately 1% of the total flow is processed continuously. With a helium or water coolant, approximately 1% of the static blanket is processed.

Cold trap technology using sodium has been used extensively in the breeder reactor program. The Clinch River Breeder Reactor (CRBR) will incorporate a sodium cold trap comparable in capacity to that required for the 17Li83Pb blanket design. Flow rates required for the DEMO design are approximately three times that used for CRBR. The tritium recovery mechanism for a cold trap has recently been studied[96] and would be incorporated into the DEMO design. Each cold trap

would require 1 d warmup to 450°C after which the tritium would be removed by pumping to the fuel cleanup units. At least four traps would be incorporated into the design, with each trap operating 6 h out-of-phase of the other to provide reliability. The sodium coolant would have to be cooled to 195°C before entering the cold trap. In Table 4-57, several cases are presented for the cold trap extraction system.

The molten salt extraction process has also been described[93] and is at the pilot-plant stage.[94] Table 4-58 contains the results for several cases considered. As noted, the tritium inventory is strongly dependent on the blanket mass. Only a small number of contactors are required. With this method, the tritium pressure could be reduced if larger fractions of blanket mass were processed.

Figure 4-51.
17 Li 83 Pb BLANKET - TRITIUM EXTRACTION CONCEPTS

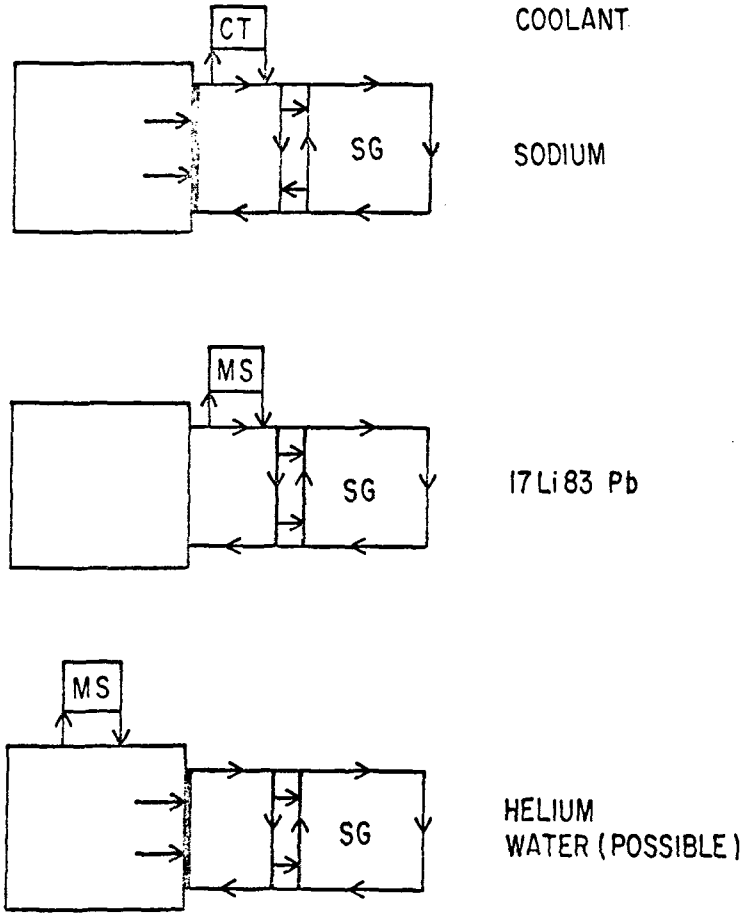

Table 4-56. Blanket/Coolant Parameters for 17Li83Pb[a]

	17Li83Pb	Sodium	Helium
Coolant			
Weight, kg	6×10^6	8×10^5	2×10^5
Volume, m^3	680	810	1299
Surface Area,[b] m^2	403	2052	3970
Thickness, mm	5	5	5
Surface Area,[c] m^2	4914	4775	9187
Thickness, mm	10	10	10
Blanket			
Weight, kg	6×10^6	3.6×10^6	3.6×10^6
Volume, m^3	680	403	403
Surface Area, m^2	5317	2052	3970
Thickness, mm	5	5	5
Breeding Ratio	1.05-1.3	1.05-1.3	1.03-1.3
Tritium Bred, g/d	147-182	147-182	147-182
Steam Generator			
Coolant Wall, mm	10	10	10
Steam Wall, mm	12.7	12.7	12.7
Surface Area, m^2	3693	3693	5899
Helium Gap			
Volume, m^3	11	11	18
Thickness, mm	3	3	3
Tritium Pressure, Pa	$\sim 10^{-12}$	$\sim 10^{-12}$	$\sim 10^{-12}$
Oxygen Pressure, Pa	1.4	1.4	1.4
Hydrogen Pressure, Pa	$\sim 10^{-12}$	$\sim 10^{-12}$	$\sim 10^{-12}$

[a] Ferritic steel structure assumed.

[b] Surface within blanket.

[c] Surface, blanket and piping.

Table 4-57. Summary of Sodium Cold Trapping at 115°C as Tritium Recovery Method for 17Li83Pb

Breeding ratio	1.3	1.3	1.3
Weight sodium, kg	8×10^5	8×10^5	8×10^5
Fraction processed	0.02	0.01	0.005
Time to steady state, h	37	60	88
Tritium pressure, Pa	0.026	0.098	0.123
Tritium Concentration kg/kg	1.4×10^{-7}	2.4×10^{-7}	4.1×10^{-7}
Tritium inventory, g			
Sodium	110	190	330
17Li83Pb	200	200	200
Cold Trap	180	180	180

Table 4-58. Summary of Molten Salt Extraction as Recovery Method for 17Li83Pb

Breeding ratio	1.05	1.05	1.3	1.05	1.3
Weight 17Li83Pb, kg	6×10^6	6×10^6	6×10^6	1.7×10^6	1.7×10^6
Fraction Processed	0.05	0.01	0.01	0.01	0.01
Frequency, No./d[a]	60	114	119	379	396
Contactors	11	2	2	2	2
Electrolytic Zone					
Volume, m^3	0.03	0.05	0.05	0.2	0.2
Surface Area, m^2	6	2	2	7	7
Tritium Pressure, Pa	37	256	359	256	359
Tritium Level, kg/kg					
Salt	4×10^{-8}	1×10^{-7}	1×10^{-7}	3×10^{-8}	4×10^{-8}
17Li83Pb	3×10^{-8}	7×10^{-8}	8×10^{-8}	7×10^{-8}	8×10^{-8}
Tritium Inventory, g					
Salt	2	1	1	0.1	0.1
17Li83Pb	158	408	483	122	145

[a]Number of times fraction is processed per day.

4.4.6.2 Tritium Inventory

In comparing the three tritium extraction systems studied, one finds that the inventory in all three systems is similar, Table 4-59, as is the tritium pressure in the blanket. The main difference is noted in the tritium pressures achieved in the coolant. To all intents, the systems are equivalent.

4.4.6.3 Tritium Leakage

With the 17Li83Pb system, secondary containment of all coolant lines outside the blanket is required. In addition, 1.4 Pa oxygen has to be added to all secondary enclosures filled with helium to ensure (1) that an oxide layer is formed to impede permeation, and also (92) to convert T_2 to T_2O. The equilibrium constant for the equilibrium

$$T_2 + \frac{1}{2} O_2 = T_2O$$

is $\sim 5 \times 10^{19}$ $Pa^{1/2}$ at 500°C.[97] Thus with 1.4 Pa oxygen, the tritium pressure is $\sim 10^{-12}$ Pa and the T_2O pressure is $\sim 10^{-3}$ Pa provided the helium is processed through molecular sieves to remove the T_2O. (A low flow rate would be required.) In addition, the helium gap would reduce the H_2 influx from the steam generator. At 50 atm. the hydrogen pressure would be 6×10^{-3} Pa which would result in an influx of $< 4 \times 10^{-4}$ g/d. The secondary tritium permeation data is summarized in Table 4-60.

The reference designs used incorporated ferritic steel as the alloy of choice (to reduce tritium inventories by about two orders of magnitude) and used molten salt extraction with either 17Li83Pb or helium coolant and a cold trap with sodium coolant. Any of these systems appear feasible from the tritium standpoint.

4.4.7 Thermal-Hydraulic Analysis

To be completed.

Table 4-59. Comparison of Different Tritium Extraction Methods for 17Li83Pb

	17Li83Pb	Sodium	Helium
Breeding ratio	1.3	1.3	1.3
Fraction processed	0.01	0.01	0.01
Tritium pressure, Pa			
17Li83Pb	359	>100	359
Coolant	--	0.1	10^{-3}[b]
Tritium inventory, g			
17Li83Pb	483[a]	200	290
Coolant	--	190	0.2
Other[c]	1	~180	1.0
Alloy (Fe)	~13	~5	~10

[a] For 6×10^6 kg; if 4×10^6 kg, inventory is 290 g.

[b] T_2O pressure; $T_2 \sim 10^{-12}$ Pa.

[c] Molten salt or cold trap.

Table 4-60. Tritium Permeation into Secondary Enclosures for 17Li83Pb Blanket

	17Li83Pb	Sodium	Helium
Piping			
Surface Area, m^2	1221	1082	3288
Pressure T_2 Pa	200	0.05	10^{-12}[a]
Permeation, g/d	75	1	8×10^{-6}
Permeation, barrier,[b] g/d	0.08	0.001	4×10^{-9}
Steam Generator Gap			
Surface Area, m^2	3693	3693	5899
Permeation, g/d	75	1	1.6×10^{-5}
Permeation, barrier[b], g/d	0.08	0.001	4×10^{-8}
Pressure T_2	10^{-12}a	$<10^{-12}$[a]	$<10^{-12}$[a]
Permeation, g/d	6.5×10^{-3}	$<1 \times 10^{-3}$	4×10^{-8}
Permeation, barrier,[b] g/d	0.06	$<10^{-2}$	$<10^{-9}$

[a]Presence of 1.4 Pa oxygen, T_2O pressure = 0.14 Pa.

[b]Barrier effectiveness assumed 1000X.

4.4.8 Materials Compatibility

Compatibility with the structural material is a key feasibility question for the Li-Pb breeder concept. The maximum blanket operating temperature may be limited by corrosion/compatibility criteria. Since the data base for this system is very limited, much of the compatibility assessment must be extrapolated from available results from similar types of systems. Critical compatibility issues are of two types: (1) those problems related to corrosion/mass transfer effects, and (2) those problems related to effects on the mechanical integrity of the structure. Reference 93 is a recent summary on the corrosion and compatibility considerations of liquid metals for fusion reactor applications.

4.4.8.1 Corrosion/Mass Transfer

Relatively little experimental data exist for the corrosion of structural alloys in the 17Li-83Pb alloy system. Therefore, the importance of these effects must be deduced from fundamental solubility data and results from similar types of systems. General aspects of the compatibility problem can be summarized as follows:

- Nickel is highly soluble in both lead and lithium, therefore alloys with significant concentrations of nickel will generally exhibit high corrosion rates.

- Preliminary static capsule tests with Type 316 SS and HT-9 alloy indicate much higher (about 100 x) corrosion rates at 500°C in 17Li-83Pb than in lithium under similar conditions.[99] Much lower corrosion rates have been reported in static tests at 350 and 400°C.[100]

- Corrosion/mass transfer effects in circulating systems are generally much greater than in static systems.

- Preliminary results indicate that corrosion of ferrous alloys in 17Li-83Pb is more similar to testing in pure lead than in pure lithium.

- Ferritic steels with low or no nickel are more resistant to attack than austenitic steels.

- Results from Fe-2-1/4Cr-1Mo tests indicate that the extent of penetration by Li-3.5 Pb is quite sensitive to the alloy microstructure. Results for 17Li-83Pb were less sensitive to alloy microstructure.

- The importance of impurities in the liquid metal has not been investigated. Nonmetallic impurity effects are generally important in liquid metal systems of interest for practical applications.

- Pure iron is probably more resistant to corrosion than most ferrous alloys. Minimal alloying is probably desirable from a compatibility viewpoint.

- The refractory metals, e.g., vanadium and niobium alloys, are expected to be much more corrosion resistant than stainless steels or ferritic steels.

Obviously more data are required before the extent of corrosion/mass transfer in a practical system can be reliably assessed.

4.4.8.2 Effects on Mechanical Properties

Possibly a greater concern than the corrosion/mass transfer effects are potential stress-corrosion or liquid metal embrittlement effects on the structural alloys exposed to the Li-Pb alloy. The heavy liquid metals, e.g., lead, bismuth, and tin, generally produce much more severe embrittling effects than the alkali metals. An important aspect of this problem is that it occurs at relatively low temperatures.

Armco iron and low-alloy steels wetted with lead, bismuth, or lead-bismuth eutectic showed severe ductility loss between 200 and 400°C.[101-103] The largest drop of ductility was observed at approximately 350°C. Specimens exposed to embrittling metals failed as a result of the growth of a brittle crack, whereas in an inert environment they failed by ductile fracture. The

temperature range for embrittlement extends considerably below the melting point of the melt and is related to the temperature interval of reduced plasticity of "blue brittleness" of specimens tested in vacuum. Stress relaxation in this temperature range is inhibited and thus promotes strain hardening, which is more pronounced in specimens deformed in liquid metals [101, 106].

The influence of lead-bismuth eutectic environment on the fatigue strength of ferritic and austenitic steels has been investigated at temperatures between 300 and 600°C [105,106]. The fatigue strength of various grades of steels when wetted by molten lead-bismuth eutectic was substantially reduced by penetration of the liquid metal along the grain boundaries. The deleterious effects of liquid lead-bismuth eutectic can be prevented by the formation of an oxide film on the steel surface, which if maintained, inhibits the wetting of the steel by the liquid metal. Surface oxides are not expected to be stable in the Li-Pb system. The weakening effect of lead-bismuth eutectic can also be eliminated by controlling the cyclic frequency. The fatigue life of low-alloy steel tested in liquid lead-bismuth at a strain rate of 8.0×10^{-6}/s was about the same as that in air, but a drastic reduction in fatigue strength was observed at a strain rate of 5.3×10^{-3}/s [107,108]. The reverse strain-rate effect in liquid metals is explained by accelerated grain boundary diffusion of liquid metal under high cyclic stresses. The absence of the harmful effects at slow strain rates is associated with the relaxation of local stresses such that conditions conducive to grain-boundary diffusion by the liquid metal cannot be produced. Tests of austenitic steel under stress in 17Li-83Pb at 350°C show microcracks after 500 h. [100]

4.4.8.3 Design Limitations

The data base on compatibility of candidate structural alloys is insufficient to provide definite conclusions. However, based on the available information, the following conclusions are provided as a basis for the present design study:

- Corrosion rates of austenitic steels with significant nickel concentrations are believed to be excessive. Hence, these alloys have not been selected as the candidate structural materials for the Li-Pb breeder concepts.

- Although corrosion rates of ferritic steels are predicted to be quite high, these alloys are proposed for the reference structural material with a maximum temperature limit of 450°C.

- Although data for refractory metals are practically nonexistant, corrosion rates are predicted to be much lower than those for the ferritic steels. Therefore, vanadium-base alloys are proposed as the backup structural material.

4.4.9 Design Configuration

This section provides a description of the conceptual design for the 17Li-83Pb liquid metal breeder reference blanket design (Sec. 4.4.9.1) and the related energy conversion system (Sec. 4.4.9.2). Rationale for blanket design detail choices is given in Sec. 4.4.9.3, and operational and safety considerations are discussed in Sec. 4.4.9.4.

4.4.9.1 Design Description

The Li-Pb alloy reference blanket design is illustrated in Figure 4-43. Because it is cooled by liquid sodium, it is similar to the water-cooled Li_2O solid breeder reference blanket design described in Section 4.3.9.1, and the rationale described therein for selection of design details is generally applicable. Therefore, this section and the three following will focus on the difference in the Li-Pb reference blanket design as compared to the design of the Li_2O blanket. The principal differences are (1) coolant tube arrangement and thermal-hydraulic parameters, (2) module structural arrangement, and (3) the addition of resistance heaters. Materials and selected design options for the Li-Pb reference blanket are listed in Table 4- 61.

Table 4-61. STARFIRE/DEMO Li-Pb Alloy Breeder Reference Design Description

Selected Materials	
- Tritium Breeder	Liquid 17Li-83Pb Alloy
- Coolant	Liquid Sodium ($\lesssim$ 0.5 MPa)
	- Inlet temperature $\simeq$ 275°C
	- Outlet temperature $\simeq$ 400°C
- Structure	Ferritic Stainless Steel
Selected Design Options	
- First Wall	Be-clad Corrugated Panel
- Breeder Coolant Containment	Small-diameter Tubes
- Other	
	- Toroidal direction for coolant flow
	- Dual parallel primary coolant loops
	- Maintenance by sector removal and replacement

The module first wall is the same as for the Li_2O blanket, except that the thickness and channel size in the corrugated sheet are reduced since sodium coolant pressures are low. Coolant tube spacing, both poloidally and radially (depthwise), is altered from that of the Li_2O blanket to account for (1) the different nuclear heating rate with depth into the blanket, and (2) the higher thermal conductance at the outer surface of the coolant tubes.

Module structure is modified somewhat to react the gravity loads resulting from the large mass of lead contained within each module. The toroidally-oriented internal frames are spaced ~ 20 cm apart poloidally, and connect the first wall structure to the back wall of the module. The internal frames extend to the side walls of the module, and are welded to them around each frame's perimeter to form a number of pressure-tight compartments within the module. The breeder gravity load (for the vertical or slanted modules) is thus taken in large part by these frames. The frames are stiffened by shallow ribs spaced ~ 10 cm apart in the toroidal direction, to react the gravity loads to the module's back wall.

Resistance heaters arranged in dual parallel circuits are attached to the two sides of the module extending toroidally and to the back wall. During a startup these heaters are used to raise the blanket temperature above the 98°C melting point of sodium, at which time the two coolant circuits are filled with sodium. The sodium is heated outside the reactor and then circulated through the blankets to bring their temperature above the 240°C Li-Pb melting point to the temperature selected for beginning the plasma burn.

The tritium removal scheme, as discussed in Section 4.4.2.1, is to permit tritium permeation from the Li-Pb through the coolant tube walls into the sodium. A portion of the sodium coolant flow is diverted outside the reactor to the tritium processing equipment which uses cold trapping to extract the tritium from the sodium.

4.4.9.2 Energy Conversion System

The basic elements and arrangement of the energy conversion system for the sodium-cooled Li-Pb breeder concept is illustrated in Figure 4-52. The system is similar to that shown for the Li_2O reference blanket in Figure 4-17 with the primary differences being (1) deletion of the pressurizers, and (2) addition of dump tanks and transfer pumps. Major parameters of this system are listed in Table 4.62.

The future detail design of the steam generators for this system is expected to borrow heavily from the active and extensive program of steam generator development for LMFBRs, which builds on earlier efforts [74] to develop steam generators for the Clinch River Breeder Reactor Plant (CRBRP). Three steam generator types are being developed: (a) single-wall tube, hockey stick configuration; (b) single-wall tube, helical coil configuration; and (c) double-wall straight tube configuration. Prototype tests have been conducted or are planned for all three designs. The selected alloy for each is 2-1/4 Cr-1 Mo ferritic steel, based on its good performance in actual service and on current development activities. Materials and process development and qualification efforts are underway in critical areas such as double-wall tube fabrication and welding and inspection techniques. The development program for sodium-heated LMFBR steam generators, together with similar programs for other components such as pumps, is expected to result within the next 10 years in a proven technology base adequate for design and construction of sodium-heated STARFIRE/DEMO energy conversion system components.

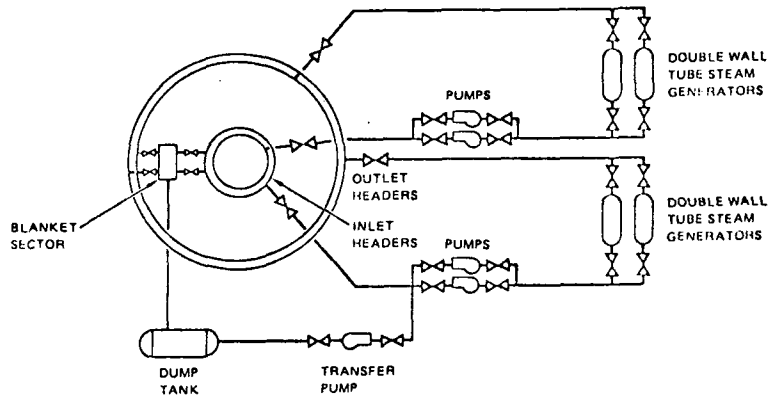

Figure 4-52. Schematic of Energy Conversion System for Li-Pb Breeder/Coolant Blanket Concept.

Table 4-62. Major parameters for primary loop (sodium-cooled Li-Pb alloy breeder blanket)

Coolant	Liquid sodium
Heat Load	850 MW
Blanket Outlet Temperature	$\sim 400^0$C
Blanket Inlet Temperature	$\sim 275^0$C
Operating Pressure	< 0.5 MPa ($\lesssim$ 70 psig)
Maximum Li-Pb Temperature	$\sim 450^0$C
Number of Independent Loops	2
Maximum Pipe Size	$\sim$ 1.0 m I.D.
Maximum Velocity	$\sim$ 20 m/s
Pumping Power	$\sim$ 20 MW
Coolant Volume	$\sim$ 300 m^3
Number of Steam Generators	2 per loop
Number of Pumps	2 per loop
Pump Capacity	50% of total required capacity

4.4.9.3 Rationale for Design Detail Selection

The rationale for selecting a sodium-cooled approach to the Li-Pb alloy breeder blanket rather than a self-cooled approach was discussed in Section 4.4.2.3. Section 4.3.9.3 presented the rationale for the design details selected for the Li_2O solid breeder reference blanket, most of which were also selected for the soldium cooled Li-Pb alloy reference blanket. Two specific choices which require additional discussion are: (1) use of single-wall breeder coolant tubes instead of double-wall tubes; and (2) internal structural arrangement.

Single-wall breeder coolant tubes are considered to give adequate protection against the development of leaks through which the coolant could contact the Li-Pb breeder. Inspection methods developed within the LMFBR program for small-diameter seamless ferritic steel tubing should result in very low prob-

abilities of through-crack occurrence in service. Also, the consequences of any sodium-to-breeder leak are expected to be small, because of the low reactivity between liquid sodium and liquid Li-Pb. However, if double-wall tubes with intermediate zone leak detection capability are later shown to be desirable, they can be incorporated into the design with minimal impact.

The internal structural arrangement illustrated in Figure 4-43 is a preliminary choice. The primary design load on the module is the ~ 1.0-1.7 MPa pressure on the first wall acting toward the plasma chamber center during a plasma disruption (Chapter 5). This load is adequately reacted by frames oriented normal to the first wall and connected to the back wall. The toroidal plane selected for the frames simplifies their integration with the toroidally-oriented coolant tubes. The gravity load of the high-density Li-Pb must also be reacted, however, and the module internal pressure resulting from the Li-Pb static head must be accommodated. To meet these requirements, the internal frames are extended toroidally to the module end walls (in the poloidal plane) and are welded to the walls to form multiple pressure-tight compartments within each module. This reduces Li-Pb static head to < 10 psi for any compartment. The loads acting on the frames and first wall in the vertical or 45° modules are beamed to the back wall through small stiffeners on each frame, spaced ~ 10 cm apart. The gravity load of the Li-Pb in each compartment is reacted by the first wall (top horizontal module), the back wall (bottom horizontal module), the frames (side vertical modules), or some combination of these (45° modules). Thus, all Li-Pb gravity loads are ultimately reacted by back wall, which is attached to major sector support structure. Further design and analysis effort is needed, however, to determine whether this structural arrangement is preferable to simply increasing the module wall thickness to adequately react the gravity loads and hydrostatic head for a full module.

4.4.9.4 Operation/Safety Considerations

The most important safety considerations for the Li-Pb alloy reference blanket are (1) the consequences of a coolant tube rupture in the steam generator, and (2) removal of blanket afterheat in a reactor accident situation. These considerations and the reasons for their importance are discussed in Table 4-63.

A sodium coolant tube rupture within a module for the Li-Pb reference blanket is not expected to have serious consequences. The sodium/Li-Pb interaction will not produce high pressures inside the module, and the module walls are designed to withstand the relatively low MPa maximum sodium coolant pressure. Thus the accident should be contained within the single faulted module, so that secondary accidents (e.g., module rupture) will not occur.

The designs proposed for LMFBR steam generators use primary coolant tubes manufactured, inspected and installed to very high standards. Regardless, a coolant tube rupture within the steam generator is still a possibility. However, the pressure pulse created will be contained by the thick shell of the steam generator and any damage will be confined to the internals. Thus the reactor will not be affected and reactor operation can continue after a brief downtime, assuming a spare steam generator is included in the plant design (nominally for use during maintenance of one of the other steam generators).

The safe removal of blanket afterheat following an accident involving a primary coolant loop is important to the protection of plant capital investment. If not adequately cooled, the activated blanket structure could overheat past the temperature limit for safe sense of the component. In a worst case, the blanket structure could weaken sufficiently to permit rupture and thus release large quantities of Li-Pb and sodium into the plasma chamber. It is because of these possibilities that the provision of either dual parallel primary coolant circuits, or an independent emergency coolant loop for all modules, is considered virtually a necessity for power reactor blankets. The relative design simplicity of providing dual circuits for the sodium-cooled Li-Pb blanket is a significant advantage for this approach.

Table 4-63. Principal operation/safety considerations for Li-Pb breeder reference blanket

Concern	Importance	Remarks
o Breeder/coolant[1] contact as result of small or large coolant leak	o Module internally pressurized to coolant pressure	o No breeder/coolant[1] chemical reaction o Module designed to withstand coolant pressure
o Coolant/water[1] contact in steam generator as result of small or large coolant leak	o Coolant/water[1] reaction can damage steam generator internals	o Steam generator shell sized to withstand full steam/water pressure o Damage limited to a single steam generator o LMFBR technology development minimizes risk
o Safe removal of blanket afterheat following a coolant loop accident	o Temperature increases in blanket can lead progressively to annealing of structure, which precludes reuse	o Dual parallel coolant[1] loops nearly eliminate possibility of unacceptable temperature increases o Further work needed to determine whether safe afterheat removal without active cooling (via conduction and radiation) is feasible

[1]Assumes Li-Pb breeder cooled by sodium.

REFERENCES FOR CHAPTER 4

1. C. C. Baker, et al., "STARFIRE - A Commerical Tokamak Fusion Power Plant Study," Argonne National Laboratory, ANL/FPP-80-1 (1980).

2. W. M. Stacey, Jr., et al., "U.S. Contribution to the International Tokamak Reactor Phase-I Study," Georgia Institute of Technology, US-INTOR/81-1 (1981).

3. B. Badger, et al., "A Wisconsin Toroidal Fusion Reactor Design: UWMAK-I," University of Wisconsin, UWFDM-68 (1974).

4. B. Badger, et al., "UWMAK-III, A Conceptual Tokamak Power Reactor Design," University of Wisconsin, UWFDM-112 (1975).

5. B. Badger, et al., "UWMAK-III, A Noncircular Tokamak Power Reactor Design," University of Wisconsin, UWFDM-150 (1976).

6. D. L. Smith, et al., "Fusion Reactor Blanket/Shield Design Study," Argonne National Laboratory, ANL/FPP-79-1 (1979).

7. J. S. Karbowski, et al., "Tokamak Blanket Design Study," Oak Ridge National Laboratory, ORNL/TM-7049 (1979).

8. D. L. Smith, et al., "A Physical Sputtering Code for Fusion Applications," Proc. 9th Symp. on Engineering Problems of Fusion Research, Chicago, IL, (October 26-29, 1981) (to be issued).

9. J. Roth, J. Bohdansky, and W. Ottenberger, "Data on Low Energy Light Ion Sputtering," Max-Planck Institute fur Plasma-Physik, IPP-9/26 (1979).

10. B. J. Merrill, "INTOR First Wall Erosion During Plasma Disruption, Proc. 9th Symp. on Engineering Problems of Fusion Research, Chicago, IL, (October 26-29, 1981) (to be issued).

11. A. M. Hassanein, G. L. Kulcinski, and W. G. Wolfer, "Vaporization and Melting of Materials in Fusion Devices," University of Wisconsin, UWFDM-422 (1981).

12. R. W. Schrage, A Theoretical Study of Interphase Mass Transfer, Columbia University Press (1953).

13. S. I. Anisimov and A. Kh. Rakumatulina, Sov. Phys. JETP, 37, 442 (1973).

14. P. Wienhold, F. Waelbroeck, J. Winter, and I. Ali-Khan, "Tritium and Vacuum," European Contribution to the International Tokamak Reactor Phase-I Workshop, INTOR/NUC/81-11, Chapter VI-3 (June 1981).

15. J. Bartlit, P. A. Finn, and M. A. Abdou, U.S. Contribution to the International Tokamak Reactor Phase-I Workshop, INTOR/NUC/81-11, Chapter XI (June 1981).

16. J. T. Bell, J. D. Redman, and F. J. Smith, Proc. 24th Conf. on Remote Systems Technology (1976).

17. K. L. Wilson and M. I. Baskes, J. Nucl. Mater., 76 and 77, 291 (1978).

18. K. L. Wilson and M. I. Baskes, J. Nucl. Mater., 74, 179 (1978).

19. R. G. Hickman, UCRL-75354 (1974).

20. I. Ali-Khan, et al., J. Nucl. Mater., 76 and 77, 337 (1978).

21. M. I. Baskes, Sandia Laboratories, Livermore, CA, SAND80-8201 (1980).

22. H. H. Anderson and J. F. Ziegler, Hydrogen, Vol. 3, Pergamon Press (1977).

23. M. R. Louthan, Jr. and R. G. Derrick, Corr. Sci., 15, 565 (1975).

24. G. C. Wood, Corr. Sci., 2, 173 (1962).

25. K. L. Wilson, et al., "Trapping of Deuterium in Helium-Damaged Steels: He^+ Fluence Dependence," Proc. 2nd Topical Meeting on Fusion Reactor Materials, Seattle, WA (August 9-12, 1981) (to be issued).

26. J. Bohdansky, et al., J. Nucl. Mater., 93 and 94, 594 (1980).

27. V. A. Maroni and E. H. VanDeventer, "Materials Considerations in Tritium Handling Systems," Proc. 1st Topical Meeting on Fusion Reactor Materials, Miami, FL (1979).

28. M. I. Baskes, J. Nucl. Mater., 92, 318 (1980).

29. K. L. Wilson, "Hydrogen Recycling Properties of Stainless Steels," Proc. 2nd Topical Meeting on Fusion Reactor Materials, Seattle, WA (August 9-12, 1981) (to be issued).

30. M. Braun, et al., J. Nucl. Mater., 93 and 94, 861 (1980).

31. R. A. Kerst, in Ref. 29, Seattle Meeting.

32. S. Myers, in Ref. 29, Proc. of the Environmental Degradation of Engineering Materials VPi, Blacksburg, VA (September 21-23, 1981).

33. F. Waelbroeck, et al., J. Nucl. Mater., 85 and 86, 345 (1979).

34. I. Ali-Khan, et al., (to be published).

35. F. Waelbroeck, J. Winter, and P. Wienhold, in Ref. 29, Seattle Meeting.

36. M. I. Baskes, in Ref. 29, SAND80-8201 (1980).

37. I. Ali-Khan, et al., J. Nucl. Mater., 74, 132 (1978).

38. M. I. Baskes, J. Nucl. Mater., 99, 337 (1981).

39. P. Wienhold, et al., J. Nucl. Mater., 93 and 94, 866 (1980).

40. P. Wienhold, et al., J. Nucl. Mater., 93 and 94, 540 (1980).

41. P. Wienhold, et al., J. Nucl. Mater., 85 and 86, 1001 (1979).

42. F. Waelbroeck, et al., J. Nucl. Mater., 93 and 94, 839 (1980).

43. N. Saitoh, et al., "Hydrogen Permeation and Diffusion under Ion Bombardment," Technology Reports of the Osaka University, No. 2564, Vol. 30 (1980).

44. H. K. Perkins and T. Noda, J. Nucl. Mater., 71, 349 (1978).

45. M. S. Ortman and E. M. Larson, University of Wisconsin (unpublished data).

46. R. M. Arons, et al., "Preparation Characterization and Chemistry of Solid Ceramic Breeding Materials," Proc. 2nd Topical Meeting on Fusion Reactor Materials, Seattle, Wa (August 9-12, 1981) (to be published).

47. R. G. Clemmer, "The Development of Tritium Breeding Blankets for DT-Burning Fusion Reactors," Proc. 4th Topical Meeting on the Technology of Controlled Nuclear Fusion, USDOE Rep. CONF-801011 (1980) P. 526, and references therein.

48. D. L. Smith, et al., "Analysis of In-Situ Tritium Recovery from Solid Fusion Reactor Blankets," Proc. 4th Topical Meeting on the Technology of Controlled Nuclear Fusion, USDOE Rep. CONF-802022 (1980) p. 560, and references therein.

49. D. Okula and D. K. Sze, "Tritium Recovery from Solid Breeders: Implications of the Existing Data," University of Wisconsin, UWFDM-351 (1980) and references therein.

50. J. W. Davis, et al., Proc. Workshop on Tritium Breeding Solids-Research and Development, USDOE Rep. DOE/ET-52039/1 (1981) and references therein.

51. S. Nasu, "Data Base for Breeder Choice," Japan Atomic Energy Agency, JAERI-M-8510 (1979), K. Shiraishi, et al., pp. 63-75; also published as App. C, Ref. 5.

52. M. Tetenbaum, Argonne National Laboratory (personal communication).

53. P. A. Finn, et al., "Solid Oxide Compounds -- Properties Necessary for Fusion Applications," Proc. 9th Symp. on Engineering Problems of Fusion Research, Chicago, IL (October 26-29, 1981) (to be published).

54. O. K. Chopra and D. L. Smith, "Interactions of Solid Ceramic Breeding Materials with Structural Alloys," Proc. 2nd Topical Meeting on Fusion Reactor Materials, Seattle, Wa (August 9-12, 1981) (to be published).

55. L. Yang, et al., "Irradiation Study of Lithium Compound Samples for Tritium Breeding Application," General Atomic Company, GA-A16407 (1981).

56. T. Takahashi and T. Kikuchi, J. Nucl. Mater., 91, 93 (1980).

57. P. A. Finn, Argonne National Laboratory, Private Communication (1980).

58. G. K. Johnson, R. T. Grow, and W. N. Hubbard, J. Chem. Thermodynamics, 7, 781 (1975).

59. M. Tetenbaum, Argonne National Laboratory, Private Communication (1981).

60. S. Nasu, "A Preliminary In-Pile Test of Tritium Release from Li_2O Pellets", Japan Atomic Energy Research Institute, JAERI-memo 9276 (1980).

61. D. L. Smith, et al., "Fusion Reactor Blanket/Shield Design Study," Argonne National Laboratory, ANL/FPP-79-1, pp. 4-26 (1979).

62. JANAF Thermochemical Tables, Dow Chemical Company, Midland, MI (1974).

63. J. Berkowitz, D. J. Meschi, and W. A. Chopka, J. Chem. Phys., 33, 553 (1960).

64. A. B. Johnson, et al., "Tritium Production from Ceramic Targets," Battelle Northwest Laboratory, BNWL-2097 (1976).

65. J. R. Hoffman, Nucl. Sci. Eng., 68, 73 (1978).

66. R. Bird, et al., Transport Phenomena, John Wiley & Sons, Inc., New York (1960).

67. R. A. Graham, Masters Thesis, University of Florida.

68. G. R. Youngquist, Ind. Eng. Chem., 62, 8, 52 (1970).

69. S. Chapman and T. G. Cowling, Mathematical Theory of Non-Uniform Gases, Cambridge University Press (1951).

70. T. Kurasawa, et al., J. Nucl. Mater., 80, 48 (1979).

71. T. Kurasawa, et al., J. Nucl. Mater., 92, 67 (1980).

72. J. E. Draley, et al., "Corrosion of Some Reactor Materials in Dilute Phosphoric Acid,"Argonne National Laboratory, ANL-6206 (1961).

73. "Blanket/Shield and Power Conversion System for Small Field-Reversed Mirror Fusion Reactor," General Atomic Company, GA-A1553 (1979).

74. C. C. Stone, et al., Nucl. Technol., 55 (1981).

75. B. Badger, et al., "WITAMIR-I, A Wisconsin Tandem Mirror Reactor Design," University of Wisconsin, UWFDM-400 (1980).

76. "STARFIRE - A Commercial Tokamak Reactor: Interim Report," Argonne National Laboratory, ANL/FPP/TM-125 (1979).

77. G. L. Stephens and D. J. Campbell, "Program THTB, for Analysis of General Transient Heat Transfer Systems," General Electric Company, RGO/FPD647 (1961).

78. J. Jung, Nucl. Technol., 50, 60 (1981).

79. W. M. Stacey, Jr., et al., "U.S.-INTOR: U.S. Contribution to the International Tokamak Reactor Workshop, Phase-I," USA INTOR/80-1 (1980).

80. J. Jung, Nucl. Sci. Eng., 65, 130 (1978).

81. D. L. Smith (ed.), "First-Wall Systems," Chapter VII, in INTOR-International Tokamak Reactor Phase I Conceptual Design, IAEA, Vienna (1981)

82. J. Jung and M. Abdou, Trans. Am. Nucl. Soc., 34, 645 (1980).

83. D. K. Sze, R. G. Clemmer, and E. T. Cheng, "Li-Pb, A Novel Material for Fusion Applications," Proc. 4th Topical Meeting on Technology of Controlled Nuclear Fusion, USDOE Rep. CONF-801011, p. 1786 (1981); also, University of Wisconsin, UWFDM-378.

84. N. J. Hoffman, A. Darnell, and J. A. Blink, "Properties of Lead-Lithium Solutions," ibid., p. 1745; also, Lawrence Livermore Laboratory, UCRL-84273.

85. P. A. Finn, et al., Trans. Am. Nucl. Soc., 34, 55 (1980).

86. M. L. Saboungi, J. Marr, and M. Blander, J. Chem. Phys., 68(4), 1375 (1978).

87. H. Kottowski, Ispra, Personal Communication to R. Clemmer, Argonne National Laboratory (November 12, 1981).

88. H. R. Ihle and C. H. Wu, "The Activity of Lithium and the Solubility of Deuterium in Lithium-Lead Alloys," Proc. 10th Symp. on Fusion, Padova, Italy, Pergamon Press, New York, pp. 639-644 (1979).

89. E. M. Larsen, M. S. Ortman, and K. E. Plute, "Comments on the Hydrogen Solubility Data for Liquid Lead, Lithium, and Lithium-Lead Alloys and Review of the Tritium Solubility Model for Lithium-Lead Alloys," University of Wisconsin, UWFDM-415 (1981).

90. E. Veleckis, Argonne National Laboratory, Personal Communication to N. Hoffman, ETEC, Canoga Park, CA (June 15, 1981).

91. E. Veleckis, R. M. Yonco, and V. A. Maroni, "The Current Status of Fusion Reactor Blanket Thermodynamics," Argonne National Laboratory, ANL-78-109 (1979).

92. V. A. Maroni and E. H. VanDeventer, "Materials Considerations in Tritium Handling Systems," Proc. 1st Topical Meeting on Fusion Reactor Materials, Miami, FL (1979).

93. W. Calaway, Nucl. Technol., 39, 63 (1978).

94. V. A. Maroni, R. D. Wolson, and G. E. Staahl, Nucl. Technol., 25, 83 (1975).

95. K. Natesan and D. Smith, Nucl. Technol., 22, 138 (1974).

96. S. B. Skladzien, D. J. Raue, and C. C. McPheeters, "Method for Regenerating Sodium Cold Traps," Argonne National Laboratory, ANL-81-52 (1981).

97. V. A. Maroni, "An Analysis of Tritium Distribution and Leakage Characteristics for Two Fusion Reactor Reference Designs," Argonne National Laboratory, CEN/CTR/TM-9 (1974).

98. P. F. Tortorelli and O. K. Chopra, "Corrosion and Compatibility Considerations of Liquid Metals for Fusion Reactor Applications," Proc. 2nd Topical Meeting on Fusion Reactor Materials, Seattle, WA (August 10-12, 1981) (to be issued).

99. P. F. Tortorelli, Oak Ridge National Laboratory, Personal Communication.

100. Data from Ispra, INTOR-International Tokamak Reactor Phase-I, Conceptual Design, IAEA, Vienna (1981) (in press).

101. V. V. Popovich and I. G. Dmukhovskaya, Sov. Mater. Sci., 14, 365, English Translation (1977).

102. I. G. Dmukhovskaya and V. V. Popovich, Sov. Mater. Sci., 15, 366, English Translation (1979).

103. N. N. Breyeer and K. L. Johnson, J. Test. Eval., 2, 471 (1974).

104. V. V. Popovich, Sov. Mater. Sci., 15, 438, English Translation (1979).

105. A. L. Bichuya, et al., Sov. Mater. Sci., 4, 12, English Translation (1968).

106. A. L. Bichuya, Sov. Mater. Sci., 5, 352, English Translation (1969).

107. E. S. Nikolin and G. V. Karpenko, Sov. Mater. Sci., 4, 15, English Translation (1968).

108. M. I. Chaevskii and A. L. Bichuya, Sov. Mater. Sci., 5, 82, English Translation (1969).

CHAPTER 5

CONFIGURATION AND MAINTENANCE

Chapter 5

Table of Contents

Chapter 5

List of Figures

Chapter 5

List of Tables

5.1 Introduction

The reactor configuration and maintenance approach are major factors in determining the economic viability of commercial fusion reactors. DEMO should utilize a reactor configuration and maintenance approach that typifies a commercial reactor so that shortcomings can be identified and modifications incorporated prior to construction of the first commercial demonstration reactor. In addition, cost of electricity (COE) will be one of the most important aspects for commercial reactors so emphasis in DEMO should be placed on reducing the elements that contribute to COE, namely:

- o Outage rate (reliability and lifetime)
- o Capital cost
- o Replacement approach (time)

Design choices can affect the outage rates but quantative data on the reliability and lifetime of components is presently lacking. Data on the required design margins, redundancy levels, specific component designs, etc. will become available as reactors such as TFTR and FED begin operations. Availability analyses of tokamaks has provided some guidance to DEMO such as to indicate that some components (e.g. magnets) will have to be significantly more reliable than other components (e.g. first wall) if a reasonable availability is to be achieved.

All DEMO components should be prototypical of a commercial reactor. Enhancing maintainability is a primary goal of the DEMO design even at the expense of a modest increase in capital cost. The experience gained through design, construction and operation of a commercially relevant reactor configuration is expected to outweigh any cost differences.

The component replacement approach for DEMO should be as close as possible to that expected for commercial reactors. Similar access provisions, module configuration, sealing approaches, leak isolation techniques, sector removal approach, etc. should be utilized so that design improvements can be identified. A difference between DEMO and the first commercial demonstration

reactor; however, is that DEMO needs only to show that the method is viable for a first demonstration commercial reactor. For example DEMO costs may dictate that less sophisticated maintenance tools be used. These tools may require more time to perform tasks but this is acceptable if no feasibility question exists.

The STARFIRE/DEMO study has emphasized design for ease of replacement (maintenance). Minimum capital cost has been emphasized until it impacts maintenance. At that point we have let maintenance dominate. For example, the numbers and size of TF coils has been reduced as much as possible compatible with replacing one blanket sector per TF coil. Reducing the number of TF coils leads to use of fewer first wall blanket sectors, fewer seals, joints and pipes which might fail and to fewer components resulting in less total time for component replacement.

A total remote maintenance approach was selected for DEMO based on the desire to minimize radiation exposure to workers. It is believed that if remote maintenance is desired in a commercial reactor then DEMO should show its viability for all maintenance operations. Workers can be utilized in the radiation environment as a backup to the maintenance system given the developmental nature of DEMO. The key issues addressed in the DEMO effort have been selection of the number of TF coils, minimizing their size, identification of the location of the vacuum boundary, selecting the number and configuration of blanket shield sectors and selecting the maintenance approach.

This chapter first summarizes the DEMO design approach and then is followed by discussions of the key issues noted above.

5.2 Reference Reactor Configuration

The reactor configuration is made up of 8 TF coils, 8 shield sections, 8 blanket sectors, 8 limiter modules, 8 EF coils, 4 OH coils and 4 CF coils. Also included are 2 REB launchers. A layout of the reactor is shown in Figure 5-1. The reactor is designed for complete reassembly by remote maintenance. Sketches of the blanket, shield and TF coil are shown in Figures 5-2, 5-3 and 5-4 respectively.

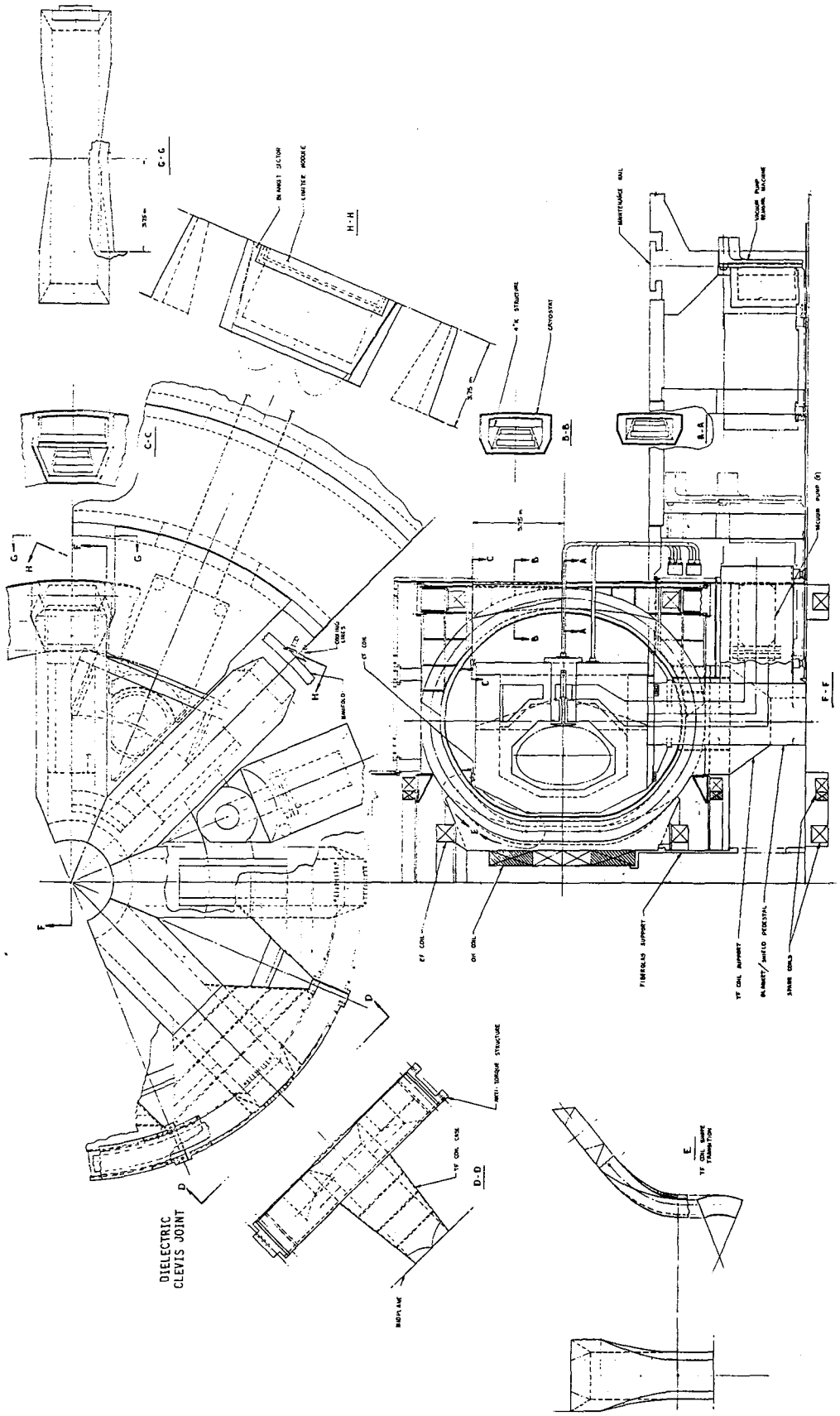

Fig. 5-1. Reactor layout.

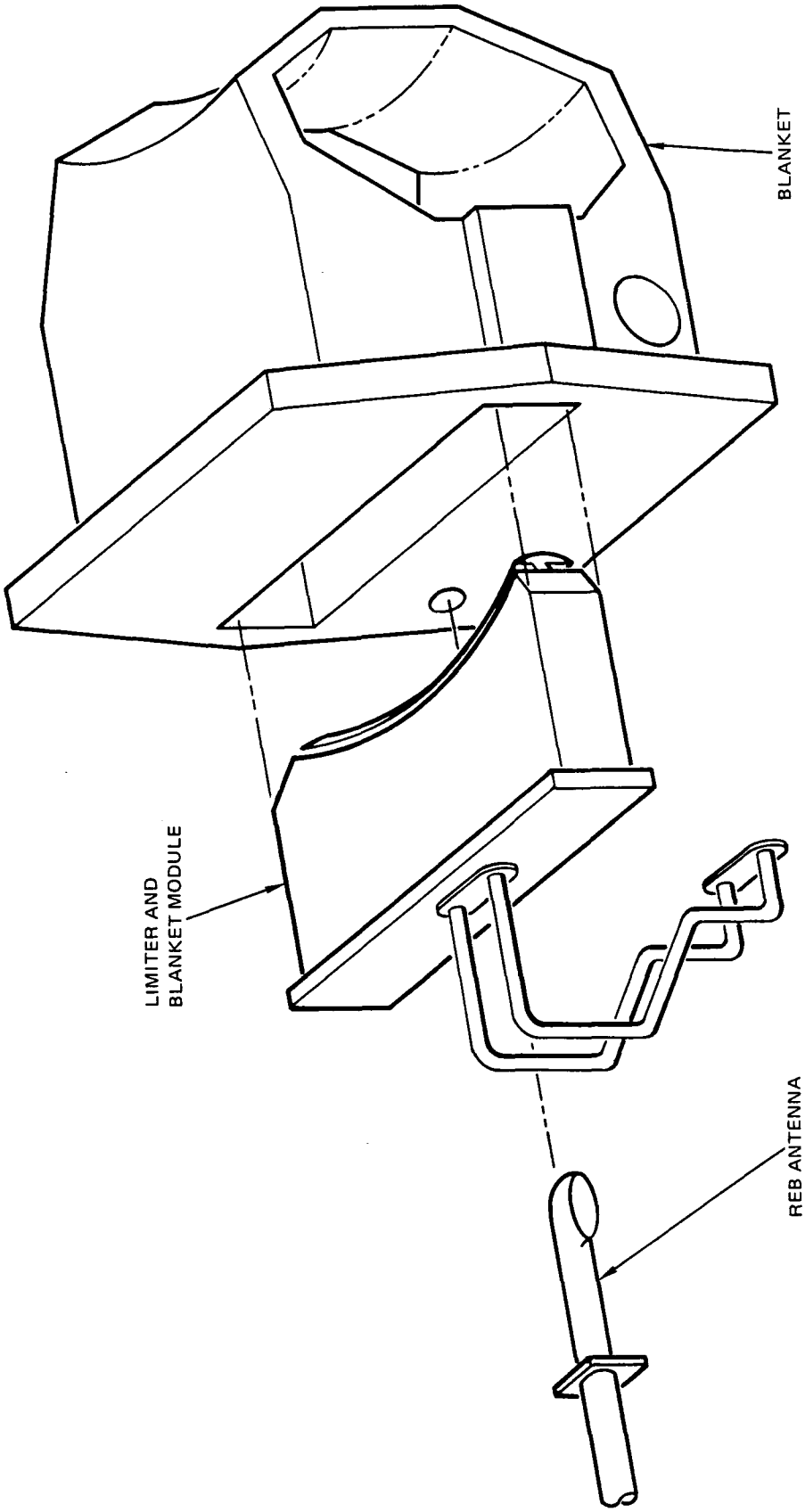

Fig. 5-2. Blanket sector.

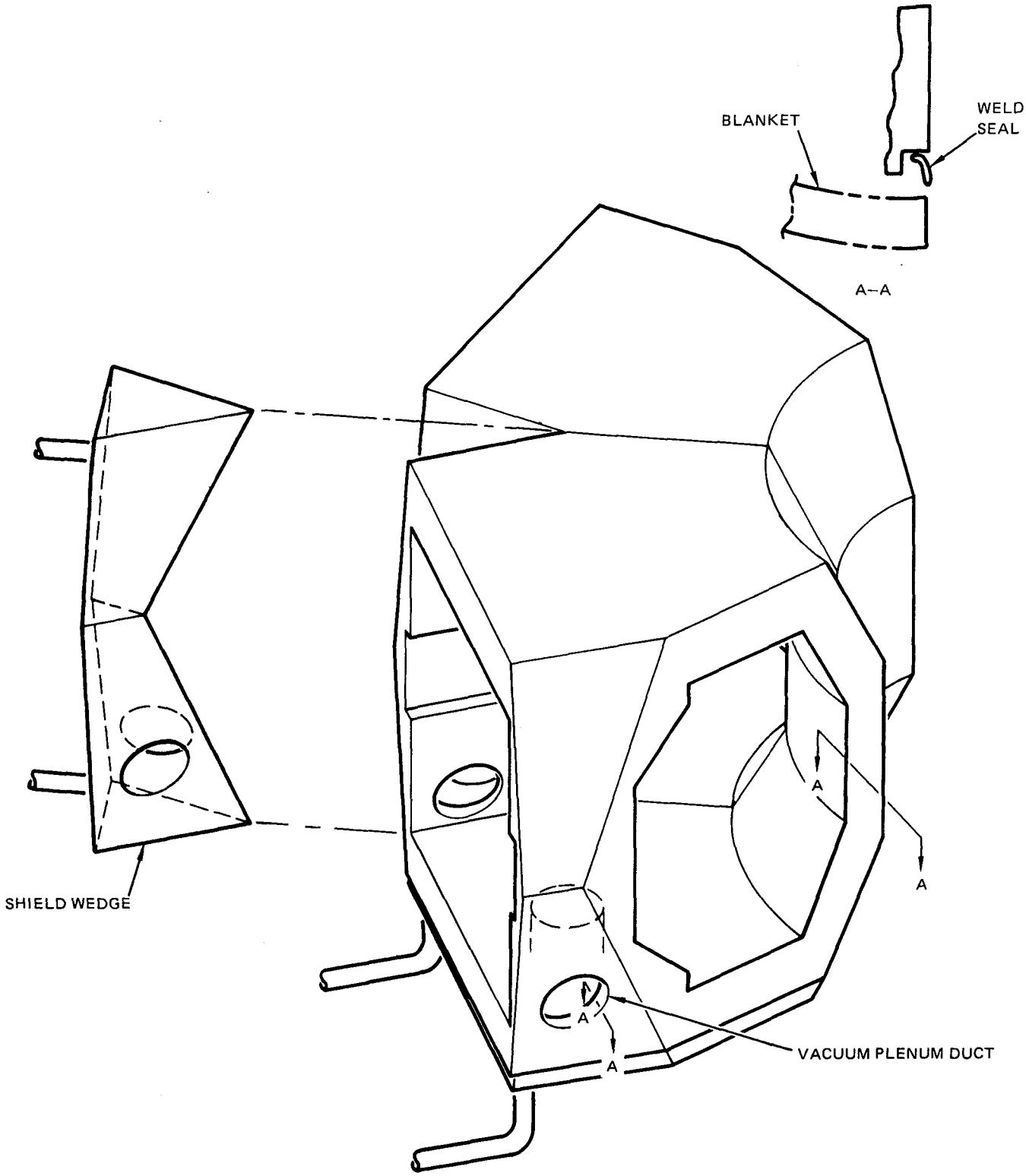

Fig. 5-3. Shield sector.

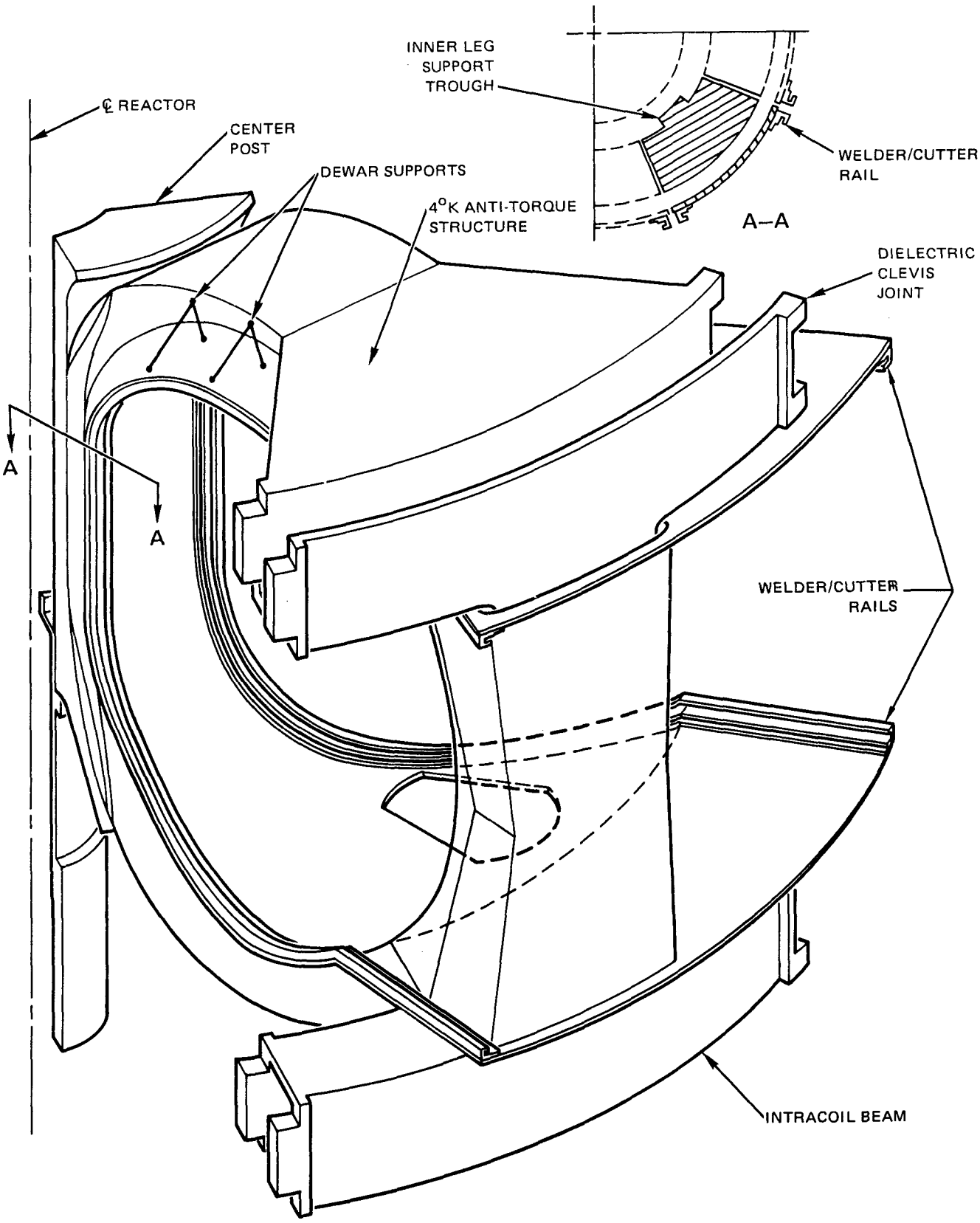

Fig. 5-4. TF coil configuration.

The TF coils are designed for a 10T peak field and utilize NbTi in a bath cooled tank. The coil vertical support is provided by the center post and an outer support pedestal of G-10 fiberglass. The half height of the coil is 5.46 m and the outer leg radius is 11.6m. The overturning forces are reacted through a 4°K beam structure which leaves a 6.2 m wide x 7.5 m high opening between TF coils for blanket installation. The in-plane loads on the upper and lower portions of the TF coil are supported by the center post which extends outward ~1.5 m. This permits use of a shortened TF coil which follows a pure tension shape in areas away from the center post. The OH and EF coils are supported inside the common vacuum tank from the TF coils. The upper and inner OH and EF coils can be replaced by removing the upper dome of the vacuum tank. Spares have been included for the lower OH and EF coils because of the consequences associated with their replacement (rewind in-place or disassemble the reactor).

The vacuum boundary for the plasma chamber is located at the shield. The blanket/shield sector doors provide the vacuum enclosure with dual elastomer seals which have intermediate pumping to permit the system to tolerate some leakage. The shield is installed as 8 sectors which form a pocket for the blanket. The pocket shield sectors are seal welded together to form the vacuum boundary. Two dielectric breaks are required in sectors 180° apart. The TF, CF, EF and pocket shield sectors are designed to last the life-of-the-plant and should not require replacement; however, provisions are made for remotely replacing them since "Murphy's Law" says it is prudent.

The blanket, limiters, vacuum pumps and REB current drive launchers are remotely replaceable. These components are designed so they may be replaced independent of each other except for the blanket which will require removal of limiter and REB antennas with the blanket sector.

The vacuum pumps are located in the reactor building basement and can be maintained independent of other reactor components. Each of the 8 pumps are manifolded into a common plenum inside the blanket sector shield door cavity so that two of the eight can be regenerated while the other six are operating. A regeneration time of 2 hours is anticipated which implies 6 hours

between pump regeneration. Dual gate valves are included on each pump for redundancy and to permit pump removal without breech of vacuum.

The anti-torque structure consists of a 4°K bending beam structure that forms a ring at the top and bottom of the coils in addition to the outer legs of the TF coil. This structural approach is based on the design development work done for INTOR and FED. Additionally the shield rests on pedestals which are made up primarily of the shielding that surrounds the vacuum ducts. The TF coil vertical supports are via the center post and G-10 fiberglass support paths under each TF coil. A common vacuum tank encloses all TF, EF and OH coils and the center post. The weights of the major components are summarized in Table 5-1.

5.3 Design Approach Selection

The DEMO configuration has been selected to enhance the maintainablility of the reactor without critically detracting from the reactor performance or increasing cost. Many of the STARFIRE considerations have been carried directly into DEMO especially in areas where little effort has been expended for DEMO. Areas where major differences occur are in the number of TF coils, TF coil shape, TF coil support and selection of one blanket sector per TF coil. Eight TF coils are utilized instead of twelve. The modification is required due to the decision to use one blanket sector per TF coil which results in use of a larger coil relative to the plasma. The TF coil shape is more circular than Dee but is still pure tension in areas not supported by the center post. This shape was chosen to minimize the stored energy of the TF and EF coil systems. The 4°K overturning structure design of INTOR and FED has been adopted for DEMO. Steady state operation minimizes fatigue concerns with this structure. A single blanket sector is used per TF coil because it simplifies sector removal, significantly reduces the number of cooling lines and simplifies limiter replacement. The object of identifying a design configuration at this point is to provide a focal point for design trades in the major systems and to identify critical areas for further considerations.

Key areas where further design work is planned include:

Table 5-1. Major Component Weights

	Per Sector/Item (Metric Tons)	Total (Metric Tons)
Shielding (Excludes sector door)	439	3512
TF Coil (8)	400	3200
EF Coil (R = 1 m)	42	84
EF Coil (R = 2 m)	55	110
EF Coil (R = 4 m)	56	112
EF Coil (R = 11.5 m)	315	630
		936
OH Coil (R = 1 m)	63	126
OH Coil (R = 3.6 m)	36	72
		198
CF Coil (R = 4.4 m)	12	24
CF Coil (R = 8 m)	21	42
		66
Limiter Module	50	400
Sector Removal:		
1 FW/B Segment	44	2448
1 Door	263	
	306	
Total Weight		10,760

TF Coil Design Modification for Enhanced Replacement

The DEMO TF coil has been designed for remote replacement; however, it would be highly desireable to develop a method of eliminating the welded common vacuum tank at the centerpost. Methods of surrounding the inner leg with a separate vacuum tank generally result in an excessive heat leak and are not compatible with the 4°K support structure. (See paragraph 5.5)

Vacuum Boundary Location

The vacuum boundary location tradeoff has indicated substantial benefits (e.g. no dielectric vacuum joints) and penalties of larger surface areas and volumes for vacuum pumping and increased difficulty of replacing the TF coil if the plasma vacuum boundary is located at the TF coil vacuum tank as opposed to the shield. Further trade studies are required. (See paragraph 5.3.4)

Electromagnetic Loading

The electromagnetic loads on the first wall/blanket sectors, current drive launchers and poloidal coils of the DEMO reactor need to be evaluated.

Inversion Probability at Limiter

The probability that particles entering the limiter slot will remain in the slot must be determined with more accuracy. The number of vacuum pumps and ducts can change significantly with this criteria. (See paragraph 5.4)

5.3.1 TF Coil Configuration

The TF coil system probably has the largest single effect on the overall reactor configuration. The number of coils will determine how many components are required and the basic size of each component. In general a lower number of TF coils means fewer components, joints, valves and connections and, in all likelihood results in a higher reliability of the system. Fewer parts also imply fewer maintenance operations and therefore less time for maintenance. The above considerations lead to higher availabilities for lower numbers of TF coils, hence our incentive to reduce the number of coils as much as possible.

5.3.1.1 Number of TF Coils

Consideration of the access requirements of the blanket and shield and the ripple limits imposed on the TF coil system has resulted in selection of 8 TF coils with an outer leg radius of 11.6m. The resulting ripple is 2.1 percent peak-to-peak at the outer edge of the plasma and 0.9 percent at R_o + a/2.

Ripple Requirements

Ripple requirements for tokamaks have not been well established; however, the currently suggested limits are:

- 0.6 Percent peak-to-peak at R_o + a/2
- Three Percent peak-to-peak at the outer plasma edge (R_o + a)

The 0.6 percent peak-to-peak ripple limit has been mutually arrived at by members of a ripple limit workshop (1). This limit is compatible with current transport codes. A second ripple limit of three percent peak-to-peak at the plasma edge has been discussed more recently as a possible alternative. DEMO has utilized this limit for its design. Peak-to-average ripples of other designs are given in Table 5-2.

Table 5-2. Field Ripple for Design Studies

	PEAK-TO-AVERAGE RIPPLE (%)		
LOCATION	R_o	R_o + a/2	R_o + a
STARFIRE	0.09%	0.40	1.47
INTOR	0.10	-	0.50
FED	0.10	0.30	0.80
INTOR MODIFIED	-	0.50	1.50
DEMO	0.145	0.45	1.05

TF Coil Outer Leg Radius Selection

A simplified equation (2) has been utilized to determine the TF Coil ripple; this relationship is:

$$R_2 = 1.1\ R/\delta^{1/N}$$

where R_2 = outer leg radius (m)

R = radius where ripple is measured (m)

δ = peak-to-peak ripple

N = number of TF coils

A plot of the outer leg radius as a function of ripple is shown in Figure 5-5 for the two plasma zones of interest. The ripple limit of three percent is met at an outer leg radius of 11.1 m but, this radius was too small to permit sector installation. (See next section: Access Requirements.) Seven coils would have resulted in a peak-to-peak ripple at R_o + a of 3.8 percent if the access limited radius of 11.4 m was used.

Access Requirements - The access required for installation of one first wall/blanket sector per TF coil can be estimated using simple geometry calculations. Assumptions in these calculations included the geometry shown in Figure 5-6 and an assumption that the full blanket depth is desired at the reactor midplane. Additionally, assumptions for the shield sectors are that a 30 cm thick outer frame and a 10 cm shielding step are required. The shield sector clears the TF coil vacuum tank by 10 cm. The vacuum tank thickness, superinsulation and liquid nitrogen shroud make up a 20 cm layer enclosing the 4°K cold case. These calculations result in the mechanical access constraint that is shown in Figure 5-5. Further refinement of the ripple calculations and ripple limits and better definition of the structural support, vacuum tank and shielding step designs are required. The total access to the blanket sectors varies less than 1 m in total perimeter for changes from 8 to 12 TF coils. As more coils are used, each sector becomes proportionally narrower.

5.3.1.2 TF Coil Cross Section

The center post portion of the TF coil is frequently designed with flat sides to make the coil simpler to fabricate. However, if the coil is pancake wound, as is anticipated for the DEMO coil, the only added expense of a more closely fitting cross section is that of machining that portion of the coil case along the inner leg and in a transition area at the top and bottom inner leg. The two options are shown in Figure 5-7. A comparison of the fabricated cost of each case indicates that a $20/kg cost is incurred for a welded plate dewar and that an additional $10/kg can pay for machining in grooves. On this

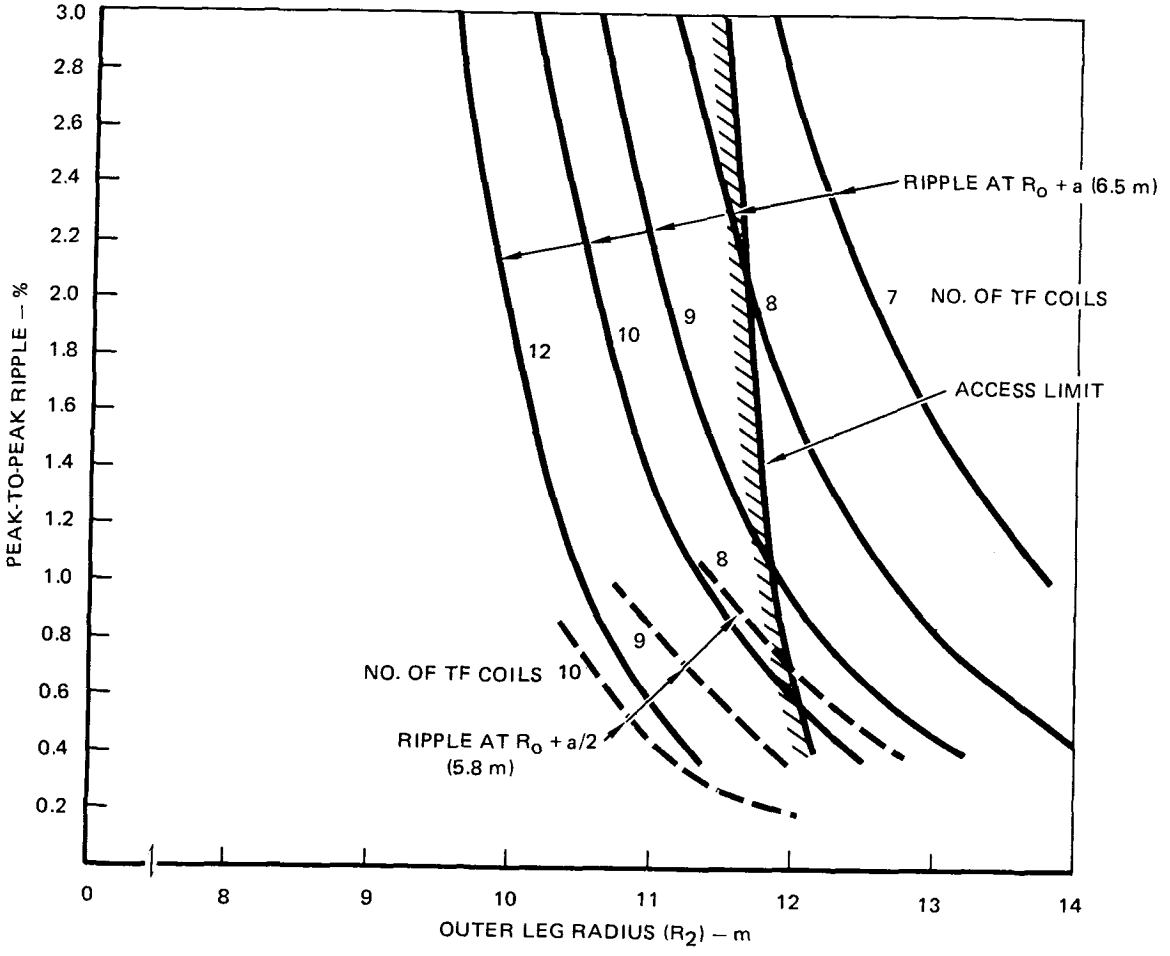

Fig. 5-5. TF coil ripple with mechanical access constraints for sector installation superimposed.

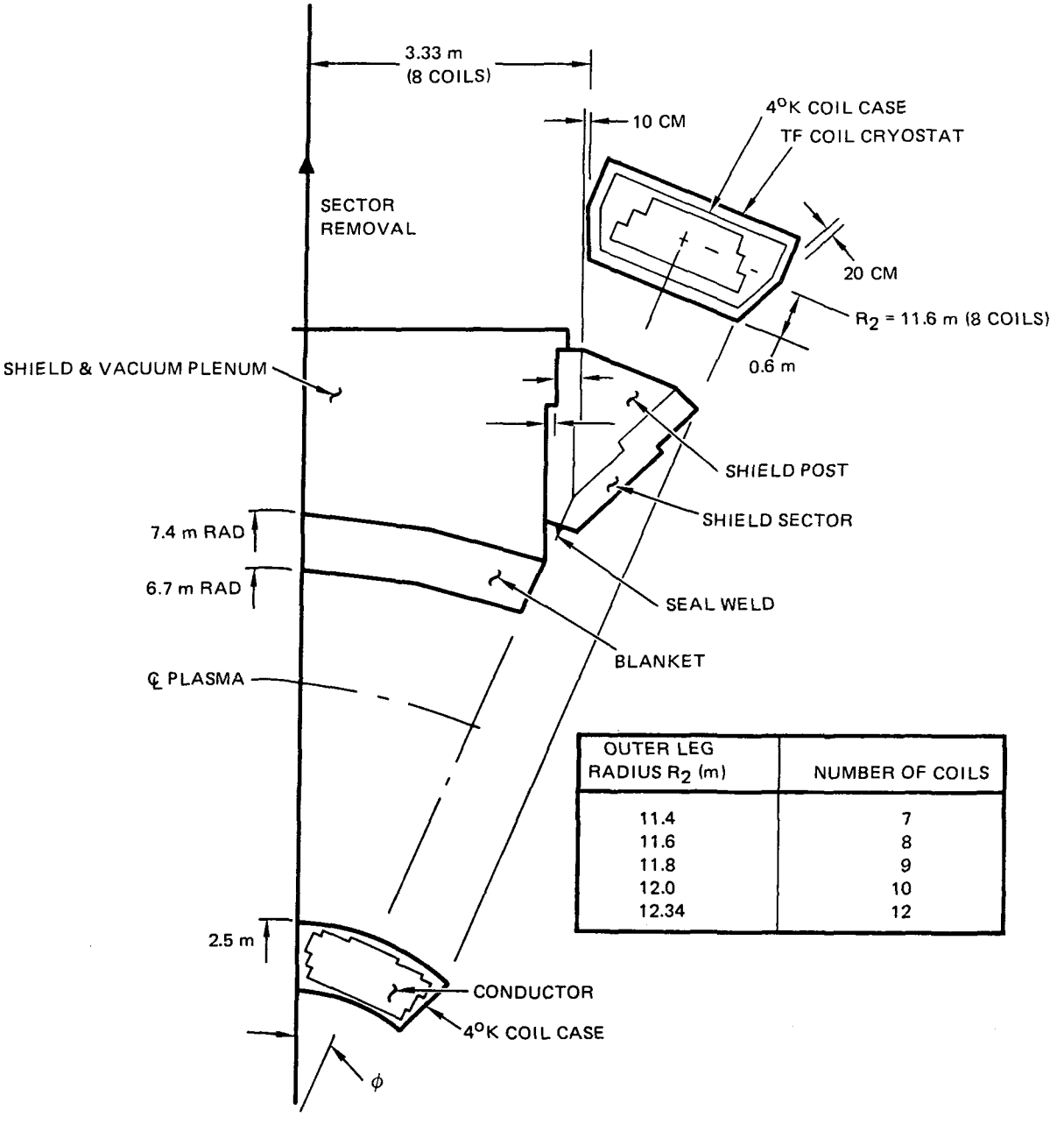

OUTER LEG RADIUS R_2 (m)	NUMBER OF COILS
11.4	7
11.6	8
11.8	9
12.0	10
12.34	12

Fig. 5-6. Access geometry of reactor.

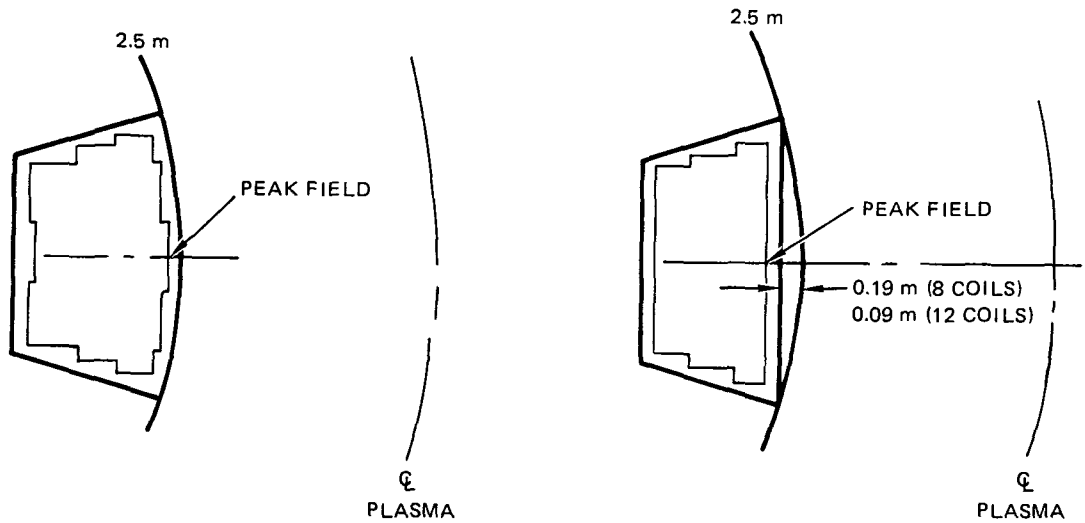

COST/LB	$30/KG	$20/KG
MANUFACTURED COST OF INNER LEG STRUCTURE	$1.9 m	$1.3 m

Fig. 5-7. TF coil inner leg shape comparison.

basis it costs ~$0.6M more for the machining coil case. This is more than offset by locating the peak field coil turns as much as 19 cm closer to the plasma which minimizes the field requirements and major radius of the reactor. A preliminary cost evaluation based on STARFIRE indicates this can decrease the cost by as much as $50 M (3).

5.3.1.3 Coil Shape

Conventional TF coil designs utilize a pure tension shape per Moses and Young's criteria (12) using a straight center post. As a result the total stored energy in the EF coil system is very dependent on the outer TF coil radius because every 1 m change in radius increases the coil height by ~ 2 m. This provides a great incentive for minimizing the outer leg radius. In STARFIRE this design approach resulted in the use of two blanket sectors per TF coil and complicated the maintenance operations.

The DEMO design utilizes a modified coil shape as proposed by the UWMAK II design (4). DEMO utilizes a non-straight center post and a modified pure tension shape so that a shorter magnet can be used. The conventional coil shape and DEMO modified shape are shown in Figure 5-8. A resulting 1.43 m decrease in total height occurs. The shape was selected by plotting a series of pure tension shapes with a given R_2 needed for blanket access. After layout of the options it was found that the 5.46 m half height design could be used and still permit sector installation and removal. The inner leg shape was then modified by deviating from the pure tension shape on the inner leg. To reduce in-plane bending stresses as as result of this modification, the center post was brought out to the point where the deviation was started. This allows the center post to pick up any loads that would be imposed in the coil case by deviation from the pure tension shape. The benefits of shortening the TF coil height include a reduction in reactor building height and reduction in EF coil stored energy.

Reduction of each 1 m in building height saves approximately 600 m^3 in reactor building volume (Based on STARFIRE); this represents ~$3M in cost savings alone. Additionally savings in stored energy costs are approximately $3 M/GJ (5).

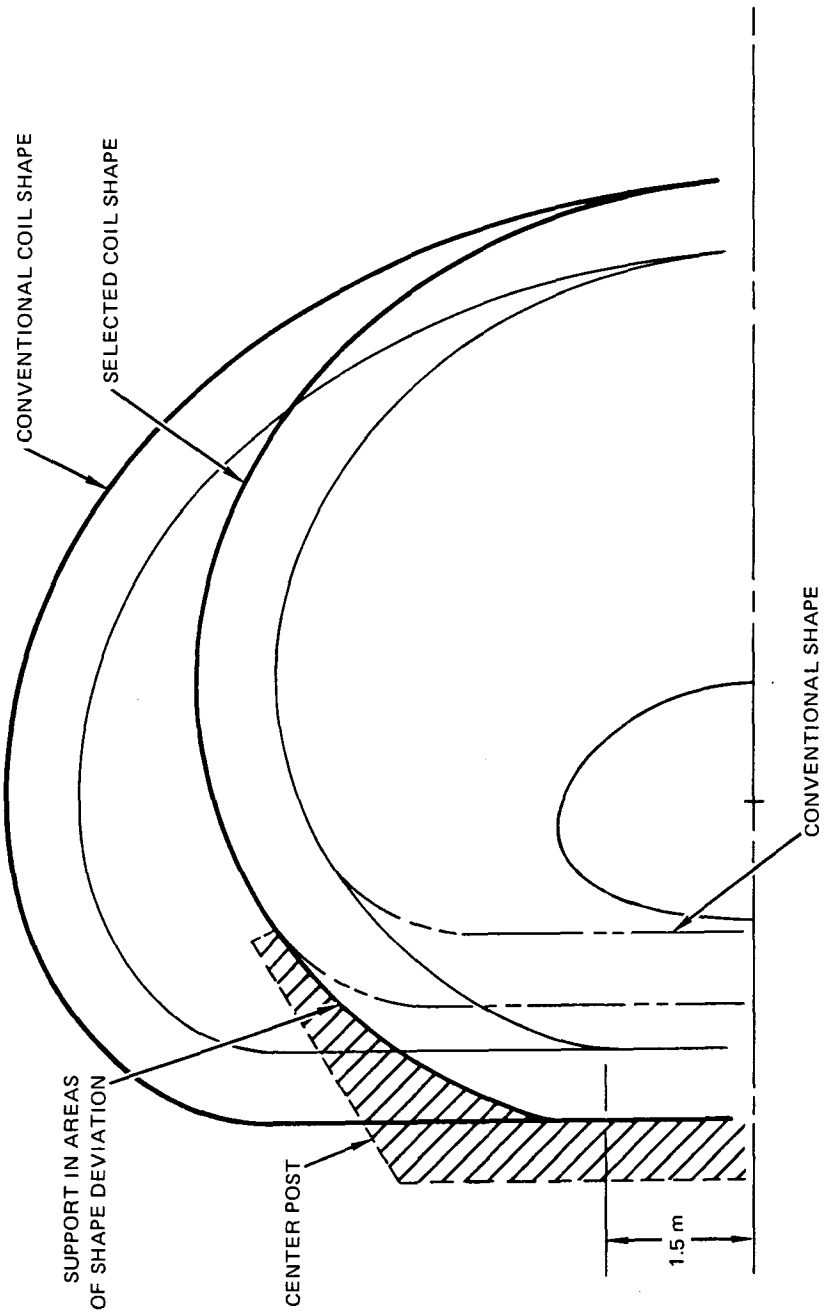

Fig. 5-8. TF coil shape options.

A survey of EF stored energy was performed for several standard pure tension TF coil designs, Figure 5-9, and plotted as a function of the product of H_{max} and R_2 of the TF coil. This is shown in Figure 5-10. As indicated a significant incentive exists for minimizing TF coil size. The outer leg size is fixed by access for maintenance but the height is not until it starts to interfere with the blanket/shield installation. The resultant stored energy of ~4GJ is substantially less that the ~14 GJ that would have been required for a pure tension shape. This represents ~$30 M in cost savings.

5.3.1.4 TF Coil Intracoil Support

The DEMO intracoil support structure has been defined utilizing the 4°K cold support system of FED and INTOR. The out-of-plane loads were assumed to be approximately two times those of FED based on a ratio of the plasma currents. The design criteria used was the smaller of 1/3 F_{TU} (ultimate strength) or 2/3 F_{TY} (yield strength) at 4°K. For welded 316 LN steel this results in a design allowable stress of 372 mpa (54 ksi). It was assumed that 82 percent of the overturning moment (10) was taken in the outer leg of the TF coil and fixed end beams calculations were performed. The design criteria and a structural deflection limit of one cm were used to define the beam cross section required. The design and cross section is shown in Figure 5-11. The trapezoidal shape of the outer leg was selected because it provided maximum access for blanket and shielded installation. The equivalent cross section makes a transition to the basic cold case shell where it rests against the center post.

The intracoil beam (see Figure 5-4) was sized to give approximately the same moment of inertia as the outer TF coil leg and found to require a 1.2 m X 1.8 m solid area. This size was then replaced with a more practical built up grid of structural elements. The grid elements are compared to the solid beam in Figure 5-11. The grid elements extend from either side of the TF coil case and are pinned to adjacent coil structures through a dielectric clevis joint between coils (see Figure 5-1). This joint permits removal and replacement of any TF coil without cutting and welding the basic structure. The outer EF coil is supported from a structural tray which serves as a cap member for the bending beam intracoil structure.

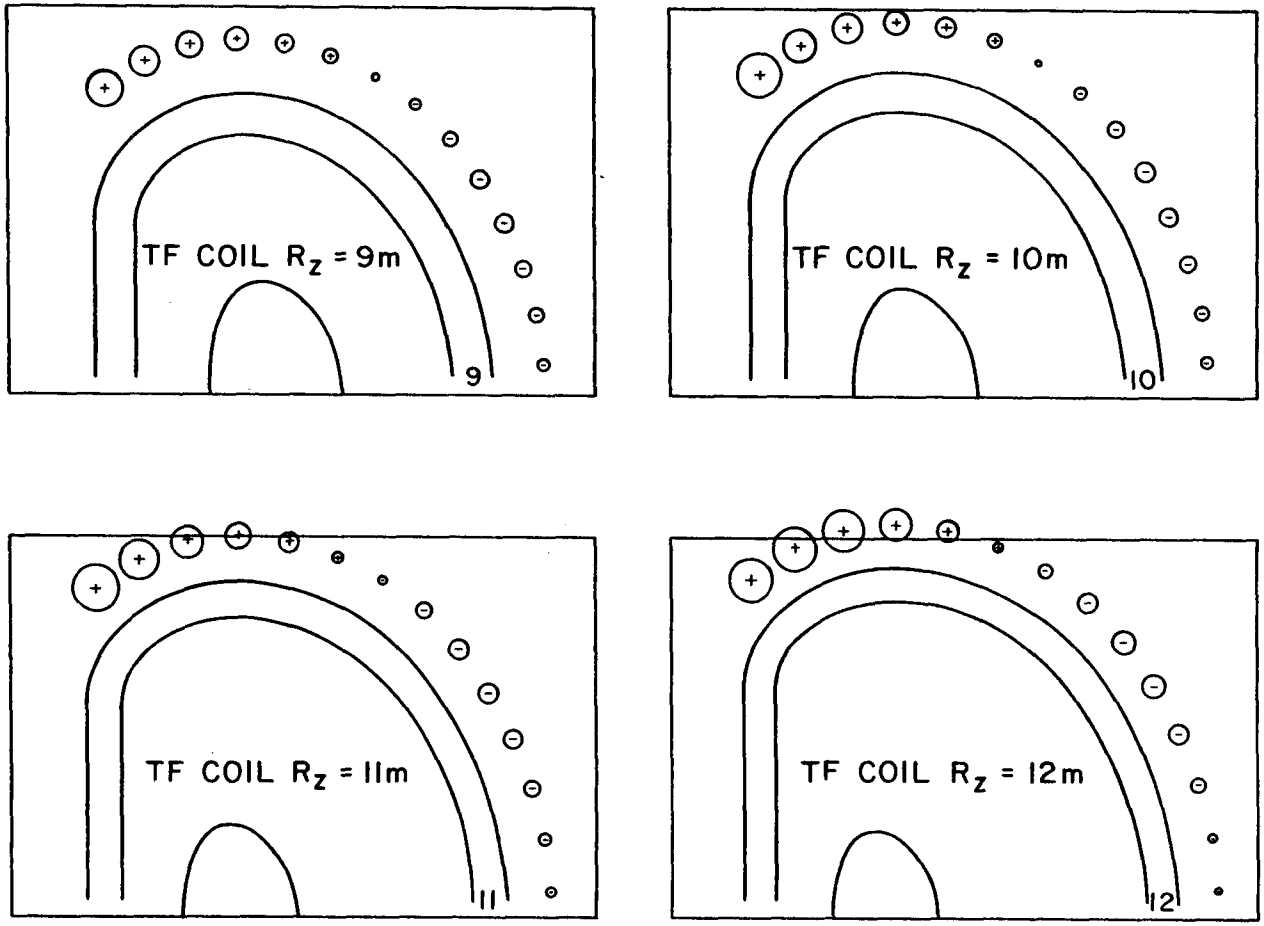

RO - 5.20 FWALL - 25.00 ASP - 4.00 KAPPA - 1.60 DEITY - 0.20

ALPHA - 1.40 BETAT - 0.08 Q(A) - 1.92 DELM - 0.780 BMAX - 10.00

Fig. 5-9. EF coil location as a function of TF coil outer radius.

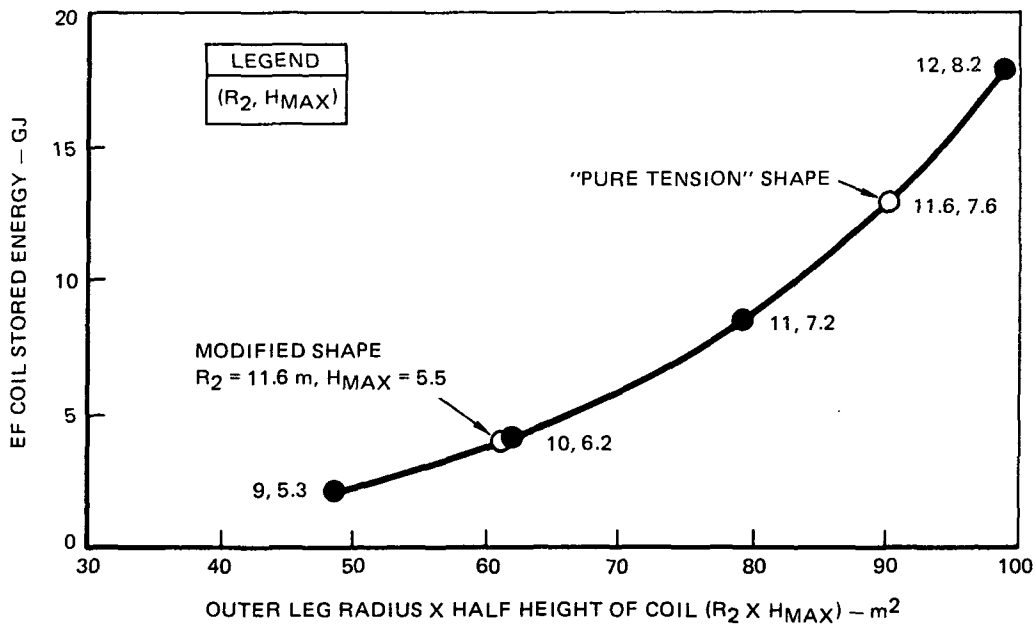

Fig. 5-10. EF coil stored energy.

MATERIAL: WELDED 316 LN STAINLESS STEEL
F_{tu} = 161 KSI, F_{ty} = 100 KSI

ALLOWABLE STRESS: SMALLEST OF 1/3 F_{tu} OR 2/3 F_{ty} = 54 KSI

OUT OF PLANE LOAD: FED = 11.5 (10^6) LB

DEMO = 2 X FED = 23 (10^6) LB

ASSUME 82% CARRIED IN OUTER LEG
(1.9 X 10^7 LB)

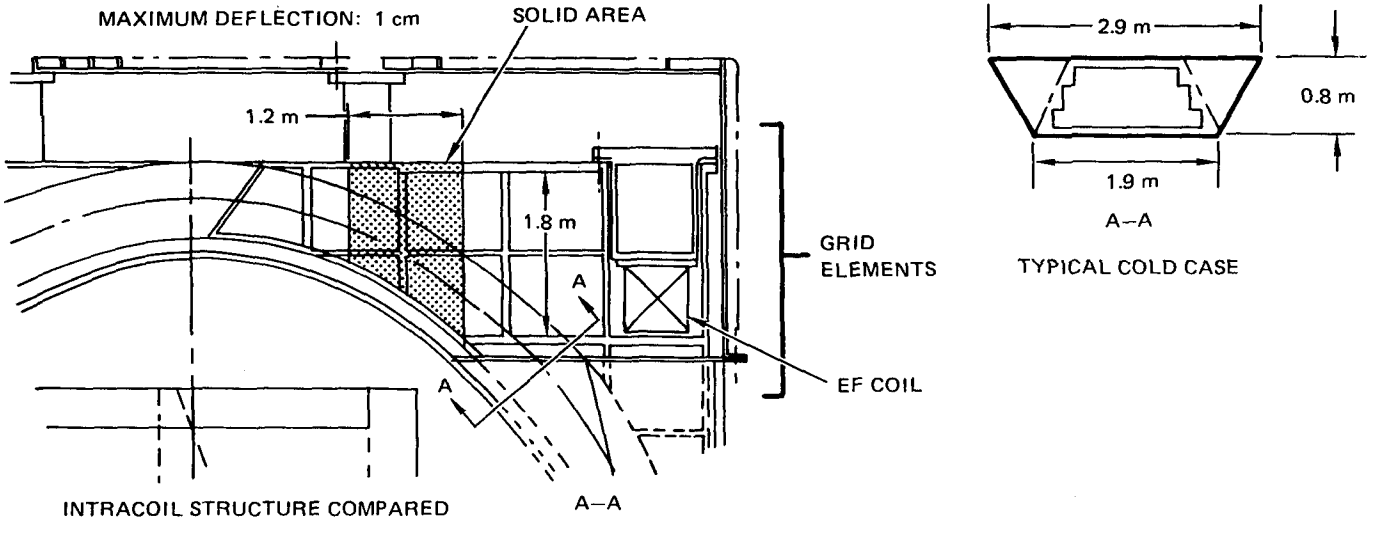

Fig. 5-11. TF coil anti-torque structures design criteria.

The preliminary sizing work is felt to establish feasibility of this concept based on the substantial background provided by the FED and INTOR work.

5.3.1.5 Vacuum Tank

The TF, EF and OH coils are enclosed in a common vacuum tank which consists of a top panel, a lower enclosure and eight segments that are attached to the 4°K TF coil case. An isometric was shown in Figure 5-4. Local support struts are provided to isolate the room temperature vacuum tank from the 4°K coil case. The common vacuum tank approach was selected to minimize the heat leak. Enclosing individual coils in separate vacuum tanks at the center post results in a large heat leak along the sidewalls. The use of 4°K intracoil support structure to react overturning loads requires a common vacuum tank at the top and bottom of the reactor. This vacuum tank can enclose the EF/OH coils without additional complexity.

Each segment of the TF coil vacuum tank segment incorporates a welder/cutter track that doubles as a structural support. This is discussed in Section 5.5. The TF coil dewar dome is designed as a flat panel grid structure to save in overall building height. Each 1 meter in height is equivalent to ~$3M in savings on the building cost. The atmospheric loads are supported with local G-10 fiberglass support rods. The total atmospheric load on the dome is ~300,000 kg of force which can be reacted through ~750 cm^2 of G-10 fiberglass with a total heat leak of ~3 watts through ~1 m long struts. This loss of 4°K cooling can be readily offset for less than the savings in building costs.

5.3.2 Poloidal Coil Systems

The poloidal coil systems consist of the Equilibrium Field (EF) coils, the Ohmic Heating (OH) coils and Control Field (CF) coils. The EF coils provide the field which maintains the plasma at equilibrium with the desired shape, position and current profile. The OH coils are used to provide an inductive voltage over several seconds to initiate a certain portion of the plasma current that is sustained with a current drive system. These coils are all superconducting and are located outside to TF coil to avoid the need for

in-situ winding. The CF coils are located inside the TF coils. They are normal conducting coils that include segments to permit removal and replacement. These coils are closer to the plasma so they can respond to plasma motion more quickly and without the excessive power demands that would be required of the EF coil system. The CF coil design has been taken from STARFIRE (5).

EF Coils - The analyses utilized the least squares method for fitting to the external field that is required for MHD equilibrium and for minimizing the EF coil stored energy. The EF coils were designed to be located ~1 m away from the TF coils and outside of the shaded areas in Figure 5-12 which represent the access requirement of blanket sector installation, the vacuum duct and the center-post. The ~1 m gap between TF and EF coils has been shown (11) to reduce the overturning moments significantly. Independent of the locations of the other coils, the outboard coil leads to lower stored energy if it is closer to the midplane than access permits. The difference between the points labeled s and u corresponds to ~1 GJ. The use of the large inboard coil helps offset the energy requirements of locating the outboard coils above and below the access envelope. If necessary a design could be obtained, however, with no inboard EF coils. The coils in the upper corner are not sensitive as to their placement, but only to the rough net current near this location. Replacing them by a single coil costs ~.2 GJ, however.

OH Coils

The analyses utilized the least squares method to create a zero field inside the plasma to provide 17 volt-seconds and to minimize the stored energy. The 17 volt-seconds is provided to help bring the plasma current to ~1 MA. The inboard coils were made the same thickness as the inboard EF coil. More volt-seconds would require a more vertically elongated coil. The position of the upper coil is somewhat flexible. It was placed beside the upper EF coil for convenience. (It could not be as low as the next lower EF coil.)

The OH system would be charged and run to zero field, then turned off. For this reason the EF and OH systems were not decoupled. They could be

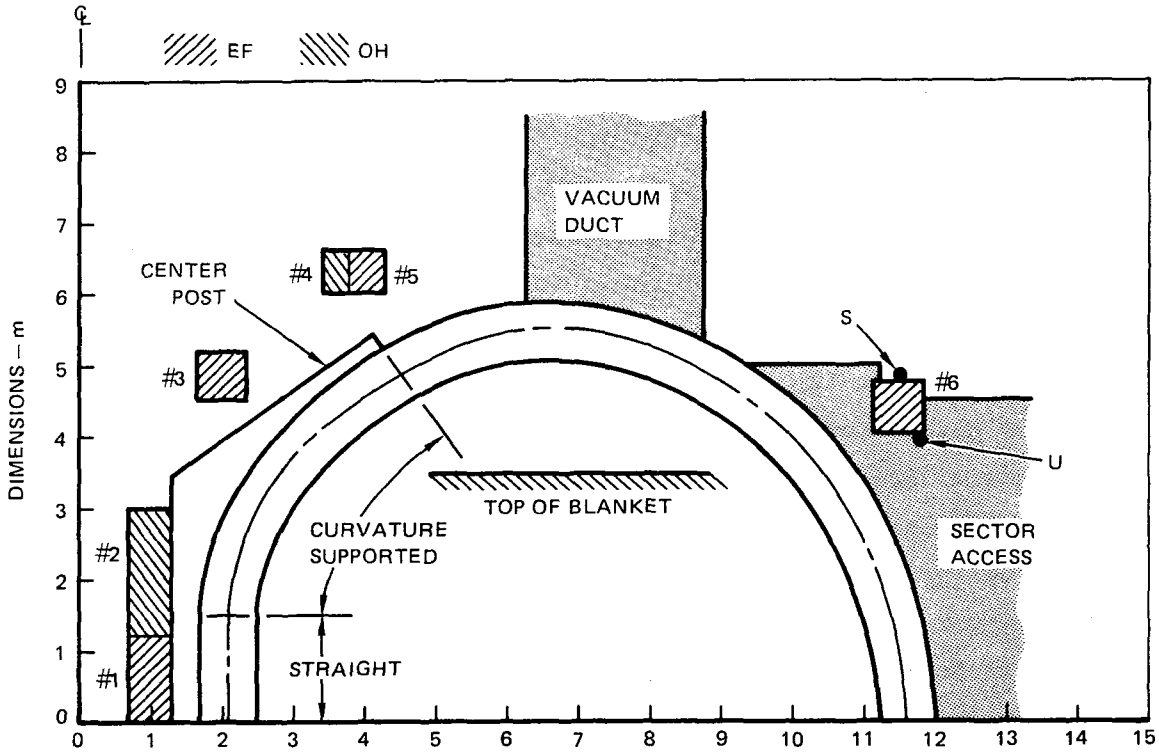

Fig. 5-12. EF/OH coil locations and constraints.

designed to be decoupled while the OH coil is on. Recent indications from TFTR are, however, that the voltage problems can be handled via a control system.

The coil locations and sizes are shown in Table 5-3. These locations are shown in Figure 5-12. A summary of the system parameters is given in Table 5-4. Plots of the resulting field are shown in Figure 5-13. These fields were used for determining the overturning forces on the TF coil.

5.3.3 Out-of-Plane Forces and Overturning Moments

The support of a TF coil system against out-of-plane forces from the poloidal field (PF) coils is one of the most serious problems encountered in a tokamak reactor design. It has caused great problems in the INTOR and FED design studies, particularly because of fatigue problems in those two reactors, which are designed for a lifetime of order one million pulses. Similar considerations arise in the DEMO design although steady state operation minimizes the concern. The overturning moment on each DEMO TF coil, from the PF coils, is calculated to be 805 MN-m. Table 5-5 compares the overturning moments of several recent reactor designs. Note that the DEMO numbers are small only in comparison with the other studies.

Table 5-5. Comparison of Overturning Moments

Reactor Design	Moment per Coil (MN-m)	Moment per Coil Normalized to 8 coils (MN-m)
DEMO	805	805
FED	620	775
STARFIRE	1500	2250
WILDCAT (DD)	3900	5850

Figure 5-14 shows the distribution of bending moment along the TF coil circumference. It can be seen that most of the moment is contributed by the upper (and lower) portion of the coil, and that the smaller moments acting on the inner and outer legs cancel only a small fraction (18%) of the moment.

Table 5-3. DEMO EF and OH Coil Locations

As Circular Coils	No.	R (m)	Z (m)	a (m)	I (mA)
	1A	1.00	0.30	.339	-6.34
	1B	1.00	0.90	.339	-6.34
	2	2.00	4.82	.401	8.91
	3	4.00	6.32	.296	4.34
	4	11.50	4.40	.382	-8.06
	5A	1.00	1.50	.339	-6.34
	5B	1.00	2.10	.339	-6.34
	5C	1.00	2.70	.339	-6.34
	6	3.56	6.32		-3.26

As Square Coils	No.	R (m)	Z (m)	ΔR (m)	ΔZ (m)	I (mA)
	1	1.00	0.60	0.60	1.20	-12.67
	2	2.00	4.82	0.71	0.71	8.91
	3	4.00	6.32	0.52	0.52	4.34
	4	11.50	4.40	0.68	0.68	-8.06
	5	1.00	2.10	0.60	1.80	-19.00
	6	3.56	6.32	0.36	0.52	-3.26

Table 5-4. System Parameters

System	Stored Energy (GJ)	Current (MAT)	Volume* (M^3)	Volt-Sec to Plasma (V-S)
EF	4.78	68.9	102.0	-42.3
OH	0.57	44.5	21.9	-17.0
Plasma	0.43	9.0		

*Current Density $\sim$ 17.6 MA/m^2

Inductive Volt-Sec to Initiate Current: -95.6

EF-OH Energy ($1/2\ M_{OH,EF}\ I_{OH}\ I_{EF}$): -0.047 GJ

EF-Plasma Energy ($1/2\ M_{EF,P}\ I_{EF}\ I_P$): -0.19 GJ

OH-Plasma Energy ($1/2\ M_{OH,P}\ I_{OH}\ I_P$): -0.76 GJ

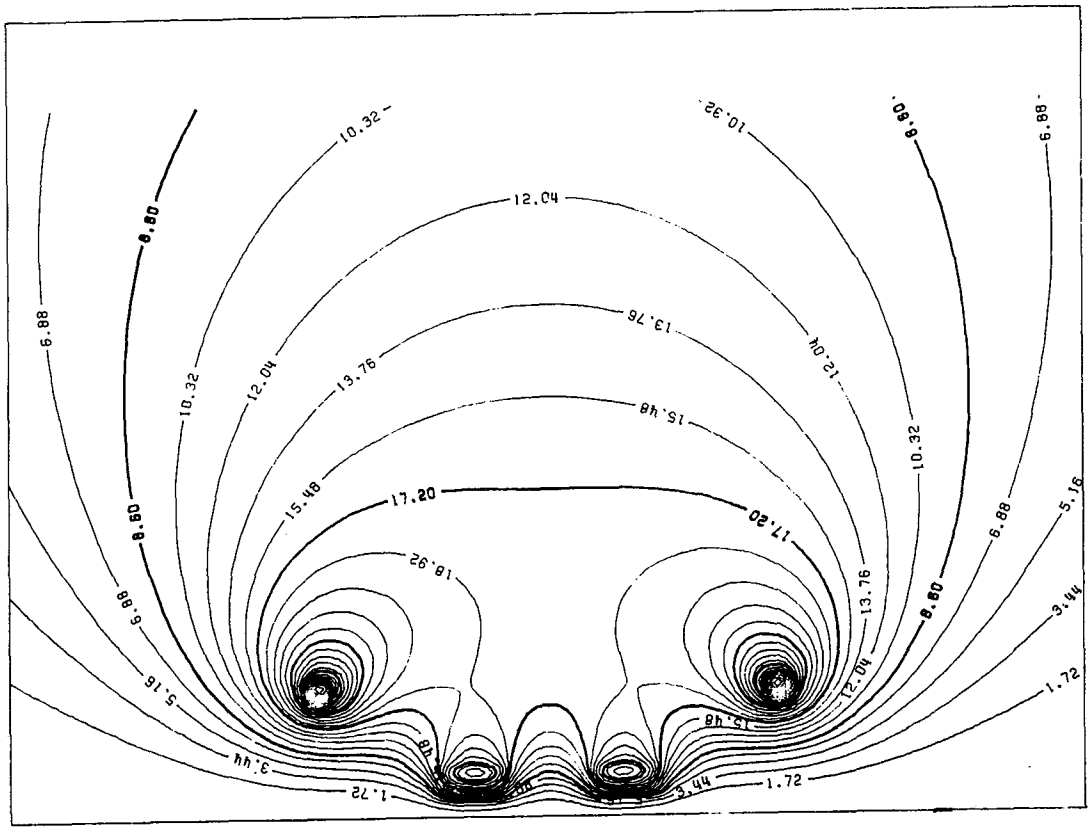

13b. OH field.

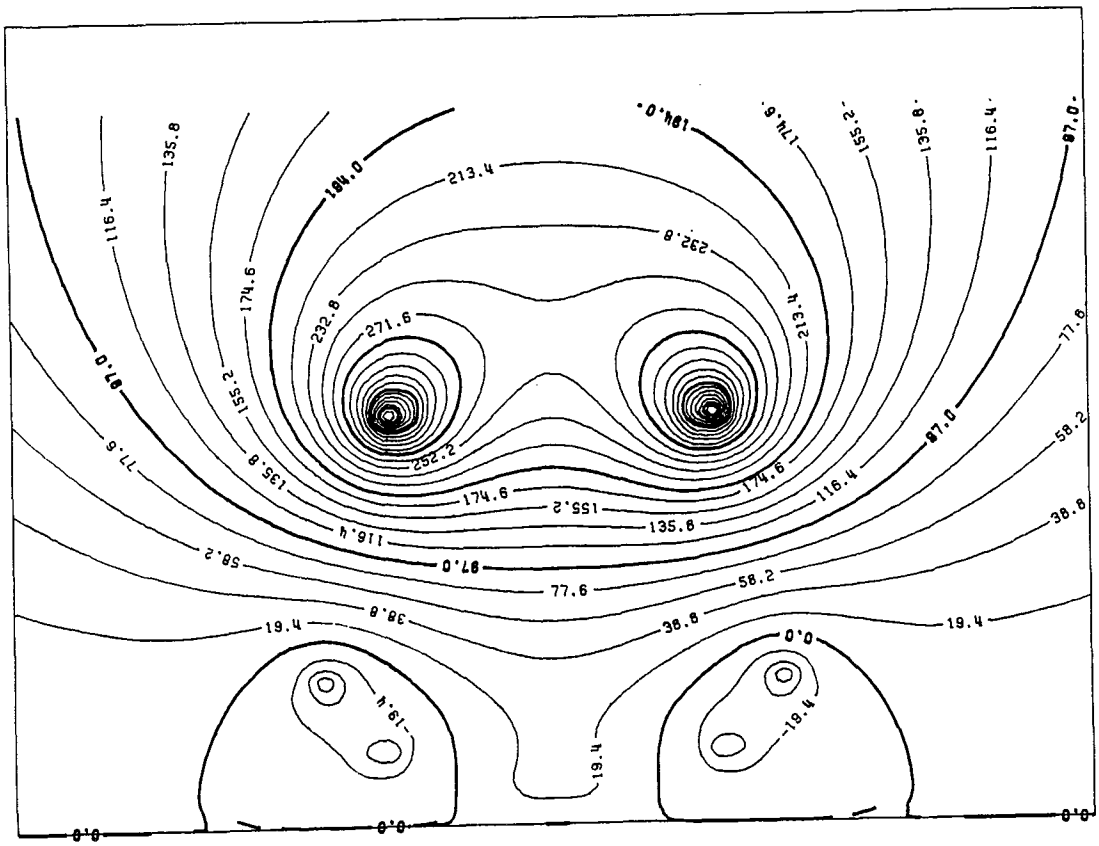

13a. EF field.

Fig. 5-13. Magnetic field plots.

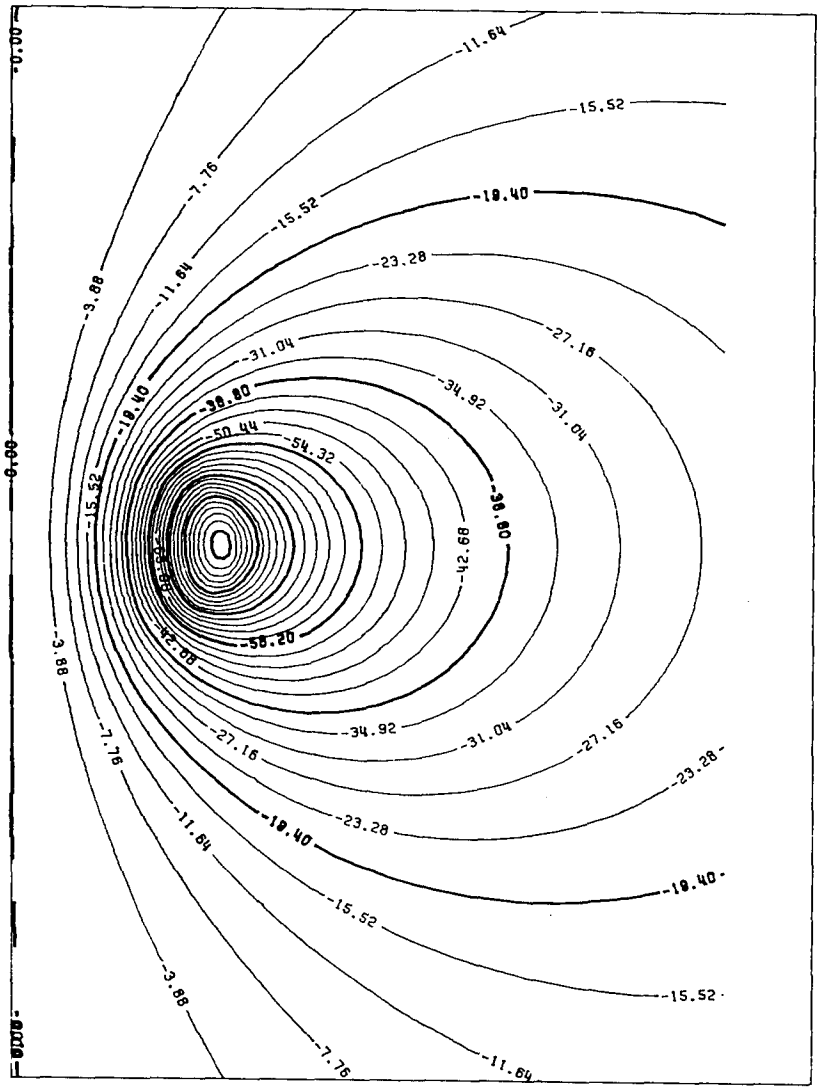

13c. Plasma field.

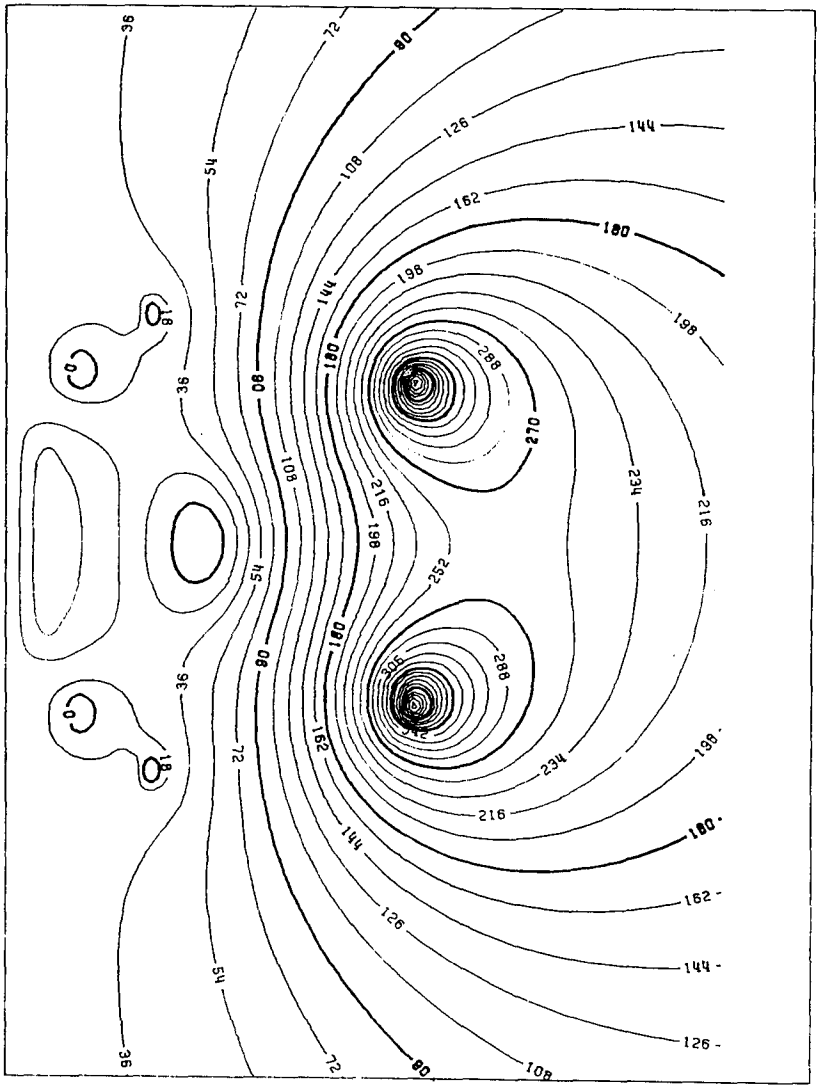

13d. Total field (excluding OH).

Fig. 5-13. Magnetic field plots (continued).

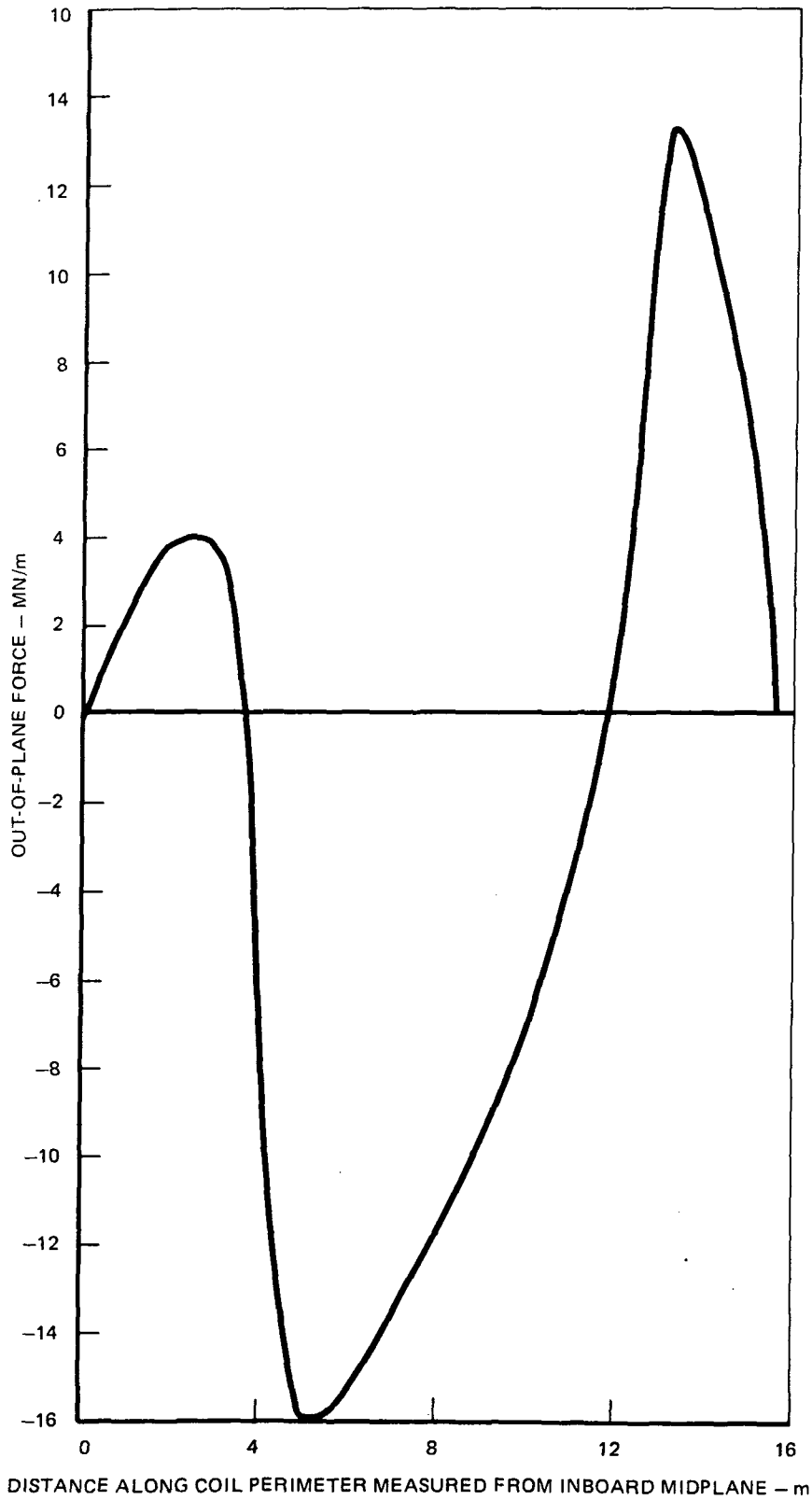

Fig. 5-14. Out-of-plane force distribution on TF coil.

5.3.4 First Wall/Blanket/Shield Configuration

The first wall/blanket/shield (FW/B/S) design has been selected based on the perceived needs of a commercial reactor. It is believed that a configuration that gives every possible advantage to remote maintenance is required if DEMO is to achieve a 50 percent availability. Furthermore, it is believed that if a commercial reactor is to achieve a ~70 percent availability all forthcoming reactors must utilize reactor revelant configurations so the normal evolution of desirable maintenance features, maintenance equipment and component reliabilities can occur. This evolutionary process will lead to improved access, new machines, addition of redundancy and addition of design margins to specific areas of the reactor and plant design. Detailed design of the blanket interior is discussed in Chapter 4.

The design philosophy that has been adopted for the first wall/blanket/shield is as listed below:

- o Remove and replace coolant joints outside the vacuum boundary
- o Flat seals (planar)
- o Mechanical seals for scheduled replacement items
- o Weld seals for life-of-plant components.

It is generally accepted that sector removal of the FW/B/S is superior to in-situ repair (6). The logic is that removal and replacement of large sectors can be done more rapidly and with simplier maintenance equipment than with in-situ maintenance. With in-situ maintenance, many more maintenance operations must be performed before the plant can be restarted. With sector-removal, repair can be made in the hot cell while the plant is operating. Secondly, the hot cell repair will provide greater access and more elaborate maintenance equipment. The limiter and current drive antenna can be removed without removing the blanket sector.

The blanket and shield are made in sectors; however, most of the shield remains in place during blanket removal to minimize the weight of the removed sector and to minimize the shield gap size that would be required for rapid replacement. The shield door is attached to the blanket sector (Figure 5-3) and is removed as an integral part. Blanket modules are replaced in the

shield door structure in the hot cell. The shield sector (Figure 5-4) incorporates frames at either side of the blanket access opening to provide a continuous seal flange surface.

Vertical structural support of the blanket and shield is provided by the vacuum duct shielding. Lateral support for seismic events is provided by the bridge panel from the floor to the shield.

All coolant line disconnects have been located outside the plasma vacuum boundary to avoid the need for leak-free pressurized coolant ducts. Welded leak-free joints inside the vacuum chamber have the disadvantages of (1) contamination during weld preparation and welding and of requiring rewelding of irradiated material to virgin material during replacement; (2) welded joints require more time for replacement than mechanized joints. Leak-free mechanical joints for a pressurized coolant inside a vacuum are even more difficult to achieve than atmosphere to vacuum. The only vacuum tight disconnects that are normally opened for maintenance are atmosphere-to-vacuum at the vacuum pumps and valves, current drive antenna, limiter, sector door and fueling mechanism.

Mechanical seals have been selected for all scheduled replacement items. An ethylene-propylene elastomer seal has been chosen for all mechanical seals based on STARFIRE (5). Table 5-6 shows a comparison of the options including welded seals. All mechanical seals have been kept in a single plane to minimize the difficulties of providing a uniform clampup force on the seal and minimizing tolerance requirements between mating parts.

An advantage of the elastomer seal is the ease of obtaining an initial seal; however, it has two limitations; bakeout temperature, and radiation damage resistance. Bakeout temperature requirements of ~150°C are considered the most serious limitation in DEMO. Because of its developmental nature, DEMO is expected to have many outages and require frequent breech of the vacuum. As a result, a system which can be baked to modest temperatures is desirable to minimize start-up time. Currently, it is planned to provide bakeout to the system while actively cooling the elastomer seal flange.

Table 5-6. Sealing Methods

	Repeatibility	Rad. Damage Limit	Ease of Sealing	Bakeout	Durability
Elastomer	Many times	Least ($\sim 10^8$ rad.)	Most repeatable	$\sim$ 150°C	Least
Metal	1-2 times	$> 10^{10}$ rad.	Requires careful surface finish and clampup	> 300°C	Least
Welded	5-10 times	Greatest ($> 10^{10}$ rad.)	Requires closely controlled weld prep.	$\sim$ 400°C	Greatest

Potentially glow discharge cleaning offers an alternative to heating and should be considered further. Elastomers are susceptible to radiation damage but STARFIRE neutronics calculations (7) have shown that doses can be maintained at acceptable levels when seals are located outside of the shield. The low partial pressures of tritium are not expected to seriously degrade the seals (8). Seals in DEMO are located at the shield exterior and also have acceptable radiation levels. High frequency 35 GHz microwaves have also been shown to cause excessive heating in elastomer seals in EBT-S (9). The REB launchers or the 82 MHZ fast wave current antennas do not pose this problem.

Metal seals are acceptable from all standpoints except they are generally very susceptible to physical damage (e.g. scratches), and require extreme care to effect a seal repeatability.

Welded seals have been selected for all life-of-plant components. These components are those where replacement capability is provided but where replacement is not planned unless they fail. Welded seals offer the advantage of radiation resistance and reliability once they have been made and verified. In event replacement is required, more time can be allocated for remaking these seals. All shield sector seal welds have been made in a single plane. Triple point seal welds have been avoided in replacement of shield sectors. These occur when a weld must cross or butt to another weld. These welds create close fit up requirements, permit little motion, and require welding around square corners.

Selection of Number of Sectors

Three primary options considered in selecting the number of sectors and method of removing the large sectors are shown schematically in Figure 5-15. Option A requires use of one sector per TF coil and has been used in FED and INTOR and has been selected for use in DEMO. Option B was used in the STARFIRE design. With option C composite sectors consisting of the blanket sector and outboard shielding are used. This design requires one sector be located under the TF coil and one sector between TF coils which increases the difficulty of sealing between sectors.

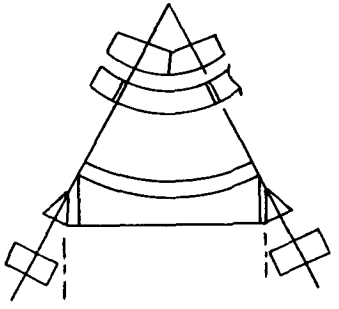

A. ONE/TF

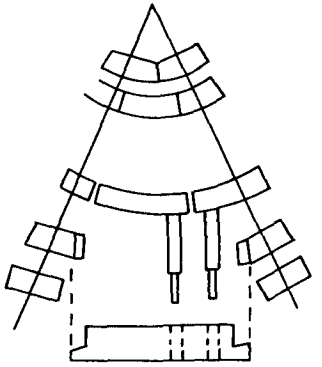

B. TWO/TF

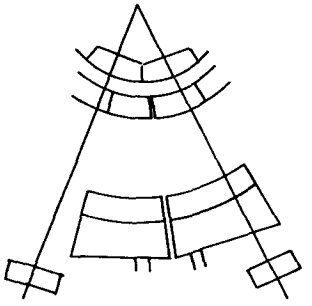

C. TWO/TF*

	A. ONE/TF	B. TWO/TF	C. TWO/TF*
NUMBER OF LARGE REMOVABLE PARTS	1	3	2
NUMBER OF CONNECTIONS/TF COIL	14	~ 30	~ 28
LIMITER	6 (BKT MODULE)	4	12
SHIELD	2	2	4
BLANKET (COOLANT & TRITIUM PURGE)	4	8	8
VACUUM BOUNDARY SEALS	2	16 (INCLUDES 14 CONNEC. PENE.)	4
REMOVAL DIRECTION	RADIAL	RADIAL + TRANSLATION	RADIAL + TRANSLATION
TF COIL OUTER LEG RADIUS	~11.6 m	~9.5 m	~ 9.5 m
LIMITER REPLACEMENT	INDEPENDENT	AFTER SECTOR REMOVAL	SEQUENCED LIMITER REMOVAL
STORED ENERGY	5 GJ MODIFIED PURE TENSION TF	2-3 GJ	2-3 GJ
			*REQUIRES TRIPLE POINT SEALS WHICH MAY BE UNRELIABLE AND TAKE A DISPROPORTIONATE AMOUNT OF TIME TO REPLACE

Fig. 5-15. One blanket sector per TF coil is preferred.

Our comparison will develop the rationale for selecting Option A over the other two concepts. The three key assumptions in the rationale are as follows. First it is believed that sector weight and size (within a factor of two) will have little impact on the time required for component removal/replacement. Second it is believed that the number of connections made to reactor components will directly affect the time required for replacement. Third, the failure rates of the first wall and limiters are expected to be the same regardless of the number of components but the failure rate of connections and maintenance equipment is not.

The STARFIRE concept (Column B) was derived because of the perceived impact of stored energy on the overall system. STARFIRE utilized a "pure-tension" magnet per the Moses and Young criteria (12) and resulted in very tall magnets for an outer leg radius large enough to replace a single sector/TF coil. DEMO has decreased the TF coil height by modifying the TF coil shape (see paragraph 5.3.1.3) and minimized the amount of stored energy.

The third option shown in Column C is deemed feasible only if a triple point seal can be used. A radial view looking in at adjacent sectors is shown in Figure 5-16. Two things are evident. The limiter cannot be removed from the sector under the TF coil without removing the other limiter and numerous triple point seals are required. Triple point seals require very close fit up during installation and can likely be accomplished only by welding. The problems of developing a triple point seal weld are expected to be difficult. As a result, this option was not pursued.

A comparison of the changeout times and failure rates for the three options are given in Table 5-7. The number of steps required in sector change out is a minimum for the one sector per TF coil, and it requires ~ 1/2 as long for replacement as the other two options. A comparison of the relative failure rates is made by assigning failure rates of Y and Z to components used in concept A. The total failure rate of concept A is taken as X. If the failure rate is dominated by the wall or components such as the limiter, then the overall failure rate of the alternative approaches will be equal. If, however, the failures are dominated by connections or replacement equipment then

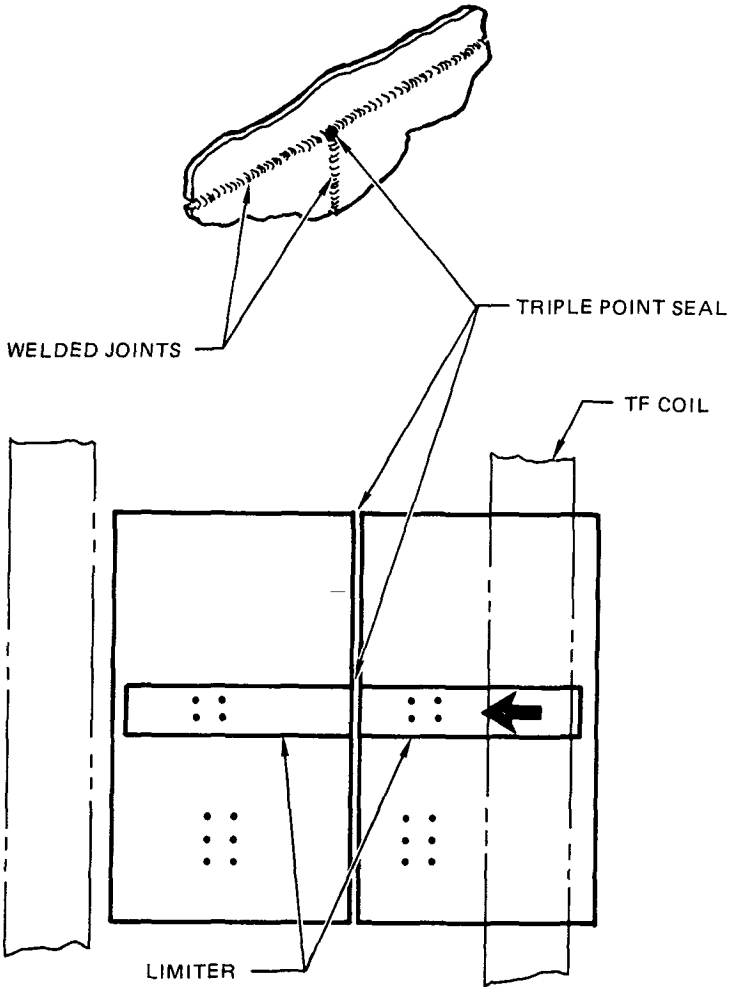

Fig. 5-16. Two sector per TF coil option with triple point seals.

Table 5-7. Blanket Removal Changeout Steps

A. One Sector/TF		B. Two Sectors/TF		C. Two Sectors/TF	
0. Shutdown	24 hrs	Shutdown	24 hrs	Shutdown	24 hrs
1. Disconnect 28 Connections	28 hrs	Disconnect 60 Connections	60 hrs	Disconnect 56 Connections	56 hrs
2. Unlatch Door Air to Vac Seal	2 hrs	Disconnect 16 Air to Vac Connections	16 hrs	Cut Door Seal Weld	4 hrs
3. Remove Sector	4 hrs	Remove Shield Door	4 hrs	Remove Sector A	4 hrs
4. Reverse of Above (+50% Time)	48 hrs	Remove Blanket Sector #1	4 hrs	Remove Sector B	6 hrs
5. Startup	24 hrs	Remove Blanket Sector #2	4 hrs	Reverse of Above (+50% Time)	98 hrs
		Reverse of Above (+50% Time)	123 hrs	Startup	24 hrs
		Startup	24 hrs		
Total Time to Replace	∿ 5 days		∿ 10 days		∿ 9 days
Failure Rate					
Wall	Same		Same		Same
Components	Same		Same		Same
Seal Components	Y		2Y		2Y
Removal Process Equip.	Z		3Z		3Z
Total Failure Rate	X		X to ∿ 2X		X to ∿ 2X

concept B and C can have a failure rate two times as large as concept A. The true failure rate is likely to be somewhere in between.

Based on the above, it is clear that one sector per TF coil offers clear advantages over two sectors per TF coil. The penalties in stored energy of the larger TF coil leg radius do not appear to overwhelm the choice so it is recommended that the DEMO utilize one sector per TF coil. Addition of a divertor would require an increase in the stored energy and needs further assessment.

Dielectric Break Design

The dielectric break in the shield is formed at the outer surface of the shield where the radiation dose level is anticipated to be $<10^9$ RADS based on the STARFIRE (7) analysis. It is expected that the dielectric break will be fabricated as a permanent part of the shield sector, last the life-of-the-plant and be subjected to bakeout heat loads only. The dielectric break design is shown in Figure 5-17. It consists of dual metal spring seals that are coated with polyimide (*). The concentric seals provide the dielectric break and vacuum wall. The seal is bakeable to ~ 300°C and seals more readily than a bare metal seal. It also permits the polyimide to flow somewhat without loss of sealing. The design also incorporates intermediate vacuum pumping so it is tolerant of some leakage.

Vacuum Boundary Location

Primary options considered for the plasma chamber vacuum boundary were locations at the shield and at the interior surface of the TF coil vacuum tank. Both concepts are shown in Figure 5-18. Key considerations in the comparison are given in Table 5-8.

An advantage of combining the TF coil common vacuum tank with the plasma chamber vacuum boundary is that it can potentially simplify the reactor design by eliminating the need for seals and dielectric breaks between shield sectors

(*) MDAC proprietary.

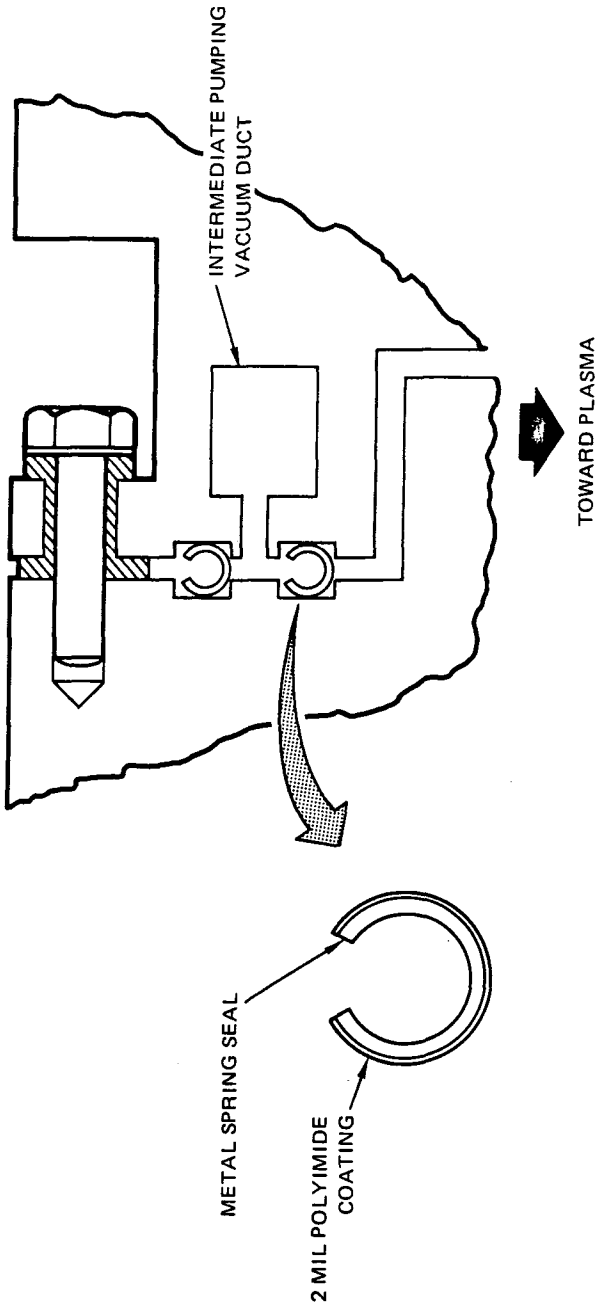

Fig. 5-17. Dielectric break design.

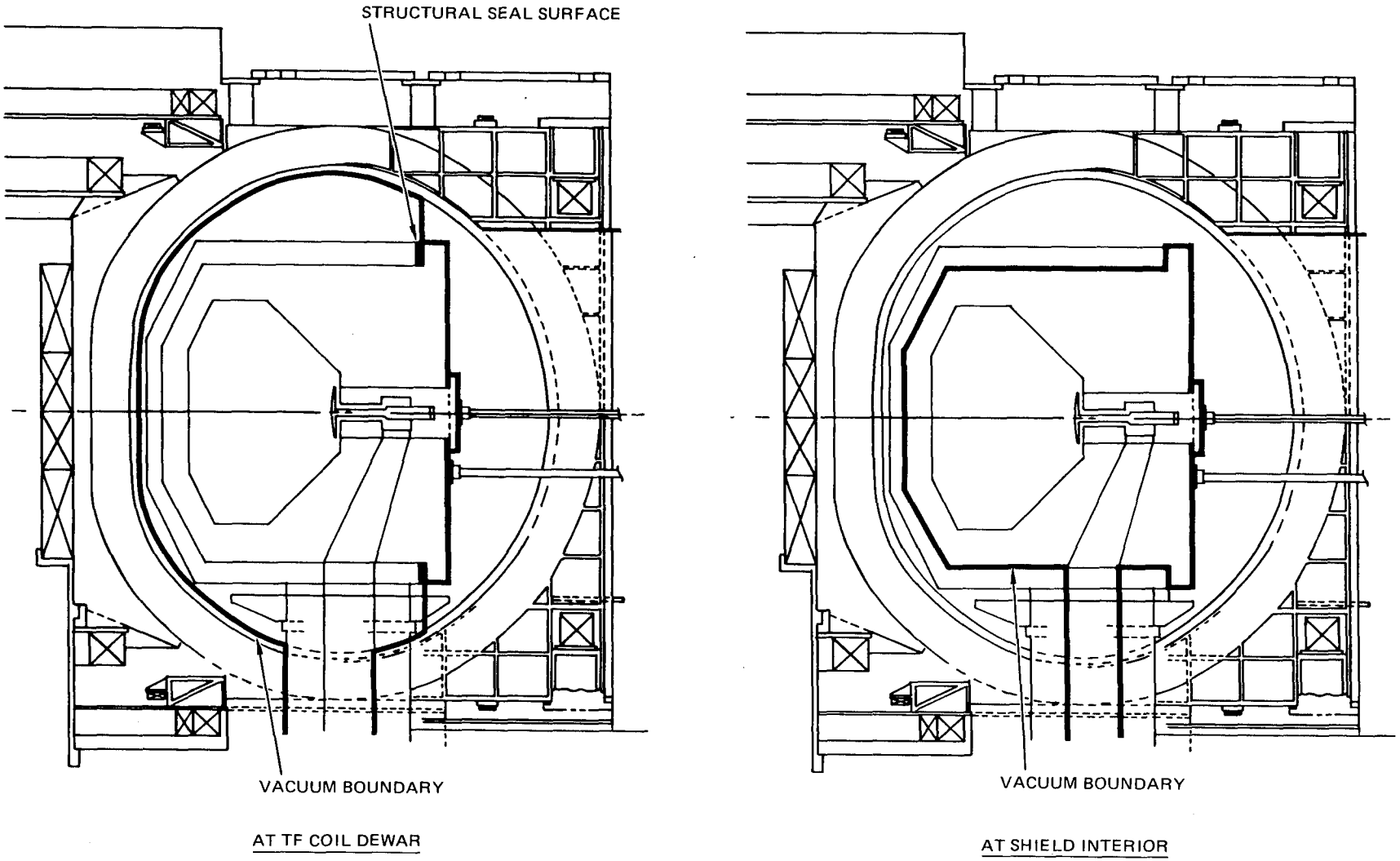

Fig. 5-18. Vacuum boundary location options.

Table 5-8. Vacuum Boundary Location Options

	At TF Coil	At Shield Interior
Pumped Volume	$\sim$ 1100 m^3	$\sim$ 300 m^3
Exposed Surface Area	$\sim$ 4400 m^2	$\sim$ 1500 m^2
Bakeout	< 150°C Glow Discharge Only	$\sim$ 300°C Heating by Coolant
Leakage-In Door	Forced Outage	Forced Outage
Leakage-In Other Areas	Continued Operation	Forced Outage
Segment Joints	Intersector Contactor Vacuum Gap	Intersector Contactor Dielectric Break or Resistance Control
Trim Coil Operation	Potential for Arcing	Operation in Air
TF Coil Replacement	Severely Complicates Removal	No Impact

and can permit limited operation with a leak between the TF coil and plasma chamber volumes. The wall between the TF coil and plasma chamber volumes is required to avoid the need for TF coil warm up when the plasma volume is opened.

Disadvantages of the common TF coil vacuum tank and plasma chamber wall are a severe complication in the TF coil replacement process, increased volume and surface areas, and complications in the bakeout process. An added complication is the potential for arcing of the control coils that would be located in the vacuum.

Removal of a TF coil will require cutting the vacuum tank. A method for accomplishing this is discussed in paragraph 5.5. Addition of a seal flange to the area between TF coils would require that a several centimeter thick structural sealing surface member be cut and rewelded remotely in replacing a TF coil. Although this may be feasible, no concepts for readily accomplishing it are apparent.

A common TF coil and plasma chamber wall would also complicate the bakeout process by limiting the amount of heat that could be put into the structure without creating excessive thermal stresses in the transition to unheated areas of the top and bottom of the reactor. If the problems of TF coil replacement and chamber bakeout can be overcome, this option is attractive since it also eliminates the need for a vacuum tight dielectric break in the shield.

DEMO has chosen to leave the vacuum boundary at the shield; however, further consideration is planned.

Intrasector Connector

The use of individually replaceable blanket sectors may require a conducting shell near the first wall. This shell provides stabilization to the plasma by permitting image currents to be created by any plasma motion and reduces the demands on the control (CF) coil system. The intrasector connector must be located near the plasma to reduce the electromagnetic forces that

are generated on the blanket walls as the currents flow radially to the connectors and to prevent arcing. Additionally these connectors must be capable of carrying the full plasma current during a disruption until it decays in the blanket. An additional desireable feature of this system is that it be switchable so that it can be left open during reactor OH coil heating.

Investigation for FED (13) disclosed several connector options. Of these three are selected for consideration here. The concepts are shown in Figure 5-19. Each must permit ~1cm of change in the gaps between blanket sectors due to thermal growth.

Any of the three options are acceptable to DEMO. Uncertainities in the design include the current-carrying capacity of the contacts in vacuum and the contact pressures required to avoid contact welding. Options such as sacrificial carbon arc pads were not considered in DEMO because of the volumes of material that would be vaporized and the uncertainty of where the arc would strike.

5.4 Vacuum Pumping System

The vacuum pumping system consists of eight cryosorption pumps located in the reactor building basement. Six of these pumps operate continuously while the other two are regenerated. Each pump can be isolated from the plasma chamber by use of a gate valve. Redundant gate valves are provided so operation can continue after a single valve failure.

Liquid pool cryopumps are seen as the best choice for the DEMO reactor. Two advantages of such pumps are their very high pumping speeds and their cleanliness. Capture probabilities for helium as high as 0.2 have already been achieved, and there remains potential for improvement. Possible pathways by which hydrocarbons or other contaminants could reach the plasma are eliminated, since such cryopumps have no working fluids or moveable parts. They are reliable and low cost. The thermal shielding they require does not present a major obstacle and they are compatible with the magnetic fusion environment. Although they require regeneration, this process can be combined with fuel gas recovery operations.

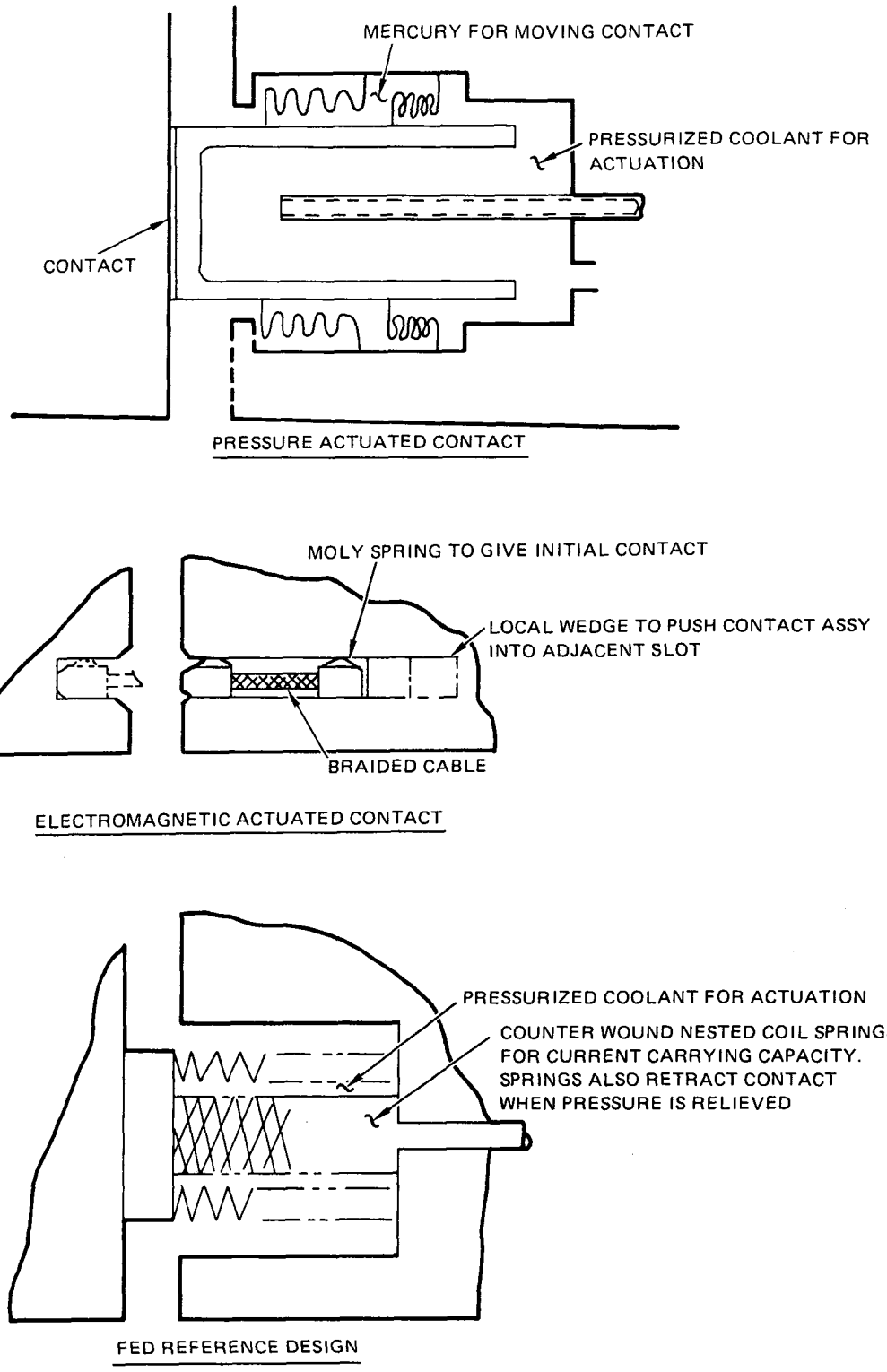

Fig. 5-19. Intersector connector.

The required pumping speed of the system is 3.2×10^{20} atoms/sec of helium and 4×10^{21} molecules/sec of deuterium and tritium (see Chapter 3). This gas load is compatible with the use of cryosorption pumps.

The gases are pumped through a limiter slot, through the blanket, into a plenum and then into circular ducts to the pump as shown in Figure 20. The total conductance of the limiter slots is 8.2×10^5 ℓ/sec. The slot extends from the leading edge of the limiter to the limiter stem where incoming particles impact the surface. The rest of the vacuum pumping system from the limiter stem through the vacuum pump has a conductance of 1.4×10^5 ℓ/sec if eight pumps are operating and a conductance of 1.1×10^5 ℓ/sec if six pumps are in operation. As a result the ratio of system conductance to slot conductance (γ) is:

8 pumps operating: $\gamma = 5.8$

6 pumps operating: $\gamma = 7.5$

5.4.1 Vacuum Pump Location

The vacuum pumps were located in the reactor building basement where they could be maintained independent of the basic reactor. For conductance improvement it was desired to locate the pumps as close to the plasma as possible. Mechanical constraints imposed by the TF coils limit the pumps to ~ 3.5m below the blanket as shown in Figure 5-20.

The nuclear heating rates in the cryosorption pump was determined utilizing the work of Fisher and Watson (14). They show a critical surface heat load of 2.3×10^{-2} watts on a 320 cm^2 cryo panel. For an equivalent panel of 0.3 cm thickness this corresponds to 2.2×10^{-4} w/cm^3. A margin of safety of 2 should be included on this design and therefore a heating rate of ~ 4×10^{-4} w/cm^3 is deemed acceptable.

Scaling of the STARFIRE nuclear heating rates (7) indicates that this heating rate will occur when the pump is approximately 5.5m from the inside of this shield without bends in the duct. A single bend was put in the duct to prevent the pump from requiring a deeper reactor building basement. The bend

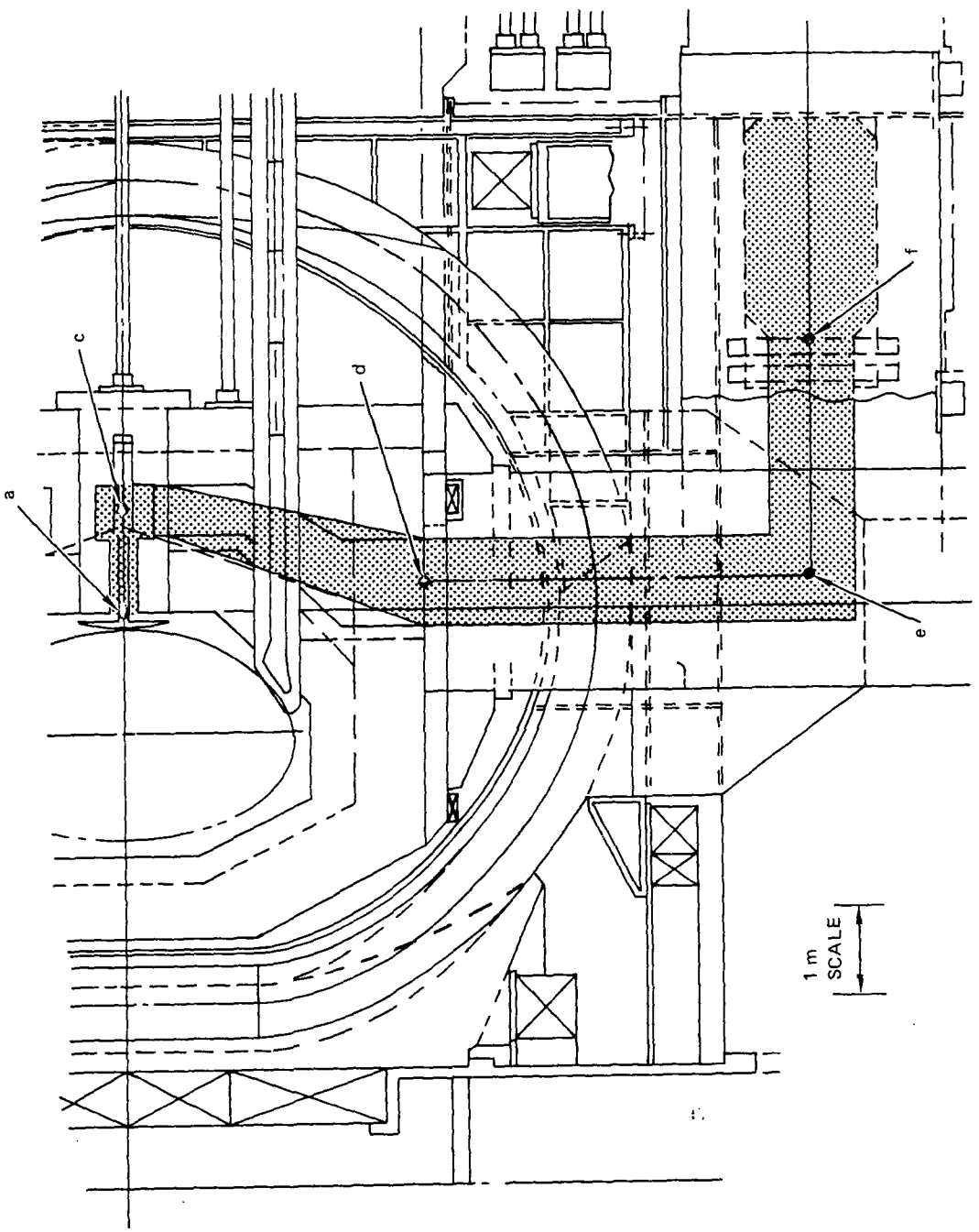

Fig. 5-20. Vacuum pumping system.

also reduces the nuclear heating by approximately a factor of ten (7). The anticipated heating rate in the pump is expected to be $< 10^{-5}$ w/cm^3.

Pump locations at the top and side of the reactor were considered prior to selection of the basement location. Pumps on the side of the reactor provide direct access by maintenance equipment but must be removed for blanket replacement and may interfere with movement of other maintenance equipment. Pumps at the top of the reactor provide a maximum access for maintenance but interfere with simultaneous maintenance of other components.

5.4.2 Conductance Analysis

Slot Conductance - Each limiter slot has the form of a cylindrical annulus. To calculate its conductance, molecular flow was assumed. The slot was treated as equivalent to a tube of the same length but of rectangular cross section. The wide dimension a of this cross section is equal to the first wall circumference while the narrow dimension b is equal to the distance of the limiter from the first wall.

The conductance of such a rectangular tube, under the restriction that a>>b and that a>> the length ℓ, is given by

$$C = 3.638 \sqrt{\frac{T}{M}}\, ab\, \alpha$$

where C is the conductance in liters/sec, a and b are in cm, T is the absolute temperature of the gas at the inlet, and M is its molecular weight. In this expression the factor α is the probability that a given molecule which enters the inlet of the conductance will exit via its outlet, and all the other factors describe the rate at which molecules enter the inlet. It is important to note that this formula is based on the assumption that the molecular velocities at the inlet are randomly directed and have magnitudes in accordance with the temperature T.

Values for the transmission probability α for the tube of rectangular cross section were obtained by linear interpolation from a table in Reference

15, which lists α as a function of the ratio ℓ/b of length to narrowest cross-sectional dimension. Data from this table are shown graphically in Figure 5-21.

The validity of this procedure was checked by comparing its results with those of Monte Carlo calculations of the transmission probability for the conductance of the annular space between two concentric cylinders. These results are reported in Reference 16. The good agreement between the two sets of results is shown in Table 5-9. Each of the Monte Carlo results in this table was obtained by treating 5000 individual molecules; the maximum standard deviation listed for these figures was 2.2% of the probability shown.

The last row of figures in Table 5-9 corresponds to the dimensions pertinent to the DEMO reactor; first wall radius 680 cm; limiter height 8 cm and length of limiter slot 35 cm. The corresponding transmission probability obtained by interpolation from the data of Reference 15 is α = .3843. The corresponding conductance predicted by the proceeding equation is 4.1×10^5 liters/sec. if it is assumed that the gas temperature of the neutral atoms from the back surface of the limiter is 300°K. Since the limiter slots are equivalent to two such conductances, the total slot conductance is 8.2×10^5 liters/sec for helium.

R_o/R	ℓ/R	α, Monte Carlo Results Reference (16)	α from Reference (15)	ℓ/b
.9	.25	.488	.499	2.5
.9	.5	.351	.358	5
.9	.75	.279	.302	7.5
.75	.5	.541	.541	2
.988	.052	-	.384	4.4

Table 5-9: Comparison of transmission probabilities predicted for a cylindrical annulus by Monte Carlo analysis to probabilities predicted for the rectangular tube corresponding to the "unwrapped" annulus by interpolation from data of Figure 5-21. R_o = inner radius, R = outer radius, ℓ = length, b = $R-R_o$.

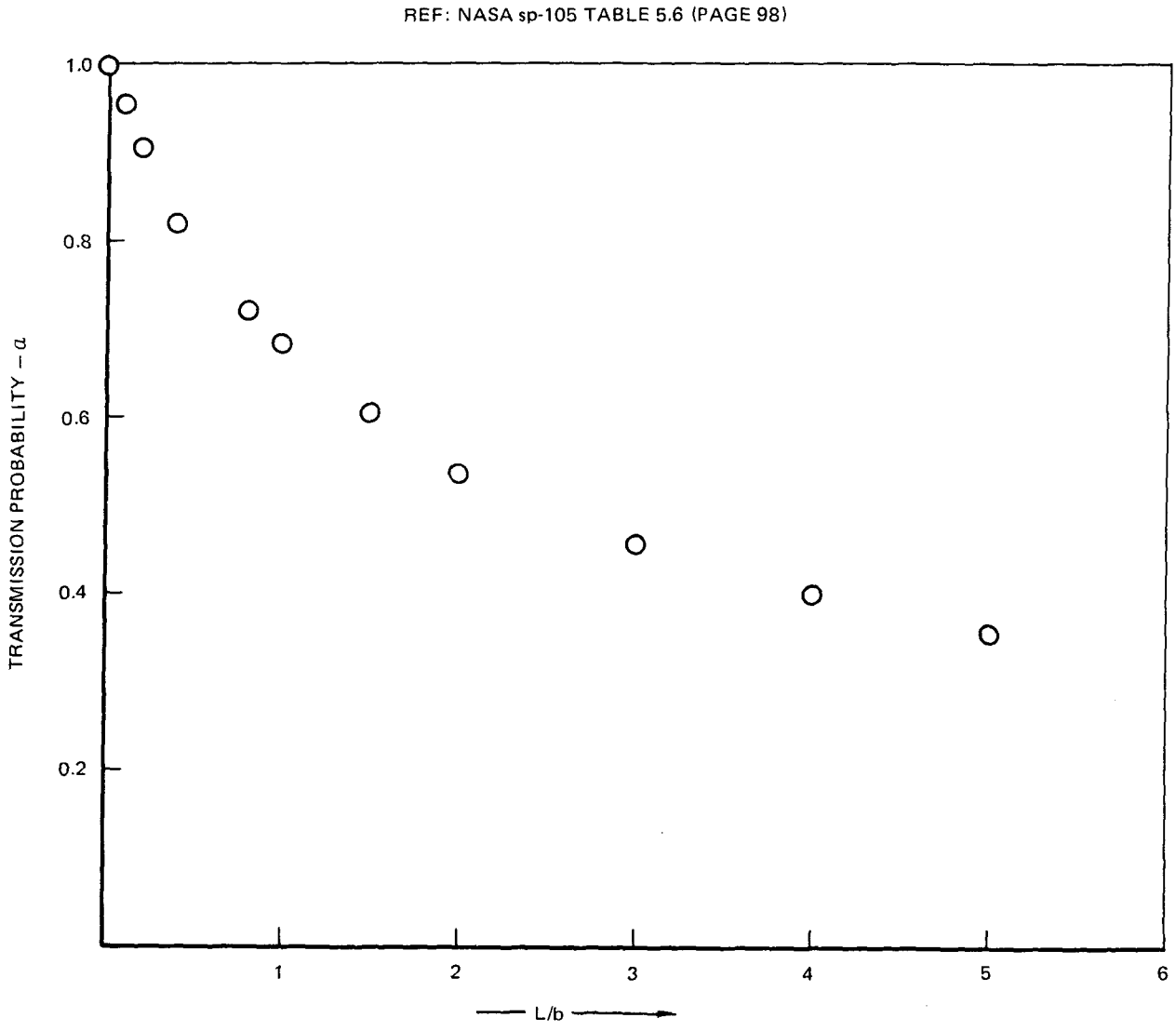

Fig. 5-21. Transmission probability of a rectangular duct.

Vacuum System Conductance

The vacuum system conductance is equal to the effective pumping speed at the back of the limiter slot which is calculated from the previously mentioned equation, $C = 3.638 \sqrt{T/\tilde{M}}\, A\alpha$, where A is the cross sectional area of the limiter duct. The vacuum system transmission probability α is obtained by combining the pump capture probability in an appropriate way with the transmission probabilities of each ductwork element between the pump and the back of the limiter slot.

This procedure will be described with reference to Figure 5-20, which shows a cross-sectional view of the vacuum system. The first conductance encountered is the limiter duct. This conductance is approximated by a short duct of rectangular cross section. The wide cross-section dimension, equal to the circumference of the first wall, was taken as $a = 2\pi \times 6.8 = 42.73$ meters. The narrow cross-section dimension b was 15 centimeters. The length ℓ, from point a to point c in Figure 5-20, equaled 1 meter. Since a was considerably larger than both ℓ and b, the transmission probability can be obtained from the table in Reference 15 as described in the previous section. The transmission probability was found to be .32 for the limiter duct. Combined with the total inlet area of the two ducts, and again under the assumption that the gas at the inlet is room temperature helium, this implies a total limiter duct conductance of 1,300,000 liters/second.

The plenum region, from c to d in Figure 5-20, was also approximated as a tube of rectangular cross section. Again the wide cross section dimension a, corresponding to the inner circumference of the plenum and taken as approximately 49 meters, was considerably larger than either the length $\ell = 3$ meters or the narrow cross section dimension b = 45 to 100 cm. The value for α was taken as 0.39, leading to a conductance of 2.7×10^6 liters/second under the assumptions described above.

From d to e in Figure 5-20 is a duct of round cross-section. Transmission probabilities for round tubes are given as a function of length to diameter ratio by equation 3.109 of Reference 17. Taking the length as 480 cm and the diameter as one meter leads to $\alpha = .2$. The corresponding conductance,

again under the assumption of room temperature helium at the inlet, is 5.0 x 10^4 liters/second for each duct. There are eight such ducts, one leading to each of the eight pumps. In a similar way, the conductance of the horizontal round tube attached to the pump inlet was found to be approximately 7.8 x 10^4 liters/sec.

Each pump itself is characterized by a "capture probability" which is the probability that a molecule entering the pump inlet will be pumped rather than eventually move back out the inlet. The pumping speed of the pump is related to its capture probability by the equation $C = 3.638 \sqrt{T/M}\, A\alpha$. For purposes of combining the effects of the pump with upstream ductwork, the pump is equivalent to a conductance element having the same inlet area, having its downstream end immersed in a perfect vacuum, and having conductance equal to the pumping speed. The pump capture probability was taken as 0.2 for helium, based on experience with cryopumps. Combined with a one meter inlet diameter, this led under the usual assumptions to an equivalent conductance of 4.9 x 10^4 liters/second for each pump.

After conductances are obtained for each element in the system of Figure 5-20, it is necessary to combine them in order to get an effective net conductance or pumping speed for the system. The conductance of each pump was combined with that of the round tube connected to its inlet to produce an equivalent conductance using the approximation:

$$\frac{1}{C_{eq}} = \frac{1}{C_T} + \frac{1}{C_p} - \frac{1}{(3.638\ \sqrt{T/M}\ A)}$$

where C_T is the conductance of the tube and C_p is that of the pump. The final term in this expression is a correction term applicable when the two conductances are on the same axis. T is the absolute temperature of the gas, M is its molecular weight and A is the duct area.

This equivalent conductance was multiplied by eight to account for the number of pumps, and the product conductance was combined with the conductances of the plenum, the round tubes from the plenum, and the limiter ducts through successive applications of the equation:

$$\frac{1}{C_{Total}} = \frac{1}{C_1} + \frac{1}{C_2}$$

For these cases the correction term is not used. The total conductance C_S of the entire vacuum system consisting of limiter ducts through pump was found to be 140,000 liters/second for the system shown in Figure 5-20. A summary of the system conductances is shown in Table 5-10.

Resulting Conductance ratio γ; discussion

The conductance C_S of the limiter slots, 823 m^3/sec, together with the conductance C_R of the vacuum system found to be 140 m^3/sec, establishes the value of the conductance ratio $\gamma = C_S/C_R$. For this case we obtain $\gamma = 5.9$ with 8 pumps operating and 7.6 with only 6 operating.

The significant of γ, as discussed in volume I of the STARFIRE report (5), is that together with the inversion probability, it determines the transmission probability for helium through the limiter slots and vacuum system. For a given value of the inversion probability, as γ decreases the transmission probability increases so that it is desirable to minimize γ.

The inversion probability describes the extent to which the limiter slots are "one-way" conductances. This effect arises because molecules which have been neutralized at the back surface of the limiter and are on trajectories which would taken them back through the limiter slots to the plasma stand a good chance of being ionized by incoming hot electrons. Once ionized, they are accelerated toward the back of the limiter slot. The inversion probability expresses the statistical chance that this process will occur.

The calculation of the inversion probability requires the solution of a neutral transport equation, together with models of the incoming plasma; see for example FED[19]. This has not been done yet for DEMO; however, other designs such as FED have high, predicted inversion probabilities. Because of the inversion process, the removal efficiency of the system is not calculated in the manner usually employed for vacuum conductance problems. For example, if the inversion probability is one, the removal efficiency is independent of the vacuum system design, since all molecules at the inlet of the vacuum

Table 5-10. Conductance Values for the Vacuum System

Item	Conductance (ℓ/sec)	Figure 20 Reference Points
Limiter Duct	1.3×10^6	a to c
Plenum	2.7×10^6	c to d
Vertical Duct	5.0×10^4 (each)	d to e
Horizontal Duct	7.8×10^4 (each)	e to f
Pump	4.9×10^4 (each)	f to pump surfaces
Total	1.4×10^5 ℓ/sec	
Limiter Slot	8.2×10^5 ℓ/sec	Plasma to a

system (the back of the limiter slot) will be removed from the plasma. The transmission probability of the entire system is then independent of the conductance ratio γ, since it is already at its maximum value because of its dependence on the inversion probability. However, a complication with this type of system is that the inversion process will probably only function for a gamma below some maximum value; otherwise there is too much neutral gas in the limiter slots which may overwhelm the ability of the incoming plasma to ionize and return the neutral helium. The maximum value of gamma is design dependent and needs to be determined by detail plasma and vacuum system analyses of the limiter slot region. A ball park value of gamma equal to five has been assumed for the present.

Several approaches could lower the value for γ if necessary. Lowering the slot conductance C_S in the numerator of the expression for γ is probably the easiest possibility. This conductance scales with slot width (w) approximately as $C_S \propto w^2$, i.e. a strong scaling, while particle flow to the slot scales weakly with w (see for example, FED report[19]).

The other way to a lower γ is to increase the conductance of the vacuum system, C_R. This includes shortening the ductwork between the back of the limiter slots and the pump, or increasing the size of the ductwork. More pumping can be applied by the use of improved pumps, or a greater number of pumps of the same type. In general, decreasing γ by increasing its denominator C_R tends to be a simple approach in that one is less likely to encounter complicated tradeoffs with helium removal rate requirements or inversion probability mechanisms. On the other hand, increasing C_R would seem to be a more expensive way to decrease γ than decreasing C_S.

Vacuum Wall Cleaning

It will be necessary to clean all vacuum surfaces in DEMO prior to initiation of plasma operation. Low level impurities residing on vacuum surfaces are desorbed during operation and degrade the plasma. Desorption may be thermally induced or may be the result of ion impingement. The level of desorbed gases can be reduced by careful cleaning of all surfaces during fabrication and installation and by careful operation after start-up. In-situ

cleaning methods must however be employed. Those most commonly used are vacuum bakeout and glow discharge cleaning. Both processes will be used on DEMO.

Two cleaning scenarios are anticipated for DEMO. The first involves the cleaning processes during instruction in preparation for start-up. The second scenario addresses the cleaning associated with up-to-atmosphere maintenance periods.

Cleaning during construction is essential in ultra high vacuum (UHV) facilities. Material selection and chemical cleaning processes will be carefully controlled. Assembly will include commonly used UHV techniques including gloves, clean tools, clean room environment, etc. When construction is complete and vacuum vessel is verified to be leak tight, the vacuum system will be pumped to below 1×10^{-6} torr and in-situ cleaning will be initiated. The coolant for the first wall/blanket will be heated externally and circulated to raise the temperature of the first wall and blanket to $\sim 300^{0}C$, providing a vacuum bakeout. It is anticipated that the temperature of the shield will reach $\sim 100^{0}C$ during this bakeout. To accelerate the removal of adsorbed gases, a concurrent glow discharge cleaning will be performed. A low power Taylor Discharge Cleaning (TDC) method has been successfully employed (18) to reduce impurity levels to $Z_{eff} \approx 2.0$. The discharge parameters will be the same as those proposed for STARFIRE (5), and should limit cleaning times to 3 to 5 days.

Another cleaning scenario is that required after a major vacuum system opening for maintenance. The amount of time required for cleaning becomes quite critical, as it affects the reactor availability. After the completion of maintenance and the vessel is verified to be leak tight, it will be pumped to below 1×10^{-6} torr and the vacuum bakeout and glow discharge cleaning will be performed. The approach will be exactly as described above, except that the number of pulses can probably be reduced by a decade, since precautions will be taken to maintain a known gaseous environment throughout the maintenance period. Based on STARFIRE, carbon dioxide would be the backfill gas during maintenance; however its effect on cleaning time has not been fully

investigated. Discharge cleaning with 10^4 to 10^5 TDC pulses, and a choice of the proper backfill gas, is expected to result in a total cleaning time of approximately 1.5 days.

Some aspects of the cleaning operation merit further investigation. The shield temperature will reach 100°C, which may not be sufficient for UHV cleaning. Normal bakeout temperatures are in the range of 250°C. The shield however will not be exposed to ion bombardment during operation and thus may not require cleanliness levels such as those on the first wall. Several surfaces, including parts of the blanket, the limiter slots, and the shield, will not be exposed to glow discharge cleaning. These same surfaces however will not experience ion induced desorption and thus may not require stringent cleanliness.

5.5 Maintenance

The DEMO reactor is being developed for total remote maintenance. The remote maintenance approach was chosen because it will result in the minimum radiation dose to plant workers. The reactor building will be exposed to tritium by permeation and releases during maintenance. Some activation outside the shield may also result from neutron streaming and spread of particulate matter. Use of remote equipment will permit maintenance with a minimal cool-down or clean-up period. In any event when the shield is opened personnel access will not be possible.

The design philosophy being followed is to maintain the radiation levels within the reactor building to < 2.5 mrem/hr within 24 hours after reactor shutdown if all the shielding is inplace; to design all components for complete remote maintenance, and to identify contact maintencance operations where personnel can safely be used with significant economic savings. When the blanket sectors are pulled from the reactor no personnel can be in the reactor building; however, there may be periods when personnel entry is possible.

The 2.5 mrem/hr radiation criteria will limit the activated volumes of material in the reactor building and may permit human access if tritium and

activation products can be controlled. The criteria should not be taken as assurance that contact maintenance can be performed over the life of the plant and designs should be developed accordingly. When the reactor is in place and operating, it may be possible to utilize personnel for some contact maintenance operations.

All components within the reactor building are replaceable. Some are replaced on a scheduled maintenance basis while others are designed for life-of-plant and are replaced only in the event of failure. Items designed for life-of-plant include the overhead crane, TF, EF and CF coils, coolant piping, reactor support structure and radiation shielding. These items represent more than 90% of the reactor total weight. The blanket assembly, impurity control components, current driver, pumps, valves, fueling mechanism, power supplies, maintenance equipment etc. are maintained on a scheduled basis. Spares are provided for all scheduled maintenance components, so that as one part is removed a pretested replacement is available and reactor operation can commence while repairs to the damaged components are being made. The spares for the superconducting EF coils trapped below the TF coils are stored in place so reactor disassembly is unnecessary in event of a failure. These coils are designed for life-of-plant but the consequence of their failure suggests in place spares are prudent.

The number of different maintenance operations planned in the reactor building are minimized by using a component "remove and replace" approach. This permits each maintenance action to be preplanned and designed for use with simple push, pull types of operation. This approach increases the speed of maintenance operations and simplifies maintenance equipment design requirements. Once the damaged or end-of-life components are removed from the reactor they are transported to a hot cell where more time is available for checkout, repair or disposal. The hot cell will have extensive maintenance capability for testing, component replacement, cutting, welding, machining, pinpoint leak location, and other repair.

Redundancy is planned for reactor auxiliary subsystems to permit continued operation of the plant until a scheduled maintenance period or until

the component can be replaced in-service. The particular components where redundancy is planned will be defined as the design progresses; however, candidate systems include redundant power supplies, vacuum pumps, current drivers, some valves, pumps and fueling mechanisms.

Availability goals have been established as 50 percent for extended periods of operation. The DEMO design must be developed around features which enhance maintence if this goal is to be met.

Maintenance Features

The design is being developed to keep the top and sides of the reactor clear for access by maintenance equipment. Components are also being combined where practical to minimize the number of assemblies and improve access. For example, the shield duct around the vacuum duct provides support for the blanket and shield system and the shield door is combined with the blanket sector.

The blanket is replaceable as a 1/8 sector of the torus. Each blanket sector incorporates an integral first wall, limiter and current drive antenna. The limiter and current drive antennas can be removed independently of the blanket. The life goals for limiter and antenna are 4 years and the blanket life goal is 8 years. The coolant is manifolded and valved so that individual replaceable components can be valved off for leak isolation. All lines to the blanket, limiter and current drive antenna utilize mechanical disconnects. Coolant leaks will be detected by sequentially reducing the pressure in individual components and monitoring the change of the partial pressure of coolant in the plasma chamber with a gas analyzer. This technique requires valves that isolate individual components from their coolant loop. Detection of vacuum seal leaks to the vacuum chamber will be accomplished by injecting helium in to a cavity between dual seals.

The shield is designed to last the life-of-plant and will be replaced only in event of unscheduled failures. A shield door is provided as a part of each blanket sector. The door is sealed with redundant seals that are shielded locally to reduce the radiation damage. The seals are replaced each

time the door is opened. The basic shield consists of sectors welded together to form the vacuum boundary. Cutting and rewelding the poloidal seals is required if shield sector replacement is required.

The TF coils are also life-of-plant components. They utilize a common welded dewar in the center post region. Weld tracks are provided to permit coil replacement.

The EF and CF coils are also life-of-plant. CF coils are inside the TF coil and are segmented to permit removal. The external EF coils are superconducting. Those on the top and sides of the reactor can be removed for replacement. Spare EF coils are provided for those trapped below the TF coils. In event of failure, the failed coil is cut out and the spare raised into position.

The vacuum system utilizes redundancy to improve and minimize the effects of failures. Eight compound cryo pumps with isolation valves are provided. Six are required for operation. More pumps may need to be added if the tritium inventory becomes excessive. External valves and pumps leading to the tritium processing system utilize redundancy.

The power supplies are assumed redundant and include a replacement capability during operation. The power supply systems are located outside the primary confinement building and can be repaired during plant operation.

Failed redundant heat transport system conponents, with exception of a few in-line valves, can be replaced during reactor operation using remote/hands-on maintenance equipment.

Blanket and Component Replacement

Blanket and shield sector replacement will utilize the rail mounted approach selected for STARFIRE so that an accurate reference point is available for maintenance operations. A cross section showing the maintenance equipment for removal of these sectors is shown in Figure 5-22.

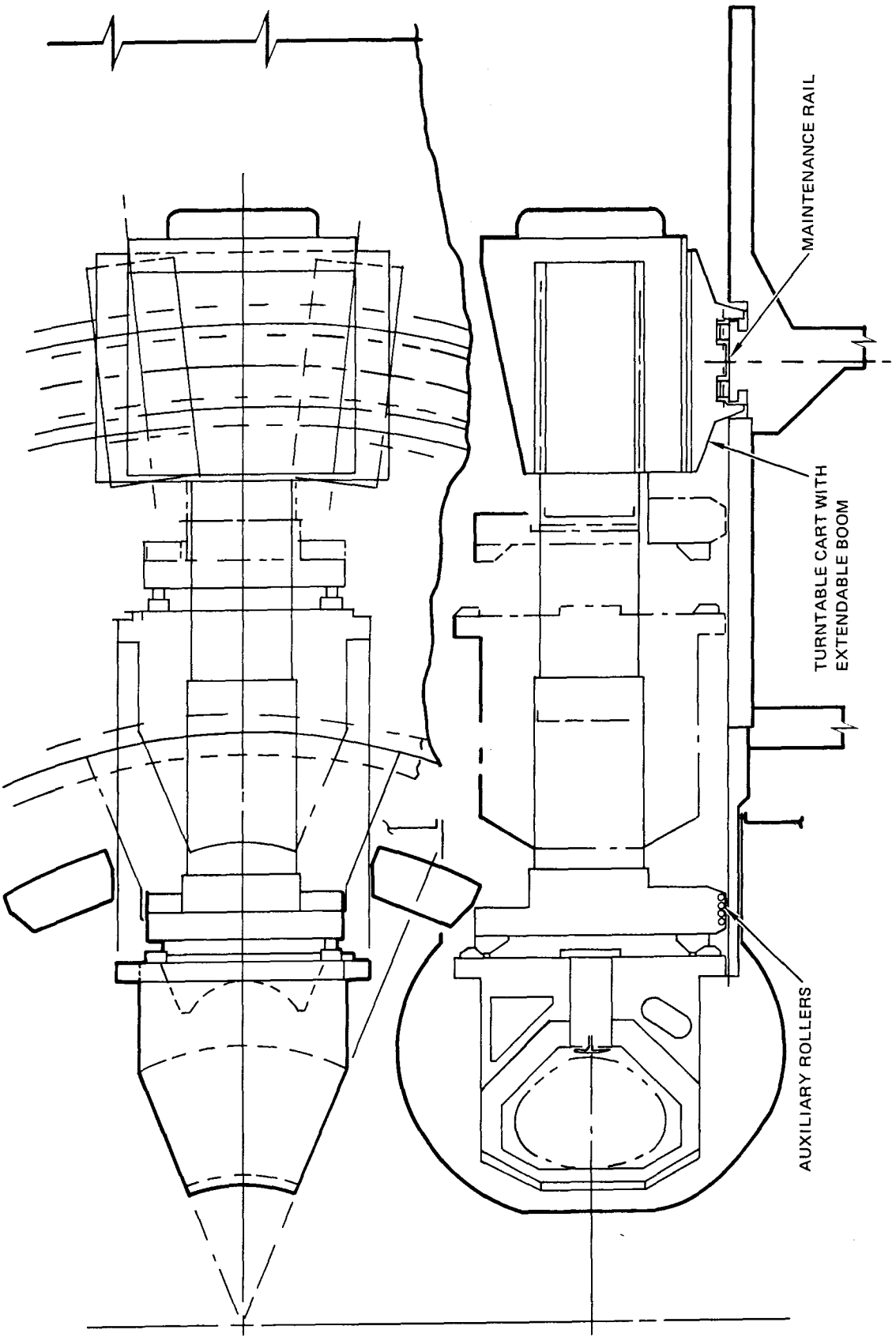

Fig. 5-22. Removal of blanket/shield sector.

The replacement sequence would be as follows:

1. Discharge TF coils
2. Drain or purge fluid lines
3. Move multipurpose manipulator into place
4. Disconnect and remove limiter module fluid lines
   2-limiter coolant
   2-blanket module coolant
   2-tritium purge
5. Disconnect and remove current drive antenna leads
6. Disconnect and remove 2 door cooling lines
7. Disconnect and remove blanket sector fluid lines (2-coolant, 2-tritium purge)
8. Remove multipurpose manipulator
9. Move blanket sector removal machine into place
10. Unlatch sector door
11. Remove blanket sector
12. Reverse Steps 1 to 10
13. Bakeout chamber
14. Restart plasma

It is anticipated that the above operation can be accomplished in approximately 1 1/2 weeks. The most time-consuming aspect of this operation is expected to be removal and replacement of fluid lines. It is assumed that mechanically operated joints will be available for this operation where either a built in actuator or a single drive point is utilized. Self aligning guide pins will be essential for line reinstallation. A multipurpose manipulator which incorporates a storage rack for removal cooling lines is used for this task.

Replacement of a limiter module or current drive antenna is expected to require only 1 or 2 days less than the time for replacement of the blanket sectors since all of the same basic steps are required.

Vacuum Pump Replacement

The vacuum pumps and values are located in the reactor basement and can be replaced independently of the blanket components. A separate maintenance cart is provided for pump replacement and a catacomb is located in the basement to permit access to all 8 pumps.

TF Coil Replacement

Coil removal requires the vacuum tank top panel to be removed, magnet leads disconnected, structural attachments disconnected, blanket and shield removal, cutting the vacuum tank welds and separating the 4°K structure. The two major problems that dominate remote TF coil replacement are (1) cutting and rewelding the common vacuum tank and (2) disconnecting the 4°K structure between TF coils.

Cutting and rewelding the common vacuum tank requires that a welder track be built-in and that assembly tolerances be acceptable. The DEMO design is shown in Figure 5-23. Two 10 cm high welder tracks are permanently attached to the vacuum tank at each joint. These rails have steps to prevent neutron streaming. Two seal welds are used between each TF coil so that tracer gas can be injected for leak detection. The two weld tracks are then held together by segmented structural clamps that keep the pressure loads out of the seal weld. Varying width clamps are provided to overcome tolerance build up during reassembly. The structural clamps also provide the rigidity required for rewelding. Clamps can be removed and relocated behind the welder periodically to maintain track position. In the inner shield area this clamp will be near continuous to provide shielding.

Although a detailed study has not been made yet, it is believed that a system of this type is required before remote TF coil replacement is feasible. It would surely decrease the time required for remote coil replacement by 1 to 2 months as compared with attempting to remotely install a similar track that has sufficient rigidity.

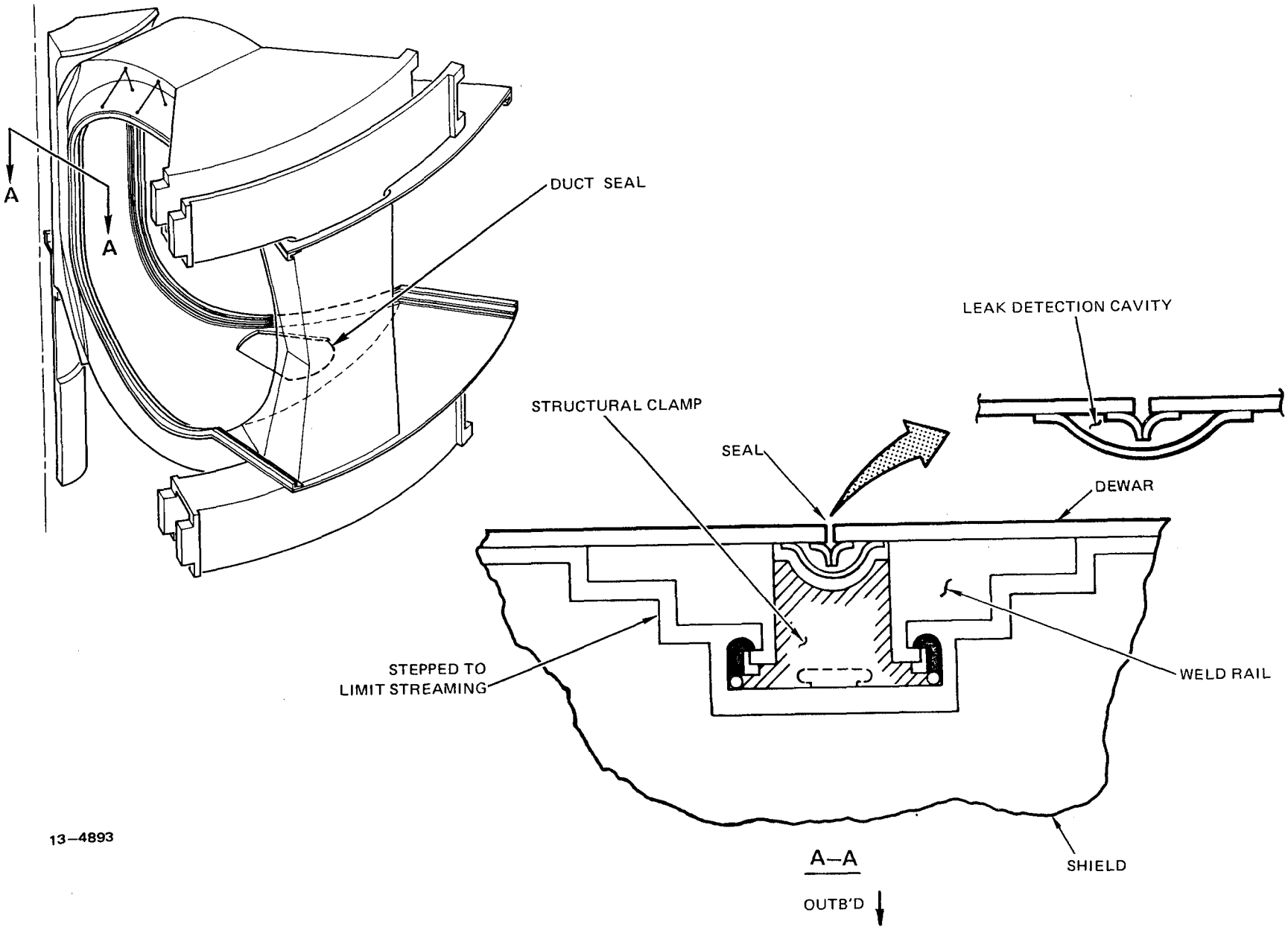

Fig. 5-23. TF coil welded dewar.

References for Chapter 5

1. D. K. Bhadra, T. W. Petrie, V. A. Puron, J. M. Rawls, Ripple Burn Control, GA15924, May 1980, p. 11.

2. Joel Schultz, Junior Woodchuck Manual, (MIT, May 30, 1980)

3. Verbal Communication, Les Waganer, MDAC, 11/24/81.

4. B. Badger et al, UWMAK II, A Conceptual Tokamak Power Reactor Design, UWFDM 112, University of Wisconsin, October 1975.

5. C. Baker, et al, STARFIRE - A Commercial Reactor Study, ANL/FPP/80-1.

6. G. M. Fuller, H. S. Zahn et. al, Developing maintainability for Tokamak Fusion Power Systems, DOE COO-4184-6, p. 7-10, Nov. 1978.

7. C. Baker, et. al., STARFIRE, ANL/FPP/80-1, Chapter 11

8. Verbal communication, Don Coffin, LASL, 10/20/81.

9. D. A. Gueritt, Intrinsic Engineering Problems for Elmo Bumpy Torus-Scale, 9th Symposium on Engineering Problems of Fusion Research, Chicago, October 1981.

10. C. A. Flanagan, et. al., Initial Trade and Design Studies for the Fusion Engineering Device, ORNL/TM-7777, June 1981.

11. W. M. Stacey, et. al., Tokamak Experimental Power Reactor Studies, ANL/CTR-75-2.

12. R. W. Moses, Jr., and W. C. Young, Analytic Expressions for Magnetic Force on Sectored Toroidal Coils, Proc. of the Sixth Symposium on Engineering Problems of Fusion Research, p. 917 (1975).

13. Ken Black, FED Shield Inner Wall Electrical Contact, Informal Memo, MDAC, 4 Sept 1981.

14. P. W. Fisher and J. S. Watson, Cryosorption Vacuum Pumping of Deuterium helium and hydrogen at 4.2 K for CTR Applications, ORNL, Presented at NAS, Washington, D. C. Nov 14-19, 1976.

15. NASA SP-105 Vacuum Technology and Space Simulation, Santeler, Holkeboer, Jones & Pagano (1966).

16. D. H. Davis, "Monte Carlo Calculation of Molecular Flow", J. Appl. Phys. VR31, No. 7, pp. 1169-1176 (1960).

17. Vacuum Technology, A. Roth, North-Holland (1976)

18. Dylla, H. F. et. al., Observation of Cleanliness in Residual Gas and Surface Composition with Discharge Cleaning in PLT, PPPL-1485.

19. FED Device Design Description, ORNL TM 79/48, to be published.

APPENDIX

APPENDIX A

STARFIRE/DEMO WORKSHOP

Agenda

Wednesday, January 20

9:00 - 10:30 a.m.	Plenary Overview Session
10:30 - 12:30 p.m.	Parallel Working Groups (Presentations by STARFIRE/DEMO Team)
12:30 - 1:30 p.m.	Lunch
1:30 - 5:00 p.m.	Parallel Working Groups (General Discussions)

Thursday, January 21

8:30 - 12:00 noon	Parallel Working Groups (General Discussions)
12:00 - 1:00 p.m.	Lunch
1:00 - 4:00 p.m.	Plenary Wrap-up Session (Presentations by Working Group Chairmen)

APPENDIX B

STARFIRE/DEMO WORKSHOP

Working Groups

Group	Chairman
DEMO Objectives and Parameters	W. Stacey
Plasma Engineering - Current Drive	D. Cohn
Reactor Configuration and Maintenance	T. Shannon
Impurity Control Systems	J. Schmidt/M. Sabado
First Wall/Blanket Design	G. Kulcinski/K. Schultz

APPENDIX C

STARFIRE/DEMO WORKSHOP

List of Participants

Name	Organization
M. Abdou	Argonne National Laboratory
J. Anderson	Los Alamos National Laboratory
V. Bailey	Pulse Sciences, Inc.
C. Baker	Argonne National Laboratory
J. Baublitz	DOE/Office of Fusion Energy
W. Bauer	Sandia Laboratories-Livermore
S. Berk	DOE/Office of Fusion Energy
M. Billone	Northwestern University
K. Black	McDonnell Douglas Astronautics Company
C. Boley	Argonne National Laboratory
W. Briggs	McDonnell Douglas Astronautics Company
J. Brooks	Argonne National Laboratory
Y. Cha	Argonne National Laboratory
J. Citrolo	Princeton Plasma Physics Laboratory
R. Clemmer	Argonne National Laboratory
D. Cohn	Massachusetts Institute of Technology
J. Crocker	EG&G Idaho, Inc.
J. Davis	McDonnell Douglas Astronautics Company
D. DeFreece	McDonnell Douglas Astronautics Company
D. Driemeyer	McDonnell Douglas Astronautics Company
D. Ehst	Argonne National Laboratory
G. Emmert	University of Wisconsin
K. Evans	Argonne National Laboratory
J. Fillo	Brookhaven National Laboratory
P. Finn	Argonne National Laboratory
C. Flanagan	Fusion Engineering Design Center
S. Freije	TRW, Inc.
Y. Gohar	Argonne National Laboratory
R. Gold	Westinghouse Electric Corporation
S. Grotz	University of California-Los Angeles
F. Heck	Westinghouse Electric Corporation
H. Helava	Physics International Company
H. Herman	Argonne National Laboratory
N. Hoffman	ETEC/Rockwell International
G. Hollenberg	Hanford Engineering Development Laboratory
P. Hsu	EG&G Idaho, Inc.
J-H. Huang	University of Wisconsin
J. Jung	Argonne National Laboratory
M. Kazimi	Massachusetts Institute of Technology
G. Kulcinski	University of Wisconsin
D. Kummer	McDonnell Douglas Astronautics Company
B. Kusse	Cornell University
R. Lari	Argonne National Laboratory
Y. Li	University of Wisconsin

STARFIRE/DEMO WORKSHOP PARTICIPANTS (cont.)

Name	Organization
S. Majumdar	Argonne National Laboratory
L. Masson	EG&G Idaho, Inc.
R. Mattas	Argonne National Laboratory
D. Mattox	Sandia Laboratories-Albuquerque
T. Mau	University of California-Los Angeles
R. McGrath	Pennsylvania State University
A. Mense	McDonnell Douglas Astronautics Company
G. Miley	University of Illinois
B. Misra	Argonne National Laboratory
G. D. Morgan	McDonnell Douglas Astronautics Company
R. Nygren	Argonne National Laboratory
A. Opdenaker	DOE/Office of Fusion Energy
J. Perkins	University of Wisconsin
K. Plute	University of Wisconsin
G. Proulx	Physics International Company
J. Rest	Argonne National Laboratory
R. Rose	Westinghouse Electric Corporation
M. Sabado	Ebasco Services, Inc.
J. Santarius	University of Wisconsin
J. Schmidt	Princeton Plasma Physics Laboratory
K. Schultz	General Atomic Company
L. Sevier	General Atomic Company
T. Shannon	Fusion Engineering Design Center
D. Smith	Argonne National Laboratory
C. Singer	Princeton Plasma Physics Laboratory
W. Stacey	Georgia Institute of Technology
L. Stewart	Exxon Nuclear Corporation
V. Stubblefield	McDonnell Douglas Astronautics Company
I. Sviatoslavsky	University of Wisconsin
A. Tobin	Grumman Aerospace Corporation
C. Trachsel	McDonnell Douglas Astronautics Company
L. Turner	Argonne National Laboratory
D. Vieth	DOE/Office of Fusion Energy
D. Vrabel	INESCO, Inc.
K. Wakefield	Princeton Plasma Physics Laboratory
N. Young	Ebasco Services, Inc.

APPENDIX D

STARFIRE/DEMO WORKSHOP

Recommendations

I. DEMO Objectives and Basic Parameters

A. Role of DEMO in the Fusion Program

The design team views the DEMO as the device which follows the FED and assumes the present concept definition of the FED for the purpose of defining the DEMO. The working group agreed that this was a reasonable ground rule but noted that the definition of the DEMO depends upon the definition of the FED in this "roll-forward" context.

The design team has not attempted to define the DEMO in a "roll-back" context, i.e., the device which precedes a first "STARFIRE-like" commercial plant. The working group agreed that the DEMO concept definition should not be constrained by the ground rule that the DEMO be the only step between the FED and a "STARFIRE-like" commercial plant. In fact, it was the general feeling of the working group as well as that design team that an intermediate device will be required between a DEMO defined in the "roll-forward" context discussed above and a "STARFIRE-like" commercial plant.

B. Major Parameters

The major parameters and characteristics for the DEMO that have been chosen by the design team were felt by the working group to be appropriate given the above role of the DEMO. It was noted that the DEMO parameters are similar to the INTOR and ETF parameters, except that the DEMO has more ambitious availability and tritium breeding objectives and somewhat more optimistic assumptions about β. The working group felt that achieving a tritium breeding ratio greater than one should be a DEMO objective and that the possibility that it may be necessary for the maximum toroidal field to exceed 10 T to achieve the wall load objective should be recognized.

C. DEMO Objectives

The working group felt that the objectives identified by the design team were appropriate. In addition, because of its unique large-volume, high-fluence capability, the DEMO will, by necessity, serve an important role as a test facility for materials damage, advanced blanket concepts, and possibly other non-electric applications of fusion. The working group agreed that this

testing mission, previously associated with the ETF, would have to be fulfilled by the DEMO and that this should be explicitly stated as an objective.

D. Relationship of DEMO to FED

The fact that the DEMO concept is defined within the "roll-forward" context of being the device which follows FED implies a strong, direct relationship between the DEMO and FED concept definitions. The working group agreed that a more ambitious FED concept would allow a more aggressive DEMO concept in terms of availability, neutron wall load, etc., and could reduce the testing mission of the DEMO. A sufficiently ambitious FED concept could lead to a DEMO concept sufficiently advanced to eliminate the need for an additional device between the DEMO and a "STARFIRE-like" first commercial plant.

In a different vein, it is the role of FED to demonstrate certain technological systems which would then be extrapolated to the DEMO, while other technological systems will be first demonstrated in the DEMO. The working group felt that this point should be kept in mind by the design team.

E. Ground Rules for the FY 1982 Study

The schedule for the DEMO relative to the FED was discussed. The working group agreed that a success-oriented schedule should be the working base assumption for the study. Specifically, the DEMO design should be assumed to proceed in parallel with the final stages of the FED construction and initial operation. However, major commitment of money for DEMO component fabrication, etc., would be made only after sufficient FED operation to obtain the relevant information to confirm the design.

In examining the DEMO design, the working group concluded that the design basis philosophy is a mixture of "conservative" and "aggressive" assumptions. The working group agreed that the design team was justified in making "aggressive" assumptions about high-leverage items that have the potential for dramatically improving the concept.

The emphasis recommended by the design team (i.e., primary emphasis upon key technical issues and R&D needs definition and somewhat less emphasis upon a full-fledged point design) was supported by the working group. The working group felt that there should also be a strong emphasis upon identifying the sources of the information which must constitute the design basis for the DEMO.

F. Other Considerations

The idea of upgrading the FED, after it has accomplished its mission, to also accomplish the DEMO mission was discussed. This could reduce the cost of two separate devices but could lead to higher initial costs and technology requirements for the FED. The working group did not suggest that the design team consider this possibility this year.

The fact that increased international cooperation could, or perhaps must, play a major role in providing the design basis for the DEMO was discussed. This cooperation could take the form of coordinated planning of several "FED-like" devices or collaboration in one such device (e.g., INTOR) as well as collaboration in supporting R&D.

II. Plasma Engineering-Current Drive

On the basis of the survey presented in the draft interim report and from the experience of the reviewers in this working group, the various current drives were rated based on the following key issues: Physics - physics confidence level, experimental basis; margin of degraded performance relative to theoretical prediction which is acceptable; and recommended experiments. Technology - margin of degraded performance of future technology which is tolerable; required advances in technology; reliability, lifetime, and maintainability; and recommended technology R&D. A summary of the recommendations made for each of the current driver systems follows.

A. REB

1. Physics

In regard to the physics confidence level, results are promising, but it must be shown that beams can penetrate in a real reactor. In addition, the scaling of high alpha (anomalous resistance) results to a reactor is a concern. Concerning the margin for degraded performance, there is a very significant margin factor of 10 over minimum acceptable value of I/P, which is encouraging. Multiple pulses in a medium-size tokamak is a high priority item for the experimental tokamak program.

2. Technology

The margin of degraded performance is large with regard to efficiency. Required advances in technology are minor, except for materials issues concerned with lifetime. Reliability and maintainability have not been studied. Technology R&D is not as high a priority as experiments. Technology improvements should automatically accompany the experiments.

B. Waves

1. Physics

In regard to physics confidence level, experimental verification of theoretical prediction is generally poor. For example, lower hybrid experiments do not agree with theory at higher density. However, LH has effectively driven large currents at low density. There are no experiments on HSMS. There is little margin of degraded performance here. It is recommended that HSMS experiments be initiated and that LH experiments at higher density, higher temperature be continued. Also, experiments on LSMS waves (trapped electron effects) should be performed.

2. Technology

There is little margin in performance of projected technology (little margin in overall efficiency). The main problem here is materials development in antennas. Some tube development is necessary (high power tubes). Also, it is recommended that radiation-resistant antennas be developed.

C. Neutral Beams

1. Physics

The physics confidence level is very good except for questions concerned with collective effects (injection above Alfven velocity). The margin of degraded performance is low, but improvement by using pulsed scenarios is promising. Recommended experiments include injection at high velocities ($V > V_{Alfven}$) typical of negative ion neutral beam technology.

2. Technology

Negative ion systems with $E_b > 0.5$ MeV and efficiency > 0.50 are needed. In addition, ESQ (electrostatic quadrupole) accelerators and/or laser neutralizers may be essential. However, development of ESQ technology represents very significant extrapolation, and our present perspective is speculative. Regarding radiation hardening, neutron damage problems do not appear to be prohibitive. (FED study was encouraging.) With respect to reliability and maintainability concerns, these relatively complex systems have possible adverse effects on reactor maintenance. Finally, an aggressive negative ion neutral beam development program is needed to pursue this option. Experiments with a small-scale ESQ device should be considered.

D. General Recommendations to the DEMO Team and Fusion Community

The following general recommendations are offered to the DEMO team as well as the fusion community: 1) A medium-size tokamak facility is needed to study various current drive techniques and long-pulse physics/engineering issues. 2) Supporting test stands are needed. 3) REB current drive studies are the most important physics experiments since REB has the highest margin of safety, because very little work has been done, and because there is no on-going work. 4) The use of REB in the DEMO should be explored further.

III. Reactor Configuration and Maintenance

This working group addressed the issues in the areas of design philosophy and reactor design. The stated DEMO design philosophy provides a good basis for configuration development. The working group recommends that the project assign high priority to the following major issues: TF coil replacement, overall maintenance system, EF coil structural design, TF coil shape and structural reinforcement, and the relationship between the number of components and reactor availability. Specific issues are discussed below.

A. Prototypical Components

It is believed that the goal of utilizing prototypical commercial subsystems for the DEMO is essential for satisfying its objectives. This includes the use of similar components (limiter or divertor, vacuum pumps, superconducting magnets, etc.) and the same configuration and maintenance approach.

B. Minimum Number of Components

The argument presented by the DEMO team that increased availability is possible by minimizing the number of components is believed to be valid. This leads to reducing the number of TF coils because the number of components is directly proportional to the number of TF coils. Decreases in numbers of components reduces the replacement time without a corresponding decrease in reliability. Further work is recommended to provide more backup calculations and specific examples.

C. Remote Maintenance

The working group agreed with the choice of fully remote maintenance but recommends that references to manned backup be deleted because it may weaken the development of remote maintenance techniques.

It is recommended that DEMO place emphasis on defining the maintenance system to establish the feasibility of fully remote maintenance and to provide information about its impact on configuration and cost. This effort should include a listing of the major maintenance operations, a reactor building layout, development of basic requirements and design concepts for the equipment, and identification of the high priority R&D needs.

The track-mounted manipulator was endorsed as a good concept but it was agreed that more detailed design is required.

Cost estimates for making the TF coils large enough to permit removal of a single sector per TF coil were questioned. FED estimates project a difference of $150 M to $300 M, whereas DEMO estimates project approximately $60 M for a 2-m larger outer leg radius. Maintenance costs should be acknowledged as significant but necessary.

TF coil replacement was recognized as the most significant maintenance problem. The approach presented for DEMO incorporates features that are a step in the right direction but must be developed more fully. The working group recommends a major effort on this task since tokamak engineering may hinge on this issue.

D. Magnet Cryostat Design

The use of a common magnet vacuum dewar is appropriate at the inner leg of the TF coil. It is suggested, however, that the possibility of combining the common dewar with the inner shield be investigated. The flat top of the cryostat appears to provide substantial cost savings but should be evaluated further.

E. Blanket/Shield Concept

The design approach is considered appropriate and, in particular, the use of a single straight line motion for sector removal is considered essential by the working group.

F. Availability

The 50% availability goal is appropriate for the DEMO, but it is not apparent as to how fusion will achieve this goal. It is recommended that a reliability and maintenance time assessment be performed for the approximately 10 major systems.

G. TF Coil Shape

The reduced height TF coil was endorsed as appropriate for decreasing reactor plant capital costs. The interface between the pure tension shape and

the extended center post should be analyzed in more detail to assure the bending moments are manageable.

H. Structural Design

It is recommended that a set of firm design criteria (number of disruptions, etc.) be developed for the design effort. A specific problem that should be addressed in detail is the non-uniform loading and support of the poloidal coils.

I. Electromagnetics

The dielectric break and first wall connector pose a significant risk and require early demonstration. Current generation devices utilize bellows for resistance control.

J. Vacuum Pumping

It is recommended that a larger percentage of redundancy be added in the vacuum system. It was felt that an increase in duct and pump size could provide added redundancy without adding much cost. This would also reduce the tritium inventory by permitting recycling of more than two pumps simultaneously and could decrease the reliance of the inversion probability at the limiter on vacuum system conductance.

The use of elastomer seals in the vacuum door, limiter, and REB antenna were endorsed as desirable. The bakeout limitation of 150°C will prevent the local areas from being baked to 250°C with the blanket. The impact of the reduced bakeout capability should be included.

The automatic clamps for disconnecting vacuum joints is very appropriate. However, a simplified design is needed.

IV. Impurity Control Systems

A. Physics

1. Introduction

The working group reviewed the assumptions, models, and physics results on which the DEMO impurity control system design is based. In general, the modelling results are realistic and based on presently accepted physics assumptions. Several of the important concepts and associated models have been pioneered by the DEMO team. These developments will certainly contribute to the FED/INTOR design effort.

2. Discharge Physics

The modelling of the overall discharge, which serves as a basis for the impurity control system design, is realistic and self-consistent. However, three factors appear to reduce the overall reactivity more than would seem necessary: a) the helium level is high (i.e., 8%), b) the beryllium level is high (i.e., 2.6%), and the discharge appears not to be operated at optimum temperature and density. Since the reactivity is the primary product of the reactor, a better combination of contamination, temperature, beta, and wall load should be considered.

3. Edge Conditions

The models used to study the edge conditions appear to be realistic and well developed. The choice of three edge conditions to study (i.e., 10 eV, 100 eV, and 1.5 keV) is a sensible approach to the uncertainties in edge conditions. The design group should keep in mind the fact that the 1.5 keV reference condition may be difficult to realize. This is born out by the fact that the maximum temperature obtained in the modelling studies (for 10% particle removal) was 560 eV. Unaccounted-for effects (i.e., secondary electrons, increased edge radiation, etc.) will tend to decrease this temperature while it is very important for the beryllium design to maintain a high temperature.

4. Erosion and Redeposition

The model used to estimate the material erosion and redeposition on DEMO is one of the first attempts to address this question for a reactor. The studies indicate a several millimeter per year erosion or buildup rate for the conditions considered. This net rate is the difference between a much larger erosion and redeposition rate. For this reason it is very sensitive to uncertain edge and material conditions. The panel was concerned that redeposited material properties, such as the sputtering coefficient, could be quite different from those assumed. In addition, potential flaking could significantly alter the results. We recommend that the DEMO team analyze the sensitivity to these and other factors.

The single element decision (i.e., walls and limiters of the same material) will be very restrictive for future design considerations. The studies should reexamine the need for this requirement.

The 0.3 cm/year buildup on the limiter will likely come from a region of the wall of similar area. The effect of a localized wall erosion at this rate should be considered.

5. Power Loads

The model used to calculate the power loads is realistic. The choice of the level of the power load will affect the position of the channel and the associated helium pumping. In addition, moving the limiter to the bottom can reduce the loads or increase the helium pumping. Since the helium level is high and, thereby, affecting reactivity, these factors should be considered in reoptimizing the design to reduce this contamination level.

6. Impurity Control

Modelling the impurity flow and associated level is difficult. However, the models used here are realistic in their embryonic form. The projected level of beryllium contamination is about 2.6%. This causes a reduction in reactivity of 20-25%. Uncertainties in modelling and associated potential increases in this level would be serious. Consideration should be given to reoptimizing the design to reduce this contamination level.

7. Helium Removal

The helium removal characteristics of the DEMO pumped limiter have not been considered in detail. However, other studies indicate that this type of limiter will suffice for helium removal.

The helium level is projected to be about 8%. This will have a significant (i.e., ~ 20-25%) effect on reactivity. Because of the importance of this helium level, the pumping characteristics of the limiter should be studied.

B. Engineering

1. Ripple Field

It was agreed that both limiter and pumping space benefit from an evenly distributed heat load in the toroidal direction. The presence of a ripple field will produce unequal toroidal loading on the present limiter configuration. This should be investigated further.

2. Disruptions

Recent experimental evidence indicates that a disruption will go to the surface that is in contact with the plasma prior to the disruption. This is regardless of whether the surface is the inner wall, upper wall, or outer wall. Evidence also indicates that the thermal quench part of the disruption will be on the order of 200-500 μs, and the E/M part will occur on the order of presently accepted design values of a few milliseconds. The DEMO limiter design should be consistent with present knowledge of plasma disruptions.

In addition, an investigation of current flow during disruptions should be made. It was not clear that major forces will not occur from current flowing down a limiter arm, through the structure, to the next limiter. Arcing may also occur between adjacent limiter (type)/structures during a disruption because limiters could be at different potentials. These phenomena will have a major effect on the limiter (and support) design (and stress).

3. Limiter Thickness

The possibility of making the limiter blade thicker should be investigated. Since the flux lines do not dictate the present shape of the rear surface of the limiter and conductance is not a problem, the possibility for a thicker blade exists. This would produce a stronger design, less flexible in bending, and allow for incorporation of structural support into the blade separate from the cooling structure (e.g., stainless or inconel could be used as a spine, surrounded by a copper cooling sheath, similar to the FED design).

4. Stress Analysis

Substantial concern was expressed about the use of ASME Stress Criteria in the limiter analysis. This code allows $(P_L + P_B + Q) \leq 3\ S_m \sim$ Ultimate Strength. It treats the thermal load as a secondary stress. For an irradiation embrittled material, this criteria is not conservative.

The effects of irradiation creep and property changes on the limiter model should be estimated (for a first-order analysis). Some of these effects are/can be handled by finite element Structural Analysis Codes. The hand analysis presented cannot adequately model irradiation effects, much less accurately portray the shear stress state at the coating/substrate interface. Irradiation effects will have a major impact on limiter stresses and, therefore, limiter life.

As mentioned above, the shear stresses at the coating/substrate interface have not been investigated. These should be investigated since they will be a major factor in coating adherence. In addition, the Be/Cu interface will have a reduction in strength due to possible tritium buildup along it.

It is probable that cracks will occur in the coating from operations/disruptions. These could propagate into the irradiation-embrittled substrate. The subsequent leak into the torus would vaporize the water coolant. It is recommended that some fracture mechanics investigation of the coating be undertaken.

5. Materials

The scheme presented for erosion control of the limiter has interesting possibilities. If the impurity material being transported by the plasma and deposited onto the limiter is the same material, problems arising from impurity modification of limiter substrates may be avoided. There are, however, a substantial number of questions that need answers before this solution can be validated as a conceptual design.

Some basic tests and analyses should be undertaken to verify, to the first order, some critical material properties and morphology. Suggested areas for investigation are: erosion rates vs. redeposition rates; strength and physical properties of the redeposited material; effects of impurities (since plasma will contain them) on properties which will stress the material; reduce the uncertainties in sputtering parameters since they will greatly affect the strength and physical properties; investigate the applicability of spalling (bond properties, adhesions, sticking), since experimental evidence shows that a large probability for it exists; investigate the effects on design/maintenance of high locked-in stresses from high temperature deposition in the cooled-down limiter structure after operation; redo stress analysis using finite element techniques and properties from materials investigation since present stress analysis does not properly reflect changes in the redeposited material; and do not underestimate or neglect the irradiation effects which will also alter the materials properties.

6. Summary

The erosion-redeposition scheme presented to the attendees was inventive. It certainly addressed the erosion problem designers of impurity control systems must increasingly face. Like many areas of research, the first cut at a solution reveals many more questions. Some of these questions must be answered in order to verify that continued research and/or acceptance of the concept has merit.

It is recommended, therefore, that the fusion community pursue this concept: that a modest materials investigation program be initiated to validate some basic assumptions; that all the limiters, regardless of location, be designed for disruptions; and that issues raised above be addressed by the component design staff.

V. First Wall/Blanket Design

A. First Wall/Limiter Design

1. Critical Issues

a. Tritium Permeability

The main question here is the rate at which energetic hydrogen isotopes, implanted in the first surface region will permeate through the first wall into the coolant. The three main issues discussed in this area relate to: model development, experimental verification of models, and anticipated first wall composition in a "real" fusion environment. Most of the discussion related to the question of whether T_2 loss rate could be held to less than 20 curies per day.

It appears that the development of models for tritium permeability through metals in an energetic hydrogen plasma environment is proceeding at a reasonable pace for this project. The current models are felt to be representative of the physics of T_2 permeation, but the models also contain a large number of parameters whose values are poorly known. The rather large number of these uncertain parameters does not generate much confidence in the predictions of actual permeation rates in the DEMO. There was a great deal of discussion about the need to measure some of the more critical parameters in the models such that the range of uncertainties could be reduced. The need for sensitivity studies to discover the most important parameters was brought up several times in the session.

Finally, there seemed to be some disagreement of how well we might be able to predict the actual first wall conditions in a "real" fusion environment. Topics such as the degree of contamination from oxygen or carbon, the rate at which the surface is "cleaned" by sputtering, the change in alloy composition in the near-surface region due to preferential diffusion of the low atomic weight elements, etc., were discussed. Another area of concern was the effect of implanted helium on the trapping of the hydrogen isotopes as they permeate through the wall. Radiation trapping of the permeating hydrogen isotopes was also discussed, but no firm conclusions were drawn.

b. Disruptions

It was generally agreed that there has been considerable progress in this area, at least in understanding the nature of the problem. However, it was also evident that the consequences of disruptions were far

from being adequately understood. This problem was felt to be of a "go or no-go" magnitude in the DEMO and, therefore, still deserves further analysis. The major issues discussed were: model development, spatial and temporal variations of heat flux during a disruption, melt layer stability, and mechanical response to the Be coating.

The progress in model development has been very encouraging in the past two years, mainly because of the INTOR Project. The DEMO can, and should, benefit from this work. However, the uncertainty over the spatial variation in the deposited energy or the time-related behavior is still unacceptably large. For example, the DEMO team used an overall "peaking" factor (that is, the maximum flux divided by the average flux if the energy went uniformly to the first wall) as a factor of five. Several members felt that such a value was too low, and that factors of 10 to 15 might be more appropriate on the first wall and the values may be even higher on limiters. Disruption times of tens of milliseconds were appropriately analyzed, but it was pointed out that the consequences of shorter disruption times and high peaking factors need to be assessed further.

The stability of the melt layer was frequently discussed, but other than recognizing the problem, the issue of how the melt layer would react to the rapidly changing magnetic field and/or the gravitational forces was not addressed. It appears that this problem is not easily modeled and may not be solvable during the time period of this study. However, it was pointed out that the melt layer stability was also of the "go or no-go" nature for the DEMO.

Finally, there were a large number of questions about the mechanical stability of the Be/SS bond after being subjected to repeated shock waves generated during the short deposition time of a disruption.

c. Be Coatings

The use of relatively thick Be coatings ($\sim$ 5-10 mm) to protect the first wall and plasma during disruptions was discussed in some detail. The major concern in this area seemed to be on the stability of the Be/SS bond due to forces that might be generated during operation. These include neutron-induced swelling of the Be, temperature variations during power load changes, or even irradiation-induced creep relaxation of the base structural material

2. Recommendations to the DEMO Team

a. Tritium Permeability

The main recommendation to the design team is to conduct a sensitivity analysis on the parameters in the current T_2 permeation models. The results of such a parametric analysis can be then used to identify those critical parameters which need to be measured experimentally (after the STARFIRE/DEMO study is completed).

b. Disruptions

The three main recommendations in this area are: 1) The effects of higher peaking factors and shorter disruption times need to be assessed with respect to the survivability of the first wall. Such analysis should incorporate the vapor shielding effects as well as the possibility that the vaporized material might be swept away by the rapidly changing magnetic fields. 2) An attempt should be made to model (analytically) the stability of the melt layer in Be or SS. Because of the short time available in FY 1982, such an analysis can only be of a scoping nature, but it is felt that ignoring the problem at this time will detract from the credibility of the current design. 3) An analysis of the effect of disruptions on the limiter alone needs to be made. Thus far, only the effect of disruptions on the first wall have been addressed. The same variations in peaking, time duration, and melt layer stability as applied to the first wall should also be included.

c. Be Coatings

There are several near-term recommendations for this area: 1) The effect of higher charge exchange (CX) fluxes near the pumping parts or limiters needs to be addressed. Thus far, the CX flux is assumed to be uniformly distributed, a rather unlikely situation. 2) A general analysis of the Be/SS and Be (redeposited)/Be (old)/SS bonds needs to be instigated. The ability of those bonds to withstand frequent changes in the temperatures, slowly induced neutron or helium gas bubble swelling, and the propagation of cracks perpendicular or parallel to the plane of the bond needs to be assessed. 3) If the Be coating falls off for any reason, the consequences to the DEMO design need to be examined. Such failures could result in the melting of the steel during the disruptions or the propagation of cracks through steel which is embrittled due to neutron or hydrogen effects. 4) An assessment of the Be resource implications of the DEMO design should also be included.

3. Recommendations to the Fusion Community

a. Tritium Permeation

The major concern here is that there is very little experimental information on the permeation of energetic hydrogen isotopes through metals or coatings. Without such information, the predictions of current theories will always be viewed with some skepticism. Such experiments must be conducted on well-characterized surfaces because of the uncertainty over contamination, near-surface chemical changes, or microstructural changes associated with bubbles. It is also recommended that such permeation studies be conducted under conditions where a high population of radiation-induced defects are present during the permeation phase of the hydrogen isotopes.

b. Disruptions

The major recommendation in this area is to conduct experimental tests of the "vapor shield" model recently proposed in the magnetic fusion area. Such tests are needed to see if we can actually take advantage of this mechanism to reduce the vaporization during a disruption to acceptable levels in large tokamaks.

c. Be Coatings

In addition to the modeling studies of a Be coating on steel, there is a need to fabricate and test thick Be coatings under the conditions which may be present in a tokamak-like DEMO. The failure conditions and failure rate with respect to transient or steady-state heat fluxes need to be established. It would also be helpful to simulate dimensional changes due to neutron swelling of either the Be or the steel substrate.

B. Lithium Oxide Blanket

1. Critical Issues

a. Materials Issues

The major issues discussed were the evaluation of the properties and temperature limits of solid lithium compounds, the statements made about helium cooling, the concern about fabrication and availability of the desired solid breeder configurations, and the embrittlement of ferritic steel by hydrogen. The DEMO team has collected the available thermophysical property data base and has developed operating temperature windows to stay within the constraints established by sintering and compatibility concerns, mass transport of the lithium materials in the purge stream, and tritium release. The working group indicated that further consideration of the temperature

limits is needed and that experimental studies are probably needed in order to define these limits. Evaluation of the thermophysical properties of the lithium materials in the configurations/morphologies is needed and should be guided by consideration of the sensitivity of the design to these properties. Fabrication development is needed to show the desired configurations can in fact be made but should wait until the need for special configurations (e.g., bi-modal pore distribution) is verified by experiment.

A sharp discussion was generated on the question of helium cooling. While the choice of water cooling for the DEMO was generally accepted as being a reasonable choice, strong opinions were presented that the statements made in the draft report and the review presentations about helium being undesirable were not justified or substantiated. It was pointed out that all of the issues raised for helium were highly design-dependent and that a good candidate design for helium had not been developed or evaluated. It was suggested that it was not necessary for the DEMO to make any statements on the viability of helium and that the statements that were made were not justified.

b. Tritium Release and Recovery

Partially as a result of the STARFIRE Workshop held one year ago, experimental work in FY 1981 was focused on the issue of T_2O solubility in Li_2O. This work appears to have resolved the concerns about large tritium inventories in a Li_2O blanket. The issues now appear to be concerns about the rate of diffusion out of Li_2O, understanding of the rate-limiting effects and temperature constraints, and selection of material configurations/morphologies to optimize tritium release. Preliminary information from the TULIP experiment appears to indicate that small grain sizes and complicated configurations will not be needed to achieve good release. This issue needs to be explored thoroughly as soon as possible as it strongly impacts the need for developing complicated fabrication techniques for lithium compounds. It may be possible to do some simple "go/no-go" type experiments to define the need for more detailed evaluations. If tritium is adequately released from simple, high-density sintered pellets with large grain sizes, the need for investigation of the detailed release mechanisms and development of complicated configurations may be obviated.

c. Design Considerations

One of the consequences of the narrow operating temperature window assumed by the DEMO team for Li_2O is the challenge to develop a credible design that stays within those limits. Maintenance of the proper narrow gap between the breeder material and the coolant tubes is particularly important, especially considering the poloidal variations of the wall loading. Design solutions that are developed will need testing of their thermal-hydraulic/thermomechanical behavior to verify that the correct temperature distributions can in fact be achieved and to insure that the conditions that maintain these distributions are stable with time during operation.

The choice of whether or not to include breeding of tritium in the inboard blanket has not yet been made for the DEMO. The issues, pro and con, concerning the choice have not yet been fully identified or discussed, although Li_2O blankets that include beryllium to enhance breeding performance were discussed and appear quite interesting. The consensus of the working group appeared to be that there are no strong arguments against inboard breeding and a decision not to use the inboard direction would have to be justified. Although the question of lithium burnup was raised several times in the DEMO review, the degree of burnup was not quantified nor were the consequences discussed. This is one of the aspects that must be considered in estimating the DEMO blanket lifetime.

2. Recommendations to the DEMO Team

a. Materials Issues

Most of the materials issues require experimental efforts that are beyond the scope of the STARFIRE/DEMO study. Several issues, however, can and should be examined further during the study. The narrow operating temperature window for Li_2O is presently set by tritium inventory concerns on the lower side and lithium compound vaporization concerns on the upper side. The lower limit of 410°C was set during the STARFIRE design on the basis of tritium inventory. It should be reexamined in light of the newly discovered very low solubility of LiOH in Li_2O. The upper limit of 670°C is based on keeping expected weight loss by mass transport below 1% of the weight loss due to burnup. This appears to be a tight limit. The impact of increasing this to 10% or even 100% of the burnup weight loss should be considered. The limit imposed by radiation-induced sintering appears to be as high as 750°C for Li_2O. The DEMO team should be more specific about what determines the operating lifetime of the Li_2O (i.e., neutron swelling, burnup, etc.).

The issues, pro and con, regarding helium cooling should be examined by the DEMO design team with knowledgeable groups in the fusion design community. It is not clear that a head-to-head comparison between water and alternate coolants, including helium, is possible or needed for the STARFIRE/DEMO study. It is recommended that the DEMO team meet with groups that have developed helium-cooled blanket designs and learn of the technical aspects of these designs. Since the points raised in the DEMO report and review are highly design dependent, it appears necessary to modify the statements made in the DEMO report accordingly.

b. Tritium Release and Recovery

Resolution of the questions concerning release of tritium from solid breeder materials requires further experimental data. It does appear that recent information from experiments (e.g., TULIP at ANL and OG-5 at General Atomic Company) may help interpret the various analytical model results. The DEMO team should incorporate these recent experimental results into their design, analysis, and evaluation efforts.

c. Design Considerations

The DEMO team has done a good job of identifying the sensitivity of the solid breeder blanket to the maintenance of a proper thermal conductance between the solid breeder and the coolant tube. It is recommended that the team try to develop design solutions to insure maintenance of this gap. It appears that use of annular pellets around the cooling tubes and wire-wrap on the cooling tubes may be a solution. Use of the coolant pressure to maintain thermal contact could also be considered. The design must include consideration of reasonable hot-spot (and cold-spot) factors and partial power operation which will affect the blanket temperature profiles. An important factor will be the cost asociated with the possible need for different thermal designs at different poloidal positions around the blanket. This could incur large design, fabrication, and spare parts costs.

The question of inboard breeding must be resolved and a recommendation made. The team appears to presently be leading toward not breeding in the inboard blanket region. A case has not been made that this is in fact desirable. The blanket lifetime limits (burnup, radiation damage, etc.) must be explored and a lifetime limit identified.

3. Recommendations to the Fusion Community

a. Materials Issues

The bases for specification of operating temperature limits are, for the most part, analytic calculations of tritium release and theoretical expectations for sintering, vaporization transport, etc. It is important that an experimental basis for these limits be established. This includes the effects of sintering and radiation effects, compatibility concerns, and mass transport of the solid breeder constituents. In addition, further evaluation of the thermophysical properties of the breeding materials is needed. Although a good start has been made in recent years, more work remains to be done. As the understanding of the critical parameters associated with tritium release improves, the specification of the required breeder material configurations and morphologies will become firmer. At that time, it will be necessary to develop techniques for economical fabrication of the desired materials.

b. Tritium Release and Recovery

The concerns associated with tritium release from solid breeders are still predominantly based on theoretical predictions. There is a strong need for experimental support for the tritium behavior models. When these models are understood and when blanket designs using these models are done, demonstration of prototypical solid breeder blanket tritium recovery systems is needed.

c. Design Considerations

The concern about temperature control in solid breeder blankets is a generic issue and is not confined to the DEMO blanket concept. As a result, the fusion design community must attempt to develop design concepts that will accommodate or, better, avoid the concerns about maintenance of proper gap thermal conductance that were identified by the DEMO team.

C. Lithium-Lead Breeding Blanket

1. Critical Issues

a. Compatibility

The main issue discussed here was to establish upper and lower operating temperature limits for the Pb-Li alloys. Unfortunately, there is very little data on which to base such determinations, and the upper limit of 450°C (or even lower) is made from inference to Li compability data. The only data available to date is on samples in a static test environment, and there

is a real need for data in a dynamic (i.e., flowing liquid metal) environment. There was considerable disagreement on how one could extrapolate the present static test data to a dynamic limit for Pb-Li alloys.

Similar problems exist when trying to predict embrittlement of austenitic or ferritic steels. Inferences from pure Pb embrittlement of ferritic steels at the melting point of Pb were not deemed to be adequate to place a lower temperature limit on Pb-Li blanket operation.

b. Tritium

The main issue discussed in this area was the relative merits of recovering tritium via the molten salt technique versus removal by vacuum pumping above the surface of the molten metal. Pros and cons of both systems were discussed, but the major reason against vacuum pumping appears to be associated with the extremely large pumping capacity (and cost) required to reduce the inventory down to the tens of grams level.

Because of the high vapor pressure of T_2 above the Pb-Li alloy, containment of the tritium will be a major problem. It appears that special coatings to reduce the permeation rate by a factor of one hundred or more will be required to meet leakage rates of greater than or equal to 20 curies per day.

The breeding of T_2 from Pb-Li alloys was discussed, but there seemed to be no doubt that breeding ratios of more than 1.0 could be achieved. If the Li is highly enriched in the Li-6 isotope, it appears that sufficient breeding on the outside could be accomplished to use "non-breeding" blankets on the inboard side.

Finally, the safety of Pb-Li alloys was briefly discussed, with the general conclusion being that such alloys are significantly safer than Li, but quantitative values could not be agreed upon by the group.

c. Coolants

The main issue discussed revolved around the coolants that should be used for the Pb-Li breeding blanket. The options included helium, sodium, water, and $Pb_{83}Li_{17}$. In the first three cases, the Pb-Li would be present in a static blanket where thin tubes would carry the coolants through the Pb-Li alloy. In this last case, the $Pb_{83}Li_{17}$ itself would move through the blanket. The helium looked unattractive because of the low maximum operating temperature. The water was unattractive because of safety and the difficulty of removing T_2. The sodium has some attractive features such as an

established technology, low T_2 solubility, and low pressure. However, the MHD drop in sodium (which would have to be flowing at a much higher velocity than $Pb_{83}Li_{17}$ itself) was not calculated. Furthermore, the use of Na coolant on the inboard side of a tokamak would also present severe MHD pressure loss problems.

2. Recommendations to the DEMO Team

a. Compatibility

The main area that could be addressed within the time frame of this study would be a parametric analysis of the quantitative consequences of the various corrosion rates. There are two main points here: the thinning of the blanket walls, and the deposition of corrosion products throughout the system. An assessment of "sacrificial" deposition surfaces in the colder parts of the heat transport system may alleviate the "plugging" problem.

b. Tritium

It was evident that further analyses of gas sparging versus gas pumping extraction techniques would be helpful. There are several reasons suggested why gas sparging may be better than the pumping techniques or the molten salt techniques.

c. Coolants

A quantitative analysis of the MHD pressure drops in the sodium-cooled Pb-Li blankets and the self-cooled designs should be made. Particular emphasis should be paid to the inboard side of the tokamak design.

An overall cost analysis (mills/kWh not $/kWh) of the Pb-Li versus Li versus Li_2O breeding blankets should be conducted. This analysis should take into account the increased or reduced shield thickness required to protect magnets as well as pumping power costs and efficiency analyses.

3. Recommendations to the Fusion Community

a. Compatibility

It appears that the most critical tests that can be performed over the next few years are in flowing Pb-Li systems. Such data and the experience with such loops is absolutely essential to establishing realistic operating limits. It is also necessary to investigate the effects of high magnetic fields on the corrosion rates and embrittlement tendencies of these systems. If ferritic steels look promising with Pb-Li alloys, then the effects of such steels on magnetic field asymmetries needs to be assessed. The effect of the fields on stresses in the magnetic blankets also needs to be

examined, especially where tubes enter or exit from high magnetic field regions.

b. Tritium

An experimental demonstration of the extraction of T_2 from Pb-Li alloys via molten salt, gas sparging, or gas pumping techniques is vital. The effects of impurities and corrosion products also need to be included in such an assessment.

c. Coolants

Quantitative experimental information on the interaction of Pb-Li and H_2O is urgently needed. Since Pb-Li alloys are perceived to be safer to work with than Li or Na, such data will confirm or deny this impression.

Distribution for ANL/FPP/TM-154

Internal:

M. Abdou
C. Baker
E. Beckjord
C. Boley
J. Brooks
F. Cafasso
Y. Cha
R. Clemmer
D. Ehst
K. Evans
P. Finn
Y. Gohar
L. Greenwood
D. Gruen
H. Herman
C. Johnson
J. Jung
M. Kaminsky
S. Kim
Y-K. Kim
R. Kustom
R. Lari
B. Loomis
S. Majumdar
ANL Patent Dept.
V. Maroni
R. Mattas
B. Misra
J. Norem
W. Praeg
J. Rest
J. Roberts
D. Smith
H. Stevens
L. Turner
FP Program (50)
ANL Contract File
ANL Libraries (2)
TIS Files (6)

External:

DOE-TIC, for distribution per UC-20 (119)
Manager, Chicago Operations Office, DOE
President, Argonne Universities Association
AUA Special Committee for the Fusion Program:
- G. Miley, University of Illinois
- S. Baron, Burns & Roe, Inc.
- H. Forsen, Bechtel National, Inc.
- F. Loeffler, Purdue University
- M. Lubin, Standard Oil Company of Ohio
- P. Reardon, Princeton Plasma Physics Laboratory
- K. Symon, University of Wisconsin

S. Abdel-Khalik, University of Wisconsin
N. Amherd, Electric Power Research Institute
J. Anderson, Los Alamos National Laboratory
D. Anthony, General Electric Company
V. Bailey, Pulse Sciences, Inc.
S. Ball, Physics International Company
K. Barry, The Ralph M. Parsons Company
J. Baublitz, DOE/Office of Fusion Energy
W. Bauer, Sandia Laboratories-Livermore
S. Berk, DOE/Office of Fusion Energy
L. Berry, Oak Ridge National Laboratory
D. Bhadra, General Atomic Company
M. Billone, Northwestern University
K. Black, McDonnell Douglas Astronautics Company
R. Blanken, DOE/Office of Fusion Energy
P. Bonanos, Princeton Plasma Physics Laboratory
R. Boom, University of Wisconsin
R. Botwin, Grumman Aerospace Corporation
W. Briggs, McDonnell Douglas Astronautics Company
T. Brown, Fusion Engineering Design Center

J. Cannon, Oak Ridge National Laboratory
G. Carlson, Lawrence Livermore National Laboratory
J. Cecchi, Princeton Plasma Physics Laboratory
R. Cherdack, Burns & Roe, Inc.
J. Chi, Westinghouse Electric Corporation
C. Chu, General Atomic Company
J. Citrolo, Princeton Plasma Physics Laboratory
M. Clarke, Combustion Engineering
F. Clinard, Los Alamos National Laboratory
M. Cohen, DOE/Office of Fusion Energy
D. Cohn, Massachusetts Institute of Technology
R. Conn, University of California-Los Angeles
B. Coppi, Massachusetts Institute of Technology
B. Cramer, Fusion Engineering Design Center
J. Crocker, EG&G Idaho, Inc.
J. Davis, McDonnell Douglas Astronautics Company
M. Davis, Sandia Laboratories-Albuquerque
S. Dean, Fusion Power Associates
D. DeFreece, McDonnell Douglas Astronautics Company
J. DeVan, Oak Ridge National Laboratory
C. Dillow, McDonnell Douglas Astronautics Company
D. Dingee, Battelle-Pacific Northwest Laboratory
R. Dowling, DOE/Office of Fusion Energy
D. Driemeyer, McDonnell Douglas Astronautics Company
G. Emmert, University of Wisconsin
J. Fillo, Brookhaven National Laboratory
N. Fisch, Princeton Plasma Physics Laboratory
P. Fischer, Oak Ridge National Laboratory
C. Flanagan, Fusion Engineering Design Center
S. Freije, TRW, Inc.
G. Fuller, Fusion Engineering Design Center
W. Getty, University of Michigan-Ann Arbor
J. Gilleland, General Atomic Company
R. Gold, Westinghouse Electric Corporation
R. Gross, Columbia University
S. Grotz, University of California-Los Angeles
G. Haas, DOE/Office of Fusion Energy
S. Harkness, Bettis Atomic Power Laboratory
P. Haubenreich, Oak Ridge National Laboratory
C. Head, DOE/Office of Fusion Energy
F. Heck, Westinghouse Electric Corporation
H. Helava, Physics International Company
M. Hoffman, Lawrence Livermore National Laboratory
N. Hoffman, ETEC/Rockwell International
G. Hollenberg, Hanford Engineering Development Laboratory
J. Holmes, Hanford Engineering Development Laboratory
P. Hsu, EG&G Idaho, Inc.
J-H. Huang, University of Wisconsin
D. Hwang, Princeton Plasma Physics Laboratory
D. Jassby, Princeton Plasma Physics Laboratory
A. B. Johnson, Battelle-Pacific Northwest Laboratory
C. Karney, Princeton Plasma Physics Laboratory
M. Kazimi, Massachusetts Institute of Technology
R. Krakowski, Los Alamos National Laboratory

O. Krikorian, Oak Ridge National Laboratory
G. Kulcinski, University of Wisconsin
D. Kummer, McDonnell Douglas Astronautics Company
B. Kusse, Cornell University
L. Lidsky, Massachusetts Institute of Technology
Y. Li, University of Wisconsin
P. Lykoudis, Purdue University
J. Maniscalco, TRW, Inc.
L. Masson, EG&G Idaho, Inc.
D. Mattox, Sandia Laboratories-Albuquerque
T. Mau, University of California-Los Angeles
C. Maynard, University of Wisconsin
D. McAlees, Exxon Nuclear Corporation
R. McGrath, Pennsylvania State University
A. Mense, McDonnell Douglas Astronautics Company
B. Merrill, EG&G Idaho, Inc.
D. Metzler, Fusion Engineering Design Center
D. Mikkelsen, Princeton Plasma Physics Laboratory
R. Moir, Lawrence Livermore National Laboratory
D. B. Montgomery, Massachusetts Institute of Technology
G. D. Morgan, McDonnell Douglas Astronautics Company
G. Nardella, DOE/Office of Fusion Energy
A. Opdenaker, DOE/Office of Fusion Energy
R. Parker, Massachusetts Institute of Technology
M. Peng, Fusion Engineering Design Center
J. Perkins, University of Wisconsin
G. Peuron, General Atomic Company
K. Plute, University of Wisconsin
D. Post, Princeton Plasma Physics Laboratory
G. Proulx, Physics International Company
T. Reuther, DOE/Office of Fusion Energy
F. Ribe, University of Washington
J. Rome, Oak Ridge National Laboratory
R. Rose, Westinghouse Electric Corporation
S. Rosenwasser, INESCO, Inc.
P. Rutherford, Princeton Plasma Physics Laboratory
M. Sabado, Ebasco Services, Inc.
P. Sager, Fusion Engineering Design Center
J. Santarius, University of Wisconsin
J. Schmidt, Princeton Plasma Physics Laboratory
K. Schultz, General Atomic Company
F. R. Scott, Electric Power Research Institute
J. L. Scott, Oak Ridge National Laboratory
L. Sevier, General Atomic Company
T. Shannon, Fusion Engineering Design Center
C. Singer, Princeton Plasma Physics Laboratory
P. Spampinato, Fusion Engineering Design Center
W. Stacey, Georgia Institute of Technology
H. S. Staten, DOE/Office of Fusion Energy
D. Steiner, Rensselaer Polytechnic Institute
L. Stewart, Exxon Nuclear Corporation/Princeton Plasma Physics Laboratory
W. Stodiek, Princeton Plasma Physics Laboratory
V. Stubblefield, McDonnell Douglas Astronautics Company
I. Sviatoslavsky, University of Wisconsin

D. Swain, Oak Ridge National Laboratory
D. K. Sze, University of Wisconsin
K. Thomassen, Lawrence Livermore National Laboratory
A. Tobin, Grumman Aerospace Corporation
P. Tortorelli, Oak Ridge National Laboratory
C. Trachsel, McDonnell Douglas Astronautics Company
N. Uckan, Oak Ridge National Laboratory
D. Vieth, DOE/Office of Fusion Energy
D. Vrabel, INESCO, Inc.
K. Wakefield, Princeton Plasma Physics Laboratory
W. Wiffen, Oak Ridge National Laboratory
H. Willenberg, Mathematical Sciences Northwest, Inc.
K. Wilson, Sandia Laboratories-Livermore
G. Woodruff, University of Washington
H. Woodson, University of Texas-Austin
N. Young, Ebasco Services, Inc.
Bibliotheque, Service du Confinement des Plasmas, C.E.A Fusion, Seine, France
Bibliothek, Max-Planck-Institute fur Plasmaphysik, West Germany
I. A. Knobloch, Max-Planck-Institute fur Plasmaphysik, West Germany
C.E.A. Library, Seine, France
C.-S. Li, Chinese Academy of Sciences, Peking, China
Thermonuclear Library, Japan Atomic Energy Research Institute, Japan
Library, Laboratorio Gas Ionizati, Frascatti, Italy
R. Hancox, Culham Laboratory, Abingdon, Oxfordshire, England
Librarian, Culham Laboratory, Abingdon, Oxfordshire, England

☆U. S. GOVERNMENT PRINTING OFFICE: 1982—554-037/3